

**FUNCTIONALIZATION AND EXFOLIATION OF BULK GRAPHITE
INTO FEW-LAYER GRAPHENE SHEETS FOR IMPROVED HEAT
DISSIPATION**

AHMAD AMIRI

**FACULTY OF ENGINEERING
UNIVERSITY OF MALAYA
KUALA LUMPUR**

2017

**FUNCTIONALIZATION AND EXFOLIATION OF BULK
GRAPHITE INTO FEW-LAYER GRAPHENE SHEETS
FOR IMPROVED HEAT DISSIPATION**

AHMAD AMIRI

**THESIS SUBMITTED IN FULFILMENT OF THE
REQUIREMENTS FOR THE DEGREE OF DOCTOR OF
PHILOSOPHY**

**FACULTY OF ENGINEERING
UNIVERSITY OF MALAYA
KUALA LUMPUR**

2017

UNIVERSITI MALAYA

ORIGINAL LITERARY WORK DECLARATION

Name of Candidate: AHMAD AMIRI

Registration/Matric No: KHA140006

Name of Degree: **DOCTOR OF PHILOSOPHY**

Title of Project Paper/Research Report/Dissertation/Thesis (“this Work”):

**FUNCTIONALIZATION AND EXFOLIATION OF BULK GRAPHITE
INTO FEW-LAYER GRAPHENE SHEETS FOR IMPROVED HEAT
DISSIPATION**

Field of Study: **HEAT TRANSFER**

I do solemnly and sincerely declare that:

1. I am the sole author/writer of this Work;
2. This Work is original;
3. Any use of any work in which copyright exists was done by way of fair dealing and for permitted purposes and any excerpt or extract from, or reference to or reproduction of any copyright work has been disclosed expressly and sufficiently and the title of the Work and its authorship have been acknowledged in this Work;
4. I do not have any actual knowledge nor do I ought reasonably to know that the making of this work constitutes an infringement of any copyright work;
5. I hereby assign all and every rights in the copyright to this Work to the University of Malaya (“UM”), who henceforth shall be owner of the copyright in this Work and that any reproduction or use in any form or by any means whatsoever is prohibited without the written consent of UM having been first had and obtained;
6. I am fully aware that if in the course of making this Work I have infringed any copyright whether intentionally or otherwise, I may be subject to legal action or any other action as may be determined by UM.

Candidate’s Signature

Date

Subscribed and solemnly declared before,

Witness’s Signature

Date

Name:

Designation:

ABSTRACT

It is evident that the studies on exfoliation of graphite into graphene for preparing stable colloidal samples have been a major subject of interest among researchers both in academia and industry. Thus, the present research had been directed towards understanding the mechanisms of exfoliation and covalent functionalization, and exploring of viable, scalable and efficient techniques to improve the stability of graphene sheets and ultimately paving routes for applying the concept into real engineering applications. Three major topics were pursued within the current research perspective. The first topic emphasizes on the exploration of facile and economical exfoliation methods for the scalable synthesis of few-layered graphene sheets. To this end, in situ liquid phase exfoliation and functionalization was employed. Surprisingly, the morphological and statistical studies showed that more than 90% of the flakes had less than two layers and about 84% of graphene sheets were single-layered in one of the procedures. Also, the BET analysis indicated that the SSA of different graphene sheets prepared in this study was up to 1559 m²/g. The second topic focuses on the benign and facile preparation of water-based highly stable functionalized graphene nanofluids and its role on enhancing the thermo-physical properties. Water-based highly porous single layer graphene (SGr), water-based crumpled few-layer graphene (HCFLG), and water-based functionalized graphene nanoplatelets dispersions were prepared. Further, the maximum sediments of less than 2% and 13 % were obtained for water-based HCFLG and water-based SGr dispersions, respectively, which are quite impressive. Also, the addition of HCFLG and SGr into the basefluids produced noticeable increases in the thermal conductivity, up to 42.5% and 26%, respectively. Insignificant average drops of <1% in Cp were observed after addition of SGr or HCFLG into the water at the weight concentration of 0.001–0.01 wt%. Also, the density of the water-based HCFLG

nanofluids, water-based SGr nanofluids, and water/ethylene glycol-based EG-GNP nanofluids at weight concentration of 0.01% decreases by 1.01 and 0.99%, 0.87 and 0.88%, and 0.01 and 0.1%, when the temperature increases from 20 to 50 °C, respectively. The final topic deals with the field testing of various colloidal dispersions with improved stability within energy transport system. A duct with a backward-facing step experimental set-up working in transition and turbulent modes and subjected to constant heat flux was established. As compared to the base fluid, the maximum enhancement in average heat transfer coefficient for transitional and turbulent flow regimes was 271% and 177% in the presence of water-based SGr nanofluid at 0.01 wt%, respectively. The amount of enhancement was 233.5% and 199% for water-based HCFLG nanofluids, respectively. Also, the average thermal performance of car radiator in the presence of water/EG-based ethylene glycol-treated GNP nanofluids increased by 99.9%, 102.2% and 115.3% for inlet temperature of 35, 45 and 55 °C, respectively. Other characteristics of the new coolants such as weak increase in the pressure drop and required pumping power (less than 2%), low friction factor, lack of corrosive agent, and appropriate performance index ($PI > 1$) are all highly favorable for introducing new fluids for wide industrial applications.

ABSTRAK

Adalah jelas bahawa kajian mengenai pengelupasan grafit kepada graphene untuk menyediakan sampel koloid yang stabil telah menjadi subjek utama yang menarik minat di kalangan penyelidik dalam bidang akademik dan industri. Oleh itu, kajian semasa telah diarahkan ke arah memahami mekanisme pengelupasan dan pemungsaan kovalen, serta meneroka teknik yang berdaya maju, berskala dan berkesan untuk menambah baik kestabilan lapisan graphene dan seterusnya membuka laluan bagi mengaplikasikan konsep ke dalam aplikasi kejuruteraan sebenar. Tiga topik utama telah diteruskan dalam perspektif penyelidikan semasa. Topik pertama menekankan penerokaan kaedah pengelupasan yang mudah dan penggelupasan yang ekonomi untuk sintesis berskala beberapa lapisan graphene. Bagi mencapai objektif ini, pengelupasan dan pemungsaan fasa cecair in situ telah dilaksanakan. Mengejutkan, morfologi dan kajian statistik menunjukkan lebih dari 90% serpih mempunyai kurang dari dua lapisan dan kira-kira 84% lapisan graphene adalah lapisan-tunggal di dalam salah satu prosedur. Juga, analisis BET memberi indikasi bahawa SSA bagi berlainan lapisan graphene yang disediakan dalam kajian ini adalah sehingga $1559 \text{ m}^2/\text{g}$. Topik kedua fokus kepada penyediaan yang mudah dan menggalakkan bagi cecair-nano graphene yang diubahsuai fungsi berasaskan air yang sangat stabil dan peranannya ke atas mempertingkatkan ciri-ciri termofizikal. Penyebaran bagi lapisan-tunggal graphene yang sangat berliang berasaskan air (SGr), renyukan beberapa lapisan graphene berasaskan air (HCFLG) dan graphene nanoplatelet yang diubah suai fungsi berasaskan air telah disediakan. Selanjutnya, mendapan maksima kurang dari 2% dan 13% telah diperolehi bagi penyebaran renyukan beberapa lapisan graphene berasaskan air (HCFLG) dan lapisan-tunggal graphene yang sangat berliang berasaskan air (SGr), masing-masing, adalah agak menarik perhatian. Juga, dengan penambahan HCFLG dan SGr ke dalam cecair asas menghasilkan peningkatan yang ketara dalam konduktiviti haba, sehingga 42.5% dan 26% masing-masing. Purata jatuh

yang tidak ketara <1% dalam Cp telah diperhatikan selepas penambahan SGr atau HCFLG ke dalam air pada berat kepekatan sebanyak 0.001-0.01 wt%. Juga, ketumpatan cecair-nano HCFLG berasaskan air, cecair-nano SGr berasaskan air dan EG-GNP berasaskan air/etilena glikol pada berat kepekatan 0.01% masing-masing menurun sebanyak 1.01 dan 0.99%, 0.87 dan 0.88%, dan 0.01 dan 0.1%, apabila suhu meningkat dari 20 sehingga 50 °C. Topik akhir berurusan dengan bidang ujikaji pelbagai penyebaran koloidal dengan kestabilan yang telah bertambah baik dalam sistem pengangkutan haba. Set eksperimen dengan langkah saluran menghadap-kebelakang dalam mod peralihan dan gelora dan tertakluk kepada fluks haba yang berterusan telah didirikan. Berbanding dengan cecair asas, peningkatan maksima dalam purata pekali pemindahan haba bagi peralihan dan rejim aliran gelora masing-masing adalah 271% dan 177% dengan kehadiran cecair-nano SGr berasaskan air pada 0.01 wt%. Jumlah peningkatan masing-masing adalah 233.5% dan 199% bagi cecair-nano HCFLG berasaskan air. Juga, prestasi purata haba bagi radiator kereta dengan kehadiran cecair-nano etilena glikol-GNP berasaskan air/EG yang dirawat masing-masing meningkat sebanyak 99.9%, 102.2% dan 115.3% bagi suhu inlet untuk 35, 45 dan 55 °C. Ciri-ciri penyejuk yang lain seperti kelemahan meningkat dalam kejatuhan tekanan dan memerlukan kuasa mengepam (kurang dari 2%), faktor geseran yang rendah, kekurangan agen menghakis dan prestasi indeks yang sesuai ($PI > 1$) semuanya sangat diingini bagi memperkenalkan cecair baru untuk aplikasi industri meluas.

ACKNOWLEDGMENTS

“Dedication to my beloved wife, mother and father”

First and foremost, In essence, I wish to pay my uttermost tribute to Prof. Kazi Md Salim Newaz and Dr. Chew Bee Teng for their persistent guidance and supervision. The research has been made possible due to the financial aid from UMRG Grant RP012B-13AET, ministry of Higher Education High Impact Research (UM.C/625/1/HIR/MOHE/ENG/45) grants and Bright Sparks Unit which I highly indebted. I would also like to thank Dr. Mehdi Shanbedi, Prof. Zeinali Heris, Prof. Eshghi, Prof. Goodarz Ahmadi, Dr. M.N.M. Zubir and Prof. Rashidi for their helps, supports in pursuing different parts of the thesis. I would also wish to endow my deepest gratitude to my beloved wife for her enduring patience and persistence in supporting me during my emotional journey towards climbing higher academic strata. In addition, I would like to express my sincere thanks to my close associates: Dr. Houman Yarmand, Mr. Wail Sami Sarsam, and Mr. Teng Kah Hou for the series of thoughtful discussions and brainstorming sessions. My heartiest thanks are extended to my colleagues and friends who I benefited from in terms of valuable technical and academic assistances through-out the demanding research period. Finally, I wish to thank Mr. Bakri and his staffs from Garuda Mekar Sdn Bhd for their professional support in making my experimental test rig a reality. I would treasure this memorable journey as a milestone to spearhead my challenging academic carrier.

TABLE OF CONTENTS

ABSTRACT	i
ABSTRAK	iii
ACKNOWLEDGMENTS	v
LIST OF FIGURES	xii
LIST OF TABLES	xxiii
NOMENCLATURE	xxiii
LIST OF APPENDICES	xxvii
CHAPTER 1 : INTRODUCTION	1
1.1 Background	1
1.1.1 Water-based carbon nanostructures dispersions	1
1.1.2 Mass-production of graphene	3
1.2 Objectives of present research	7
1.3 Motivation of Research	8
1.4 Thesis Overview	8
CHAPTER 2 : LITERATURE REVIEW	10
2.1 Introduction	10
2.2 Direct Ultrasonic Exfoliation	13
2.2.1 Exfoliation in Organic Solvents	13
2.2.2 Exfoliation with Low Boiling Point Solvents	17
2.3 Stabilizer-Based Exfoliation	18
2.3.1 Ionic Surfactants	19
2.3.2 Nonionic Surfactants	21
2.3.3 Polymers	23
2.3.4 Pyrene Derivatives	24
2.3.5 Aromatic Stabilizers	28
2.4 Exfoliation with Ionic Solvents	28

2.5	Functionalization-Assisted Exfoliation.....	29
2.6	Thermal Exfoliation Techniques.....	34
2.6.1	Thermal Exfoliation of Graphite Oxide.....	35
2.6.2	Thermal Exfoliation of Bulk Graphite.....	39
2.7	Shear Exfoliation.....	43
2.8	Electrochemical Exfoliation.....	45
2.9	Exfoliation Summary and Conclusion.....	50
2.10	Functionalization by Covalent Bonding.....	51
2.10.1	Covalent Attachment of Organic Functionalities.....	51
2.10.1.1	Functionalization by Free Radicals.....	52
2.10.1.2	Functionalization by Dienophiles.....	56
2.11	Covalent Attachment of Functionalities to Graphene Oxides.....	62
2.12	Noncovalent Functionalization of Graphene sheets.....	63
2.13	In Situ Exfoliation and Functionalization for Applications.....	73
2.13.1	Nanofluid as a New Class of Material to Enhance Heat Transfer Performance.....	74
2.13.2	Using Graphene Based Nanofluids as Promising Candidate for Improving Convective Heat Transfer.....	76
2.14	The challenge of graphene stabilization in solvents.....	85
CHAPTER 3 : METHODOLOGY.....		89
3.1	Characterization Methods and Instruments.....	89
3.1.1	Preparation of samples for characterization instruments.....	89
3.1.1.1	Field Emission Scanning Electron Microscopy.....	89
3.1.1.2	Transmission Electron Microscopy.....	89
3.1.1.3	Atomic Force Microscopy.....	90
3.1.2	Functionality and Elemental Analysis.....	90
3.1.2.1	Fourier Transform Infrared Spectroscopy (FTIR).....	90
3.1.2.2	X-ray Photoelectron Spectroscopy.....	90
3.1.2.3	Energy Dispersive X-Ray Spectroscopy.....	91

3.1.2.4	Raman Spectroscopy.....	91
3.1.2.5	Thermogravimetric Analysis	91
3.1.2.6	Selected Area (Electron) Diffraction	92
3.1.3	Specific Surface Area.....	92
3.1.4	Thermo-physical Analysis	93
3.1.4.1	Thermal Conductivity.....	93
3.1.4.2	Differential Scanning Calorimetry.....	96
3.1.4.3	Rheometer	97
3.1.4.4	Densitometer	97
3.1.5	Stability Analysis	98
3.1.5.1	UV–Vis Spectroscopy.....	98
3.1.5.2	Zeta-Potential and Particle Size Distribution.....	99
3.1.6	Experimental system	99
3.1.6.1	Duct with a Backward-facing Step	99
3.1.6.2	Design and Construction.....	103
3.1.6.3	Car Radiator.....	113
3.1.6.4	Two Phase Closed Thermosyphon	117
3.1.6.5	Flowchart of study	118
CHAPTER 4 : RESULTS AND DISCUSSION		120
4.1	Introduction.....	120
4.2	Exfoliation, Functionalization and Characterization	121
4.2.1	Preparation of Chemically-Assisted Exfoliated, Highly-Porous, Graphene (CE-GR) and Thermally-Treated Graphene (T-GR).....	121
4.2.1.1	Chemicals.....	121
4.2.1.2	In Situ Functionalization and Exfoliation Procedure.....	121
4.2.1.3	Characterizations, Results and Discussion	125
4.2.1.4	Functionality and Quality of Graphene	125
4.2.1.5	Morphological Study	132
4.2.1.6	Summary of in Situ Functionalization and Exfoliation	140

4.2.2	Preparation of Highly-Crumpled, Few-Layered Graphene (HCG) and Highly-Crumpled Nitrogen-Doped Graphene (HCNDG).....	140
4.2.2.1	Chemicals.....	140
4.2.2.2	Exfoliation and Functionalization.....	141
4.2.2.3	Results and Discussion	142
4.2.2.4	Functionality	142
4.2.2.5	Morphological Study	146
4.2.3	Preparation of Crumpled Nitrogen-Doped Graphene (CNDG).....	154
4.2.3.1	Material and Methods	154
4.2.3.2	Functionalization Analysis	154
4.2.3.3	Morphological Study	157
4.2.4	Synthesis of Ethylene Glycol-Treated Graphene Nanoplatelets.....	158
4.2.4.1	Functionalization Procedure	158
4.2.4.2	Functionalization Analysis	160
4.2.4.3	Morphological Study	162
4.2.5	Direct Coupling of Graphene Nanoplatelets with Poly Ethylene Glycol and 4-Phenylazophenol Molecules	164
4.2.5.1	Microwave-assisted functionalization	164
4.2.5.2	Functionalization Analysis	165
4.2.5.2.1	FTIR	166
4.2.5.2.2	Raman spectroscopy.....	169
4.2.5.2.3	TGA.....	171
4.2.5.3	Morphology studies	174
4.2.6	Preparation of GNP-COOH	175
4.2.6.1	Covalent functionalization of GNP.....	175
4.2.6.2	Morphological and functionalization studies.....	176
4.3	Colloidal stability and Thermo-physical properties.....	177
4.3.1	Water-based highly crumpled few layered graphene nanofluids.....	177
4.3.1.1	Preparation	177

4.3.1.2	Colloidal Stability	178
4.3.1.3	Thermo-physical properties	179
4.3.2	Water-based chemically-assisted exfoliated single-layered graphene (SGr) nanofluids	184
4.3.2.1	Preparation	184
4.3.2.2	Colloidal Stability	185
4.3.2.3	Thermo-physical properties	187
4.3.3	Water/ethylene glycol-based crumpled nitrogen-doped graphene nanosheets nanofluids (CNDG-WEG)	192
4.3.3.1	Preparation	192
4.3.3.2	Colloidal Stability	192
4.3.3.3	Thermo-physical properties	197
4.3.4	Water/ethylene glycol-based EG-treated graphene nanosheets nanofluids	205
4.3.4.1	Preparation	205
4.3.4.2	Thermo-physical properties	206
4.3.5	Water-based carboxylated GNP nanofluids	210
4.3.5.1	Preparation of nanofluids	210
4.3.5.2	Thermo-physical properties	211
4.3.6	Water-based PEG-treated GNP and acetone-based Azo-treated GNP acetone nanofluids	214
4.3.6.1	Preparation of nanofluids	214
4.3.6.2	Colloidal Stability	214
4.4	Experimental Heat Transfer Performance of Different Thermal Equipment	217
4.4.1	Car Radiators	217
4.4.1.1	Introduction	217
4.4.1.2	Data Processing	220
4.4.1.3	Thermal performance studies	222
4.4.1.3.1	GNP-WEG	224
4.4.1.3.2	CNDG-WEG	240

4.4.2	Ducts and channels with abrupt expansion	255
4.4.2.1	Introduction.....	255
4.4.2.2	Data Processing.....	258
4.4.2.3	Heat transfer Over a Backward Facing Step Flow	261
4.4.2.3.1	Water-Based HCFLG Nanofluids	261
4.4.2.3.2	Water-Based SGr Nanofluids.....	276
4.4.3	Two-phase closed thermosyphon.....	288
4.4.3.1	Introduction.....	288
4.4.3.2	Data Processing.....	291
4.4.3.3	Heat Transfer Rate	293
4.5	Numerical Study on the Convective Heat Transfer Over a Backward-Facing Step 303	
4.5.1	Introduction.....	303
4.5.2	Numerical implementation.....	307
4.5.3	Governing equations	307
4.5.4	Physical model and assumptions.....	308
4.5.5	Grid study.....	309
4.5.6	Result and discussion	310
CHAPTER 5 : CONCLUSIONS AND RECOMMENDATIONS		318
5.1	Conclusions.....	318
5.2	Recommendations for Future Work.....	323
REFERENCES.....		324
List of Publications and Awards		357

LIST OF FIGURES

Figure 2.1: a) Graphite concentration measured after centrifugation for a range of solvents plotted versus solvent surface tension, b) Raman spectra of the graphite and few-layered graphene c) and d) TEM images of graphene (Hernandez et al., 2008).	15
Figure 2.2: a) Concentration of graphene dispersion versus sonication time. The inset illustrates solutions including graphene after 6 h and 180 h. b) Mean layer number, length, and width of flakes as a function of sonication time (Khan, O'Neill, et al., 2010).	17
Figure 2.3: (A) Topographic view of the graphene layers, (B) AFM image of a single flake. (C) Height profile of the image 2.3B. Statistical analysis of the AFM images of 60 flakes: (D) thickness, (E) length and (F) width of the flakes (Vadukumpully et al., 2009).	21
Figure 2.4: Concentration of graphene dispersions obtained by various types of surfactants (Guardia et al., 2011).	23
Figure 2.5: Molecular structures of pyrene derivatives with their names and corresponding acronyms for stabilizing graphene in the liquid media. (Niu et al., 2016)	25
Figure 2.6: (a) A typical AFM image of graphene flakes dispersed in TPA/D2O solution. (b) The thickness distribution of all the graphene flakes observed in panel (a). (c) AFM image of a mechanically exfoliated monolayer graphene (X. Dong et al., 2009)..	26
Figure 2.7: Scheme for the production of water-based graphene oxide suspension from graphite (a) a photo of bulk graphite powder, (b) a SEM image of the layer structure of graphite oxide, (c) a water-based graphene oxide suspension, (d) a AFM image of graphene oxide placed on a mica substrate, and (e) chemical structure of graphene oxide with different functional groups (S. Park & Ruoff, 2015).....	31
Figure 2.8: The procedure of preparing homogeneous colloidal suspensions of RGO (S. Park & Ruoff, 2015).	32
Figure 2.9: (a) Histogram of number of layers per graphene flakes, (b) SEM image of graphene flake, (c & d) AFM of graphene on mica and (e and f) the height profiles along the black imaged lines above in panels c and d, respectively (Zhengzong Sun et al. (2010)).	34
Figure 2.10: Thermally exfoliated graphene. (a) Tapping-mode AFM topography image of thermal exfoliation of GO. (b) A wrinkled graphene sheet with rough surface structure. (c) Contact-mode AFM image of a flake. (d) The cross-section through the line in the sheet shown in panel (c) (M. Cai et al., 2012).	36

Figure 2.11: High temperature exfoliation of graphite oxide under atmospheric pressure (top) and low-temperature exfoliation of graphite oxide (as low as 200 °C) under high vacuum (bottom) (Lv et al., 2009).....	39
Figure 2.12: (a) Graphite exfoliation after re-intercalation with sulphuric acid molecules and insertion of tetrabutylammonium hydroxide. Graphene sheets' structure after thermal exfoliation of bulk graphite (b) and graphite oxide (c) (X. Li, G. Zhang, et al., 2008).....	40
Figure 2.13: (a) and (b) SEM images of expanded graphite after inductively coupled thermal plasma treatment. (c) Raman spectra of four graphene sheets obtained with inductively coupled thermal plasma treatment method (S. Y. Choi et al., 2011).....	41
Figure 2.14: (a, b, c) Set-up of high shear mixer with close-up view of rotor and stator. (d), Mass-produced graphene–NMP dispersions via shear exfoliation. (e, f, g, h) TEM images of graphene nanosheets produced by shear exfoliation. (i), Histogram of graphene thickness and Raman spectrum (inset). (k) Diagram of rotor speed, N versus diameter, D (the red line shows a minimum shear rate of 10^4 S^{-1}). (f) TEM image of exfoliated BN flake. (Paton et al., 2014).....	44
Figure 2.15: (a) Electrochemical exfoliation of bulk graphite in the presence of acids. (b) Suggested mechanism for electrochemical Exfoliation (Parvez et al., 2013).....	47
Figure 2.16: N1s and C1s XPS spectra of the functionalized GNR and GNRs (Niyogi et al., 2010).....	53
Figure 2.17: The functionalization procedure of graphene nanosheets by polystyrene (Fang et al., 2009).....	54
Figure 2.18: Radical addition reaction mechanism. (a) Raman spectra of a mono layer graphene after and before functionalization and (b) optical image of a functionalized mono layer graphene with some holes or defects (Haitao Liu et al., 2009).....	54
Figure 2.19: (a) Schematic of Electrophilic addition reaction. (b) FTIR spectra (c) Raman spectra, and (d) energy dispersive X-ray spectroscopy traces of the triethanolamine-treated graphene nanoplatelets (EDS traces are presented for different specific surface areas).....	55
Figure 2.20: The 1,3 dipolar cycloaddition reaction for decorating the surface of graphene with azomethine ylide (left). Ethanol-based Functionalized graphene nanoplatelets dispersion (top, right). Raman spectra of (a) pristine graphene and (b) pyrrolidine functionalized graphene (bottom, right) (Georgakilas et al., 2010).....	57
Figure 2.21: (a, b, c) TEM images and (d, e) AFM images of the functionalized graphene sheets (S. Park & Ruoff, 2009).....	58
Figure 2.22: Edge-functionalization of pristine graphene with perfluorophenylazides (L.-H. Liu et al., 2010).....	59
Figure 2.23: (a) Functionalization of graphene sheets with alkyl nitrenes. (b) Raman spectra of graphene sheet before (1) and after functionalization of graphene sheets with 11-azidoundecanoic acid in 1:1 (2) and 10:1 (3) ratios (Vadukumpully et al., 2011).....	60

Figure 2.24: The photographs of functionalized graphene nanosheets dispersion in solvents after sonication: hydroxyl-functionalized graphene in water (1) and DMF (2), carboxyl-functionalized graphene in water (3) and DMF (4), poly(ethylene glycol)-functionalized graphene in water (5) and DMF (6), long alkyl chain-functionalized graphene in chloroform (7) and toluene (8), polystyrene-functionalized graphene in chloroform (9) and toluene (10), amino-functionalized graphene in water/chloroform (12), graphene oxide in chloroform (13), and reduced graphene oxide in DMF (14) (Hongkun He & Gao, 2010)..... 61

Figure 2.25: (top) The schematic of chemical functionalization of graphene sheets via aryne cycloaddition. (Bottom left) Photographs of graphene sheets and aryne-modified graphene sheets dispersions in DMF: (a) graphene sheets, (b) F- aryne-modified graphene sheets, (c) Me- aryne-modified graphene sheets and (d) H- aryne-modified graphene sheets. (Bottom right) (B) UV-vis absorption spectra of Me-aryne-modified graphene sheets dispersed in ethanol with different concentrations (J. Choi et al., 2009)..... 62

Figure 2.26: (left) AFM images of graphene oxide and (right) pyrenebutyric-treated graphene nanoplatelets on mica (Y. Xu et al., 2008)..... 64

Figure 2.27: DNA coating, metal coating and aqueous dispersion of graphene oxide and Reduced graphene oxide (Jinbin Liu et al., 2010)..... 66

Figure 2.28: TEM images of (left) 5,10,15,20-tetrakis α -2-trismethylammonium phenyl] porphyrin iron (III) pentachloride/Reduced graphene oxide; and (right) photographs of a) Reduced graphene oxide, b) 5,10,15,20-tetrakis [α -2-trismethylammonium phenyl] porphyrin iron (III) pentachloride, and c) 5,10,15,20-tetrakis [α -2-trismethylammonium phenyl] porphyrin iron (III) pentachloride (0.1 mg mL⁻¹) dispensed in water (Tu et al., 2010)..... 67

Figure 2.29: Solubility photographs of congo red-treated graphene nanoplatelets nanocomposites in (a) toluene, (b) benzene, (c) tetrahydrofuran, (d) ethyl acetate, (e) isopropanol, (f) chloroform, (g) acetone, (h) acetonitrile, (i) dimethylformamide, (j) methanol, (k) dimethyl sulfoxide, (l) water, (m) N-Methyl-2-pyrrolidone, (n) ethanol, (o) isoamyl alcohol, (p) m-cresol, (q) pyridine, and (r) 1,4-dioxane (F. Li et al., 2010). 68

Figure 2.30: (a) Photographs of reduced graphene dispersed in water and 16 different organic solvents via 5 h sonication. The photographs were taken 1 month after the preparation of the reduced graphene dispersion. (b) UV-Vis absorption spectra of reduced graphene dispersed in good solvents (E.-Y. Choi et al., 2010)..... 72

Figure 2.31: (a) The main chemical structure of poly ethylene glycol- oligomer phenylene-ethynylene (PEG-OPE). (b) The synthesis procedure of PEG-OPE-treated Reduced graphene oxide in H₂O. (c) Photograph of (A) graphene oxide and (B) Reduced graphene oxide in water and (C) PEG-OPE-treated Reduced graphene oxide and (D) PEG-OPE in methanol (Qi et al., 2010)..... 73

Figure 2.32: Thermal conductivity ratio of graphene-based nanofluids in the presence of different basefluids (Distillated water (DW) and ethylene glycol (EG)) (Kole & Dey, 2013)..... 83

Figure 2.33: Thermal conductivity of water-based nanofluids in the presence of different additives e.g. metals, metal oxide, carbon nanotubes (CNT) and graphene (Gupta et al., 2011).....	84
Figure 2.34: Thermal conductivity of graphene, graphene/SiO ₂ , and graphene/SiO ₂ -SDBS (X, Li. et al.).....	84
Figure 3.1: Schematic setup of KD2 thermal properties analyzer.....	94
Figure 3.2: Photographs of the KS-1 probe without (a–c) and with (d–f) the probe holder.....	95
Figure 3.3: Comparison between distilled water and previous data.....	96
Figure 3.4: Comparison between the measured viscosity with the standard values reported by Arnold (1970) for distilled water at 200 1/s shear rate.....	97
Figure 3.5: (Up) Photograph, schematic and (down) 2D diagram of the duct with a backward-facing step.....	101
Figure 3.6: Schematic view of the test section and the positioning of the thermocouples on the outer surface of the cylindrical tube.....	102
Figure 3.7: Photograph of the Reservoir Tank.....	104
Figure 3.8: Photograph of the Magnetic gear pump.....	104
Figure 3.9: Photograph of the Hoffman Muller inverter.....	105
Figure 3.10: Photograph of the Electromagnetic flow meter.....	106
Figure 3.11: Photograph of the Differential Pressure Transducers.....	106
Figure 3.12: Photograph of the refrigerated bath circulators.....	107
Figure 3.13: Photograph of the N8731A DC-power supplies.....	108
Figure 3.14: Photograph of the Thermocouple calibrator.....	109
Figure 3.15: Thermocouple testing.....	110
Figure 3.16: Photograph of the Data acquisition instruments.....	110
Figure 3.17: Photograph of the controlling unit that attached with SCADA system.....	111
Figure 3.18: Thermocouple installation.....	112
Figure 3.19: Photograph of the heat transfer test rig.....	113
Figure 3.20: Photographs of the experimental system.....	115
Figure 3.21: Schematic of the experimental system.....	116

Figure 3.22: (left and middle) Schematic and (right) photograph of the experimental apparatus.	118
Figure 3.23: Flowchart of phases of this study.	119
Figure 4.1: The experimental procedure for functionalization as well as exfoliation of graphite and synthesizing of CE-GR and T-GR.	124
Figure 4.2: (1) Photographs of functionalized and expanded graphite dispersed in (a) DMF, (b) DMA, (c) g-butyrolactone and (d) EG. (2) The extracted black pure graphene powder (T-GR).	125
Figure 4.3: (a) FTIR spectra of pristine graphite, CE-GR and T-GR, TGA and DTG curves of (b) pristine graphite, (c) CE-GR, (d) T-GR and (e) Raman spectra of pristine graphite, CE-GR and T-GR.	127
Figure 4.4: TGA and DTG curves of pure PEG.	127
Figure 4.5: (a) XPS survey spectra of CE-GR and T-GR. High-resolution C 1 s spectra of (b) pristine graphite, (c) CE-GR and (d) T-GR.	131
Figure 4.6: FESEM images of the CE-GR (3a-h) and T-GR (3i-l).	133
Figure 4.7: a-h , High-resolution TEM images of CE-GR (a-c) and T-GR (d-g) graphene. h, i , Electron diffraction patterns taken from the positions of the red (h) and white spots (i), respectively, of the sheet shown in d, with the peaks labelled by Miller–Bravais indices. The graphene is clearly one layer thick in (h) and two layers thick in (i). j, k , Diffracted intensity taken along the 1–210 to –2110 axis for the patterns shown in h and i , respectively. l , Histogram of the ratios of the intensity of the {1100} and {2110} diffraction peaks for all the diffraction patterns collected.	134
Figure 4.8: TEM images of the CE-GR.	135
Figure 4.9: AFM ichnography and cross-section contour of (a, c, d and e) CE-GR and (b, f, g and h) T-GR.	138
Figure 4.10: AFM ichnography and cross-section contour of (a ₁ &a ₂) CE-GR and (b) T-GR.	138
Figure 4.11: N ₂ -adsorption/desorption of the CE-GR and T-GR.	139
Figure 4.12: The experimental procedure for exfoliation of graphite and synthesizing HCG and HCNDG.	142
Figure 4.13: (a) FTIR and (b) Raman spectra of the pristine graphite, HCG and HCNDG.	144
Figure 4.14: (a) XPS survey spectra of pristine graphite, HCG and HCNDG, High-resolution C 1s spectra of (b) HCG and (c) HCNDG, N1s spectra of (d) HCG and (e) HCNDG.	146
Figure 4.15: SEM images of (a-d) HCG and (e-h) HCNDG.	147

Figure 4.16: TEM images of (a and b) HCG, (c-e) HCNDG and selected area electron diffraction (SAED) patterns of (f) panel a and (g) panel c.	148
Figure 4.17: (a-c) FESEM images and (d-g) TEM images of HCG; (h and i) selected area electron diffraction (SAED) patterns of white point in panel (f) and red point in panel (g).	149
Figure 4.18: AFM ichnography and cross-section contour of (a) HCNDG and (b and c) HCG.	151
Figure 4.19: N ₂ -adsorption/desorption of (a) the pristine graphite, (b) HCG and (c) HCNDG.	153
Figure 4.20: (a) Raman spectrum (b) XPS spectrum of and (c) high-resolution N 1s Spectra of CNDG.	156
Figure 4.21: TEM image of (a) forming C ₃ N ₄ polymer layers on the surface of the GO (b) CNDG.	157
Figure 4.22: N ₂ sorption isotherms, (insert figure) pore size distribution of the CNDG nanosheets.	158
Figure 4.23: The experimental procedure for chemical-assisted functionalization of GNP with EG.	159
Figure 4.24: (A) FTIR spectra, (B) Raman spectra, (C) thermogravimetric analysis of the pristine and EG-treated GNP and (D) photographs of EG-treated GNP dispersed in water-EG after 1 month.	162
Figure 4.25: TEM images of the (A & A1) pristine and EG-treated GNP (B, B1, B2 & B3).	163
Figure 4.26: The experimental procedure for chemical-assisted functionalization of GNP with PEG and Azo.	164
Figure 4.27: FTIR spectra of the pristine GNP as well as PEG- and Azo-treated GNP in the presence of ZnCl ₂	166
Figure 4.28: FTIR spectra of (a) PEG-treated GNP and (b) Azo-treated GNP without using catalysts.	168
Figure 4.29: Raman spectra of the (a) Azo-treated GNP and (b) PEG-treated GNP in comparison with pristine sample in the presence of different Lewis acids.	170
Figure 4.30: Thermogravimetric analysis of the (a) Azo-treated GNP and (b) PEG-treated GNP in comparison with pristine sample in the presence of different Lewis acids.	172
Figure 4.31: TEM images of (a–c) pristine sample, (d) PEG-treated GNP and (e) Azo-treated GNP.	175
Figure 4.32: FTIR spectra of pristine and acid treated GNP.	176
Figure 4.33: TEM images of (A) pristine, (B and C) acid-treated GNP.	177

Figure 4.34: The colloidal stability of HCFLG in distilled water as a function of time and weight concentration.	179
Figure 4.35: (a) Thermal conductivity and (b) specific heat capacity plots of water-based HCFLG nanofluids at different weight concentrations as well as distilled water.	181
Figure 4.36: Plots of the measured values of viscosity versus shear rate for water-based HCFLG nanofluids at different temperatures and weight concentrations. ...	183
Figure 4.37: Photographs of functionalized and expanded graphite dispersed in (a) DMF, (b) DMA, (c) g-butyrolactone and (d) EG.	185
Figure 4.38: (a) UV–Vis spectra of water-based SGr nanofluids at different concentrations and (b) the colloidal stability of SGr in distilled water as a function of time and weight concentration.	186
Figure 4.39: (a) Thermal conductivity and (b) specific heat capacity plots of water-based SGr nanofluids at different weight concentrations as well as distilled water.	189
Figure 4.40: Plots of the measured values of viscosity versus shear rate for water-based SGr nanofluids at different temperatures and weight concentrations.	191
Figure 4.41: (a) UV–Vis spectrum of CNDG-WEG at different concentrations and (b) the colloidal stability of CNDG in water-EG mixture as a function of time and weight concentration.	194
Figure 4.42: The colloidal stability of the HCND-WEG for weight concentration of 0.01 wt.% obtained by performing UV measurements for 20 days on suspensions mechanically stirred with speed range ~ 1000 rpm every day.	195
Figure 4.43: Zeta-potential and electrical conductivity of CNDG-WEG at 25 °C.	196
Figure 4.44: Zeta-potential of CNDG-WEG at weight concentrations of (a) 0.001, (b) 0.005 and (c) 0.01 wt.%.	197
Figure 4.45: Thermal conductivity plot of CNDG-WEG at different weight concentrations and pure water–EG mixture.	199
Figure 4.46: The effects of inlet temperature and weight concentration of CNDG-WEG on the specific heat capacities of coolant.	204
Figure 4.47: The relative Mo numbers of CNDG-WEG for turbulent flow conditions.	205
Figure 4.48: Photographs of EG-treated GNP dispersed in water–EG (after 1 month).	206
Figure 4.49: Thermal conductivity plot of GNP-WEG and pure water-EG mixture.	209

Figure 4.50: The effects of temperature and weight concentrations of EG-treated GNP on the specific heat capacity of GNP-WEG coolant.....	210
Figure 4.51: Thermal conductivity of GNP-based water nanofluids at different temperatures and weight concentrations.	211
Figure 4.52: Viscosity of the GNP-based water nanofluids as a function of temperature and concentration for a shear rate of 300 s^{-1}	213
Figure 4.53: Plot of absorbance versus wavelength for (1) pure PEG and PEG-treated GNP, (2) pure Azo and Azo-treated GNP, (3) photographs of (a) the pristine GNP/water and PEG-treated GNP/water catalyzed by (b) AlCl_3 , (c) FeCl_2 , (d) TiCl_4 , (e) ZnCl_2 , (4) (4) photographs of (f) the pristine GNP/acetone and Azo-treated GNP/acetone catalyzed by (g) AlCl_3 , (h) FeCl_2 , (i) TiCl_4 and (j) ZnCl_2	215
Figure 4.54: Plot of colloidal stability of PEG-treated GNP in Di-water and Azo-treated GNP in acetone in the presence of different catalysts.....	217
Figure 4.55: A comparison of the data obtained from the Gnielinsky and Dittus-Boelter correlations and the experimental data for the Water-EG mixture at the inlet temperature of $45 \text{ }^\circ\text{C}$	224
Figure 4.56: The average outlet temperature (T_{out}) as a function of flow rate for the car radiator in the presence of GNP-WEG as well as pure basefluid at inlet temperatures of (a) 35 , (b) 45 and (c) $55 \text{ }^\circ\text{C}$	226
Figure 4.57: The effects of Reynolds number and concentration of EG-treated GNP on the convective heat transfer coefficient at the inlet temperatures of (a) $35 \text{ }^\circ\text{C}$, (b) $45 \text{ }^\circ\text{C}$ and (c) $55 \text{ }^\circ\text{C}$	228
Figure 4.58: The average Nusselt numbers of GNP-WEG at different concentrations and volume flow rates for (a) $35 \text{ }^\circ\text{C}$, (b) $45 \text{ }^\circ\text{C}$ and (c) $55 \text{ }^\circ\text{C}$	230
Figure 4.59: Pressure drop of the car radiator for different flow rates and weight concentrations of GNP-WEG as well as deionized water at T_{in} of $55 \text{ }^\circ\text{C}$	231
Figure 4.60: Effect of Inlet temperature of working fluid on the pressure drop at concentration of $0.1 \text{ wt}\%$	232
Figure 4.61: Effect of volume flow rate and concentration of EG-treated GNP on the friction factor at inlet temperature of $55 \text{ }^\circ\text{C}$	233
Figure 4.62: Effect of volume flow rate and inlet temperature of working fluid on the friction factor at concentration of $0.1 \text{ wt}\%$	234
Figure 4.63: The performance index of the synthesized coolant versus flow rate at different concentrations of EG-treated GNP.....	235
Figure 4.64: The performance index of the synthesized coolant versus flow rate at different temperatures and concentration of $0.1 \text{ wt}\%$	236
Figure 4.65: Pumping power of GNP-WEG for different concentrations and temperatures.	237

Figure 4.66: Radiator Efficiency of GNP-WEG at different concentrations and volume flow rates for different inlet temperatures of (a) 35 °C, (b) 45 °C and (c) 55 °C.	239
Figure 4.67: The average outlet temperature (T_{out}) of car radiator in the presence of CNDG-WEG as well as Water-EG mixture at different inlet temperatures.	242
Figure 4.68: The effects of Reynolds numbers and weight concentrations of CNDG on the forced convective heat transfer coefficient at different inlet temperatures. .	245
Figure 4.69: The Nusselt number enhancement of CNDG-WEG at different concentrations, inlet temperatures and volume flow rates.	247
Figure 4.70: Pressure drop of the car radiator at different flow rates and weight concentrations of GNP-WEG and inlet temperatures.	249
Figure 4.71: The pressure drop of the car radiator for different T_f (the average temperature between inlet and outlet) and weight concentrations of CNDG-WEG at volume flow rate of 7 lit/min.	250
Figure 4.72: The performance index of the CNDG-WEG coolants at different flow rates, inlet temperatures and weight concentrations.	252
Figure 4.73: (a) Electrical conductivity and (b) enhancement in electrical conductivity of CNDG-WEG at different weight concentrations and temperatures (c) the ratio of the thermal conductivity (κ) to the electrical conductivity (σ) of CNDG-WEG for different weight percentages	254
Figure 4.74: Measured temperature of the heated wall (T_s), the temperature difference between the wall and the fluid bulk (T_s-T_b), local convective heat transfer coefficient (h) and Nusselt number (Nu) versus X/D for distilled water at different Reynolds numbers (Re).	263
Figure 4.75: Measured temperature of the heated wall (T_s), the temperature difference between the wall and the fluid bulk (T_s-T_b), local convective heat transfer coefficient (h) and Nusselt number (Nu) versus X/D for water-based HCFLG nanofluid at 0.001 wt%.	265
Figure 4.76: Measured temperature of the heated wall (T_s), the temperature difference between the wall and the fluid bulk (T_s-T_b), local convective heat transfer coefficient (h) and Nusselt number (Nu) versus X/D for water-based HCFLG nanofluid at 0.005 wt%.	266
Figure 4.77: Measured temperature of the heated wall (T_s), the temperature difference between the wall and the fluid bulk (T_s-T_b), local convective heat transfer coefficient (h) and Nusselt number (Nu) versus X/D for water-based HCFLG nanofluids at 0.01wt%.	267
Figure 4.78: Average heat transfer coefficient of distilled water and water-based HCFLG nanofluids over a backward-facing step.	268
Figure 4.79: The effects of Reynolds numbers and weight concentrations of HCFLG on the Nusselt numbers at different axial ratios.	270

Figure 4.80: The effects of Reynolds numbers and weight concentrations of HCFLG on the position of maximum Nusselt numbers.....	271
Figure 4.81: (a) The measured values of pressure drop in the set-up at different Re numbers for distilled water and water-based HCFLG nanofluids with different weight concentrations. (b) Experimental friction factor for distilled water and water-based HCFLG nanofluids with different weight concentrations at different Re numbers.....	273
Figure 4.82: (a) Performance evaluation criterion (PEC) and performance index (PI) of water-based HCFLG nanofluid; (b) pumping power ratio for the backward-facing step in the presence of distilled water and water-based SGr nanofluids with different weight concentrations.....	275
Figure 4.83: The temperature of the heated wall (TS) and the temperature difference between the wall and the fluid bulk (TS-Tb) for water and water-based SGr nanofluids.....	277
Figure 4.84: Experimental Nusselt number of distilled water and water-based SGr nanofluids at weight concentrations of 0.001, 0.005 and 0.01% for different Re numbers.....	279
Figure 4.85: Average heat transfer coefficient of distilled water and water-based SGr nanofluids over a backward-facing step.....	280
Figure 4.86: The effects of Reynolds number and weight concentration of SGr on the local heat transfer coefficient at different axial ratios.....	282
Figure 4.87: The effects of Reynolds number and weight concentration of SGr on the position of maximum local heat transfer coefficient.....	283
Figure 4.88: (a) The measured value of pressure drop of the set-up at different Re numbers for distilled water and water-based SGr nanofluids with different weight concentrations. (b) Experimental friction factor for distilled water and water-based SGr nanofluids with different weight concentrations at different Re numbers.	285
Figure 4.89: (a) Performance evaluation criterion (PEC) and performance index (PI) and (b) pumping power for the backward-facing step in the presence of distilled water and water-based SGr nanofluids with different weight concentrations.	287
Figure 4.90: Efficiency of thermosyphon in the presence of GNP-based water nanofluids at various concentrations.....	294
Figure 4.91: Effect of input power and concentration of GNP-based water nanofluids on the average temperature difference (ΔT) between the evaporator and the condenser.....	296
Figure 4.92: Effect of input power and concentration of GNP-based water nanofluids on the average temperature of the evaporator section.....	297
Figure 4.93: Effect of input power and concentration of GNP-based water nanofluids on the thermal resistance of thermosyphon.....	298

Figure 4.94: Effect of input power and concentration of GNP-based water nanofluids on the overall heat transfer coefficient of thermosyphon.....	299
Figure 4.95: Effect of input power and concentration of GNP-based water nanofluids on the entropy of the thermosyphon.	300
Figure 4.96: Effect of input power and concentration of GNP-based water nanofluids on the vacuum pressure drop of thermosyphon.	302
Figure 4.97: 2D geometrical configuration of backward-facing step.	308
Figure 4.98: Local Nusselt numbers for $Re = 5000$ and pure water at three different grid distributions.	309
Figure 4.99: Mesh configuration of backward facing step.	310
Figure 4.100: Streamline of velocity with weight fraction of 0.2% (a) $Re = 5000$, (b) $Re = 10,000$, (c) $Re = 15,000$, isothermal streamline with weight fraction of 0.2% (d) $Re = 5000$, (e) $Re = 10,000$, (f) $Re = 15,000$	312
Figure 4.101: Convective heat transfer coefficient as a function of different weight concentrations at different Reynolds numbers of (a) 5000, (b) 10,000, and (c) 15,000 and the local Nusselt number as a function of different concentrations at (d) $Re = 5000$, (e) $Re = 10,000$, and (f) $Re = 15,000$	314
Figure 4.102: (a) Prediction of skin friction factor, (b) the ratio of skin friction factors of EGNP to basefluid, and (c) the performance index of the synthesized coolant versus weight concentrations of EGNP for various Reynolds numbers.	317

LIST OF TABLES

Table 2.1: Summary of experiments on convective heat transfer of graphene-based nanofluids.....	79
Table 2.2: Summary of experimental results on thermal conductivity of graphene-based nanofluids.....	81
Table 3.1: Zeta potential and associated suspension stability (Vandsberger, 2009)	99
Table 3.2: Specifications and errors of the measuring instruments and sensors used in the present experiment.	103
Table 3.3: Technical specifications for V8 series inverters.	105
Table 3.4: Specifications of the refrigerated bath.	107
Table 3.5: Dimensions of the test section	111
Table 3.6: Test condition during the experiments.....	116
Table 4.1: Peak positions of various groups in C1s Spectra of pristine graphite, CE-GR and thermally-treated graphene.	132
Table 4.2: Pore structure of the CE-GR and T-GR.....	139
Table 4.3: The content distributions of N species in HCG and HCNDG.	146
Table 4.4: Pore structure of the HCG and HCNDG.....	153
Table 4.5: Identification of catalysts for formation of the electrophilic addition reactions.	171
Table 4.6: Comparative study of the functionalization of compounds in the presence of different catalysts.....	174
Table 4.7: Densities of the Di-water and water-based HCFLG nanofluids for different concentrations.	184
Table 4.8: Densities of the water and water-based SGr nanofluids for different concentrations.	192
Table 4.9: Dynamic viscosity of the CNDG-WEG as a function of temperature and weight concentration at shear rate of 140 s^{-1}	198
Table 4.10: Dynamic viscosity of the GNP-WEG as a function of temperature and weight concentration at shear rate of 140 s^{-1}	207
Table 4.11: Densities of the water-EG mixture and GNP-WEG at different concentrations.	207

Table 4.12: The average increase in the viscosity of nanofluids compared with deionized water.	214
Table 4.13: Measurement uncertainties.	261

University of Malaya

NOMENCLATURE

A	absorbency
AFM	Atomic force microscopy
B	Optical path (cm)
BET	Brunauer–Emmett–Teller
c	Molar concentration (mol/dm ³)
C_p	Specific heat capacity, J/g K
CTAB	Cetyltrimethylammonium bromide
CHF	Critical heat flux
CE-Gr	Chemically-exfoliated Graphene
CNT	Carbon nanotube
CNDG	Crumpled nitrogen doped graphene
CVD	Chemical vapor deposition method
D	Diameter, m
DGU	Density gradient ultracentrifugation
DSC	Differential scanning calorimetry
DW	Distilled water
f	Friction factor
FT-IR	Fourier transform infrared spectroscopy
GA	Gum Arabic
GO	Graphene oxide
GNP	Graphene nanoplatelets
h	Convective heat transfer coefficient
HC	Hamilton-Crosser
I	Electrical current, A

k	Thermal conductivity, W/m.K
L	Tube length, m
MWCNT	Multi-walled carbon nanotube
HCG	Highly crumpled graphene
HCFLG	Highly crumpled few-layer graphene
HCNDG	Highly crumpled nitrogen-doped graphene
NDG	Nitrogen-doped graphene
Nu	Nusselt number
P	Heater power, W
Pe	Péclet number
PEG	Poly Ethylene Glycol
PEC	Performance evaluation criterion
PI	Performance Index
Pr	Prandtl number
PVD	Physical vapor deposition method
q''	Heat flux, W/m ²
Re	Reynolds number
rGO	Reduced graphene oxide
SAED	Selected area electron diffraction
SDBS	Sodium dodecyl benzene sulfonate
SDS	Sodium dodecyl sulfonate
SEM	Scanning electron microscopy
SSA	Specific surface area
SWCNT	Single-wall carbon nanotube
T	Temperature, K
TEM	Transmission electron microscopy

TGA	Thermogravimetric analysis
T-Gr	Thermally-exfoliated graphene
THW	Transient hot-wire
U	Mean velocity, m/s
V	Volts, V
v	Mean velocity, m/s
w	Water
W	Watt
x	Axial distance
XRD	X-ray diffraction
XPS	X-ray photoelectron spectroscopy
U_{ave}	Average velocity (m/s)
m°	Mass flow rate (Kg/s)
A_c	Surface area of the cross section (m^2)
T_{sx}	The wall temperature of fluid at the axial distance x
T_{bx}	The bulk temperature of fluid at the axial distance x
XPS	X-ray photoelectron spectroscopy
R_h	Ratio of the heat transfer coefficient enhancement of new coolant to the base-fluid
$R_{\Delta p}$	Ratio of pressure drop of new coolant to the base-fluid
PLC	Programmable logic controller
RTD	Resistance temperature detector
Greek	
ΔP	pressure drop, Pa
wt%	weight percentage

ϕ	nanoparticle volumetric fraction
μ	viscosity, Pa.s
ε	Performance Index
ρ	density, kg/m ³
η	thermal performance factor
σ	Electrical conductivity

Subscripts

avg	average
b	bulk
bf	base fluid
i	inner
in	inlet
m	mean
nf	nanofluid
np	nanoparticle
out	outer
out	outlet
s & w	wall

LIST OF APPENDICES

Appendix A: UNCERTAINTY ANALYSIS.....	361
A.1 Introduction.....	361
A.2 Theory.....	361
A.3 Uncertainties.....	362
A.4 Summary.....	367
Appendix B: XRD ANALYSIS.....	368
B.1 Introduction.....	368
APPENDIX C: ANALYSIS AND INSTRUMENTS.....	369
C.1 List of sample preparation and characterization instruments.....	369

University of Malaya

CHAPTER 1: INTRODUCTION

1.1 Background

1.1.1 Water-based carbon nanostructures dispersions

Since colloidal system was first experimentally introduced within thermal engineering community, rapid growths of exploration into the fundamental theory as well as extensive research on its potentials to address persisting heat transfer limitations have shown promising results. In particular, the incorporation of colloidal system is the key to major advancement in various thermal related researches such as energy storage and conversion and thermal transport systems. It is also evident that the trend of research has seen a dramatic transition in terms of the type of material used to generate the colloidal system along with the engineered morphological structures that constitute major impact on the technological progress. This is due to the fact that these two elements govern the change in most physicochemical properties of colloids. Most of the current research efforts have focused on carbon based materials of different dimensions and morphologies owing to its superior thermal properties in comparison to oxide, metal and nitride based materials which were extensively employed in the early period of the researches. The pivotal cornerstone of this shift is associated to the growing evolution on the ability to stabilize carbon based colloids in various polar and non-polar solvents in particular the aqueous system. Nevertheless, the importance of addressing the stabilization issue also befalls on other types of colloids since the key towards incorporating this approach lies on the ability to ideally generate discrete suspension with minimal agglomeration as well as leaning towards surfactant free matrix, which is known as impact provider on the property of the colloidal systems.

The use of covalent and noncovalent functionalization to improve the stability of aggregated prone structure in colloidal system is a relatively new approach within the subject of colloidal stability. The fact that long chain molecules such as surfactant, etc.

are replaced with orderly structured nanoparticles ensures that the physical properties of the mixture remain uncompromised since nanoparticles themselves pose a relatively similar property to the host colloids. It is evident that long chain molecules are capable of improving colloidal stability, the major challenge lies on their low thermal property which is known to induce negative impact on the overall potential of the colloids. Moreover, removal of these substances also requires extended procedures and does not guaranty completely purified end products. In energy transport applications which mostly involves liquid medium, surfactant grafted on colloids will act as insulator which disturbs the phonon transport among colloids. The low degradation temperature of surfactant and other non-covalent molecules such as polymers also restrict their usage to low temperature applications. In addition, owing to the formation of foam problem associated with the use of surfactants and long-chain polymers for non-covalent functionalization of carbon-based nanostructures, covalent functionalization can be a promising alternative for preparing stable dispersion for heat transfer and fluid flow applications to meet the requirements of foam-free working fluids. These shortcomings can be addressed by employing highly covalently-functionalized carbon-based nanostructures with hydrophobic molecules, which can radically react with the carbon-based nanostructures, thus providing the overall coolant with high stability.

Considering the high thermal conductivity of free-defected graphene, they can be a superior additive to prepare highly-conductive heat transfer working fluids. Balandin et al. (2008) have reported an experimental thermal conductivity of 5300 W mK^{-1} for a single layer graphene (higher than all of the carbon allotropes). However, in order to apply few-layered graphene as an additive in various working fluids, three obstacles should be solved.

1. Finding a method for mass production of graphene with high quality and specific surface area in a commercially viable way.

2. Finding suitable functional groups for decorating on graphene sheets to reach highly-stable colloidal system, mostly, in aqueous media. Functional groups should be selected wisely to avoid re-stacking, corrosion and foaming.
3. Finding an efficient, one-pot, industrially-scalable, cost-effective and facile functionalization method for synthesizing highly soluble graphene sheets.

1.1.2 Mass-production of graphene

Over the last decade, the research on efficient, scalable and economical ways to produce high quality graphene has witnessed unprecedented breakthrough (Konstantin S Novoselov et al., 2012). It was known that several routes have been explored to exfoliate graphene which include micromechanical cleavage (KS Novoselov et al., 2005), topological growth on metal and non-metal substrate (Berger et al., 2006; Marchini et al., 2007; Ohta et al., 2008), chemical oxidation (Dikin et al., 2007; D. Li et al., 2008; Yeh et al., 2015) and solution phase processing (Athanasios B Bourlinos, Vasilios Georgakilas, Radek Zboril, Theodore A Steriotis, & Athanasios K Stubos, 2009; Hernandez et al., 2008; Matsumoto et al., 2015b; Paton et al., 2014). It is also evident that the first three approaches suffer from scalability, cost effectiveness and quality issues (Kovtyukhova et al., 2014; Loh et al., 2010; Matsumoto et al., 2015b; Sutter et al., 2008; S. Zhou et al., 2008). As a low-cost and highly scalable method, chemical exfoliation was also suggested for synthesizing mono- or few-layered graphene. This method comprises of graphene oxide (GO) synthesis through chemical oxidation of graphite and subsequently exfoliation via ultrasonic. However, the structural defects of GO cannot be completely removed even with thermal reduction and chemical treatment. Obviously, the presence of structural defects considerably restricts the applications of GO in different equipment (Becerril et al., 2008; Stankovich et al., 2007; Zhu, Murali, Cai, et al., 2010). More recently, a novel liquid-phase exfoliation illustrated significant performance in forming

2D carbon-based nanostructures. Liquid-phase exfoliation refers to a group of approaches that exfoliate bulk graphite into thin graphene (mono- or few-layered graphene) in the liquid media directly. The lack of chemical oxidation is one of the advantages with this method. On this note, special interest has been directed on liquid phase exfoliation which typically employs fluids of specific properties along with external excitation to overcome Van der Waals attraction and π - π bonding interaction between the graphene layers (W. Du et al., 2013; Hernandez et al., 2008; Lotya et al., 2009). This approach was inspired by the previous success in CNT debundling using solvents which interact strongly with nanotubes surfaces (Bergin et al., 2008; Tawfique Hasan et al., 2007). The close resemblance between CNT and graphene with respect to the mode of molecular attraction has become the premise for graphene exfoliation using similar solvents (Hernandez et al., 2008). This method was proven to address the above limitations of graphene production toward achieving mono- and/or few layered crystal exfoliation. Nevertheless, the challenge remains on producing high yield and quality in addition to defect-free pristine graphene (Bracamonte et al., 2014) in order to harness its intrinsic properties (Geim & Novoselov, 2007; K. Novoselov et al., 2005; K. Novoselov et al., 2004; Pisana et al., 2007; Y. Zhang et al., 2005). Therefore, the liquid-phase exfoliation strategy has been obtaining great attention due to its unique properties such as being cost-effective, efficient, extraordinarily versatile and potentially for large-scale production of defect free graphene (Hernandez et al., 2008; Paton et al., 2014).

Although lots of liquid-phase exfoliation approaches for scalable few-layered graphene synthesis have been emerging (Edwards & Coleman, 2013), the second fundamental problem is the difficulties in processing graphene, in particular in our study, the graphene's poor colloidal stability in most common solvents (Ayan-Varela et al., 2014). Nonetheless, many of graphene's applications cannot be fully realized due to weak solubility of graphene in most common solvents. So, graphene sheets are needed with

high solubility in different working fluids. Therefore, in order to improve the interactivity and solubility of graphene, functionalization was reported elsewhere as a general solution (Johnson et al., 2015; Zhengzong Sun et al., 2010). Thus, a method is needed for mass production of functionalized graphene sheets. In situ functionalization and exfoliation of graphite into graphene sheets can be a gateway for solving all the aforementioned problems. Accordingly, various functionalities such as amines, aryl diazonium salt, and halogens have been employed onto graphene surface and edge. Selecting an appropriate functional groups is another criterion for reaching stable dispersion. Among the various functional groups attached to the carbon-based nanostructures, amines are attached in a relatively simple procedure. In fact, the nitrogen atom of the amino group ($-NH_2$) as well as oxygen atom of the hydroxyl can easily be available for covalent bonding to other molecules. Because of this reactivity, the amine- and hydroxyl-functionalized graphenes are frequently used in fabrication of electrodes, composites, and membranes. Between all functional groups including amine molecules and hydroxyl groups, non-corrosive functional groups with hydrophilicity and preferably mono-functional groups are more favorite molecules, since they could realize high stability for graphene sheets and limits the negative effects of oxidative groups.

Also, in order to apply the different functionalities including amino or hydroxyl groups, some conventional methods such as sonication and mixing have been employed. However, these methods are often time-consuming and on a small-scale plan, as well as comprising multiple steps. Recently, the microwave radiation was proposed as an efficient and facile method for functionalization of different carbon-based nanostructures. It has also shown to result in lower structural defects on carbon nanostructures' surface compared with the conventional methods. Thus, it can be a great method for in situ functionalization and exfoliation. Noteworthy, the reaction intensifies under microwave irradiation. When carbon nanostructures are exposed to microwaves, strong absorptions

are obtained, which produces intense heating. Although the utilization of microwaves for the activation of carbon nanostructures has not been fully explored, the strong absorptions can open the door to the radical reactions. Note that the decomposition of the functional groups on functionalized flakes under microwave irradiation can also generate some pressure for overcoming the van der Waals interaction among graphene layers during the microwave procedure.

The enhancement in solubility of graphene sheets after in situ functionalization and exfoliation under microwave irradiation which can result in further enhancement in thermo-physical properties, thus paving ways for its application within thermal transport domain.

Investigation on the effect of incorporating carbon based materials in improving convective heat transfer in different thermal equipment such as heat exchanger, duct with sudden expansion, closed conduit has recently received considerable interest by researchers. Due to the enhancement in thermal conductivity of the base fluid with the addition of carbon nanostructure, the overall heat transfer performance was believed to be increased accordingly. It is worthy to mention that pristine graphene for instance exhibit more than 5000 times of the thermal conductivity of water, much higher than oxide, metal or nitride based materials. Thus, theoretically, a small amount of this highly conductive material is sufficient to cause significant change on the conductivity of the base fluid provided that a well dispersed colloidal mixture can be established. Further, the fact that only a small amount of filler material is required within the colloidal mixture along with the formation of well homogenized system implies that the viscosity will remain close to the base fluid. This condition negligibly compromises the pumping power penalty and provides favorable enhancement of the overall energy transport system. While research community within thermal engineering domain has been focusing on metal- and metal oxide-based colloids on improving heat transfer performance of

different thermal equipment such as ducts and channels with abrupt expansion, closed conduit, car radiator, two-phase closed thermosyphon, etc. It was not until recent years that attention has been increasing on switching into solution containing carbon-based additives as the heat transport medium due to the ability to tackle the stability issue.

Note that large specific surface area and outstanding thermal conductivity at room temperature make the few-layer graphene significantly promising material for heat transfer applications. Developing an efficient and quick method for mass-production of the few layer graphene, however, is critical for its large-scale industrial applications such as for developing high performance nanofluids. It is also well known that thermal conductivity and subsequently heat transfer rate improve as the specific surface area of graphene increases (Sarsam, et al., 2016a). Therefore, in order to manufacture highly-conductive nanofluids for improving heat transfer rate in different thermal equipment, materials with high specific surface areas, such as crumpled graphene or highly porous material, and in particular, few-layered graphene can be more suitable.

1.2 Objectives of present research

The objectives of the present work are:

- To determine facile and economical methods for mass production of few-layered graphene sheets via in situ liquid phase exfoliation and functionalization of graphite
- To investigate the effects of different hydrophilic functional groups and degree of functionalization on solubility of graphene sheets in aqueous media.
- To develop a quick covalent functionalization method for mass production of graphene-based nanofluids.
- To investigate the colloidal stability of covalently-functionalized graphene in aqueous media.
- To investigate the thermo-physical properties of the synthesized nanofluids.

- To investigate the effect of highly dispersed graphene based materials on improving convective heat transfer rate in different thermal equipment such as ducts with a backward-facing step, close conduit, thermosyphon, and car radiator.

1.3 Motivation of Research

The lack of a facile and economical method is one of the biggest problems for the scalable synthesis of few-layered graphene sheets. On the other hand, most of the reported researches resulted in pure graphene, which is extremely hydrophobic and do not have any tendency to solve in polar solvents. In situ exfoliation and functionalization can be a great solution to solve above-mentioned problems. To this end, introducing a strong radical reaction between graphene/graphite sheets with high-branch hydrophilic molecules can be a great solution. Moreover, performing reaction can speed the reaction. To do exfoliation simultaneously, selecting a solvent with surface energy matching the van der Waal attraction of graphite can be a great solution for mass production of functionalized graphene sheets. Covalently-functionalized graphene with hydrophilic molecules can be very good additive for enhancing thermal conductivity of conventional base fluids for improving thermal performance of heat exchangers, car radiators, two-phase closed thermosyphon, etc. Utilization of highly conductive working fluids let engineers to do effective energy optimization in different infrastructure, industry, defense etc.

1.4 Thesis Overview

This thesis consists of five chapters. Chapter 1 is the “Introduction” that provides background about the areas of this study, highlights the current problems that motivated this research, and clarifies the objectives through which the aim of this study can be reached. Chapter 2 is the “Literature Review” which comprehensively surveys the

previous published studies related to the field of study which can be categorized as: different methods for liquid-phase exfoliation, functionalization-assisted exfoliation, shear-based exfoliation, different methods for covalent functionalization of graphene sheets, non-covalent functionalization, graphene-based nanofluids, and enhancement of colloidal stability and its challenges. Chapter 3 is the “Methodology” which concerns about the devices and methods used in this study for the preparation of samples, characterization instruments and how to prepare their samples, measurement of thermophysical properties, evaluation of colloidal stability, and the experimental test setup that is built and used for investigation of the thermal performance of graphene-based nanofluids. Chapter 4 is the “Results and Discussion” which includes three main sections: i) description of new in situ exfoliation and functionalization methods and synthesis of novel graphene along with all the characterization; ii) preparation of nanofluids with the prepared graphene sheets, evaluation of colloidal stability and thermophysical properties and compare them with the recent results, iii) lists, compares and discusses the data obtained from experiments to evaluate overall performance of different thermal equipment e.g., car radiator, two phase closed thermosyphon, and heat exchangers. Finally, chapter 5 is the conclusion and recommendations in which the important outcome of this study are briefly summarized with some recommendations for future work in this research field.

CHAPTER 2: LITERATURE REVIEW

2.1 Introduction

After the discovery of carbon-based nanostructures, two-dimensional (2D) graphene has attracted intensive research attention because of its unique properties. Mono layer graphene with remarkable properties such as high thermal conductivity of the order of $5000 \text{ W m}^{-1}\text{K}^{-1}$, large specific surface area of $2630 \text{ m}^2 \text{ g}^{-1}$, high intrinsic mobility of $2 \times 10^5 \text{ cm}^2 \text{ V}^{-1} \text{ s}^{-1}$, Young's modulus of 1.0 TPa, and high electrical conductivity have high potential for different high tech applications (Geim & Novoselov, 2007; Huang et al., 2011; Konstantin S Novoselov et al., 2012; Zhu, Murali, Cai, et al., 2010). Owing to its unique properties such as low flake resistance and good transmittance, graphene was applied in different electronic devices including the organic light emitting diodes and touch screen displays. Note that the outstanding mechanical and chemical stability of 2D graphene make it unique and exclusive to rigid indium tin oxide (ITO).

In addition, possessing comprehensive absorption ranging from ultraviolet to infrared and ultrafast response, graphene could be used in different photodetectors (J. Li et al., 2014) and various optical modulators (Sensale-Rodriguez et al., 2011). Graphene has also illustrated superior potential for fabricating highly effective storage devices, such as solar cells, supercapacitors, and lithium-ion batteries.

Due to the numerous applications of graphene, there is a need to develop a commercially viable method for mass production of high quality graphene. This is a critical issue if different industries are to use novel 2D graphene material for large scale applications. To date, some methods have been reported for mass production of mono layer graphene, such as chemical vapor deposition (CVD), chemical exfoliation, exfoliation methods by micromechanical cleavage, and liquid-phase ultrasonic exfoliation. Among these methods, the CVD has been used extensively for production of graphene. In order to synthesize mono- and few-layered graphene sheets with the CVD

method, precursors react on transition metal substrates at high temperature. The CVD is able to synthesize mono- or few-layered graphene with superior quality; however, the approach requires stringent manufacturing conditions such as high vacuum and high temperature. Note that the CVD method is also size-limited, which is the major problem of this method. In addition, in CVD the transfer procedure from the surface of metal to target substrates may induce some defects, leading to low-quality graphene and associated deteriorating performance. To increase the performance of the CVD synthesis and the transfer procedures, many studies have been done (Obraztsov, 2009; Yu Wang et al., 2011); however, further discussions of the details of these procedures are outside the scope of this thesis.

The bulk graphite as a layered material possesses strong in-plane chemical bonds and weak out-of-plane interactions, which correspond to the van der Waals forces. Therefore, exfoliation of bulk graphite to thin graphene flakes with thickness of nanometer is possible. To take advantage of this idea, micromechanical cleavage was introduced (Ferrari et al., 2006; Sutter et al., 2008). However, the micromechanical cleavage has shown very low performance and can produce extremely low amount of few-layered graphene. As a low-cost and highly scalable method, chemical exfoliation was suggested for synthesizing mono- or few-layered graphene (Lomeda et al., 2008; Marcano et al., 2010; Zhengzong Sun et al., 2011). This method comprises of synthesizing graphene oxide (GO) through chemical oxidation of graphite and subsequent exfoliation via ultrasonic. However, the structural defects of GO cannot be completely removed even with thermal reduction and chemical treatment. Obviously, the presence of structural defects restricts the applications of graphene oxide in electronic and optical devices (Becerril et al., 2008; Stankovich et al., 2007; Zhu, Murali, Cai, et al., 2010). More recently, a novel liquid-phase exfoliation was introduced that shows significant performance in forming 2D carbon-based nanostructures (Hernandez et al., 2008). Liquid-

phase exfoliation refers to a group of approaches that exfoliate bulk graphite into thin graphene (mono- or few-layered graphene) directly in the liquid media. The lack of chemical oxidation is an advantage of this method.

Liquid-phase exfoliation includes:

- i) Various ultrasonic exfoliation techniques such as liquid phase exfoliation by surfactants, organic solvents, ionic liquids, and salts.
- ii) Electrochemical exfoliation in different liquid media.
- iii) Shear exfoliation method.

The liquid-phase exfoliation strategy has attracted considerable attention due to its unique properties such as being cost-effective, efficient, extraordinarily versatile and having the potential for large-scale production of defect-free graphene (Hernandez et al., 2008; Paton et al., 2014). Although a number of liquid-phase exfoliation approaches for synthesis of scalable few-layered graphene have been emerging (Edwards & Coleman, 2013), there are still difficulties with processing graphene, in particular, due to the weak solubility and the poor colloidal stability of graphene in most common solvents (Ayan-Varela et al., 2014). For example, pristine graphene tends to agglomerate in composites. Therefore, in order to improve the interactivity and solubility of graphene, functionalization was reported as a potential solution in the literature (Johnson et al., 2015; Zhengzong Sun et al., 2010). With appropriate functionalization method, the graphene can remain dispersed over a reasonable period of time.

In view of many great advantages of liquid phase exfoliation and the rapid progress that is being made in the literature, this chapter aims to provide a comprehensive review on the synthesis methods of mono- and few-layered graphene. In addition, the effective functionalization strategies for solving the lack of dispersibility of graphene in different media are also described. Also, for preparing graphene-based nanofluids, the graphene must be dispersed at an appropriate concentration in a suitable base fluid for the

heat transfer applications, and maintained in dispersed state over a reasonable period of time. Also, current functionalization strategies to solve these challenges are the second phase of this chapter (literature review). In the third section of this chapter, the functionalized graphene-based nanofluids, which present the desirable heat transfer properties and good solution dispersing ability, will be investigated.

2.2 Direct Ultrasonic Exfoliation

Direct ultrasonic exfoliation in liquid is referred to different approaches that synthesize graphene via direct ultrasonication of the bulk graphite in liquid media. In this method, two factors can critically influence the yield of exfoliation of the bulk graphite. The first factor is having a strong bath sonication or probe sonication. This is because the bulk graphite is effectively exfoliated upon exposure to the ultrasonic waves. Shear forces or cavitation bubbles created from such waves can generate high amount of energy with the collapse of bubbles in liquids that can change the main structure of bulk graphite from layered structure to single- or few-layered graphene (Mason & Lorimer, 2002). The second important factor is the liquid media used. There is commonly an energy barrier in the interlayers of the graphite, and in the subsequent stabilization of nanosheets via interfacial interactions. Different liquid media (ionic liquids, aqueous solutions of stabilizers, and organic solvent) behave differently in decreasing the potential energy barrier. To properly classify direct ultrasonic exfoliation, this part of the literature review is organized into several sections based on the liquid media used.

2.2.1 Exfoliation in Organic Solvents

This approach includes the sonication of the bulk graphite in an organic solvent and the subsequent purification procedure (Niu et al., 2016). In this method, the interfacial tension between the bulk graphite and organic solvent is the most important parameter in their interactions. As mentioned above, an appropriate organic solvent can decrease the potential energy between adjacent layers in the bulk graphite to overcome the van der

Waals attraction between layers (Blake et al., 2008; Hernandez et al., 2008; Israelachvili, 2011). In addition, the solvent–nanosheets interactions could balance the inter-sheet attractive forces to stabilize the dispersion of graphene sheets in the suspension (Hernandez et al., 2008; Israelachvili, 2011). There have been a number of investigations on the interaction between the bulk graphite and organic solvents in the pursuit of identifying the suitable solvents for efficient exfoliation, and enhancement of the stability of concentrated dispersion of graphene sheets. These are described in this section.

In a comprehensive study, Coleman's and coworkers (Hernandez et al., 2008) investigated the liquid exfoliation performance of the bulk graphite with a series of commonly-used organic solvents. They concluded that solvents with surface tension of about 40 mJ m^{-2} like *N*-methyl-2-pyrrolidone (NMP) and *N,N*-dimethylformamide (DMF) are the best candidates for mass-production of graphene sheets. In fact, surface tension of 40 mJ m^{-2} is relatively close to the surface energy of graphene, which is 68 mJ m^{-2} (Figure 2.1a). Note that the Raman spectrum of large graphene flakes shows no D band, implying the lack of structural defects after the application of ultrasonic procedure for 30 min. On the other hand, small graphene flakes show a weak D band, which is due to the edge defect as is seen in Figure 2.1b. Figures 2.1c,d shows some transmission electron microscopy (TEM) images of some graphene flakes with size of a few micrometres (Hernandez et al., 2008). Interestingly, Hernandez et al. (2008) reported that flakes with thickness of more than a few layers are rare, indicating high performance liquid exfoliation. They concluded that the graphite was extensively exfoliated and mainly single-layered and few-layered graphene was produced. Analyzing a large number of TEM images and paying attention to the uniformity of the flake edges, they found 28% of total number of flakes was monolayer graphene after sonication process in NMP. Finally, they reported a dispersion concentration of 0.01 mg mL^{-1} and a flake size range of 500 nm to 3 μm . The resulting weight fraction, however, was still too small to

meet the industrial demands of large scale graphene production. Therefore, the search for alternative organic solvents for production commercially viable graphene continues.

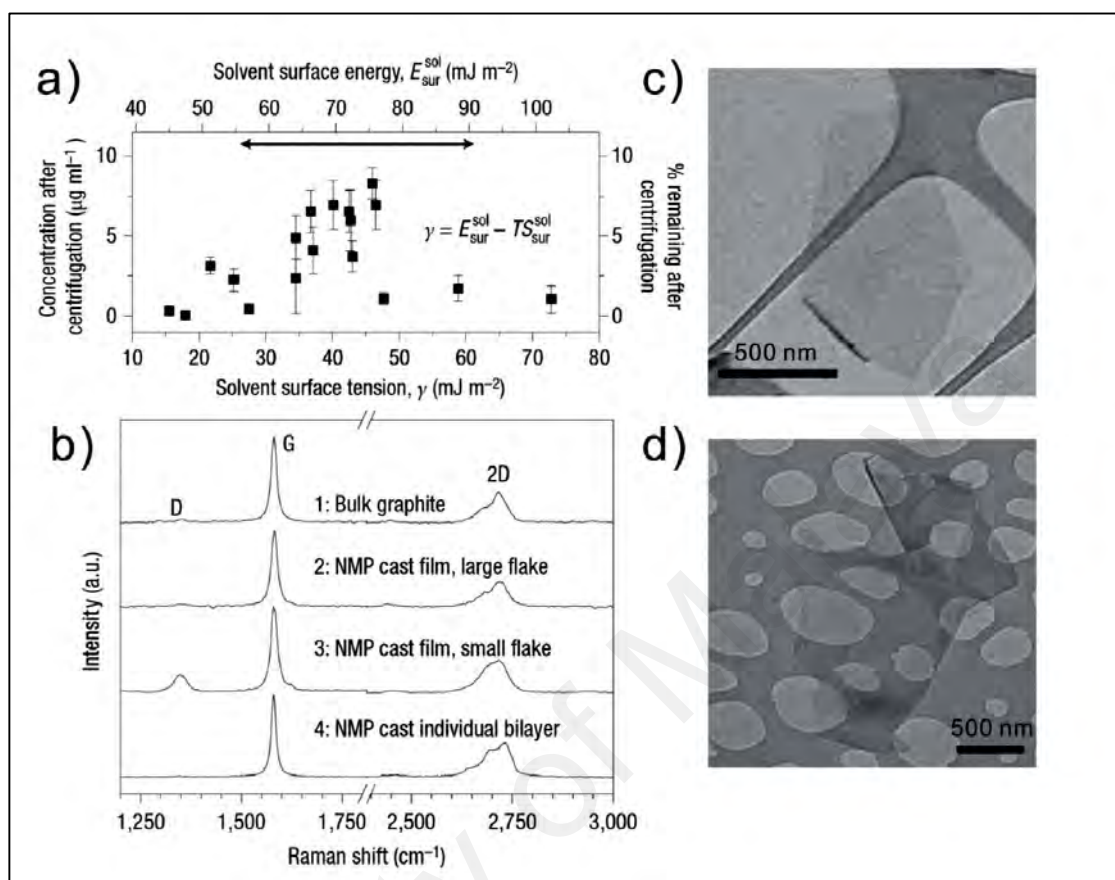


Figure 2.1: a) Graphite concentration measured after centrifugation for a range of solvents plotted versus solvent surface tension, b) Raman spectra of the graphite and few-layered graphene c) and d) TEM images of graphene (Hernandez et al., 2008).

In order to synthesize homogenous dispersions of graphene nanosheets, Hamilton et al. (2009) selected ortho-dichlorobenzene as a nonpolar solvent. Due to the surface tension of 36.6 mJ m^{-2} and via π - π stacking, ortho-dichlorobenzene can easily interact with graphene. But, the resulting weight concentration was improved to only 0.03 mg mL^{-1} , which is still quite low. In order to enhance the exfoliation yield, Bourlinos et al. (Athanasios B Bourlinos, Vasilios Georgakilas, Radek Zboril, Theodore A Steriotis, & Athanasios K Stubos, 2009) suggested the use of a peculiar series of perfluorinated aromatic molecules such as pentafluorobenzonitrile ($\text{C}_6\text{F}_5\text{CN}$), hexafluorobenzene (C_6F_6), pentafluoropyridine ($\text{C}_5\text{F}_5\text{N}$), and octafluorotoluene ($\text{C}_6\text{F}_5\text{CF}_3$). According to

their results, in addition to the surface energy matching of the solvent and graphene, the donor–acceptor interactions play an important role as a driving force for the exfoliation of the bulk graphite. Overall, they reported that the pentafluorobenzonitrile (C_6F_5CN) had the best results, showing the graphene sheets with thickness of 0.5–2 nm reaching a concentration of 0.1 mg mL^{-1} . The sequence of exfoliation yield was $C_6F_5CN > C_6F_6 > C_5F_5N > C_6F_5CF_3$. Also, a comparison between above-mentioned solvents and the analogous hydrocarbon solvents such as benzene, and toluene showed that similar solvents failed to produce stable suspension at high concentrations. In addition to the selection of appropriate solvents, other parameters including ultrasonication power and time were also studied to enhance the exfoliation performance. For instance, with a low-power ultrasonication in NMP but using a long time period (up to 460 h), Khan and coworkers (Khan, O'Neill, et al., 2010) reported increasing the graphene concentrations up to 1.2 mg mL^{-1} . The corresponding concentration of graphene versus sonication time is presented in Figure 2.2a. It is seen that the concentrations of flakes in solutions increases as the sonication time increases. However, Figure 2.2b shows that the flake dimensions reduce with sonication time. The reduction of flake size is proportional to the reverse of square root of time ($t^{-1/2}$). Undoubtedly, long sonication times resulted in inducing numerous edge- and basal plane defects. Later Khan et al. (2011) reported a higher exfoliation performance (2 mg mL^{-1}) by using a sonic tip. To enhance the exfoliation yield, they also offered a novel method in which a pre-sonication and centrifugation procedure was performed for eliminating big particles (unexfoliated graphite). Then, the mixture was sonicated via a bath sonication for 24 h in NMP again (Khan et al., 2011). They reported a significant graphene concentration of 63 mg mL^{-1} , with a flake size of about $1 \mu\text{m} \times 0.5 \mu\text{m}$ and thickness of 3–4 layers on average. These high-concentrated solutions will be useful for practical applications such as the

manufacturing of conducting films or formation of reinforced composites (Khan, May, et al., 2010).

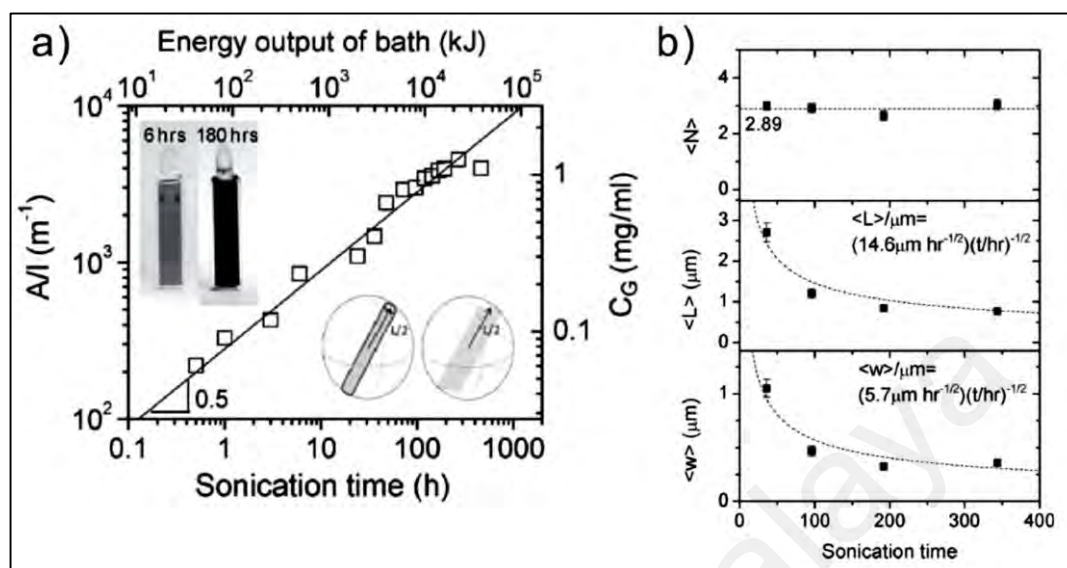


Figure 2.2: a) Concentration of graphene dispersion versus sonication time. The inset illustrates solutions including graphene after 6 h and 180 h. b) Mean layer number, length, and width of flakes as a function of sonication time (Khan, O'Neill, et al., 2010).

2.2.2 Exfoliation with Low Boiling Point Solvents

Despite great advantages for the dispersion of graphene in the aforementioned solvents such as NMP and DMF, there are also some disadvantages such as their high boiling point and toxicity. In particular, these undesirable solvent properties can hinder their applications and deteriorate the device performance (E.-Y. Choi et al., 2011; O'Neill et al., 2011). For instance, O'Neill et al. (2011) showed that the suspension of graphene with a high colloidal stability and concentration can be obtained with low boiling point solvents, such as isopropanol and chloroform. They found that the resulting graphene flake had the lateral dimensions of $1 \mu m \times 0.35 \mu m$, and the thickness of almost 10 layers on average is a suspension with the concentration of 0.5 mg mL^{-1} . In a similar work, E.-Y. Choi et al. (2011) used a volatile solvent (propanol) for exfoliation of graphite to graphene and reported a weight concentration of 1 mg mL^{-1} . Quick evaporation of

propanol could smooth the deposition procedure of graphene nanosheets onto substrates without flake aggregation.

In addition, Qian and coworkers (Qian et al., 2009) studied the effect of acetonitrile (ACN, boiling point of 81.6 °C) as a low boiling point solvent on exfoliation yield. Combined with a solvothermal procedure for producing adequate energy, ACN molecules could diffuse into the interlayers of graphite and overcome the potential barrier. They reported that a stable dispersion including monolayer and bilayer graphene was synthesized after sonication and centrifugation. Their exfoliation yield was 10–12 wt%.

In addition to exfoliation with low boiling point solvents, a solvent exchange technique was suggested by Zhang and coworkers (X. Zhang et al., 2010) for transferring graphene dispersions from high boiling point solvents into low boiling point solvents. In this method, after preparing NMP-based graphene solution, it was filtered and re-mixed into ethanol. This procedure shows a much better stability when compared with the direct exfoliation in ethanol. However, the reason for the stabilizing mechanism is not fully understood. Additional investigations were also performed with methanol, toluene, and dichloromethane, however, the graphene flakes were precipitated after centrifugation.

2.3 Stabilizer-Based Exfoliation

Based on the presented reviews in Section 2.2, it may be concluded that the direct exfoliation in organic solvents is quick and simple, but some of the associated procedures as well as most of the materials used are hazardous. To avoid these environmentally less friendly materials, another method was proposed to exfoliate bulk graphite to graphene in liquid media in the presence of stabilizers such as surfactants, polymers and pyrene derivatives. Stabilizers play a key role in tuning the surface tension of the aqueous solution, which can increase the exfoliation yield efficiently. Reviews of the related works on different kinds of stabilizer are presented in this section.

2.3.1 Ionic Surfactants

Sodium dodecylbenzene sulfonate (SDBS), which is an ionic surfactant was employed to exfoliate bulk graphite to graphene by Lotya and coworkers (Lotya et al., 2009). They reported that the obtained graphene flakes had dimensions in the range of 0.1 to 3 μm with the thickness distribution of 43% less than 5 layers. Fourier transform infrared (FTIR) and Raman spectra showed the presence of a small percentage of oxidation over the exfoliation procedure. They also reached the dispersion concentration of 0.1 mg mL^{-1} . The prepared sample was remained stable for over 6 weeks due to the strong electrostatic repulsion. Later, Lotya and coworkers (Lotya et al., 2010) used sodium cholate (SC) as an ionic surfactant to increase the dispersion concentration of graphene up to 0.3 mg mL^{-1} . After long time sonication of 400 h, TEM analysis showed the graphene flakes with a lateral size of 1 μm and 400 nm and more than 20% of flakes were mono layer.

To improve the electrical conductivity of this type of films, De and coworkers (De et al., 2010) employed an annealing stage at 500 $^{\circ}\text{C}$. Green and Hersam (2009) also employed the density gradient ultracentrifugation (DGU) method to separate graphene flakes based on their thickness. As a result, in terms of sheet resistance and transmittance, the performance of graphene-based films generated by DGU method was enhanced as compared with the common sedimentation centrifugation. In a similar work, T Hasan et al. (2010) used a mild sonication for exfoliation of the bulk graphite in aqueous solution of sodium deoxycholate (SDC) bile salt. With SDC, they could generate denser colloidal sample including graphene flakes with better stability. This enhancement in density was attributed to the highly-hydrophobic index of SDC, which significantly increases the SDC absorption on the graphitic surfaces. As a stabilizer, 7,7,8,8-tetracyanoquinodimethane (TCNQ) anion was used by Hao et al. (Hao et al., 2008) to synthesize water-based graphene solution by using expanded graphite. Via π - π stacking interactions, 7, 7, 8, 8-

tetracyanoquinodimethane could be absorbed onto the surface of graphene flakes. Also, the negative charge imposed by 7, 7, 8, 8-tetracyanoquinodimethane do not allow the exfoliated graphene sheets to aggregate due to the inherent electrostatic repulsion. Finally, they reported a successful exfoliation that produced only mono- and few-layered graphene nanosheets, though with some defects. However, the weight concentrations of the obtained samples were fairly low, of about 15–20 $\mu\text{g mL}^{-1}$. Generally, surfactants have both hydrophobic and hydrophilic chains (tail or head). The hydrophobic tail groups could absorb carbon-based nanostructures (non-polar objects) through the van der Waals interactions. On the contrary, the hydrophilic head groups are prone to dissociation and charge the flakes. So, graphene flakes in the presence of surfactants are stabilized in aqueous solution by the electrostatic repulsion between flakes. Zeta potential (ζ) is typically used to measure the electric potential of aqueous dispersions. Like anionic surfactants, cationic surfactants have been also applied as stabilizer for exfoliation of graphite to graphene. As a cationic surfactant, cetyltrimethylammonium bromide (CTAB) and acetic acid play essential roles in exfoliation of highly ordered pyrolytic graphite (HOPG) to few-layered graphene flakes through rather mild sonication (Vadukumpully et al., 2009). According to Vadukumpully's results, the hydrophobic group of long alkyl chains can adsorb via the surface of graphene (hydrophobic interactions). Also, the electrostatic charge of hydrophilic chains can prevent restacking and agglomeration. They concluded that the obtained graphene with their method had the thickness of 1.18 nm with 85% of which were less than four-layered. In addition, the average length and width of flakes were, respectively, 0.7 μm and 0.5 μm . Figure 2.3 shows the topographic view of the graphene flakes spin-coated on mica, AFM image of a graphene sheet, height profile of the Figure panel b, and statistical analysis of the thickness, length and width of the flakes. In order to increase the dispersion concentration and exfoliation yield with surfactants, an ultrasonic exfoliation procedure with the continuous addition of

surfactants was proposed by Notley (2012), resulting in significant increase in exfoliation yield. With this method, the surface tension of solutions could be kept at an optimum value of 41 mJ m^{-2} , representing an efficient exfoliation and significant growth in the weight concentration of samples. This approach was successful with the use of different types of surfactants, either ionic or non-ionic.

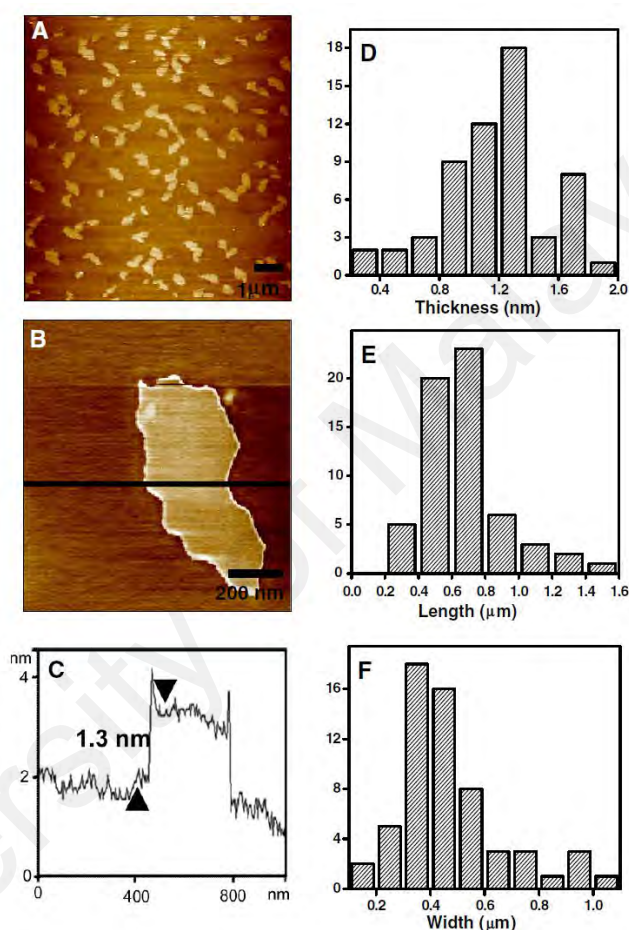


Figure 2.3: (A) Topographic view of the graphene layers, (B) AFM image of a single flake. (C) Height profile of the image 2.3B. Statistical analysis of the AFM images of 60 flakes: (D) thickness, (E) length and (F) width of the flakes (Vadukumpully et al., 2009).

2.3.2 Nonionic Surfactants

According to Guardia et al. (2011), due to the stronger steric repulsion compared to the electrostatic repulsion, non-ionic surfactants can prepare the graphene-based solution with higher dispersibility and stability compared with the ionic ones. They prepared several water-based graphene solutions by using direct bath sonication with various non-ionic surfactants and compared the results with different ionic ones. Their

findings are shown in Figure 2.4, where the weight concentrations of graphene dispersion in the presence of non-ionic surfactants are significantly larger than that for the ionic ones. P-123, which was the best non-ionic surfactant, led to the weight concentration of 0.9 mg mL⁻¹. The concentration was further grown to almost 1.5 mg mL⁻¹ after extending the sonication period to 5 h. In addition, the paper-like films obtained from this procedure had the highest electrical conductivity of 3600 S m⁻¹.

A successful two-step process was suggested by Geng et al. (Geng et al., 2010) to exfoliate bulk graphite in NMP containing nonionic porphyrin. Organic ammonium ion and porphyrin were used for exfoliation via π - π interactions with graphene. The presence of undisturbed sp² carbon networks was the main result of this novel method. In this case the stability of non-ionic surfactants was also caused by the steric effects. Also, the long hydrophilic chains of surfactants can disperse into water easily. More interestingly, if the graphene flakes get close to each other, the hydrophilic head groups of surfactants can interact to induce osmotic repulsion.

Coleman's group (Smith et al., 2010) investigated the effect steric repulsive potential barrier on the dispersion of graphene using different surfactants. They studied 12 different ionic and nonionic surfactants for identifying the main stabilization mechanism in surfactant-assisted graphite exfoliation. They found linear growth of the dispersion concentration of graphene with the increase of steric repulsive potential barrier.

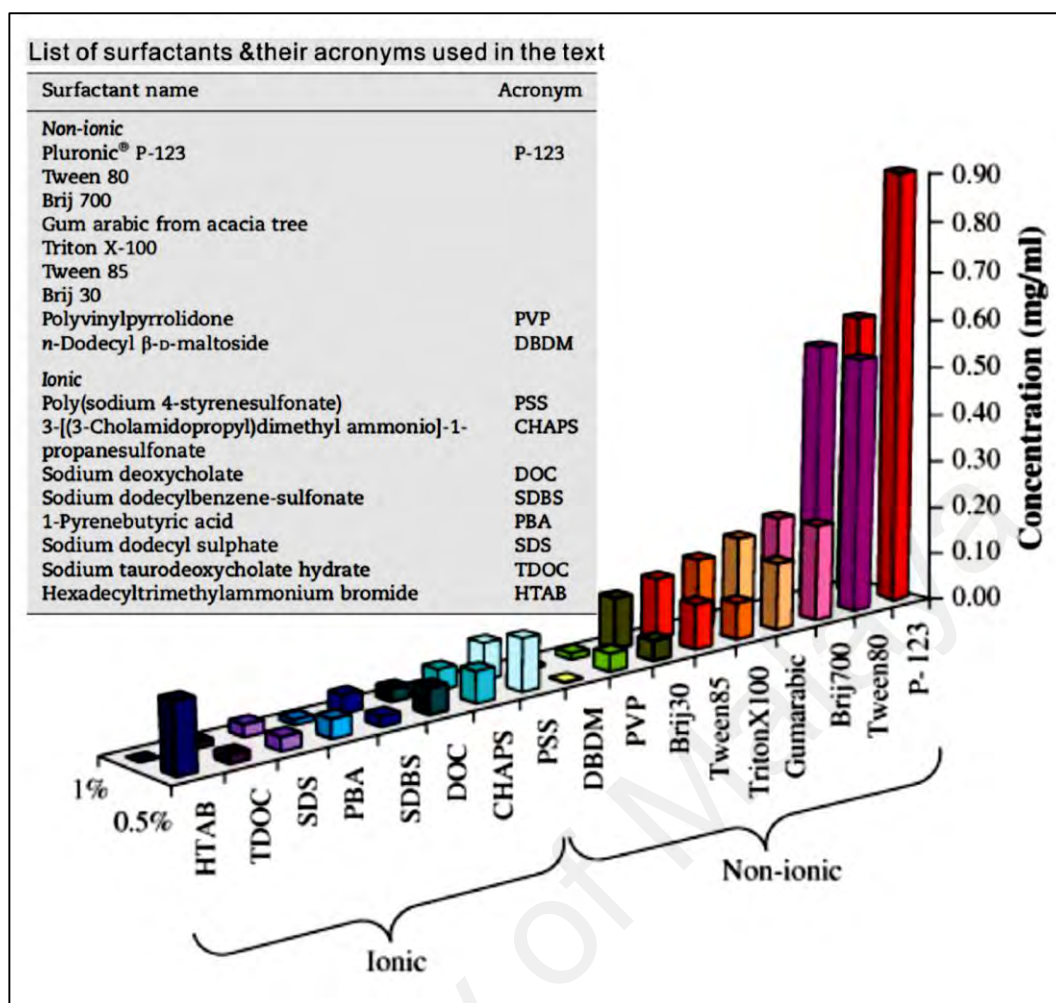


Figure 2.4: Concentration of graphene dispersions obtained by various types of surfactants (Guardia et al., 2011).

2.3.3 Polymers

Bulk graphite can be exfoliated in different media in the presence of various polymers such as polyvinyl chloride (PVC) and poly methyl methacrylate (PMMA). For example, in order to synthesize non-oxidized graphene, Bourlinos and his co-worker (Athanasios B Bourlinos, Vasilios Georgakilas, Radek Zboril, Theodore A Steriotis, Athanasios K Stubos, et al., 2009) had directly sonicated the graphite powders in water and polyvinylpyrrolidone (PVP). The PVP has good solubility in aqueous media and affinity to graphite surfaces and it is biocompatible. They reported that the resulting graphene was mostly few layered with the weight concentration of 1 mg mL^{-1} . Steric (or depletion) effect was the main mechanism for stabilization of PVP-graphene.

Using ethyl cellulose as a stabilizing polymer, Y. T. Liang and Hersam (2010) reported a high yield of graphene exfoliation in ethanol. They reached the maximum dispersion concentration of 1.02 mg mL^{-1} via iterative solvent exchange. Coleman's group (May et al., 2012) performed a study for identifying suitable type of polymer-solvent combinations for exfoliation of bulk graphite. They established a simple model based on Hildebrand solubility parameters of nanosheets, polymer and solvent. Despite the low graphene concentration on a scale of $\mu\text{g mL}^{-1}$, the proposed model was successful. Recently, Xu and coworkers (L. Xu et al., 2013) obtained graphene dispersions with good concentrations using tetrahydrofuran (THF) / hyperbranched polyethylene (HBPE). They proposed the use of a solvent/polymer pair to exfoliate graphite via absorbing HBPE on graphene flakes to generate steric stabilization for avoiding restacking. More interestingly, the characterization instruments and morphological studies showed no defect on the structure of graphene nanosheets. In addition, the produced graphene flakes had between 2 and 4 layers with length of $0.5 \mu\text{m}$ and width of $0.2 \mu\text{m}$. They reported the concentration of 3.4 mg mL^{-1} for graphene dispersion in chloroform after solvent evaporation.

In addition to the significant stabilization effect of polymers in the exfoliation procedures, they can be utilized to enhance the graphene wettability. To address this issue, Skaltsas and co-workers (Skaltsas et al., 2012) added amphiphilic block copolymers such as poly[styrene-*b*-(2-vinylpyridine)] (PS-*b*-P₂VP) and poly(isoprene-*b*-acrylic acid) (PI-*b*-PAA) to switch solubility of graphene from the organic to aqueous phase. A tip sonication was used in the presence of *o*-dichlorobenzene or NMP, however, the quality of graphene, the concentration of dispersion and the lateral size of flakes were small.

2.3.4 Pyrene Derivatives

In the exfoliation of graphite, typically the higher concentration of small molecular surfactants leads to higher concentration of graphene nanosheets in the

dispersions. Nevertheless, eliminating additional surfactants or polymers is an immense difficulty, which can reduce the exfoliation yield and impose some negative effects on the performance of composites, electronic devices and films. Therefore, finding alternative materials with low weight fraction for mass-stabilizing of graphene flakes is critical. Pyrene (Py) molecules and some of its derivatives shown in Figure 2.5 could be promising alternative materials for high-yield exfoliation of the bulk graphite. The π - π interactions between graphene and the planar surfaces of this kind of stabilizers play a key role in the exfoliation process (X. Dong et al., 2009; Jang et al., 2011; D.-W. Lee et al., 2011; F. Liu et al., 2010; Niu et al., 2016; Parviz et al., 2012; Schlierf et al., 2013; H. Yang et al., 2013; M. Zhang et al., 2010).

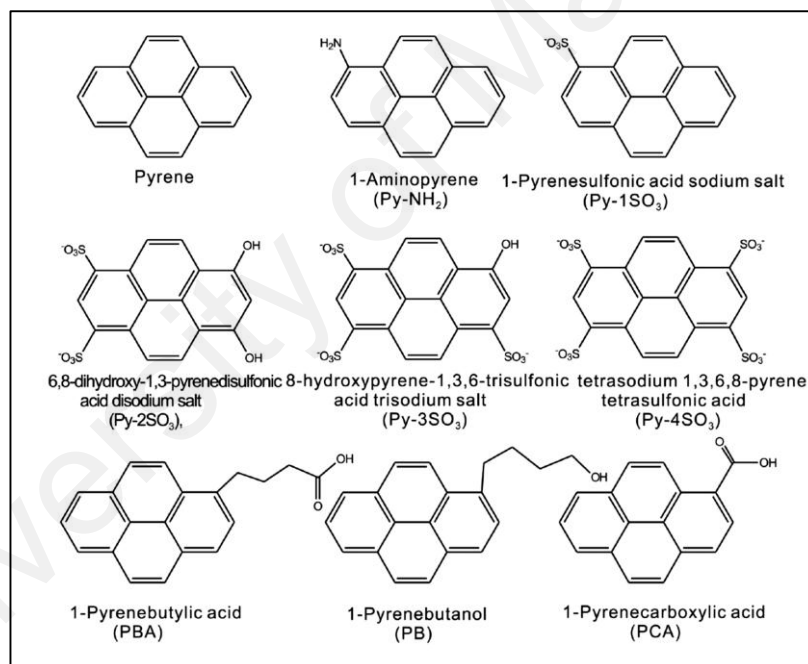


Figure 2.5: Molecular structures of pyrene derivatives with their names and corresponding acronyms for stabilizing graphene in the liquid media. (Niu et al., 2016)

In the presence of tetrasodium 1,3,6,8-pyrenetetrasulfonic acid (Py-4SO₃), Dong and coworkers (X. Dong et al., 2009) presented an efficient exfoliation technique for preparing monolayer graphene with only probe sonication. Their statistical analysis of AFM images showed that the majority of graphene sheets were mono-layered. Their AFM images are shown in Figure 2.6.

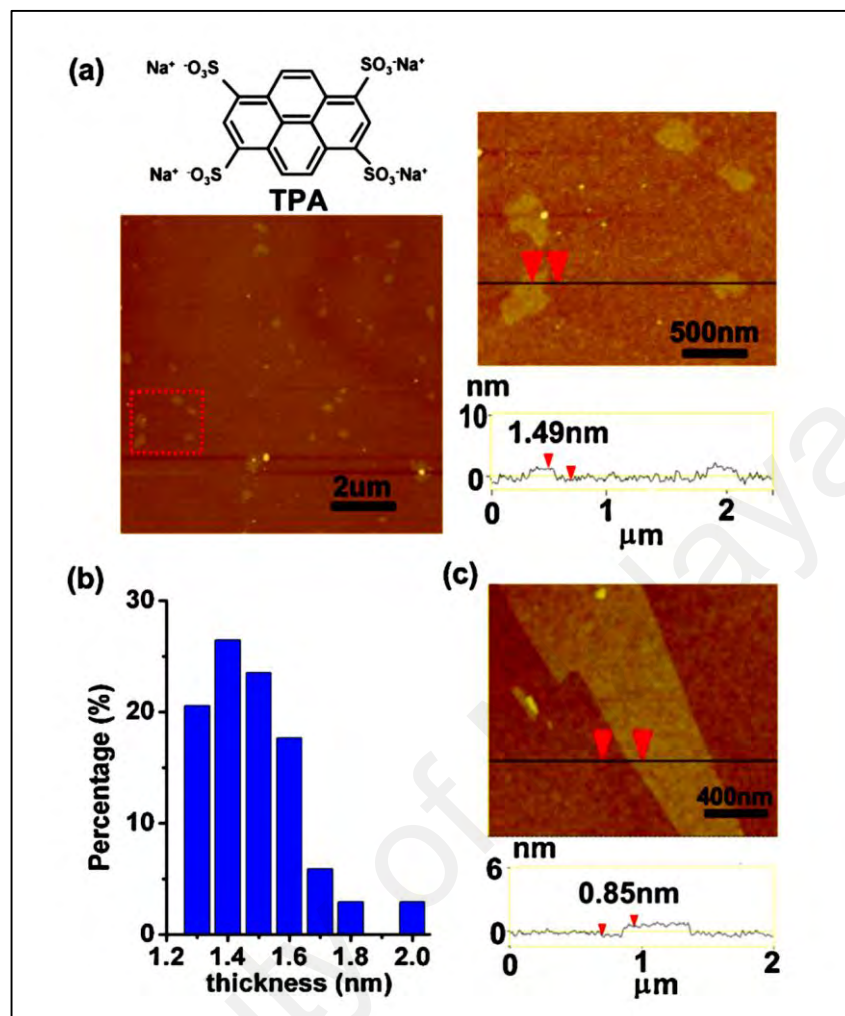


Figure 2.6: (a) A typical AFM image of graphene flakes dispersed in TPA/D2O solution. (b) The thickness distribution of all the graphene flakes observed in panel (a). (c) AFM image of a mechanically exfoliated monolayer graphene (X. Dong et al., 2009)..

In another study, pyrene derivatives, 1-pyrenecarboxylic acid (PCA) was used by X. An et al. (2010) to produce water-based graphene dispersion. Using a method of sonication of bulk graphite in aqueous solutions of pyrene molecules functionalized with water-soluble groups, including Py-NH₂ and Py-4SO₃, Zhang and coworkers (M. Zhang et al., 2010) could synthesize monolayer graphene flakes with high quality. In addition to the stabilization effect of pyrene molecules, they also played a role as the fillers (nanographene) to treat the structural defects on the surface of graphene sheets. After annealing the graphene nanosheets at 1000 °C, superior conductive transparent films with

electrical conductivity of 181200 S m^{-1} and transmittance in the visible light range of 90% were produced.

A supercritical fluid exfoliation with 1-pyrene sulfonic acid sodium (Py-1SO₃) was suggested (Jang et al., 2011) in a mixture of ethanol/water. The Py-1SO₃ molecules can attach on the surface of graphene flakes and act as electron-withdrawing groups, resulting in an electron transfer from graphene flakes to Py-1SO₃ molecules. Two main advantages were reported with the addition of Py-1SO₃ molecules. First, it could increase the exfoliation yield of bulk graphite into monolayer and bilayer graphene sheets up to 60%. Second, the Li-ions storage capacity was also increased. Similarly, Yang and coworkers (H. Yang et al., 2013) used Py-1SO₃ for exfoliation of bulk graphite to graphene sheets with only bath sonication in aqueous media. To enhance the exfoliation yield, Lee and coworkers (D.-W. Lee et al., 2011) synthesized an aromatic amphiphile molecules. These molecules have four pyrene units as an aromatic segment and a hydrophilic dendron. With non-destructive π - π stacking interactions, these molecules could easily attach on the surface of graphene flakes and subsequently facilitate the production of water-based graphene dispersions. They reported the concentration up to 1.5 mg mL^{-1} via sonication in water/methanol media.

To investigate the effects of different pyrene derivatives on exfoliation yield, Parviz et al. (2012) used various pyrene derivatives and determined the dispersion yield of graphene sheets. They found that Py-1SO₃ showed the best exfoliation performance compared with all other pyrene derivatives shown in Figure 2.5. They could reach the graphene concentration yield up to $0.8\text{--}1 \text{ mg mL}^{-1}$ in the presence of Py-1SO₃. They also showed that the functional groups with larger electronegativity is more suitable for being adsorbed on the surface of graphene sheets. Therefore, they concluded that pyrene derivatives including sulfonyl groups can be the most effective stabilizer for producing graphene flakes over a wide range of pH. In another comparative study, Schlierf et al.

(Schlierf et al., 2013) reported a novel exfoliation method in aqueous media in the presence of different pyrene sulfonic acid sodium salts such as Py-1SO₃, 6,8-dihydroxy-1,3-pyrenedisulfonic acid disodium salt (Py-2SO₃), 8-hydroxypyrene-1,3,6-trisulfonic acid trisodium salt (Py-3SO₃) and Py-4SO₃. Their results showed that the molecular dipole was not essential per se, however, it can facilitate adsorption of the molecule on the graphene flakes, enhancing lateral displacement of water molecules collocated between aromatic cores of the organic dye and graphene (Niu et al., 2016).

2.3.5 Aromatic Stabilizers

Like pyrene molecules and polymers, some polycyclic aromatic hydrocarbons such as tetrapotassium salt of coronene tetracarboxylic acid (Ghosh et al., 2010) and perylenebisimide-based bolaamphiphile detergent (Englert et al., 2009) have the ability to increase exfoliation yield of graphite. Being highly water-soluble, this type of aromatic stabilizers with bulky planar aromatic surface provides a strong interaction with the surface of graphene nanosheets via synergistic noncovalent charge-transfer and π - π stacking interactions. Like other stabilizers, the negative charge imposed on the graphene surfaces prevent them from inter and intra re-stacking, thus, leading to high level of stabilization for graphene dispersions.

2.4 Exfoliation with Ionic Solvents

Semi-organic salts with a low melting point (mostly lower than 100 °C) are commonly used as ionic solvents (X. Zhou et al., 2010), which have absorbed much attention due to their promising properties including suitable thermal stability, proper ionic conductivity, and non-flammability. According to the high dispersibility of carbon nanotubes in ionic solvents (Gunasekaran & Dharmendirakumar, 2014), it is anticipated that ionic solvents may also be utilized for stabilizing graphene flakes via Coulombic interaction. The exfoliation of bulk graphite into graphene nanosheets via tip sonication in a ionic solvent, namely, 1-butyl-3-methylimidazolium bis(trifl

uoromethanesulfonyl)imide ([Bmim][Tf₂N]) was reported (Xiqing Wang et al., 2010). They found a rather high exfoliation yield and could also synthesize a stable graphene suspension of 0.95 mg mL⁻¹. They also reported that the graphene nanosheets were few-layered with micrometer sizes. More interestingly, 1-hexyl-3-methylimidazolium hexafluorophosphate (HMIH) was found to be a significantly strong ionic solvent for exfoliation of bulk graphite, leading to a concentration of graphene dispersion up to 5.33 mg mL⁻¹ via direct sonication (Alzari et al., 2011). Quantitative analysis showed that the graphene nanosheets had the wide of 4 mm and an average thickness of 2 nm, representing almost 6–7 atomic layers. Sanjeeva Rao et al. (Rao et al., 2015) described an efficient soft processing approach for continuous synthesis of high-quality, few-layered graphene nanosheets. They used electrochemical exfoliation of graphite in the presence of environmentally friendly glycine-bisulfate ionic complex under ambient reaction conditions. The resulting graphene nanosheets were mostly 2–5 layered. They suggested that the formation of surface molecule nuclei via the polymerization of intercalated monomeric HSO₄⁻ and SO₄²⁻ ions can be the main plausible electrochemical exfoliation mechanism.

2.5 Functionalization-Assisted Exfoliation

Functionalization-assisted exfoliation is a high-performance method for exfoliation of bulk graphite into mono layered graphene via direct sonication in different solvents. Covalently oxidation-assisted exfoliation is the most common method of the functionalization-assisted exfoliation. Graphite oxide as the first resulting material can be exfoliated in different media such as water by direct sonication. The presence of polar functional groups and the increased *d*-spacing of the material were suggested as the main reasons for increasing the exfoliation yield (Stankovich et al., 2007; Stankovich, Piner, Chen, et al., 2006). Using functionalization of graphite oxide with isocyanate, Stankovich et al. (Stankovich, Piner, Nguyen, et al., 2006) performed the first graphite oxide

exfoliation in organic solvents. Such reactions decrease the percentage of hydrogen bonding in the oxide layers by changing hydrogen bond donors, e.g. hydroxyl groups, into carbamate esters and/or amides. They reached the stable monolayer graphene dispersions of 1 mg mL^{-1} in dimethylformamide (DMF) and *N*-methyl-2-pyrrolidone (NMP). In a similar study (G. L. Li et al., 2010), poly(*tert*-butyl acrylate)-functionalized graphite oxide were employed to prepare a suitable dispersion of graphene in toluene at 1 mg mL^{-1} (G. L. Li et al., 2010). Recently, exfoliation of GO in certain organic solvents such as DMF, NMP, tetrahydrofuran (THF), and ethylene glycol (EG) has also been performed with direct sonication (Paredes et al., 2008). Paredes et al. reported synthesis of stable dispersions of 1 mg mL^{-1} in the presence of organic solvents. In addition to all the advantages of graphite oxide, the oxidation of bulk graphite produces different reactive oxygen-containing functional groups on the basal planes and edges (W. Cai et al., 2008; Heyong He et al., 1998). Oxygen-containing functional groups like hydroxyl and epoxy, carboxyl and ketone groups can impart hydrophilicity to the graphene network, resulting in stable dispersion in water via direct sonication (Figure 2.7) (S. Park et al., 2008; S. Park & Ruoff, 2015).

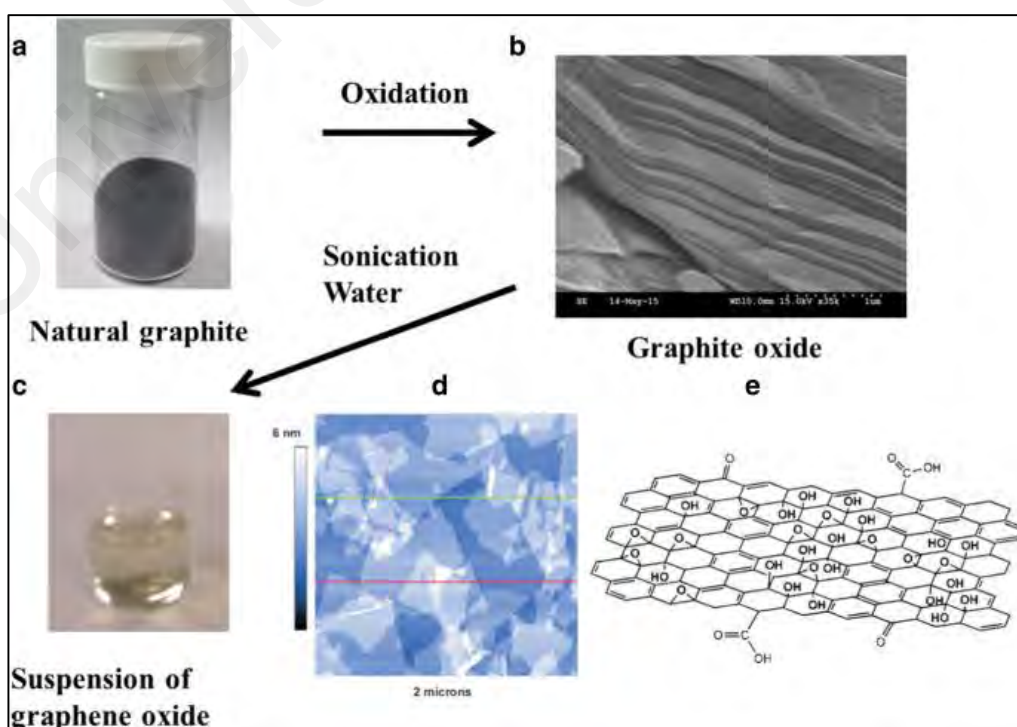


Figure 2.7: Scheme for the production of water-based graphene oxide suspension from graphite (a) a photo of bulk graphite powder, (b) a SEM image of the layer structure of graphite oxide, (c) a water-based graphene oxide suspension, (d) a AFM image of graphene oxide placed on a mica substrate, and (e) chemical structure of graphene oxide with different functional groups (S. Park & Ruoff, 2015).

Graphene oxide is heavily functionalized with many permanent chemical defects, such as holes introduced into the basal plane. These holes are not readily healed even upon annealing (Ruoff, 2008; H. Wang et al., 2009). Therefore, reduced graphene oxide (RGO) were produced via the reduction of an aqueous graphene oxide suspension with hydrazine (NH_2NH_2) or dimethylhydrazine ($\text{C}_2\text{H}_8\text{N}_2$) as a pure material (Stankovich, Dikin, et al., 2006; Stankovich, Piner, Chen, et al., 2006). Due to the promising electrical and thermal properties as well as high surface area, RGO material has shown great potential in a wide range of applications. Nevertheless, preparing stable and homogeneous suspensions of RGO platelets has been challenging. In addition, the chemical reduction of the materials with hydrazine led to agglomerated powders, which created another problem. To address these problems, a mixture of water and organic solvents (9 parts organic solvent and 1 part water) were employed (S. Park et al., 2009) and subsequently was reduced by hydrazine, leading a stable suspension of RGO for depositing films with a relatively high electrical conductivity (Figure 2.8).

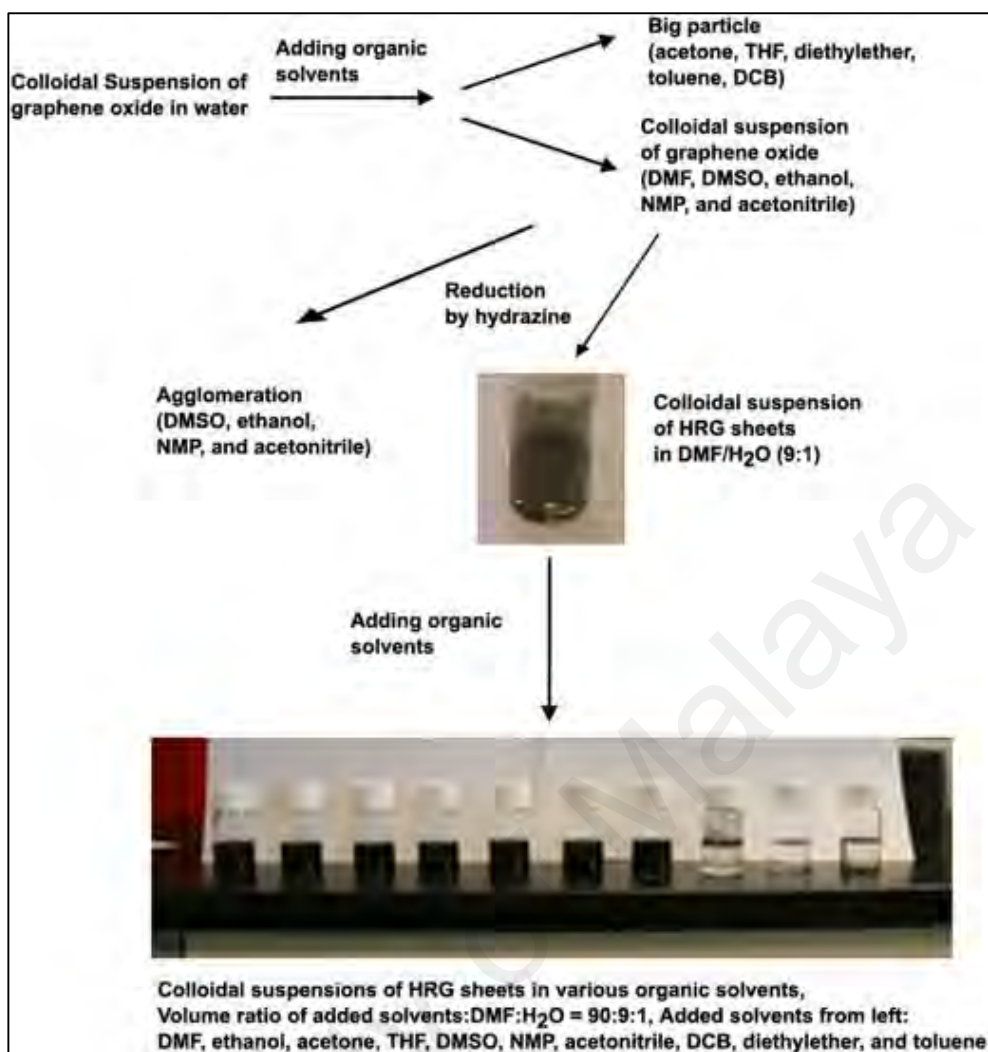


Figure 2.8: The procedure of preparing homogeneous colloidal suspensions of RGO (S. Park & Ruoff, 2015).

As a large-scale exfoliation method, the production of chemically converted graphene from the reduction of graphene oxide is a convenient method for obtaining large amounts of graphene (Stankovich et al., 2007); however, even with efficient reducing agents such as hydrazine or H_2 , and annealing at high temperature, the pure crystalline structure of graphene is not restored. Graphene oxide is heavily functionalized with many permanent chemical defects, such as holes, introduced into the basal plane. These holes are not readily healed even with annealing (Ruoff, 2008; H. Wang et al., 2009). While thermal annealing is considered as one of the best methods to heal some of holes, it does not seem to be cost-effective (Zhengzong Sun et al., 2010).

As mentioned above, a novel technique for overcoming above-mentioning drawbacks for production of single-layered and/or few-layered sheets of graphene is the liquid phase exfoliation of graphite in the presence of high surface-tension organic solvents and direct sonication (Zhengzong Sun et al., 2010). However, due to the lack of easily-miscible functional groups, such as polymers to decrease interlayer attractions, the graphene sheets suspended in the high-surface tension base fluids tend to aggregate and restacking (Lotya et al., 2009). Also, due to the strong π - π interactions, liquid-phase exfoliated graphene cannot reach stable dispersion in base fluids, leading high level of aggregation (Zhengzong Sun et al., 2010). However, due to lack of graphene-solubility, the exfoliation performances of most of the solvents suggested in previous attempts were quite low. Also, in some cases, the obtained samples are only partially exfoliated and still contain extensive amount of staked graphitic layers. To increase the efficiency of exfoliation with this method, the chemical functionalization of graphite with different functional groups, such as 4-bromophenyl, provides a new approach for improving the solubility of graphene sheets in polar, aprotic, organic solvents, allowing the exfoliation of bulk graphite with fewer problems (Lomeda et al., 2008).

Earlier, Zhengzong Sun et al. (2010) concluded that graphite can be changed to graphene by covalent functionalization of the graphite and the synthesis of a stable suspension in the presence of DMF without any added surfactant or stabilizer. They achieved both exfoliation and functionalization with a fast procedure and obtained appropriate edge-functionalization and intact pristine graphene structure in the interior basal planes. In addition, the morphological results showed that more than 70% of the graphene flakes had layers with thicknesses less than 5 nm, providing a high yield of soluble graphene. They concluded that the proposed preparation approach is significantly simpler than the multi-step approaches needed for preparing graphene oxide followed by

reduction to chemically-converted graphene and is an effective method for producing soluble graphene with high yield (Figure 2.9).

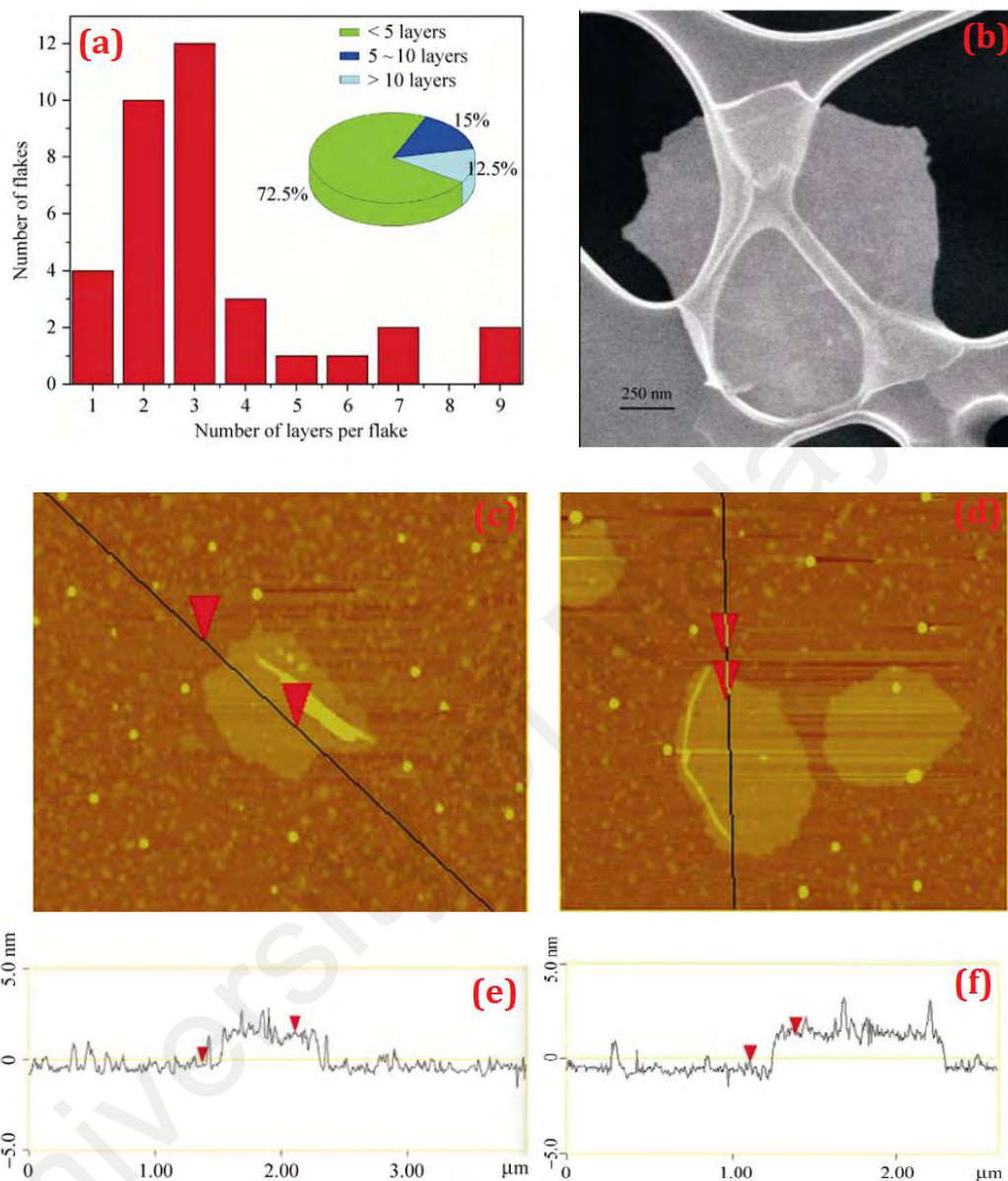


Figure 2.9: (a) Histogram of number of layers per graphene flakes, (b) SEM image of graphene flake, (c & d) AFM of graphene on mica and (e and f) the height profiles along the black imaged lines above in panels c and d, respectively (Zhengzong Sun et al. (2010)).

2.6 Thermal Exfoliation Techniques

In order to reach near-complete exfoliation of bulk graphite into mono layer graphene, thermal exfoliation techniques are shown to be a promising approach. Compared to the aforementioned exfoliation methods, thermal exfoliation approach has

the advantage of being faster and producing dry graphene (M. Cai et al., 2012; McAllister et al., 2007). For instance, Schniepp and coworkers (Schniepp et al., 2006) showed that the exfoliation could be done within seconds at high temperature. It should also be pointed out that for many applications such as electrodes in lithium batteries dry graphene is needed.

Overall, in thermal exfoliation techniques, the functional groups decorated on the graphitic layers decompose and generate gases that exert pressure on the adjacent layers during the heating procedure. Exfoliation procedure starts once this pressure exceeds the van der Waals interlayer interaction force (McAllister et al., 2007). To reach a high-yield exfoliation and generate proper pressure, the pristine graphite is required to possess interlayer functional groups. Therefore, graphite oxide, chemically-treated expanded graphite, and intercalated graphite compounds are commonly utilized instead of pure graphite as the pristine materials for thermal exfoliation.

2.6.1 Thermal Exfoliation of Graphite Oxide

Schniepp et al. (2006) proposed the use of thermal exfoliation of graphite oxide for producing mono layer graphene in 2006. For this purpose, they loaded dried GO into a quartz tube that was heated in a furnace at 1050 °C for 30 seconds. They reported that this approach leads to high-yield exfoliation of graphite oxide. Later, McAllister and coworkers (McAllister et al., 2007) proposed a new exfoliation mechanism and the reason for thermal exfoliation. They concluded that thermal exfoliation only occurred in the presence of special conditions. That is, the decomposition rate of the functional groups on graphite oxide flakes should exceed the diffusion rate of the evolved gases. This phenomenon could generate sufficient pressure for overcoming the van der Waals interaction among graphene layers. For a fast exfoliation, the experiments should be performed at a critical temperature up to 550 °C. A wrinkled graphene nanosheet with

rough surface area and a minimum thickness of 1.1 nm were shown in Figure 2.10 by M. Cai et al. (2012). Also, the high surface area of 700–1500 m² g⁻¹ and conductivities ranging of 1 × 10³ to 2.3 × 10³ S m⁻¹ were reported for the exfoliated graphene. In addition, statistical analysis revealed that more than 80% of the obtained flakes were mono-layered.

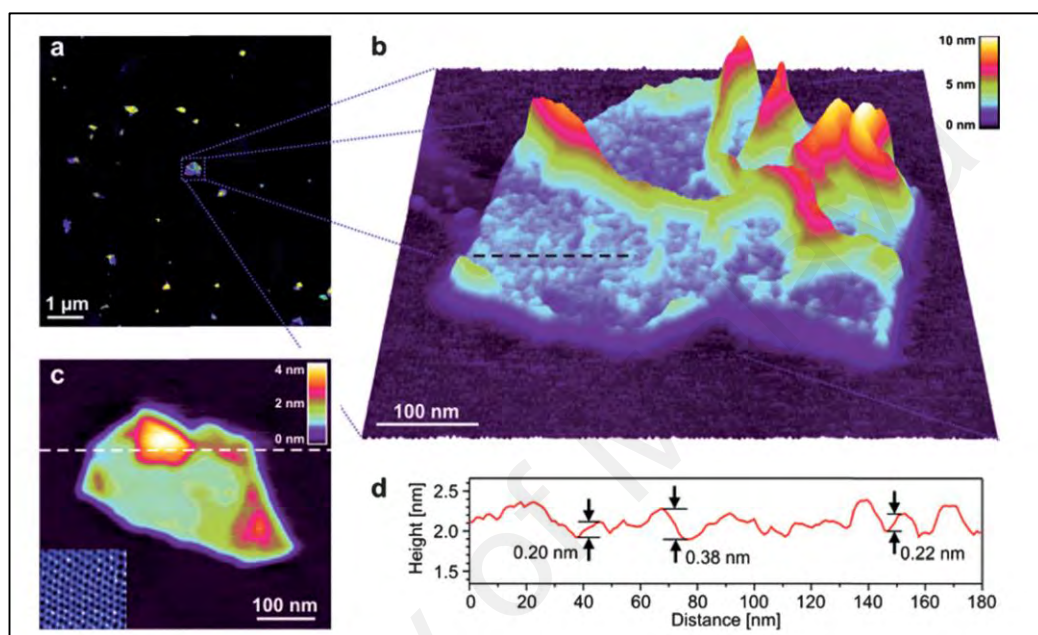


Figure 2.10: Thermally exfoliated graphene. (a) Tapping-mode AFM topography image of thermal exfoliation of GO. (b) A wrinkled graphene sheet with rough surface structure. (c) Contact-mode AFM image of a flake. (d) The cross-section through the line in the sheet shown in panel (c) (M. Cai et al., 2012).

In a similar study, Z.-S. Wu, Ren, Gao, Liu, et al. (2009) investigated the exfoliation yield using different pristine graphite flakes as starting materials and rapid heating in a furnace at 1050 °C. They reported as the lateral flake size and the crystallinity of the bulk graphite decrease, the exfoliation yield enhances. They also found an electrical conductivity of ~105 S m⁻¹ after exfoliation with the flak surface areas in the range of 50–350 m² g⁻¹.

In order to exfoliate graphite oxide, a detonation procedure was employed, in which a mixture of graphite oxide and picric acid was mixed and sealed (Can et al., 2011).

The fast explosion could generate the powerful shockwave of about 20 MPa a high temperature of 900 °C (G. Sun et al., 2008) to fully-exfoliate the bulk graphite sheets. As a result, the obtained graphene flakes were 2–5 layered with lateral size of few micrometers.

Other fast heating approaches for exfoliating graphite oxide, such as employing microwave irradiation and arc discharge, were also suggested (M. Cai et al., 2012). Using a microwave-assisted method, Zhu and coworkers (Zhu, Murali, Stoller, et al., 2010) found that the exfoliation of graphite oxide occurred in about 1 min, preparing the exfoliated graphene sheets with the surface area of 463 m² g⁻¹. They also reported a conductivity of 274 S m⁻¹ for the graphene sheets after microwave-assisted exfoliation. To increase the exfoliation yield, these microwave assisted graphene flakes activated chemically with KOH. Zhu et al. have also reported the specific surface area of 3100 m² g⁻¹ and the conductivity of 500 S m⁻¹ (Zhu et al., 2011) for highly exfoliated graphene sheets with an extensive number of holes. Using microwave-assisted method under hydrogen atmosphere, Park et al. also reached a high surface area of 586 m² g⁻¹ for a mixture of graphite oxide and graphite nanosheets. Graphite nanosheets collected all the microwave irradiation, resulting in quick heating of graphite oxide (S.-H. Park et al., 2011). Exfoliation of graphite oxide via a mixture of graphene and graphite oxide precursor was also developed (H. Hu et al., 2012).

As another high temperature thermal exfoliation, hydrogen arc discharge was used as a successful method for exfoliation of graphite. For example, Wu and coworkers (Z.-S. Wu, Ren, Gao, Zhao, et al., 2009) showed an efficient exfoliation of graphite flakes via hydrogen arc discharge, in which a sudden increase in the temperature up to 2000 °C was applied. Eighty percent of the graphene sheets obtained via hydrogen arc discharge were mono layered with a thickness of 0.9–1.1 nm and electrical conductivity of about 2 × 10⁵ S m⁻¹.

In all of the above-mentioned thermal exfoliation methods, high temperature processes were employed. As a low temperature thermal exfoliation, McAllister et al. proposed a successful quick exfoliation of graphite oxide flakes at temperature of 550 °C (McAllister et al., 2007). Later, a fast and low temperature thermal exfoliation method was proposed (Q. Du et al., 2010). The procedure included heating of graphite oxide at different temperatures of 250 °C, 300 °C, and 400 °C in air for 5 minutes. Du et al. reported the specific surface area of 328–418 m² g⁻¹ for the exfoliated graphene (Q. Du et al., 2010).

Exfoliation of graphite oxide was also investigated in different atmospheres such as hydrogen at 200 °C (Kaniyoor et al., 2010) and argon at 275–295 °C (M. Jin et al., 2010). The exfoliated graphene sheets had the specific surface area of 442 m² g⁻¹, which was similar to the value reported for exfoliation in air. Note that vacuum was also utilized to increase the exfoliation performance of graphite oxide at temperature of 200 °C (Lv et al., 2009). Due to the release of functional groups on the graphite oxide, a pressure less than 1 Pa obtained between layers, which caused an enhancement in net repulsive forces between the layers (Figure 2.11). According to the statistical analysis, over 60% of the graphene flakes were mono-layered (Lv et al., 2009). In addition, Zhang et al. (H.-B. Zhang et al., 2011) reported an even lower temperature of 135 °C for producing graphene in a vacuum oven. The exfoliated graphene had the specific surface area of 759 m² g⁻¹, which was significantly high.

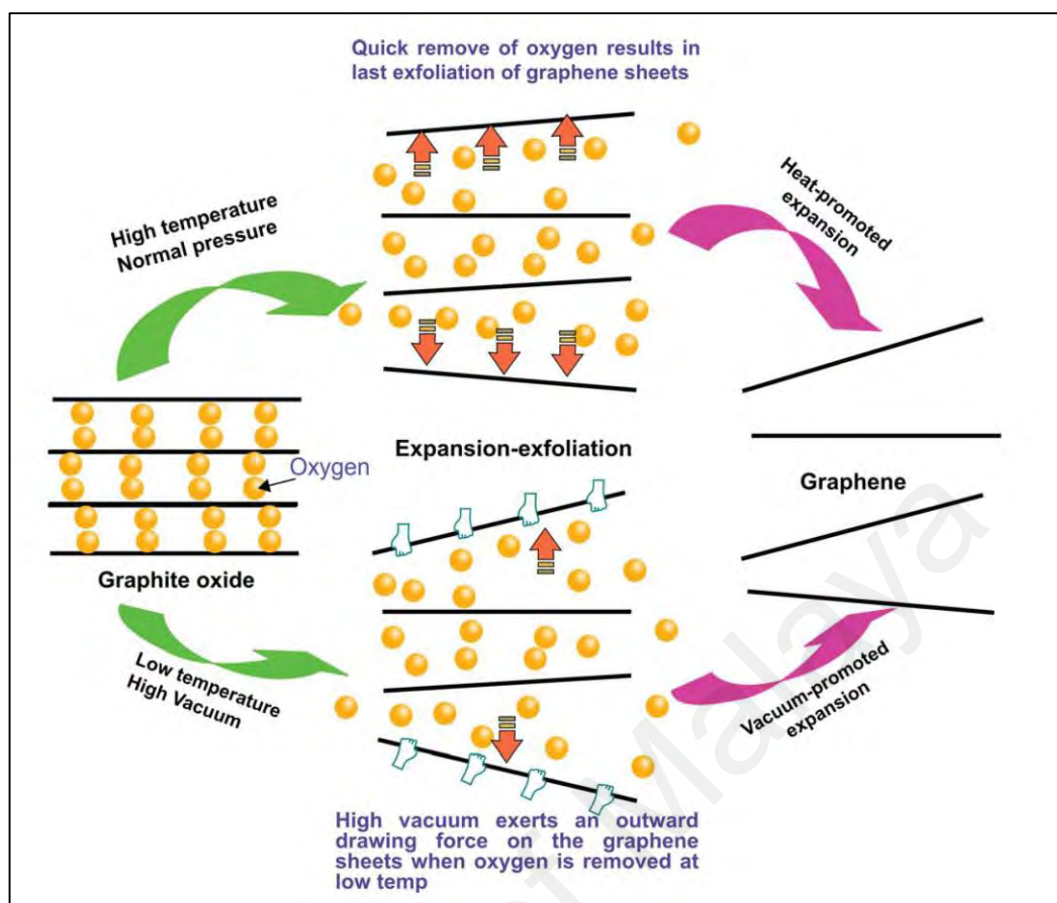


Figure 2.11: High temperature exfoliation of graphite oxide under atmospheric pressure (top) and low-temperature exfoliation of graphite oxide (as low as 200 °C) under high vacuum (bottom) (Lv et al., 2009).

2.6.2 Thermal Exfoliation of Bulk Graphite

Thermal exfoliation of bulk graphite into the graphene sheets commonly requires expanded graphite or graphite intercalation compounds as pristine materials. Clearly the raw materials in this method have less functional groups than graphite oxide, resulting in graphene sheets with higher quality (M. Cai et al., 2012). Direct heating and microwave irradiation are two common approaches to exfoliate bulk graphite to graphene sheets.

Regarding direct heating, Li et al. exfoliated the bulk graphite into the mono- and few-layered graphene sheets via a rapid heating at 1000 °C (X. Li, X. Wang, et al., 2008). The exfoliation yield, however, was as small as 0.5% of the pristine graphite. In order to enhance the exfoliation yield, a procedure including thermal exfoliation and intercalation

of graphite was suggested by the same research group (X. Li, G. Zhang, et al., 2008). Using a rapid heating, intercalating with oleum (fuming sulphuric acid) and inserting by tetrabutylammonium hydroxide (TBA) in DMF, the distance between adjacent graphite layers was increased, representing high-yield exfoliation. As a result, a stable suspension of mono-layered graphene with yield of 90% was synthesized after mild sonication in the presence of a surfactant. The graphene sheets obtained from the bulk graphite had shown a high level of quality without significant defects as compared to the graphene obtained from exfoliating graphite oxide (Figure 2.12).

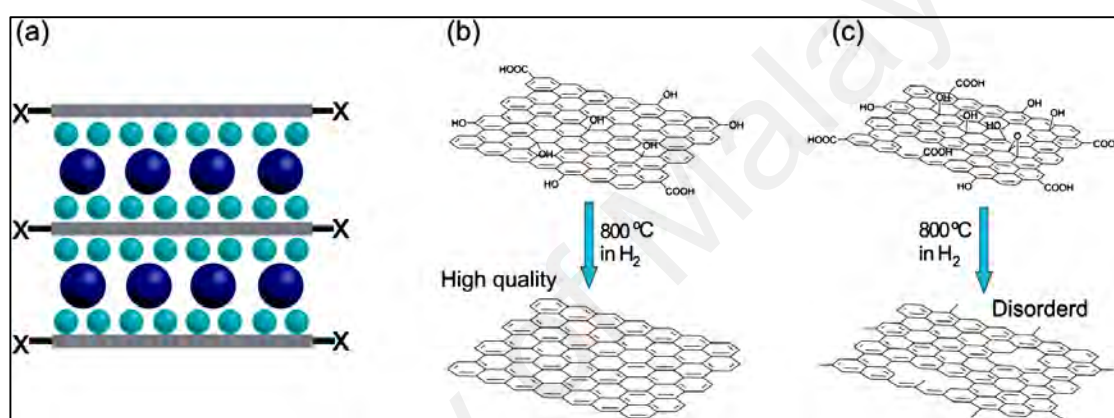


Figure 2.12: (a) Graphite exfoliation after re-intercalation with sulphuric acid molecules and insertion of tetrabutylammonium hydroxide. Graphene sheets' structure after thermal exfoliation of bulk graphite (b) and graphite oxide (c) (X. Li, G. Zhang, et al., 2008).

A rapid heating exfoliation method at 900 °C in the presence of intercalation with sulphuric acid and hydrogen peroxide was suggested by Gu et al. for producing single and multi-layered graphene from natural graphite (Gu et al., 2009). Gu and coworkers (Gu et al., 2009) finally produced multi-layered graphene sheets. Therefore, to enhance the yield of mono layer graphene, a re-exfoliation procedure was suggested by Dhakate and coworkers (Dhakate et al., 2011). After expanding graphite flakes, they were re-intercalated, re-exfoliated, sonicated and centrifuges. They have reported an overall yield

of around 4–5 wt%. using the Raman spectroscopy. Also, they found that the graphene sheets were of high quality and free of defects (Gu et al., 2009).

Choi and coworkers (S. Y. Choi et al., 2011) employed an inductively coupled thermal plasma for thermal expansion of graphite intercalation compounds. Accordingly, the inductively coupled thermal plasma could heat the graphite intercalation compounds up to 5000 °K during a millisecond time period resulting in the rapid vaporization of the intercalated species. For high-yield production of defect free graphene sheets, acoustic cavitation was subsequently utilized. Figure 2.13 shows SEM images of expanded graphite after inductively coupled thermal plasma treatment and Raman spectra of four graphene sheets. Almost 12% of the graphene sheets were mono-layered with the conductivity range of $6.6 \times 10^3 \text{ S m}^{-1}$ to $8 \times 10^3 \text{ S m}^{-1}$.

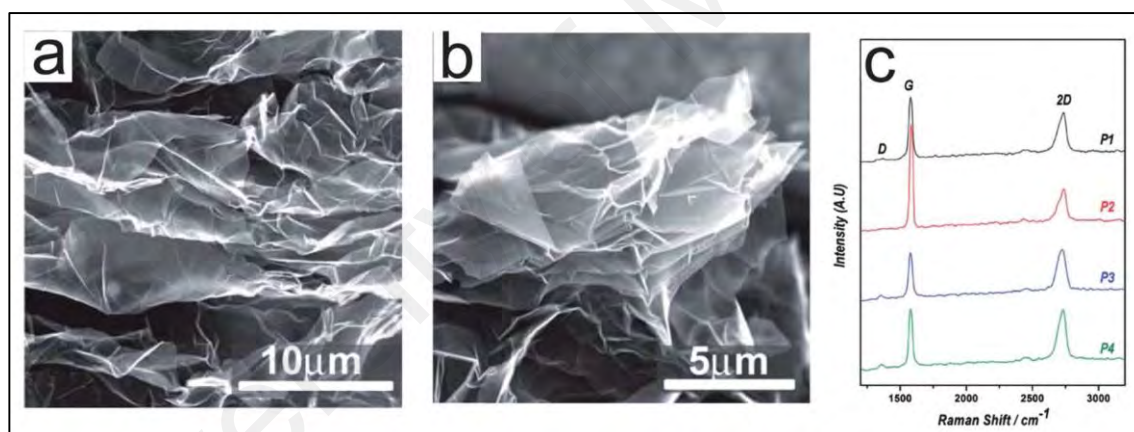


Figure 2.13: (a) and (b) SEM images of expanded graphite after inductively coupled thermal plasma treatment. (c) Raman spectra of four graphene sheets obtained with inductively coupled thermal plasma treatment method (S. Y. Choi et al., 2011).

Also, microwaves irradiation has been effectively utilized for exfoliating bulk graphite in different liquid or gas environments. As a microwave-assisted method to exfoliate bulk graphite, Janowska and coworkers attained a high-yield exfoliation of bulk graphite in an aqueous ammonia solution under microwave irradiation (Janowska et al., 2010). They produced graphene sheets with thickness less than 10 layers and a yield of almost 8 wt%. The outstanding wetting behavior of ammonia on graphite could develop the infiltration of bulk graphite, so this procedure could result in increasing the exfoliation

of graphite. Note that natural decomposition of NH_4OH to gaseous NH_3 and H_2O under microwave irradiation were also introduced as another parameter to enhance the exfoliation performance. J. Dong et al. (2010) were the first to use an ultrasonication method to prepare homogenous graphite dispersion followed by the microwave-assisted method for producing single and multilayered graphene.

Matsumoto et al. reported a microwave-assisted method for exfoliation of graphite suspended in molecularly engineered oligomeric ionic liquids (Matsumoto et al., 2015a). They reported exfoliation-efficiency of 93%, resulting in single-layer graphene with thicknesses less than 1 nm and a short processing time. The obtained graphene sheets were mostly mono-layered and damaged free. Similarly, Al-Hazmi et al. proposed a facile, cost-effective, and quick method for mass production of high quality graphene sheets (Al-Hazmi et al., 2015). After pretreatment of graphite flakes with glutaric acid, the treated graphite flakes were homogeneously dispersed into methanol and transferred into a microwave oven. A majority of graphene sheets were mono-layered and as the microwave power increased, the thickness of flakes decreased.

Highly-crumpled, few-layered graphene and highly-crumpled nitrogen-doped graphene with high surface area were produced by the present research group. These highly-crumpled materials were prepared by exfoliation of bulk graphite in the presence of liquid-phase using microwave-assisted methods.

Using ultrasonication a variety of method was proposed for the exfoliation of graphite and discussed in this section. Typically, liquid phase exfoliation is performed with ultra-sonication of bulk graphite in proper solvents that result in dispersions of defect-free graphene sheets at high concentrations. Nevertheless, exfoliation with ultrasonication has a key drawback in scalability. The production rate of few-layered graphene is measured by Eq. 2.1.

$$P_R = CV/t \quad (2.1)$$

where t , V and C are the production time, the liquid volume and the solution concentration, respectively. Eq. 1 shows that the solution concentration scales inversely with V , so the production rate could not be scaled up via adding solvent volume. This issue significantly limits the mass production of few-layered graphene by ultrasonication method (Paton et al., 2014). Shear exfoliation can address this issue and is discussed in the following section.

2.7 Shear Exfoliation

Shear mixing is a highly effective method for dispersing bulk graphite and other layered-materials that are weakly bound together in solvents (Murphy & Hull Jr, 1975; Niu et al., 2016). For this purpose, bulk graphite was pretreated with sulfuric acid to form the weakened interlayer bonding and is followed by conducting shear force exfoliation. However, the thickness of obtained sheets was high, ranging in 10 nm to 100 nm. In fact, the exfoliation performance was a function of the intercalation procedure rather than shear force, which may be considered as the main restriction for mass production of graphene. Recently, Paton and coworkers (Paton et al., 2014) addressed this issue. They showed that mass production of graphene sheets without defect is possible with use of high shear mixing of bulk graphite in proper solvents (Figure 2.14). To reach high yield exfoliation, mixers with rotating blades were utilized to form high shear rates in solvents, in which bulk graphite were loaded. The interaction between solvents and the bulk graphite permits the exfoliation. The solvents can also be used for stabilizing the produced nanosheets. The TEM images of graphene nanosheets are shown in Figure 2.14 panels (e-h). Paton et al. reported a histogram of nanosheet thickness and the presence of monolayers was confirmed by AFM and Raman spectroscopy, as shown in Figure 2.14 panel (i) (Paton et al., 2014). Accordingly, the exfoliation procedure occurred at the local shear rate up to 10^4 S^{-1} as revealed in Figure 2.14 panel (k). The scalability of this approach was studied by Paton et al.; since it is a function of the initial graphite concentration (C_i), mixing time

(t), rotor diameter (D), liquid volume (V) and rotor speed (N) (Paton et al., 2014). They found that there is a linear relationship between the production rate of 2D materials and the volume of solvents and provided initial conditions for mass production of 2D materials (Figure 2.14 panel (j)). They could exfoliate hundreds of liters with a production rate of 1.44 g h^{-1} for graphene, far larger than that of the ultrasonication approaches. This method could provide defect-free nanosheets with very low thickness and appropriate dimensions. More interestingly, shear exfoliation can be used for exfoliation of different multi-layered material into mono- and few-layered materials such as BN, WS_2 , MoSe_2 and MoTe_2 , as shown in Figure 2.14 panel (l).

For industrial applications, preparing a large quantity of mono- and few-layered graphene nanosheets with high quality is a must and this method can be a reasonable approach to reach this goal. Also, the graphene thin films obtained from this method showed a high electrical conductivity of 400 S cm^{-1} ; therefore, it can be used for solar cells applications as well as in micro-supercapacitors.

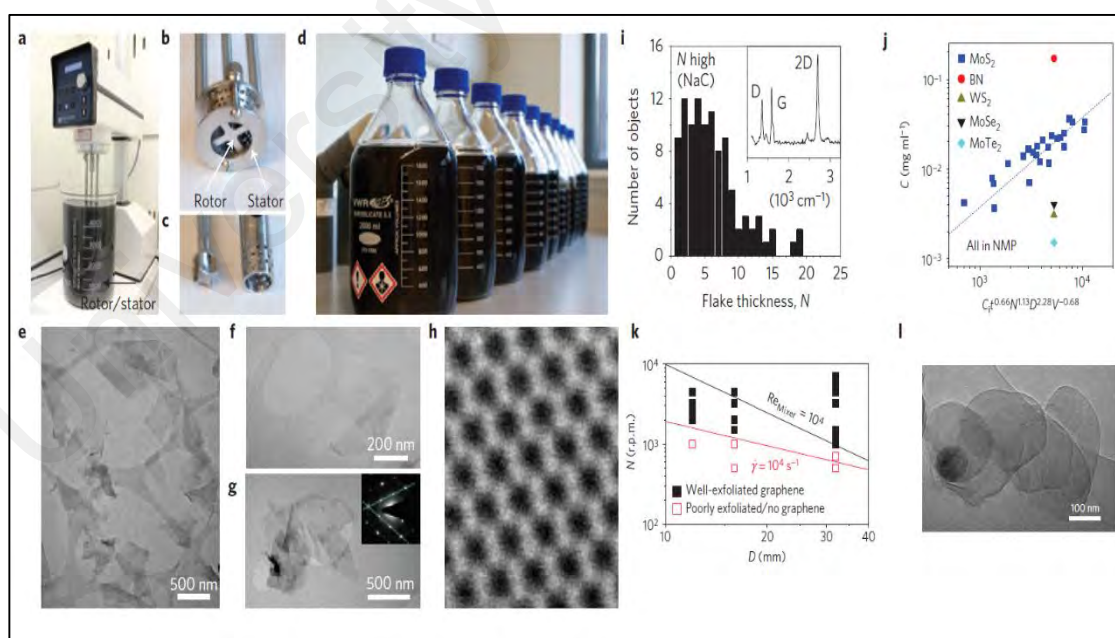


Figure 2.14: (a, b, c) Set-up of high shear mixer with close-up view of rotor and stator. (d), Mass-produced graphene–NMP dispersions via shear exfoliation. (e, f, g, h) TEM images of graphene nanosheets produced by shear exfoliation. (i), Histogram of graphene thickness and Raman spectrum (inset). (k) Diagram of rotor speed, N versus diameter, D (the red line shows a minimum shear rate of 10^4 S^{-1}). (l) TEM image of exfoliated BN flake. (Paton et al., 2014).

Shinde et al. developed a shear-assisted electrochemical exfoliation procedure to produce large graphene flakes with a high percentage of mono- and few-layered graphene (Shinde et al., 2016). The suggested method includes intercalation of sulfate ions and then shear-assisted exfoliation. Similarly, Tran et al. reported a shear-assisted exfoliation method for mass production of few-layered graphene (Tran et al., 2016). They showed a promising high-yield exfoliation of graphite into few-layered graphene by high shear mixing of bulk graphite and solvent in the Taylor vortex flow regime. They also showed that the obtained graphene was almost defect-free.

2.8 Electrochemical Exfoliation

Electrochemical exfoliation of graphite was suggested as a fast method in a two-electrode system. Simplicity of operation procedure, high yield exfoliation under different conditions, and the potential for mass production of mono layer graphene are of advantages of electrochemical exfoliation (Abdelkader et al., 2015). The main mechanism for electrochemical exfoliation is the intercalation of ionic species into multi-layered graphite under an electrochemical bias to expand the graphite layers, which can facilitate ultrasonic exfoliation as the second phase. Different anionic or cationic species have been employed to accelerate the intercalation phase. To perform anionic intercalation, bulk graphite material is installed in the setup as anode electrode and another material like platinum (Pt) as the cathode electrode. Su et al. used a graphite anode and Pt cathode to exfoliate graphite into the graphene with different electrolyte solutions, as shown in Figure 2.15a (Dimiev et al., 2011). They tested a quick electrochemical exfoliation in the presence of H₂SO₄-KOH solutions. They also studied the effects of different acids such as HBr, HCl, HNO₃ and H₂SO₄, and concluded that only H₂SO₄ is able to exfoliate bulk graphite. Note that KOH was applied for attenuating the severe oxidation effect of sulfuric acid to avoid introducing defects in graphene sheets. Despite the presence of defects, over 65% of exfoliated graphene sheets were very thin with a

thickness less than 2 nm. Similarly, Parvez et al. investigated the effect of higher acidic solution to exfoliate graphite into graphene (Parvez et al., 2013), resulting in high-performance electrochemically exfoliation (Figure 2.15b). To clear the main mechanism, water oxidation under bias voltage formed some radicals (e.g. hydroxyl and oxygen) which could easily react with edge sites and grain boundaries of graphite electrode. The presence of these defects could assist the intercalation of SO_4^{2-} into graphite interlayers. Therefore, the decomposition or release of gaseous SO_2 as well as anion depolarization expands the graphite. As a result, they could introduce a high yield of exfoliation method, representing that over 80% of graphite were exfoliated into graphene sheets with 1–3 layers. In addition, they also investigated the effects of different inorganic salts on the electrochemical exfoliation of graphite in aqueous solutions (Parvez et al., 2014; Z. S. Wu et al., 2015). Their method had a yield of 85% and produced large graphene sheets with a lateral size up to 44 μm and thickness less than 4 layers. Fabrication of a highly conductive graphene film was another advantage of this method.

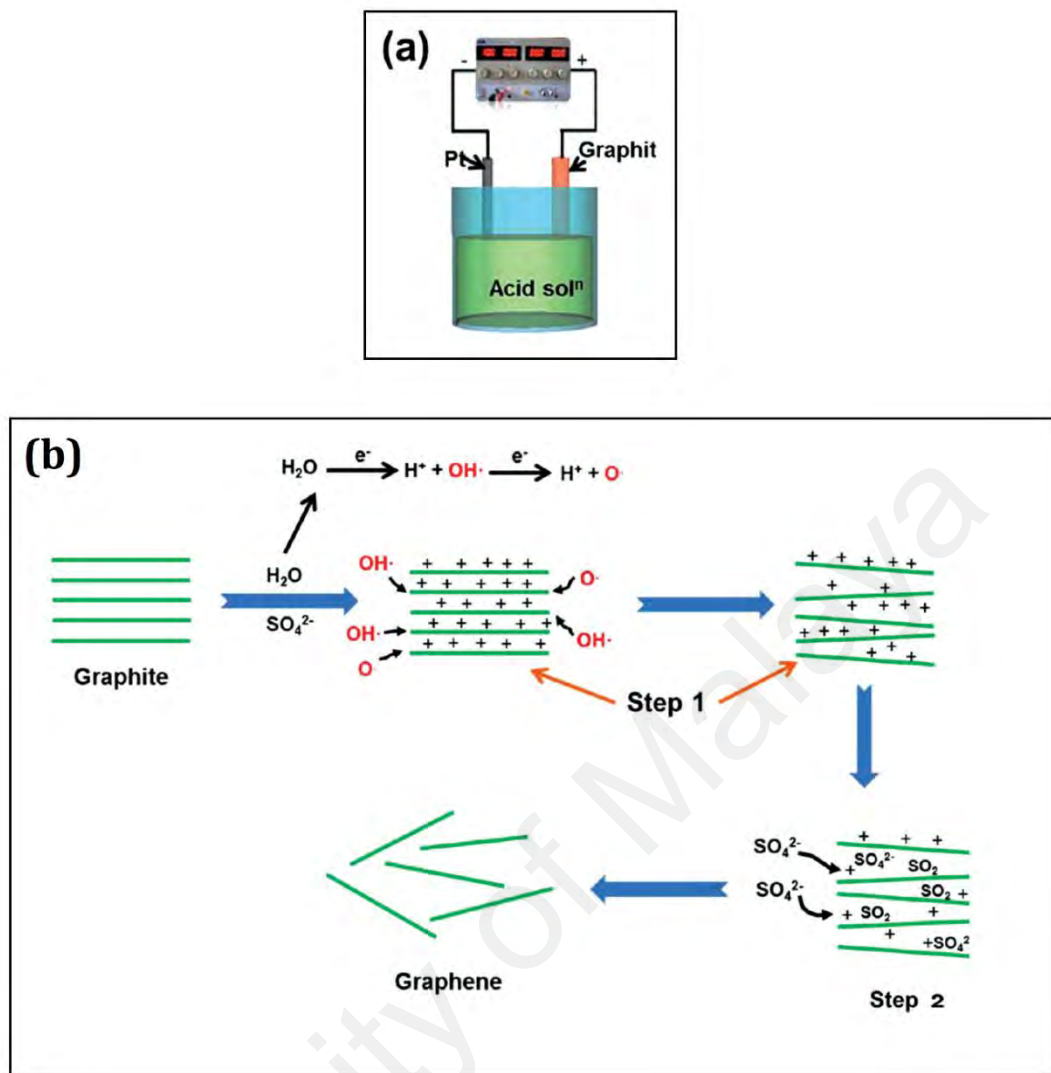


Figure 2.15: (a) Electrochemical exfoliation of bulk graphite in the presence of acids. (b) Suggested mechanism for electrochemical Exfoliation (Parvez et al., 2013).

Sulfonate salts can be suitable candidates for intercalating and subsequently exfoliation of bulk graphite. As an efficient electrolyte, poly (sodium-4-styrenesulfonate) was used by Wang et al. to synthesize graphene sheets under a voltage of 5 V (G. Wang et al., 2009). The yield of this method was 15% for production of mono- or few-layered graphene sheets. Wang and coworker. (G. Wang et al., 2009) demonstrated that the graphene dispersion has remained stable for 6 months without noticeable sedimentation. As the proposed mechanism, the edge-to-face interaction between aromatic ring of poly(sodium-4-styrenesulfonate) and the surface of graphene sheets was introduced to

facilitate the exfoliation. In a similar study, sodium dodecylbenzene sulfonate solution was selected as the electrolyte for electrochemical production of mono- and few-layered graphene by using 30 V for 48 h (Niu et al., 2016). Sodium dodecylbenzene sulfonate plays two important roles in electrochemically exfoliation of graphite: intercalant and surfactant. Mensing and coworkers (Mensing et al., 2012) proposed a quick electrochemical approach to produce graphene-metal phthalocyanines hybrid in the presence of copper phthalocyanine tetrasulfonic acid as electrolyte. The functionalized graphene was obtained using electrolysis of two graphite rod-electrodes and subsequently ultrasonication. Kuila and coworkers (Kuila et al., 2013) used 6-amino-4-hydroxy-2-naphthalene-sulfonic acid as the electrolyte and surface modifier for exfoliation of graphite anode. Functionalization of graphene and the presence of defects in graphene nanosheets were confirmed via different characterization instruments.

Liu et al. reported an electrochemical exfoliation method in the presence of 1-octyl-3-methyl-imidazolium hexafluorophosphate as an ionic liquid by using a two-graphite electrode test-rig (N. Liu et al., 2008). They could produce the graphene sheets with average thickness of 1.1 nm and the dimensions of 700 nm × 500 nm. According to their results (N. Liu et al., 2008), 1-octyl-3-methylimidazolium free radicals have enough potential to interact with π -electrons of graphene sheets, resulting an interaction between graphene sheets and ionic liquids and subsequently facilitating the exfoliation procedure.

Lu et al. utilized a new type of electrolyte, water-miscible ionic liquids such as 1-butyl-3-methylimidazolium tetrafluoroborate [BMIm][BF₄], to fabricate fluorescent carbon nanoribbons, nanoparticles, and graphene from graphite electrodes (Lu et al., 2009). According to their results, water as the main impurity in ionic liquids played a key role in performing ionic liquid-assisted electrochemical exfoliation. Using the fabrication of novel hydrogen-bonded networks, water seems to disrupt the internal organization of ionic liquids, causing anionic intercalation in the ionic liquid, expansion and exfoliation

of graphite into carbon nanoparticles, nanoribbons and graphene sheets (Lu et al., 2009). In addition, the ionic liquids electrolyte with water content higher than 10% could form soluble and oxidized carbon nanostructures. Due to high potential of this method of exfoliation, some other anionic species have also proposed to enhance the exfoliation of graphite anodes. For example, 9-anthracene carboxylate ion was applied as the electrolyte to exfoliate the graphite into the graphene sheets at constant voltage of 20 V (Khanra et al., 2012). Also, graphene sheets can be functionalized with 9-anthracene carboxylate ion during the procedure, representing oxidation of graphite over the electrochemical exfoliation. According to their proposed mechanism, 9-anthracene carboxylate ions were attached on the surface of graphite anode via electrostatic interaction, subsequently exfoliated into the graphene sheets under the electrical potential.

As another example, phosphate buffer solution was selected to perform electrochemical exfoliation of bulk graphite via cyclic voltammetry (F. Zeng et al., 2011). They showed that functionalization of graphite samples with oxygen in the intercalation procedure could weaken the interlayer attraction and, therefore, facilitate the exfoliation procedure upon the gas evolution.

According to the recent results (Abdelkader et al., 2015), the potentials needed for intercalating of anions are commonly higher than that of the potentials required for the oxidation of bulk graphite. Therefore, the formation of functionalized graphene sheets with some defects is inevitable, and this can be a harmful factor for electronic applications. In fact, after disrupting the π -electron system with functionalization, it seems impossible to reestablish the electronic structure of graphene, even by reduction (Niu et al., 2016). Therefore, the cathodic exfoliation was proposed to solve the aforementioned problem. Accordingly, Zhou and coworkers (M. Zhou et al., 2013) proposed a method for electrochemical exfoliation of a graphite cathode at low voltage (DC, 5 V) in the presence of Na^+ / DMSO as the intercalant. To produce the graphene

sheets with lower amount of functional groups (oxygen functional groups) and defects, sonication was employed (M. Zhou et al., 2013). Similarly, Yang and coworkers (Y. Yang et al., 2013) presented a high-performance cathodic exfoliation of graphite in an ionic liquid namely *N*-butyl, methylpyrrolidinium bis(trifluoromethylsulfonyl)-imide (BMPTF₂N). Their proposed mechanism of cathodic exfoliation in BMPTF₂N was the intercalation of ionic liquids cation, [BMP]⁺, under highly negatively charge, which provide conditions for graphite expansion. They also synthesized porous graphene sheets once KOH was used as the activation material.

Li⁺ can also be a promising alternative for intercalating the bulk graphite (Rocquefelte et al., 2000; Z. Zeng et al., 2011). For instance, Zeng et al. presented an efficient approach to generate mono-layered MoS₂, WS₂, TiS₂, TaS₂, ZrS₂ and graphene by a controllable lithiation procedure. They firstly put bulk layered material such as graphite into an electrochemical test-rig as cathode, and the Li foil were selected as anode for preparing the required Li ions (Z. Zeng et al., 2011). Note that the whole procedure was accomplished within 6 h at ambient temperature and the production of mono-layered materials yielded up to 92%. Also, Wang et al. reported a high-performance method for exfoliation of graphite (yield of 70%) (J. Wang et al., 2011). To this end, the negative graphite electrode was charged electrochemically and subsequently expanded in an electrolyte of Li salts and propylene carbonate (J. Wang et al., 2011).

2.9 Exfoliation Summary and Conclusion

In this part of literature review, different methods for mass production of few-layered graphene have been investigated. Selecting a cost-effective, efficient and facile method for scalable production of large quantities of few-layered graphene is the most important purpose of this part of study. Like different processing methods, liquid phase exfoliation has both merits and demerits. Among the merits, liquid phase exfoliation is obviously a scalable method, which is capable to prepare graphene nanosheets extremely

cheap. Also, it is significantly simple and prepares the practical concentrations up to 1 mg mL⁻¹. Using functionalization, the exfoliation yield can enhance. Importantly, the required graphene nanosheets for the present application, which has improved heat transfer with nanofluids, should have some properties such as high specific surface area, high thermal conductivity, superior stability in aqueous media and tend to be defect free. Nonetheless, because of significant π - π interactions and trivial interaction between pure graphene sheets and other materials, raw graphene tends to agglomerate in aqueous and organic media. To enhance the interactivity of raw graphene as well as its stability in different base fluids after exfoliation, surface functionalization was suggested as a general solution elsewhere. Accordingly, various functionalities have been applied to increase the interactivity and stability of graphene sheets in liquids. Different methods of functionalization are described in the following sections. This part of review shows all modes and methods of graphene functionalization including their classification.

2.10 Functionalization by Covalent Bonding

2.10.1 Covalent Attachment of Organic Functionalities

Numerous chemical processes for generating dispersible graphene, which are based on different exfoliation procedures, chemical vapor deposition, reduction of graphene oxide were proposed in the literature (Dreyer et al., 2010; D. Li et al., 2008). The main aim is to produce dispersible graphene sheets in various solvents which are typically achieved by covalent functionalization with organic functional groups. It is also well known that the direct dispersion of hydrophobic graphene sheets in polar solvents is a major challenge (D. Li et al., 2008). The covalent functionalization of graphene sheets is done by two methods:

- (i) Initiation of covalent bonds between C=C bonds of pristine graphene and free radicals

- (ii) Initiation of covalent bonds between oxygen groups of GO and organic functional groups.

Due to lack of defects and graphitic structure, graphene has higher thermal conductivity compared to graphene oxide (Wei Yu et al., 2011). Therefore, it is more interesting to investigate the thermal transport properties of graphene-based nanofluids, and to explore the improvement in the thermo-physical and thermal properties of basefluids. Hence, the present literature review is focused on covalent functionalization of graphene sheets.

According to the recent studies on different carbon nanostructures (Hossain et al., 2010; Niyogi et al., 2010; Sharma et al., 2010; Zardini et al., 2012), organic free radicals can be classified as the most promising organic groups for the reaction with sp^2 carbons of graphene.

2.10.1.1 Functionalization by Free Radicals

Sinitskii et al. and Kosynkin et al. prepared a reactive free radical by heating of a diazonium salt to attack the sp^2 carbon atoms of graphene, resulting in nitrophenyls-functionalized graphene (Kosynkin et al., 2009; Sinitskii et al., 2010). Upon chemically-unzipping of carbon nanotubes (CNT), the graphene sheets were generated. Similarly, Niyogi and coworkers (Niyogi et al., 2010) proposed the covalent functionalization of graphene sheets with nitrophenyls. X-ray photoelectron spectroscopy (XPS) was used to analyze the covalent attachment of the nitrobenzyl groups on the surface of graphene (Figure 2.16). There are two peaks at 406 and 400 eV in the N1s XPS spectrum of the nitrobenzyl-functionalized graphene, representing the presence of the nitrogen of NO_2 and reduced nitrogen, respectively. Note that the reactions with diazonium salts have been employed to functionalize different carbon-based nanostructures (Ghiadi et al., 2013; Z. Jin et al., 2009; Lomeda et al., 2008; Sharma et al., 2010).

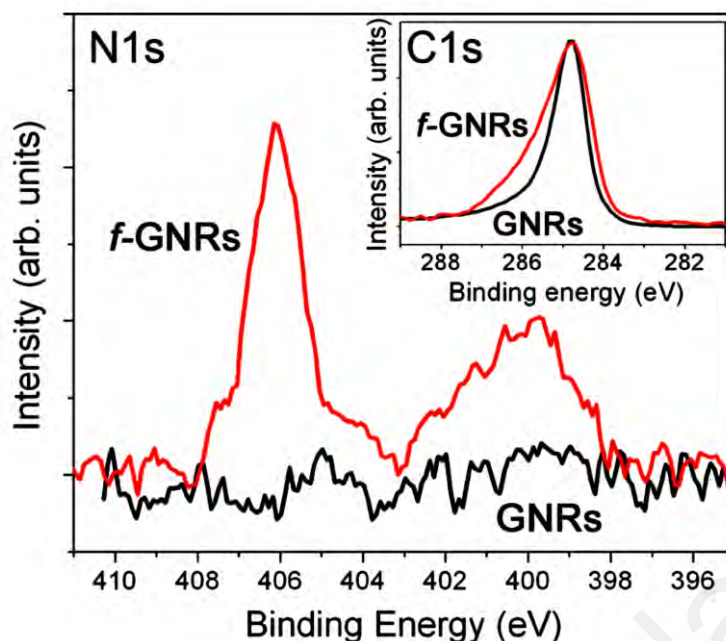


Figure 2.16: N1s and C1s XPS spectra of the functionalized GNR and GNRs (Niyogi et al., 2010).

Fang and coworkers (Fang et al., 2009) reported a promising approach to functionalize graphene nanosheets via a diazonium addition. They functionalized individual and multi-layer graphene sheets (size range: 20–40 nm) with linear polystyrene (Figure 2.17). According to their results and those of Ruoff and coworkers (S. Park & Ruoff, 2009; Zhu, Stoller, et al., 2010), as the size of graphene sheets decreases, the interlayer cohesive energy reduces, implying lower effective viscosity of suspension.

The ratio of sp^2 hybridized carbon to sp^3 ones (I_D/I_G) in the graphitic lattice is helpful to indicate the degree of functionalization. Raman spectroscopy is also a powerful instrument to measure the I_D/I_G ratio. It should be noted that pure graphene is a 2D sp^2 hybridized carbon sheet and the presence of sp^3 carbons in the lattice points to the presence of defects. Note that such defects may be present in the basal edges and/or the plane.

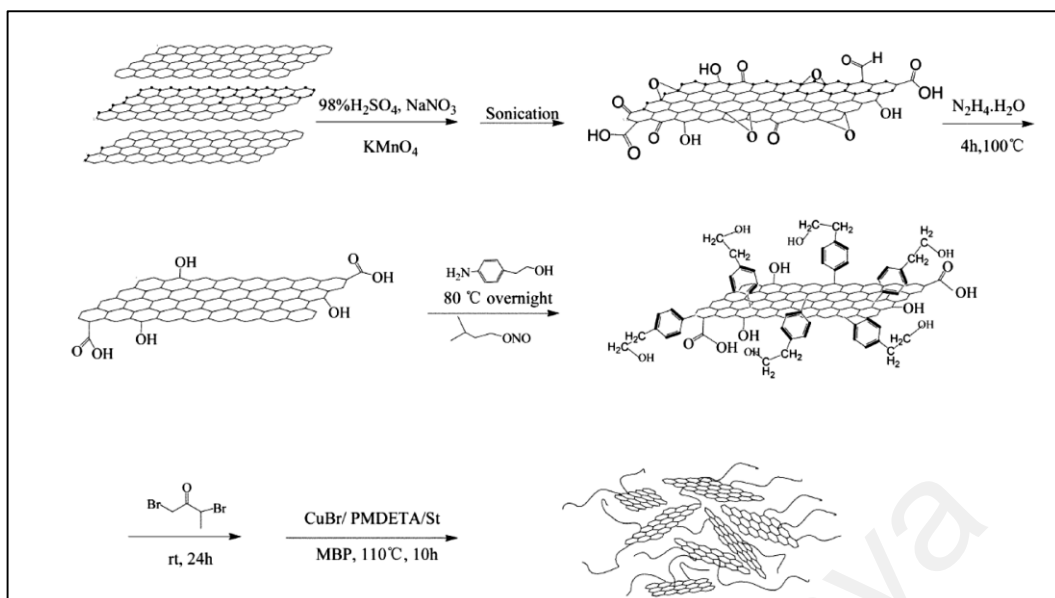


Figure 2.17: The functionalization procedure of graphene nanosheets by polystyrene (Fang et al., 2009).

Figure 2.18 panel (a) shows that the I_D/I_G ratio of samples increases from 1.7 to 2 after diazonium addition reaction (Haitao Liu et al., 2009). The functionalization of graphene sheets with phenyl groups is confirmed by the presence of a sharp D band at 1343 cm^{-1} seen in Figure 2.18 panel (b), which is in good agreement with the presence of defects on the graphene surface.

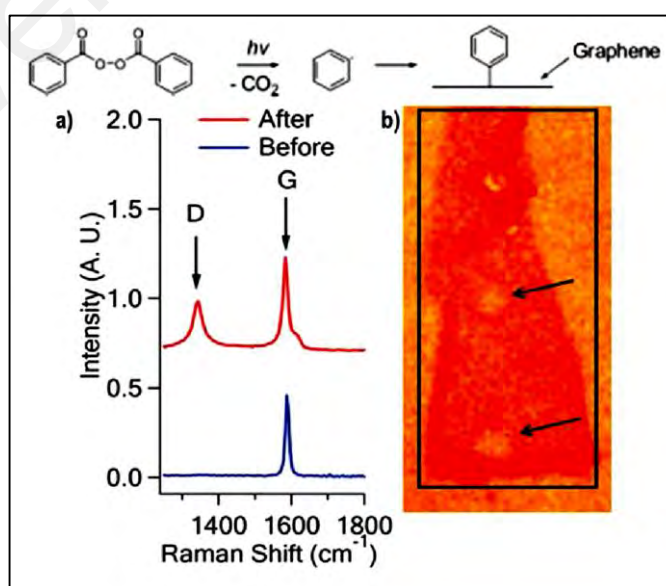


Figure 2.18: Radical addition reaction mechanism. (a) Raman spectra of a mono layer graphene after and before functionalization and (b) optical image of a functionalized mono layer graphene with some holes or defects (Haitao Liu et al., 2009).

Recently, present research group (W. Sarsam et al., 2016b) proposed a new and quick synthesis method for synthesizing triethanolamine-treated graphene nanoplatelets. Using an electrophilic addition reaction, they could functionalize graphene nanoplatelets via molecules including hydroxyl (OH) groups e.g. triethanolamine. They could synthesized water-based graphene nanoplatelets nanofluids with high stability (W. Sarsam, et al., 2016b). The triethanolamine-functionalized graphene nanoplatelets with different weight concentrations and specific surface areas showed appropriate stability in aqueous media. The direct coupling of graphene nanoplatelets with free radical of triethanolamine was confirmed by several characterization methods as shown in Figure 2.19.

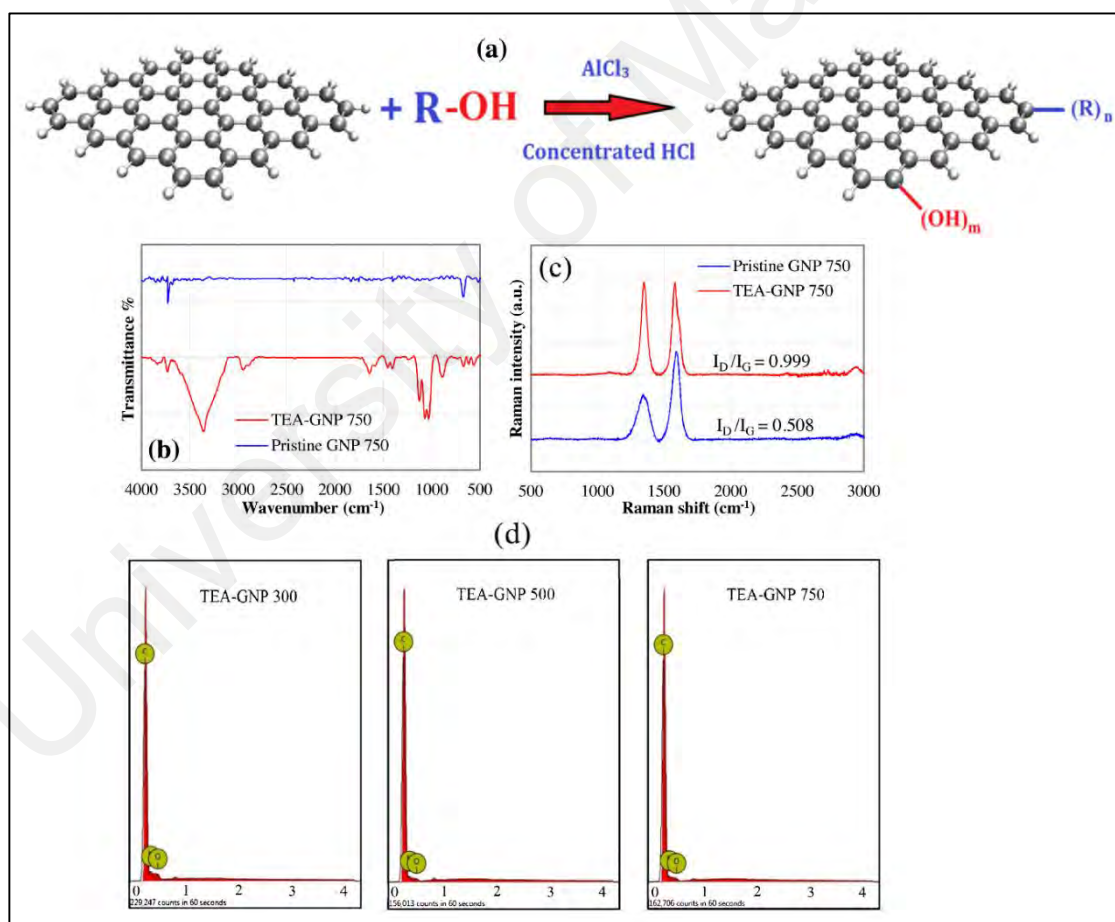


Figure 2.19: (a) Schematic of Electrophilic addition reaction. (b) FTIR spectra (c) Raman spectra, and (d) energy dispersive X-ray spectroscopy traces of the triethanolamine-treated graphene nanoplatelets (EDS traces are presented for different specific surface areas).

The higher I_D/I_G ratio of triethanolamine-treated graphene nanoplatelets compared to that of the pristine sample, where the appearance of some meaningful bands in FTIR spectrum and the presence of different elements in energy dispersive X-ray spectroscopy (EDS) results confirm the successful attachment of functional groups on graphene nanoplatelets.

2.10.1.2 Functionalization by Dienophiles

Like free radicals, dienophiles also can easily decorate on the graphene surface with quick reaction with sp^2 carbons. As one of the dienophiles, Azomethine ylide has been commonly used to functionalize different carbon-based nanostructures. In fact, Azomethine ylide reacts mostly through a 1,3 dipolar cycloaddition (Georgakilas et al., 2012). In fact, 1,3 dipolar cycloaddition reaction can be employed for a number of organic derivatives and plays a key role in increasing the performance of different applications such as nanoelectronic devices, polymer composites, drug delivery, solar cells and biotechnology (Dabiri et al., 2016; Georgakilas et al., 2008; Kostarelos et al., 2007). Georgakilas and coworkers (Athanasios B. Bourlinos et al., 2009) produced graphene sheets via direct sonication of pristine graphite in organic solvents, and subsequently performed the substitution of graphene sheets with pyrrolidine rings by a 1,3 dipolar cycloaddition of azomethine ylide (Georgakilas et al., 2010).

The dihydroxyl phenyl-functionalized graphene sheets were generated perpendicular to the graphene surface after the attachment of azomethine ylide precursors, which is shown in Figure 2.20 (Georgakilas et al., 2010). Due to the introduction of hydroxyl groups onto the graphene sheets, their dispersibility was significantly enhanced in polar solvents (e.g. ethanol). The significant increase of the ratio of I_D/I_G verified the appearance of sp^3 planar carbon atoms, implying successful functionalization (Figure 2.20).

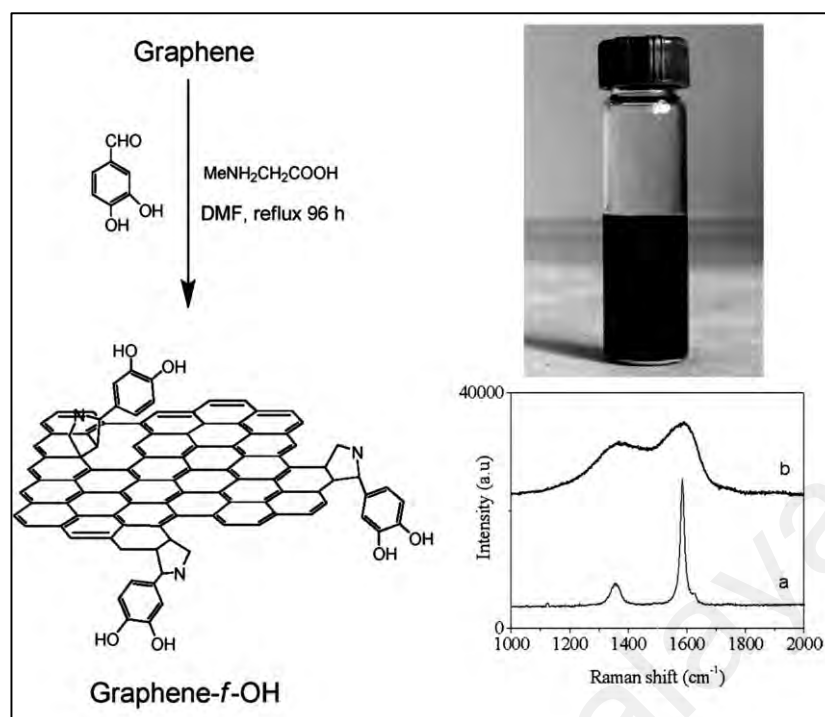


Figure 2.20: The 1,3 dipolar cycloaddition reaction for decorating the surface of graphene with azomethine ylide (left). Ethanol-based Functionalized graphene nanoplatelets dispersion (top, right). Raman spectra of (a) pristine graphene and (b) pyrrolidine functionalized graphene (bottom, right) (Georgakilas et al., 2010).

Park and Ruoff (S. Park & Ruoff, 2009) reported the prepared large few-layered graphene sheets with sizes ranging between 500 nm and 1 mm. Their morphological studies using TEM and AFM are shown in Figure 2.21. Their AFM images illustrate a mono layered graphene with a thickness of 1.5 nm. According to the recent studies (Nemes-Incze et al., 2008; S. Park & Ruoff, 2009), monolayer graphene without any modification has a thickness between 0.6 and 0.9 nm; therefore, the increase in graphene layer thickness was attributed to the functional groups across the surface of graphene sheets.

Dipolar cycloaddition can be employed for several aldehydes to yield the degree of functionalization for desirable functional groups (Georgakilas et al., 2012). Due to this flexibility, the current reaction procedure has attracted numerous researchers in this field of study.

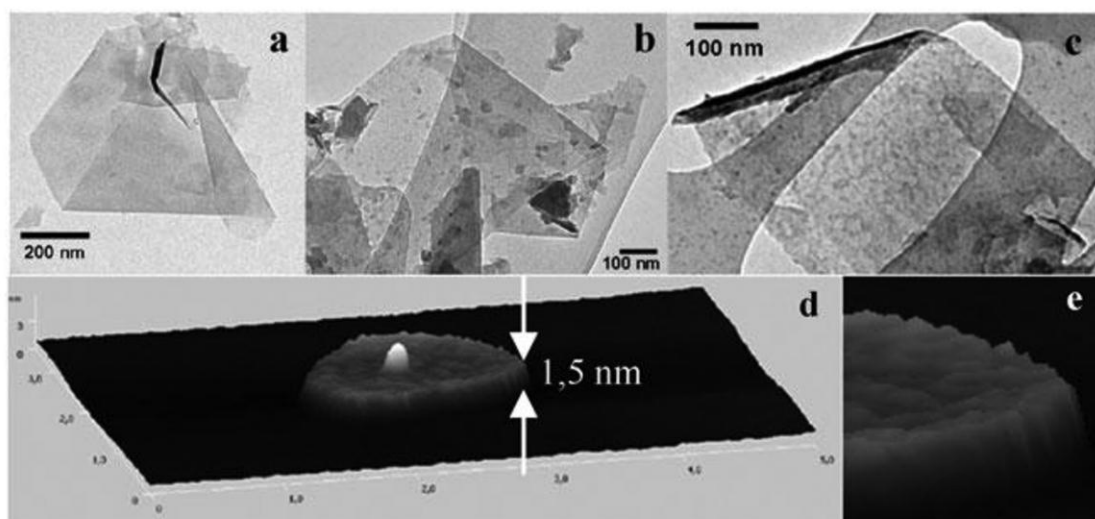


Figure 2.21: (a, b, c) TEM images and (d, e) AFM images of the functionalized graphene sheets (S. Park & Ruoff, 2009).

Zhang et al. (X. Zhang et al., 2011) utilized tetraphenylporphyrin aldehyde and sarcosin as precursors to attach tetraphenylporphyrin (TPP) on the surface of graphene sheets. Also, Quintana and coworkers (Quintana et al., 2010) used paraformaldehyde as precursor to functionalize graphene flakes with 1,3-dipolar cycloaddition reaction and NH_2 -terminated α -amino acid was obtained. To selectively bind gold nanorods, the decorated amino groups were applied.

Upon the creation of the reactive intermediate nitrene, phenyl and alkyl azides can easily attach to the graphene surface. Therefore, for producing different organic graphene derivatives, some researchers have used the effective reaction of organic azides with graphene sheets. For example, Liu and coworkers (L.-H. Liu et al., 2010) employed aforementioned method to decorate different functionalities to the graphene sheets via a three-membered aziridine ring. They have used this method for functionalization of graphene sheets with perfluorophenylazides (PFPA) with thermal and photochemical methods. Figure 2.22 shows the functionalization procedure of pristine graphite with perfluorophenylazides. Solubility of the PFPA-treated graphene sheets was significantly higher than that of pristine samples.

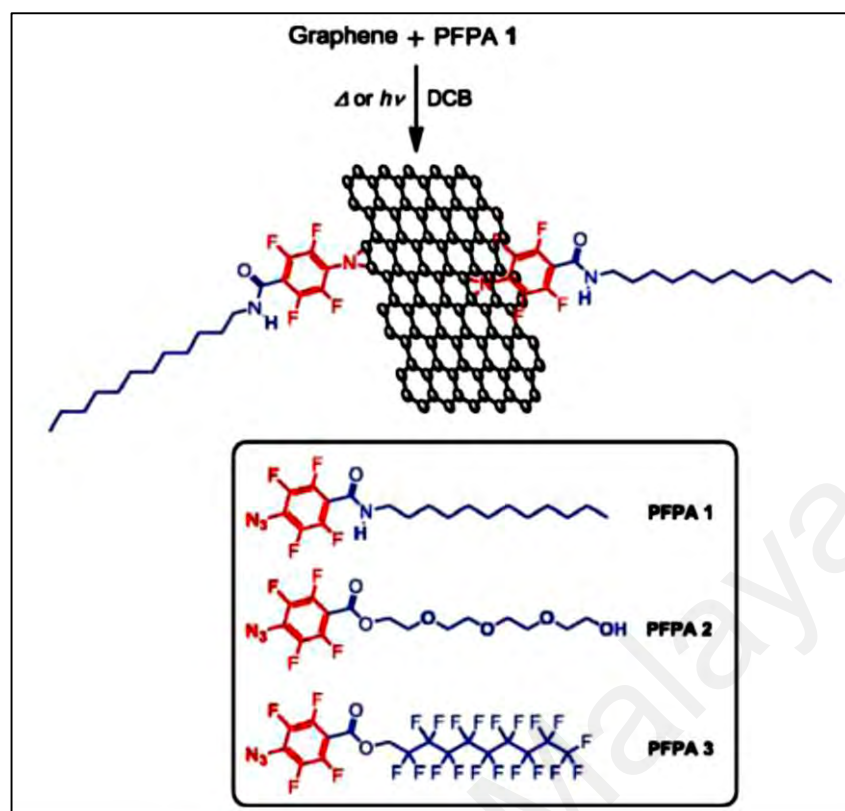


Figure 2.22: Edge-functionalization of pristine graphene with perfluorophenylazides (L.-H. Liu et al., 2010).

Nitrene addition reaction is a suitable method for functionalization of graphene sheets. Strom and coworkers (Strom et al., 2010) presented a high performance approach to functionalize graphene sheets via nitrene addition of azido-phenylalanine [Phe(N₃)]. This procedure was used to exfoliate bulk graphite into few layer graphene. Moreover, nitrene addition of azido-phenylalanine could provide a direct method for reaching high-degree of functionalization for graphene sheets. They could introduce a high degree of functionalization, representing 1 phenylalanine substituent per 13 carbons.

Vadukumpully et al. also reported a quick and efficient method for the covalent functionalization of graphene sheets (Vadukumpully et al., 2011). They functionalized dispersible surfactant wrapped graphene sheets (CTAB-graphene) with different alkylazides. Applied alkyl chains had several groups such as hexyl, hydroxyl-undecanyl, dodecyl, and carboxy-undecanyl (Vadukumpully et al., 2011). According to their

results 11-azidoundecanoic acid is the best type of azide for improving dispersibility and the alkylazides-functionalized samples illustrated high dispersibility in organic solvents like toluene and acetone. The functionalization of graphene sheets with various alkylazides is shown in Figure 2.23 panel (a). The corresponding Raman results is shown in Figure 2.23 panel (b), showing an increase in the I_D/I_G ratio after functionalization with nitrene addition method (Vadukumpully et al., 2011). Consist with Raman results, the amount of nitrene play a key role in increasing the degree of functionalization.

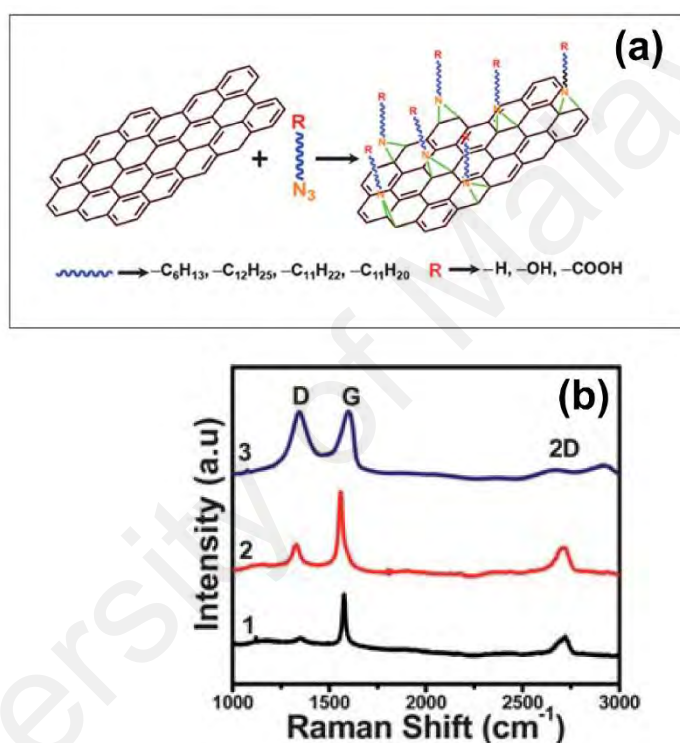


Figure 2.23: (a) Functionalization of graphene sheets with alkyl nitrenes. (b) Raman spectra of graphene sheet before (1) and after functionalization of graphene sheets with 11-azidoundecanoic acid in 1:1 (2) and 10:1 (3) ratios (Vadukumpully et al., 2011).

He and Gao introduced an efficient and useful nitrene cycloaddition reaction for functionalization of graphene sheets with polymeric chains and different functional groups (Hongkun He & Gao, 2010). Interestingly, this functionalization method can be applied to covalently bond different functional moieties and polymers to the graphene sheets, representing functionalized 2-D graphene sheets and 2-D macromolecular brushes, respectively. As a result, the treated samples demonstrated higher chemical and thermal stabilities compared to that of graphene oxide. The modified graphene sheets

showed high electrical conductivity and showed great stability and dispersibility in solvents (Hongkun He & Gao, 2010). Figure 2.24 illustrates the photographs of functionalized graphene nanosheets dispersion in various solvents after sonication. A higher dispersibility of graphene sheets in various solvents are obvious after covalently functionalization.



Figure 2.24: The photographs of functionalized graphene nanosheets dispersion in solvents after sonication: hydroxyl-functionalized graphene in water (1) and DMF (2), carboxyl-functionalized graphene in water (3) and DMF (4), poly(ethylene glycol)-functionalized graphene in water (5) and DMF (6), long alkyl chain-functionalized graphene in chloroform (7) and toluene (8), polystyrene-functionalized graphene in chloroform (9) and toluene (10), amino-functionalized graphene in water/chloroform (12), graphene oxide in chloroform (13), and reduced graphene oxide in DMF (14) (Hongkun He & Gao, 2010).

Similarly, Choi et al. proposed a method for covalent functionalization of graphene sheets with thermally generated nitrene J. Choi et al. (2009). Upon selecting the amount of nitrene in the functionalization procedure, the band gap of the functionalized graphene sheets was controlled. Zhong et al. also proposed a facile method to produce aryne-functionalized graphene sheets via aryne cycloaddition (Zhong et al., 2010). Using 2-(trimethylsilyl)aryl triate as a precursor along with reactive benzyne intermediate were employed to do aryne cycloaddition. The aryne-functionalized graphene sheets showed a significant stability in different solvents such as DMF, *o*-DCB, ethanol, chloroform, and water. The functionalization procedure resulted in the attachment of a four-membered ring, decorating graphene surface with the aromatic arene rings (Figure 2.25). Additionally, different interesting derivatives have been synthesized by substituting of

organic groups with the aryl rings. Figure 2.25 also shows the great dispersibility of functionalized graphene sheets in DMF (Zhong et al., 2010).

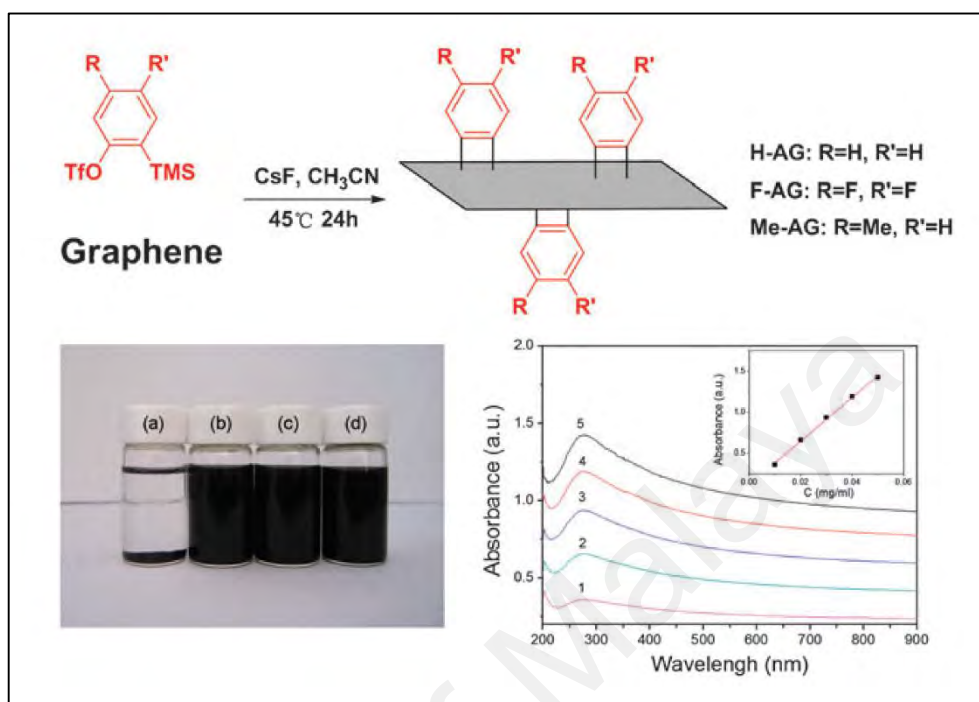


Figure 2.25: (top) The schematic of chemical functionalization of graphene sheets via aryne cycloaddition. (Bottom left) Photographs of graphene sheets and aryne-modified graphene sheets dispersions in DMF: (a) graphene sheets, (b) F- aryne-modified graphene sheets, (c) Me- aryne-modified graphene sheets and (d) H- aryne-modified graphene sheets. (Bottom right) (B) UV-vis absorption spectra of Me- aryne-modified graphene sheets dispersed in ethanol with different concentrations (J. Choi et al., 2009).

2.11 Covalent Attachment of Functionalities to Graphene Oxides

Graphene oxide is a single graphitic monolayer with randomly distributed sp^2 carbon atoms (aromatic regions) and oxygenated aliphatic regions (sp^3 carbon atoms) containing hydroxyl, epoxy, carbonyl, and carboxyl functional groups. Due to numerous defects and the presence of lots of functional groups containing oxygen on the surface of graphene oxide limits its suitability for heat transfer applications. In fact, due to the acidic groups on the hydrophilic structure of graphene oxide, it can introduce large amount of corrosion in different metal-based equipment. Also, graphene oxide mostly generates unstable dispersions in water and other polar organic solvents including ethylene glycol,

THF, and DMF (Georgakilas et al., 2012). Furthermore, exfoliated graphene oxide nanoplatelets have a tendency to aggregate through π - π stacking to produce large particles. So, in order to stabilize graphene oxide in different solutions, some protective agents were suggested (Y. Liang et al., 2009; N. Liu et al., 2008; Su et al., 2009; Watcharotone et al., 2007). It is obvious that using these stabilizers cannot be favorable for applying in technological applications and such works are however outwith the scope of this thesis.

It should be noted that a percentage of oxygen groups and defects on graphene oxide remain after any reductive treatment procedures. These defects can also decrease the properties of the reduced graphene oxide, notably its electric and thermal conductivities. For this reason and in order to reach maximum heat transfer, this study only focuses on the pristine graphene.

2.12 Noncovalent Functionalization of Graphene sheets

Upon manipulating van der Waals interaction and/or exposing ionic interaction between a molecule and graphene sheets, noncovalent functionalization of graphene is occurred. Jaegfeldt et al. reported that the pyrene moiety have a severe affinity toward the basal plane of graphite via π -stacking (Jaegfeldt et al., 1983). Similarly, a stable water-based graphene nanoplatelets dispersion was synthesized using 1-pyrenebutyrate as one of the water-soluble pyrene derivatives (Y. Xu et al., 2008). To make the stable water-based graphene nanoplatelets dispersions, graphene oxide was initially reacted with pyrenebutyric acid and subsequently the pyrenebutyric acid-treated graphene oxide was reduced chemically in the presence of hydrazine (Y. Xu et al., 2008). They finally could produce graphene oxide and pyrenebutyric-treated graphene nanoplatelets (Figure 2.26) with thickness of 1.3 and 1.7 nm, respectively.

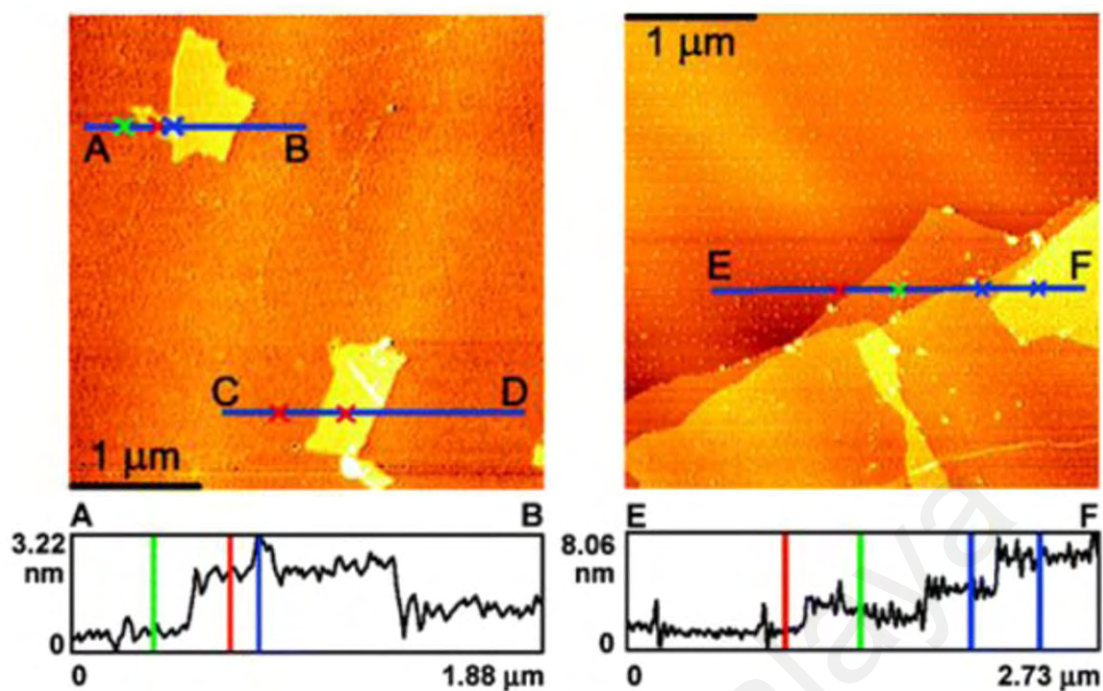


Figure 2.26: (left) AFM images of graphene oxide and (right) pyrenebutyric-treated graphene nanoplatelets on mica (Y. Xu et al., 2008).

Also, Wang et al. functionalized the graphene sheets with pyrene butanoic acid succidymidyl ester to enhance the power conversion performance of graphene (Y. Wang et al., 2009). An et al. also could prepared 1-pyrenecarboxylic acid-treated graphene films with noncovalent (π -stacked) pyrenecarboxylic acid with graphene sheets to prepare films with excellent optical and molecular sensing properties (X. An et al., 2011).

Yang et al. synthesized stable water-based graphene nanoplatelets suspensions with a high volume fractions (0.6–2 mg/mL) using the reduction of graphite oxide (Q. Yang et al., 2010). They used sodium lignosulfonate, sodium carboxymethyl cellulose, and pyrene-containing hydroxypropyl cellulose (HPC-Py) to reduce graphite oxide chemically. Kodali et al. proposed a method for noncovalently functionalization of graphene sheets via pyrenebutanoic acid-succinimidyl ester, resulting in production of flakes without disrupting structure (Kodali et al., 2010). In a majority of noncovalent functional groups, the attachment of the substituted molecules and graphene was attributed to the van der Waals interactions (Lopes et al., 2010). Recently, Su et al. offered

a promising method for functionalization of graphene sheets with pyrene and perylenediimide (Su et al., 2009). They could synthesize a stable aqueous dispersion including mostly mono and double layer graphene sheets.

As another type of noncovalent functional groups, DNA can be employed as stabilizer for developing the stability of graphene in aqueous media and other basefluids. For instance, Liang et al. could functionalize graphene sheets with single-stranded DNA, non-covalently (Y. Liang et al., 2009). They initially oxidized graphite to graphene oxide and subsequently performed the hydrazine reduction in the presence of single-stranded DNA (Y. Liang et al., 2009). The produced graphene nanosheets presented a high concentration in aqueous media, ranging as high as 2.5 mg/L.

In a similar study, for deposition of gold nanoparticles on graphene sheets, Liu et al. produced thiolated DNA oligonucleotides-functionalized graphene nanoplatelets (Jinbin Liu et al., 2010). This procedure included adsorbing thiolated DNA oligonucleotides on graphene oxide nanoplatelets and reducing thiolated DNA oligonucleotides-functionalized graphene oxide via hydrazine to thiolated DNA oligonucleotides-functionalized reduced graphene oxide (Jinbin Liu et al., 2010). The resulting functionalized materials had a unique solubility in aqueous media. Subsequently, gold nanoparticles were poured into the aqueous solutions of thiolated DNA oligonucleotides-functionalized reduced graphene oxide to form a homogenous suspension. The reported mechanism is shown in Figure 2.27.

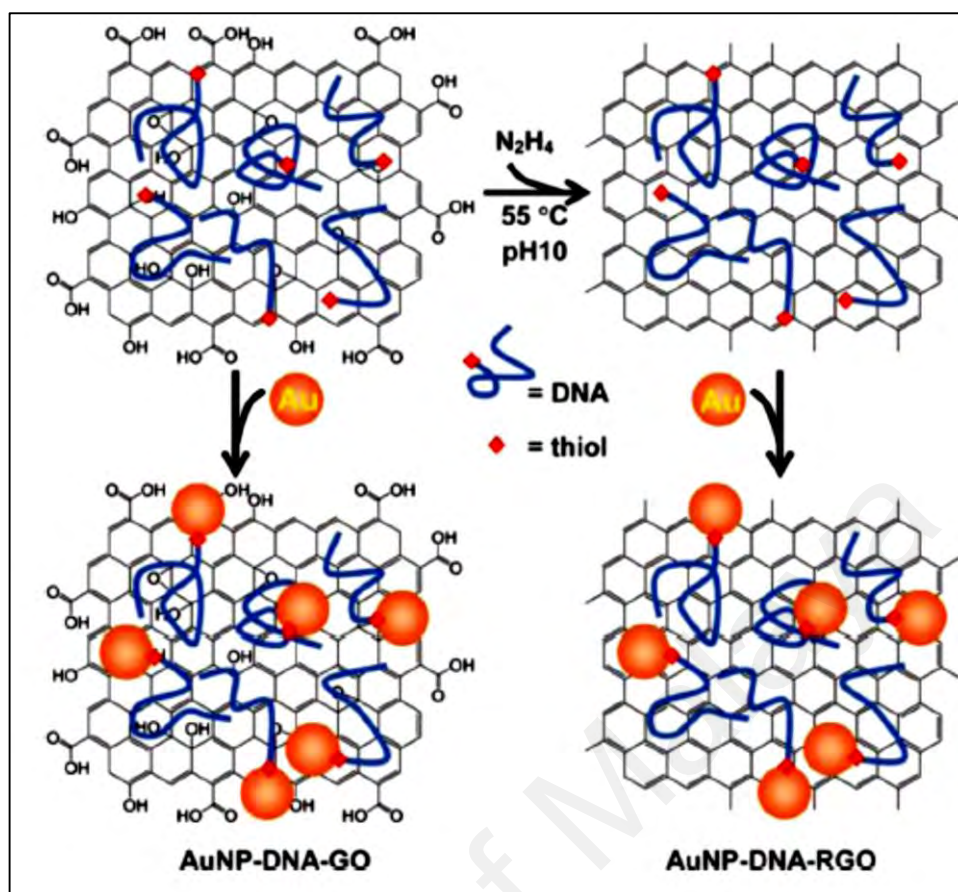


Figure 2.27: DNA coating, metal coating and aqueous dispersion of graphene oxide and Reduced graphene oxide (Jinbin Liu et al., 2010).

It is well known that methyl green has a positive charge with high solubility in aqueous media, therefore it is a promising candidate for adsorbing on the graphite surface via π - π stacking, weakening the powerful van der Waals interactions between layers. Therefore, the adsorption of methyl green onto graphite can dramatically increase the solubility of exfoliated graphene and graphite in aqueous media. To address this issue, Tu et al. functionalized graphene flakes via water-soluble picket-fence iron porphyrin (Tu et al., 2010). As shown in Figure 2.28, they presented a stable and homogenous picket-fence iron porphyrin-treated reduced graphene oxide in water (Tu et al., 2010).

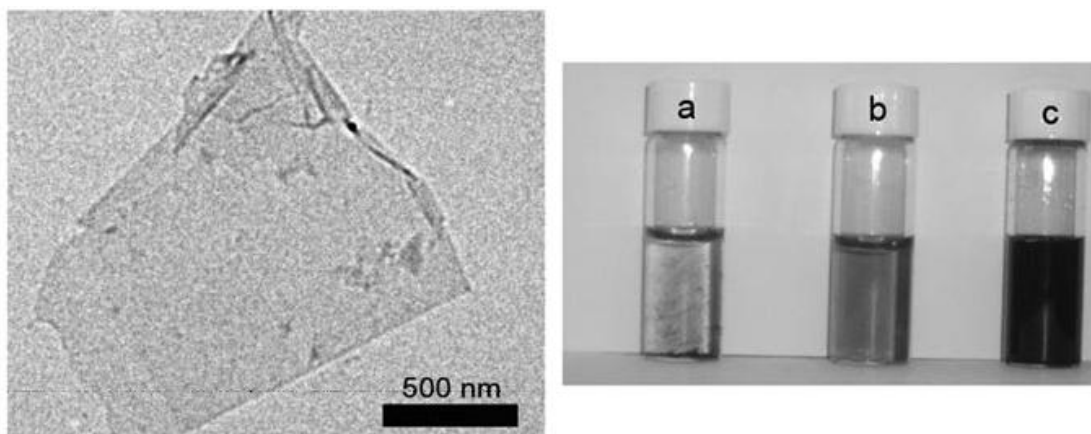


Figure 2.28: TEM images of (left) 5,10,15,20-tetrakis α -2-trimethylammoniumethylphenyl] porphyrin iron (III) pentachloride/Reduced graphene oxide; and (right) photographs of a) Reduced graphene oxide, b) 5,10,15,20-tetrakis [$\alpha\alpha\alpha\alpha$ -2-trimethylammoniumethylphenyl] porphyrin iron (III) pentachloride, and c) 5,10,15,20-tetrakis [α -2-trimethylammoniumethylphenyl] porphyrin iron (III) pentachloride (0.1 mg mL^{-1}) dispensed in water (Tu et al., 2010).

In a similar way, porphyrin-functionalized graphene nanoplatelets were synthesized via hydrazine reduction of graphene oxide with water-soluble porphyrins (Geng & Jung, 2010). Zhang et al. proposed a method for noncovalently functionalization of graphene nanoribbons with water-soluble iron (III) meso-tetrakis(*N*-methylpyridinium-4-yl) porphyrin (S. Zhang et al., 2011). They employed π - π noncovalent interaction on an electrode surface to increase the degree of functionalization. Note that the resulting Iron (III) meso-tetrakis(*N*-methylpyridinium-4-yl) porphyrin-adsorbed graphene nanoribbons composite film illustrated unique electrocatalysis for being used as a biosensor for the detection of glucose in human serum (S. Zhang et al., 2011).

Bai et al. reported a noncovalent functionalization method for synthesizing sulfonated polyaniline-graphene nanoplatelets (Bai et al., 2009). The resulting products were significantly soluble in water and remained stable for more than two weeks. Because of the electrostatic repulsion between negatively charged sulfonated polyaniline-graphene nanoplatelets as well as severe π - π stacking between the graphene basal planes and the

main structure of sulfonated polyaniline, the resulting sulfonated polyaniline-graphene nanoplatelets presented suitable stability at pH of 1–2 (Bai et al., 2009).

Li and his coworkers (F. Li et al., 2010) non-covalently synthesized an extremely soluble congo red-treated graphene nanoplatelets composite by direct coupling. They claimed that the resulting materials have significant solubility in different organic solvents as well as in water. It can be seen in Figure 2.29 that the congo red-treated graphene nanoplatelets were fully dispersed in dimethylformamide, water, ethanol, dimethyl sulfoxide, and methanol and partially dispersed in many other organic solvents. The mechanism of high dispersibility and stability of congo red-treated graphene nanoplatelets was completely explained by Hansen solubility parameters.

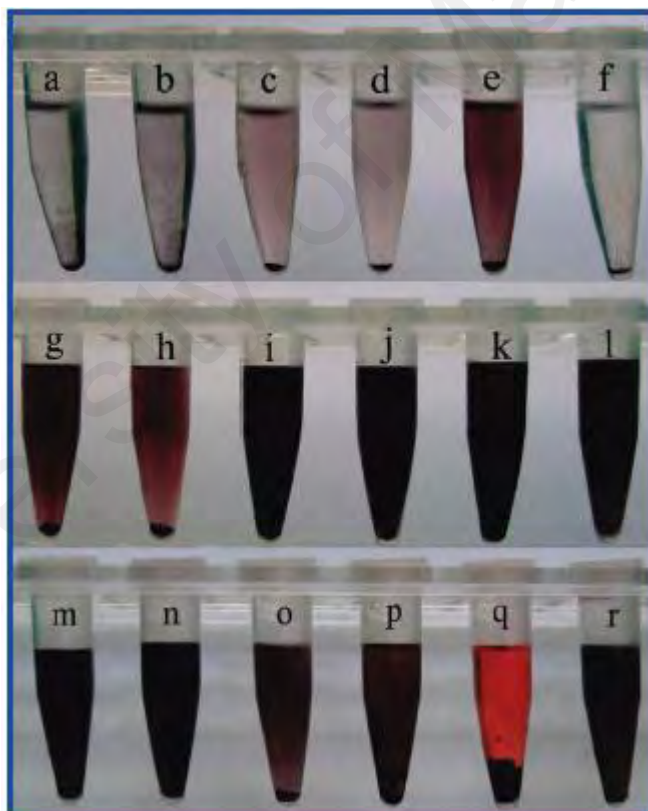


Figure 2.29: Solubility photographs of congo red-treated graphene nanoplatelets nanocomposites in (a) toluene, (b) benzene, (c) tetrahydrofuran, (d) ethyl acetate, (e) isopropanol, (f) chloroform, (g) acetone, (h) acetonitrile, (i) dimethylformamide, (j) methanol, (k) dimethyl sulfoxide, (l) water, (m) N-Methyl-2-pyrrolidone, (n) ethanol, (o) isoamyl alcohol, (p) m-cresol, (q) pyridine, and (r) 1,4-dioxane (F. Li et al., 2010).

A water-soluble aromatic electroactive dye was applied for non-covalently functionalization of graphene sheets by Liu and coworkers (Huan Liu et al., 2009). They prepared methylene green-treated graphene during the chemical reduction of graphene oxide with hydrazine. Methylene green-treated graphene showed a well-solubility in water through coulomb repulsion between methylene green-treated graphene nanoplatelets (Huan Liu et al., 2009). Also, Fang et al. investigated noncovalent functionalization of reduced graphene oxide with chitosan (Fang et al., 2010). According to their results, amino and hydroxyl groups of chitosan can be captured by graphene thorough hydrogen bonding and zwitterionic interactions, showing considerable solubility in water. It should be noted that the water-based graphene suspension is biocompatible.

As another type of non-covalent groups, polymers were introduced recently for increasing solubility of graphene sheets in aqueous media (Jo et al., 2011). Poly(3,4-ethylene dioxythiophene):poly(styrene sulfonate) (PEDOT:PSS) was used by Jo et al. (Jo et al., 2011) for noncovalent functionalization of reduced graphene oxide nanoplatelets. They have reported a significant stability for PEDOT:PSS-treated RGO suspension in aqueous media. Ghosh et al. (Ghosh et al., 2010) proposed a facile and quick method for synthesizing stable water-based single- and few-layer graphenes dispersions via non-covalent functionalization with a coronene carboxylate acceptor molecule.

To form a stable aqueous solution of single- and double-layer graphene sheets, a noncovalent functionalization of graphene sheets with thionine was suggested by Chen and coworkers (Chen et al., 2011). Some characterizations such as optical spectroscopy showed and confirmed the existence of π - π interactions between the thionine and graphene sheets. As another advantage, the conductivity of the hybrid material including functionalized graphene with thionine was almost 7 orders of magnitude larger than that observed for graphene oxide (Chen et al., 2011). Similarly, Liu and coworkers (Jingquan

Liu et al., 2010) could synthesize poly(*N*-isopropylacrylamide) [PNIPAAm]-treated graphene upon π - π stacking interactions, which resulted in an aqueous suspensions with high stability.

Yang and coworkers (H. Yang et al., 2010) also proposed an efficient technique for noncovalent functionalization of graphene sheets with poly(2,5-bis(3-sulfonatopropoxy)-1,4-ethynyl-phenylene-*alt*-1,4-ethynylphenylene) sodium salt (PPE-SO₃⁻). Highly soluble poly(2,5-bis(3-sulfonatopropoxy)-1,4-ethynyl-phenylene-*alt*-1,4-ethynylphenylene) sodium salt (PPE-SO₃⁻) in water play a key role in providing highly conductive and stable water-based graphene dispersions for long periods of time. The π stacking interaction between graphene nanoplatelets and PPE-SO₃⁻ is the main proposed mechanism. More interestingly, the successful adsorption of PPE-SO₃⁻ by graphene sheets not only was used as a stabilizer for aqueous media but also donates the resulting graphene sheets with negative charges, which provide suitable conditions for further functionalization of graphene sheets. Hemin-treated graphene hybrid nanoplatelets (H-GNs) (Guo et al., 2011) was also shown high solubility and stability in water, resulting from π - π interactions. Wang et al. proposed a green method for the formation of soluble reduced graphene oxide (Yan Wang et al., 2011). Upon the reduction of graphene oxide in the presence of green tea, the resulting green tea-treated graphene sheets showed an appropriate stability and solubility in both aqueous solution and a variety of organic solvents. Park et al. synthesized a stable and biocompatible polyoxyethylene sorbitan laurate (TWEEN)-adsorbed RGO platelets with highly stability in aqueous media (S. Park et al., 2010). By taking advantage of the solubility in water of TWEEN paper in water and the capability for being adsorbed on graphene sheets, this procedure was proposed.

The key role of Pluronic copolymer in dispersing graphene in aqueous media was investigated by Zu et al., which resulted in the aqueous graphene solutions with three months stability (Zu & Han, 2009). Liu and coworkers also synthesized an aqueous

dispersion of graphene sheets through the chemically-reduction of graphene oxide using hydrazine hydrate in the existence of a cationic polyelectrolyte namely poly[(2-ethyltrimethylammonioethyl methacrylate ethyl sulfate)-*co*-(1-vinylpyrrolidone)] (PQ11) (S. Liu et al., 2010). The resulting PQ11-attached graphene nanoplatelets remained stable for several months. As a positively charged polymer, PQ11 determines the promising capability to reduce silver salts to Ag nanoparticles.

Amine-terminated polymers were used by Choi and coworkers (E.-Y. Choi et al., 2010) for dispersing graphene sheets in different organic solvents through noncovalent functionalization. In fact, the carboxylate groups on reduced graphene oxide formed noncovalent functionalization sites for the protonated amine terminal groups of end-functional polymers. Regarding the mechanism, the phase transfer of graphene nanoplatelets from a water phase to an organic phase under sonication procedure can be facilitated by the noncovalent functionalization. They investigated the solubility and stability of reduced graphene oxide in different organic solvents, and the photographs of dispersions after one month confirmed their claim, as shown in Figure 2.30. In addition, UV-vis absorption spectroscopy was also applied for verification of dispersibility of the reduced graphene oxides (E.-Y. Choi et al., 2010).

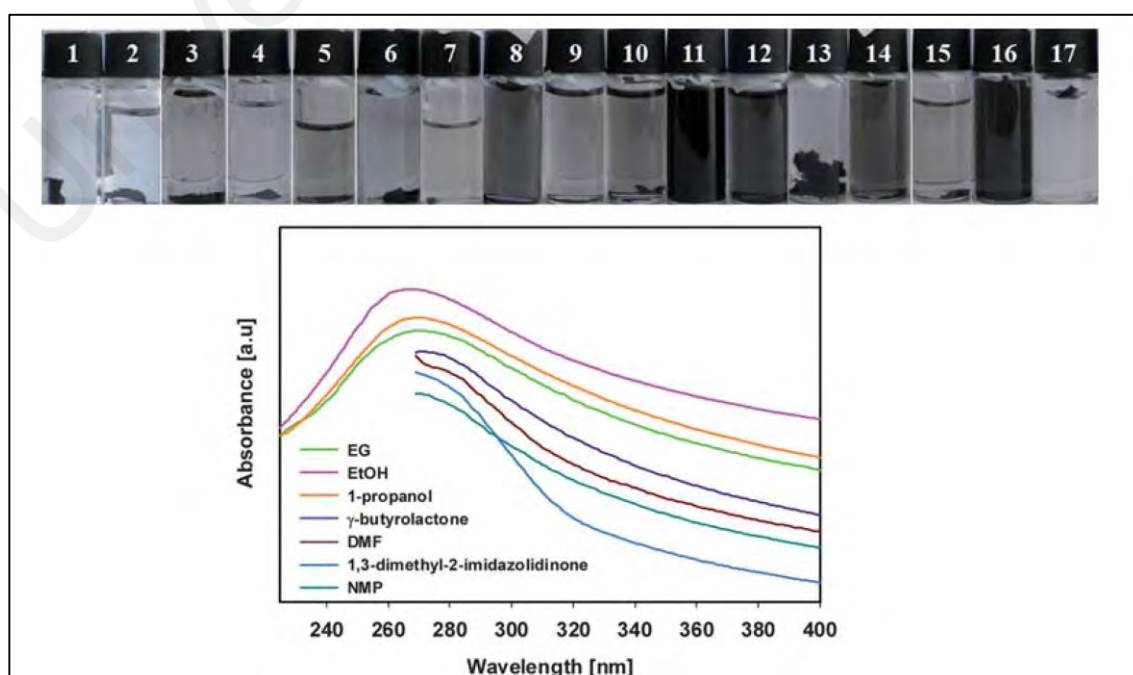


Figure 2.31: (a) The main chemical structure of poly ethylene glycol- oligomer phenylene–ethynylene (PEG-OPE). (b) The synthesis procedure of PEG-OPE–treated Reduced graphene oxide in H₂O. (c) Photograph of (A) graphene oxide and (B) Reduced graphene oxide in water and (C) PEG-OPE–treated Reduced graphene oxide and (D) PEG-OPE in methanol (Qi et al., 2010).

2.13 In Situ Exfoliation and Functionalization for Applications

As mentioned above, despite numerous studies on the applications and characteristics of graphene, researchers should find a method for mass production of graphene with high quality in a commercially viable way. Exfoliation of bulk graphite to thin graphene flakes with thickness of nanometer can be a promising method for mass production of graphene. As a low-cost and highly scalable method, chemical exfoliation was suggested for synthesizing mono- or few-layered graphene. However, the structural defects of GO cannot be completely removed even with thermal reduction and chemical treatment. Obviously, the presence of structural defects considerably restricts the applications of in thermal, electronic and optical devices (Becerril et al., 2008; Stankovich et al., 2007; Zhu, Murali, Cai, et al., 2010). More recently, a novel liquid-phase exfoliation illustrates significant performance in forming 2D carbon-based nanostructures. This liquid-phase exfoliation strategy has been obtaining great attention due to its unique properties such as being cost-effective, efficient, extraordinarily versatile and potentially for large-scale production of defect-free graphene (Hernandez et al., 2008; Paton et al., 2014). The second fundamental problem is the difficulties in processing graphene, in particular in our study, the graphene's poor colloidal stability in most common solvents (Ayan-Varela et al., 2014). As mentioned above, graphene nanosheets are extremely hydrophobic, and the interlayer cohesive energy (van der Waals interaction) enhances significantly with rising sheet dimensions (Georgakilas et al., 2012). This increase usually results in irreversible aggregation without electrostatic or steric protection. Overall, many of graphene's applications cannot be fully realized due to weak solubility of graphene in most common solvents. Grafting covalent and non-covalent functional groups can

prevent aggregation of graphene sheets, resulting in initiating nanofluids. Once functionalized with hydrophilic functional groups, the graphene-based nanofluids may open a gateway to new fields in heat transfer.

Besides presenting the exfoliation and functionalization methods for synthesizing stable dispersions, this comprehensive literature review includes experimental and theoretical works on convective heat transfer using carbon allotropes based nanofluids.

2.13.1 Nanofluid as a New Class of Material to Enhance Heat Transfer Performance

Since the dawn of industrialization, heat transfer has become the subject of interest for many researchers within the industry and academia. Nevertheless, major obstacle comes from the medium being used within the heat cycle. To date, oil, water and ethylene glycol have been extensively used as heat transfer working fluids due to their favorable attributes such as convenience in handling, disposal and recycling processes as well as their accessibility at relatively low market price. However, these fluids suffer from low thermal properties, and combined with other inherent limitations associated to the heat exchanger design such as fouling and low total surface energy, the overall heat transfer performance remains at technically low level. These impediments resort the manufacturer to design heat exchanger with extended size factor to harness the energy needed to achieve required operations within specific duration. Hence, relentless efforts have been directed on exploring the fluids that could improve heat transfer performance significantly. It is evident that the most notable and widely used technique for improving fluid properties is the addition of particles to form two-phase fluid slurries. Commonly, solid particles, such as metallic, non-metallic and polymeric are the main sources of foreign substances added into the base fluids. The effect of particle suspension of various types, sizes and volume fractions in base liquid mixture was first scientifically studied

and reported by Maxwell (Maxwell, 1881). This method has been successful up to a certain limit due to the adverse effects especially with respect to suspension stability, clogging, erosion and large increase in pressure drop. The above scenario started to change dramatically with the use of nanometer size particles ($<100\text{nm}$) (Chol, 1995). It was demonstrated that issues pertaining to the application of large particle for enhancing heat transfer properties in heat exchanger can be reduced significantly. Further, clogging and erosion problems are substantially minimized with relatively small penalty in pressure drop at low concentrations. The use of advanced techniques to uniformly disperse nanoparticles in the base fluid ensures colloidal stability to avoid deposition and settlement of particles due to the dominant effect of gravity and interparticle attractions which reduce its performance. Research conducted by Chol (Chol, 1995) on the aspect of improving the thermophysical properties of heat transfer fluids through the use of nanoparticles was among the pioneering work with regard to this subject. They coined the formation of stable suspension of these minute particles in heat transfer liquid as 'Nanofluid'. The earliest investigation on the role of nanofluid in improving heat exchanger performance was conducted by Pak and Cho who performed an experimental study to highlight the effect of adding nanoparticle in water as the base fluid in convective mode (Bock Choon Pak & Young I Cho, 1998). Since then, a lot of researchers have participated in nanofluid related studies. Most experiments were conducted on the basis of investigating heat transfer effect with particle of different type and morphological properties suspended in different heat transfer fluids under both laminar and turbulent regime (Murshed et al., 2008; Bock Choon Pak & Young I Cho, 1998; Zubir, Badarudin, Kazi, Huang, Misran, Sadeghinezhad, Mehrali, Syuhada, et al., 2015; Zubir, Badarudin, Kazi, Huang, Misran, Sadeghinezhad, Mehrali, & Yusoff, 2015; Zubir, Badarudin, Kazi, Misran, et al., 2015). Among the most notable and frequently cited research works, the

studies on formulating thermo-physical and heat transfer properties which are the pivotal elements in determining nanofluid performance.

2.13.2 Using Graphene Based Nanofluids as Promising Candidate for Improving Convective Heat Transfer

The critical demand for highly efficient thermal transport solution has become the major challenge for industries particularly in the realm of energy and power supply. This lies from the fact that many physical processes involve heat transportation between different energy conversion devices in order to harness the useful energy. At the core of heat transport system, specific priority has been given to address the limitation on the medium employed to complete the energy conversion process. Conventionally, water has been used as heat carrier especially in oil and gas refinery plants, nuclear and coal based electrical power plants and centralized cooling and heating systems (S. Lee et al., 1999). The reason being that water is abundant, inexpensive and readily available in its processed form without requiring additional chemical synthesis prior to its usage. The purification and post treatment processes are relatively straight forward and do not require specific protocols for handling and disposal. However, it is also acknowledged that water suffers from several drawbacks, particularly on the aspect of its heat transfer properties. Measurement of the thermal conductivity for instance reveals extremely low magnitude in comparison to solid metal which contributes the major obstacle in attaining high level of heat exchange. Theoretically, a low thermal conductivity of water implies an increase in thermal resistance by which the heat exchange medium would act as insulator, compromising efficient heat conduction process. This impediment has prompted researchers to explore innovative approaches such as modification of heat exchanger surface and configurations, resizing of heat exchanger unit as well as adjusting operating flow conditions as ways to boost the heat transfer efficiency. About two decades ago,

Chol (Chol, 1995) has successfully demonstrated the addition of controlled amount of sub-micron size, high thermal conductivity ceramic-based materials in aqueous system that produces significant improvement to the overall thermal conductivity of the host solutions. This research has inspired the long time ambition for achieving much compact but high efficiency heat exchanger unit that would match the rapid increase in processing capacity of integrated circuit technology for instance. Since then, booming research efforts have seen exponential growth on the number of nanofluid related publications. The research in nanofluids is classified into three main categories:

i) Addressing the role of quantum physics on describing the nanofluid property enhancement (Eapen et al., 2007),

ii) Exploring different materials along with other mechanistic effects such as concentration, particle morphological structure, state of suspension stability and external excitation on tailoring the thermo-physical properties of nanofluid (Chon & Kihm, 2005), and

iii) Unraveling the role of nanofluid in enhancing the performance of boiling and convection heat transfer processes (You et al., 2003).

Studies have shown that nanofluid demonstrates novel characteristics previously not found in base fluid alone namely strong temperature dependent thermal conductivity, significant enhancement of thermal conductivity at very low particle loading, anomalous increase in critical heat flux in pool boiling and prominent increase in heat transfer coefficient at low concentration and beyond the increase on thermal conductivity alone (Zheng et al., 2011).

It is evident that tremendous amount of research efforts have been dedicated on studying the effect of adding oxide, nitride, and carbide ceramics nanoparticles, carbon nanotube and their composites on physicochemical property of heat transfer fluid. It is worthy to note that while the study of ceramic-based nanofluid is well-established within

the scope of heat transfer subject, lack of work has been emphasized on the effect of incorporating different carbon allotropes on augmenting the thermo-physical nature of host fluids (Sundar et al., 2014). Using different base fluids including water and ethylene glycol, many studies were performed on dispersing various types of carbon based-nanostructures such as single-walled carbon nanotubes (Nanda et al., 2008; Z. Sun et al., 2008), multi-walled carbon nanotubes (Shanbedi, Heris, Amiri, Adyani, et al., 2014), graphene (W. Sarsam et al., 2016; W. Sarsam et al., 2016a) and nitrogen doped graphene for synthesizing highly-conductive nanofluids. The unique properties of few-layer graphene have attracted the attention of a large number of scientists in different fields (Shanbedi, et al., 2015). In particular, large specific surface area and outstanding thermal conductivity at room temperature make the few-layer graphene an ideal material for heat transfer applications. In recent years, researchers have gradually shifted their attention to the use of graphene based nanofluids (S. D. Park et al., 2010; Zhenyu Sun et al., 2013). This is largely due to the ability to address the persisting issues on maintaining the long term stability as well as the discovery of much effective stabilizing approaches that uses substances highly benign to the environment, low in molecular weight, as well as requiring low amount in comparison to the conventional strategies. As mentioned in functionalization section, a large number of research findings have been documented focusing the effect of stable carbon based colloidal suspensions in changing the physicochemical properties of the host fluid as well as its role in improving different modes of heat transfer processes. On this note, it is worthy to highlight that a significant rise in thermal conductivity enhancement was reported with the addition of very low particle loading while the rheological penalty was found to be insignificant (Baby & Ramaprabhu, 2010; Mehrali, Sadeghinezhad, Latibari, Kazi, et al., 2014; S. S. Park & Kim, 2014; Wei Yu et al., 2011). It was also discovered that substances containing phenolic components served as the effective carbon allotrope stabilizers which interact

via π - π aromatic stacking between benzene ring structures while abundance of oxygen based functional groups provides the necessary hydrophilic feature to maintain the solubility of carbon allotropes in aqueous solvent (Yan Wang et al., 2011).

Recently Mehrali et al. (Mehrali, Sadeghinezhad, Latibari, Kazi, et al., 2014) have shown that nanofluids containing graphene nanoplatelets (GnP), having close reminiscence to ideal graphene, demonstrates high thermal conductivity at very low weight percentages, which correspond to the previous study on functionalized reduced graphene oxide (RGO) (Baby & Ramaprabhu, 2011a). Further, the increase in rheological penalty was reported to be minimal, which paves promising avenues for its application in thermal transport system that strongly requires efficient heat transfer and energy conversion. Motivated by the above findings, further study conducted by Sadeghinezhad et al. on the effect of GnP based nanofluid on the convective heat transfer performance shows an anomalous increase in heat transfer coefficient, far greater than the thermal conductivity enhancement alone (Sadeghinezhad et al., 2014; Sadeghinezhad et al., 2015). Similar works on graphene based colloidal systems earlier conducted by Baby et al. (Baby & Ramaprabhu, 2011a; Baby & Sundara, 2011) have also shown similar trend of heat transfer enhancement. Part of the successful incorporation of graphene in convective heat transfer application is attributed to the series of innovative synthesis and stabilization techniques employed for improving its solubility as well as restoring of the conjugated aromatic structure of the planar region which holds the key for ballistic phonon and electron transport (Gupta et al., 2011). Some of the recent experimental studies on convective heat transfer coefficient in the presence of graphene-based nanofluids are illustrated in Table 2.1. It can be seen that heat transfer rate increases significantly in the presence of graphene as additive.

Table 2.1: Summary of experiments on convective heat transfer of graphene-based nanofluids.

Investigator	Geometry	Range of Re number	Nanoparticle	Maximum enhancement in convective heat transfer coefficient or Nu
(Baby & Sundara, 2011)	Straight stainless steel tube (<i>Length of 108 cm and diameter of 23 mm</i>)	4500–15,500	Copper oxide-treated graphene	81–232%
(Baby & Ramaprabhu, 2011a)	Straight stainless steel tube (<i>Length of 108 cm and diameter of 23 mm</i>)	4500–15,500 250–1000	Hydrogen-exfoliated graphene (HEG)	21–171% 59–219%
(Baby & Ramaprabhu, 2011b)	Straight stainless steel tube (<i>Length of 108 cm and diameter of 23 mm</i>)	4500–15,500 250–1000	Silver-decorated HEG	105–188% 188–327%
(Yang et al., 2011)	Straight stainless steel tube (<i>Length of 2.68 m and diameter of 1.3462 cm</i>)	290–1550	diamond-graphene	<i>Nu</i> (3–6%)
(Baby & Sundara, 2013)	Straight stainless steel tube (<i>Length of 108 cm and diameter of 23 mm</i>)	250–1000	Silver-decorated (MWNT-HEG) hybrid	570%
(Sadeghinezhad et al., 2014)	Straight stainless steel tube (<i>Length of 1400 mm and diameter of 10 mm</i>)	5000–22,000 5000–22,000	Graphene nanoplatelet (GNP)	13–160% Pressure drop increments of 0.4% and 14.6%
(Akhavan-Zanjani et al., 2014)	Straight stainless steel tube (<i>Length of 2740.2 mm and diameter of 4.20 mm</i>)	4000–10,850 4000–10,850	Graphene	6.04% Pressure drop increments of 0.8%
(Sadeghinezhad et al., 2015)	Straight stainless steel tube (<i>Length of 1400 mm and diameter of 10 mm</i>)	5000–22,000 5000–22,000	Graphene nanoplatelet (GNP)	13–160% Pressure drop increments of 0.4% and 14.6%
(Zubir, Badarudin, Kazi, Huang, Misran, Sadeghinezhad, Mehrali, Syuhada, et al., 2015)	Straight stainless steel tube (<i>Length of 1400 mm and diameter of 10 mm</i>)	4583–14,065	Reduced graphene oxide (RGO) and its hybrid complexes	144%
(Mehrli, Sadeghinezhad, Rosen, Latibari, et al., 2015)	Straight stainless steel tube (<i>Length of 1400 mm and diameter of 10 mm</i>)	5000–22,000 5000–22,000	Graphene nanoplatelet (GNP) with different specific surface area	83–200% Pressure drop increments of 0.06% and 14.7%
(Mehrli, Sadeghinezhad, Rosen, Akhiani, et al., 2015)	Straight stainless steel tube (<i>Length of 2000 mm and diameter of 4.5 mm</i>)	290–2300	Graphene nanoplatelet (GNP)	15%
(Ahmad Ghoozatloo et al., 2014)	Circular copper tube (<i>Length of 1 m and diameter of 1.07 cm</i>)	Re number of 1940 and constant heat flux of 420.5 W	Graphene	27.2%
(Hajjar et al., 2014)	Straight brass tube	4500–15,500	Graphene	171%

(A Ghozatloo et al., 2014)	Straight copper pipe	2840	graphene	42.4% in Ethylene glycol-based nanofluids
----------------------------	----------------------	------	----------	---

Thermal conductivity of graphene-based nanofluids is one of the most important heat transfer parameters. Table 2.2 summarizes some of the measured thermal conductivities by different researchers of graphene-based nanofluids.

Table 2.2: Summary of experimental results on thermal conductivity of graphene-based nanofluids.

Investigator	Particle type	Base fluid	Particle concentration	Maximum enhancement	Temperature
(Wei Yu et al., 2010)	Graphene oxide nanosheets	Ethylene glycol	1–5 vol%	10.5–61%	10–60 °C
(Baby & Ramaprabhu, 2010)	Exfoliated graphene	Water	0.005–0.056 vol%	14–64%	25–50 °C
		Ethylene glycol		4–7%	
(Martin-Gallego et al., 2011)	Functionalized graphene sheets [FGS]	Water	0.2–1 wt%	10–70%	30–60 °C
(Baby & Sundara, 2011)	Copper oxide-decorated graphene (CuO/HEG)	Water	0.005–0.05 wt%	23–90%	25–50 °C
		Ethylene glycol	0.01–0.07 wt%	17–23%	
(Baby & Ramaprabhu, 2011a)	Hydrogen-exfoliated graphene	Water	0.005–0.05 wt%	10–75%	25–50 °C
		Ethylene glycol	0.05–0.08 wt%	1–5%	
(Wei Yu et al., 2011)	Graphene oxide nanosheets	Ethylene glycol	2–5 wt%	Up to 86%	10–60 °C
(Baby & Ramaprabhu, 2011b)	Silver-decorated graphene	Water	0.005–0.05 wt%	7–86%	25–70 °C
		Ethylene glycol	0.01–0.07 wt%	3–14%	
(Aravind & Ramaprabhu, 2011)	Graphene nanosheets	Water	0.008–0.138 vol%	2.4–17%	25 °C
		Ethylene glycol		2.4–6.5%	
(Zhenyu Sun et al., 2013)	Few-layer graphene	Polymer	0.55–1 vol%	18–25%	10–60 °C
(Dhar et al., 2013)	Poly-dispersed graphene	Water	0.05–0.2 vol%	3–30%	25–50 °C
(Ghozatloo et al., 2013)	Functionalized Graphene	Water	0.01–0.05 wt%	3.8–17%	10–50 °C
(Kole & Dey, 2013)	Functionalized graphene nano-sheets (GnS)	Water + Ethylene glycol	0.041–0.395 vol%	Up to 15%	10–70 °C
(Gupta et al., 2011)	graphene nano-sheets	Water	0.05–0.2 vol%	Up to 27%	30–50 °C
(Yang et al., 2011)	Diamond-treated graphene	Silicon oil	0.35–5.2 vol%	Up to 10%	Room Temperature
(Baby & Sundara, 2013)	MWCNT-graphene hybrid	Water	0.005–0.04 vol%	1–20%	25–50 °C
(X. Li et al., 2014)	SiO ₂ -coated graphene	Water	0.1 wt%	Up to 20%	15–65 °C
(Hajjar et al., 2014)	Graphite oxide (GO)	Water	0.05–0.25 wt%	14.75–47.57%	10–40 °C
(Mehrali, Sadeghinezhad, Latibari, Mehrali, et al., 2014)	Nitrogen-doped graphene (NDG)	Water	0.01–0.06 wt%	22.15–36.78%	15–40 °C

(Mehrali, Sadeghinezhad, Latibari, Kazi, et al., 2014)	Graphene nanoplatelets (GNP)	Water	0.025–0.1 wt%	Up to 27.64%	15–40 °C
(S. S. Park & Kim, 2014)	Graphene	Water	0.001–0.01 vol%	6.24–14%	25 °C
(J. Liu et al., 2014)	Graphene	Water	0.01–0.03 wt%	3–22.9%	25–200 °C
(Akhavan-Zanjani et al., 2014)	Graphene	Water	0.005–0.02 wt%	6.04–10.3%	25–45 °C
(Zubir, Badarudin, Kazi, Huang, Misran, Sadeghinezhad, Mehrali, Syuhada, et al., 2015)	Reduced graphene oxide (RGO), RGO-CNT, RGO-GNP	Water	0.05 wt%	15–17%	30 °C
(Zubir, Badarudin, Kazi, Huang, Misran, Sadeghinezhad, Mehrali, & Yusoff, 2015)	Reduced graphene oxide (RGO), RGO-CNT, RGO-CNF, RGO-GNP	Water	0.05 wt%	2–30%	25–40 °C
(Haque et al., 2015)	MWCNT and graphene	Water	Mass ratios were 1/3, 3/1, 1/1, 1/2 and 2/1	Up to 5.546%	20–40 °C
(G.-J. Lee & Rhee, 2014)	Graphene nanoplatelets	Ethylene glycol	0.5–4 vol%	Up to 32%	10–90 °C
(Ma et al., 2013)	Functionalized graphene nanosheets	Silicon oil	0.01–0.07 wt%	Up to 18.9%	20–60 °C
(Shende & Sundara, 2015)	Nitrogen doped graphene	Ethylene glycol	0.005–0.03 vol%	Up to 15.1%	25–50 °C
		Water	0.005–0.02 vol%	Up to 17.7%	

It can be seen that all of the researchers show a significant increase in the thermal conductivity of different basefluids with loading of graphene sheets. Also, Figure 2.32 illustrates the thermal conductivity enhancement of pure water-, ethylene glycol- and ethylene glycol/water mixture-based graphene nanofluids, which were reported by other researchers (Baby & Ramaprabhu, 2011a; Gupta et al., 2011; Kole & Dey, 2013).

Interestingly, the measured results are close to each other. Figure 2.33 compare the amount of enhancement in thermal conductivity of nanofluids with different nanostructures loading at temperature of 30 °C. Note that the rate of thermal conductivity enhancement in the presence of graphene and carbon nanotubes as additives are significantly higher than that of the metallic nanofluids.

Figure 2.34 presents the thermal conductivity of the water-based graphene nanofluids, water-based graphene/SiO₂¹ as covalent nanofluids and water-based graphene/SiO₂-SDBS as non-covalent nanofluids. It can be seen that the covalent nanofluids showed higher thermal conductivity than that of non-covalent functionalization. Li and coworker investigated the effect of SiO₂/graphene nanofluid and reported that the low thermal conductivity of the water-based graphene nanofluid is highly depended to the stability of dispersion (X. Li et al., 2014).

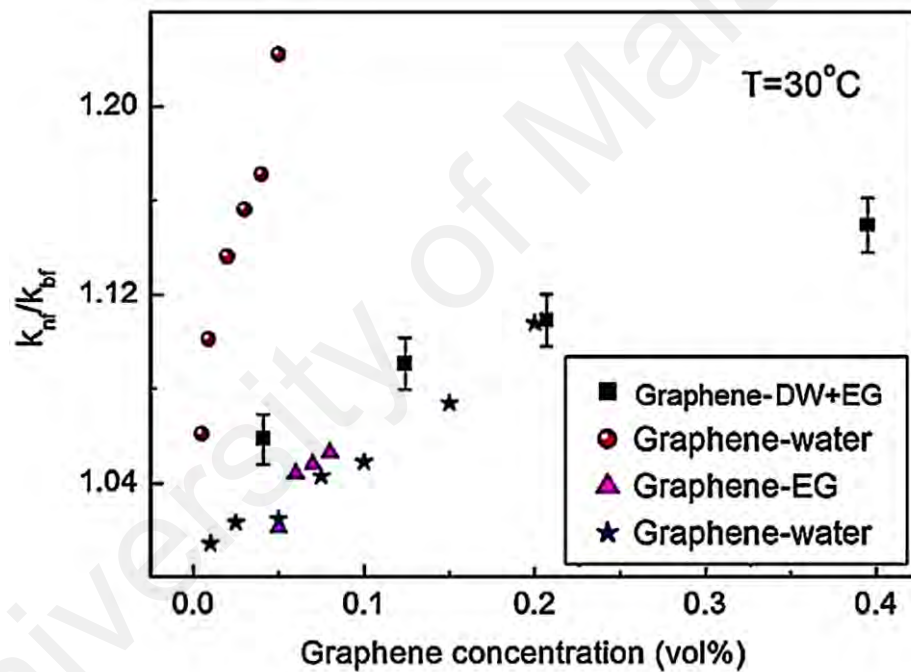


Figure 2.32: Thermal conductivity ratio of graphene-based nanofluids in the presence of different basefluids (Distillated water (DW) and ethylene glycol (EG)) (Kole & Dey, 2013).

¹ Silicon Dioxide-decorated graphene

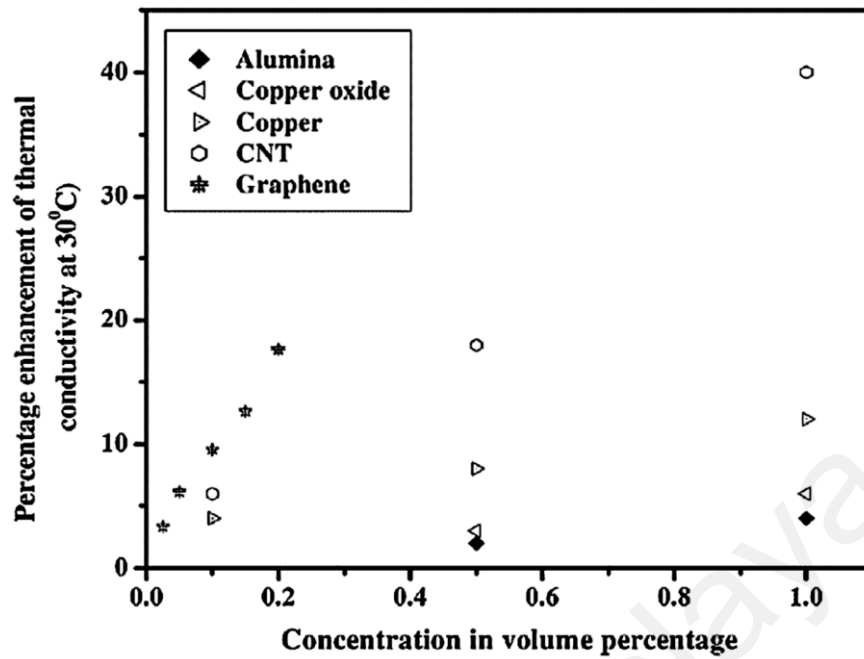


Figure 2.33: Thermal conductivity of water-based nanofluids in the presence of different additives e.g. metals, metal oxide, carbon nanotubes (CNT) and graphene (Gupta et al., 2011).

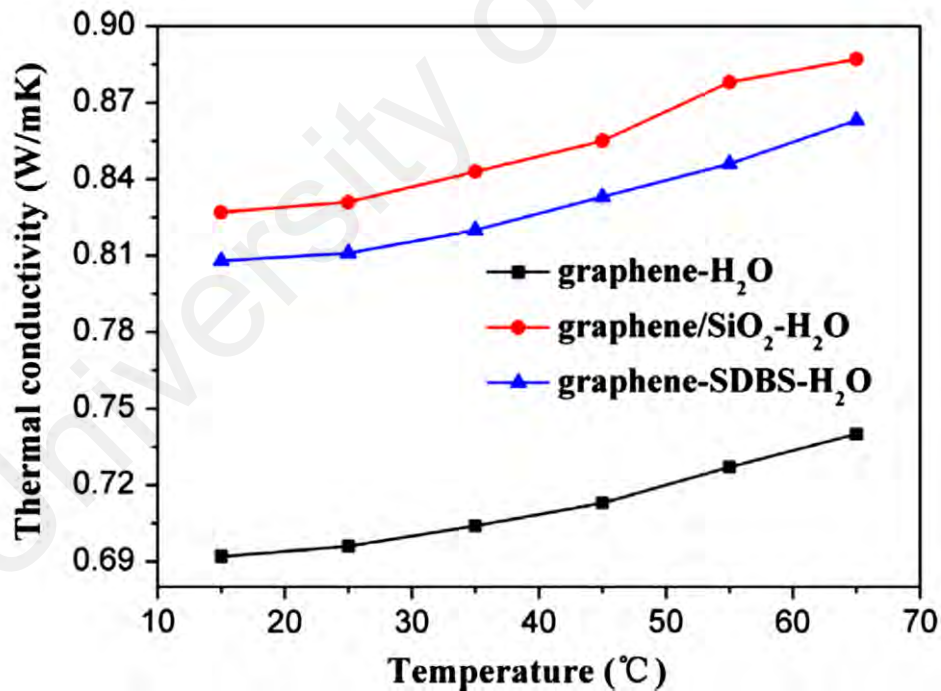


Figure 2.34: Thermal conductivity of graphene, graphene/SiO₂, and graphene/SiO₂-SDBS (X, Li. et al.)

2.14 The challenge of graphene stabilization in solvents

As mentioned in previous sections, using different base fluids including water and ethylene glycol, many studies were performed on dispersing various types of carbon based-nanostructures such as single-walled carbon nanotubes (Nanda et al., 2008; Z. Sun et al., 2008), multi-walled carbon nanotubes (Shanbedi, Heris, Amiri, Adyani, et al., 2014), graphene (W. Sarsam et al., 2016; W. Sarsam et al., 2016a) and nitrogen doped graphene (Amiri et al., 2016) for synthesizing highly-conductive nanofluids. The unique properties of few-layer graphene have attracted the attention of a large number of scientists in different fields (M. Shanbedi, et al., 2015). In particular, large specific surface area and outstanding thermal conductivity at room temperature make the few-layer graphene an ideal material for heat transfer applications. Developing an efficient and quick method for mass-production of few layer graphene, however, is critical for its large-scale industrial applications such for developing high performance nanofluids. It is also well known that the thermal conductivity and subsequently the heat transfer rate improve as the specific surface area of graphene increases (W. Sarsam et al., 2016a). Therefore, in order to manufacture highly-conductive nanofluids for improving heat transfer rate in different thermal equipment, materials with high specific surface areas, such as crumpled graphene, and in particular, few-layered graphene are used. Crumpling the 2D graphene with chemical treatment can be an approach to achieve materials with high specific surface area and pore structures. Thus, highly-crumpled few layer graphene or highly-porous graphene with large specific surface area seem to have the ideal properties.

There are, however, a number of challenges. To fully exploiting the properties of graphene with large specific surface area as an additive in base fluids requires a method for the mass production of these remarkable materials. The second problem is the lack of stability of carbon-based nanostructures in aqueous media. To solve the first problem, numerous studies have been performed. As a large-scale exfoliation technique, the

production of chemically converted graphene from the reduction of graphene oxide is a convenient method to obtain large amounts of graphene (Stankovich et al., 2007); however, even with efficient reducing agents such as hydrazine or H₂, and annealing at high temperature, the original crystalline structure of graphene is not restored, reducing all the unique properties. Also, graphene oxide is heavily functionalized with many permanent chemical defects, such as holes, introduced into the basal plane. These holes are not readily healed even upon annealing (Ruoff, 2008; Stankovich et al., 2007; Zhengzong Sun et al., 2010; H. Wang et al., 2009). As a new method to overcome the above-mentioned defects, the liquid phase exfoliation of graphite in the presence of high surface-tension organic solvents, along with continuous sonication (Hamilton et al., 2009; Hernandez et al., 2008), opened a new gateway to achieve few-layered graphene.

There are, however, other issues. The π - π interactions leads to high level of aggregation and the liquid-phase exfoliated graphene cannot reach stable dispersion in base fluids (Zhengzong Sun et al., 2010). However, due to lack of graphene-solubility, the exfoliation performances of most of the solvents used in previous studies (Niu et al., 2016) were quite low. To increase the efficiency of exfoliation with this method and solving the problem of low stability, in situ chemical functionalization and exfoliation of graphite with different functional groups, such as 4-bromophenyl, were used, providing a new approach for improving its solubility in polar, aprotic, organic solvents (Lomeda et al., 2008). For example, Sun et al. concluded that graphite can be changed to graphene by covalent functionalization of the graphite and the synthesis of a stable suspension in the presence of DMF without any added surfactant or stabilizer (Zhengzong Sun et al., 2010). Also, they achieved both exfoliation and functionalization with a fast procedure and obtained suitable edge-functionalization and intact pristine graphene structure in the interior basal planes. Thus, finding a method for mass-production of highly-crumpled few

layer graphene or highly-porous graphene with hydrophilic functional groups to prepare highly-stable nanofluids is the major goal of this study.

Availability of highly-stable superconductive nanofluid opens a new gateway for economical increase in the performance of thermal loops in industrial applications (W. An et al., 2016; Bellos et al., 2016; Delfani et al., 2016; Kaloudis et al., 2016; Tong et al., 2015). Ducts and channels with abrupt expansion, two-phase closed thermosyphon, closed ducts and heat exchangers are broadly applied in different industrial applications and heat transfer equipment.

To reach high performance equipment, owning working fluid with superior thermal capability is essential. Herein, after synthesizing superior graphene based working fluids, heat transfer rate of new coolants is investigated in different equipment.

The research investigation reported different experimental results in Tables 2.1 and 2.2 show the superior increase of thermal parameters in the presence of graphene. However, more experimental research works are required to:

- Find a method for mass production of functionalized few-layered graphene with high specific surface area.
- Find a suitable covalent functional groups to reach completely stable dispersion including graphene.
- Find the effects of covalently and non-covalently functionalization on heat transfer parameters.
- To fully exploiting the thermo-physical and rheological properties of graphene-based nanofluids
- To investigate the effect of specific surface area of graphene nanosheets as additives.
- To investigate convective heat transfer coefficient of different thermal equipment such as ducts and channels with abrupt expansion (backward

facing step), two-phase closed thermosyphon, closed conduct, and car radiator.

University of Malaya

CHAPTER 3: METHODOLOGY

3.1 Characterization Methods and Instruments

As discussed above, in order to confirm the exfoliation and functionalization, carbon-based nanostructures should be analyzed with different morphological, structural and elemental analysis. Also, in order to check the stability and thermo-physical properties, some common methods are used which are discussed in this chapter. In addition, to investigate heat transfer rate of synthesized nanofluids, some test-rigs should be employed. In this chapter, all of the used equipment are introduced.

3.1.1 Preparation of samples for characterization instruments

3.1.1.1 Field Emission Scanning Electron Microscopy

Field emission scanning electron microscopy (FESEM) is utilized for inspecting topographies of specimens at very high magnifications using a piece of equipment called the scanning electron microscope. Herein, scanning electron microscopy (Cold-Emission FESEM SU8000, Series UHR) was employed to study surface morphology of carbon-based nanostructures.

3.1.1.2 Transmission Electron Microscopy

Transmission electron microscopy (TEM) is the primary technique to verify single particle dimensions, the main structures of flakes and to identify the thickness of sheets. The electron beam can be used to see features on the nanometer level. A major drawback to the use of TEM is that samples must be dried out of solution in order to be attached to the carbon matrix (lacey carbon grid) and placed in the vacuum chamber of the TEM; therefore, the particles are not exactly in the colloid state and agglomeration might occur during drying. However, TEM can be used in combination with dynamic light scattering to acquire exact sizing in nanofluid form. Another drawback of TEM is the cost and time investment needed to prepare and view the samples. It was decided that only some initial imaging will be done as a feasibility study. In this study, 120kV High-Contrast/High-

Resolution Digital TEM HT7700 was employed to study surface morphology of graphene sheets, and thickness. As a TEM sample, each sample powder was dispersed in a suitable solvent, followed by dropping on a lacey carbon grid and subsequently dried under vacuum. An ultrasonic processor (Misonix Inc., Farmingdale, New York, NY, USA) with output of 600 W was used for performing sonication. All samples sonicated with 85% of total power of ultrasonic processor.

3.1.1.3 Atomic Force Microscopy

AFM observation was conducted for the slightly sonicated samples on the freshly cleaved mica surfaces (Multi Modes 8, Bruker, frequency of 1 Hz) in tapping and ScanAsyst mode was used to depict the dimensions.

3.1.2 Functionality and Elemental Analysis

3.1.2.1 Fourier Transform Infrared Spectroscopy (FTIR)

The infrared spectra of samples were studied by Fourier transform infrared spectroscopy (Bruker IFS 66/S) in the region of 400–4000 cm^{-1} at room temperature (around 25 °C), and all samples were placed on KBr pellets.

3.1.2.2 X-ray Photoelectron Spectroscopy

X-ray photoelectron spectroscopy (XPS) is a surface-sensitive quantitative spectroscopic technique that measures the elemental composition at the parts per thousand range, empirical formula, chemical state and electronic state of the elements that exist within a material. XPS spectra are obtained by irradiating a material with a beam of X-rays while simultaneously measuring the kinetic energy and number of electrons that escape from the top 0 to 10 nm of the material being analyzed. X-ray photoelectron spectroscopy (model: Kratos Analytical XSAM HS spectrometer) with an Al-K α X-ray source was used to identify the bonded elements in the carbon nanostructures over exfoliation and functionalization.

3.1.2.3 Energy Dispersive X-Ray Spectroscopy

Energy dispersive X-Ray spectroscopy (EDS or EDX) is a chemical microanalysis technique used in conjunction with scanning electron microscopy (SEM). Desktop scanning electron microscope (Phenom ProX, Netherlands) was used to do EDS analysis of graphene sheets. Also, combustible elemental analysis (CHNS/O) was performed using a Perkin Elmer 2400 series II and was used to measure carbon, oxygen, nitrogen and hydrogen elemental content. The instrument was used in CHN operating mode to convert the sample elements to simple gases (CO_2 , H_2O and N_2). The PE 2400 analyzer automatically performed combustion, reduction, homogenization of product gases, separation and detection.

3.1.2.4 Raman Spectroscopy

Raman spectroscopy is a spectroscopic technique used to observe vibrational, rotational, and other low-frequency modes in a system. To investigate functionalization and explore alterations in the layers, Raman spectra were obtained via a Renishaw confocal spectrometer at 514 nm at room temperature (around 25 °C).

3.1.2.5 Thermogravimetric Analysis

Thermogravimetric Analysis (TGA) is a type of elemental study that is performed on samples to determine changes in weight in relation to change in temperature. Simultaneous TGA-DTA/DSC measures both heat flow and weight changes (TGA) in a material as a function of temperature or time in a controlled atmosphere. Simultaneous measurement of these two material properties not only improves productivity but also simplifies interpretation of the results. The complementary information obtained allows differentiation between endothermic and exothermic events which have no associated weight loss (e.g., melting and crystallization) and those which involve a weight loss (e.g., degradation).

In this study, the thermogravimetric analysis was measured by a Perkin Elmer TGA-7 in the atmosphere of air. The weight loss of graphene samples was analyzed in TGA as a function of temperature at the heating rate of 10 °C/min up to a temperature of 900 °C under 50 cm³/min flow rate of air and nitrogen.

3.1.2.6 Selected Area (Electron) Diffraction

Selected area electron diffraction (SAED) is a crystallographic experimental technique that can be performed inside a transmission electron microscope (TEM). In a TEM, a thin crystalline specimen is subjected to a parallel beam of high-energy electrons. As TEM specimens are typically ~100 nm thick, and the electrons typically have an energy of 100–400 kiloelectron volts, the electrons pass through the sample easily. In this case, electrons are treated as wave-like, rather than particle-like. Because the wavelength of high-energy electrons is a few thousandths of a nanometer, and the spacing between atoms in a solid is about a hundred times larger, the atoms act as a diffraction grating to the electrons, which are diffracted. Some fraction of them will be scattered to particular angles, determined by the crystal structure of the sample, while the others continue to pass through the sample without deflection.

Therefore, SAED can be used as a definitive identification of graphene sheets. For identification of monolayers by electron diffraction, the ratio of the intensity of the {1100} to the {2110} peaks gives an unambiguous local identification of monolayer, bilayer, and multilayer to provide information on the yield of graphene sheets with different layers.

3.1.3 Specific Surface Area

The specific surface area of carbon-based nanostructures is determined by physical adsorption of a gas on the surface of the solid and by calculating the amount of adsorbate gas corresponding to a monomolecular layer on the surface. Physical adsorption results from relatively weak forces (van der Waals forces) between the adsorbate gas

molecules and the adsorbent surface area of the test powder. The determination is usually carried out at the temperature of liquid nitrogen. The amount of gas adsorbed can be measured by a volumetric or continuous flow procedure. Herein, to investigate the effects of functionalization, exfoliation and thermal treatment on the specific surface area of carbon nanostructures, N₂ adsorption–desorption isotherms were measured by a surface area analyzer (Quantachrome Autosorb-1 analyzer at 77 K). Sometimes, CO₂ adsorption-desorption was also employed to assess micropores (pores less than 1 nm) in the low-pressure region.

3.1.4 Thermo-physical Analysis

3.1.4.1 Thermal Conductivity

An important property to be characterized in this study is the thermal conductivity of the nanofluid. In order to select the desired fluids to be fully characterized, enhanced thermal conductivity is possibly the most important element in this study, because it points to the nanofluid with high heat transfer potential. There is an inexpensive commercially available system for the measurement of the thermal conductivity (Mehrali, Sadeghinezhad, Tahan Latibari, et al., 2014). The Decagon Devices KD₂ thermal properties analyzer (KD2 Pro, Decagon Devices, Inc., USA), after some initial testing, is used on all samples at room temperature as a first check. In later sections, the transient hot wire method, on which the KD₂ operates, will be described in full along with the true thermal conductivity measurement apparatus. The accuracy of the KD₂ is given as 5% by the manufacturer over a span of temperatures of 0 to 60°C. However it is found, through trial and error, that the KD₂ operates very accurately if the probe is setup perfectly vertical and an isothermal bath is used to maintain the sample at 25°C. These measures prevent convection problems and the external boundary effect problems. A schematic of the KD₂ setup with the isothermal bath is shown in Figure 3.1.

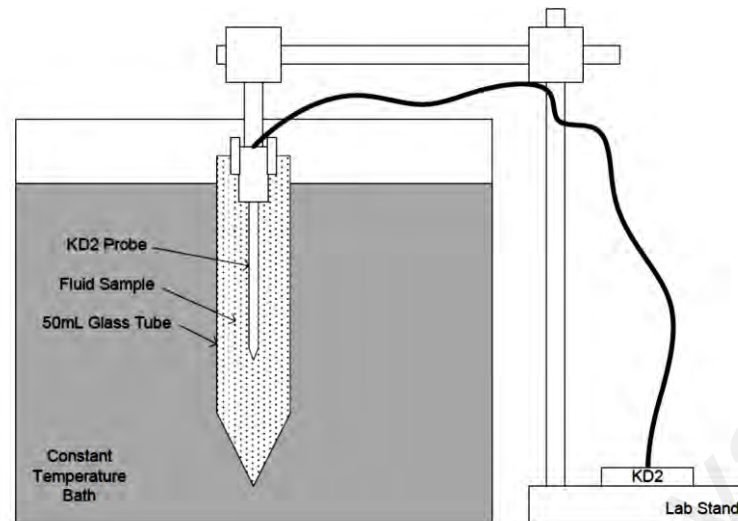


Figure 3.1: Schematic setup of KD2 thermal properties analyzer.

Thermal conductivity of working fluids was measured using KD2 Pro thermal properties analyzer device (Decagon devices, Inc., USA) with an accuracy of almost 5%. The transient hot wire method is the main operation principle. The KS-1 probe used in this study is a single needle sensor with length of 60 mm and diameter of 1.3 mm (Figure 3.2a and b). In order to obtain low error in measuring and reading, the main problem is the alignment of the probe in the center of sample's vial (Figure 3.2b and c). For graphene-based nanofluids with dark color, the problem has become more serious, where this condition creates the visual alignment of the probe impossible. So, a probe holder was fabricated to confirm the highest alignment of the probe inside the vial without the need for frequent check of alignment. Simply, the holder has two Teflon pieces interconnected with three bolts and nuts embedded in the lower part. The utilization of the holder dramatically decreased the amount of error in readings. More details about the holder are illustrated in Figure 3.2 panels (d–f).

Also, two water baths were applied to maintain the temperature of samples stable during measurements. A refrigerated bath circulator “WiseCircu WCR-P6” (Daihan Scientific Co., Ltd., Korea) was employed for temperature lower than 35 °C. By contrary,

a heating bath circulators “Lab. Companion CW-05G” (Jeitech Co., Ltd., Seoul, Korea) was also employed for high temperature than ambient. Both aforementioned circulators were 1.04 kW with an accuracy of 0.1 °C. More than 12 readings were performed and the measuring readings with device error < 0.01 were recorded, following by calculating as the average value of readings with the lowest error.

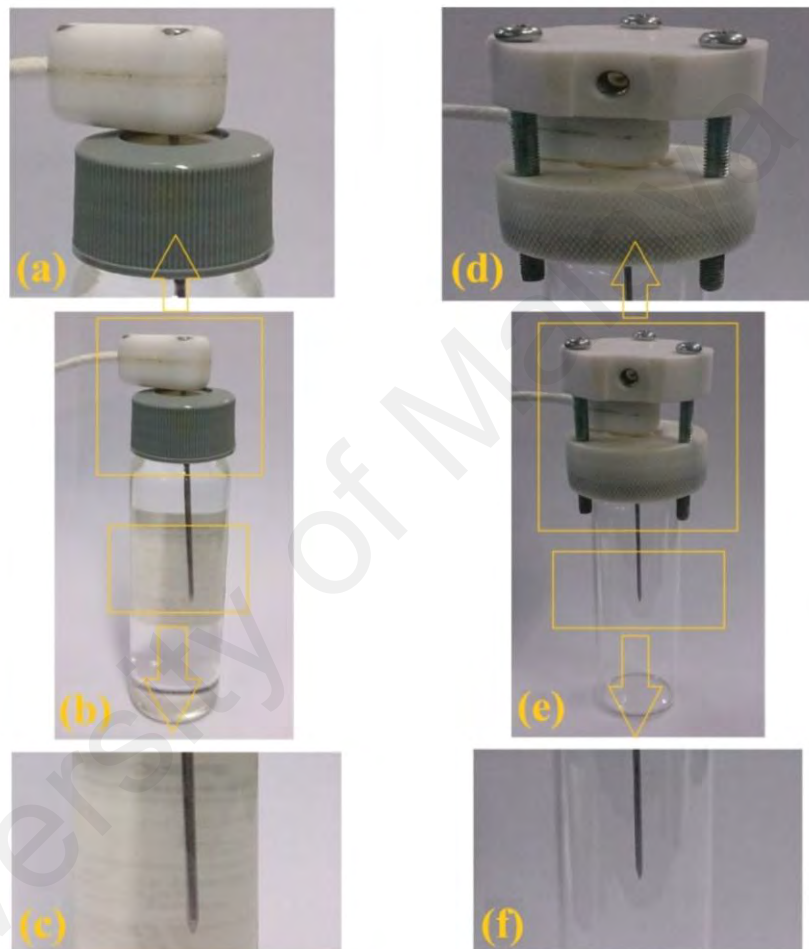


Figure 3.2: Photographs of the KS-1 probe without (a–c) and with (d–f) the probe

As mentioned above, the KD2 Pro thermal properties analyzer has a design uncertainty of 5%. In order to investigate the validity of KD2 Pro thermal properties analyzer results, the measured data for distilled water was compared with standard data reported by Arnold (1970), as shown in Figure 3.3. It can be seen that the KD2 Pro analyzer underestimate the measured values of thermal conductivity with a maximum

error of 4.08%. So, it confirmed that the device is satisfactorily working within its designed accuracy and can be reliable.

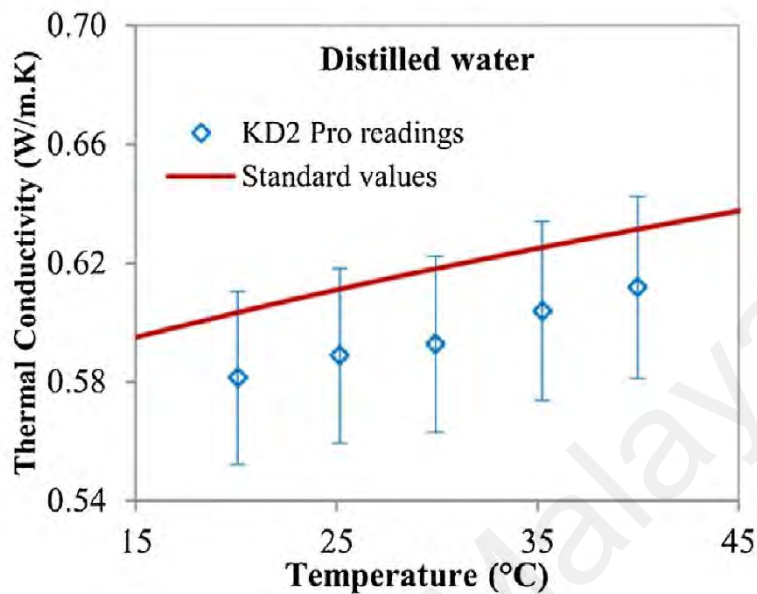


Figure 3.3: Comparison between distilled water and previous data

3.1.4.2 Differential Scanning Calorimetry

Differential scanning calorimetry (DSC) is a powerful tool to measure the heat capacity of nanofluids. The difference in the amount of heat flow required for heating up a sample pan and reference pan are measured as a function of temperature. During the whole process, the sample and reference pans are maintained at nearly the same temperature throughout the experiment. The heat capacity of the reference pan is already known. By measuring the difference in heat flow, the heat capacity of the sample is obtained. If there are phase transitions happened in the sample pan, more or less heat will need to flow to it than the reference to maintain both at the same temperature, so endothermic or exothermic peaks are shown on the DSC curves, corresponding to melting or freezing, respectively. The phase transition temperatures and latent heats are determined according to the DSC curves. The heat capacity of all working fluids was obtained on a differential scanning calorimeter (two models: Perkin Elmer Diamond DSC

and METTLER TOLEDO 820C-Error $\pm 0.25-1^{\circ}\text{C}$) at a heating rate of $5^{\circ}\text{C}/\text{min}$ in purified nitrogen atmosphere.

3.1.4.3 Rheometer

The viscosity of nanofluids is an important parameter for characterizing the suitability of the nanofluids for heat transfer applications. To investigate the effect of carbon nanostructure loading in base fluids on viscosity behavior, the viscosity of graphene-based nanofluids should be measured at different rotor RPMs, showing Newtonian or non-Newtonian behaviors. Herein, the rheological behavior of nanofluids was measured on Anton Paar rheometer (Physica MCR 301). The accuracy and reliability of the Anton Paar rheometer were validated by comparing its data at 200 1/s shear rate with the standard values presented by Arnold (1970), as shown in Figure 3.4, and a maximum error of 1.04% was found.

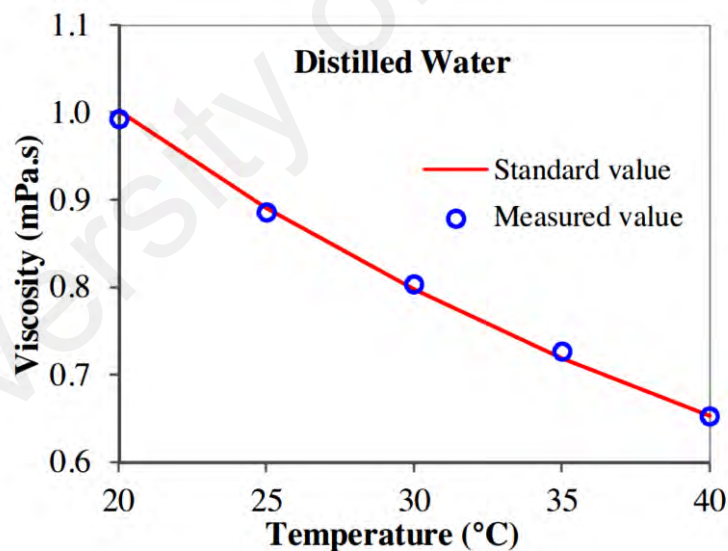


Figure 3.4: Comparison between the measured viscosity with the standard values reported by Arnold (1970) for distilled water at 200 1/s shear rate.

3.1.4.4 Densitometer

Density is another thermo-physical property of fluids affecting convective heat transfer. Force Tensiometer K100 (KRÜSS Ltd., Germany) and DM40 (Mettler Toledo,

Malaysia) were used to measure surface tension and the density of nanofluids. Accuracy of equipment is 0.0001 g cm^{-3} and it has temperature controller.

3.1.5 Stability Analysis

3.1.5.1 UV–Vis Spectroscopy

The UV–Vis spectroscopy is a common method, which is utilized for the investigation of the stability of nanofluids including solid particles. According to the Beer–Lambert’s law, there is a direct connection between the absorbance of a solution and the concentration of the absorbing species such as particles in the solution. Consist with this law, the absorption spectrum of our prepared nanofluids exhibits a maximum peak at around 265 nm corresponding to π – π transition of conjugation system in the polyaromatic structures. The band gap energy, E_g , can be measured from UV–Vis absorption by Tauc’s equation (Hadadian et al., 2014) given as,

$$(\alpha h_\nu)^n = B(h_\nu - E_g) \quad (3-1)$$

where α , h_ν , n , E_g and B are, respectively, absorption coefficient, photon energy, the nature of optical transition, band gap energy and a material constant. Plotting $(\alpha h_\nu)^n$ against the photon energy and extrapolating the linear region of the curve to the x-axis give the optical band gap. Regarding the dispersion state and the long-term stability, the colloidal stability of the carbon-nanostructures in base fluid is investigated quantitatively by UV–Vis spectroscopy.

The light transmission of all samples were measured with a Shimadzu UV spectrometer (UV-1800) operating between 190 and 1100 nm. The nanofluid solution was diluted with distilled water to allow sufficient transmission while each measurement was repeated three times to achieve a better accuracy.

3.1.5.2 Zeta-Potential and Particle Size Distribution

In order to investigate the influence of functionalization and volume fraction of carbon nanostructures on dispersion state, zeta-potential and particle size distribution can be applied. The zeta-potential and polydispersity index (PDI) are commonly utilized as an index of the magnitude of electrostatic interaction between colloidal particles and thus can be considered as a measure of the colloidal stability of the solution. According to White et al. (2007) results, the zeta potential must be as large as possible (positively or negatively) to make a common repulsive force between the particles. Table 3.1 lists the zeta potential and associated suspension stability (Vandsberger, 2009).

Table 3.1: Zeta potential and associated suspension stability (Vandsberger, 2009)

Z potential (mv)	Stability
0	Little or no stability
15	Some stability but settling lightly
30	Moderate stability
45	Good stability, possible settling
60	Very good stability, little settling likely

Zetasizer Nano (Malvern Instruments Ltd., United Kingdom) at 25 °C was used to measure zeta potential. Also, the particle size distribution change was analyzed using the dynamic light scattering (DLS) method to check the aggregate size over time. For performing measurements, the samples were transferred into the folded capillary cell (polycarbonate with gold plated electrodes) for investigation of particle size distribution using the same device (Zetasizer Nano (Malvern Instruments Ltd., United Kingdom)) at 25 °C.

3.1.6 Experimental system

3.1.6.1 Duct with a Backward-facing Step

Figure 3.5 illustrates the experimental set-up of the present study, which includes a flow loop, heating and cooling sections, measuring instruments, data acquisition and control unit. The flow loop consists of a magnetic flow meter, tank, pump, differential

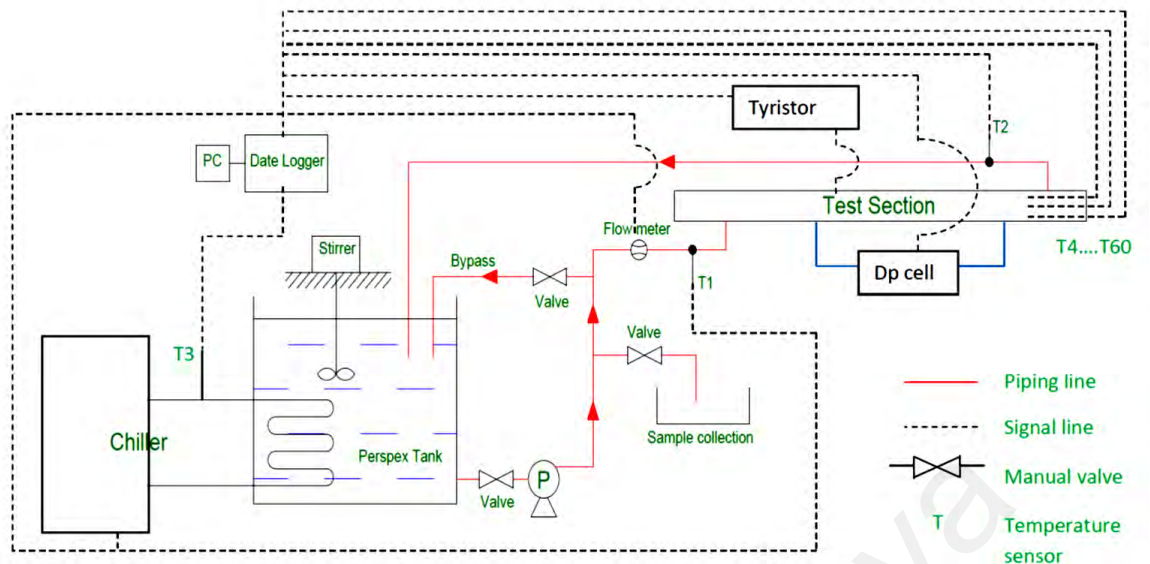


Figure 3.5: (Up) Photograph, schematic and (down) 2D diagram of the duct with a backward-facing step.

The geometrical dimensions of the tube were 12.7 mm inlet diameter, 800 mm upstream length, 25.4 mm outlet diameter and 800 mm downstream length for an expansion ratio of 2. At the test section, the downstream part was a heated straight stainless steel tube, with all the outer walls were insulated. The test section was also heated by using two programmable DC power supplies (N8731A Power Supply, Agilent Technology) with outputs of 8V and 400A current with the maximum power of 3200 W. Sixteen K type thermocouples (Omega) were installed on the test section by using high temperature epoxy glue on the outer surface of the test section. The positioning of the thermocouples on the outer surface of the cylindrical tube is schematically shown in Figure 3.6. Thermocouples were installed at outer surface of the cylindrical tube in order to avoid boundary layer interruption originating from the thermocouple probe protruding into the conduit inner surface. The boundary conditions of the experiments were maintained as follows: After expansion, there was a constant heat flux of 600 W provided by DC power supplies. Also, the inlet fluid rate was in the range of 1 to 16 Lit/min.

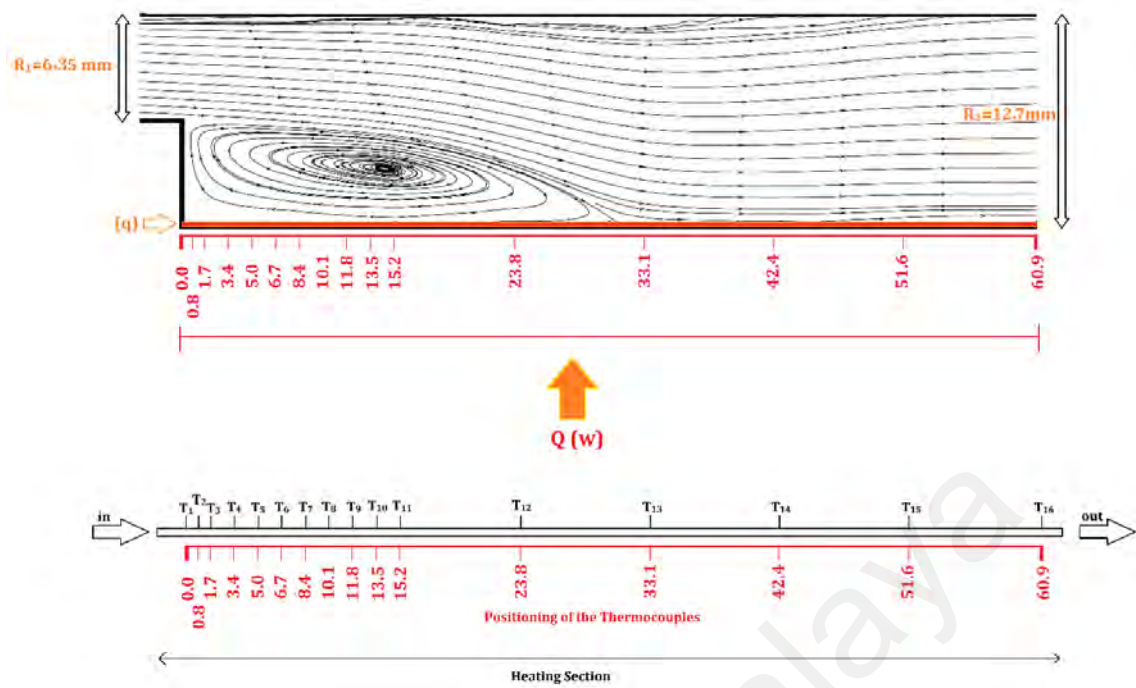


Figure 3.6: Schematic view of the test section and the positioning of the thermocouples on the outer surface of the cylindrical tube.

The thermocouples were flush mount to avoid interaction with the flow boundary layer originating from the thermocouple probe protruding into the conduit inner surface. Furthermore, two RTD (PT-100) sensors (Omega) were used to measure and record the working fluid inlet and outlet temperatures. All of the thermocouples as well as RTDs were calibrated with the use of Ametek temperature calibrator (AMETEK Test & Calibration Instruments, Denmark). The RTDs and thermocouples were connected to the PLC and SCADA system for the continuous monitoring and recording of the temperature data by the WINCC software in a computer. To eliminate or minimize the amount of heat loss, two thick layers of white glass wool wrapping were used, and also rubber insulation dressing was also applied. Two K-type thermocouples were installed on the outermost surface of the insulation to measure the amount of heat loss. Moreover, all the pipes were warped with the rubber insulation to reach steady state condition in terms of temperature and the given flow rate. Note that there are conduction and convection heat transfer simultaneously in the present system. Therefore, further calibration test was needed to

determine the exact temperature at the inner surface of the test section. Therefore, a Wilson plot was used for this purpose. The inlet temperature of bulk fluid and heat flux at different locations “x” of the duct were formulated as mentioned in the data processing section. The specifications and the accuracy of the measuring instruments and sensors used in the present experimental setup are presented in Table 3.2.

Table 3.2: Specifications and errors of the measuring instruments and sensors used in the present experiment.

Measured parameter	Instrument and sensor type	Operating	Error
Surface temperature	Type K thermocouple	0-300°C	±0.1°C
Bulk Temperature	RTD (PT-100) sensor	0-200°C	±0.1°C
Fluid flow rate	N-FLO-25 Electromagnetic flow meter	0.03 m/s ~ 12 m/s	±0.5%
Fluid pressure drop	Foxboro™ differential pressure transmitter	0-25 kPa	±0.075%
Cooling unit	WiseCircu, DAIHAN Scientific, Refrigerated circulating bath	2.2 kW	±0.1°C

3.1.6.2 Design and Construction

Some basic requirements are developed as design considerations for the convection loop. These requirements are generated in order to meet certain goals: some to mimic heat exchanger conditions, some to meet existing equipment and lab requirements, and finally some arbitrary conditions.

The reservoir tank is a Jacketed Stainless steel made and in cylindrical shape with a capacity of 20 liters. The reservoir is kept 30 cm above the gear pump so that the pump will have adequate pressure avoiding it to run dry. At the bottom of the reservoir a piping connects to the gear pump while at the top a bypass line, return line and top stirrer to mixing fluid inside the tank are connected (Figure 3.7).



Figure 3.7: Photograph of the Reservoir Tank.

The gear pump used for the experiment is a liquid flow sealed gear pump (Cole-Parmer magnetic drive pump), see Figure 3.8. It is rated for a maximum flow of 64 LPM and max head is 6.3M. This pump is capable of operating at variable speed with the maximum rated speed as 3200 RPM. The suction side of the pump is connected to the reservoir.



Figure 3.8: Photograph of the Magnetic gear pump.

The pump is capable of operating with water up to 80°C, due to the shaft seal limitations. After rough estimation of the total loop pressure losses, assuming 10mm inner

diameter tubing, and from knowledge of the pump characteristic curve, it is found that the pump should be capable of pumping around 10LPM. This will deliver a significantly turbulent flow rate for water at room temperature, up to Reynolds number of 20,000. Therefore, the pump is deemed usable for the experiment. A Hoffman Muller inverter was used to control the speed of the pump, see Figure 3.9.



Figure 3.9: Photograph of the Hoffman Muller inverter.

The specifications of the inverter are presented in Table 3.3.

Table 3.3: Technical specifications for V8 series inverters.

Items	Contents
Model	HM-V8A11P5B
Input	AC, 1PH, 230V, 50/60HZ
Output	3PH, 1.5KW, 7A, 0-650HZ

The electromagnetic flow meter (N-FLO-25) was used to measure fluid flow rate (Figure 3.10). A magnetic flow meter (mag flowmeter) is a volumetric flow meter which does not have any moving parts and is ideal for wastewater applications or any dirty liquid which is conductive or water-based working fluids. Magnetic flowmeters are also ideal for applications where low pressure drop and low maintenance are required.



Figure 3.10: Photograph of the Electromagnetic flow meter.

The operation of a magnetic flow meter or mag meter is based upon Faraday's Law, which states that the voltage induced across any conductor as it moves right angles through a magnetic field is proportional to velocity of that conductor. As stated above, the flow meters come calibrated from the manufacturer.

A smart differential pressure transmitter (Model Foxboro™) with accuracy of $\pm 0.075\%$ of span connected to the inlet and outlet of the test section was used in this test (see Figure 3.11).



Figure 3.11: Photograph of the Differential Pressure Transducers.

A refrigerated bath circulator (DAIHAN-brand, WCR- P30) was used to balance the heat input, which is inside the jacketed tank (Figure 3.12). This refrigerated bath has:

1. RS232C Interface for remote monitoring and controlling with PC
2. Stainless steel bath (#304) for Superior Durability & High Thermal Efficiency.

3. Powerful Circulation Pump ensures Temperature Uniformity: Internal and External Circulation.
4. Locking Mode Supported for Experimental Safety (Input to Jog-Shuttle can be Disabled)



Figure 3.12: Photograph of the refrigerated bath circulators.

The specification of the refrigerated bath is listed in Table 3.4.

Table 3.4: Specifications of the refrigerated bath.

Items	Contents
Capacity & Models	30 L, WCR- P30
Temp. Range & Accuracy	-25°C~ +150°C, ±0.1°C
Temp. Resolution	0.1°C-Display, 0.1°C-Control
Temp. Uniformity & Probe	±0.2°C at -10°C, PT100
Heating Power	2.2 kW
Refrigerator	7/8 HP
Cooling Capacity	at +20°C 631 W at 0°C 429 W at -20°C 284 W
Refrigerant	CFC -Free(R-404A) Refrigeration System

Two N8731A DC-power supplies (Keysight (Agilent) Technologies) with maximum power output of 400A and output voltage of 8V were used to supply enough energy for heating of working fluid homogeneously (Figure 3.13). Two DC power supplies

were conducted in parallel to reach the given amount of output power in a small length. Both DC power supplies used AC electricity as an energy source and convert the input voltage to a higher or lower AC voltage by a transformer. Also, a rectifier is employed for converting the transformer output voltage to a varying DC voltage, which in turn is passed through an electronic filter to convert it to an unregulated DC voltage.



Figure 3.13: Photograph of the N8731A DC-power supplies.

There are two different type of thermocouples used for the experiment. The thermocouples used for the bulk fluid inlet and outlet (bulk) temperatures in respect to the test section are thermocouples from Omega (Model: PR-12-2-100-1/8-6-E-RP) with Temperature Range -50 to 250 °C. These are RTD sensor (PT-100) thermocouples with 3mm sheath diameter and 100mm length. The tips of the thermocouples are inserted into the middle of the flow path of the fluid. The thermocouple is then attached to the data acquisition unit where the bulk temperatures are recorded and analyzed.

Another kind of thermocouples used for surface temperature is type-K from Omega with Liquid Crystal Polymer Molded Transition Junction Rated to 260°C . This type-K thermocouple has 1mm sheath diameter and 5mm length. The thermocouples were supplied with specification from the manufacturer as ± 0.1 °C accuracy.

All thermocouples are not calibrated in the technical sense and they are tested with standard temperatures to ensure no manufacturing or connection flaws are creating

erroneous readings. The heat transfer results are directly affected by the temperature measurements. Thus, all the thermocouples (Type-K and RTD sensor) used in this experiment must be calibrated to determine their accuracy. The thermocouples are calibrated by two ways:

1. 650SE - Reference Temperature Calibrator

The system provides significant improvement in the calibration accuracy up to $\pm 0.04^{\circ}\text{C}$ with the use of an external reference sensor. Axial homogeneity in the calibration well is important, as the typical thermo-sensitive element of a sensor can vary from 5mm to 60mm. The actual temperature in the well will inherently deviate from the ideal temperature as a function of the proximity to the bottom of the well (Figure 3.14).



Figure 3.14: Photograph of the Thermocouple calibrator.

2. The thermocouples are immersed in well mixed boiling-water bath which is at 100.16°C for the laboratory pressure and a well-mixed ice-water bath is maintained at 0°C (Figure 3.15).

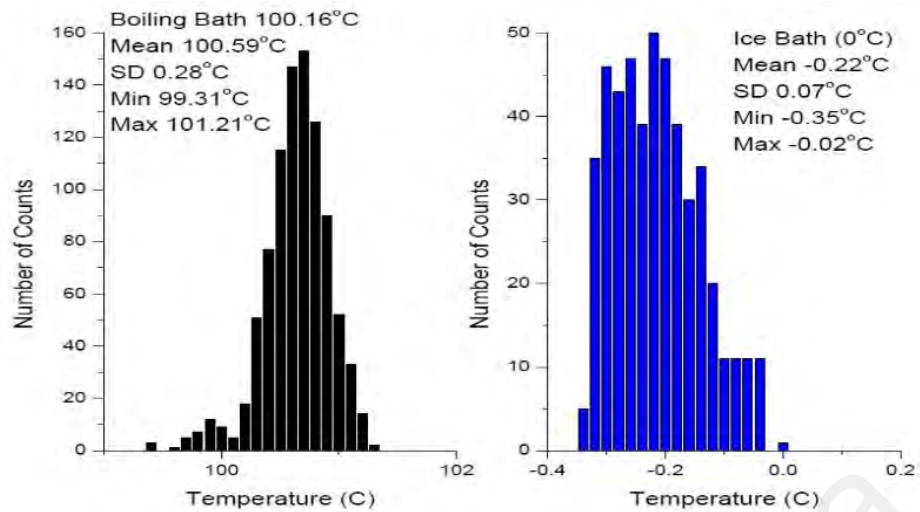


Figure 3.15: Thermocouple testing.

Graphtec (midi logger gl220) data acquisition systems are used in this study (Figure 3.16). Meanwhile, data loggers are connected to a PC for continuous data logging and monitoring.



Figure 3.16: Photograph of the Data acquisition instruments.

All the type-K thermocouples are attached to the channels of Graphtec data logger. This multi-channel data logger provides 10 analog measurement channels, in addition to four channels each of discrete logic and pulse inputs. The GL220 supports one external trigger input and four alarm outputs. The GL220 connected to a PC to allow data upload in real time as well as remote configuration and real time data acquisition.

The RTD sensors, flow meter, and pressure transducer are attached to the channels of standard PID temperature controller (Scada Autonics) (Figure 3.17). All thermocouples were connected to the PLC and SCADA system for the continuous monitoring and recording of the temperature data by the WINCC software in a computer. The system linked to the PC with the USB cable and RS485 communication (Modbus RTU) to log the data in real time.



Figure 3.17: Photograph of the controlling unit that attached with SCADA system.

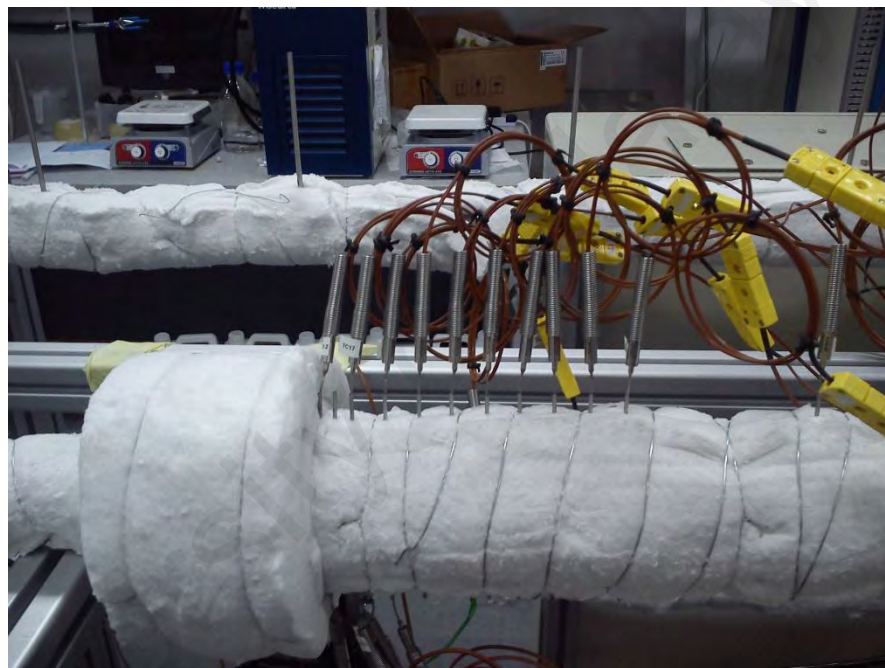
The amount of the heating power is measured by output voltage and current supported by both DC power supplies.

Note that the heat transfer test section is the main part and design of that takes much effort and it was constructed by the Advanced Fluid dynamics lab, University of Malaya. The sectional view of the experimental test section is presented in Figure 3.6 and major dimension of the test section are tabulated in Table 3.5.

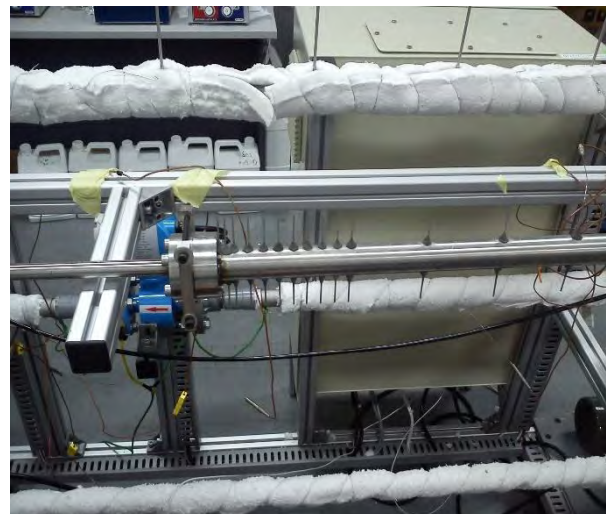
Table 3.5: Dimensions of the test section

Parameters	Values
Overall length	700 mm
Diameter before step	12.7 mm
Diameter after step	25.4 mm
Heating length	800 mm
Expansion Ratio	1/2

The heat transfer test section included two straight stainless steel 316 tube with a length of 700 mm and 800 mm. Sixteen grooves were cut along the tube length that was used to house the thermocouples. The grooves were cut as deep as possible while ensuring that the inside surface of the pipe was not disturbed. The distance between groove surface and inner surface of the tube was maintained at 1mm. Also, to keep thermocouple in location the stainless steel tubes with 2 mm outer diameter were installed and fixed with high temperature epoxy glue (Figure 3.18). The thermocouples were installed inside the tube and filled by thermo-oil to confirm the uniform heating to thermocouple sensors.



High temp. Epoxy up to 200°C



Thermo-wells installation

Figure 3.18: Thermocouple installation.

The thermocouples were calibrated to measure the surface temperature according to Equation (3.1).

$$T_W = T_{Tc} - \frac{\dot{q}}{\lambda/x} \quad (3.1)$$

This experimental system was designed and constructed to perform experiments and investigated the convection heat transfer coefficient and pressure drop over a backward facing step at constant heat flux (Figure 3.19).



Figure 3.19: Photograph of the heat transfer test rig.

3.1.6.3 Car Radiator

To study the thermal properties of coolant, an automobile radiator was also employed and is shown in Figure 3.20. The experimental system consisted of a closed loop of working fluid. To measure temperatures, the working fluid, after being warmed in a feed reservoir, was pumped into the radiator using 2.0 cm inner diameter tubes and was subsequently cooled over flowing through the radiator. The working fluid was returned to the main tank after passing through the radiator. The size of feed reservoir

was 22.5 liters (Figure 3.20) and, in every circulation, 25 liters of working fluids was nourished by a tank located on the top of the reservoir. To enhance the accuracy of the experiments, the radiator system was completely closed, which was performed via an air drain mounted on the top of the feeding repository. Moreover, to keep temperature of the working fluid steady, eight electrical elements with the power of 18 kW and a controller were used. Three calibrated thermocouples (PT100-type) were inserted into the calming and mixing chamber of the flow at inlet and outlet of the radiator for measuring the bulk temperatures of working fluids, and also eight K-type thermocouples were soldered at axial diameter on the outer surfaces of the radiator to measure wall temperatures. The accuracy of all the thermocouples was ± 0.1 °C at full scale. Due to very small thickness (2.0 mm) and very large thermal conductivity of the tubes, it was reasonable to equate inside temperature of the tube with the outside one.

The test section included a storage tank, a centrifugal pump, heating elements, flow meter, a forced draft fan, a cross flow heat exchanger and flow lines. The experimental setup was totally a closed system and worked under pressure (0.25 kPa) and the working fluid filled the whole storage tank in all the experiments. Additionally, the flow rate in the system was regulated by adjusting a globe valve on the recycle line. Three layer insulated tubes (Isopipe 0.75 in diameter) were applied as a connecting line. A flowmeter (Instrument Company LZT) was used to measure and manipulate the flow rate. When the flow rate was adjusted at the beginning of the experiments, it was monitored continually during the experiments. When it was fixed at our desired flow rate for at least 15 minutes, the results were recorded. The accuracy of the flowmeter was around 2.0%. A fin-and-tube type radiator with 40 vertical tubes (circular shaped cross section) was the main part of set-up, which schematically shown in Figure 3.21. All mechanical parts of the experimental setup were made of aluminum. For cooling the working fluid, a forced fan (Techno pars: 1,400 rpm) was installed behind the radiator. Air and fluid had indirect

cross flow contact and heat exchanged between hot fluid flowing in the tube-side and air crossing the tube bundle. In addition, a U-tube manometer with carbon tetrachloride (CCl_4) as the manometer liquid was provided for determining pressure drop through the radiator. Constant velocity and temperature of the air in the experiments were considered in order to clearly investigate internal heat transfer. Also, the design of the system allowed filling the heat exchanger from up and down. In this study, all the experiments were run while the radiator was filled from up to down.



Figure 3.20: Photographs of the experimental system.

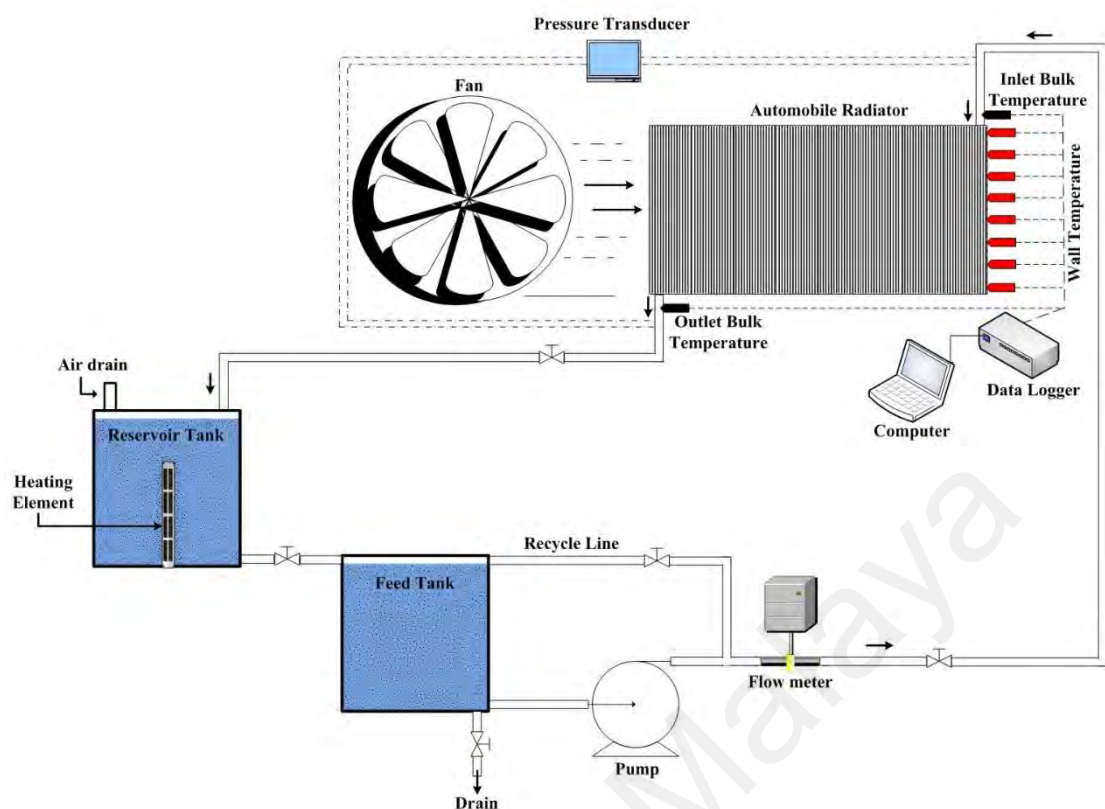


Figure 3.21: Schematic of the experimental system

All tests were carried out in triplicate to consider the average and improve the accuracy. Table 3.6 illustrates some essential parameters of experiments as well as experimental set up.

Table 3.6: Test condition during the experiments.

Volumetric flow rate (lit.min⁻¹)	3-8
Nanoparticle concentration (weight %)	0-0.2
Type of Nano-structures	Graphene nanoplateless and nitrogen doped graphene
Reynolds number	2000–8000
Inlet temperature (°C)	35, 45, 55

3.1.6.4 Two Phase Closed Thermosyphon

Figure 3.22 illustrated the schematic and photograph of the thermosyphon as an experimental apparatus used in the current study. The thermosyphon consisted of a copper tube with a length of 1000 mm and inner diameter of 20 mm. The apparatus was fabricated of three parts: the evaporator, the adiabatic region, and the condenser part. The evaporator part was made-up of a straight 20 mm inner diameter copper tube with a length of 350 mm. The adiabatic part was 250 mm long and the condenser part was also fabricated from a straight copper tube with an inner diameter of 20 mm and a length of 400 mm, and was placed in the top of the thermosyphon. Also, the condenser section comprised of a shell as heat exchanger with the diameter of 40 mm and length of 400 mm surrounding the main pipe with an inner diameter of 20 mm.

The apparatus uses 10 K-type thermocouples, with four installed in the evaporator section and another four in the condenser region. An electric heater was placed at the evaporator section which was isolated with a fireproof blanket with a thickness of 20 mm. A power supply, a water storage tank, and a vacuum pump to remove the non-condensate gases from the thermosyphon are other parts of the experimental setup. Two K-type thermocouples were also used to report the temperatures of input water and output water in the shell. A cooling system was also used to control the temperature of the storage tank.

The flow rate of the input water was measured with the flow control valve and was kept at 250 mL/min with $\pm 1.0\%$ margin of errors. Also, the ammeter, thermocouples and voltmeter with a 0.001 A, 0.1 °C and 0.1 V margin of errors were maintained respectively, to measure the different thermal parameters.

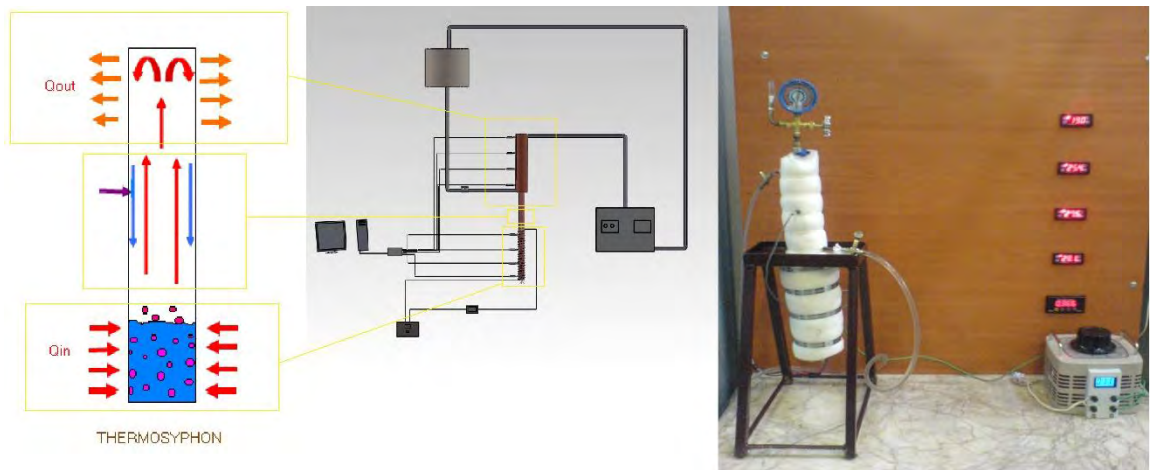


Figure 3.22: (left and middle) Schematic and (right) photograph of the experimental apparatus.

Overall, the image of all the characterization instruments employed in this study for analyzing the samples in terms of structures and morphology are shown in Appendix C.

3.1.6.5 Flowchart of study

Figure 3.23 shows the phase of this study. In fact, this study has 3 phases including material preparation and characterization, investigation of colloidal stability and thermophysical properties, and investigation of heat transfer in different equipment. In phase of material preparation and characterization, 6 graphene-based additives were synthesized, analyzed and utilized as additive for preparing different nanofluids. The second phase includes the investigation of colloidal stability of the prepared nanofluids, continuing with checking thermophysical properties. The third phase of study includes the investigation of heat transfer rate of car radiator, ducts and channels with abrupt expansion and two-phase closed thermosyphon in the presence of the prepared nanofluids.

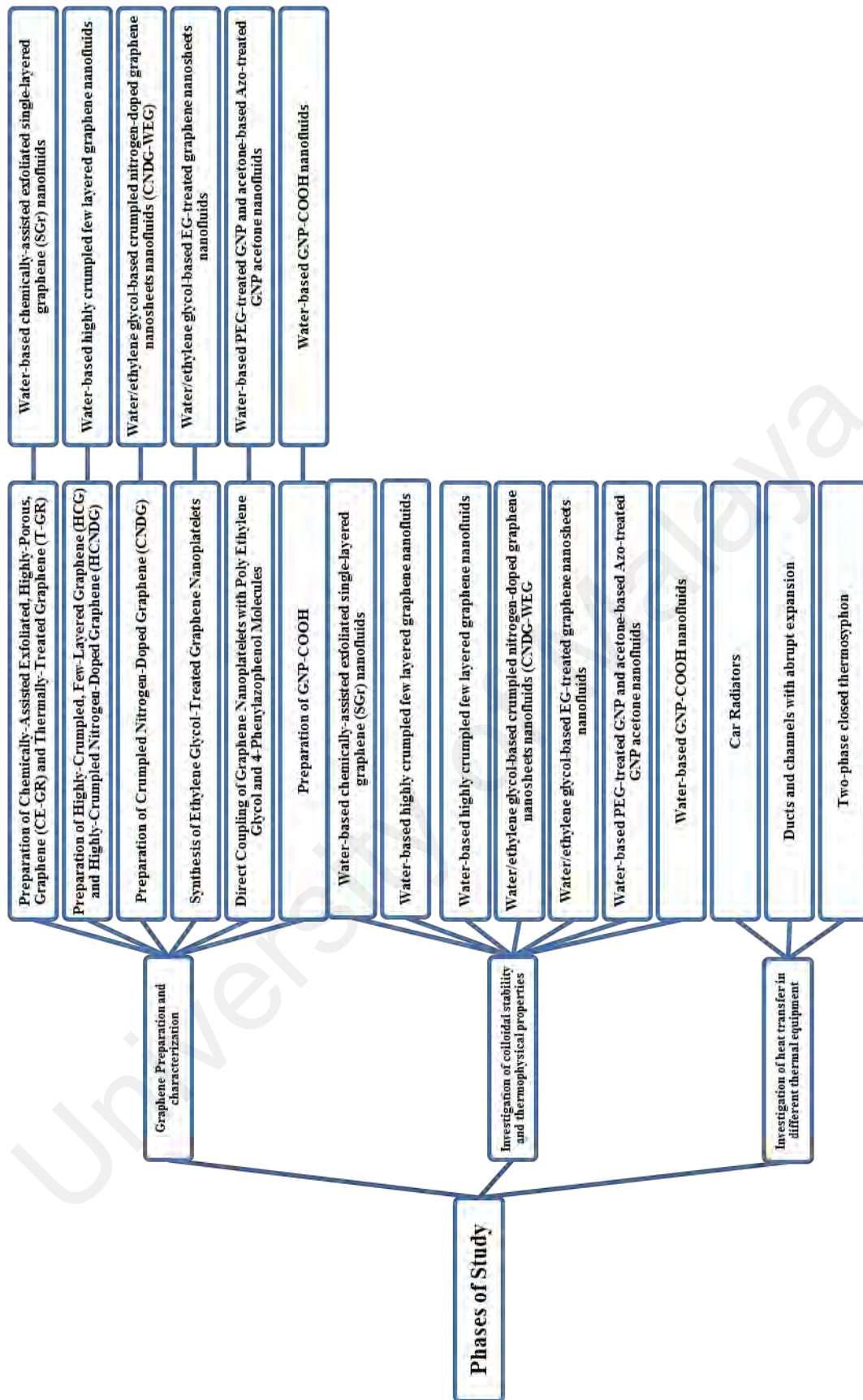


Figure 3.23: Flowchart of phases of this study.

CHAPTER 4: RESULTS AND DISCUSSION

4.1 Introduction

As mentioned in chapter 2, the liquid-phase exfoliation strategy has been obtaining great attention due to its unique properties such as being cost-effective, efficient, extraordinarily versatile and potentially for large-scale production of defect-free graphene (Hernandez et al., 2008; Paton et al., 2014). Although lots of liquid-phase exfoliation approaches for scalable few-layered graphene synthesis have been emerging (Edwards & Coleman, 2013), the second fundamental problem can be the difficulties in processing graphene, in particular in this study, the graphene's poor colloidal stability in most common solvents (Ayan-Varela et al., 2014). With introducing functionalization, graphene can remain dispersed over a reasonable period of time, which is a one of the most important goal of this study.

In view of great advantages of liquid phase exfoliation along with in situ functionalization that is being made, this chapter aims to provide a list of synthesized graphene materials and their production methods. Besides the proposed methods and introduction of materials, different characterization methods including morphological and elemental analysis were employed to confirm the present claims regarding synthesizing of materials.

The goals of this chapter are to propose some exfoliation and functionalization methods and mechanisms, investigate the exfoliation yield and functionalization degree as the first phase of study. The second phase includes the investigation of colloidal stability and thermophysical properties of the prepared nanofluids. The third phase of study includes the investigation of heat transfer rate of different thermal equipment e.g., car radiator and heat exchangers in the presence of prepared nanofluids. To have an overview on the whole thesis, the readers are referred to the flowchart represented in chapter 3.

4.2 Exfoliation, Functionalization and Characterization

4.2.1 Preparation of Chemically-Assisted Exfoliated, Highly-Porous, Graphene (CE-GR) and Thermally-Treated Graphene (T-GR)

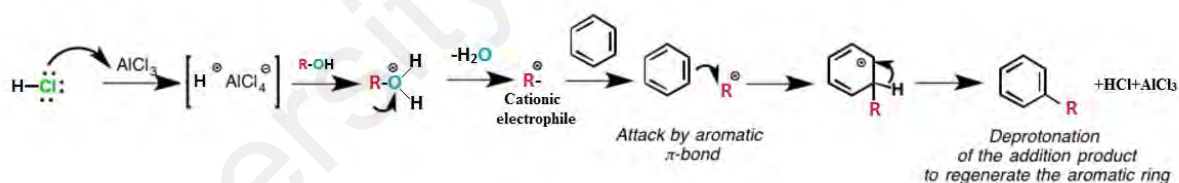
4.2.1.1 Chemicals

All reagents such as Tetrahydrofurfuryl polyethylene glycol ((PEG, $C_5H_9O(C_2H_4O)_{n=2,3}OH$, MW~200), $AlCl_3$, N,N-dimethylformamide (DMF), N,N-Dimethylacetamide (DMA), γ -butyrolactone (GBL), ethylene glycol (EG), polytetrafluoroethylene (PTFE) binder and HCl with analytical grade were obtained from Sigma-Aldrich and were employed without additional purification. The natural graphite with 100 mesh (<150 μm) and purity of 99.9% was obtained from Alfa Aesar.

4.2.1.2 In Situ Functionalization and Exfoliation Procedure

Figure 4.1 shows the experimental procedure for functionalization, as well as the exfoliation of graphite to produce chemically-assisted exfoliated, highly-porous, graphene (CE-GR) and thermally-treated graphene (T-GR). Regarding functionalization, in a typical experiment, the pristine graphite (10 mg) and 185.4 mg of $AlCl_3$ as a Lewis acid were ball-milled and poured into a Teflon reaction vessel and 200 ml of PEG were gradually added during sonication for 30 min at room temperature to obtain a homogeneous suspension under nitrogen atmosphere. A special white smoke was seen during adding the PEG. Also, concentrated hydrochloric acid (0.5 mL) was added dropwise to the graphite suspension during the sonication process. Then, the mixture was poured into a Teflon vessel, sealed and transferred into an industrial microwave and irradiated at 150 °C at an output power of 700 W for 20 min (with frequently of 5 min sonication and 5 min placed under microwave irradiation). An electrophilic addition reaction occurred between the PEG and the graphite, resulting in the attachment of the PEG groups and hydroxyl groups to the exposed edges and side of the expanded graphite flakes, thereby producing functionalized, expanded graphite. Microwave irradiation was

used to increase the speed of the reaction and the functionalization yield. With a Lewis acid (AlCl_3) as a catalyst and trace concentrated hydrochloric acid to protonate alcohols, electrophilic addition reactions were carried out between PEG and graphene through a microwave-induced method. A primary alcohol in the presence of Lewis acids and concentrated hydrochloric acid can be protonated and resulted in an electrophilic species (carbocation or protonated alcohol). This electrophile (in the case of poly ethylene glycol) is a stabilized cationic electrophilic reagent with significantly superior reactivity in the presence of microwave irradiation (Vázquez & Prato, 2009; Zhu, Murali, Stoller, et al., 2010). These types of carbocations were described by Olah et al. (1975). By protosolvation of a cationic electrophile, an active electrophilic reagent is suitable for electrophilic aromatic substitution, which in the case of the graphene flakes, an electrophilic addition reaction was occurred. The formed cations in the first step of electrophilic addition reaction on flakes reacts with nucleophiles (Olah et al., 1975; Singh, 2004). The mechanism of reaction is as follows:



Also, the reaction intensifies under microwave irradiation. When carbon nanostructures are exposed to microwaves, strong absorptions are obtained, which producing intense heating. Although the utilization of microwaves for the activation of carbon nanostructures has not been fully explored, the strong absorptions can open the door to the similar electrophilic addition reactions (W. Lin et al., 2010; Vázquez & Prato, 2009). In addition, the edges of the expanded graphite were more available for reaction with the functional groups than the basal plane surfaces, which were stacked with strong π - π interactions. Note that the decomposition of the functional groups on functionalized

flakes under microwave irradiation can also generate some pressure for overcoming the van der Waals interaction among graphene layers during the microwave procedure.

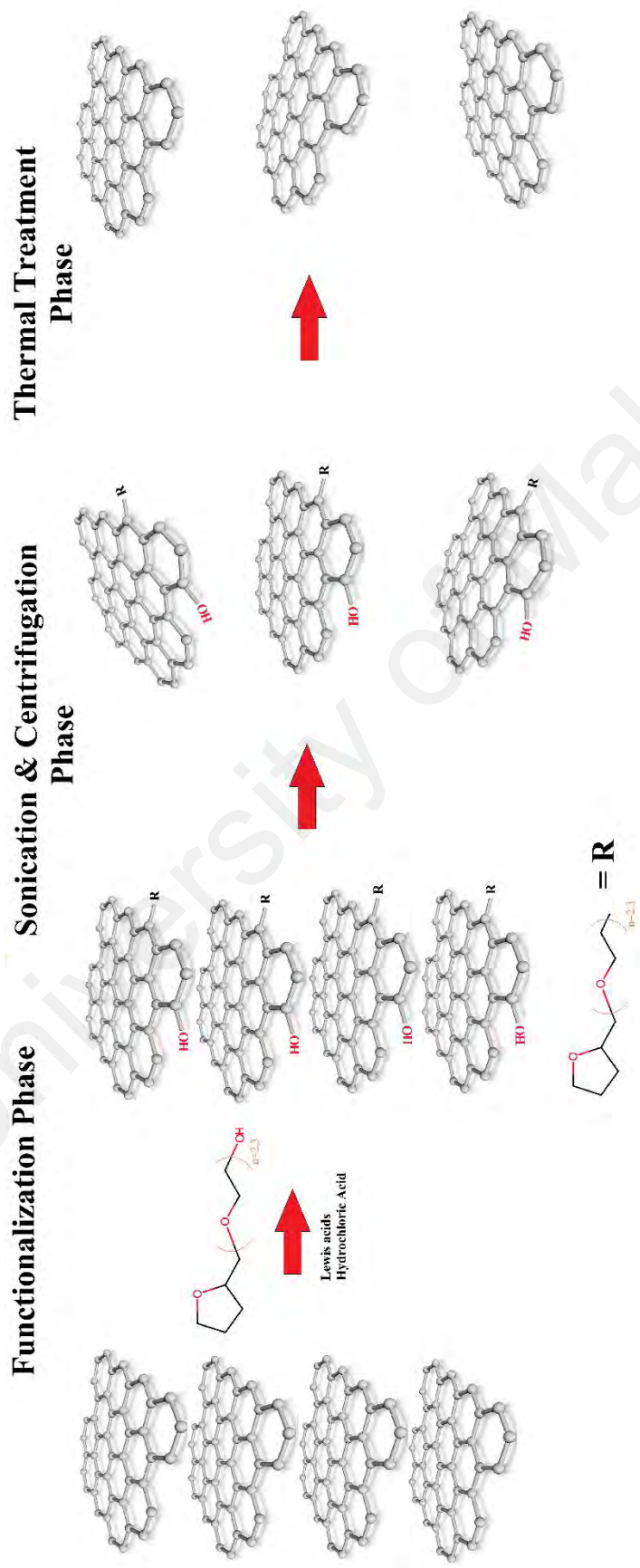


Figure 4.1: The experimental procedure for functionalization as well as exfoliation of graphite and synthesizing of CE-GR and T-GR.

Subsequently, the resulting black ink-like dispersion was left for 24 hr to separate large unstable graphite aggregates. The functionalized graphite unlike unstable graphite aggregates was expanded and was much more soluble in dimethylformamide (DMF), Dimethylacetamide (DMA), γ -butyrolactone (GBL) and ethylene glycol (EG) than the pristine graphite, as shown in Figure 4.2, panel 1. It is noteworthy that a majority of flakes remained stable for more than 1 week. Also, plot of absorbance versus wavelength for various colloidal solutions were studied to trace the presence of functionalized graphite within the binary system. Figure 4.2 show the plot of absorbance intensity versus wavelength and the colloidal stability of PEG-treated graphite in different solutions for expanded graphite in EG, DMA, DMF and GBL taken at specific period.

Then, the homogeneous suspension of PEG-treated graphite in EG was poured into another vessel that contained 450 ml of EG, and the mixture was sonicated for 2 hr to completely disperse the functionalized graphite flakes; this was followed by 30 min of centrifugation at 3000 rpm to collect the supernatant, which was filtered, washed, dried, and denoted as CE-GR after ball-milling the dry-powder for another 30 min. Part of the CE-GR was used for testing and the remainder was set aside for further treatment.

In order to obtain pure graphene without functional groups, thermal treatment up to 500 °C under a nitrogen atmosphere was applied for 15 min to remove all PEG molecules or other impurities. The product was labeled as T-GR. The pure graphene powder that was extracted was black (Figure 4.2 panel 2), which was a significant contrast with the shiny, metallic grey pristine graphite.

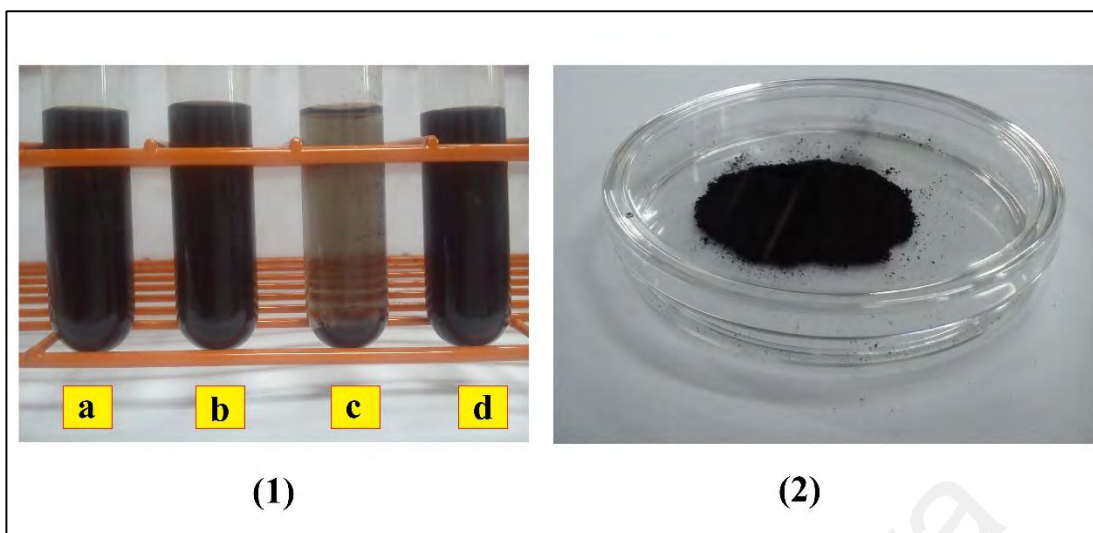


Figure 4.2: (1) Photographs of functionalized and expanded graphite dispersed in (a) DMF, (b) DMA, (c) g-butyrolactone and (d) EG. (2) The extracted black pure graphene powder (T-GR).

4.2.1.3 Characterizations, Results and Discussion

Graphene graft copolymers is first synthesized by covalent functionalization of graphite with the monofunctional, tetrahydrofurfuryl-terminated polyethylene glycol to increase the dispersibility and wettability of the individual graphite and expanding flakes. The monofunctional group, as a covalent group, prevents cross-linking of the graphite (Kalinina et al., 2011a). Also, another promising approach was followed for the exfoliation of graphite to produce just highly-porous, single-layered graphene as a quick method for application to the high-conductive nanofluids.

4.2.1.4 Functionality and Quality of Graphene

As mentioned above, covalent functionalization occurs through the formation of an electrophilic addition reaction between graphite and the PEG chain under microwave irradiation, which was verified by FTIR spectroscopy.

Figure 4.3(a) shows the FTIR spectra of pristine graphite, CE-GR, and T-GR. It is seen that the FTIR spectrum of pristine graphite provided no evidence of PEG. The peaks at 1471, 1535 and 1577 cm^{-1} were respectively consistent with the bending vibration of the CH_2 group, stretching vibrations of the $\text{C}=\text{C}$ and $\text{C}=\text{O}$. In contrast, the

FTIR spectrum of CE-GR had two peaks in the range of 2800-3000 cm^{-1} , which were associated with the C-H stretching vibration³¹. The peak at 1548 cm^{-1} was consistent with C=O or C=C stretching vibrations, which are infrared-activated by extensive functionalization. Also, the OH stretching vibration produced a weak peak at 3455 cm^{-1} , indicating the presence of hydroxyl groups attached to the graphite. The FTIR spectrum of the treated samples also had a peak at 1460 cm^{-1} , representing the bending vibration of the CH₂ group. The peak at 1182 cm^{-1} was in agreement with the stretching vibration of the C-O groups. In contrast to the CE-GR, T-GR showed no evidence of PEG molecules, which confirmed that all of the functional groups had been removed. The FTIR spectrum of T-GR shows two weak peaks in the range of 2800-3000 cm^{-1} , which were associated with the C-H stretching vibration. The lack of above-mentioned peaks in T-GR spectrum shows the prepared graphene was almost pure and that a majority of the functional groups had been removed (Ou et al., 2012; Pan et al., 2013; Radic et al., 2013).

To provide evidence supporting the above statements, thermogravimetric analysis (TGA) was used to detect quantitatively the weight fraction (loading) of organic groups attached to the graphite. Figure 4.3 panels b, c, and d show the TGA curves of the pristine graphite, CE-GR, and T-GR samples, respectively. Also, Figure 4.3 panels b, c, and d show the differential thermogravimetric analysis (DTG) curves of the pristine graphite, CE-GR, and T-GR powders after filtration. It is apparent that there was no significant weight loss with pristine graphite, which was thermally stable when heated to 770 °C under an air flow rate of 50 cm^3/min . The DTG curves also show that there were two phases of degradation with the CE-GR sample. CE-GR illustrates a mild weight loss in the temperature range of 100–205 °C, which was due to the decomposition of the covalently-grafted organic addends (PEG).

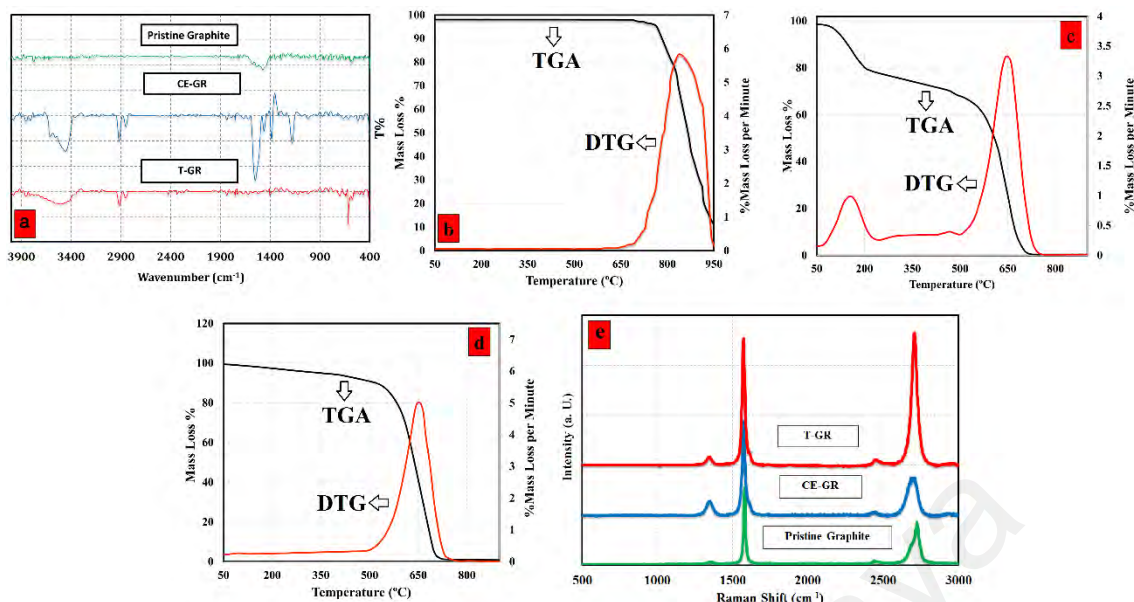


Figure 4.3: (a) FTIR spectra of pristine graphite, CE-GR and T-GR, TGA and DTG curves of (b) pristine graphite, (c) CE-GR, (d) T-GR and (e) Raman spectra of pristine graphite, CE-GR and T-GR.

To address this issue, the TGA and DTG curves of pure PEG are also shown in Figure 4.4. It can be seen that the main weight loss occurred over the temperature range of 110-200 °C, which is in agreement with our claim.

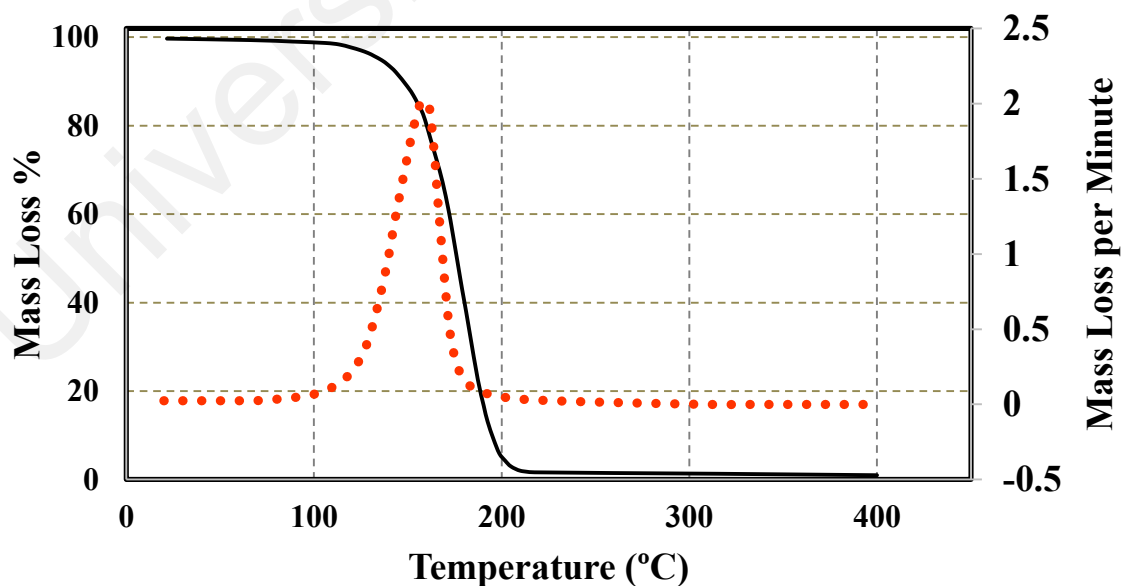


Figure 4.4: TGA and DTG curves of pure PEG.

Because the PEG molecules were used initially to achieve exfoliation and expand the layers, the weight loss that occurred up to 500 °C was attributed to the PEG that was trapped within the graphene layers. Also, the second phase of degradation was associated with the decomposition of the graphitic carbon. It is noteworthy that the results suggest that CE-GR had an appropriate degree of functionalization. Also, the weight loss obtained by our method was greater than those reported by conventional methods (Kalinina et al., 2011a), suggesting a strong functionalization of carbon nanostructures with organic molecules.

To achieve pure graphene, the remaining PEG that was decorated on the structure of CE-GR was removed by thermal treatment under a nitrogen atmosphere at temperatures up to 500 °C for 15 min. Figure 4.3(d) shows the TGA and DTG curves of the T-GR after freeze drying. As observed in the DTG curve, the only obvious peak was the graphitic peak. Also, the graphitic structure of T-GR remained stable up to 750 °C, indicating that the prepared graphene is totally pure and those functional groups can be removed with a simple and fast method (Lv et al., 2009). In addition, the decomposition temperature of both products are same and shifted towards lower temperatures compared to the pure graphite, indicating that the number of layer per flakes decreased.

The Raman spectra of the pristine graphite, CE-GR, and T-GR are shown in Figure 4.3, panel (e). A feeble D band can be seen at 1344 cm^{-1} , and there are fairly strong G and 2D bands at 1568 and 2695 cm^{-1} , respectively. The ratio of the intensities of the D-band to the G-band (I_D/I_G) is considered to be the amount of disordered carbon (sp^3 -hybridized carbon) relative to graphitic carbon (sp^2 -hybridized carbon). In functionalization studies of carbon nanostructures, the higher intensity ratio of I_D/I_G indicates the higher disruption of aromatic π - π electrons, implying the partial damage of graphitic carbon produced by expansion and edge functionalization (Lv et al., 2009). Although the D bands of all of the samples had weak peaks, the I_D/I_G ratios of CE-GR

were relatively higher than those of pristine graphite, which confirmed the successful functionalization via an electrophilic addition reaction under microwave irradiation (McAllister et al., 2007). Also, the Raman results of CE-GR showed lower I_D/I_G ratios than the graphene oxide and/or chemically-converted graphene (Dikin et al., 2007), implying that there were fewer defects on the basal planes of the CE-GR.

Also, the poor D-mode (I_D/I_G) of T-GR, which was in agreement with the DTG and TGA results, confirmed that the prepared graphene was totally pure and that the functional groups had been removed completely. Surprisingly, the G peak in the spectra of CE-GR and T-GR retained their intensities after the electrophilic addition reaction (insignificant decrease in G mode with CE-GR sample), which confirmed that the quality of the graphene layers that were obtained was preserved. Also, the higher intensity ratio of $I(2D)/I(G)$ confirms the presence of few-layer graphene.

Raman spectroscopy can obviously distinguish a single layer from a bilayer and/or from a few layers by focusing on the shape, size, and intensity of the 2D bands (Ferrari et al., 2006). According to the results of Ferrari et al. (2006), as the layer of graphene increases, the 2D band becomes much broader and up-shifted. Accordingly, a considerable change in sizes, shapes, and intensities of the 2D peaks of CE-GR and T-GR are more obvious than they are for the pristine graphite. It can be seen that the 2D band of the pristine graphite includes a coupled peak, i.e., D_1 and D_2 peaks, which produced a broad peak (Ferrari et al., 2006). However, single, sharp 2D peaks were shown in the Raman spectra of CE-GR and T-GR. This change in the 2D bands observed in the CE-GR and T-GR samples potentially verified the presence of few-layer flakes sheets.

The natures of pristine graphite, CE-GR, and T-GR were studied by X-ray photoelectron spectroscopy (XPS), as illustrated in Figure 4.5a. It can be seen that C1s and O1s peaks appeared at almost 284.5 eV and 531.8 eV, respectively. Based on these results, pristine graphite presents a very small amount of oxygen. Upon functionalization,

the intensity of the O1s peak increased considerably. It is obvious that PEG functionalities may explain the higher content of oxygen in the CE-GR sample. The amount of oxygen in T-GR decreased after thermal treatment in nitrogen as compared with the CE-GR sample, and, interestingly, it was a bit lower than the amount of oxygen in pristine graphite. The decrease in the O component that was obtained after thermal treatment was associated with the loss of the functional groups between the graphene layers, which was in agreement with the FTIR, TGA, DTG, and Raman results. To investigate the nature of the functional groups, further study was conducted using high-resolution C1s scans. Figures 4.5b-d present the deconvoluted C1s XPS spectra of pristine graphite, CE-GR, and T-GR (Lotya et al., 2009).

Pristine graphite (Figure 4.5b) mainly had a peak around 284.7 eV that corresponded to the C=C network. The peaks corresponded to the sp^3 C-C is observed at 285.2 eV, indicating the presence of the sp^3 carbons of PEG units (Z. Wang et al., 2014). The minor O component in pristine graphite presents in the form of the C=O group at 287.5 eV. In CE-GR (Figure 4.5c), the presence of considerable number of functional groups was apparent. The peak at ~ 286.1 eV corresponded to the C-O groups, which resulted from the hydroxyl (C-OH) and/or the epoxide (C-O-C) groups. Clearly the hydroxyl (C-OH) group and the epoxide group had similar C1s binding energies (Lotya et al., 2009).

The C_{ring} carbon in the furan ring bonded to two hydrogen atoms also was present to a considerable extent in CE-GR at ~ 285 eV indicating the functionalization of pristine graphite with PEG molecules. The presence of furan signals could be indicative of the lack of a ring-opening reaction. The C1s XPS spectra of T-GR (Figure 4.5d) show a significant decrease in the extent of functional groups. In T-GR, a majority of the functional groups, such as C=O, C_{ring} , and C-O, was reduced or removed. Also, in the C 1s spectra, the intensity of the peak corresponding to sp^2 -hybridized carbon (at 284.7 eV)

increases continually from CE-GR to T-GR, revealing the effective removal of functional groups from CE-GR and partial restoration of the conjugated graphene sheets (Z. Wang et al., 2014).

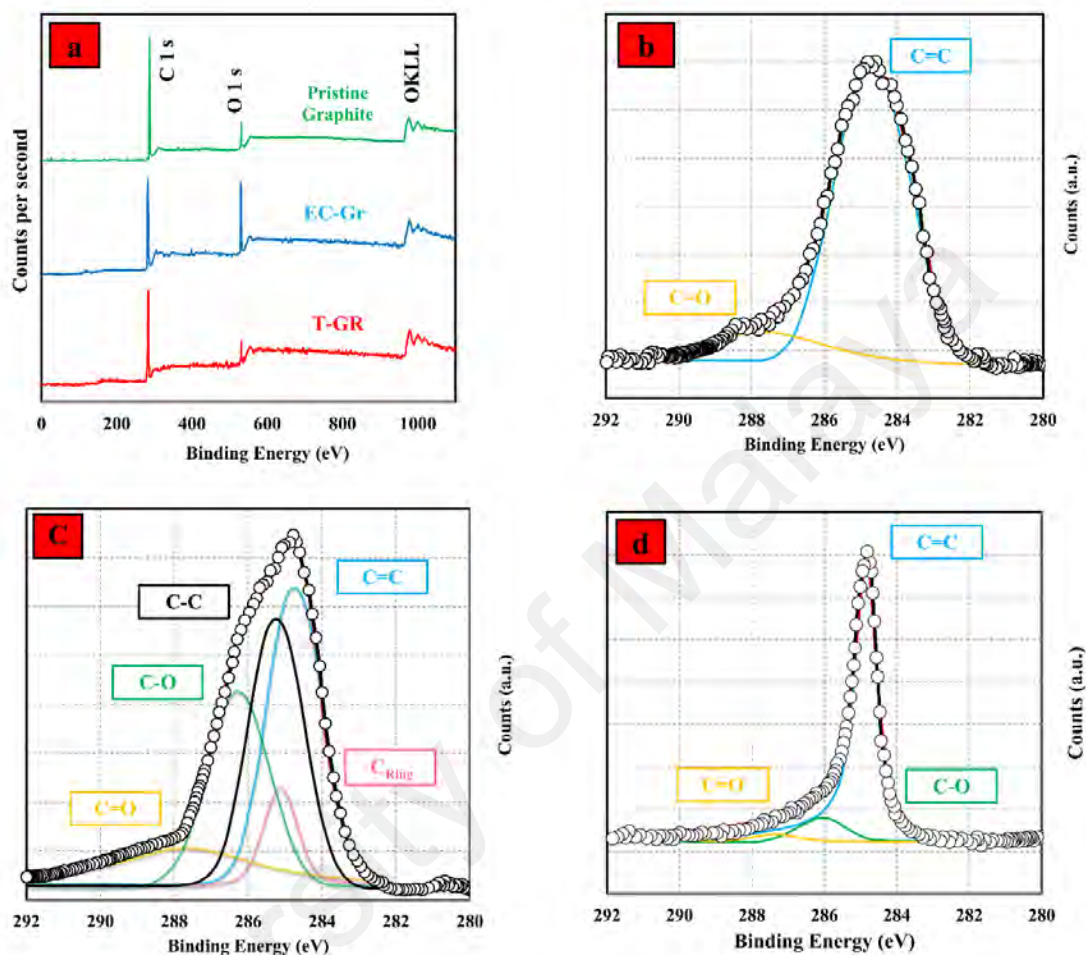


Figure 4.5: (a) XPS survey spectra of CE-GR and T-GR. High-resolution C 1 s spectra of (b) pristine graphite, (c) CE-GR and (d) T-GR.

Overall, the above results along with the ratio of $I_{D/G}$ in Raman spectra clearly indicate the strong covalent linkage of PEG moieties to the graphite. Also, the sharp and symmetric C 1s peak of T-GR at 284.8 eV confirmed the presence of a graphitic structure with minimal functional groups, indicating that a large number of covalent-functional groups on CE-GR removed after the thermal treatment (Zhengzong Sun et al., 2010). The peak positions and their interpretation are presented in Table 4.1.

Table 4.1: Peak positions of various groups in C1s Spectra of pristine graphite, CE-GR and thermally-treated graphene.

sample	functional group peak positions (eV)				
	C=C	C-C	C-O	C=O	C _{ring}
Pristine Graphite	284.7	---	---	287.7	
CE-GR	284.6	285.2	286.1	287.6	285
T-GR	284.8	---	286.1	287.3	---

4.2.1.5 Morphological Study

Figure 4.6 illustrate the FESEM images of the (a-h) CE-GR and (i-l) T-GR that show a high yield exfoliation was achieved. Note that, for CE-GR samples, high-resolution imaging of FESEM (Figure 4.6) was obtained with no pretreatment, such as surface sputtering with a thin gold layer, suggesting that the samples had high conductivity (Lv et al., 2009).

Figure 4.6 shows the exfoliations of the multi-layered graphite into single- or few-layered graphene, which was obtained by microwave-assisted functionalization along with physical cracking by a sonicator, demonstrating a marked reduction in thickness by chemical-mechanical cracking with no significant damage to the size of the grains. The mentioned approach is able to open the graphite layers swiftly, and it produces CE-GR and T-GR with appropriately uniform surfaces.

It is worth mentioning that the FESEM pictures of samples showed some crumpled and curved sheets that were transparent to the electron beam. Also, such a worm-like surface, with crumpled and curved sheets, is due to strict exfoliation and functionalization. Although FESEM images cannot distinguish the precise thickness of flakes and functional groups, the planar morphology of graphene layer, the exfoliation and formation of low-layered graphene are clearly seen from these pictures. It is worth mentioning that FESEM clearly showed intense cleavage surfaces of graphite by

functionalization under microwave irradiation and sonication. Some of T-GR images show that the extent of wrinkles, which commonly developed during functionalization and were attributed to the addition of functional groups, almost decreased after thermal treatment. This may be a result of decomposition of functional groups (PEG) during the thermal-treatment procedure. More evidence in this regard is provided by transmission electron microscopy and atomic force microscopy in the following section.

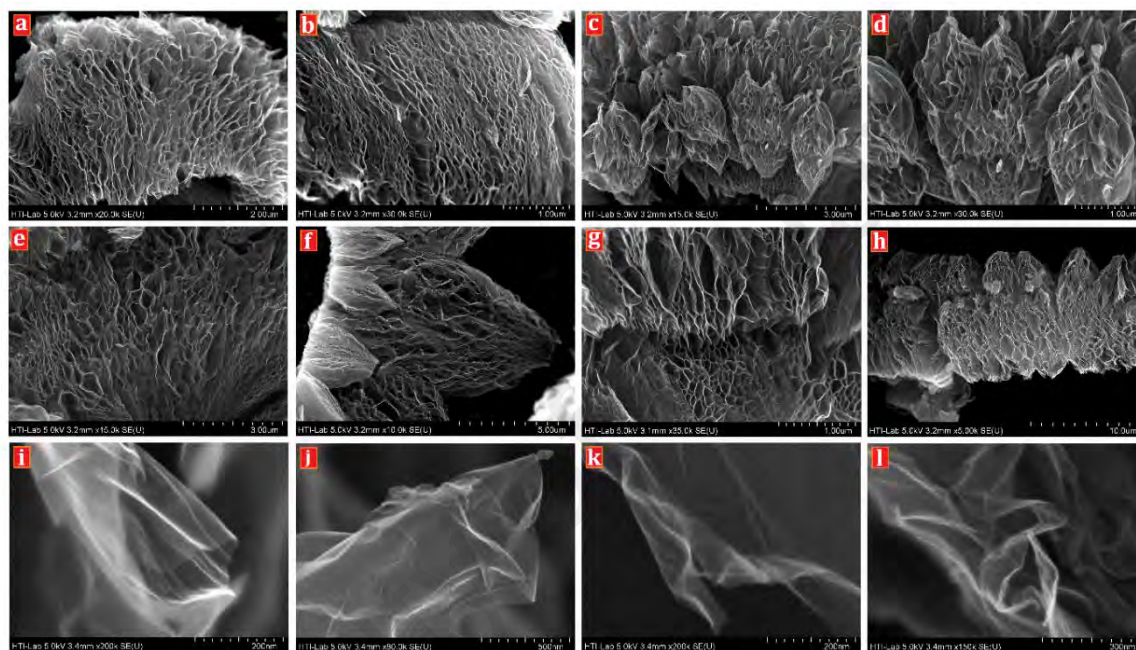


Figure 4.6: FESEM images of the CE-GR (3a-h) and T-GR (3i-l).

Figure 4.7 shows the transmission electron microscopy (TEM) images and selected areas electron diffraction (SAED) patterns of CE-GR and T-GR. Figures 4.7a-c show the TEM images of CE-GR, which included some individual graphene sheets with wrinkled morphology and folded edges. It can be seen that large graphene nanosheets (a few hundred square nanometers) resemble crumpled silk veil waves. Figure 4.7 (panels d, e, f, and g) illustrate TEM images of the T-GR sample, which comprised of a single/few-layered graphene with large grain sizes.

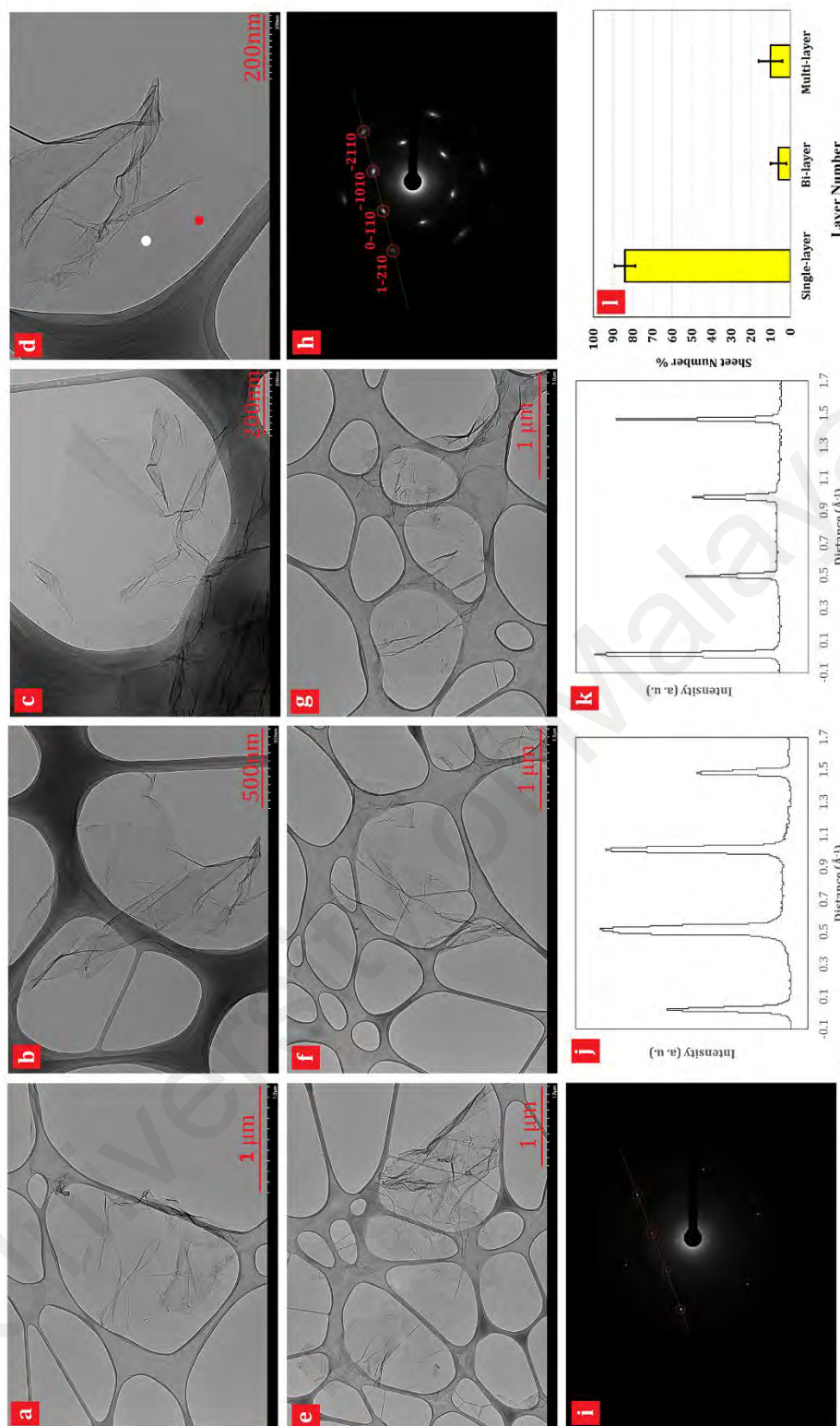


Figure 4.7: **a-h**, High-resolution TEM images of CE-GR (**a-c**) and T-GR (**d-g**) graphene. **h, i**, Electron diffraction patterns taken from the positions of the red (**h**) and white spots (**i**), respectively, of the sheet shown in **d**, with the peaks labelled by Miller-Bravais indices. The graphene is clearly one layer thick in (**h**) and two layers thick in (**i**). **j, k**, Diffracted intensity taken along the 1–210 to –2110 axis for the patterns shown in **h** and **i**, respectively. **l**, Histogram of the ratios of the intensity of the {1100} and {2110} diffraction peaks for all the diffraction patterns collected.

In addition, some of the small and big holes are obvious in Figure 4.8.

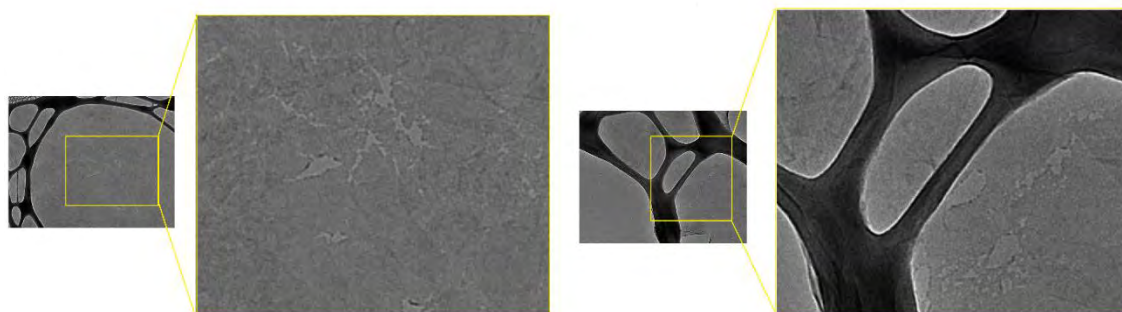


Figure 4.8: TEM images of the CE-GR.

A more definitive identification of graphene can be made by analysis of electron diffraction patterns (Hernandez et al., 2008; J. Meyer et al., 2007). For identification of monolayers by electron diffraction, the fact that the ratio of the intensity of the $\{1100\}$ to the $\{2110\}$ peaks gives an unambiguous local identification of monolayer, bilayer, and multilayer can be used to provide information on the yield of monolayer graphene. The recent results were reported experimental intensity ratios of $I_{\{1100\}}/I_{\{2110\}} \approx 0.4$ for bilayer graphene and $I_{\{1100\}}/I_{\{2110\}} \approx 1.4$ for monolayer graphene (J. Meyer et al., 2007; Shen & Lua, 2013). Also, a bimodal distribution is obtained, with peaks centered at $I_{\{1100\}}/I_{\{2110\}}=0.56$ and $I_{\{1100\}}/I_{\{2110\}}=1.45$, representing bilayer and monolayer graphene, respectively, which agreed well with other reported results (Hernandez et al., 2008; Shen & Lua, 2013). Other quantities are caused by multilayer graphene. As an example of this, Figure 4.7d shows what appear to be a graphene monolayer and a graphene bilayer, respectively. Figure 4.7d is particularly interesting as almost the middle side of the flake consists of at least two layers, whereas on the edge side, a single monolayer protrudes. Figure 4.7h shows the normal-incidence electron diffraction pattern of the flake in Figure 4.7d, taken with beam position close to the red dot. Figure 4.7i shows normal-incidence selected-area diffraction patterns for the flake in Figure 4.7d, taken with beam position close to the white dot. In both cases, the patterns show the typical sixfold symmetry expected for graphite/graphene (J. C. Meyer et al., 2007), permitting to label the peaks

with the Miller–Bravais (hkil) indices. Also, the hexagonal patterns are similar to those in other researches' reports for single-layer and bilayer graphene.

The main difference between Figures 4.7h and 4.7i is that for the multilayers (or bilayer) (Figure 4.7i), the $\{2110\}$ spots appear to be more intense relative to the $\{1100\}$ spots. As mentioned above, this identification of AB stacking in these thin multilayers allows us to differentiate monolayer from bilayer as well as multilayer graphene by inspection of the intensity ratio $I_{\{1100\}}/I_{\{2110\}}$. To this end, a line section is plotted through the $(1-210)-(0-110)-(-1010)-(-2110)$ axis for the patterns in Figure 4.7h and 4.7i in Figure 4.7j and 4.7k, respectively. In Figure 4.7j, it can be seen that the inner peaks, $(0-110)$ and (-1010) , are more intense than the outer ones, $(1-210)$ and (-2110) , confirming that the region marked by the red dot in Figure 4.7d is monolayer. Conversely, Figure 4.7k shows inner peaks that are less intense than the outer ones, confirming that the area around the white dot in Figure 4.7d consists of more than one layer. By analysing a large number of TEM images and their electron diffraction patterns based on the intensity ratio $I_{\{1100\}}/I_{\{2110\}}$, paying close attention to the uniformity of the flake edges, the flake thickness statistics could be generated as shown in Figure 4.7l. The distribution of the number of layers per flakes was obtained by analyzing 3 batches of flakes (first group 97 flakes, second group 50 flakes and third group 50 flakes). The results suggested that about 84% and 6% of the sheets were single- and bi-layered, respectively (Figure 4.7l). Also, it is rarely (almost 10% of flakes) observed large objects with thickness of more than a few layers. Thus, the present authors believe that, graphite has been extensively exfoliated to give monolayer as is obvious in FESEM images as well.

AFM was utilized for the further morphological characterization of the thin-layered graphene and for the investigation of the thicknesses of the CE-GR and T-GR flakes. AFM samples were prepared by sonicating CE-GR and T-GR sheets in DMF without any additives. Figure 4.9 and Figure 4.10 present typical AFM images in which

no graphene sheets were identified as being layered over other sheets, and there were more than 50 and 20 flakes (Figure 4.9 and Figure 4.10) in CE-GR and T-GR images, respectively, and, interestingly, all of the sheets were single-layer sheets.

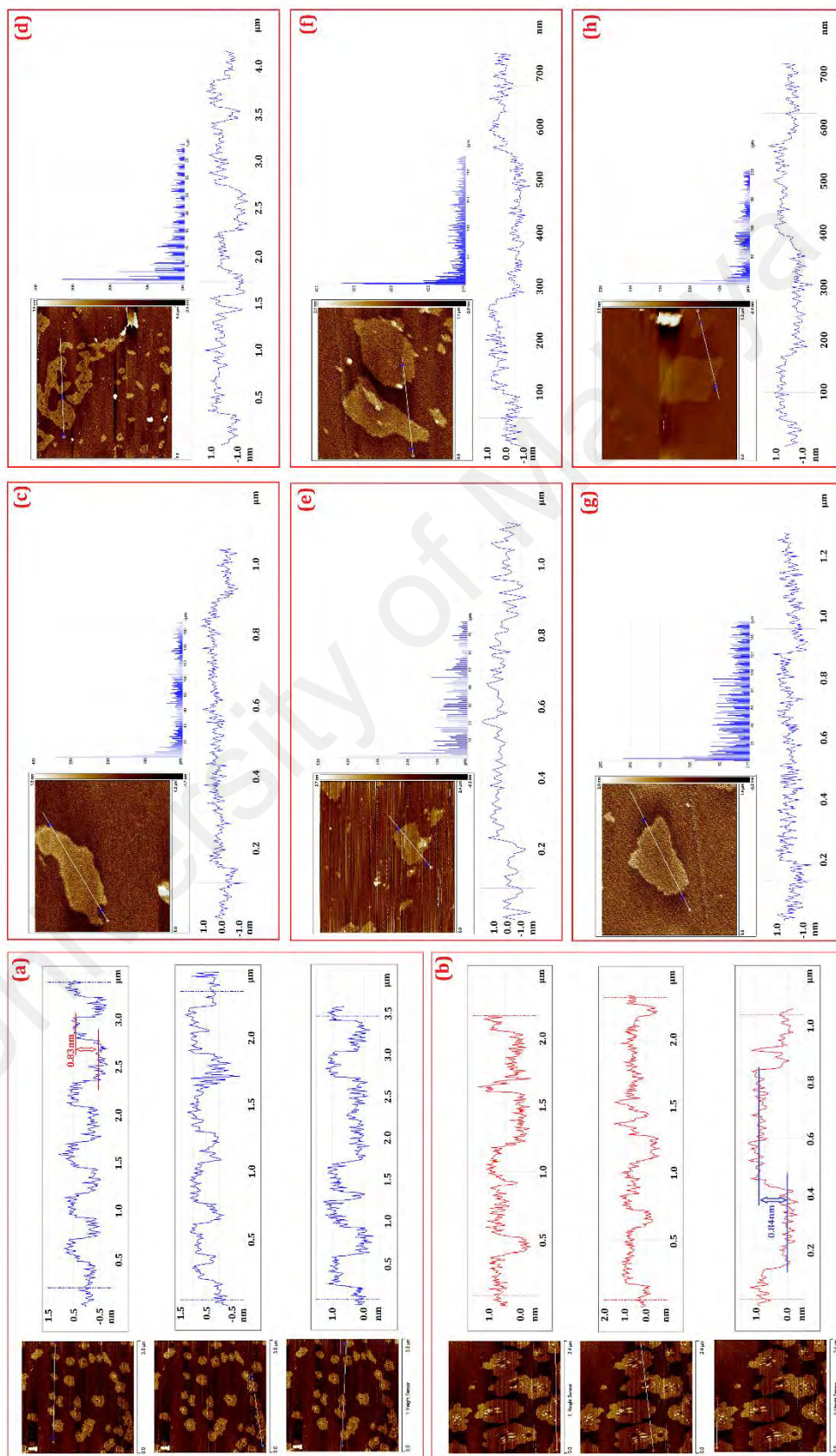


Figure 4.9: AFM ichtnography and cross-section contour of (a, c, d and e) CE-GR and (b, f, g and h) T-GR.

As shown in Figure 4.9 and Figure 4.10, both samples indicated that all of the sheets had thicknesses of less than 1 nm. With a maximum height of 1 nm in both figures, the CE-GR and T-GR samples showed the thickness of one layer, which some of them was decorated with many large and small holes and it is attributed to severe side functionalization by the electrophilic aromatic substitution under microwave irradiation. Also, some of flakes shows no big holes. It is worth to note that for energy applications, some defects or functional groups can be beneficial by representing high specific surface area.

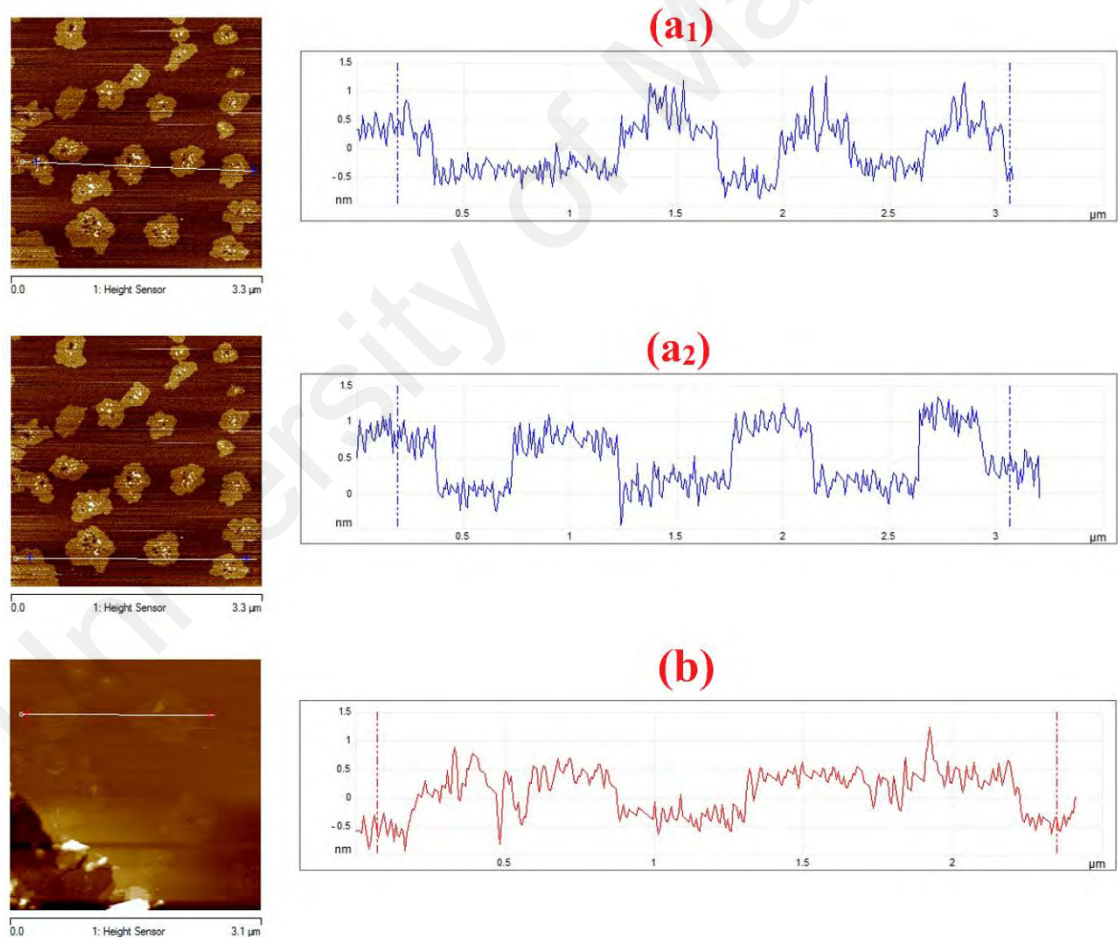


Figure 4.10: AFM ichtnography and cross-section contour of (a1&a2) CE-GR and (b) T-GR.

To investigate the effects of functionalization and thermal treatment on the specific surface area of CE-GR and T-GR, N₂ adsorption–desorption isotherms were measured by a surface area analyzer (Quantachrome Autosorb-1 analyzer at 77 K). The N₂ adsorption–desorption isotherms of the CE-GR and T-GR are shown in Figure 4.11 and Table 4.2. The nitrogen adsorption isotherms exhibit a mixture of type IV and type V with a pronounced hysteresis at a high relative pressure region, implying the presence of a large number of mesopores in both samples. In addition, CO₂ adsorption-desorption was performed to assess micropores (pores less than 1 nm) in the low-pressure region. BET analysis indicated that the specific surface area of CE-GR and T-GR were up to 761 and 1559 m²/g, respectively.

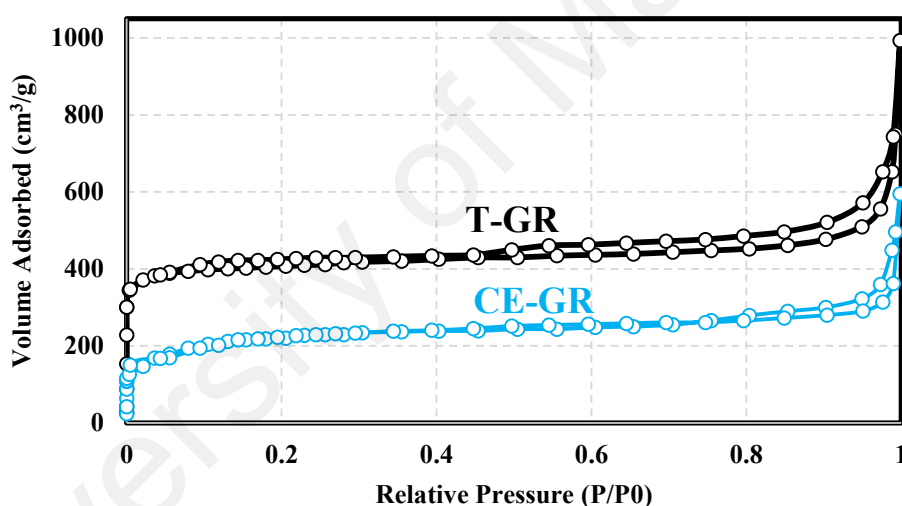


Figure 4.11: N₂-adsorption/desorption of the CE-GR and T-GR.

Also, the pores in T-GR have a well-defined micro-mesopore size distribution as shown in Table 4.2, with a huge increase in pore volume (up to 4.53 cm³/g) relative to CE-GR. This larger specific surface area of T-GR suggests that the introduction of PEG between the 2D graphene sheets can increase the layer-to-layer stacking to a greater extent than T-GR or the filled the porous area.

Table 4.2: Pore structure of the CE-GR and T-GR

Sample	S_{BET} ($m^2 g^{-1}$)	pore volume ($cm^3 g^{-1}$)		
		Micropore	Mesopore	Total
CE-GR	761	0.77	2.15	2.92
T-GR	1559	0.92	3.61	4.53

4.2.1.6 Summary of in Situ Functionalization and Exfoliation

Single-layered graphenes were produced by a potentially industrially-scalable, cost-effective, liquid-phase exfoliation in the presence of chemical-mechanical treatment. First, graphite-polyethylene glycol (PEG) was synthesized by covalent functionalization under microwave irradiation to enhance its dispersibility in polar aprotic organic solvents. Few-layer graphenes were obtained from PEG-treated graphite. Functionalization was confirmed by characterization instruments, and, after exfoliation, the statistical studies concerning the distribution of the number of layers indicated that about 90% of few-layered graphene had one and two layers, about 84% of which were single-layered. The few-layered graphenes illustrated promising potential in transferring energy. The highly-porous, single-layered structure of graphene provides a special condition for employing as additive in nanofluids due to the specific surface area of the sheets, which will be discussed in depth in the chapters 6 and 7.

4.2.2 Preparation of Highly-Crumpled, Few-Layered Graphene (HCG) and Highly-Crumpled Nitrogen-Doped Graphene (HCNDG)

4.2.2.1 Chemicals

Chemical materials and solvents were obtained from Sigma-Aldrich in analytical grade without future purification. Graphite (purity of 99.9%) was received from Alfa Aesar and applied without extra purification. Also, a Millipore PTFE membrane (pore size of $0.45 \mu m$) was purchased from Whatman Co.

4.2.2.2 Exfoliation and Functionalization

Schematic procedure of exfoliation of graphite flakes to HCG and HCNDG with cyanamide is depicted in Figure 4.12. Mechanism for the graphite exfoliation and/or HCG/HCNDG preparation includes generation of semi-stable diazonium ion, which then initiates a radical reaction with flakes. Then treated graphite with higher dispersibility in DMF open a new gateway for expanding graphite to graphene flakes by inserting between layers. In a typical experiment, pristine graphite (10 mg) and deionized water (30 mL) were poured into a 100 mL vessel. The reaction vessel was sonicated for 5 minutes and the cyanamide (4 equiv per graphite) and isoamyl nitrite (2 equiv per graphite) were added during sonication time, then poured into a Teflon vessel and placed in a microwave chamber for 15 min at 700W. The mixture was then mixed vigorously on a stirrer at 80 °C overnight. The obtained product was followed by cooling to the room temperature, filtered on a PTFE filter and washed with deionized water, methanol and acetone. Thus, a semi-stable diazonium ion produced and then resulted in a radical reaction with graphite flakes. The product was removed from the filter and sonicated for 1 hr in DMF. The resulting black ink-like dispersion was left to sit 24 hrs to separate large unstable graphite aggregates. The dispersed cyanamide-treated graphene was collected by a low speed centrifugation of 1000 rpm for 30 min.

The filtrated supernatant was then dried and denoted as HCG, comprising graphene flakes were reserved for further treatment. To prepare HCNDG, the resulting HCG materials was then placed to a furnace under nitrogen atmosphere and heated at 900 °C to decompose the functionality including amine group into the nitrogen-containing species such as $C_2N_2^+$, $C_3N_2^+$, $C_3N_3^+$ (Fischer et al., 2007; Fischer et al., 2008; Z. Wen et al., 2012), that prepare nitrogen sources for changing HCG into HCNDG.

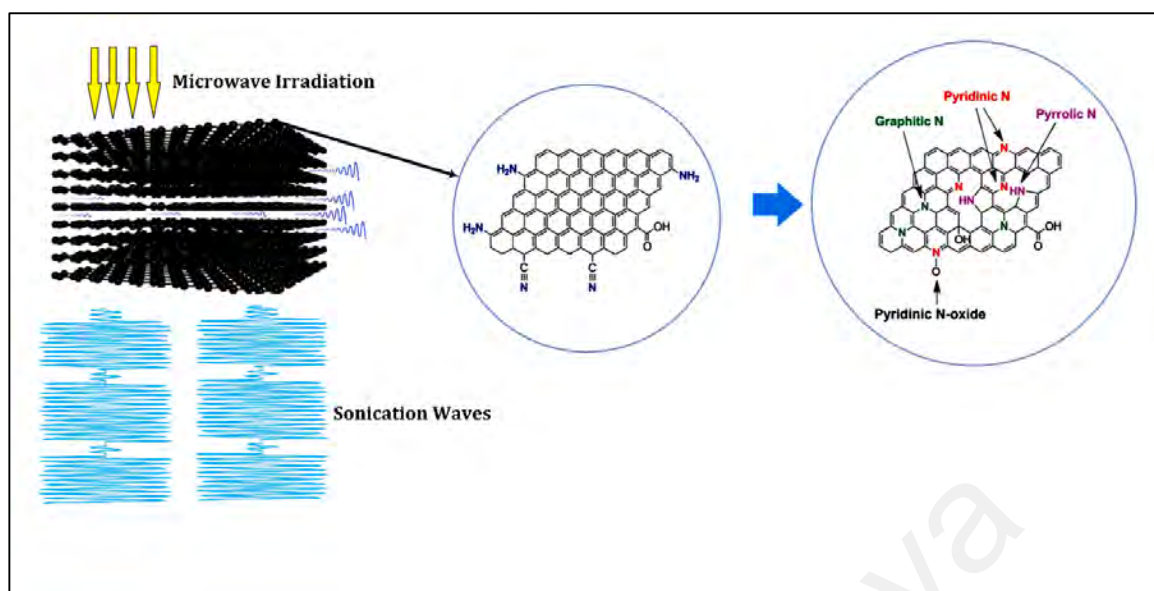


Figure 4.12: The experimental procedure for exfoliation of graphite and synthesizing HCG and HCNDG.

4.2.2.3 Results and Discussion

First, highly-crumpled graphene (HCG) and nitrogen-doped graphene (HCNDG) were synthesized with a low-cost and efficient approach. Then, both HCG and HCNDG materials were analyzed in terms of surface area, structure and morphology to investigate the exfoliation and functionalization yield.

4.2.2.4 Functionality

Figure 4.13 presents the Fourier transform infrared spectroscopy spectra of HCG and HCNDG. While there is no cue of functional groups in pristine graphite, it can be seen that both of the HCG-based and HCNDG-based samples illustrate significant peaks in their spectra. The FT-IR spectrum of HCG shows two new peaks at 1151 and 2268 cm^{-1} , which were attributed to the $\text{C}-\text{N}$ and $\text{C}\equiv\text{N}$ stretching vibrations on the HCG generated by the attachment of the $-\text{C}\equiv\text{N}$ chain of cyanamide during the diazonium treatment. Also, the peak at 3436 cm^{-1} can be assigned to $\text{N}-\text{H}$ stretching vibration. For HCNDG, the peak at 1151 cm^{-1} , corresponding to the stretching vibration of $\text{C}-\text{N}$, shifted to 1193 cm^{-1} . More importantly, the peak at 1550 cm^{-1} was associated with the stretching vibrations of $\text{C}=\text{N}$,

which provided evidence of the doping of nitrogen atoms into the HCG framework. In addition, two other peaks, one at 2851 cm^{-1} and one at 2921 cm^{-1} , are consistent with the $\text{sp}^3\text{ C-H}$ and $\text{sp}^2\text{ C-H}$, respectively, which resulted from hydrogenation at the edges and the size reduction. It can be seen that the peaks at 3436 and 2268 cm^{-1} , which were attributed to the $\text{C}\equiv\text{N}$ and N-H stretching vibrations, respectively, were removed in the FT-IR spectrum of the HCNDG after heating at $900\text{ }^\circ\text{C}$. However, the new peak at 1550 cm^{-1} that was associated with the stretching vibrations of $\text{C}=\text{N}$ was a suitable substitute for above-mentioned groups.

Raman characterization is a strong measurement for analyzing structure, sp^2 and sp^3 hybridized carbon atoms in carbon-based nanomaterials, functionalization, and exfoliation by following alterations in hole and electron doping (Das et al., 2008; Das et al., 2008; L. Feng et al., 2013). The Raman spectra of the pristine graphite, HCG, and HCNDG are presented in Figure 4.13, panel (b). While the pristine graphite is weak in terms of D intensity, the fairly strong D, G and 2D bands in the HCG and HCNDG samples can be seen at 1351 , 1578 , and 2699 cm^{-1} , respectively. The ratio of the intensities of the D-band to those of the G-band (I_D/I_G) was considered to be the amount of disordered carbon (sp^3 -hybridized carbon) relative to graphitic carbon (sp^2 -hybridized carbon). In edge-functionalization and/or nitrogen doping studies of graphene, the higher intensity ratio of I_D/I_G indicates the higher disruption of aromatic π - π electrons, implying partial damage of the graphitic carbon produced by expansion and/or doping (Lv et al., 2009). The I_D/I_G ratio of HCG was relatively higher than that of pristine graphite, which confirmed the successful functionalization via a diazonium reaction under microwave irradiation. Also, the Raman results of HCNDG showed a higher I_D/I_G ratio than that of the pristine graphite as well as HCG, implying that the N-doping procedure was performed. Also, the G and 2D peaks in the spectra of HCG and HCNDG retained their

intensities after the diazotiation, which confirmed that the quality of the graphene layers was preserved.

Obviously, Raman spectroscopy can distinguish a single layer from a few layers by focusing on the shape, size, and intensity of the 2D bands (Ferrari et al., 2006; Hernandez et al., 2008). According to the results of Ferrari et al. (Ferrari et al., 2006), as the layer of graphene increases, the 2D band becomes much broader and up-shifted. Accordingly, a noticeable change in sizes, shapes, and intensities of the 2D peaks of HCG and HCNDG are observed clearly as compared with the pristine graphite. It can be seen that the 2D band of the pristine graphite includes a coupled peak, i.e., D1 and D2 peaks, which produced a broad peak (Ferrari et al., 2006; Hernandez et al., 2008). However, single, sharp 2D peaks were shown in the Raman spectra of HCG and HCNDG. This change in the 2D bands observed in the treated samples potentially verified the presence of single layered- or few layered- graphene and nitrogen-doped graphene.

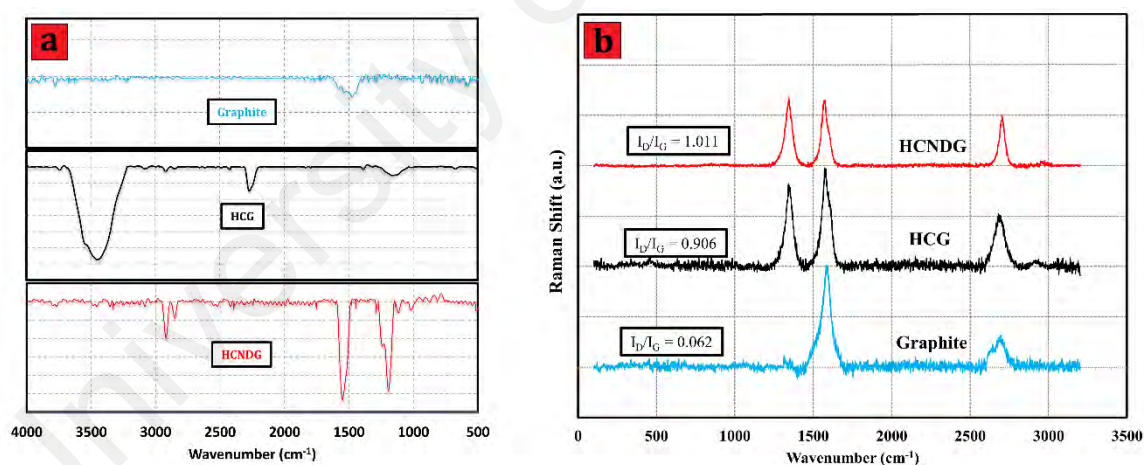


Figure 4.13: (a) FTIR and (b) Raman spectra of the pristine graphite, HCG and HCNDG.

The nature and amount of nitrogen-containing groups in pristine graphite, HCG, and HCNDG were studied by X-ray photoelectron spectroscopy (XPS), which are illustrated in Figure 4.14a. The survey spectra of HCG and HCNDG have C1s at around 286 eV, N 1s at 399eV, and O1s at 530 eV. Based on the results, all samples present a

very small amount of oxygen, and pristine graphite doesn't illustrate any nitrogen molecule in its structure. Upon exfoliation and functionalization, the intensity of the N 1s peak increased considerably. The cyanamide functionalities (especially the C≡N chain) may explain the higher content of nitrogen in the HCG sample. More interestingly, the amount of nitrogen in HCNDG presents a similar result with HCG after thermal treatment in a nitrogen atmosphere. The insignificant decrease in the N component which was obtained after thermal treatment in the nitrogen atmosphere was in agreement with the FTIR, Raman, C 1s, and N 1s results.

Figure 4.14, panels (b) and (c), present the XPS C1s spectra of HCG and HCNDG, respectively. Both HCG and HCNDG mainly had peaks around 284.6 eV, which corresponded to the C–C/C=C network. Although the intensity of the oxygen element is insignificant, the minor O component in HCG and in HCNDG presents two peaks in the form of the C=O and O–C=O groups at around 286.8 and 288.5 eV, respectively. Also, the C–N peak centered at 285.6 eV was observed in both the HCG and HCNDG spectra.

The N 1s spectrum of HCG (Figure 4.14d) composed of two peaks at about 399.2 and 401.8 eV, which would be assigned the bonding configurations of amine functional groups and C≡N or that was detected by FTIR discussed above. However, Figure 4.14e (HCNDG spectrum) shows an asymmetric N1s spectrum, which can be decomposed into four peaks, i.e., pyridinic N (~ 398.5 eV), pyrrolic N (~ 399.8 eV), graphitic N (~ 401 eV), and N-oxides of pyridinic N (~402.1 eV). Interestingly, the functional groups, including the nitrogen groups in HCG, change into more thermally-stable graphitic N after annealing, as illustrated in Figure 4.14e.

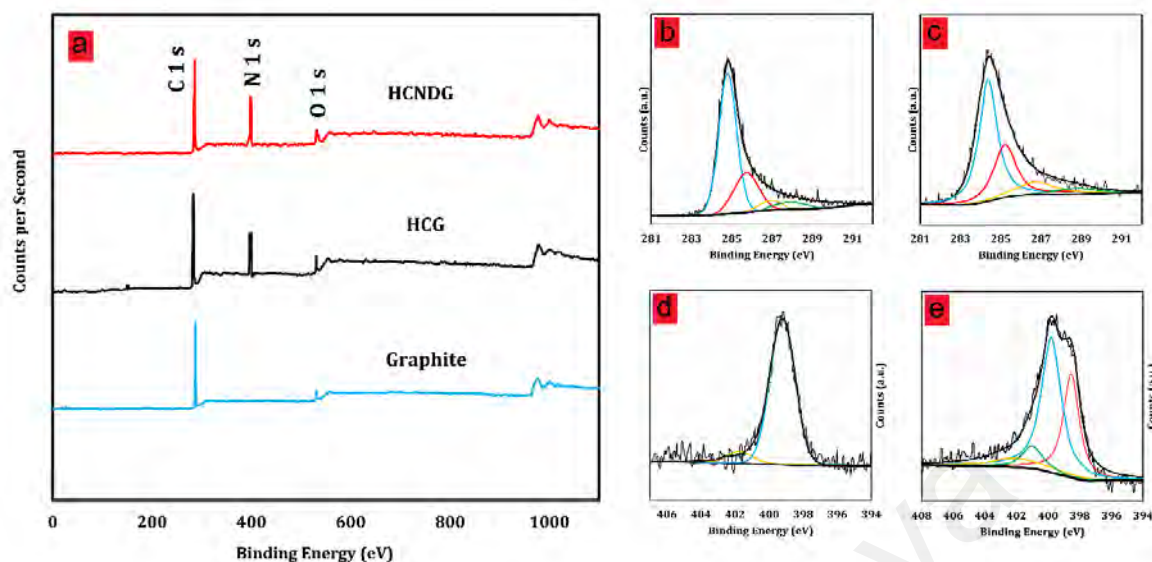


Figure 4.14: (a) XPS survey spectra of pristine graphite, HCG and HCNDG, High-resolution C 1s spectra of (b) HCG and (c) HCNDG, N1s spectra of (d) HCG and (e) HCNDG.

The distributions of the content of N species and their interpretation are presented in Table 4.3. The elemental analysis showed that the nitrogen weight content in the resulting HCG and after annealing (HCNDG) at 900 °C were 17.57% N and 10.32 % N, respectively.

Table 4.3: The content distributions of N species in HCG and HCNDG.

Materials	C%	N%	N/C	Pyridinic N	Pyrrolic N	Graphitic N	N-oxides of pyridinic N
HCG	69.13	17.56	0.254	---	---	---	---
HCNDG	79.75	10.32	0.129	4.12	4.72	0.81	0.67

4.2.2.5 Morphological Study

Figures 4.15a-d show the SEM images of highly-crumpled, few-layered graphene and exfoliated HCG, which were achieved by using a diazonium reaction under microwave irradiation along with physical cracking by a sonicator, demonstrating a noticeable reduction in thickness. The proposed method is able to expand the graphite layers swiftly by initiating a semi-stable diazonium ion and radical reaction with layers. The SEM images of HCG (Figures 4.15a-d) showed homogenous, crumpled structures.

Such a worm-like surface, with crumpled and curved sheets, was due to strict functionalization and nitrogen impurity. The HCNDG (Figures 4.15e-h) also showed the distinct, crumpled structures with 2D geometry, as did HCG. The crumpled structures of HCNDG were attributed to nitrogen doping (Z. Wen et al., 2012). More evidence of this is presented by transmission electron microscopy (TEM) and atomic force microscopy (AFM) in the following section.

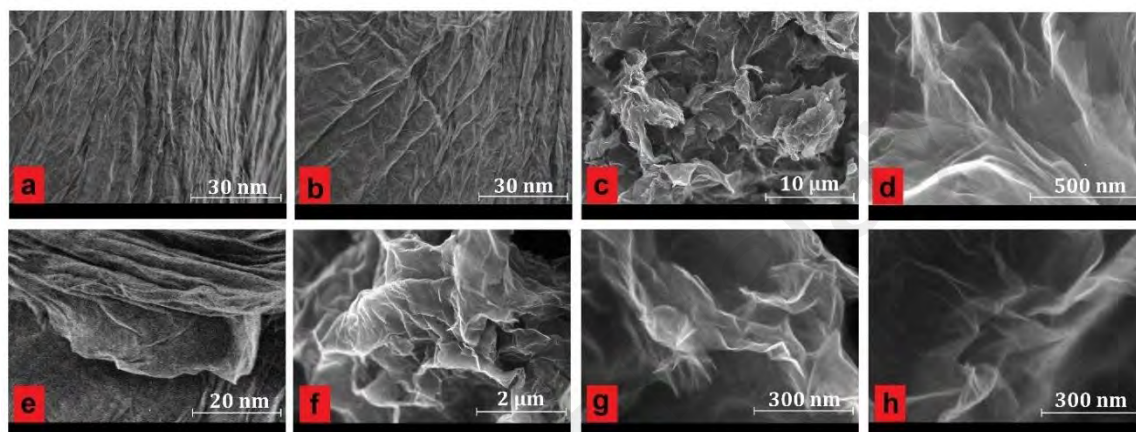


Figure 4.15: SEM images of (a-d) HCG and (e-h) HCNDG.

Figure 4.16 shows the TEM images and select area electron diffraction (SAED) patterns of HCG and HCNDG. Figures 4.16a and 4.16b show the TEM images of HCG, in which the crumpled structure can be distinguished. This figure shows a large number of few-layered graphene nanosheets with wrinkled morphology and folded edges. Figures 4.16 c-e show the TEM images of the HCNDG sample, which was comprised of a few-layered graphene with wrinkled morphology and folded edges. A set of highly-crumpled, individual graphene flakes with suitable transparency and without observable graphite crystalline structure in Figures 4.16a-e confirmed that these wrinkles resulted from the crumpling of graphene rather than stacking, which is in agreement with the sharp 2D bands in the Raman spectra. As further evidence, the crystalline structures of HCG and HCNDG were verified by selected area electron diffraction (SAED), as shown in Figures 4.16f and 4.16g, respectively. Selected area electron diffraction (SAED) of both samples

illustrated a ring-like diffraction pattern with dispersed bright spots (that were stronger in HCNDG). Such an amorphous structure was attributed partially to the existence of functional groups with abundant defective edges for HCG and nitrogen doping defects for HCNDG, which was in agreement with the high intensity of the D band in the Raman spectra of both samples (C. Hu et al., 2015; G. Wang et al., 2008). A ring-like diffraction pattern demonstrated the loss of long-range ordering in the sheets (G. Wang et al., 2008).

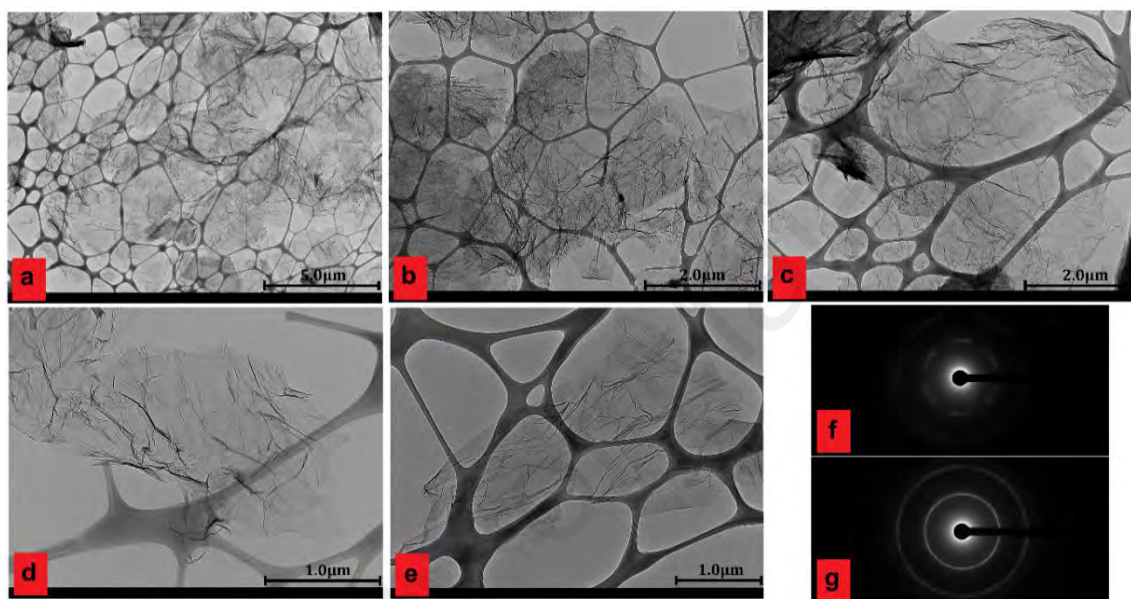


Figure 4.16: TEM images of (a and b) HCG, (c-e) HCNDG and selected area electron diffraction (SAED) patterns of (f) panel a and (g) panel c.

Figures 4.17a–c show the field emission scanning electron microscope (FESEM) images of HCG. The in situ exfoliation and functionalization procedure is able to expand the bulk graphite layers swiftly by initiating a semi-stable diazonium ion and radical reaction with layers. The FESEM images of HCG shown in Figures 4.17a–c illustrate homogenous highly crumpled structures with 2D geometry. Such a worm-like surface, with fully crumpled and curved sheets is due to the strong functionalization. More evidence of the crumpled structure is presented by the transmission electron microscopy (TEM) images shown in Figures 4.17d–g. These TEM images of HCG clearly show large few-layered graphene crumpled flakes with wrinkled morphology and folded edges. The

TEM images in the figures show no observable graphite crystalline structure, which is in agreement with the sharp 2D bands in the Raman spectrum of HCG. As further evidence, the crystalline structure of HCG was confirmed via selected area electron diffraction (SAED), as shown in Figures 4.17 panels (h) and (i). Figure 4.17 panel (h) shows the normal-incidence electron diffraction pattern of the flake in Figure 4.17f, taken with beam position close to the white dot in this figure.

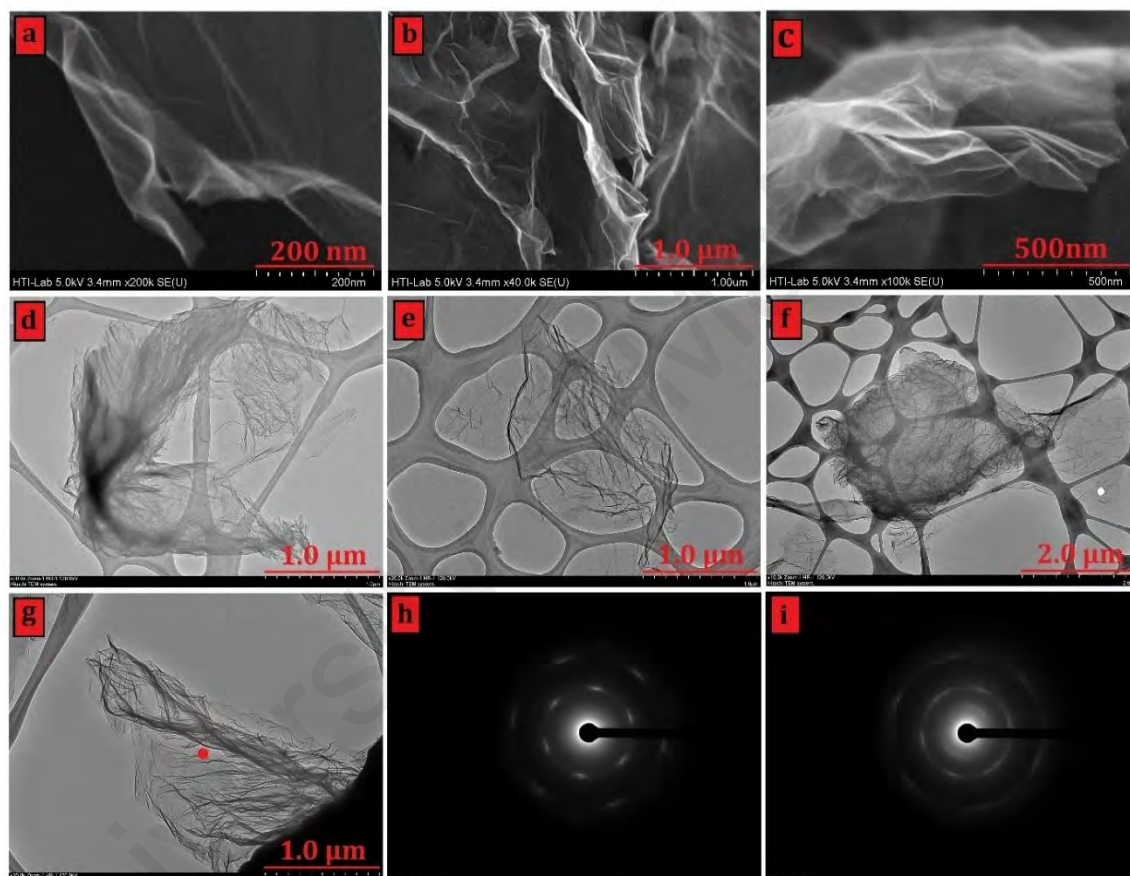


Figure 4.17: (a-c) FESEM images and (d-g) TEM images of HCG; (h and i) selected area electron diffraction (SAED) patterns of white point in panel (f) and red point in panel (g).

Figure 4.17i shows the normal-incidence selected-area diffraction patterns for the flake in Figure 4.17g, taken with beam position close to the red dot. In one of the cases, the patterns show the typical six-fold symmetry expected for graphite/graphene (J. C. Meyer et al., 2007), allowing labeling the peaks with the Miller–Bravais (hkil) indices (J. C. Meyer et al., 2007). Also, the hexagonal patterns are similar to those in reported by

other researches (Hamilton et al., 2009; Khan, O'Neill, et al., 2010) for single-layer and few layer graphene.

In another case, selected area electron diffraction of the HCG sample also shows a ring-like diffraction pattern with the dispersed bright spots. Such an amorphous structure was attributed partially to the presence of functional groups with abundant defective edges for HCG, which is in agreement with the high intensity D band in the Raman spectrum of HCG sample (C. Hu et al., 2015; G. Wang et al., 2008). A ring-like diffraction pattern suggests the loss of long-range ordering in the sheets (G. Wang et al., 2008).

AFM was used for the further morphological characterization of the thin-layered HCG and HCNDG for the investigation of the thicknesses of the flakes in the final product. AFM samples were prepared by sonicating HCG and HCNDG sheets in ethanol for two minutes in a bath sonicator without any additives. Figure 4.18 shows typical AFM images of HCG and HCNDG in which one highly-crumpled sheet was investigated, and, interestingly, the other sheets were mostly few-layered, which is in agreement with the sharp 2D bands of the Raman results and XRD results (Appendix B). As shown in Figure 4.18, the sheets had mostly the thicknesses of about 1 nm, which can be considered to be the thickness of one layer, including the wrinkled morphology.

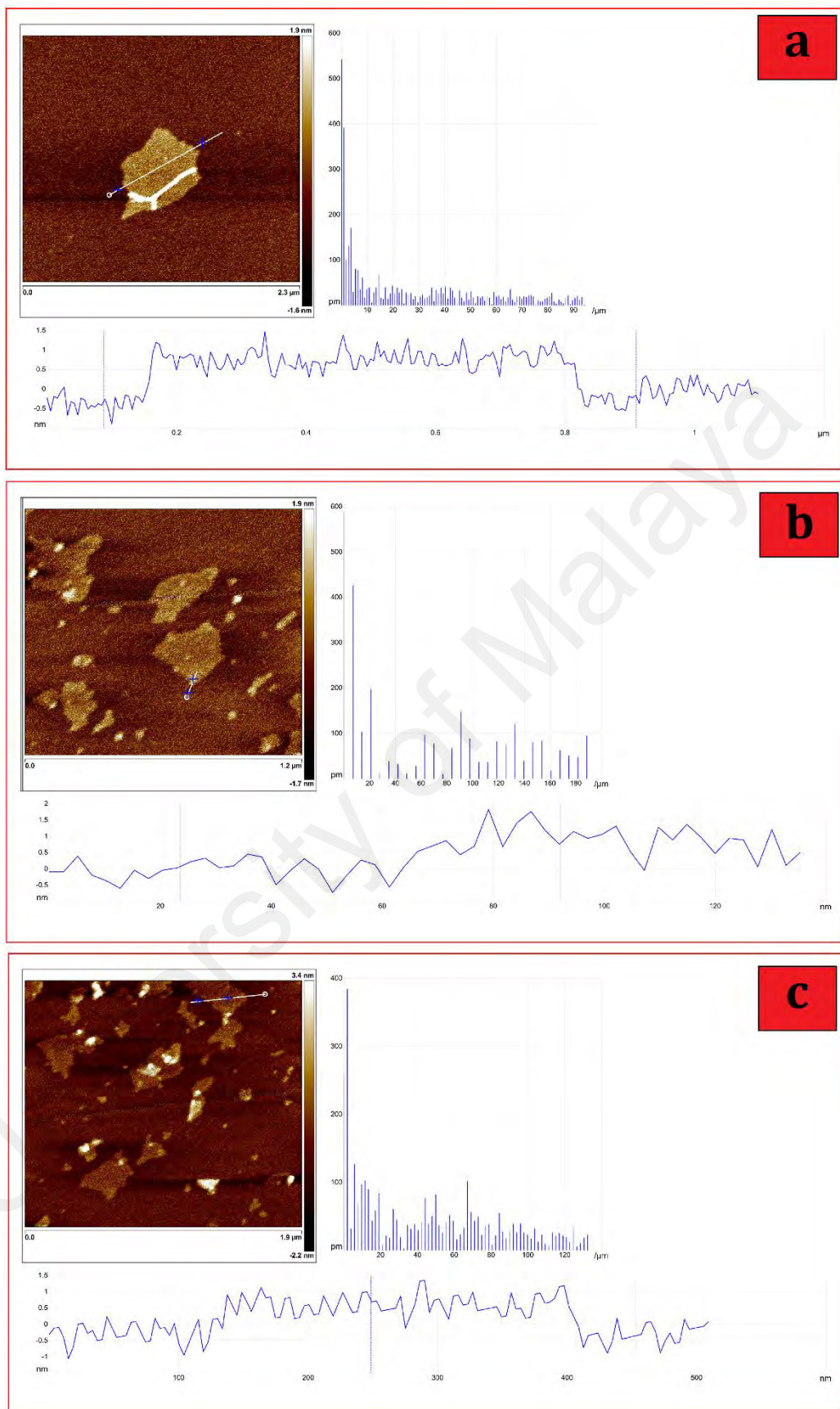
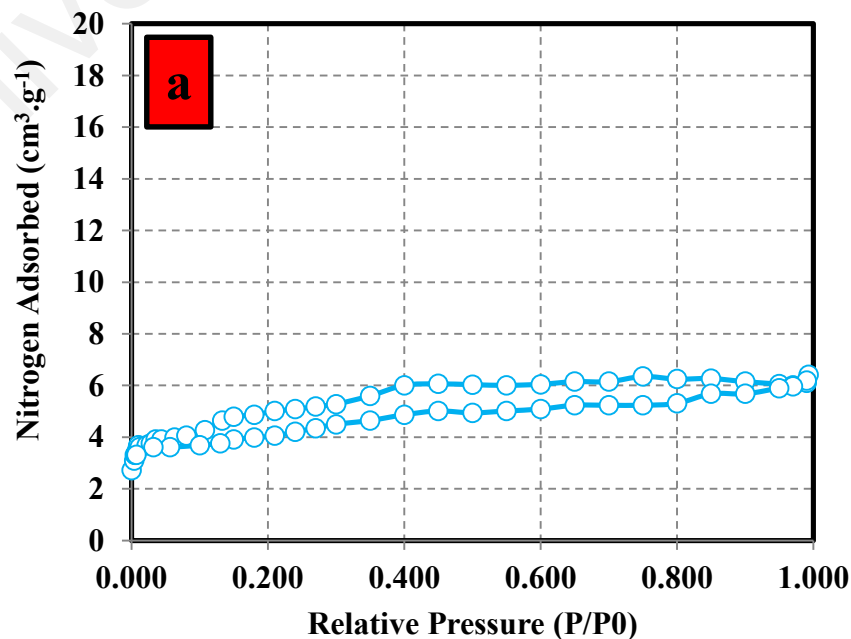


Figure 4.18: AFM ichnography and cross-section contour of (a) HCNDG and (b and c) HCG.

To investigate the effects of exfoliation and functionalization on the specific surface area of HCG and HCNDG, N₂ adsorption–desorption isotherms were measured by a surface area analyzer (Quantachrome Autosorb-1 analyzer at 77 K). The N₂ adsorption–desorption isotherms of the HCG and HCNDG are illustrated in Figure 4.19 and Table 4.4. The comparison between the BET results of this study and previous studies (Jeong et al., 2011; Z. Wen et al., 2012) of graphene materials showed a significant increase in the specific surface area. Also, it can be seen that the N₂ adsorption amount of the HCNDG was greater than that of HCG. The specific surface area of HCNDG after annealing at the high temperature of 900 °C was 1689 m² g⁻¹, but that of HCG was just 1568 m² g⁻¹. This lower specific surface area of HCG suggested that the introduction of functional groups between the 2D graphene sheets can fill the porous area. By looking at the dependence of thermal conductivity of nanofluids on the specific surface area (W. Sarsam et al., 2016a), the HCG and HCNDG with appropriate surface area can be the suitable candidates for fabricating graphene-based nanofluids. Note that the highly crumpled nature of the samples can be an advantageous property for preparing highly conductive nanofluids.



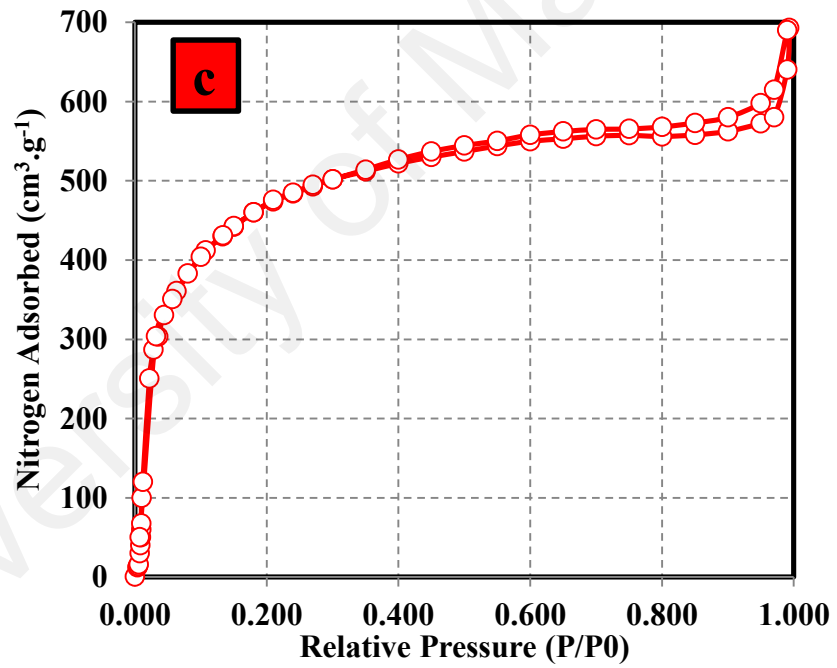
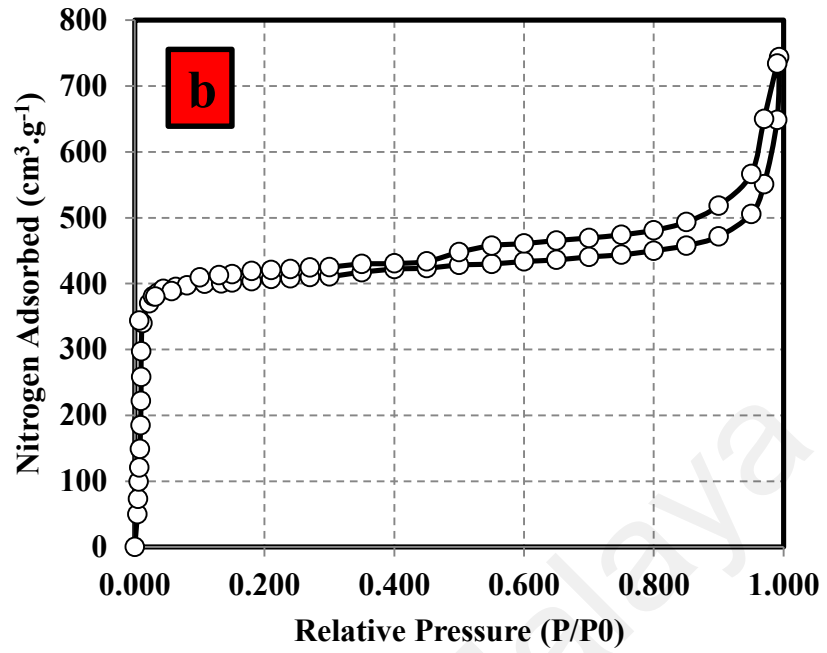


Figure 4.19: N₂-adsorption/desorption of (a) the pristine graphite, (b) HCG and (c) HCNDG.

Table 4.4: Pore structure of the HCG and HCNDG.

Sample	S_{BET} ($\text{m}^2 \text{g}^{-1}$)	Total pore volume ($\text{cm}^3 \text{g}^{-1}$)
Pristine Graphite	85	0.3
HCG	1568	1.33
HCNDG	1689	1.39

4.2.3 Preparation of Crumpled Nitrogen-Doped Graphene (CNDG)

4.2.3.1 Material and Methods

To prepare CNDG, first graphene oxide (GO) was prepared by using Hummers method (Z. Wen et al., 2012). Typically, 10.0 ml cyanamide (NH_2CN) was poured into 100 ml GO solution (1 mg/ml) under stirring. The obtained solution was then heated at 90 °C until completely dry, which followed by a reaction between oxygen-containing groups in GO and amine groups in cyanamide to form amides and/or alkylammonium ions via ring-opening aminations of epoxides. Due to the electrostatic interactions between negatively charged GO and positively charged cyanamide during drying, the rest of NH_2CN was deposited on the GO surface. The obtained product (GO- NH_2CN) was then placed into a furnace and heated at 400 °C to induce the polymerization of cyanamide. As forming a thin C_3N_4 polymer layer on the surface of the GO, the calcination temperature was set at 900 °C for the production of CNDG (Z. Wen et al., 2012). After drying, in the case of preparing coolants, the CNDG was weakly dispersible in both media of deionized water and ethylene glycol at room temperature. So, to provide better dispersion with known weight concentrations, the given amount of CNDG was mixed with Gum Arabic by a ratio of 0.5:1 and then poured into a vessel filled with the given amount of water and ethylene glycol with a volumetric ratio of 40:60.

4.2.3.2 Functionalization Analysis

As mentioned above, Raman characterization is a strong measurement for analyzing structure, sp^2 and sp^3 hybridized carbon atoms in carbon based nanomaterials, functionalization and exfoliation by following alterations in hole and electron doping (Gharehkhani et al., 2015; Seyed Shirazi et al., 2015; Yarmand et al., 2015). The Raman spectrum of the CNDG is illustrated in Figure 4.20a. Strong D and G bands in CNDG sample can be seen at 1346 cm^{-1} and 1588 cm^{-1} , respectively. The ratio of the intensities

of the D-band to the G-band (I_D/I_G) is considered to be the amount of disordered carbon (sp^3 -hybridized carbon) relative to graphitic carbon (sp^2 -hybridized carbon). The I_D/I_G ratio of CNDG material represents a high intensity ratio of 1.28, indicating the high disruption of aromatic π - π electrons and partial damage of graphitic carbon with N-doping (Lv et al., 2009). In addition, the 2D-band peak, which is characteristic for multi-layer graphene structures, can be hardly observed. The 2D peak suggest the defective structure of graphene due to N doping (Kudin et al., 2008).

The nature and amount of nitrogen-containing groups in CNDG was studied by X-ray photoelectron spectroscopy (XPS), which is illustrated in Figure 4.20b. The survey spectrum of CNDG has C1s at around 285 eV, N1s at 399 eV and O1s at 530 eV. The high resolution XPS of N1s spectrum of the CNDG (Figure 4.20c) reveals an asymmetric N1s spectrum, which can be decomposed into four peaks, including pyridinic N (ca. 397.7 eV), pyrrolic N (ca. 399.2 eV), graphitic N (ca. 400.1 eV) and N-oxides of pyridinic N (401.8). XPS results confirms the presence of N doping and is in good agreement with Raman results. Also, N 1s results confirms the presence of three common bonding configurations.

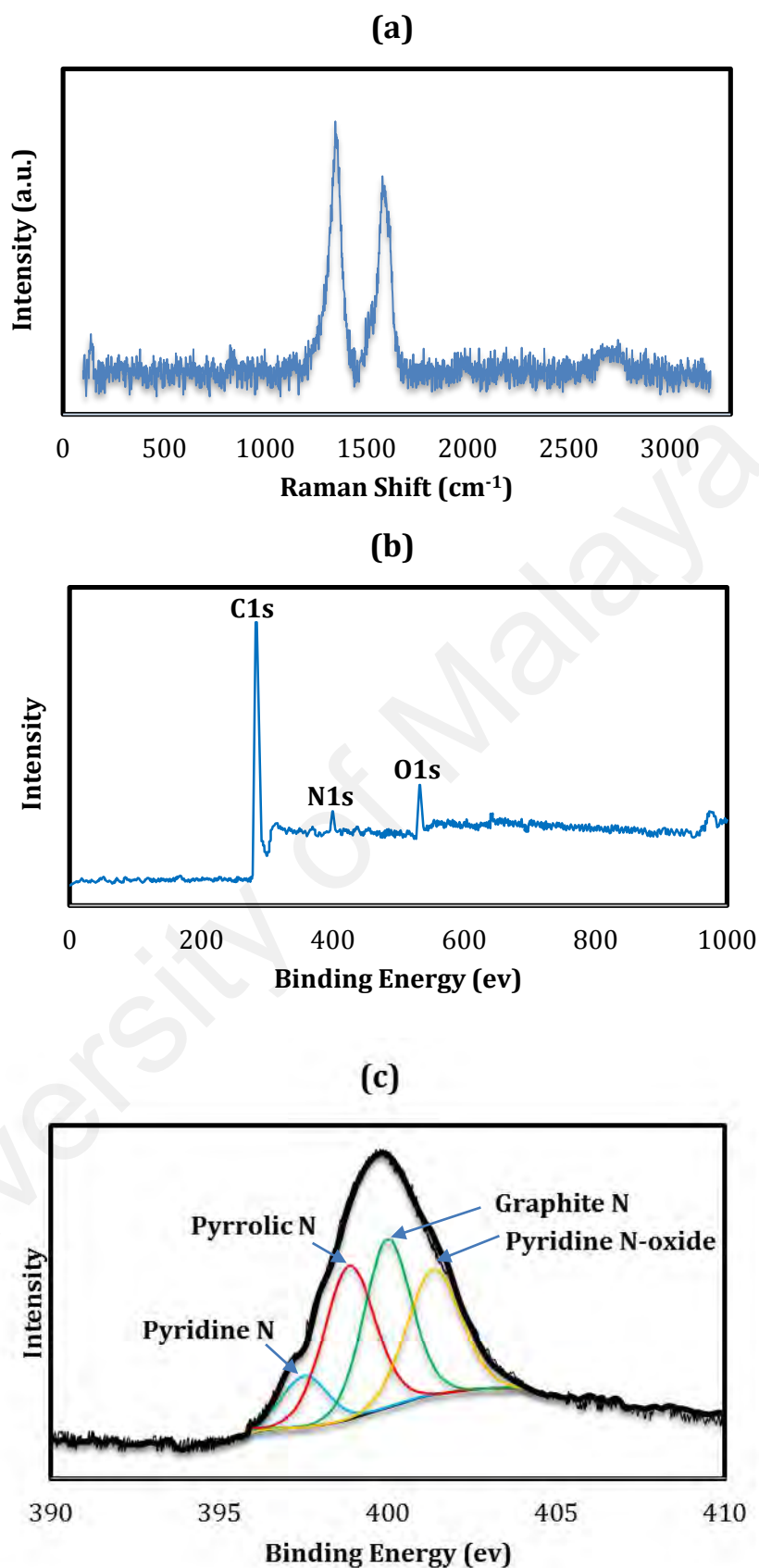


Figure 4.20: (a) Raman spectrum (b) XPS spectrum of and (c) high-resolution N 1s Spectra of CNDG.

4.2.3.3 Morphological Study

Figure 4.21 illustrates the transmission electron microscopy (TEM) images of CNDG. Figure 4.21a and 4.21b show the TEM images of GO-C₃N₄ and CNDG, respectively. The GO-C₃N₄ sample was prepared by adding 4.0 ml of cyanamide in 20 ml GO solution. First, a thin thickness of C₃N₄ polymer is obvious on the surface of all GO flakes, revealing that the reaction between GO and cyanamide was completely successful (Z. Wen et al., 2012). After annealing at 900 °C and/or N doping, TEM image of the CNDG with crumpled structure can be observed. Figure 4.21b shows a CNDG nanosheet with wrinkled morphology and folded edges, which confirms that these wrinkles are resulted from the crumpling of graphene as well as stacking.

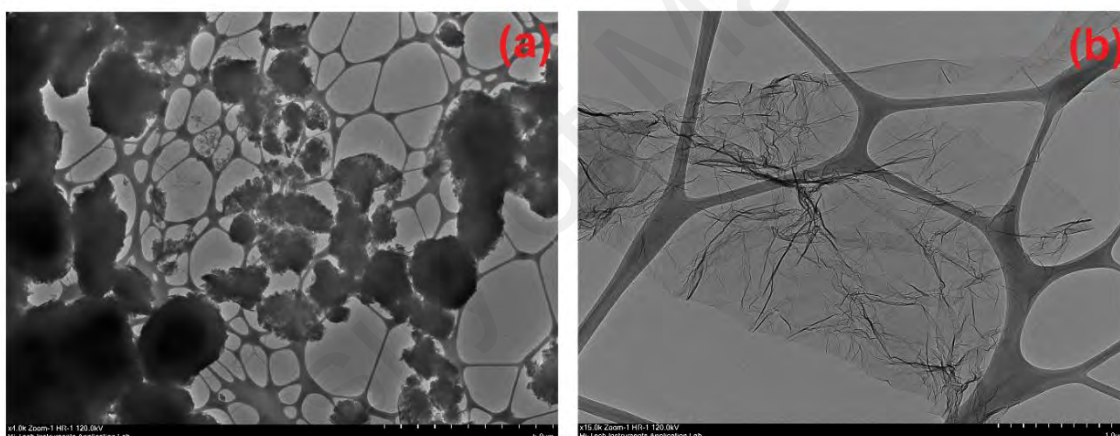


Figure 4.21: TEM image of (a) forming C₃N₄ polymer layers on the surface of the GO (b) CNDG.

Also, N₂ adsorption–desorption isotherms were measured by a BET surface area analyzer at 77 K. The N₂ adsorption–desorption isotherms of the CNDG is illustrated in Figure 4.22. The CNDG has the high specific surface area of 1175 m²g⁻¹, total pore volume of 1.11 cm³g⁻¹ and average pore diameter of 2.93 nm. This high specific surface area of CNDG can be suggested for preparing coolant based recent researches results.

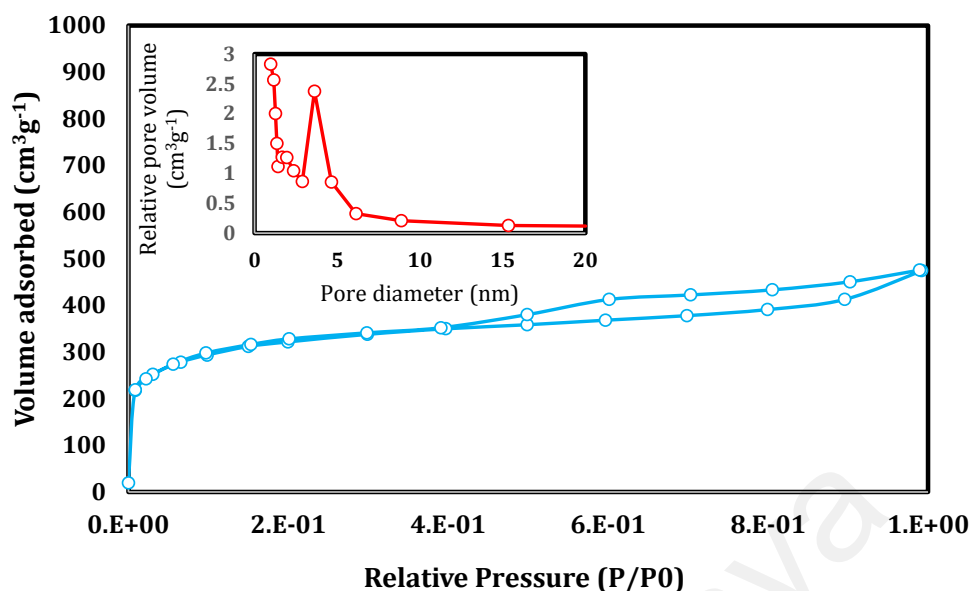


Figure 4.22: N₂ sorption isotherms, (insert figure) pore size distribution of the CNDG nanosheets.

4.2.4 Synthesis of Ethylene Glycol-Treated Graphene Nanoplatelets

4.2.4.1 Functionalization Procedure

Figure 4.23 illustrates the experimental procedure for chemical-assisted functionalization of graphene nanoplatelets (GNP) with ethylene glycol (EG). In a typical experiment, the pristine GNP (0.5 g) and AlCl₃ (9.27 g) were first poured into a planetary ball-mill container, fixed and agitated at 500 rpm for 1h. The resultant mixture was then transferred into a Teflon vessel filled with 80 ml of anhydrous EG and sonicated for 15 min with a probe-sonicator to attain a relatively homogeneous suspension. The concentrated hydrochloric acid (1 ml) was added drop by drop into the vessel over sonication time. The suspension was then sealed and placed in an industrial microwave (Milestone MicroSYNTH programmable microwave system), followed by irradiating at 150 °C for 15 min. The reaction mixture was subsequently filtered through a PTFE membrane and followed by washing with abundant DI water to eliminate any unreacted materials and then dried for 48 h at 50 °C. The EG-treated GNP was much more soluble in both water and EG than the pristine GNP. The easily-miscible EG functionalities can

explain a significant increase in dispersibility of the functionalized GNP with EG in both media of water and EG.



Figure 4.23: The experimental procedure for chemical-assisted functionalization of GNP with EG.

Recently, the same functionalization procedure was employed to decorate different alcohols on the surface of carbon nanotubes (Tian et al., 2008). An electrophilic addition reaction occurred between the EG and the GNP, resulting in the attachment of the EG groups and hydroxyl groups to the exposed edges and side of the GNP flakes, thereby producing functionalized GNP. Microwave irradiation was used to increase the speed of the reaction and the functionalization yield. With a Lewis acid (AlCl₃) as a catalyst and trace concentrated hydrochloric acid to protonate alcohols, electrophilic addition reactions were carried out between PEG and graphene through a microwave-induced method. A primary alcohol in the presence of Lewis acids and concentrated hydrochloric acid can be protonated and resulted in an electrophilic species (carbocation or protonated alcohol) (Tian et al., 2008). This electrophile (in the case of poly ethylene glycol) is a stabilized cationic electrophilic reagent with significantly superior reactivity in the presence of microwave irradiation (Vázquez & Prato, 2009; Zhu, Murali, Stoller, et al., 2010). These types of carbocations were described by Olah et al. (1975). By protosolvation of a cationic electrophile, an active electrophilic reagent is suitable for electrophilic aromatic substitution, which in the case of the GNP flakes, an electrophilic addition reaction was occurred. The formed cations in the first step of electrophilic addition reaction on flakes reacts with nucleophiles (Olah et al., 1975; Singh, 2004).

Also, the reaction intensifies under microwave irradiation. When carbon nanostructures are exposed to microwaves, strong absorptions are obtained, which producing intense heating. Although the utilization of microwaves for the activation of carbon nanostructures has not been fully explored, the strong absorptions can open the door to the similar electrophilic addition reactions (W. Lin et al., 2010; Vázquez & Prato, 2009). In addition, the edges of the GNP flakes were more available for reaction with the functional groups than the basal plane surfaces.

4.2.4.2 Functionalization Analysis

To analyze functional groups, various characterizations methods such as FTIR and Raman spectroscopy as well as TGA were employed. Also, the morphology/structure of EG treated GNP was studied by TEM. FTIR was employed to investigate chemical groups which attached to the GNP. Figure 4.24a illustrates the FTIR spectra of EG-treated GNP as well as a pristine sample. In contrast to the pristine sample, EG-treated GNP demonstrates low infrared absorption intensities as the cues of EG molecules. Two broad peaks at 3486 and 1141 cm^{-1} are consistent, respectively, with the O–H and C–O stretching vibrations. These peaks could be due to the reaction of one of the hydroxyl groups of EG with GNP and/or the attached hydroxyl groups on the GNP. The peak at 1592 cm^{-1} is related to the C=C graphitic stretching mode of GNP, which is infrared-activated by functionalization. A couple of peaks at the ranges of 2850–3000 cm^{-1} and a peak at 1403 cm^{-1} are consistent, respectively, to the stretching and in-plane bending vibrations of the C–H bond. Based on the results of FTIR, the alkyl and hydroxyl groups are successfully attached to the GNP material through an electrophilic addition reaction under microwave irradiation (Kalinina et al., 2011b; Mehdi Shanbedi et al., 2013; Zardini et al., 2012; Zardini et al., 2014).

As extra evidence, Raman spectra can provide fundamental information to evaluate the modification and functionalization of GNP. Figure 4.24b is shown the Raman

spectra of the pristine and EG-treated GNP, which illustrates the amorphous/disorder (D mode) and tangential (G mode) bonds at 1346 and 1573 cm^{-1} . The D band is commonly attributed to the amorphous (sp^3) carbon, is due to disruption of aromatic π -electrons, and G band is related to the graphitic carbon (sp^2) (Zardini et al., 2012; Zardini et al., 2014). It can be seen that the intensity ratios of the D–G band (I_D/I_G) is larger than that of pristine sample, indicating some sp^2 hybridized carbons changed to the sp^3 hybridization. Raman spectra can be considered as one of the strongest evidence for studying covalent functionalization (Tian et al., 2008), which provided a strong confirmation from the results.

TGA (Figure 4.24c) traces of the pristine and EG-treated GNP provide more evidence about functionalization by thermal analysis of samples (Zare-Zardini et al., 2015b). While there is no significant weight loss in the trace of pristine GNP, a steady weight loss between 140 and 500 $^{\circ}\text{C}$ is seen in the EG-treated GNP trace, confirming the decomposition of the functional groups. Also, the obtained results indicate that the functionalization of GNP with EG is successful, since a steady weight loss observed in EG-treated GNP curve. As expected, the EG-treated GNP can easily disperse in a mixture of water-EG as a base-fluid (Figure 4.24d), pointing to the easily-miscible EG functionalities. EG as a functional group, not only provide suitable dispersibility, but also synthesized coolant suspension which has no corrosive function for different metals or engines.

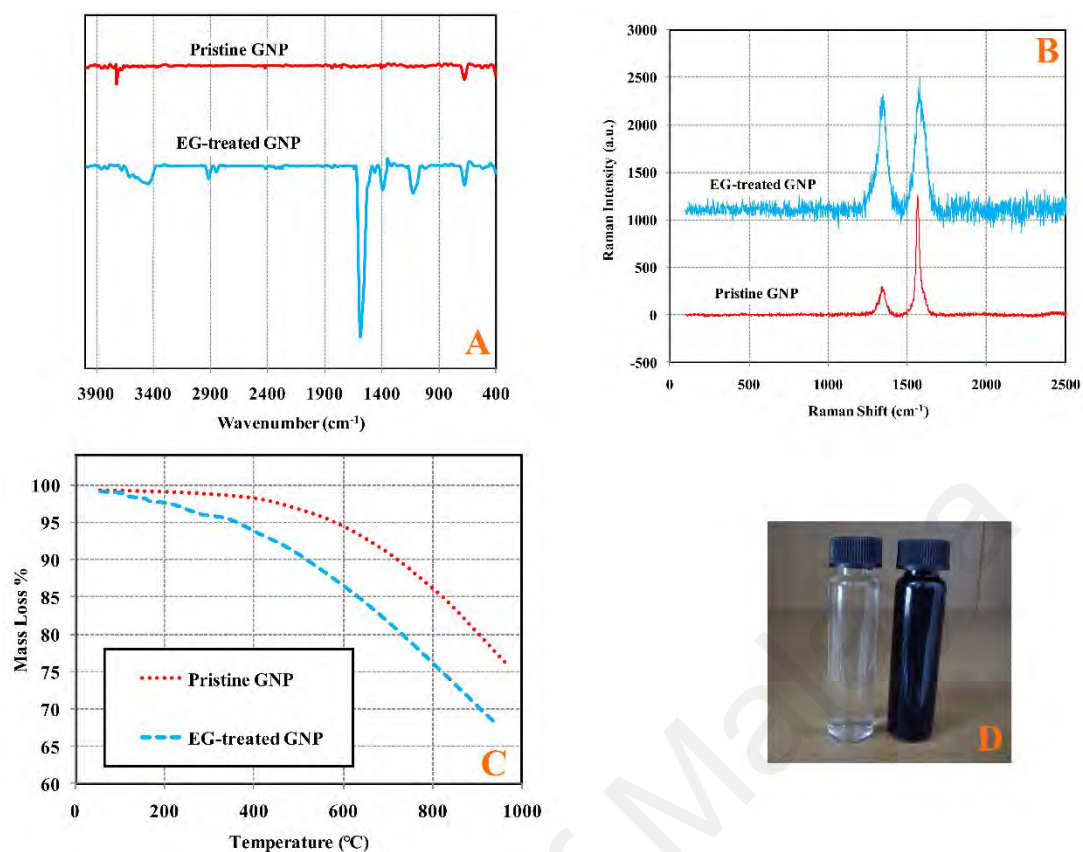


Figure 4.24: (A) FTIR spectra, (B) Raman spectra, (C) thermogravimetric analysis of the pristine and EG-treated GNP and (D) photographs of EG-treated GNP dispersed in water-EG after 1 month.

4.2.4.3 Morphological Study

Figure 4.25 shows the TEM images of the pristine GNP and EG-treated GNP. TEM Image of the pristine GNP (Figure 4.25a) demonstrate two flakes with relatively smooth layer's surface and edge. Although TEM images for the EG-treated GNP (Figure 4.25b) could not distinguish minute functional groups, surface deterioration and wrinkles of the GNPs that formed as a result of covalent functionalization with EG, which could clearly have been observed. The lines seen in the TEM images are wrinkles on the GNP surface due to the inherent instability of 2D structures. The increase of these lines after functionalization can be attributed to the enhancement of wrinkles (waviness) during the sonication and microwave procedures, resulting from the flexibility of GNP flakes after treatment or higher wettability of flakes (Q. Zhang et al., 2013). Obviously, higher tendency for wrinkling indicates an increase in the wettability of GNP's surface due to

covalent functionalization with EG. The easily-miscible ethylene glycol functionalities may explain the increased wettability of the treated samples. Consequently, higher dispersion stability was obtained (Kamiya et al., 2012; Wei et al., 2011). Furthermore, all TEM images illustrate multi-layered graphene sheets with average diameter around 2 μm and the EG-treated GNPs sheets preserved their shape and size as compared with the pristine sample.

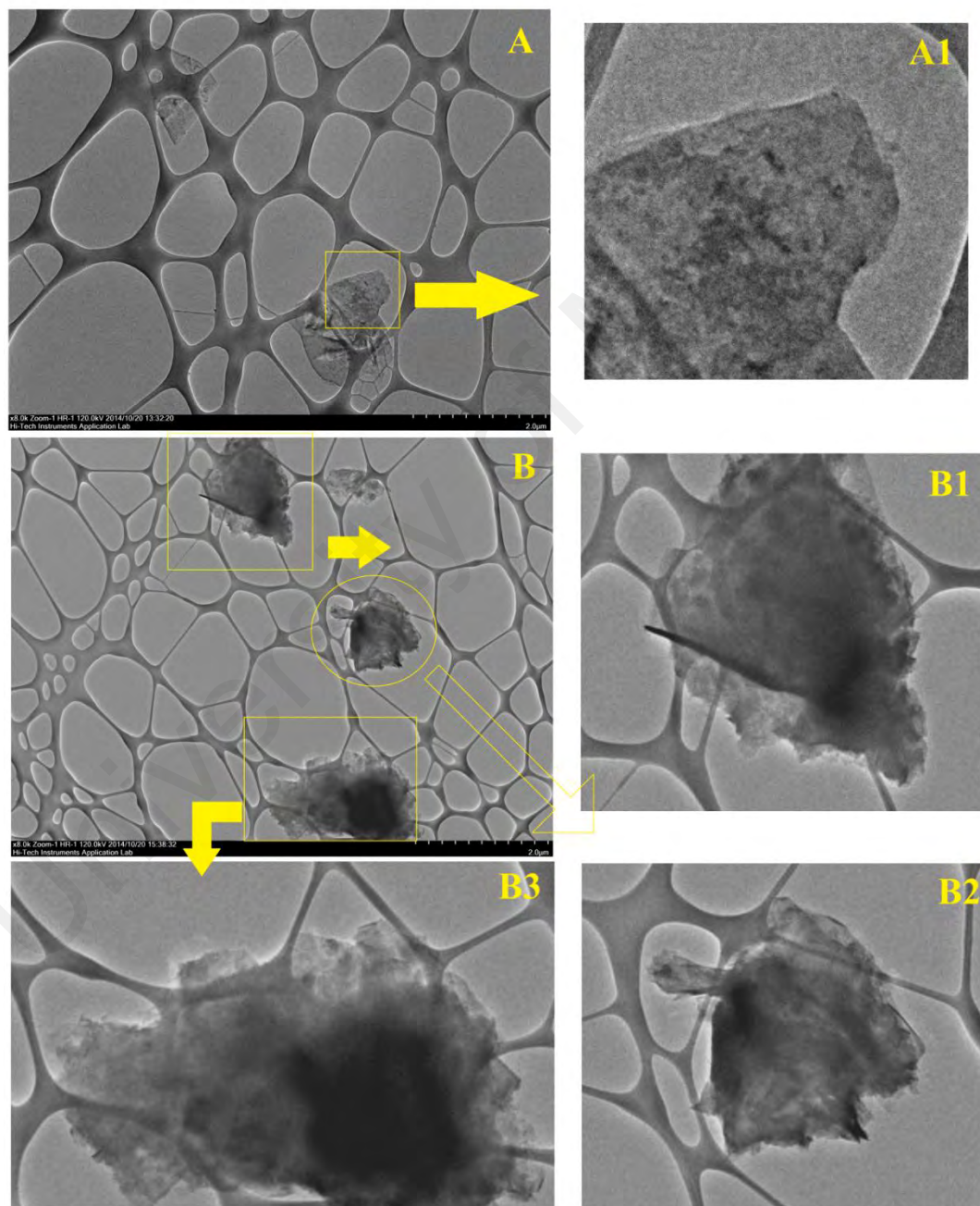


Figure 4.25: TEM images of the (A & A1) pristine and EG-treated GNP (B, B1, B2 & B3).

4.2.5 Direct Coupling of Graphene Nanoplatelets with Poly Ethylene Glycol and 4-Phenylazophenol Molecules

4.2.5.1 Microwave-assisted functionalization

The schematic diagram of functionalization procedure of GNP with Azo and PEG is illustrated in Figure 4.26.

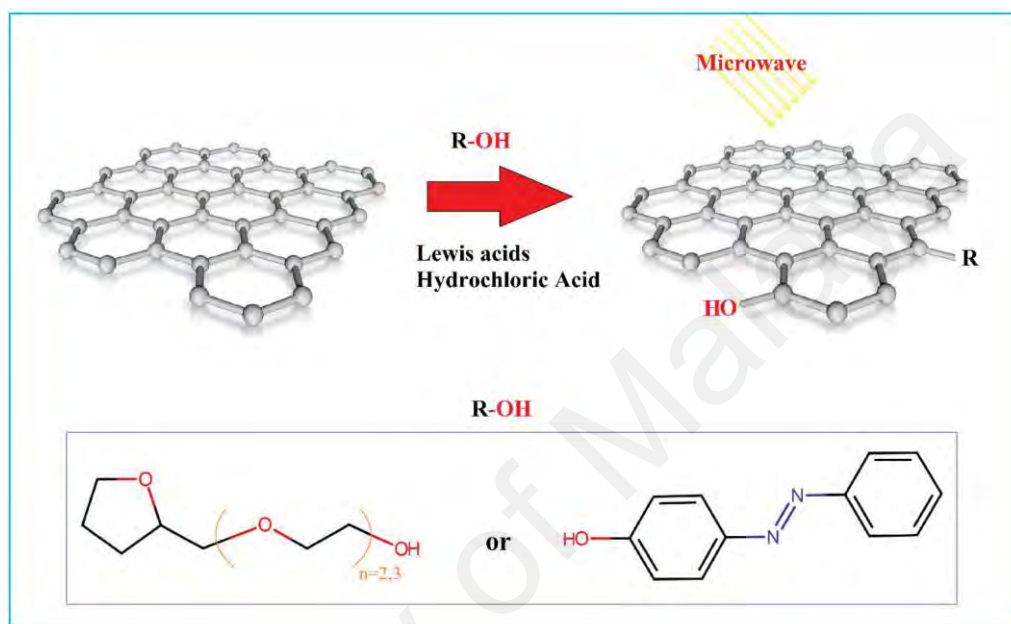


Figure 4.26: The experimental procedure for chemical-assisted functionalization of GNP with PEG and Azo.

Regarding PEG-treated GNP, in a typical experiment, pristine GNP (10 mg) and one of the Lewis acids (1.4 mmol) were poured into a planetary ball-mill container, fixed and agitated with 500 rpm for 15 min. The resultant mixture was then transferred into a Teflon vessel filled with 25 ml PEG and sonicated for 15 min with a probe-sonicator to reach a relatively homogeneous suspension. The concentrated hydrochloric acid (0.5 ml) has been added dropwise to the GNP suspension over the sonication process. The mixture was then heated in an industrial microwave (Milestone MicroSYNTH programmable microwave system) up to 120 °C with output power of 700 W for 30 min. The reaction mixture was cooled to the room temperature and then filtered through a 0.22 μm Teflon

membrane. The filter cake was thoroughly washed with DMF and abundant deionized water to remove any unreacted materials and then dried under vacuum at 50 °C.

The same procedure is carried out for the functionalization of Azo. However, since Azo is solid in the room temperature, it was first sonicated in THF (25 ml) for 30 min at 60 °C. The used amount of this precursor was as same as the molar equivalent of Azo. Since Azo did not react with GNP at 120 °C, its treatment temperature in the microwave chamber was increased to 180 °C. Also, since different kinds of Lewis acids can demonstrate the different degree of functionalization, four catalysts of ZnCl₂, FeCl₂, TiCl₄ and AlCl₃ have been employed and their performance have been compared.

4.2.5.2 Functionalization Analysis

In different applications of GNP, the covalent functionalization of GNP with Azo and PEG were commonly reported. Here, Tetrahydrofurfuryl polyethylene glycol and 4-phenylazophenol which are the monofunctional oligomers were used in order to prevent cross-linking between the GNP flakes. Noteworthy, PEG was also used, which has been utilizing as one of the base materials in the biomedical applications. Also, Azo-treated GNP has several promising properties in charge transfer and preparing long-term solar thermal storage. To realize this issue, a green, cheap and fast technique (microwave) should be developed to enhance the degree of functionalization and decrease the time of interaction and defects. Thus, after functionalization with molecules including hydroxyl (-OH), GNP samples were characterized by FTIR spectroscopy, TGA and Raman spectroscopy. Also, several simple Lewis acids catalyzed the reaction and their effectiveness for the functionalization process has been reported. Microwaves irradiation has also been employed in the direct coupling reaction and producing hot sites on the surface of GNP in the presence of metallic catalysts.

4.2.5.2.1 FTIR

The covalent functionalization, which had been occurred through the formation of an electrophilic addition reaction between the GNP and PEG and/or Azo, was investigated by FTIR spectroscopy. To complete the reaction, four catalysts of ZnCl_2 , FeCl_2 , TiCl_4 and AlCl_3 were applied separately. Figure 4.27 shows the FT-IR spectra of pristine GNP, PEG-treated GNP and Azo-treated GNP in the presence of ZnCl_2 .

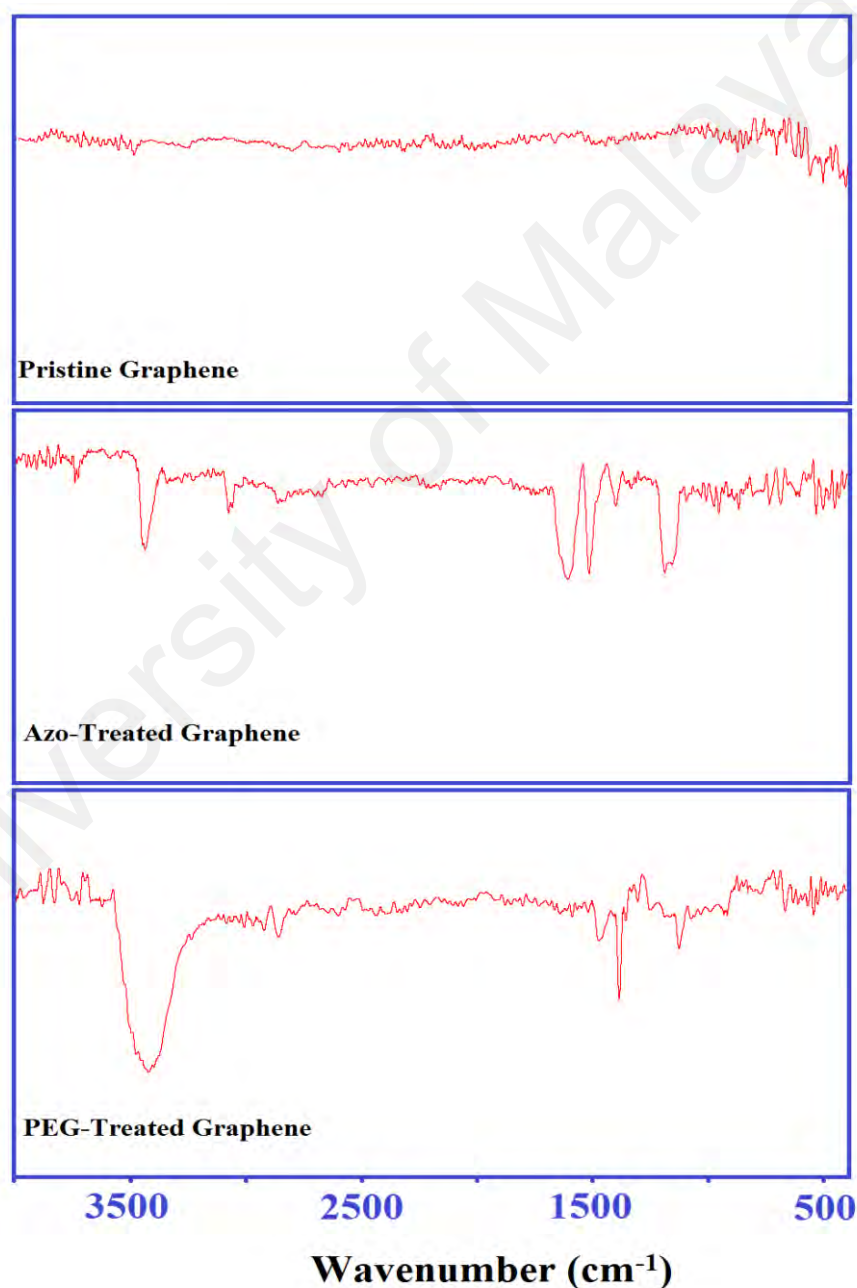


Figure 4.27: FTIR spectra of the pristine GNP as well as PEG- and Azo-treated GNP in the presence of ZnCl_2 .

In contrast to the pristine GNP, Azo/PEG-treated GNP shows the cues of different molecules on the main structures. The spectrum of treated GNP with PEG represents a peak at 1122 cm^{-1} , which could be attributed to the C–O stretching vibrations. Also, another weak peak centered on 1385 cm^{-1} is attributable to the CH_2 bending vibration. The broad peak at 3442 cm^{-1} is in agreement with stretching vibration of O–H. The peaks at the range of $2850\text{--}2918\text{ cm}^{-1}$ corresponds to the C–H stretching vibration (Zardini et al., 2014). The deformation vibration of the CH_2 group provides a peak at 1460 cm^{-1} (Kalinina et al., 2011a).

Regarding Azo-treated GNP, a peak at 1180 cm^{-1} is consistent to the C–C stretching vibrations. A couple peaks in the range of $3020\text{--}3100\text{ cm}^{-1}$ are in agreement with the C–H stretching vibration. Also, the peaks at 1396 and 1509 cm^{-1} are respectively related to the ν^{cis} and ν^{trans} of N=N stretching vibration (Y. Feng et al., 2013). The presence of azobenzenes bound to the GNP is also supported by the observation of new bands in the FTIR spectra of Azo-treated GNP that can be assigned to the C=C stretch (1602 cm^{-1}) and the O–H bend (3451 cm^{-1}).

In order to evaluate the specific role of Lewis acids, our experimental procedure was also done without using Lewis acids as catalyst (Figure 4.28). As could be seen, in the absence of Lewis acids, FTIR spectra show just low intensities for all samples. However, using Lewis acids was led to the aforementioned peaks for PEG and Azo. Unfolding C–O, CH_2 , O–H, C–H, =C–H, N=N, and C=C peaks in these samples with Lewis acids could highlight the essential role of Lewis acid in PEG and Azo functionalization.

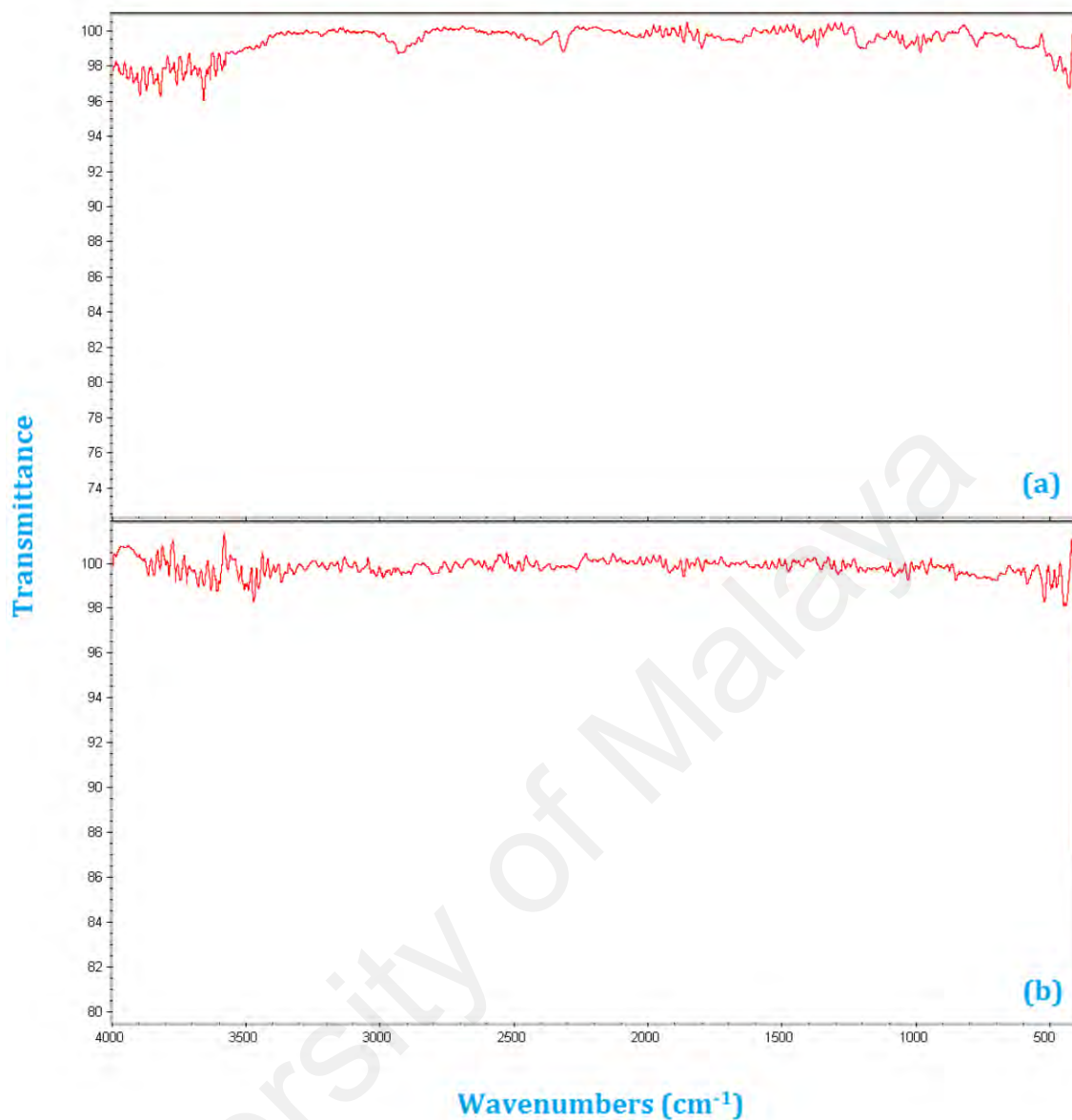


Figure 4.28: FTIR spectra of (a) PEG-treated GNP and (b) Azo-treated GNP without using catalysts.

Reaction products showed approximately similar trends in presence of other Lewis acids as the catalysts. Since the FTIR spectra of pristine GNP, PEG-treated GNP and Azo-treated GNP show similar peaks in presence of different kinds of catalysts, the quantitative tests such as Raman spectroscopy and TGA has been considerably employed to characterize various functional groups, indicating essential information for estimation

of the covalent functionalization and compare the performance of functionalization in presence of different catalysts.

4.2.5.2.2 Raman spectroscopy

Raman spectroscopy is applied to present fundamental information for investigation of the covalent modification of GNP. Figure 4.29 panels (a) and (b) show the Raman spectra of pristine GNP and functionalized GNP with Azo & PEG, respectively. This technique established an eminent sensitivity to the disordered band on the structure depending upon the optical skin depth (Shirazi et al., 2015). Raman spectra of the pristine and functionalized samples with Azo & PEG are illustrated the D and G bands at around 1341 and 1572 cm^{-1} , respectively. The D band around 1341 cm^{-1} is connected to the amorphous carbon, which resulted from addition of functional groups to the main backbone of GNP. In contrast, the tangential G-mode of GNP at 1572 cm^{-1} is associated with the motion in opposite direction of two high carbon atoms in a graphitic framework (Shirazi et al., 2015). The G band implies the existence of crystalline graphitic carbon in GNP. Previous researches (E.-Y. Choi et al., 2010; Fu et al., 2013), confirmed that GNP functionalization is one of the main causes of different results on the shift of the D and G bands. Raman spectra can be applied to characterize the amount of disordered carbon relative to the graphitic carbon by measuring the ratio of D to G bands (I_D/I_G). Hence, it can be seen that the intensity ratio (I_D/I_G) of all functionalized samples increased as compared with pristine GNP, which verify successful functionalization, indicating an improvement in the structure defects or disruption of aromatic π -electrons on the GNP framework (Ghiadi et al., 2013; Zare-Zardini et al., 2015a). Again, the higher values of I_D/I_G determined by Raman spectroscopy indicate the higher degree of covalent functionalization. Also, the results suggest different intensity ratios (I_D/I_G) in the presence of different catalysts, which first confirmed functionalization of GNP in the presence of

all catalysts and then the influence of Lewis acids on the reaction products. Therefore, it is also categorized some catalysts for this reaction, which can enhance the direct coupling reaction in the presence of microwave irradiation. Thus, GNP was reacted with PEG and/or Azo under microwave irradiation in the presence of a series of potential catalysts, of which results are indicated in the Table 4.5.

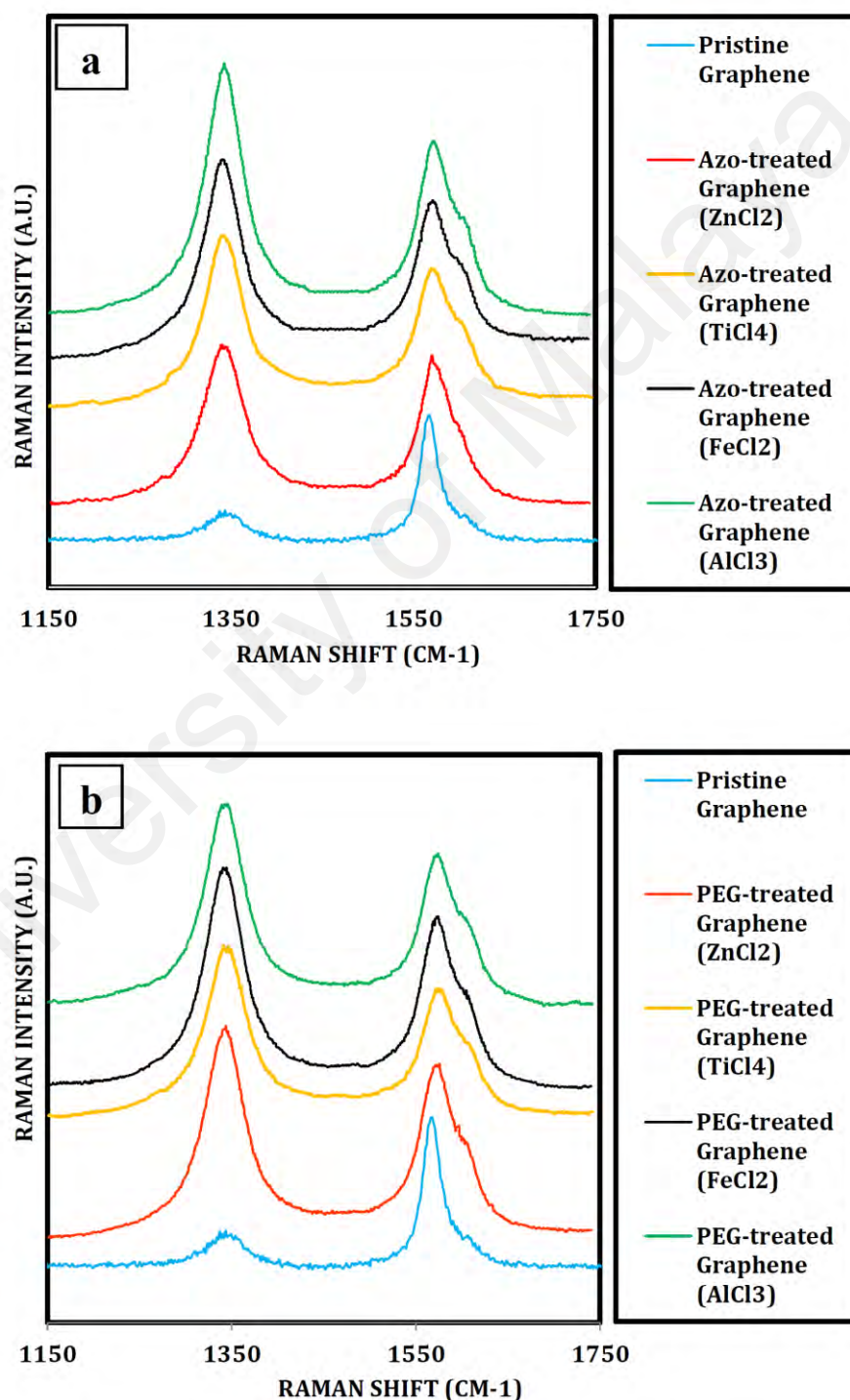


Figure 4.29: Raman spectra of the (a) Azo-treated GNP and (b) PEG-treated GNP in comparison with pristine sample in the presence of different Lewis acids.

Table 4.5: Identification of catalysts for formation of the electrophilic addition reactions.

I_D/I_G				
Pristine GNP	0.459			
Material/Catalyst	ZnCl ₂	TiCl ₄	FeCl ₂	AlCl ₃
Azo-treated GNP	1.187135	1.450617	1.409756	2.238462
PEG-treated GNP	1.392157	1.405556	1.554839	1.778761

According to the values of I_D/I_G determined by Raman spectroscopy in Table 4.5, it could be recognized that all of the catalysts (ZnCl₂, TiCl₄, FeCl₂ and AlCl₃) led to successful reaction between GNP and Azo/PEG. With the above catalysts loading and under same conditions, the best result was obtained by AlCl₃. The use of alternative catalysts led to the good development of I_D/I_G ratio, especially for AlCl₃. Based on the observed Raman results, the sequence of I_D/I_G for functionalization in the presence of different catalysts was AlCl₃ \gg FeCl₂ $>$ TiCl₄ $>$ ZnCl₂.

Interestingly, G-bands of the treated GNP samples in the presence of different catalysts show a redshift (around 20 cm⁻¹), implying weakening of graphitic (sp²) carbon moieties (Khare et al., 2005). This could again confirm functionalization of GNP.

4.2.5.2.3 TGA

TGA can present valuable information about the quantitative extent of functional groups on GNP because of lower degradation temperature of organic functional moieties than graphitic layers of GNP. Figures 4.30a and b represent further evidence of the functionalization of GNP with Azo and PEG, respectively. Further evidence from TGA traces of the treated GNP with Azo and PEG demonstrated functionalization of GNP in the presence of different kinds of catalysts which had applied here.

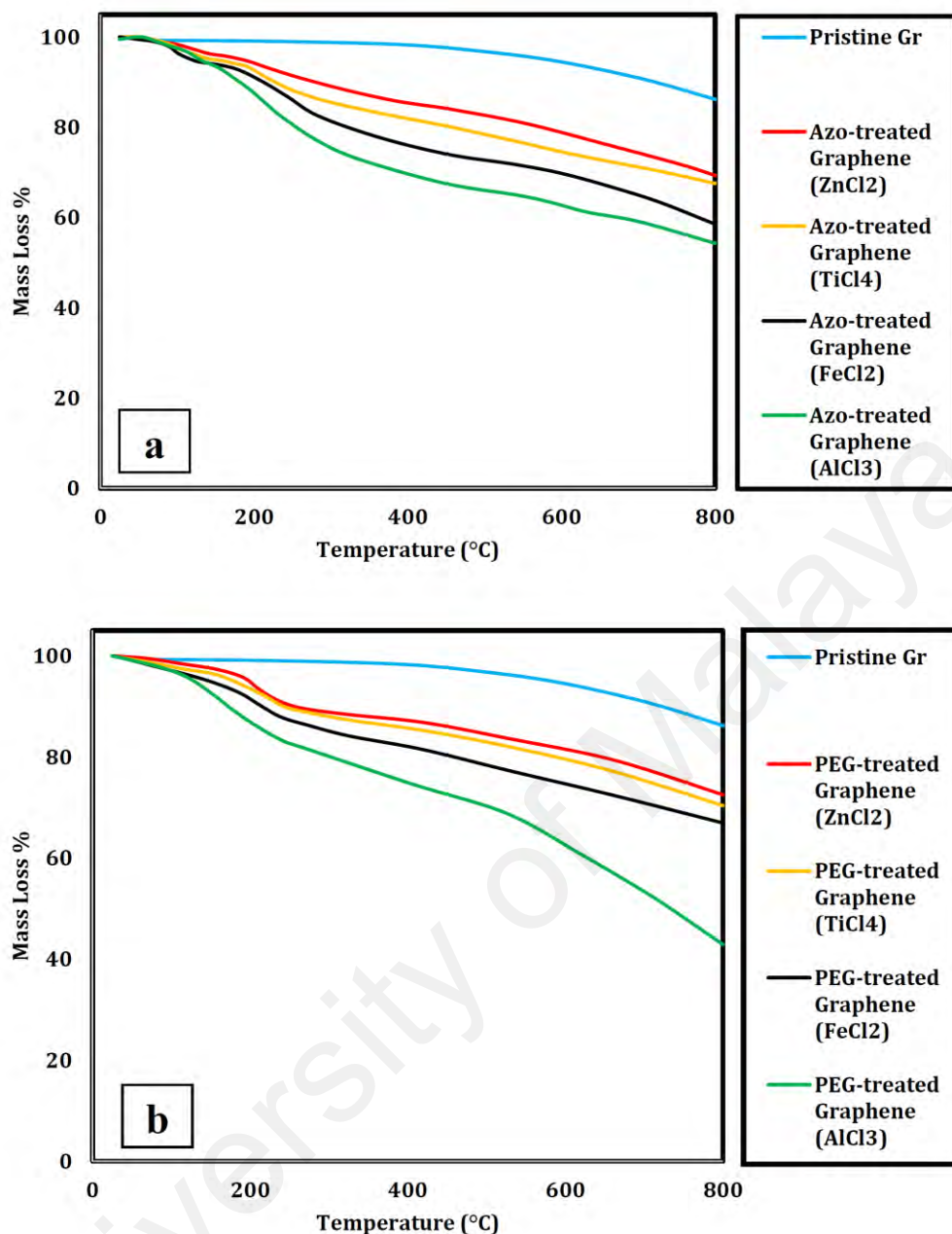


Figure 4.30: Thermogravimetric analysis of the (a) Azo-treated GNP and (b) PEG-treated GNP in comparison with pristine sample in the presence of different Lewis acids.

Despite the fact that TGA curve of pristine GNP illustrates no considerable weight loss up to 400 °C as the thermal degradation of main graphitic structures, an obvious weight loss for the treated samples can be occurred in temperature range of 0–400 °C in all the samples. In the curve of functionalized samples with PEG, the sharp weight loss (the first weight loss) presented in temperature range of 100–250 °C can be attributed to the functionality of PEG as an unstable organic moieties decorated on the edge of GNP.

The TGA curves of various functionalized samples in the presence of different kinds of catalysts demonstrate different weight loss at mentioned temperature range, which may be due to the fact that employed Lewis acids have different activities and lead to different conversion.

Regarding Azo-treated GNP, the first sharp weight loss explained in the temperature range of 150–350 °C, which may be attributed to the functionality of Azo. According to the TGA results for both PEG- and Azo-treated GNP, the use of AlCl₃ as catalysts can provide the best reaction performance at same catalyst loading, which also confirmed by Raman results. So, hydroxyl (–OH) group can be decorated on the edge of GNP by an efficient method including an electrophilic addition reaction under microwave irradiation. It was discovered that all catalysts employed here noticeably accelerated the reaction. According to the results of TGA and Raman spectroscopy, ZnCl₂ has the least reactive activity for electrophilic addition reaction under microwave irradiation. Interestingly, in order to quantify the functionalization yield, Moaseri et al. (2014) have introduced the degree of functionalization from the TGA results. On the basis of this weight loss, the following formula employed to calculate the degree of functionalization of GNP:

$$\text{Degree of Functionalization} = \frac{\text{mmol of attached functional group}}{\text{grams of Graphene}}$$

The degree of functionalization might be measured as an extent of functionalization improvement. Table 4.6 demonstrates the amounts of the degree of functionalization for the treated samples with Azo and PEG as well as pristine GNP. Based on the determined values of the degree of functionalization, all the treated GNP represent different results in the presence of various catalysts. Also, these results can confirm the Raman results for functionalization with Azo and PEG. In agreement with

Raman results, AlCl_3 and ZnCl_2 have the maximum and minimum performances in functionalization among the selected catalysts. On the other hand, the second weight loss interval at more than 400 °C corresponds chiefly to the degradation onset temperature of main graphitic structures in nitrogen atmosphere.

Table 4.6: Comparative study of the functionalization of compounds in the presence of different catalysts

Material/Catalyst	Degree of Functionalization (mmol/gr)			
	AlCl_3	FeCl_2	TiCl_4	ZnCl_2
PEG-treated GNP	1.702125378	1.136362242	0.869564197	0.762194244
Azo-treated GNP	2.423127591	1.728406126	1.436165044	0.957884155

4.2.5.3 Morphology studies

Figure 4.31 depicts the TEM images of pristine GNP as well as Azo- and PEG-treated GNP. First, the multi-layered structure of the GNP is obvious in the TEM images of pristine Gr (Figure 4.31a), which has almost smooth surface (Figure 4.31b and c). Although TEM images are not able to distinguish minuscule functional groups, whereas any change in morphology and surface deterioration can be considered as an evidence in TEM images. Pristine sample (Figure 4.31a–c) shows a GNP flake with relatively smooth layers' surface and edge. Unlike pristine sample, the PEG-treated GNP (Figure 4.31d) and Azo-treated GNP (Figure 4.31e) provide edges with high defect density. Such higher roughness indicates the partial damage of graphitic carbon, in the effect of our severe functionalization under microwave irradiation. Also, the lines seen in the TEM images can be wrinkles on the GNP surface, which is due to the inherent instability of the 2D structures. The obtained increase of such lines after functionalization can be attributed to the enhancement of wrinkles (waviness) during the microwave procedures, resulting from appropriate flexibility of GNP flakes after treatment.

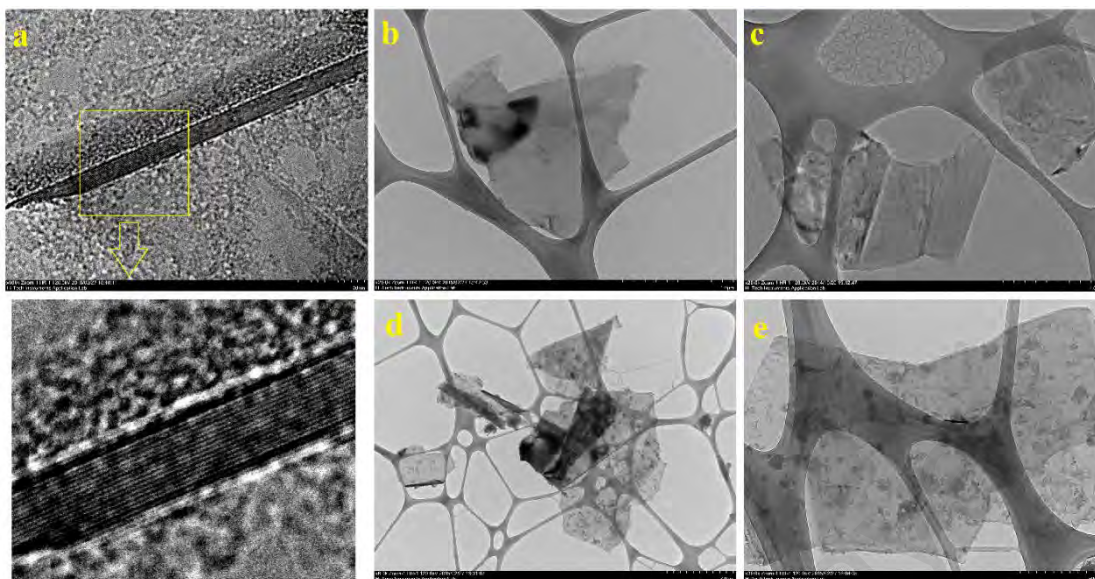


Figure 4.31: TEM images of (a–c) pristine sample, (d) PEG-treated GNP and (e) Azo-treated GNP.

4.2.6 Preparation of GNP-COOH

4.2.6.1 Covalent functionalization of GNP

Based on the technique explained by Y. Wang et al. (2006) with slight modification, carboxylation of GNP was performed. In order to generate carboxylated GNP, the GNP (1 g) with a mixture of HNO_3 and H_2SO_4 (1:3 volume ratio) were first sonicated for 0.5 h at room temperature in a closed vessel. The GNP suspension was then poured into a Teflon reaction vessel and placed in an industrial microwave (Milestone MicroSYNTH programmable microwave system) with output power of 700 W and heated up to 90 °C for 15 min. The resulting suspension was cooled at room temperature and then diluted with 200 mL deionized water to reduce the intensity of acids for filtration stage. The GNP suspension was filtered through 45 μm polytetrafluoroethylene (PTFE) membrane, and the filtrate was continually washed with the deionized water to remove any unreacted acids. The functionalized sample was dried overnight at 40 °C in a vacuum.

4.2.6.2 Morphological and functionalization studies

Figure 4.32 shows FTIR spectra of GNP-COOH as well as pristine GNP. In contrast to the pristine GNP, acid treated GNP sample obviously shows the cues of carboxylic groups. In the FTIR spectrum of GNP-COOH, a broad peak at 3327 cm^{-1} was associated with the O-H stretching vibrations (Zardini et al., 2012). GNP-COOH sample also illustrates a peak at 1667 cm^{-1} , which could be attributed to the C=O. It is obvious that the carboxyl group has a sharp peak, resulting from the oxidation stage by nitric/sulfuric acid. Also, another peak centered on 1573 cm^{-1} is attributable to the C=C stretching vibration, which can be resulted from edge-defected sites. The mentioned picks, which are insignificant in the pristine spectrum, can confirm GNP carboxylation.

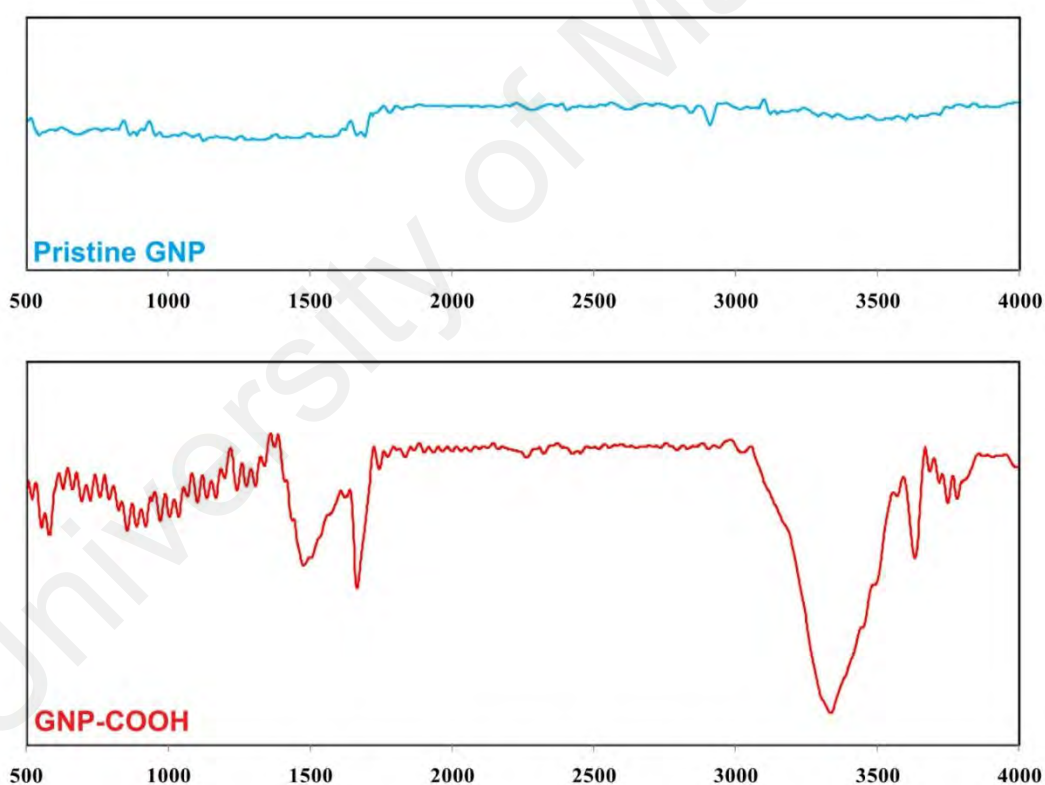


Figure 4.32: FTIR spectra of pristine and acid treated GNP.

Figure 4.33 illustrates the TEM images of pristine GNPs and acid treated GNPs. Although TEM images are not able to distinguish minute functional groups, it can show

the surface deterioration and change of the GNPs that formed as a result of acid treatment. In pristine sample, one can see multi-layered GNPs with relatively smooth layers and low edge-defected GNPs. On the other hand, the acid treated samples provide higher surface roughness on the GNPs. Such higher roughness implies the partial damage of graphitic carbon, in effect of severe carboxylation. Also, the lines seen in the TEM images are wrinkles on the surface of the GNP due to the inherent instability of the 2D structures. The increase in these lines with functionalization may just be a result of increased wrinkling (waviness) during the sonication process.

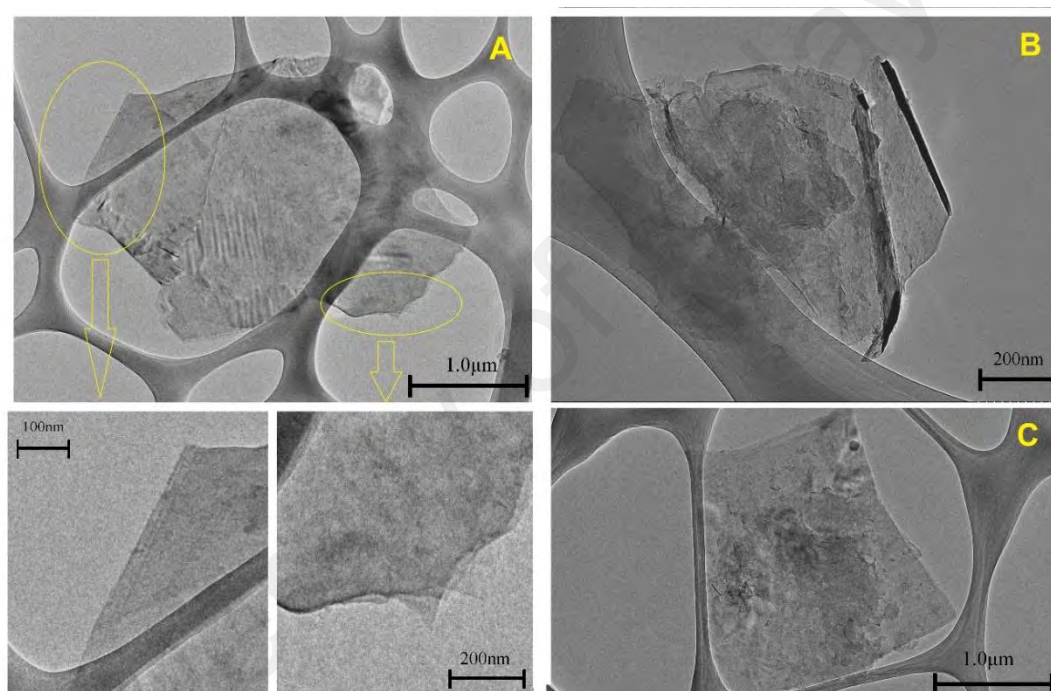


Figure 4.33: TEM images of (A) pristine, (B and C) acid-treated GNP.

4.3 Colloidal stability and Thermo-physical properties

4.3.1 Water-based highly crumpled few layered graphene nanofluids

4.3.1.1 Preparation

To synthesize water-based HCFLG nanofluids, the obtained HCFLG (section 4.2.2) was mixed with Gum Arabic by a ratio of 0.5:1 and then poured into a vessel filled with the given amount of water and finally sonicated with a probe-sonicator for 10 min.

4.3.1.2 Colloidal Stability

The UV–Vis spectroscopy is a common method, which is utilized for the investigation of the stability of nanofluids including solid particles. According to the Beer–Lambert’s law, there is a direct connection between the absorbance of a solution and the concentration of the absorbing species such as particles in the solution. Considering this law, the absorption spectrum of the prepared nanofluids exhibits a maximum peak at around 265 nm corresponding to π – π transition of conjugation system in the polyaromatic structures. The band gap energy, E_g , can be measured from UV–Vis absorption by Tauc’s equation (Hadadian et al., 2014) given as equation no. 4.1,

$$(\alpha h_\nu)^n = B(h_\nu - E_g) \quad 4.1$$

where α , h_ν , n , E_g and B are, respectively, absorption coefficient, photon energy, the nature of optical transition, band gap energy and a material constant. Therefore, the UV–vis spectrum for the distilled water-based HCFLG nanofluids with different weight concentrations was investigated and photometric analysis of the UV–vis spectrometer was employed to trace the weight concentrations of samples versus time. To this end, a standard curve was drawn for each concentration. Figure 4.34 shows the colloidal stability for distilled water-based HCFLG nanofluids versus time. It is seen that the concentration of the samples decreases slightly with time because of agglomeration and sedimentation. Figure 4.34, however, shows that the relative reduction of weight concentration for all of the samples after 30 days was less than 2%. The high colloidal stability of distilled water-based HCFLG nanofluids is attributed to the small particle size associated with very high specific surface area ($1568 \text{ m}^2/\text{g}$).

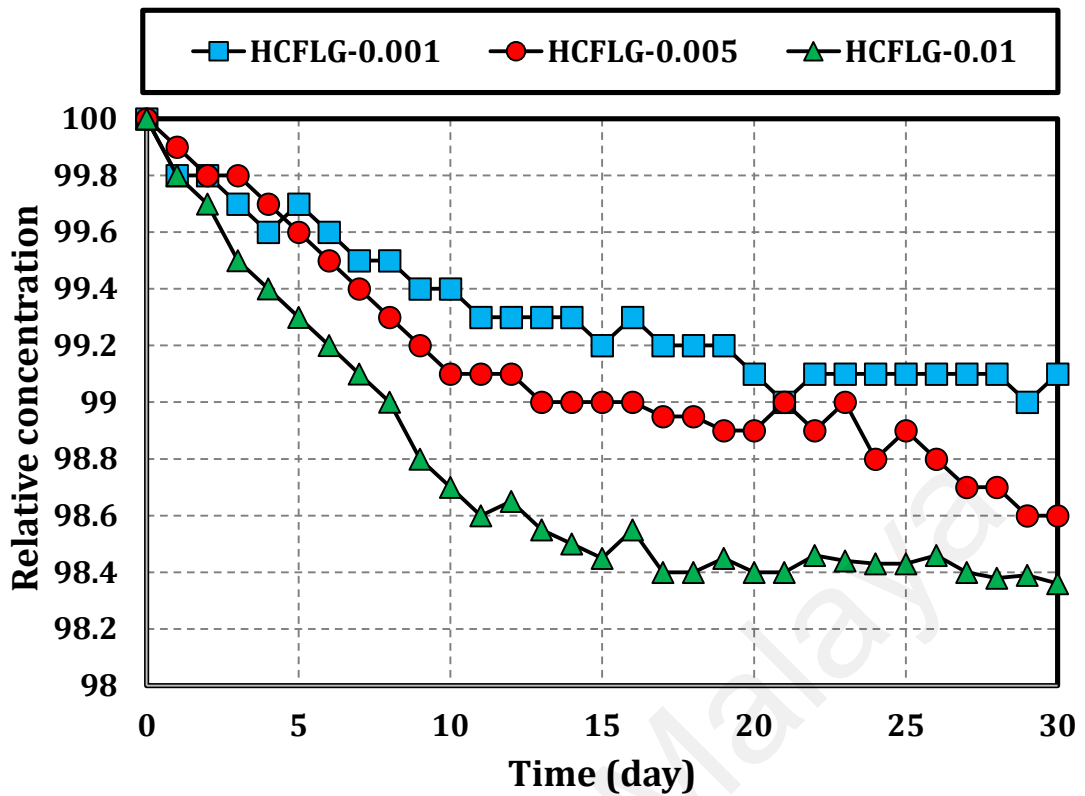


Figure 4.34: The colloidal stability of HCFLG in distilled water as a function of time and weight concentration.

4.3.1.3 Thermo-physical properties

Thermal conductivity is an important thermo-physical properties and was measured by a KD2 Pro analyzer based on the transient hot wire technique. The measured values of thermal conductivity of distilled water and distilled water-based HCFLG nanofluids are shown in Figure 4.35(a). As expected, this figure shows that the measured thermal conductivity increases with temperature. In the recent study (W. Sarsam et al., 2016b), it has been found that the higher specific surface area leads to the higher thermal conductivity of water-based graphene nanofluids. Since HCFLG has high specific surface area, the increase of thermal conductivity of the nanofluids is consistent with the earlier findings.

From Figure 4.35(a) it can be seen that all the samples were prepared with very low weight concentration, nevertheless, the amount of enhancements in thermal

conductivity of different samples are significant. As the concentration was increased from 0.0 wt% to 0.01 wt%, the figure shows that the thermal conductivity of water-based HCFLG nanofluids increases from 0.642 to 0.915 W/mK at 50 °C, which represents 42.5% enhancement. This amount of enhancement is quite impressive for the low weight concentration of 0.01wt%. Also, for distilled water, Figure 4.35(a) showed that the increase in temperature from 20 to 50 °C resulted in 8.6% increase in the thermal conductivity, while for water-based HCFLG nanofluids at 0.001 wt%, 0.005 wt%, and 0.01 wt% concentrations, the increase in thermal conductivity were 20.8%, 23.8%, and 21.9% respectively. Keblinski et al. (2002) and Eastman et al. (2004) suggested some potential mechanisms for the increase in the thermal conductivity in the presence of nanoparticles. These are, Brownian motion, molecular-level layering of the liquid at the liquid/particle interface, fluctuation of fluid velocity due to drag of Brownian nanoparticles, thermophoresis, reduction in thermal boundary layer thickness, nature of heat transport in nanoparticles, and effects of nanoparticle clustering. According to the recent studies (S. Choi et al., 2001; Godson et al., 2010; Huxtable et al., 2003; Kang et al., 2006; Nan et al., 1997), the thermal conductivity of nanofluids is affected by the thermal conductivities of the basefluid and nanoparticles, temperature, concentration, specific surface area, shape/geometry of nanostructures etc. The present results show that the specific surface area of nanoparticles also affects the thermal conductivity as well as the colloidal stability.

In Figure 4.35b, the effects of temperature and weight concentration of HCFLG on the specific heat capacity of distilled water-based HCFLG nanofluids are studied. It is seen that an increase in the weight concentration of HCFLG leads to a drop in the specific heat capacity. In particular, an average drop of 0.1–0.5% is observed for weight concentrations of 0.001–0.01 wt%. Specific heat capacity of distilled water-based

HCFLG is lower than that of water due to the lower specific heat capacity of HCFLG loaded in the base fluid.

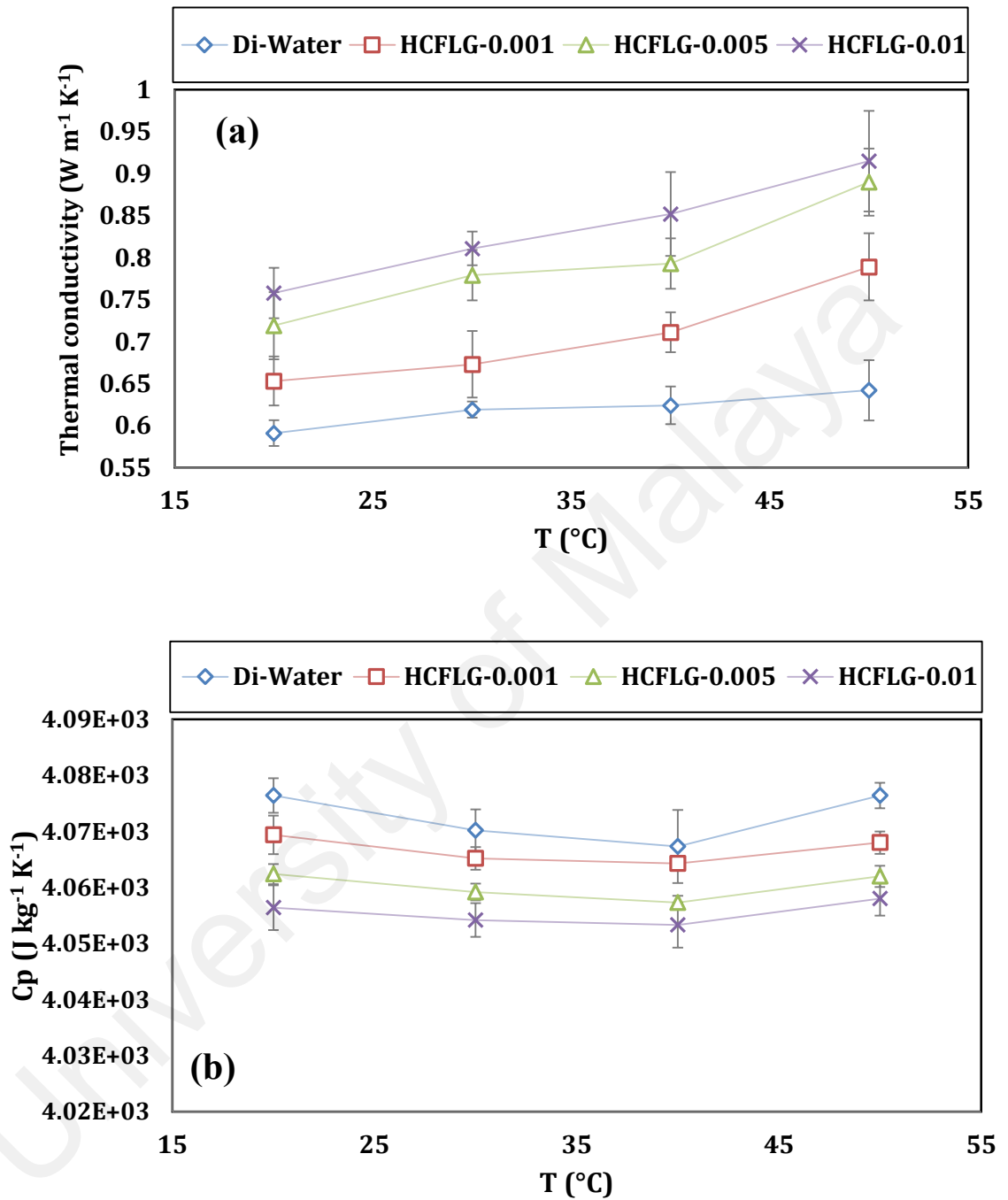
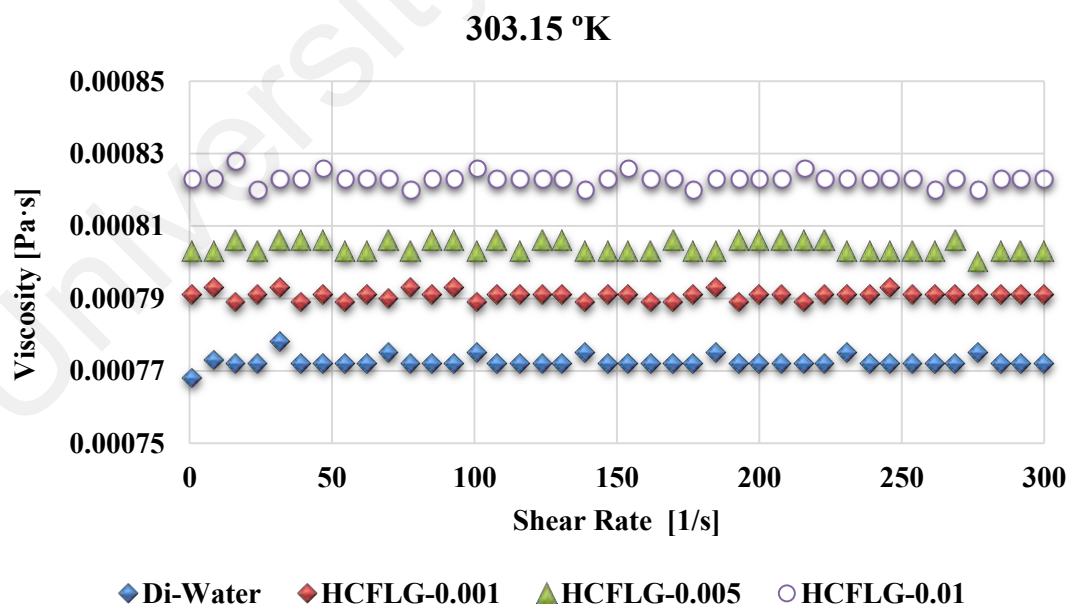
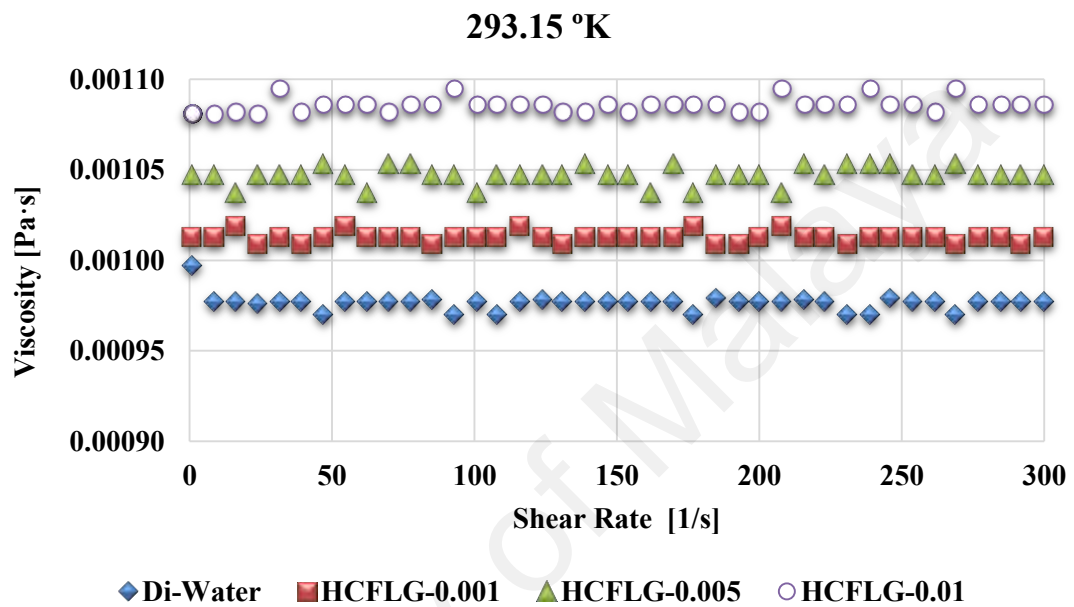


Figure 4.35: (a) Thermal conductivity and (b) specific heat capacity plots of water-based HCFLG nanofluids at different weight concentrations as well as distilled water.

The measured values of viscosity are plotted in Figure 4.36 as function of shear rate for water-based HCFLG nanofluids and weight concentrations, as well as, distilled

water at various temperatures. This figure shows that the effective viscosity of water-based HCFLG nanofluids is higher than water and increases as weight concentration increases. Furthermore, the effective viscosity decreases with increase of the temperature. Figure 4.36 also shows that the behavior of water-based HCFLG nanofluids is Newtonian with almost constant viscosity for different values of shear rate.



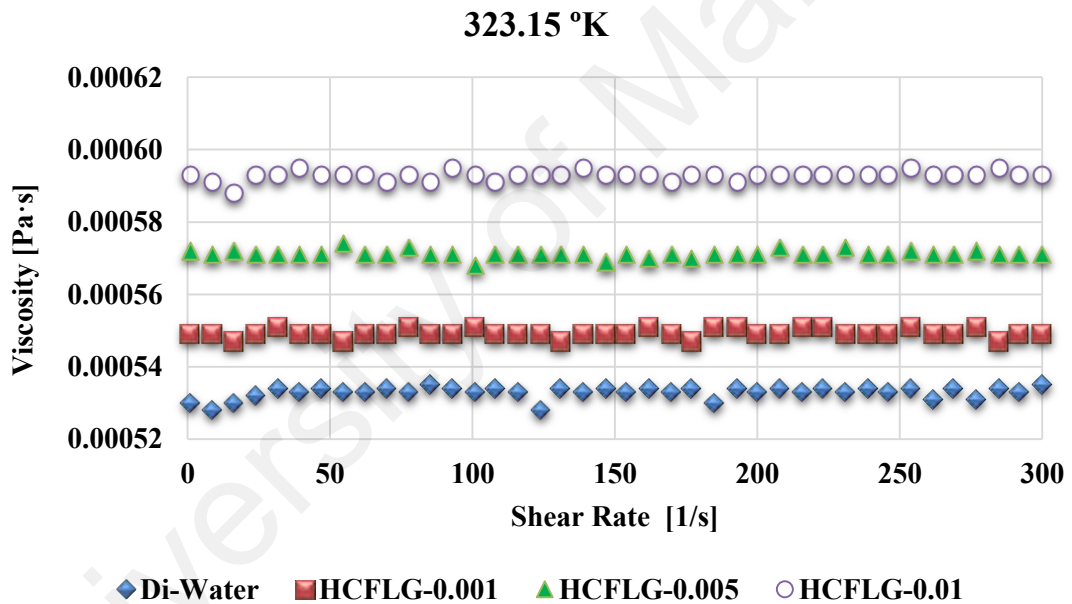
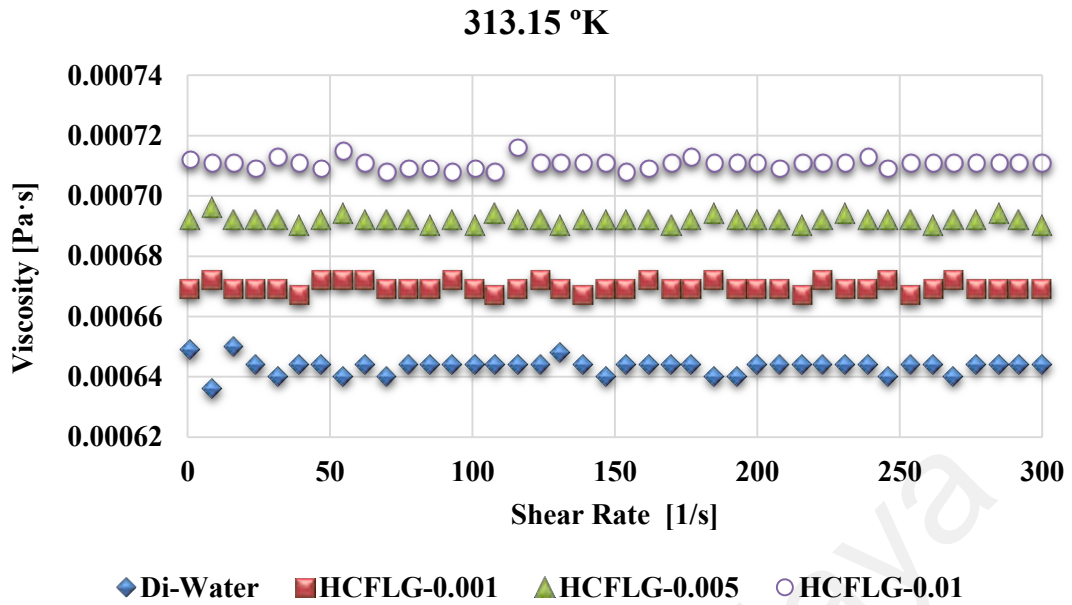


Figure 4.36: Plots of the measured values of viscosity versus shear rate for water-based HCFLG nanofluids at different temperatures and weight concentrations.

The densities of water-based HCFLG nanofluids and water are measured as functions of temperature and weight concentrations, and the results are shown in Table 4.7. It is observed that the density of water-based HCFLG nanofluids as well as water decreases by increasing the temperature, which may be related to the thermal expansion of liquid. Also, there is an upward trend between the density of samples and weight

concentrations of HCFLG, therefore as the weight concentration increases, the density grows. Since the density of solid particles is commonly more than the liquids, the density of prepared samples increases with concentration, which can be a reasonable issue. Also, as the temperature increases, the density insignificantly enhances. For example, the density of the Di-water and water-based HCFLG nanofluids at weight concentration of 0.01% decreases by 1.01% and 0.99% respectively, when the temperature increases from 20 to 50 °C.

Table 4.7: Densities of the Di-water and water-based HCFLG nanofluids for different concentrations.

T (°C)	Density (kg/m ³)			
	Di-Water	HCFLG-0.001	HCFLG-0.005	HCFLG-0.01
20	997.78	998.18	999.79	1001.80
30	995.18	995.58	997.20	999.23
40	991.80	992.20	993.84	995.88
50	987.68	988.092	989.74	991.80

4.3.2 Water-based chemically-assisted exfoliated single-layered graphene (SGr) nanofluids

4.3.2.1 Preparation

Based on the results in section 4.2.1, the functionalized graphite was expanded and was much more soluble in DMF, DMA, g-butyrolactone (GBL) and EG than the pristine graphite, as shown in Figure 4.37. It is noteworthy that a majority of flakes has remained stable for more than 1 week. The easily-miscible tetrahydrofurfuryl polyethylene glycol (PEG) functionalities may explain the higher dispersion of the functionalized and expanded graphite.

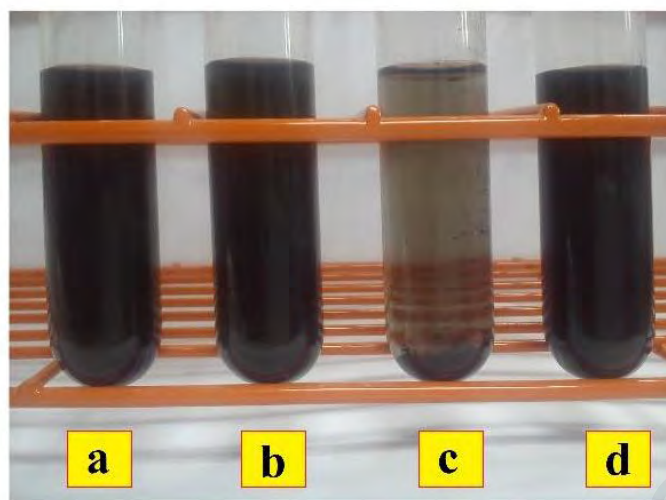


Figure 4.37: Photographs of functionalized and expanded graphite dispersed in (a) DMF, (b) DMA, (c) g-butyrolactone and (d) EG.

To synthesize water-based SGr nanofluids, the given amount of chemically-assisted exfoliated single-layered graphene after preparation (Section 4.2.1) poured into a vessel filled with the given amount of water and finally sonicated with a probe-sonicator for 15 minutes to reach homogenous suspension. Three different weight concentrations of 0.001%, 0.005% and 0.01% were prepared for next phase of study.

4.3.2.2 Colloidal Stability

As mentioned in section 3.1.5, the UV–Vis spectroscopy is a common method, which is utilized for investigation of the stability of nanofluids including solid particles. Therefore, the UV–vis spectrum for the distilled water-based SGr nanofluids with different weight concentrations was investigated and photometric analysis of the UV–vis spectrometer was employed to trace the weight concentrations of samples versus time. To this end, a standard curve was drawn for each concentration. The UV–vis spectrum for the water-based SGr nanofluids with different weight concentrations is presented in Figure 4.38 panel (a), from which it can be seen that the peak value of absorbance for all samples due to the presence of SGr in the wavelengths of 265 nm. Figure 4.38 panel (b) illustrates the colloidal stability for distilled water-based SGr nanofluids versus time. From this figure, the concentration of the samples decreases with

time because of agglomeration and sedimentation. According to the presently obtained results, the remaining weight concentration for all of the samples in aqueous media after 30 days were less than 15%. Also, the sediment of all samples remain almost constant after 23 days, representing almost 15%. Representing these results, the suitable colloidal stability of distilled water-based SGr nanofluids is attributed to hydrophilic functional PEG, the small particle size of SGr associated with very high specific surface area. Mostly, the easily-miscible PEG functionalities may explain the higher dispersion of the SGr in aqueous media (Kalinina et al., 2011a).

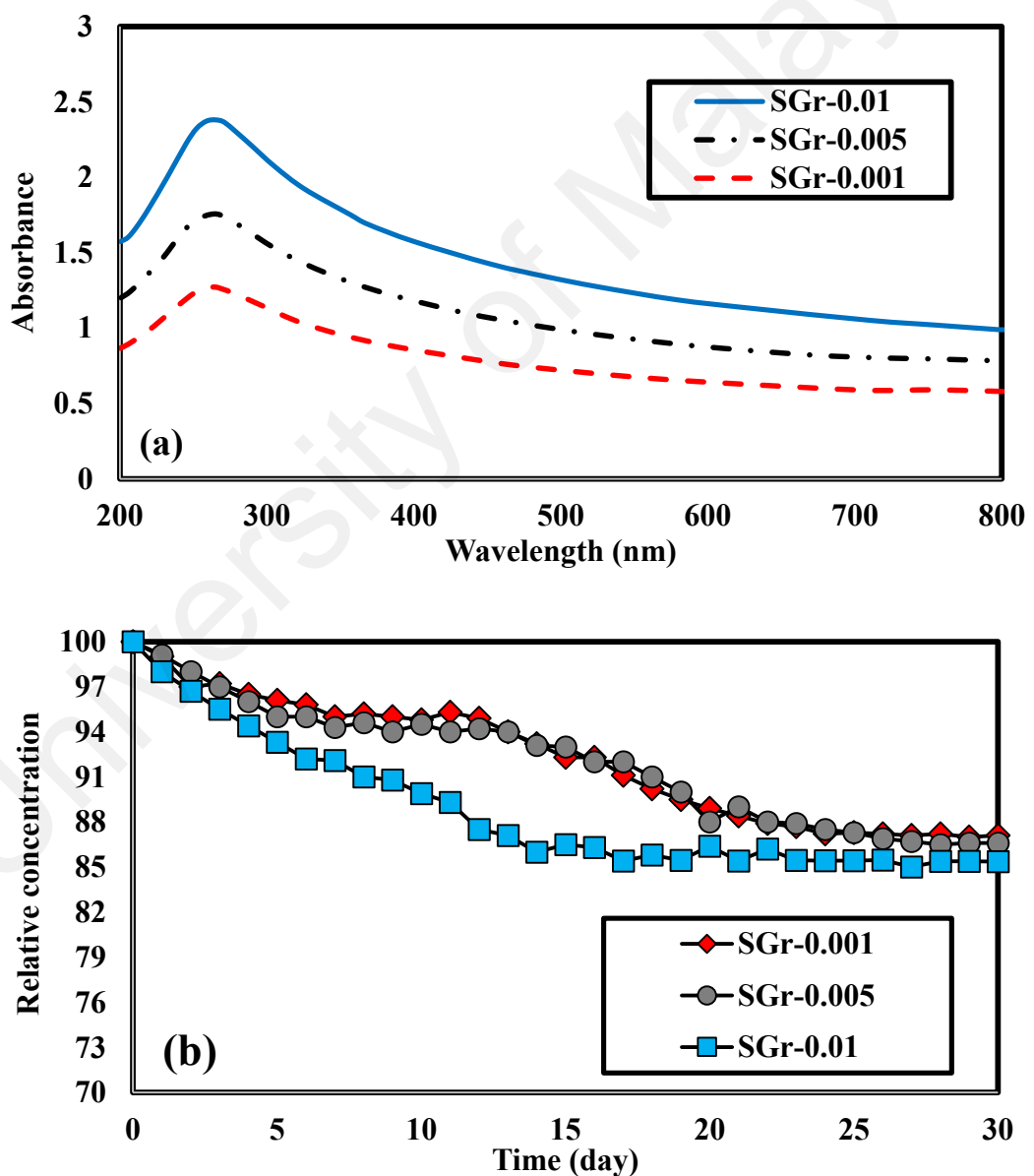


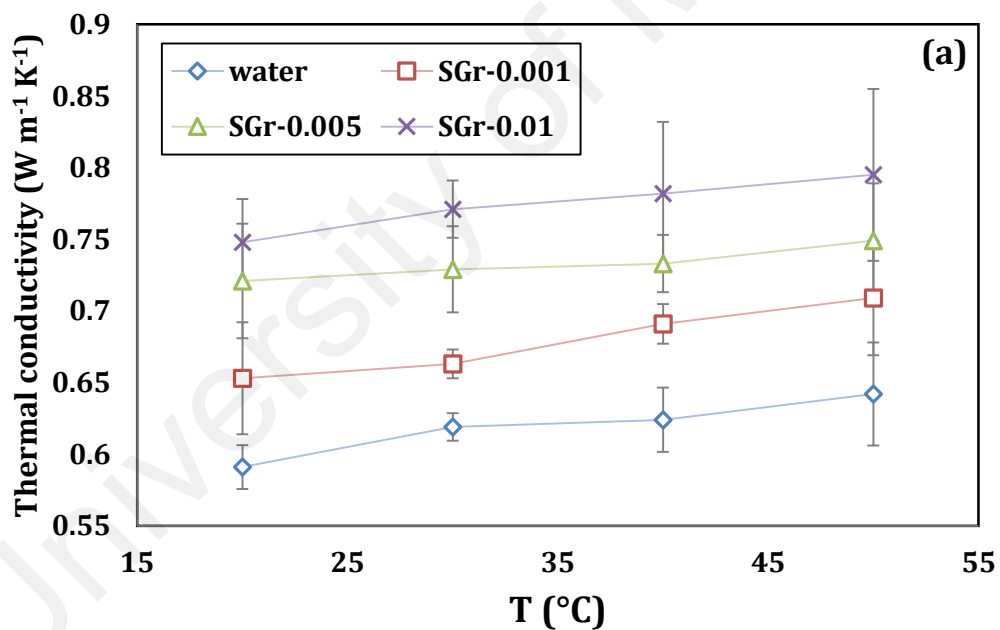
Figure 4.38: (a) UV–Vis spectra of water-based SGr nanofluids at different concentrations and (b) the colloidal stability of SGr in distilled water as a function of time and weight concentration.

4.3.2.3 Thermo-physical properties

As one of the most fundamental thermo-physical properties, thermal conductivity was obtained by using the KD2 Pro analyzer based on the transient hot wire technique. The measured values of thermal conductivity for distilled water and distilled water-based SGr nanofluids are shown in Figure 4.39 panel (a). From which, it can be first concluded that as temperature increases, the measured thermal conductivity increases, which is an expected phenomenon. According to Sarsam et al. (2016b), the higher specific surface area of graphene means the higher thermal conductivity for nanofluids loaded with graphene flakes. Therefore, the synthesized material with superior specific surface area was estimated to represent high thermal conductivity at low weight concentration. Obviously, all the nanofluids samples were arranged at low weight concentrations, however the amount of enhancements for different samples were fairly significant. From Figure 4.39 panel (a), there is more than 25% increase in the thermal conductivity of water-based SGr nanofluids for different temperatures and at the weight concentration of 0.01%. For example, water-based SGr nanofluids increased from 0.624 to 0.782 W/m °K at 40 °C for concentration of 0.01%, representing 25.3% enhancement as compared with water. This amount of enhancement was brilliant for the low weight concentration of 0.01wt%. Regarding the mechanism of increasing thermal conductivity with loading graphene in base fluid, Keblinski et al. (2002) and Eastman et al. (2004) reported four potential mechanisms to introduce reasons for the enhancement, i.e., Brownian motion, molecular-level layering of the liquid at the liquid/particle interface, the nature of heat transport in the nanoparticles, and the effects of nanoparticle clustering. In addition, according to the recent studies (S. Choi et al., 2001; Godson et al., 2010; Huxtable et al., 2003; Kang et al., 2006; Nan et al., 1997), some basic parameters such as thermal conductivities of the basefluid and nanoparticles, temperature, concentration, specific surface area, shape or geometry of nanostructures play key roles in determining the

thermal conductivity of nanofluids. Herein, the results show that the specific surface area of nanoparticles has a direct effect on the thermal conductivity as well as colloidal stability.

As another thermo-physical property, the specific heat capacity of distilled water-based SGr nanofluids and distilled water are illustrated in Figure 4.39 panel (b) for different temperatures and weight concentrations. It is seen that an increase in the weight concentration of SGr leads to a small drop in the specific heat capacity. Commonly, average drop of 0.1–0.5% in the specific heat capacity of distilled water-based SGr nanofluids as compared with base fluid indicated an insignificant decrease. Specific heat capacity of distilled water-based SGR is lower than that of water due to the lower specific heat capacity of SGr loaded in the basefluid.



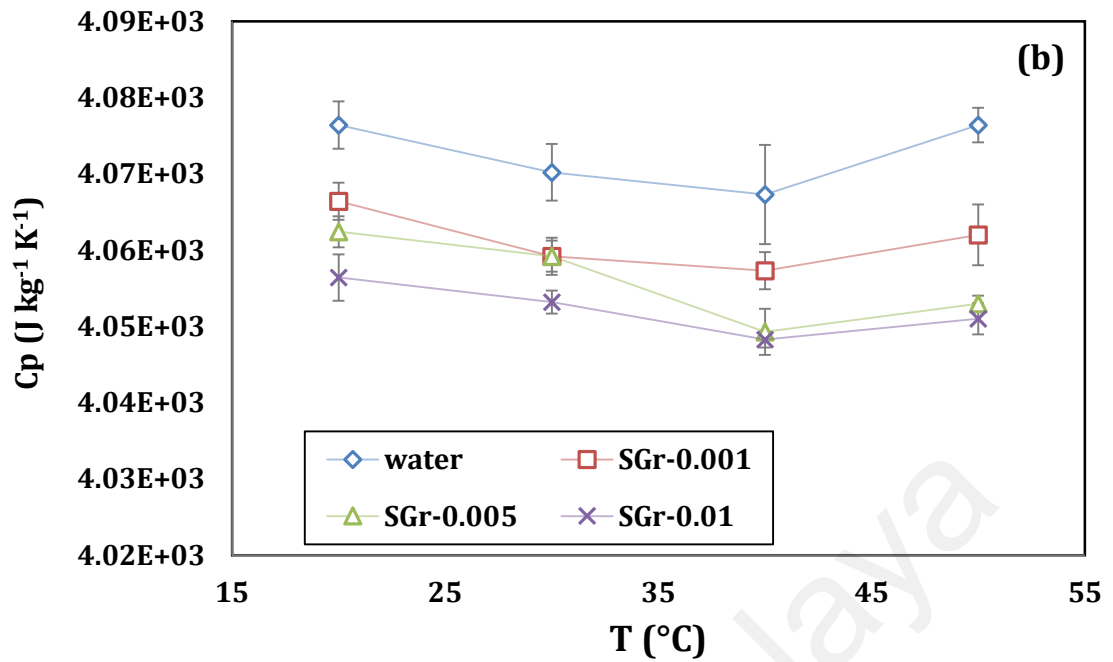
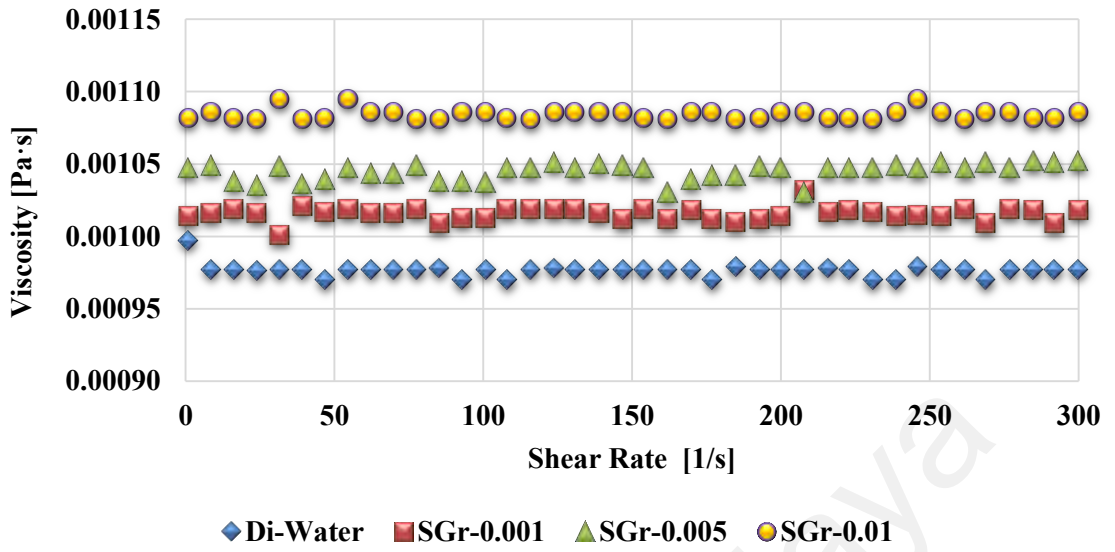


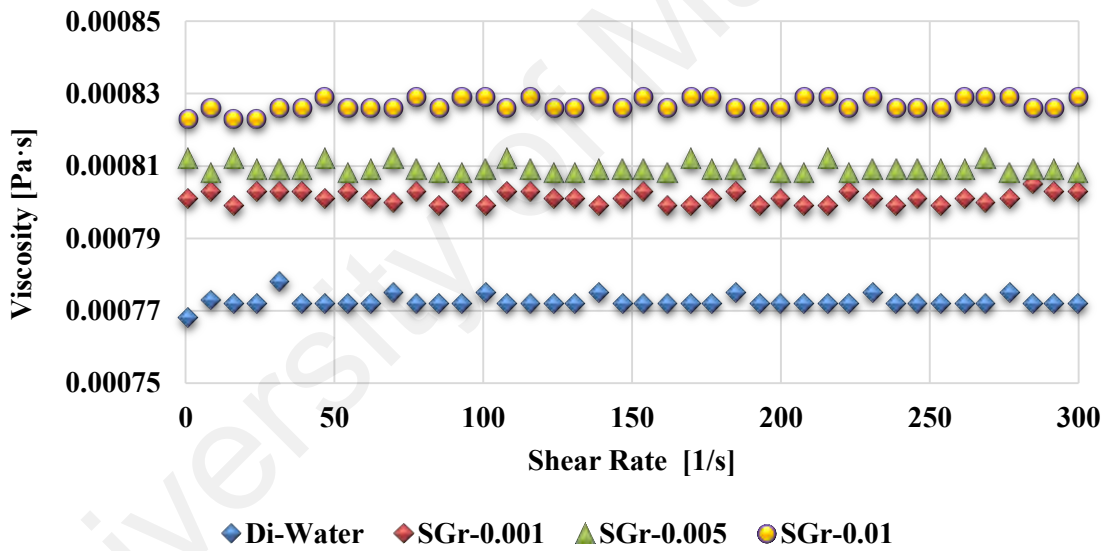
Figure 4.39: (a) Thermal conductivity and (b) specific heat capacity plots of water-based SGr nanofluids at different weight concentrations as well as distilled water.

The measured values of viscosity as functions of shear rate, weight concentration, and temperature are plotted in Figure 4.40 for water-based SGr nanofluids as well as distilled water. From which, it is seen that the measured viscosity increases with weight concentration and decreases with temperature. Also, it can be found that the behavior of water-based SGr nanofluids was quite Newtonian with almost constant viscosity at different values of shear rate. The amount of fluctuation in viscosity is insignificant and negligible. From Figure 4.40, it can clearly be found that viscosity of water-based SGr nanofluids was higher than that of water alone and increases as weight concentration increases.

293.15 °K



303.15 °K



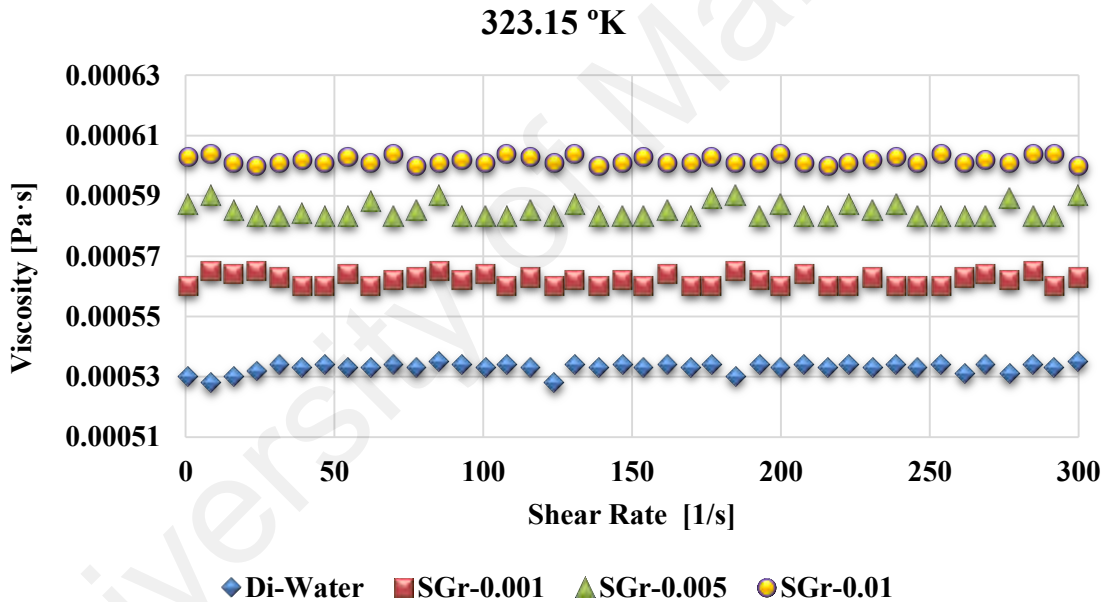
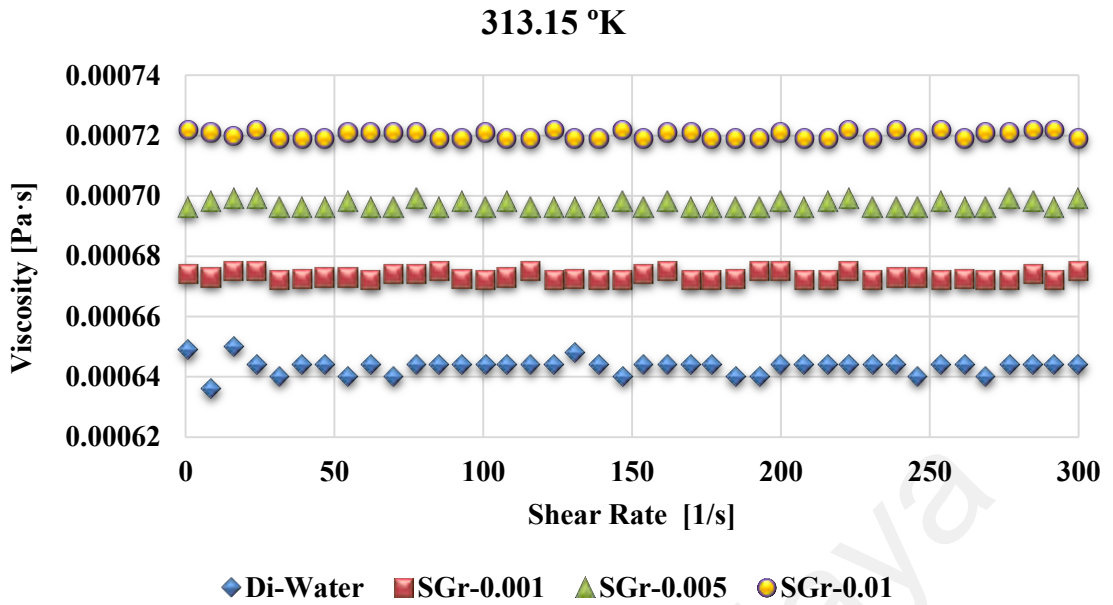


Figure 4.40: Plots of the measured values of viscosity versus shear rate for water-based SGr nanofluids at different temperatures and weight concentrations.

The densities of water-based SGr nanofluids and water are measured as functions of temperature and weight concentration, and the results are shown in Table 4.8. It is observed that the density of water-based SGr nanofluids as well as water decreases by increasing the temperature, which may be related to the thermal expansion of liquid. Also, there is an upward trend between the density of samples and weight concentration of SGr,

therefore as the weight concentration increases, the density grows. Since the density of solid particles is commonly more than the liquids, and the density of the prepared samples increases with concentration, which can be a reasonable issue. Also, as the temperature increases, the density insignificantly enhances. For example, the density of the Di-water and water-based SGr nanofluids at weight concentration of 0.01% decreases from 1.01% to 0.96%, when the temperature increases from 20 to 50 °C.

Table 4.8: Densities of the water and water-based SGr nanofluids for different concentrations.

T (°C)	Density (kg/m ³)			
	Di-Water	SGr-0.001	SGr-0.005	SGr-0.01
20	997.78	998.58	1001.79	1005.80
30	995.18	996.01	999.35	1003.52
40	991.80	992.61	995.89	999.98
50	987.68	988.52	991.87	996.05

4.3.3 Water/ethylene glycol-based crumpled nitrogen-doped graphene nanosheets nanofluids (CNDG-WEG)

4.3.3.1 Preparation

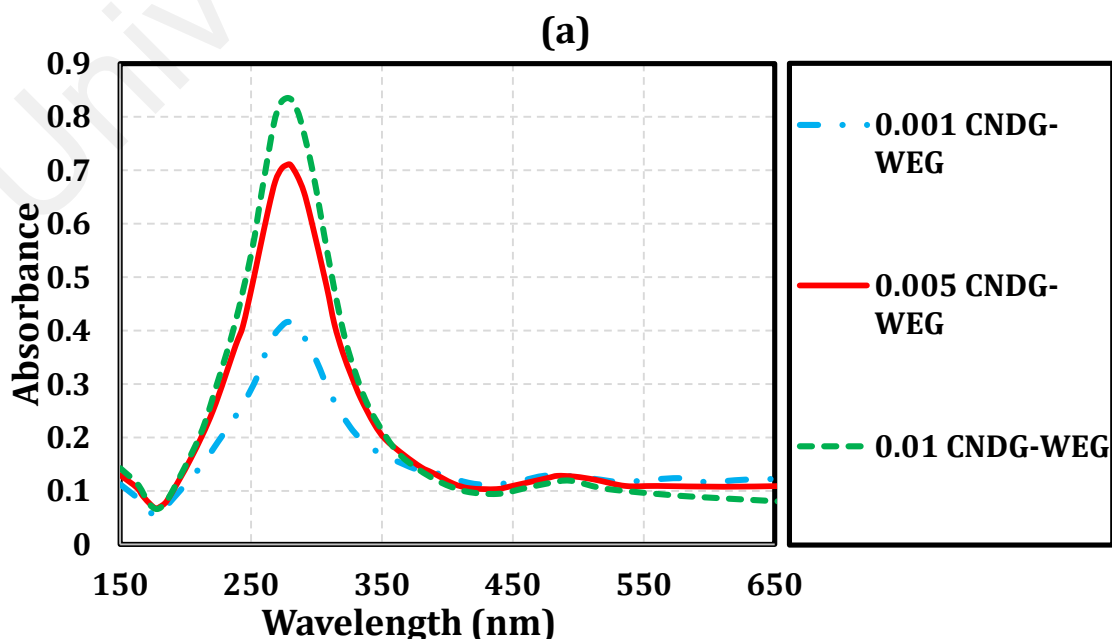
After preparing CNDG (section 4.2.3), the CNDG was weakly dispersible in both the media of deionized water and ethylene glycol at room temperature. So, to provide better dispersion with known weight concentrations, the given amount of CNDG was mixed with Gum Arabic by a ratio of 0.5:1 and then poured into a vessel filled with the given amount of water and ethylene glycol with a volumetric ratio of 40:60.

4.3.3.2 Colloidal Stability

Figure 4.41a illustrates the UV–vis spectra of the CNDG for different weight concentrations. As mentioned above, UV–Vis spectroscopy is commonly utilized for investigation of the stability of coolant including solid nanoparticles and is able to measuring the sedimentation time. According to the Beer–Lambert’s law, the absorbance

of a solution is directly proportional to the concentration of the absorbing species such as particles in the solution. The absorption spectrum exhibited a maximum peak at around 277 nm corresponding to $\pi-\pi^*$ transition of conjugation system in the polyaromatic structures. The band gap energy can be measured from UV– Vis absorption using Tauc's equation (Eq. 4.1) (Hadadian et al., 2014).

Plotting $(\alpha h\nu)^n$ in Eq.1 against the photon energy and extrapolating the linear region of the curve to the x-axis provides the optical band gap. Regarding the dispersion state and the long-term stability, the colloidal stability of the CNDG in water-ethylene glycol mixture in the presence of GA is investigated quantitatively by UV–Vis spectroscopy. The stability of CNDG-WEG dispersion of 0.001, 0.005 and 0.01 wt.% were examined by UV– Vis spectroscopy (Figure 4.41b). The relative concentration calculated by absorbance at the wavelength of 277 nm was plotted against time during 30 days. It can be seen that the relative concentration of CNDG-WEG decreases insignificantly over the aforementioned period of time. As a result, the maximum sediment of 26% was obtained for highest weight concentration of 0.01 wt.%, which confirmed the suitable dispersibility of CNDG in the mixture of water and ethylene glycol.



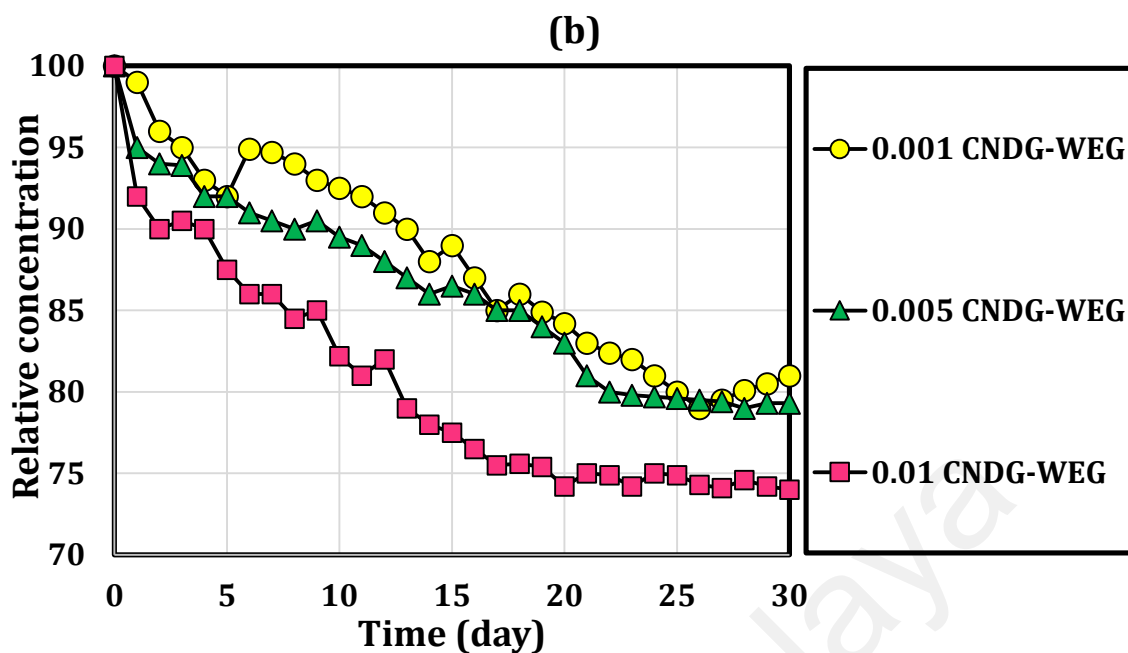


Figure 4.41: (a) UV–Vis spectrum of CNDG-WEG at different concentrations and (b) the colloidal stability of CNDG in water-EG mixture as a function of time and weight concentration.

To check whether the decrease in signal intensity by time is just due to reversible particle settling or gradual irreversible particle aggregation, Figure 4.42 is plotted. The colloidal stability of the HCND-WEG for weight concentration of 0.01 wt.% obtained by performing UV measurements for 20 days on suspensions mechanically stirred every day. The stirring was performed for 15 min at room temperature with speed range ~ 1000 rpm. The measurement was again carried out at peak wavelength of each material to trace the alteration in the intensity which can be further used to describe the suspension stability for CNDG-WEG with different intervals. It can be seen that all colloidal mixtures show almost 1% decrease (can be attributed to the error in measurement) in the relative concentrations as the time progressed, indicating that the colloidal suspensions have been remained stable for 20 days without irreversible particle aggregation.

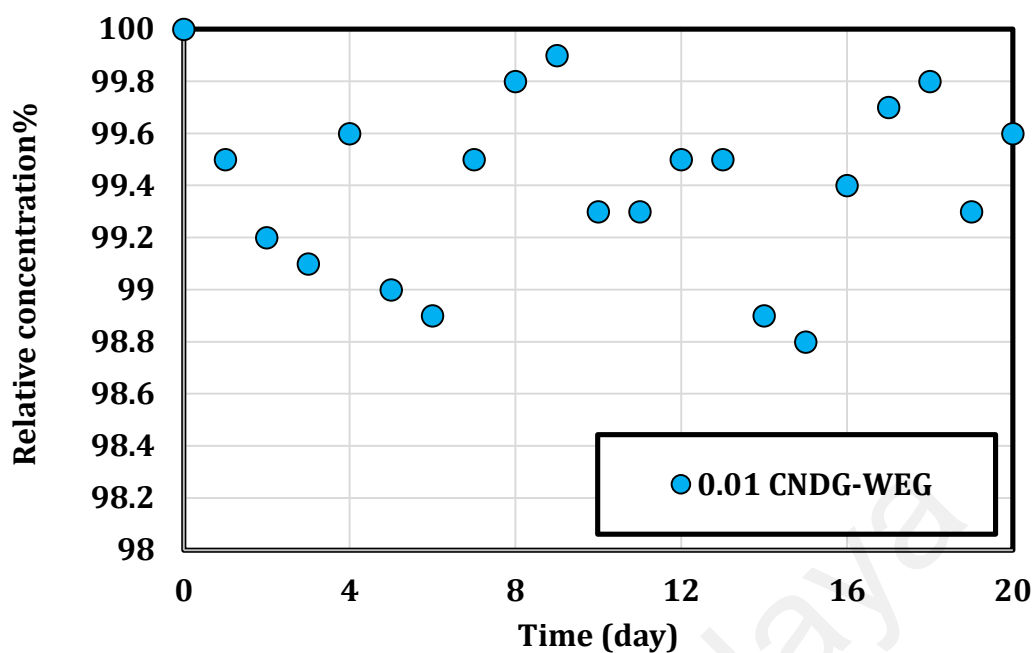


Figure 4.42: The colloidal stability of the HCNDG-WEG for weight concentration of 0.01 wt.% obtained by performing UV measurements for 20 days on suspensions mechanically stirred with speed range ~ 1000 rpm every day.

The feasibility of forming stable CNDG-WEG dispersions through electrostatic stabilization was examined by the zeta potential analysis. The zeta potential values more negative than -30 mV or more positive than +30 mV are generally considered to represent sufficient mutual repulsion to ensure the stability of a dispersion (S. Park & Ruoff, 2009). Concerning the CNDG-WEG interface, it is known that GNDG nanosheets have negative charges when they are dispersed in water-EG mixture (S. A. Hasan et al., 2012). As shown in Figure 4.43, zeta potential of CNDG-WEG coolant at pH ~ 7 was highly negative revealing strong repulsive forces between CNDG nanosheets. As the figure shows, by increasing the weight concentration from 0.001 to 0.01 wt.%, zeta potential decreased from -47.7 to -57 (Figure 4.44). The increase in nitrogen group and acidity (unreacted COOH) of the suspension by increasing CNDG loading indicates that more number of protons (H^+) are released through deprotonation of pyrrolic N and/or remaining acidic-groups. The electrostatic repulsion between CNDG nanosheets can also be considered as one of the reasons in the preventing of the CNDG sheets from aggregating (C.-J. Shih et

al., 2011). The negative zeta potential value indicates that the surface charges are negative. Also, it can be concluded that higher weight concentration means higher electrical conductivity, which can be a reason for decreasing trend of zeta potential (or higher absolute amount of zeta potential).

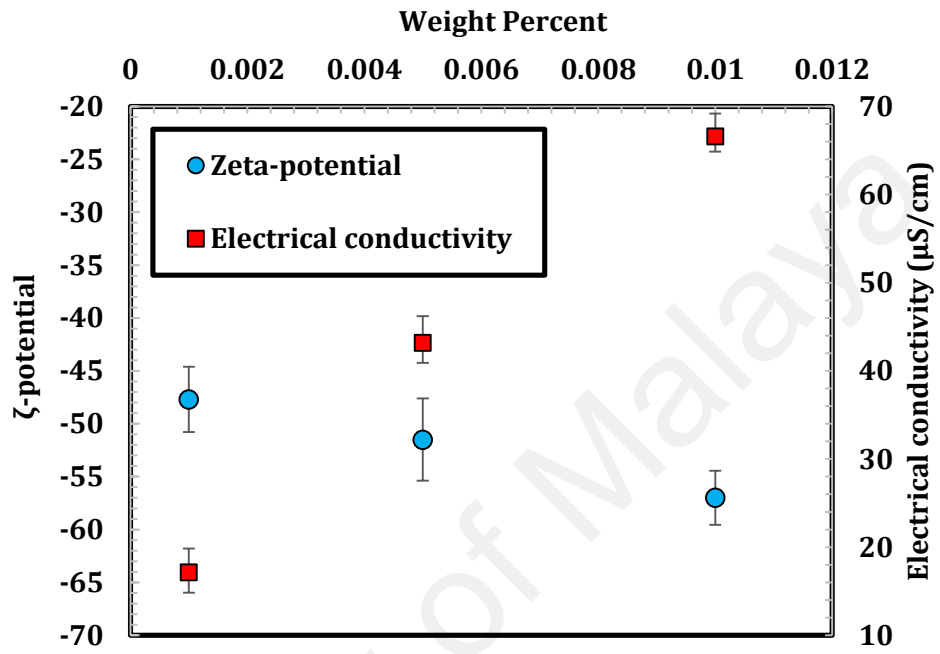


Figure 4.43: Zeta-potential and electrical conductivity of CNDG-WEG at 25 °C.

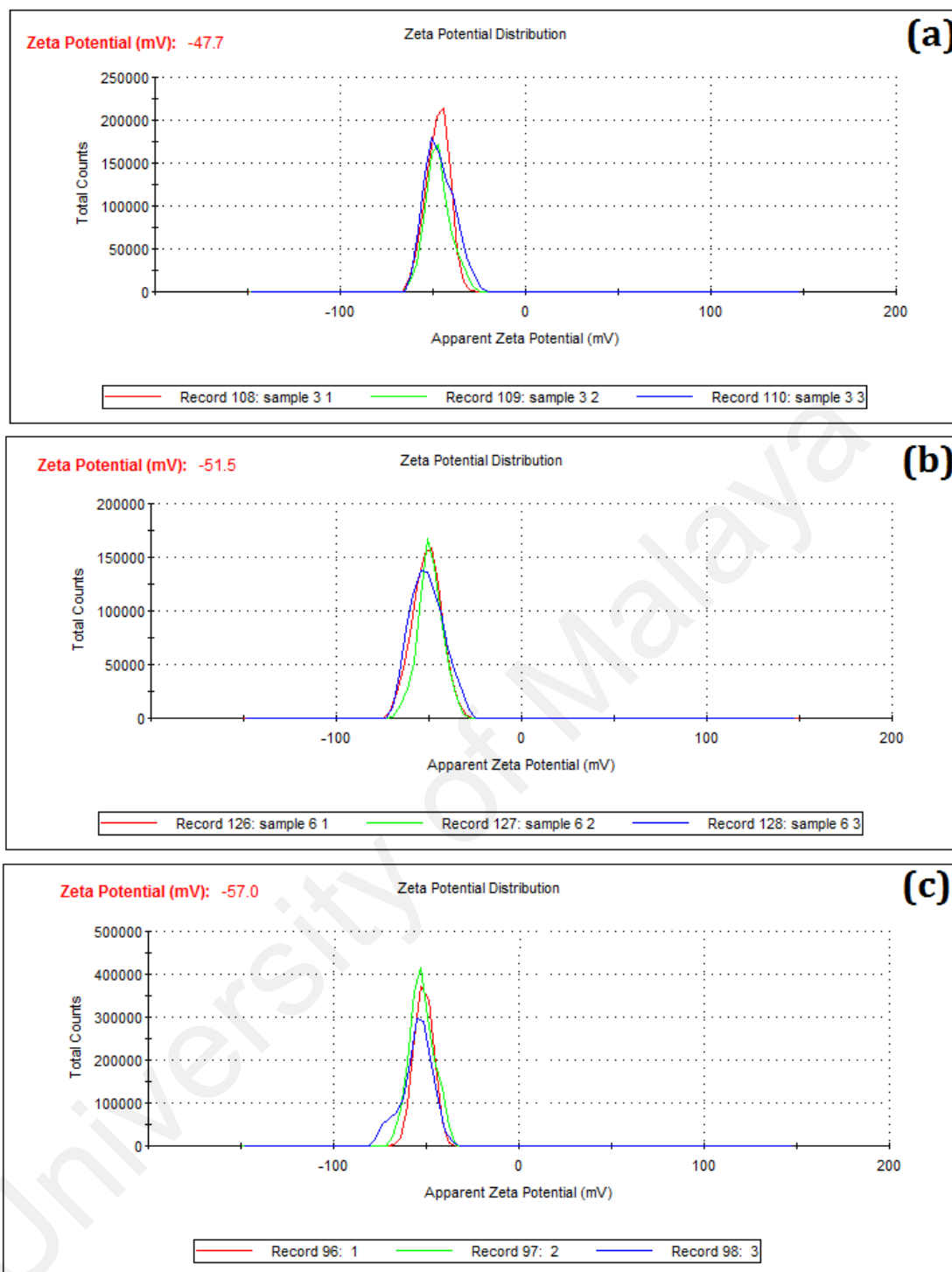


Figure 4.44: Zeta-potential of CNDG-WEG at weight concentrations of (a) 0.001, (b) 0.005 and (c) 0.01 wt.%.

4.3.3.3 Thermo-physical properties

The effective viscosities of DI water-EG and CNDG-WEG mixtures were determined for temperature range of 25-65°C. The dynamic viscosity of the CNDG-WEG as a function of temperature and weight concentration was determined at high shear rate of

140 s⁻¹ and the results are indicated in Table 4.9. Like other coolants, the rheological behavior of CNDG-WEG indicates two typical characteristics: (i) an improvement of viscosity with increased concentration of CNDG, and (ii) a decrease in viscosity with increasing temperature, which is the result of the intermolecular forces of the fluid being weakened. It can be observed that there is a little increase in the CNDG-WEG viscosity with increase in weight concentration. Pumping power increases with increasing viscosity of the working fluid and it can be considered as a negative economic indicator in a loop system. Table 4.9 shows an insignificant increase in the viscosity with the CNDG loading. In addition, viscosity decreases with the increase in temperature, which is consistent with Ko et al. (2007) and S. J. Aravind et al. (2011).

Table 4.9: Dynamic viscosity of the CNDG-WEG as a function of temperature and weight concentration at shear rate of 140 s⁻¹.

Temperature (°C)	μ (g/ms)			
	water/EG	0.001 CNDG- WEG	0.005% CNDG-WEG	0.01% CNDG- WEG
25	3.964±0.014	3.970±0.03	3.981±0.022	3.994±0.024
35	2.981±0.016	2.987±0.031	2.996±0.038	3.011±0.046
45	2.207±0.018	2.211±0.042	2.224±0.044	2.234±0.041
55	1.663±0.02	1.669±0.034	1.678±0.062	1.689±0.042
65	1.317±0.034	1.322±0.054	1.335±0.052	1.344±0.032

Figure 4.45 indicates the plot of thermal conductivity of CNDG-WEG as a function of temperature and concentration. Three different weight concentrations of 0.001 wt.%, 0.005 wt.% and 0.01 wt.% are considered and the variation of thermal conductivity with concentration and temperature are examined. In this study, CNDG-WEG with low concentrations of CNDG is considered to prevent sharp increase in effective viscosity. Figure 4.45 indicates that thermal conductivity of CNDG-WEG is higher than that of water-EG. It can also be observed that thermal conductivity of the base fluid and the prepared coolants at various weight concentrations increase by increasing the

temperature. For CNDG-WEG samples, the increase in thermal conductivity with temperature is more sensible. Therefore, it supports that the temperature plays an important role in increasing the thermal conductivity of CNDG-WEG coolant. The enhancement of thermal conductivity with increase of temperature is attributed to the Brownian motion of the nanoparticles, which are suspended in the base-fluid (Aravind et al., 2011). Figure 4.45 also indicates that CNDG-WEG samples show larger enhancement in thermal conductivity at higher weight concentration of CNDG.

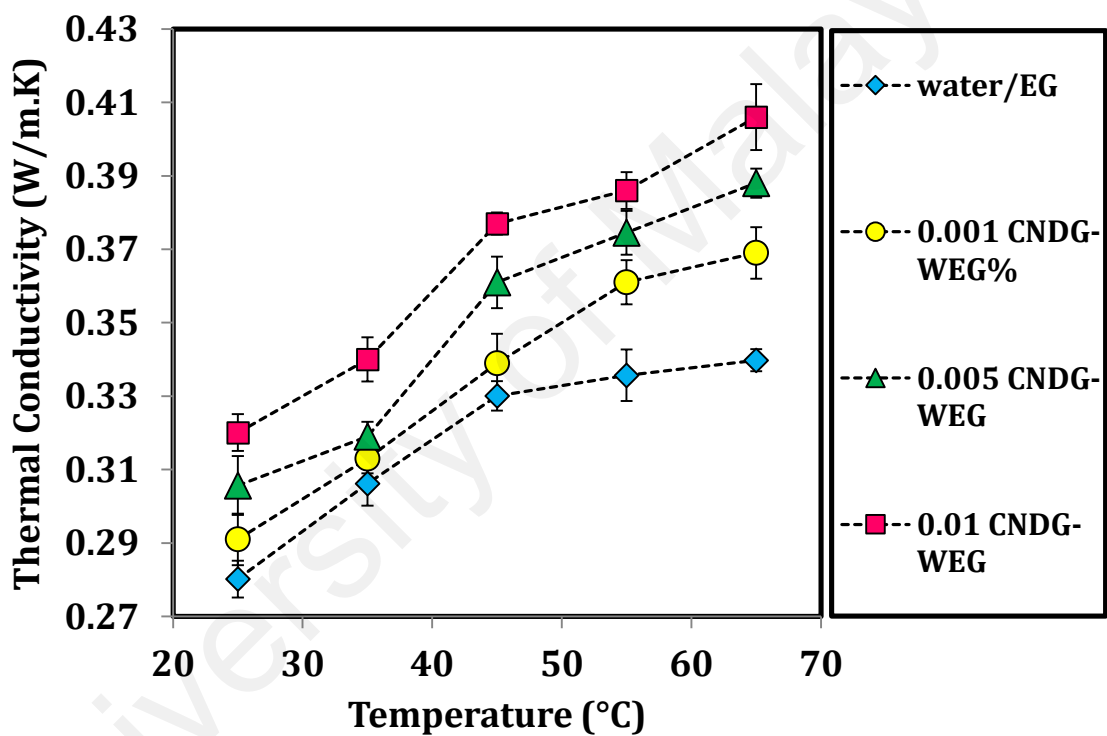


Figure 4.45: Thermal conductivity plot of CNDG-WEG at different weight concentrations and pure water-EG mixture.

According to (Aravind et al., 2011; Jha & Ramaprabhu, 2008), the formation of surface nanolayers plays a key role in heat transfer for CNDG base-fluids. Liquid molecules create layers around the CNDG, so enhance local ordering of the liquid layer at the interface region. Therefore, the liquid layer at the interface would indicate a higher thermal conductivity compared to the base-fluid. The higher slope in thermal conductivity of CNDG-WEG coolant with concentration of 0.01 wt.% shows higher rate of formation

of the surface nanolayers. Layering of base fluid molecules on the surface of nanoparticles in a nanofluid should be studied using nuclear magnetic resonance (NMR). Professor Buongiorno and his coworker from Massachusetts Institute of Technology (Gerardi et al., 2009) show a thin ordered layer of liquid molecules surrounds each nanoparticle with NMR method. This ordered layer increases the nanoparticle effective volumetric fraction; however, the nanofluid thermal conductivity appears to be unaffected by this layer. Numerous researchers applied the concept of liquid/solid interfacial layer to show the different enhancements of the thermal conductivity in nanofluids. Some studies (W Yu & Choi, 2003, 2004) proposed some models according to the conventional theory by considering a liquid molecular layer around the nanoparticles. However, some theoretical and experimental studies e.g. Xue et al. (2004) and Gerardi et al. (2009) showed that the thermal transport in layered liquids had no effect on the heat transfer characteristics and it is not adequate to explain the increased thermal conductivity of suspensions included nanoparticles.

In order to elucidate the reasons for the strange growth in thermal conductivity of nanofluids, Keblinski et al. (2002) and Eastman et al. (2004) suggested four potential mechanisms e.g. molecular-level layering of the liquid at the liquid/particle interface, Brownian motion of the nanoparticles, the nature of heat transport in the nanoparticles, and the effects of nanoparticle clustering. They suggested that the effect of Brownian motion can be neglected since influence of thermal diffusion is higher than Brownian diffusion. However, they only measured the cases of stationary nanofluids. Xinwei Wang et al. (1999) concluded that the thermal conductivity of nanofluids is a function of the particle structure and microscopic motion (Brownian motion and inter-particle forces).

Also, Xuan and Li (2000) argued that some effective reasons for improving the thermal conductivity of nanofluids e.g. the increased surface area by suspended nanoparticles, the increased thermal conductivity of the fluid, the interaction and collision

among particles, the intensified mixing fluctuation and turbulence of the fluid, and the dispersion of nanoparticles. Khaled and Vafai (2005) also studied the effect of thermal conductivity on heat transfer enhancement of nanofluids. These results suggested that utilization of a dispersive element in the core region has no effect on the heat transfer rate. However, the corresponding dispersive elements led to almost 21% enhancement in Nusselt number for a uniform tube supplied by a fixed heat flux as compared to the uniform distribution for the dispersive elements. These results suggest a conceivable elucidation for the enhanced thermal conductivity of nanofluids which can regulate partially by the dispersive properties.

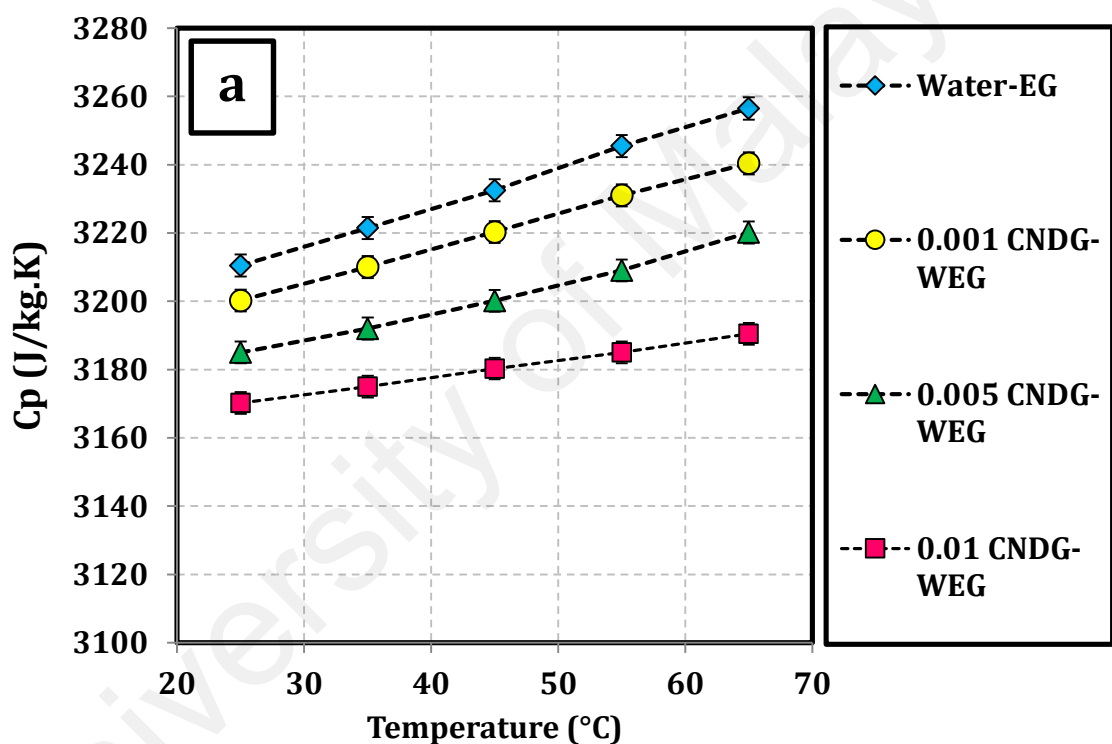
Wen and Ding (Ding & Wen, 2005; D. Wen & Ding, 2005) investigated the influence of particle migration on heat transfer characteristics in nanofluids flowing through mini-channels theoretically. The influence of shear-induced and viscosity-gradient-induced particle migration and the self-diffusion due to Brownian motion on heat transfer rate were investigated. Their results illustrated a considerable non-uniformity in particle concentration and thermal conductivity over the test-section due to particle migration, which resulted in a higher Nusselt number as compared to the uniform distribution of thermal conductivity. Koo and Kleinstreuer (2005) discussed the effects of Brownian, thermo-phoretic, and osmo-phoretic motions on the effective thermal conductivities. They proposed that Brownian motion is a much more vital factor than the thermo- and osmo-phoretic motions. However, their claim has not been confirmed by experiment yet. Evans et al. (2006) proposed that the effect of Brownian motion on the thermal conductivity enhancement of the nanofluid is insignificant and it alone is not able to reach this amount of extraordinary thermal transport properties. They employed the molecular dynamics simulations and the effective medium theory, but, they just focused on the stationary fluids, which weakens their results.

Rather than abovementioned reasons, the effect of surface charge state of the nanoparticle in suspension on the thermal conductivity was experimentally studied by Lee et al. (D. Lee et al., 2006). They illustrated that the pH value of the nanofluid strongly influenced the heat transfer rate of the fluid. With farther diverged pH value from the isoelectric point of the particles, the nanoparticles in the suspension got more stable state to change the thermal conductivity. That may partially explain the disparities between different experimental data since many researchers used surfactants in nanofluids, but with insufficient descriptions. Vadasz (Vadasz, 2006) demonstrated that the transient heat conduction process in nanofluids may provide a valid explanation for the apparent heat transfer enhancement by adopting a variation of the classical heat conduction method in porous media to the problem of heat conduction in nanofluid. Hence, so far there are no general mechanisms to rule the strange behavior of nanofluids including the highly improved effective thermal conductivity, although many possible factors have been considered, including Brownian motion, liquid–solid interface layer, ballistic phonon transport, and surface charge state. However, there are still some other possible macro-scale explanations such as heat conduction, particle-driven natural convection, convection induced by electrophoresis, thermo-phoresis, etc.

In this section, the effects of temperature in a range of 25 to 65 °C as well as weight concentration of CNDG on the specific heat capacity of CNDG-WEG coolant is studied. Figure 4.46a indicates an increase in the weight concentrations of CNDG leads to a drop in the specific heat capacity. In particular, an average drop of 1.2 % to 2% is observed for weight concentration of 0.001 to 0.01 wt. %, respectively. Also, as the temperature increases specific heat capacity increases gradually. Specific heat capacity decreases in the presence of CNDG-WEG which can be attributed to the lower specific heat capacity of CNDG loaded in water-EG mixture than that of the base-fluid. Figure 4.46a also indicates that heat capacity of base-fluid increases with temperature, so it is expected that

there would be a rising trend of the specific heat capacity in the presence of CNDG. However, the specific heat capacities curves of CNDG-WEG indicate almost the same slopes, which is consistent with Bock Choon Pak and Young I. Cho (1998) results.

Figure 4.46b shows the average drop in C_p as the functions of temperature and weight concentration of CNDG in basefluid. It is seen that the amount of drop in C_p increases with increasing temperature and/or weight concentration. At weight concentration of 0.01 wt.%, the drop in C_p increases by an average of 2.026%, which is an insignificant change.



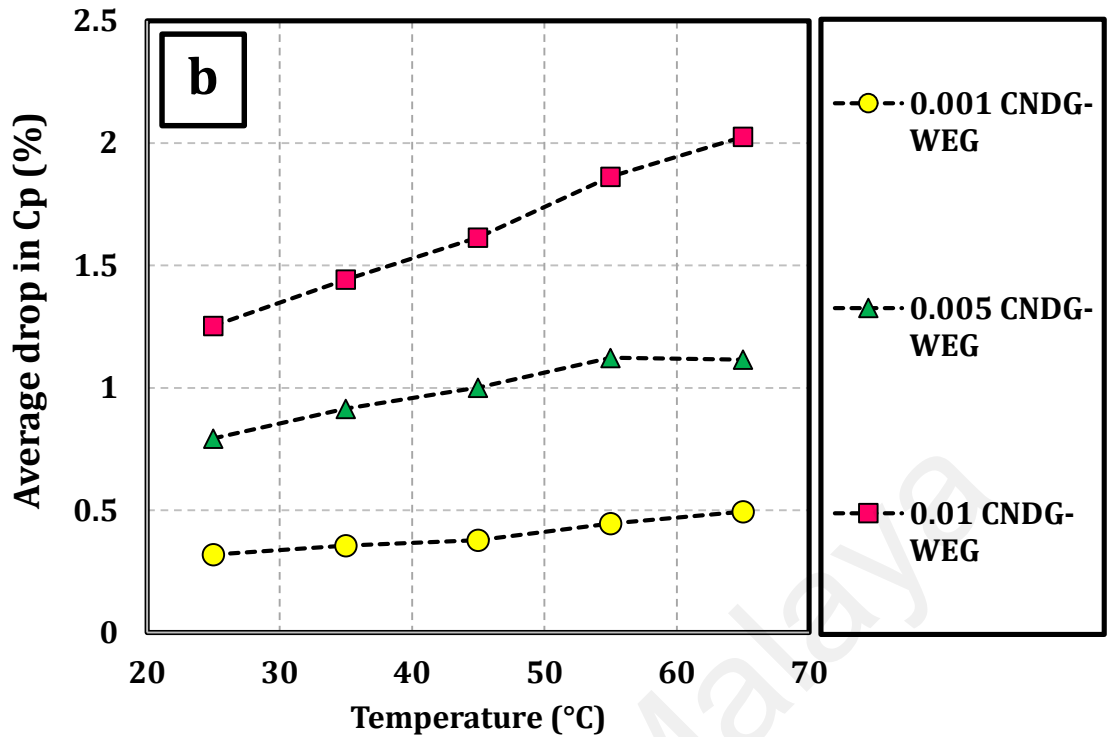


Figure 4.46: The effects of inlet temperature and weight concentration of CNDG-WEG on the specific heat capacities of coolant.

Note that some of the thermo-physical properties have shown negative effects by nanoparticle loading. It is well known that under different flow regimes, the heat transfer rate of coolants depends on the whole of thermo-physical properties of the fluid, and can be evaluated from the Mouromtseff number, Mo (Halelfadl et al., 2014; Minea et al.; W Yu et al., 2010; Wenhua Yu et al., 2009a; Wenhua Yu et al., 2013). Mouromtseff number is a figure of merit to evaluate and compare the heat transfer capability of alternative thermal fluids. This number is defined by Eq. 5.2. Higher the Mouromtseff number, better the potential of the nanofluid as coolant. At the constant flow velocity for a turbulent flow, the relative Mo number ratio with the heat transfer coefficient is predicted by the Dittus–Boelter equation as expressed by different researchers (Minea et al.; Wenhua Yu et al., 2013):

$$\frac{Mo_{nf}}{Mo_{bf}} = \left(\frac{\rho_{nf}}{\rho_{bf}}\right)^{0.8} \left(\frac{Cp_{nf}}{Cp_{bf}}\right)^{0.4} \left(\frac{\mu_{nf}}{\mu_{bf}}\right)^{-0.4} \left(\frac{k_{nf}}{k_{bf}}\right)^{0.6} \quad 4.2$$

To elucidate the potential of the samples, the Mouromtseff number ratios (or equivalently or heat transfer coefficient ratios) calculated from Eq. (5.2) for the CNDG-WEG nanofluids at various particle weight concentrations of 0.001, 0.005, and 0.01 % in turbulent flow with the heat transfer coefficients are predicted by the Dittus–Boelter equation and plotted as a function of the temperature in Figure 4.47. It can be seen that the Mouromtseff number ratios of the CNDG-WEG over the base fluid are bigger than 1 for all the weight concentrations and temperatures. These results also show that the temperature effect is one of the important factors affecting the Mouromtseff number ratios. Also, these levels of heat transfer (Mouromtseff number ratios) enhancement at different temperatures are very attractive for the common high- and low-temperature heat transfer applications.

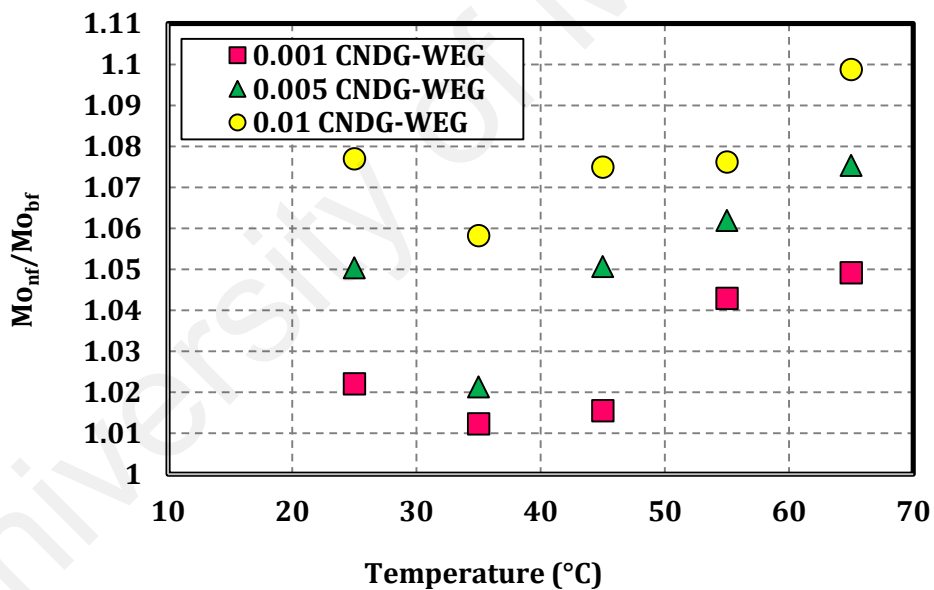


Figure 4.47: The relative Mo numbers of CNDG-WEG for turbulent flow conditions.

4.3.4 Water/ethylene glycol-based EG-treated graphene nanosheets nanofluids

4.3.4.1 Preparation

After preparation of the EG-treated GNP (section 4.2.4), as expected, the EG-treated GNP can easily be dispersed in a mixture of water–EG as a base-fluid (Figure 4.48) due to easily-miscible EG functionalities. EG as a functional group, not only

provide suitable dispersibility, but also the synthesized coolant suspension has no corrosive effect on different metals or engine parts. The easily-miscible EG functionalities could be responsible for a significant increase in dispersibility of the functionalized GNP with EG in both the media of water and EG. EG-treated GNP based water–EG coolant (GNP-WEG) were synthesized at different weight concentrations.



Figure 4.48: Photographs of EG-treated GNP dispersed in water–EG (after 1 month).

4.3.4.2 Thermo-physical properties

The effective viscosities of DI water-EG and GNP-WEG mixtures were measured at the temperature range of 25-65 °C. The dynamic viscosity of the GNP-WEG as a function of temperature and weight concentration was measured at high shear rate of 140 s⁻¹ and the results are shown in Table 4.10. Similar to other coolants, the rheological behavior of GNP-WEG shows two typical characteristics: (i) an enhancement of viscosity with increasing concentration of EG-treated GNP, and (ii) a decrease in viscosity with increasing temperature, which is due to weakening of the intermolecular forces of the fluid itself. It can be seen that the enhancement in the GNP-WEG viscosity are insignificant with increase in weight concentration, which can show a positive point of the chemical treatment. In addition, the data are in agreement with the results of Ko et al. (2007) and Aravind et al. (2011), that the viscosity decreases with the increase in temperature.

Table 4.10: Dynamic viscosity of the GNP-WEG as a function of temperature and weight concentration at shear rate of 140 s^{-1} .

Temperature (°C)	Dynamic Viscosity (Kg/ms)				
	Water-EG	0.01 wt%	0.05 wt%	0.1 wt%	0.2 wt%
25	0.003964	0.003973	0.003998	0.004025	0.004041
35	0.002981	0.002992	0.003017	0.003039	0.003054
45	0.002207	0.002215	0.002241	0.002259	0.002271
55	0.001663	0.001671	0.00169	0.001701	0.001725
65	0.001317	0.001322	0.001347	0.00136	0.001381

The densities of GNP-WEG and water-EG mixture are measured as functions of temperature and weight concentration, and the results are shown in Table 4.11. It is seen that the density of GNP-WEG as well as the base-fluid decreases by increasing the temperature, which may be related to the thermal expansion of liquid. There is also a rising trend between the density of GNP-WEG and weight concentration of EG-treated GNP, thus as the weight concentration increases, the density increases. Since the density of GNP is more than the base-fluid, so the density of coolant increases with the increase of concentration. Also, as the temperature increases, the density insignificantly decreases. The density of the base-fluid and GNP-WEG at concentration of 0.2 wt.% decreases by 2.8% and 2.5%, when the temperature increases from 25 to 65 °C.

Table 4.11: Densities of the water-EG mixture and GNP-WEG at different concentrations.

Temperature (°C)/Concentration	Density (gr/cm^3)				
	Water-EG	0.01 wt%	0.05 wt%	0.1 wt%	0.2 wt%
25	1.09982321	1.09994778	1.101983503	1.10299683	1.104208119
35	1.09366946	1.094165487	1.096322453	1.098499797	1.100104057
45	1.08801264	1.089026592	1.091542659	1.093332825	1.0949418
55	1.08069657	1.081705683	1.083884427	1.085250272	1.087515955
65	1.069211456	1.070680665	1.072951395	1.074180889	1.076157721

Figure 4.49 shows the thermal conductivity plot of GNP-WEG as a function of temperature and concentration. Four different weight concentrations of 0.01%, 0.05%,

0.1% and 0.2% are considered and the variation of thermal conductivity with concentration and temperature are studied. To prevent sharp increase in the effective viscosity, GNP-WEG at low concentrations of EG-treated GNP has been considered in this study. Figure 4.49 clearly shows that the thermal conductivity of GNP-WEG is higher than that of water-EG. Also, it can be seen, as the temperature increases, the thermal conductivity of the basefluid and coolants at various weight concentrations increase. The increase in thermal conductivity with temperature is more sensible in GNP-WEG. Thus, it confirms that the temperature plays a key role in increasing the thermal conductivity of GNP-WEG coolant. The main mechanism for thermal conductivity enhancement with increase of temperature is attributed to the Brownian motion of the nanoparticles suspended in the base-fluid (Aravind et al., 2011). Figure 4.49 also shows that GNP-WEG samples exhibits larger thermal conductivity enhancement at higher weight concentration of EG-treated GNP.

According to the recent researches (Aravind et al., 2011; Jha & Ramaprabhu, 2008), the formation of surface nanolayers in GNP base-fluids plays an important role in energy transfer. Liquid molecules generate layers around the GNP, thereby enhancing the local ordering of the liquid layer at the interface region. Thus, the liquid layer at the interface would exhibit a higher thermal conductivity compared to the base-fluid. The higher slope in thermal conductivity of GNP-WEG coolant with concentration of 0.2 wt% indicates the higher rate of formation of the surface nanolayers.

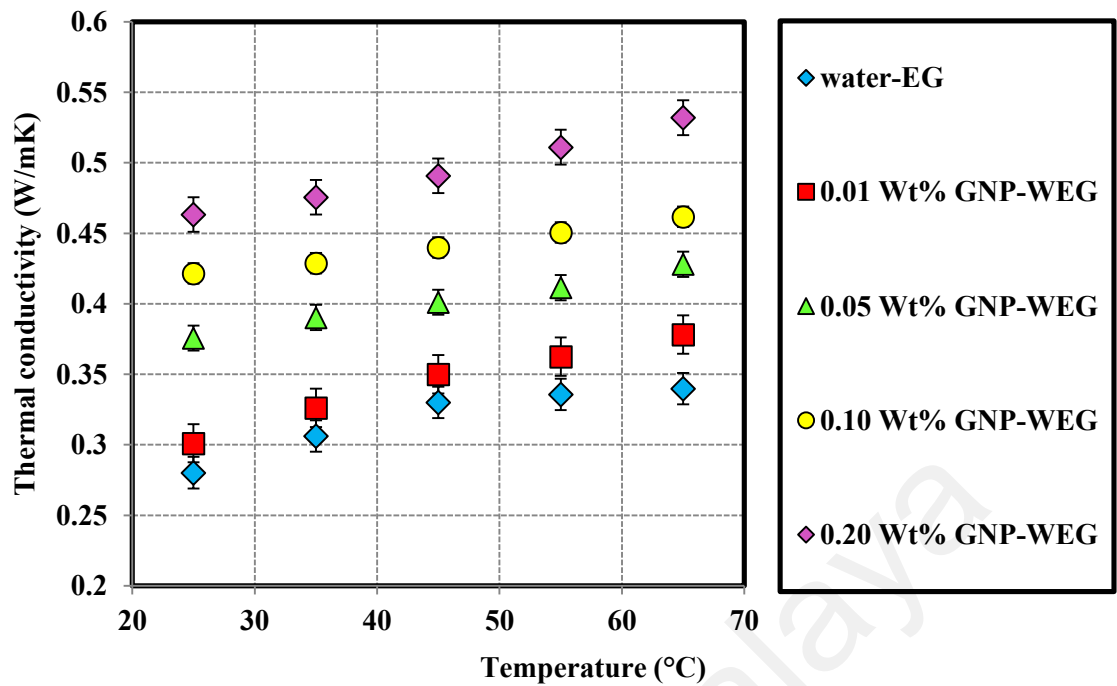


Figure 4.49: Thermal conductivity plot of GNP-WEG and pure water-EG mixture.

The effects of temperature in a range of 25 to 65 °C as well as weight concentrations of EG-treated GNP on the specific heat capacity of GNP-WEG coolant is studied in this section. Figure 4.50 shows that an increase in the weight concentrations of EG-treated GNP leads to a drop in the specific heat capacity. More specifically, an average drop of 0.6% to 5% are seen, respectively, for the weight concentrations of 0.01 to 0.2%, respectively. Also, it is seen that the specific heat capacity increases gradually with the increases of temperature. The drop in the specific heat capacity of GNP-WEG is attributed to the lower specific heat capacity of EG-treated GNP loaded in water-EG mixture than that of the base-fluid.

Figure 4.50 also shows that the heat capacity of the base-fluid increases with temperature and, therefore, a rising trend of the specific heat capacity in the presence of GNP-WEG is expected. In contrast, the specific heat capacity curves of GNP-WEG show almost same slopes, which is in agreement with the results of Pak and Cho (Bock Choon Pak and Young I. Cho (1998).

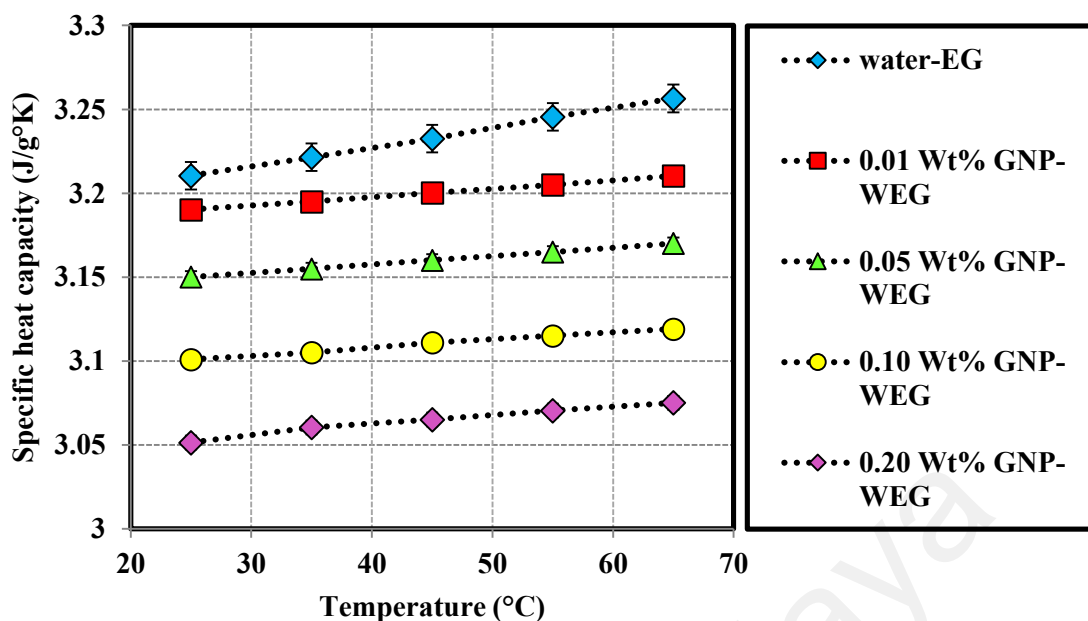


Figure 4.50: The effects of temperature and weight concentrations of EG-treated GNP on the specific heat capacity of GNP-WEG coolant.

4.3.5 Water-based carboxylated GNP nanofluids

4.3.5.1 Preparation of nanofluids

In the case of covalent nanofluids, the carboxylated GNPs (GNP-COOH) produced after microwave phase (section 4.2.6) were highly dispersible in the deionized water at room temperature. Dispersed GNPs at concentration of 0.1 wt% was easily obtained in water in the presence of COOH groups. The dispersions results illustrated no sign of GNP sedimentation after 1 month under ambient conditions.

To provide non-covalent nanofluids at the known weight concentrations, the estimated amount of pristine GNP was first weighted, followed by pouring a weight ratio of SDBS/pristine GNP (0.5:1) into a vessel filled with the required distilled water (Botelho et al., 2011).

In the current study, two aqueous nanofluids comprising of GNP-COOH and GNP-SDBS at concentrations of 0.025, 0.05 and 0.1 wt% were prepared. To obtain stable and homogeneous suspensions, GNP-COOH and GNP-SDBS samples were sonicated in water about 10 min.

4.3.5.2 Thermo-physical properties

Figure 4.51 shows the thermal conductivity of water-based nanofluids including GNP-COOH and GNP-SDBS at the weight concentrations of 0.025%, 0.05% and 0.1% and at different temperatures. In Figure 4.51, one can clearly see that the thermal conductivity of water based GNP-COOH and GNP-SDBS nanofluids are higher than that of water. In addition, the thermal conductivity increases as the concentrations of GNP in the water-based nanofluids increases. In nanofluids, the main mechanism of thermal conductivity enhancement can be attributed to the Brownian motion of the suspended particles as it is one of the most dominating functions of temperature (S. J. Aravind et al., 2011). Figure 4.51 also shows that the thermal conductivity for GNP-COOH prepared nanofluid is higher than that of GNP-SDBS. For nanofluids comprising of carbon nanostructures like GNP with chemical functionalization, in addition to the Brownian motion of GNP, the formation of surface nanolayers dominate the energy transfer in the nanofluids.

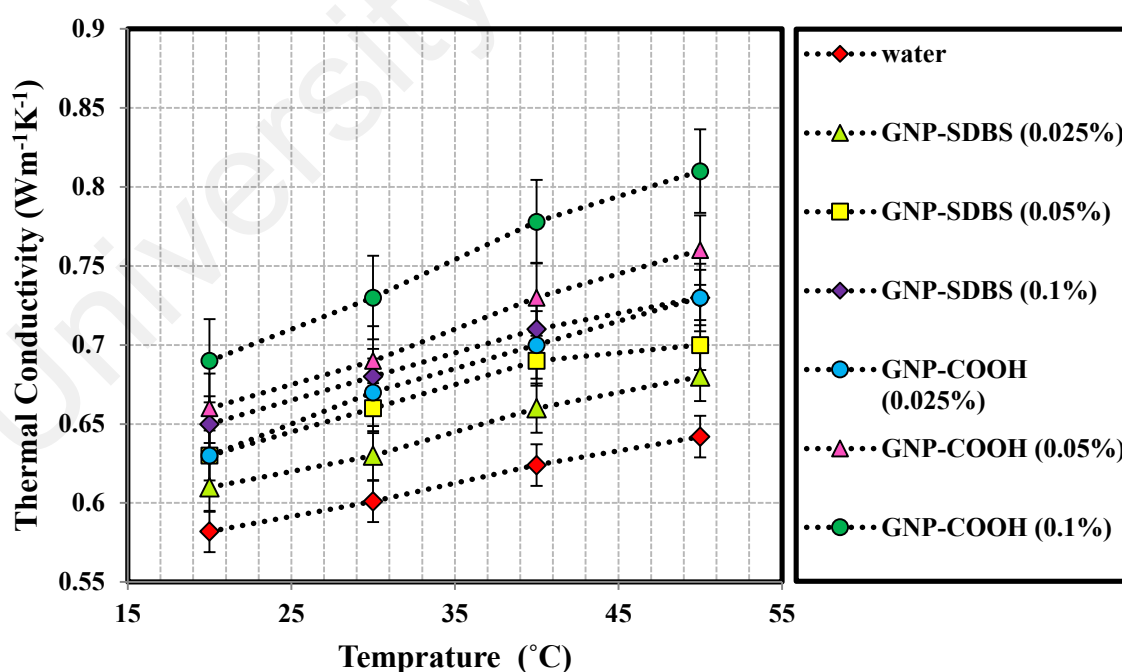


Figure 4.51: Thermal conductivity of GNP-based water nanofluids at different temperatures and weight concentrations.

The higher thermal conductivity of GNP-COOH can be attributed to the higher effective heat transfer area in the presence of covalent functional groups. Liquid molecules create layers around the GNP, thereby increasing the local ordering of the liquid layer at the interface region. The liquid layer at the interface would reasonably have a higher thermal conductivity than the bulk liquid (S. J. Aravind et al., 2011). Thus, the nanolayer is considered as an essential parameter in increasing the thermal conductivity of the GNP-based nanofluids. On the other hand, absorbing non-covalent groups on the surface of GNP can reduce the generation of layers around the nanostructures by decreasing the effective heat transfer area, since non-covalent groups warp around the GNP flakes and thereby decreasing the local liquid layer at the interface area of GNPs. Also, the generation of more hydrophilic phase on the GNP surface by addition of oxygen-containing functional groups (COOH) may result in the more homogeneous dispersion in basefluids (Jha & Ramaprabhu, 2008).

Thus, when surfactant like SDBS is utilized to increase the dispersibility of carbon nanostructures, surfactants tend to wrap around them, preventing the enhancement of nanolayer, leading to lower microconvection (Duan et al., 2011; Kim et al., 2010).

Furthermore, Figure 4.51 confirmed that the thermal conductivity of nanofluids is a function of temperature. In all samples, an increase in temperature results in an enhancement of thermal conductivity, with the higher slope in covalent water-based nanofluids, which can validate the presence of higher Brownian motion (Duan et al., 2011; Jha & Ramaprabhu, 2008).

The viscosity of nanofluids is another important parameter for characterizing the suitability of the nanofluids for heat transfer applications. Figure 4.52 shows the measured viscosity of the prepared GNP nanofluids versus temperature for a shear rate of 300 s^{-1} at various concentrations. It is seen that both the GNP-COOH/water and GNP-SDBS/water

have higher viscosities than that of the deionized water. As expected, the viscosity of all the samples decreases as temperature increases at a constant concentration.

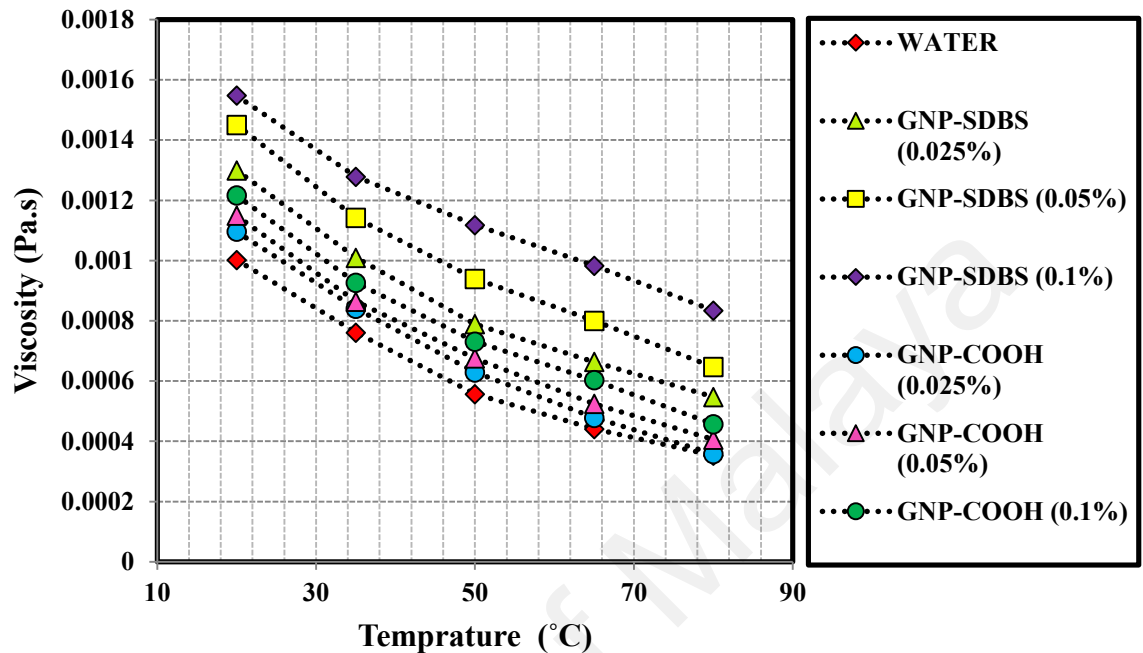


Figure 4.52: Viscosity of the GNP-based water nanofluids as a function of temperature and concentration for a shear rate of 300 s^{-1} .

As can be seen in Figure 4.52, the GNP-SDBS/water nanofluids have significantly higher viscosity than those of covalent nanofluids (GNP-COOH/water) under similar experimental conditions. This infers that surfactants such as SDBS and GA are the main reason for the increase of viscosity of nanofluids. Interestingly, the viscosity of GNP-SDBS/water nanofluid at concentration of 0.025% is larger than that of GNP-COOH/water nanofluid at the concentration of 0.01%, which is due to the influence of surfactants or non-covalent functionalization on nanofluids viscosity.

Table 4.12 shows the average percentage increase in viscosity of the nanofluids compared with the deionized water. The percentage increase is evaluated as shown in Equation 4.3.

$$\text{Percentage increase} = \frac{\mu_{\text{nanofluid}} - \mu_{\text{water}}}{\mu_{\text{water}}} \quad 4.3$$

Table 4.12: The average increase in the viscosity of nanofluids compared with deionized water.

Percentage increase of nanofluid viscosity for different temperatures and concentrations						
<i>T</i> (°C)	GNP-SDBS 0.025 wt%	GNP-SDBS 0.05 wt%	GNP-SDBS 0.1 wt%	GNP-COOH 0.025 wt%	GNP-COOH 0.05 wt%	GNP- COOH 0.1 wt%
20	29.7%	44.7%	54.5%	9.4%	14.7%	21.4%
35	32.7%	50.0%	68.0%	10.5%	13.5%	21.7%
50	41.6%	68.7%	100.7%	13.0%	21.3%	31.3%
65	50.4%	81.4%	122.9%	8.4%	18.9%	36.8%
80	55.0%	83.2%	136.4%	1.4%	15.0%	29.4%

4.3.6 Water-based PEG-treated GNP and acetone-based Azo-treated GNP acetone nanofluids

4.3.6.1 Preparation of nanofluids

In the case of covalent nanofluids, tetrahydrofurfuryl polyethylene glycol-treated GNP (PEG-treated GNP) and 4-phenylazophenol-treated GNP (Azo-treated GNP) produced after microwave phase were highly dispersible in some of the solvents at room temperature (section 4.2.5). Dispersion of the treated GNPs at the concentration of 0.1 wt% was easily obtained in some solvents in the presence of functional groups. The dispersions results illustrated a small amount of GNP sedimentation after 1 month under ambient conditions.

4.3.6.2 Colloidal Stability

Plot of absorbance versus wavelength for different colloidal solutions (PEG-treated GNP based water and Azo-treated GNP based acetone) were investigated to indirectly trace the presence of specific particles within the binary system. Figure 4.53 panels (1) and (2) show the plot of absorbance intensity versus wavelength for each bimodal system taken at a specific period of time. The measurements were performed

after 5 days of sample preparation to remove any non-reacted negligibly charged colloids which rapidly agglomerated and settled at the bottom of the sampling bottle. The results suggested that the hybrid colloidal mixtures exhibit almost the same trends to the single absorbance spectral curves of PEG and/or Azo colloids. This observation verified the fact that PEG and/or Azo remain within the colloidal mixture, implying successful functionalization and good stability.

Unsurprisingly, the functionalized GNP with PEG and Azo could easily disperse in water and acetone solvents, respectively. Figure 4.53 panels (3) and (4) depict the appreciably higher dispersibility of PEG-treated GNPs in water and Azo-treated GNP in acetone, respectively, as compared with the pristine sample. The easily-miscible PEG and Azo functionalities may explain the higher dispersion of the functionalized GNP.

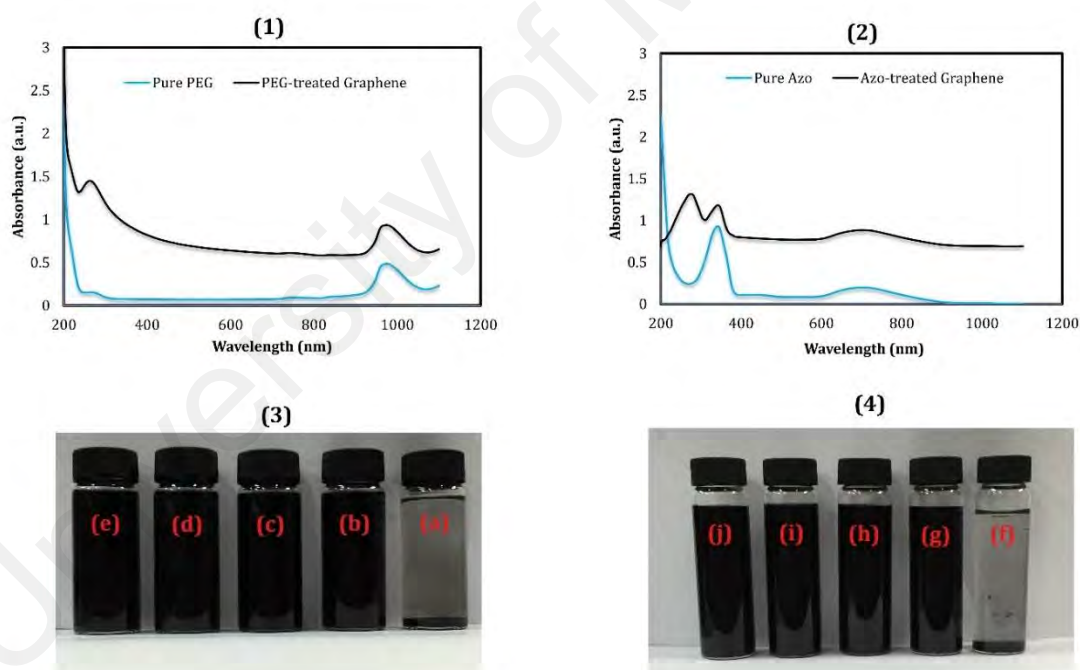
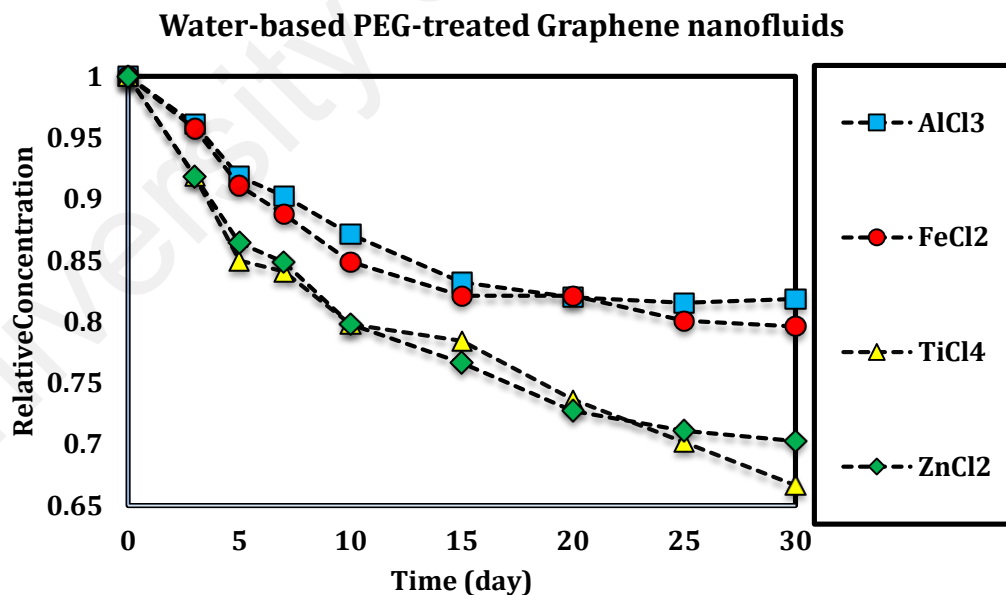


Figure 4.53: Plot of absorbance versus wavelength for (1) pure PEG and PEG-treated GNP, (2) pure Azo and Azo-treated GNP, (3) photographs of (a) the pristine GNP/water and PEG-treated GNP/water catalyzed by (b) AlCl_3 , (c) FeCl_2 , (d) TiCl_4 , (e) ZnCl_2 , (4) photographs of (f) the pristine GNP/acetone and Azo-treated GNP/acetone catalyzed by (g) AlCl_3 , (h) FeCl_2 , (i) TiCl_4 and (j) ZnCl_2 .

To investigate the colloidal stability of PEG-treated GNP in water and Azo-treated GNP in acetone, further measurements were conducted to observe the chronological

progress of the suspension's light absorbance with respect to time, which is illustrated based on relative concentration in Figure 4.54 panels (a) and (b), respectively. The measurement was carried out at peak wavelength of each material to trace the alteration in the intensity which can be further used to describe the suspension stability at the constant GNP concentration of 0.05% wt. It can be seen that all the colloidal mixtures (produced by different catalysts) show a downward trend of relative concentration as the time progressed, indicating that the level of particle concentration and thus the stability subsided. Also, the relative concentration (absorbance intensity) for both colloids including PEG- and Azo-treated GNP show the minimum amount of sediment for the treated samples in the presence of AlCl_3 and maximum amount in the presence of ZnCl_2 .

High absorbance intensity was also recorded within the early days of the observational period, but the magnitude significantly drop after several days, which can be attributed to the aforementioned gravity driven sedimentation (Chang et al., 2011).



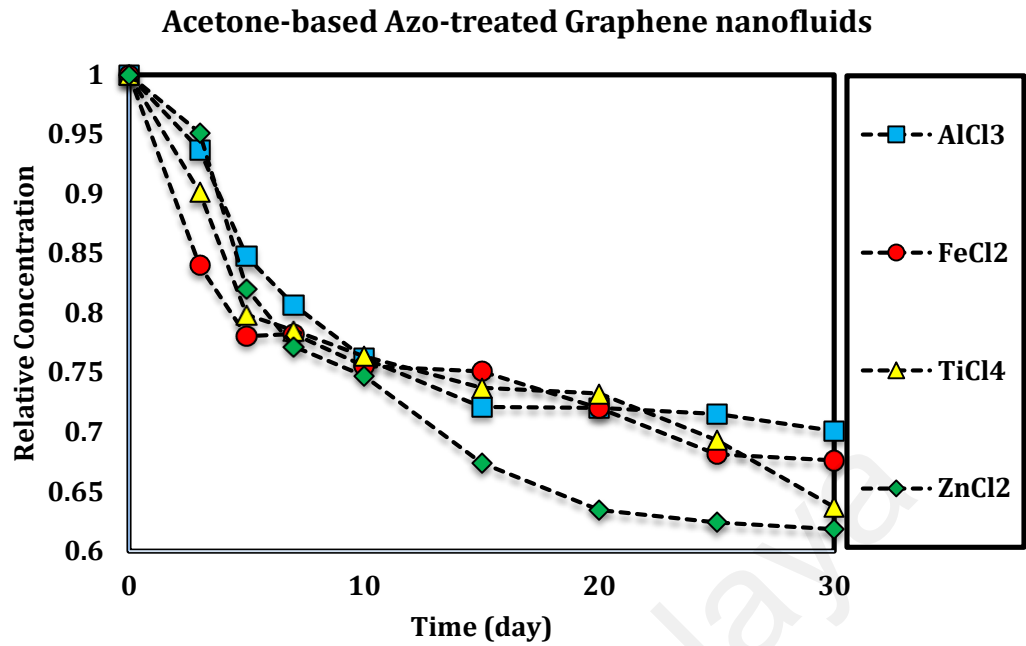


Figure 4.54: Plot of colloidal stability of PEG-treated GNP in Di-water and Azo-treated GNP in acetone in the presence of different catalysts.

4.4 Experimental Heat Transfer Performance of Different Thermal Equipment

4.4.1 Car Radiators

4.4.1.1 Introduction

Heat transfer is an essential part of the wide range of fields of studies and in industries e.g. oil and gas, electrical, food and nuclear, automotive industries, etc. Among different industries, automotive industry is one of the world's most important economic sectors by revenue and has a special effect on the other industries. Generation of highly efficient engines for automotive industries is one of the most important goals of automotive industries. Increasing of the thermal efficiency of radiator by optimizing the size (De Carli et al., 2015; Hatami et al., 2015; Rashidi & Abbasbandy, 2011), addition of fins, and use of micro-channels have been suggested and employed (Imke, 2004). However, there are some limitations in applying many of the conventional methods, such as lack of space, for increasing the cooling rate (Kulkarni et al., 2008). On the other hand, conventional base-fluids such as water and ethylene glycol (EG) have poor thermal

conductivity, which intensify the reduction of engine efficiency. To solve this issue, high performance heat transfer fluids can be utilized in the car radiators.

To enhance the heat transfer properties of conventional base-fluids and heat transfer rate in heat exchangers, addition of different particles, in particular carbon nanostructures such as carbon nanotubes (CNT), graphene nanoplatelets (GNP) and few-layered graphene (Gr), has been suggested as a promising approach (Chandrasekaran et al., 2014; S. U. S. Choi & Eastman, 1995; Dalir et al., 2015; Mohammad Zadeh et al., 2015; Saidi & Karimi, 2014; X. J. Wang et al., 2014).

Jha and Ramaprabhu (2008) studied the influence of Cu-loaded carbon nanotubes (Cu-CNTs) in deionized water (DI water) and Cu-CNTs in EG on the thermal conductivity. They obtained a significant enhancement at a very low volume fraction, which attributed to the well-dispersibility of Cu-CNTs in the working fluids as well as the formation of hydrophilic CNT. A similar study was conducted by this group which showed noticeable enhancement in the thermal conductivity and heat transfer rate enhancements of CNT-based water nanofluids and the reason was attributed to the thinning of the thermal boundary layer by CNT resulting to reduction in thermal resistance (Aravind et al., 2011; Aravind & S. Ramaprabhu, 2013).

The intrinsic heat transfer capacity of the carbon nanostructures could be considered as the main factor for thermal improvement. For working fluids including carbon nanostructures such as CNT and graphene, the chemical surface effects and surface area of carbon nanostructures can dominate the extent of energy transfer in the prepared coolants (Murshed et al., 2006; Shanbedi et al., 2015). Murshed et al. concluded that liquid molecules form layers around the carbon nanostructures, thus increasing the local ordering of the liquid layer at the interface region. It is obvious that the liquid layers at the interface would fairly have a higher thermal conductivity than the bulk liquid. Therefore, in addition to the effect of Brownian motion of carbon nanostructures, the

prepared nanolayer around nanostructures play a vital role in enhancing the thermal conductivity of carbon nanostructures-based nanofluids (Murshed et al., 2006).

It is also well known that thermal conductivity and subsequently heat transfer rate improve as the specific surface area of graphene increases (W. Sarsam et al., 2016a). Therefore, in order to manufacture highly-conductive nanofluids for improving heat transfer rate in different thermal equipment, materials with high specific surface areas, such as crumpled graphene, and in particular, few-layered graphene should be used. Thus, carbon nanostructures with high surface area can provide better condition for enhancing heat transfer rate and thermal conductivity of working fluid. To reach a carbon nanostructure with high surface area and for preparing high-performance heat transfer coolant, modification of graphene should be elaborately designed by taking the morphology and pore structure into consideration. It is also noteworthy that N-doping performs an important role in regulating the electronic, thermal and chemical properties of carbon materials because of the similar atomic size and the availability of five valence electrons to form strong valence bonds with carbon atoms. Nitrogen-doped graphene materials with large mesopores favorable for heat transfer were found to exhibit a good coolant property as an additive and significantly well-dispersed suspension (Seyed Shirazi et al., 2015). The higher electronegativities of N ($x = 3.04$) than that of C atoms ($x = 2.55$) in N-doped graphene resulted in a significant surface charge state of nanoparticles, leading to the excellent stabilized colloidal suspension (Xie et al., 2015). A significant enhancement in thermal conductivity as well as in electrical conductivity of dispersed NDG in the ethylene glycol (EG) (Seyed Shirazi et al., 2015) confirms its potential application towards nanofluids. Although various studies conducted on the thermal and electrical conductivity of composite material suspensions, no investigation has yet performed on the nanofluids containing crumpled N-doped graphene in water-EG

media. The crumpled nitrogen-doped graphene (CNDG) seems to meet both above-mentioned criteria and thus it is attractive and novel for coolant applications.

To this end, an efficient and facile method for fabricating highly crumpled nitrogen-doped graphene nanosheets (CNDG) with high surface area is employed (section 4.2.2) to reach a carbon nanostructure with the above-mentioned properties. After investigation of functionality and morphology (section 4.2.2), the thermo-physical and colloidal stability of coolants containing CNDG and EG-treated GNP and the cooling potentials of synthesized coolants have been investigated in terms of the steady-state forced convective heat transfer. In addition, physical insight was prepared to clarify the improved heat transfer coefficient of CNDG-based water-ethylene glycol coolant (CNDG-WEG) and EG-treated GNP-based water coolants (GNP-WEG).

4.4.1.2 Data Processing

The thermo-physical properties such as thermal conductivity, density, specific heat capacities and viscosity at different concentrations were measured experimentally. A study on the heat transfer behavior and energy management of the synthesized coolant in the car radiator was performed via evaluating the convective heat transfer coefficient (h), Nusselt number (Nu), friction factor (f), pressure drop (ΔP), and pumping power (W). The convective heat transfer coefficient was attained via evaluating the values of the inlet, outlet, wall and bulkfluid temperatures as well as the flow rates. The Reynolds number was calculated using equation 4.4,

$$Re = \frac{\rho U D}{\mu} \quad (4.4)$$

where D , U , ρ and μ are the inner diameter of the tube, the flow velocity, density and viscosity of working fluid, respectively.

According to the Newton's cooling law, the convective heat transfer coefficient (h) can be calculated from equation 4.5,

$$h = \frac{q}{A(T_b - T_w)} \quad (4.5)$$

where T_b and T_w are the average temperature of the bulkfluid and the radiator tube wall, respectively. Also, heat transfer rate is obtained by using equation 4.6.

$$q = \dot{m} C_p (T_{in} - T_{out}) \quad (4.6)$$

where \dot{m} is the mass flow rate, T_{in} and T_{out} are the inlet and outlet temperature of the bulkfluid respectively of the car radiator. Considering the same value for q in the equations (4.7) and (4.8), the convective heat transfer coefficient and Nusselt number are respectively obtained from the equation 4.7 and 4.8 respectively.

$$h = \frac{\dot{m} C_p (T_{in} - T_{out})}{A(T_b - T_w)} \quad (4.7)$$

$$Nu = \frac{\dot{m} C_p (T_{in} - T_{out}) D}{A(T_b - T_w) K} \quad (4.8)$$

In Equations (4.7) and (4.8), C_p , A and K are introduced as the specific heat capacity, spherical area of radiator tubes, and the thermal conductivity of the fluids, respectively. In Eq. (6.5), Nu is the average Nusselt number for the entire radiator. The pressure drop of working fluid flowed through the radiator was measured by a differential pressure transducer for different concentrations of nanoparticles. Also, the empirical friction factor was measured from the pressure drop of synthesized coolants through the radiator. That is represented by equation 4.9 (Samira et al., 2014),

$$f = \frac{2 \Delta P \rho D}{G^2 n L} \quad (4.9)$$

where ΔP is pressure drop, n is the number of tube passes, L is the tube length of radiator and G is the mass flow rate per unit area defined as,

$$G = \frac{\dot{m}}{A} \quad (4.10)$$

Employing new type of working fluid (GNP-WEG) as a new coolant for car radiator requires investigation of performance of the coolant as well as their suitability as

appropriate alternative candidate for a range of Reynolds numbers and temperatures. According to Samira and coworkers (Samira et al., 2014), using of nanofluids in a car radiator provides enhancement in both pressure drop (negative effects) and heat transfer coefficient (positive effects). To assess the effectiveness of nanofluids, a performance index (ε) is selected as an appropriate parameter (Equation 4.11) to clarify the range of temperature and velocity that can be used by the synthesized coolant (Samira et al., 2014):

$$\varepsilon = \frac{h_{nf}/h_{bf}}{\Delta P_{nf}/\Delta P_{bf}} = \frac{R_h}{R_{\Delta P}} \quad (4.11)$$

where R_h is the ratio of the heat transfer enhancement of the new coolant (GNP-WEG) to the base-fluid and $R_{\Delta P}$ is the ratio of pressure drop of synthesized coolant to the base-fluid. To study the energy saving in the turbulent region, the pumping power can be measured as follows by equation (4.12) (Mansour et al., 2007).

$$\frac{W_{nf}}{W_{bf}} = \left(\frac{\mu_{nf}}{\mu_{bf}}\right)^{0.25} \left(\frac{\rho_{bf}}{\rho_{nf}}\right)^2 \quad (4.12)$$

where W_{nf} and W_{bf} are the pumping power in the presence of nanofluid and basefluid, respectively.

4.4.1.3 Thermal performance studies

Prior to carrying out the set of detailed experiments on the GNP-WEG and CNDG-WEG as the novel coolants for car radiator, a set of initial experiments has performed for water-EG mixture as the base-fluid, in order to assess the accuracy and reliability of the experimental set-up. The empirical correlations of Gnielinsky and Dittus-Boelter (Dittus & Boelter, 1985; S. Zeinali Heris et al., 2013) were selected for comparison with the obtained results especially for test of accuracy of the set-up in the turbulent region. These correlations are stated by equations 4.13 and 4.14, respectively.

$$Nu = \frac{\left(\frac{f}{8}\right) (Re - 1000) Pr}{1 + 12.7 \left(\frac{f}{8}\right)^{0.5} \left(Pr^{\frac{2}{3}} - 1\right)} \quad (4.13)$$

$$Nu = 0.002515 Re^{1.015} Pr^{0.4} \quad (4.14)$$

The Gnielinski correction obtained by equation (4.13) is valid for the range of $3000 < Re < 5 \times 10^6$ and $0.5 < Pr < 2000$. The friction factor, f , is obtained From Equation 4.15 (Filonenko, 1954):

$$f = (0.79 \ln Re - 1.69)^{-2} \quad (4.15)$$

The comparison of the average Nusselt number measured experimentally for the base-fluid at a constant inlet temperature of 45 °C with the empirical correlations is shown in Figure 4.55. It can be seen that the experimental data are in reasonable agreement with the predicted values from the Gnielinski equation and the Dittus–Boelter equation and most of the experimental data are within $\pm 15\%$ of the predicted values, which is within the generally-accepted deviation range.

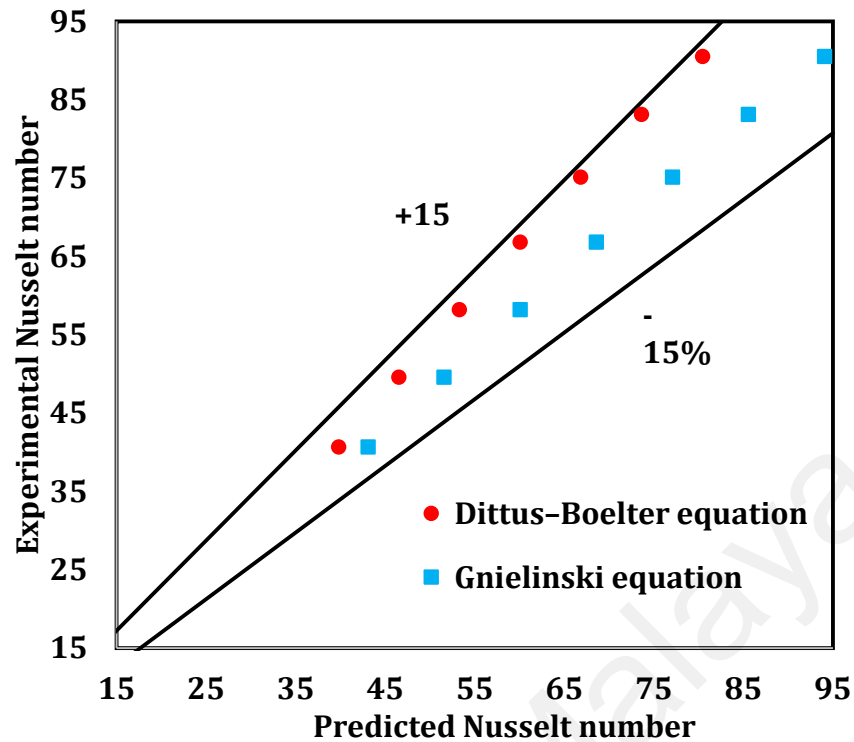


Figure 4.55: A comparison of the data obtained from the Gnielinsky and Dittus-Boelter correlations and the experimental data for the Water-EG mixture at the inlet temperature of 45 °C.

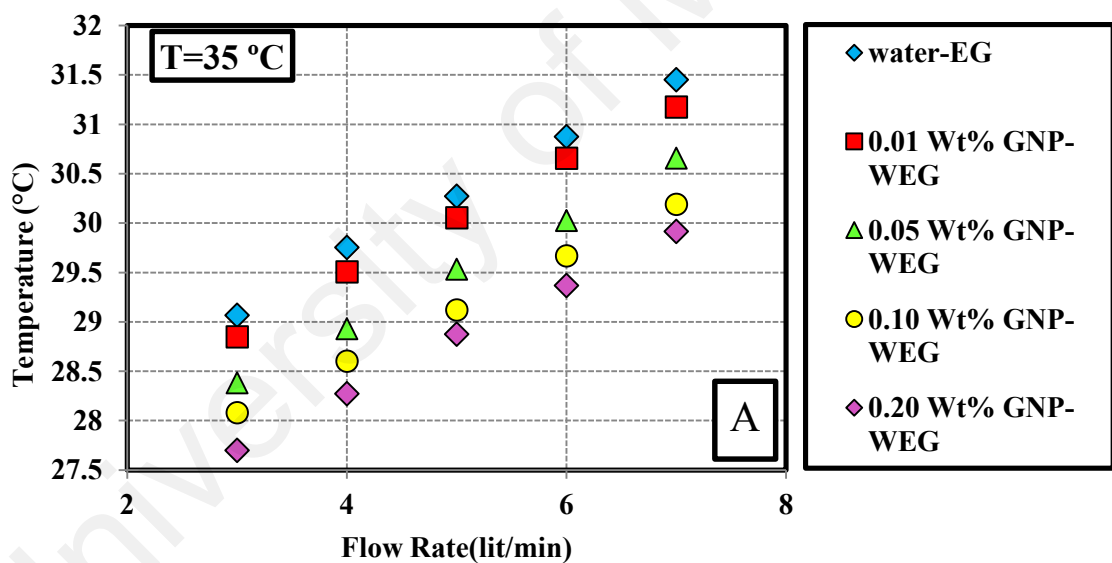
This figure, in particular, shows good agreement between the experimental measurements and the Gnielinsky correlation for different Reynolds numbers. The average error is 2.4%, which is quite reasonable. In addition, the correlation of Dittus-Boelter provides an acceptable agreement with the experimental data for the water-EG mixture. Figure 4.55 also shows the expected trend of increase of Nusselt number with Reynolds number.

4.4.1.3.1 GNP-WEG

Figure 4.56 (A-C) presents the average outlet temperature (T_{out}) of the car radiator as a function of flow rate for the GNP-WEG as coolant fluid for inlet temperatures of 35, 45 and 55°C and at different weight concentrations of EG-treated GNP. These figures show an increasing trend of T_{out} with volume flow rate and a downward trend of T_{out} with concentration of EG-treated GNP. That is, T_{out} decreases

as the concentration of EG-treated GNP in base-fluid increases. As mentioned above, higher weight concentration means higher thermal conductivity of the working fluid, leading to higher heat transfer or lower difference between temperatures of bulk fluid and the radiator tube wall. Also, as the volume flow rate in circulation system increases, the connection time for transferring energy in car radiator (time for transferring heat between air and tube surface) decreases, causing higher outlet temperature.

In addition, it is seen that the average outlet temperature increases with the increase of inlet temperature. The drop in the car radiator temperature is associated with the increase of EG-treated GNP concentration which is related to the improvement of the thermal conductivity of the water-EG mixture in the presence of EG-treated GNP.



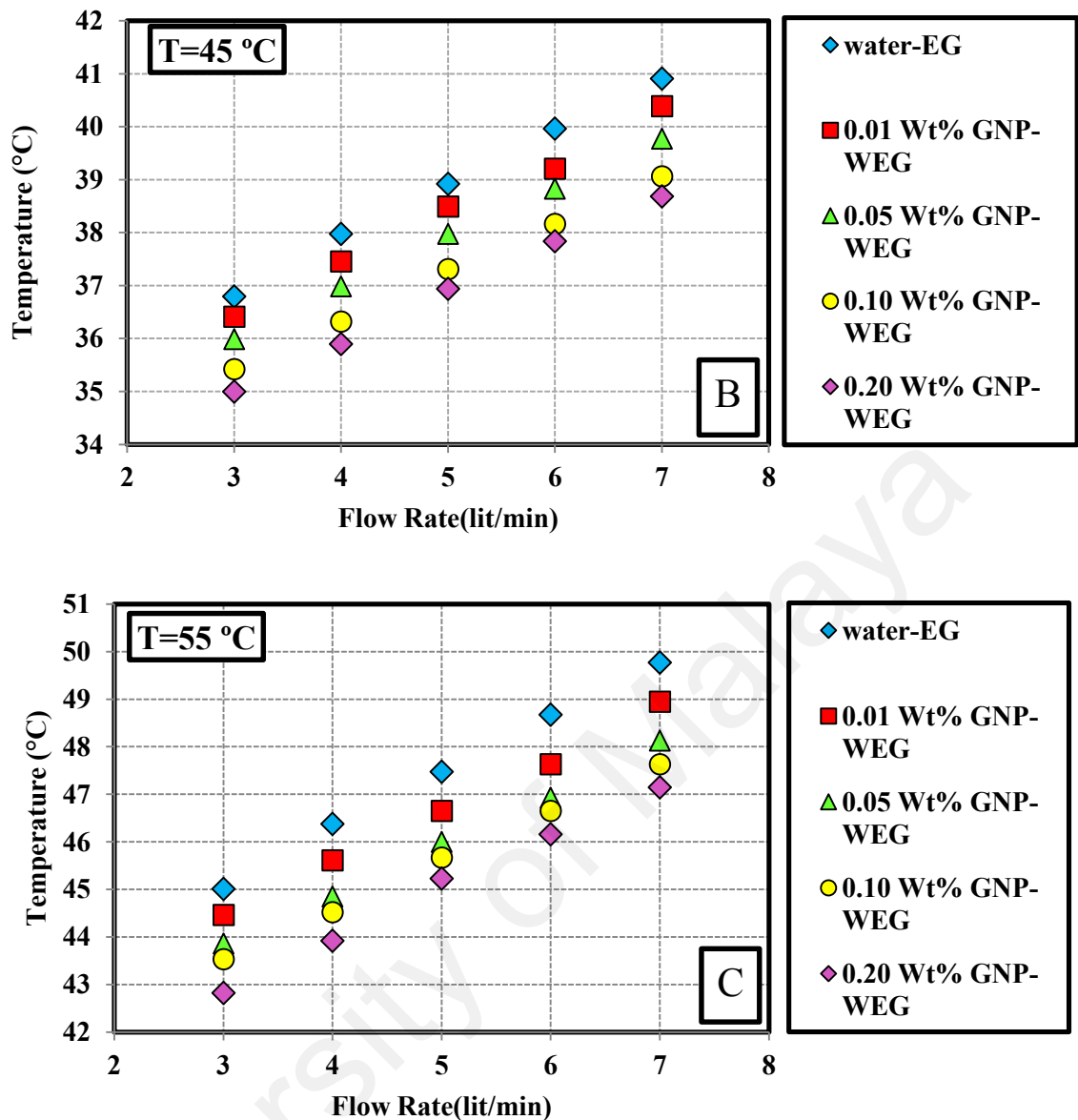
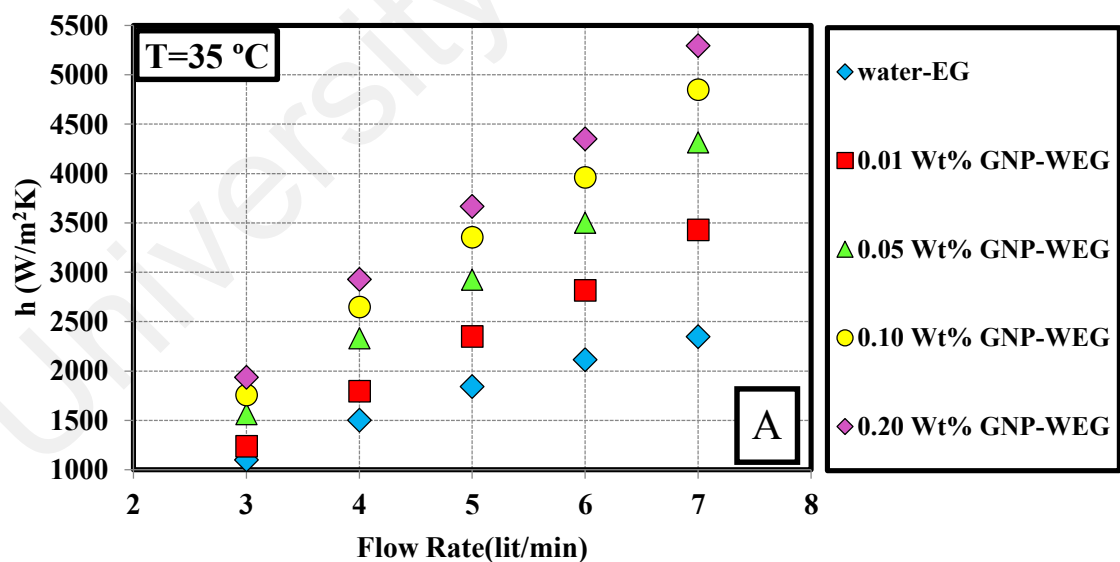


Figure 4.56: The average outlet temperature (T_{out}) as a function of flow rate for the car radiator in the presence of GNP-WEG as well as pure basefluid at inlet temperatures of (a) 35, (b) 45 and (c) 55 °C.

Variations of the convective heat transfer coefficient of EG-treated GNP dispersed in a mixture of DI water-EG are studied and the results are presented in this section. Figures 4.57A, 4.57B and 4.57C present the comparison of convective heat transfer coefficients of GNP-WEG for different weight concentrations at three different temperatures. It is seen that the augmentations of the convective heat transfer coefficient of GNP-WEG significantly exceed those of the thermal conductivity enhancements for

different weight concentrations. The maximum thermal conductivity and convective heat transfer coefficient enhancements for GNP-WEG are 65% and 130% respectively at the weight concentration of 0.2 wt% and volume flow rate of 7 lit/min. The reason for larger enhancement of the convective heat transfer compared to that of thermal conductivity was introduced by Aravind and coworkers (Aravind et al., 2011; Aravind & S. Ramaprabhu, 2013) using a simple analogy that the convective heat transfer is proportional to $k/\delta t$, where δt is the thickness of thermal boundary layer. Thus, to increase the convective heat transfer coefficient, k can be increased and/or δt can be decreased. According to the recent studies (Aravind et al., 2011; Ding et al., 2006b), carbon nanomaterials such as CNTs and graphene have a tendency to decrease the thermal boundary layer thickness. Higher thermal conductivity or lower difference between temperatures of bulk fluid and tube wall in radiator can be introduced as the main reason for aforementioned enhancement in the convective heat transfer coefficient. More studies, typically flow visualization studies, should be conducted to get a clearer picture of the heat transfer enhancement mechanism.



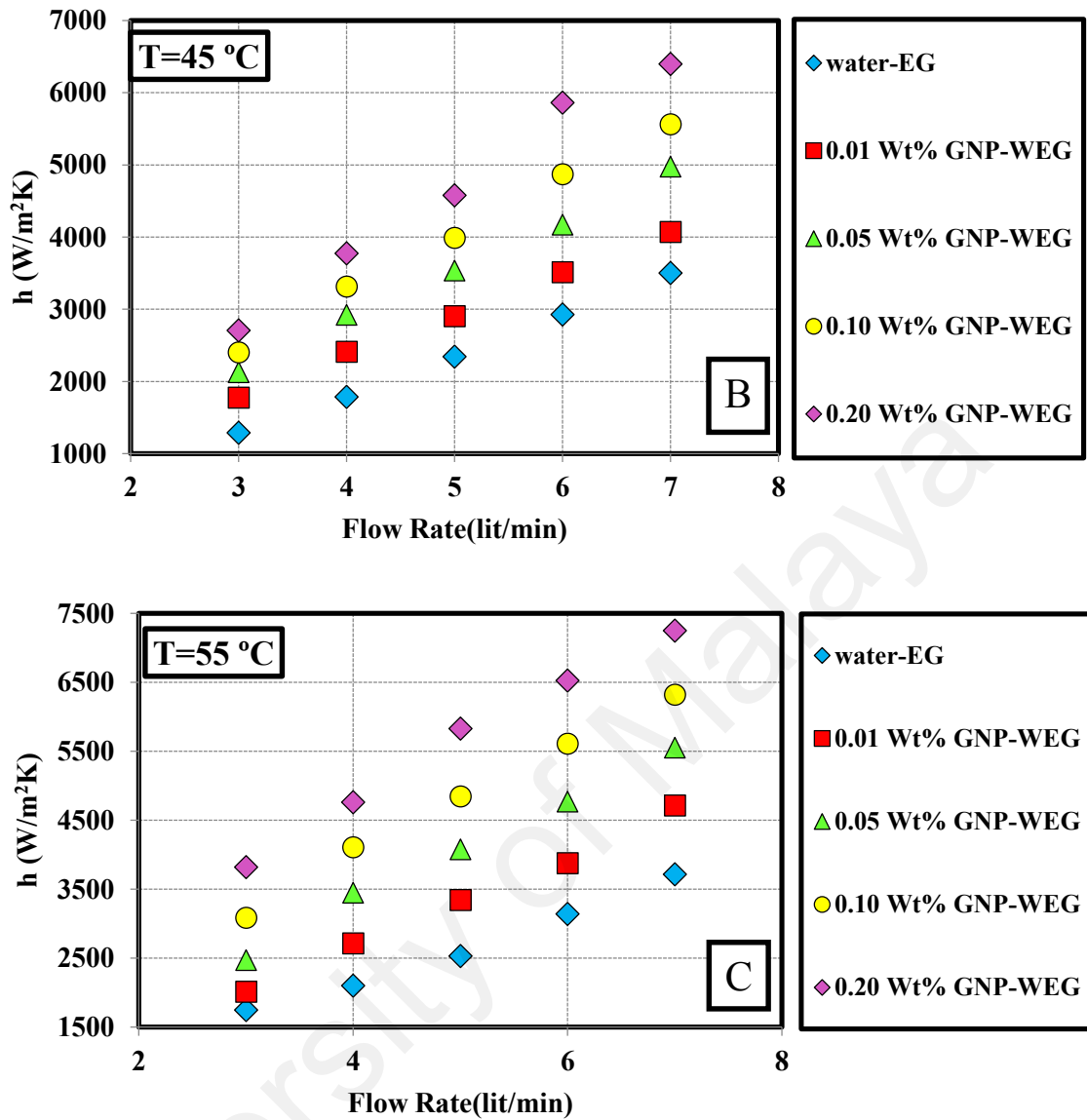
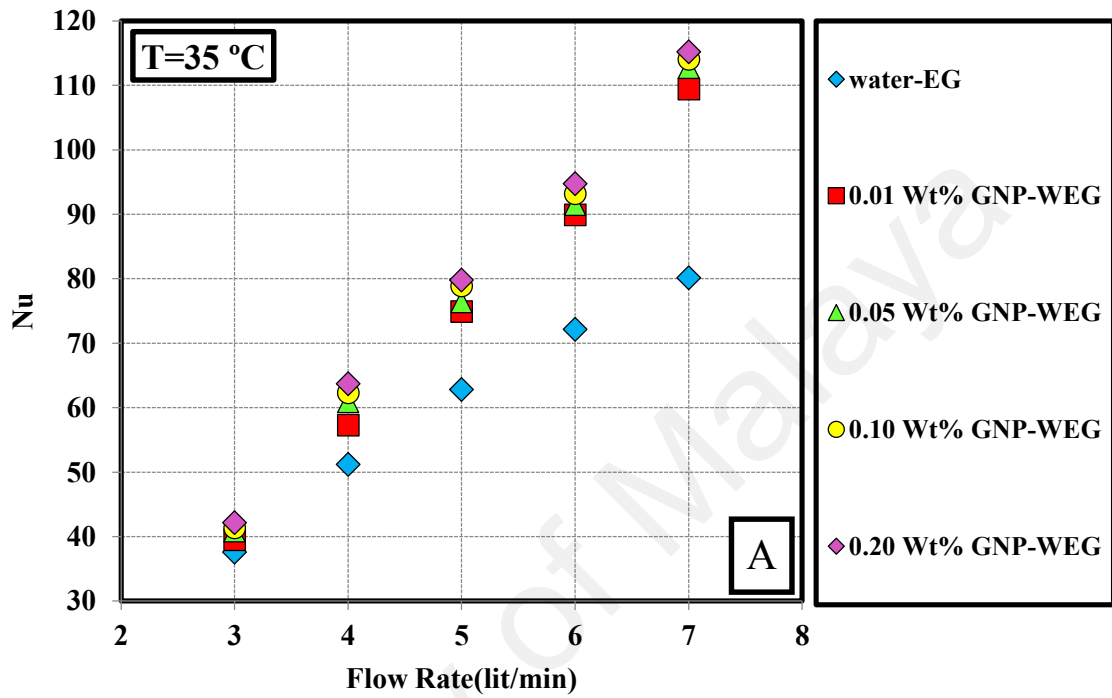


Figure 4.57: The effects of Reynolds number and concentration of EG-treated GNP on the convective heat transfer coefficient at the inlet temperatures of (a) 35 °C, (b) 45 °C and (c) 55 °C.

In order to evaluate the ratio of convective to conductive heat transfer of GNP-WEG coolants, experiments are performed for different weight concentrations (0.01, 0.05, 0.1, and 0.2 %), volume flow rates and inlet temperatures and the average Nusselt numbers are evaluated and presented in Figure 4.58 (A-C). This figure shows that for the GNP-WEG coolants the Nusselt number increases significantly compared to the base-fluid. The higher Nusselt number for the GNP-WEG coolant is attributed to the decrease in circulation temperature by increasing thermal conductivity of working fluid, which

decreases the temperature difference between the tube wall and bulk fluid in the car radiator. The lower temperature difference between the tube wall and the working fluid explains the increase in the heat transfer rate. This in turn could lead to a decrease in the size of radiator or heat exchanger.



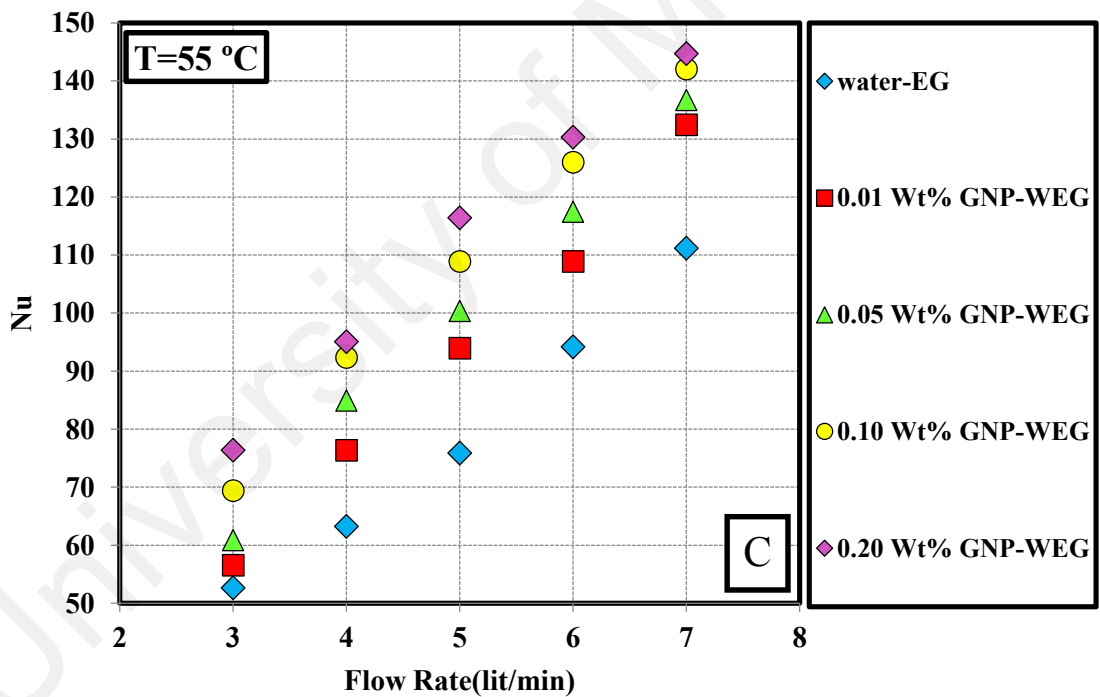
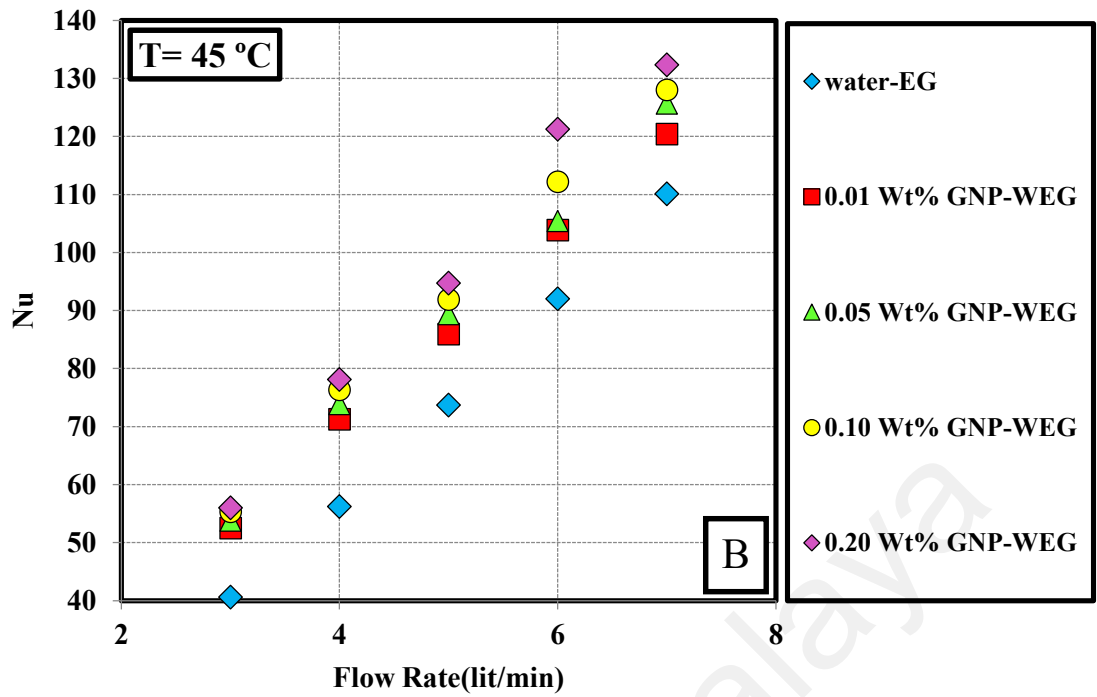


Figure 4.58: The average Nusselt numbers of GNP-WEG at different concentrations and volume flow rates for (a) 35 °C, (b) 45 °C and (c) 55 °C.

Figure 4.59 represents plots of the pressure drop of the car radiator for different flow rates and weight concentrations of GNP-WEG as well as DI water at T_{in} of 55 °C. It

is seen that as the volume flow rate and concentration of EG-treated GNP increases, the pressure drop increases. The pressure drops for the coolant suspensions at low concentrations of 0.01 and 0.05 are quite close to that for the mixture of DI water-EG. Figure 4.59 shows that the pressure drop for the GNP-WEG at the concentration of 0.2 wt% and flow rate of 7 lit/min has the highest pressure drop for the current range of measurements. It is also noteworthy that the pressure drop and viscosity curves exhibit similar trends, which can be attributed to the direct relationship between pressure drop and viscosity.

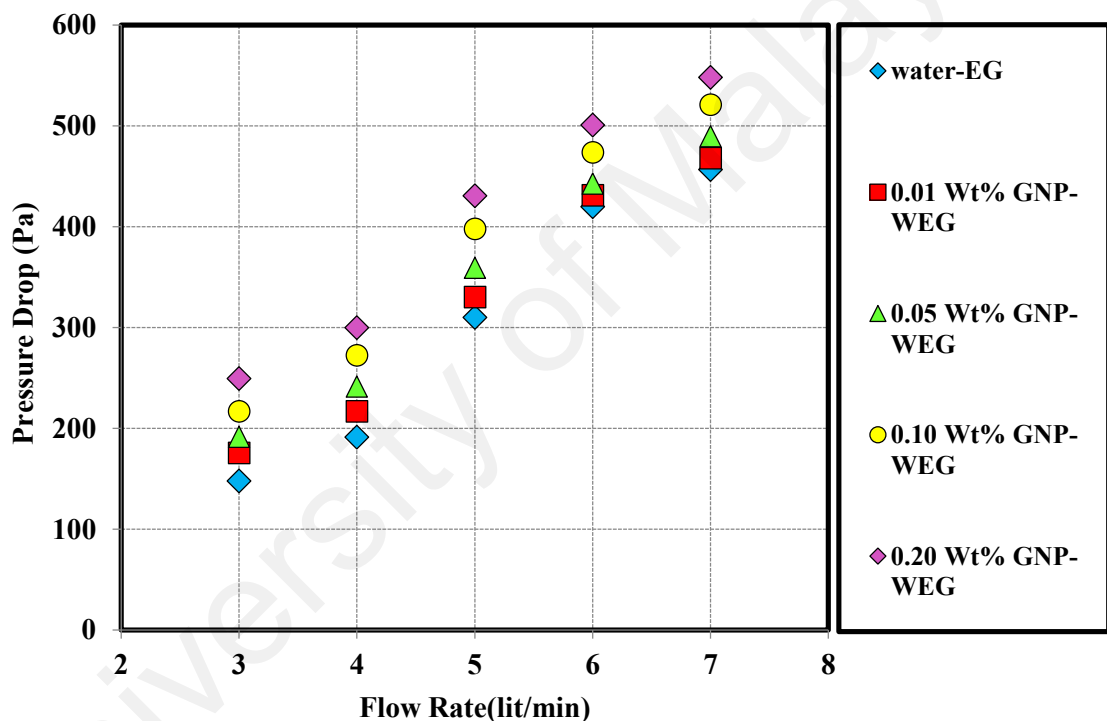


Figure 4.59: Pressure drop of the car radiator for different flow rates and weight concentrations of GNP-WEG as well as deionized water at T_{in} of 55 °C.

Also, the influence of inlet flow temperature and flow rate on pressure drop at the concentration of 0.1 wt% of EG-treated GNP is shown in Figure 4.60. Expectedly, as the temperature increases, the amount of pressure drop decreases, which can be resulted from reducing viscosity at higher temperature and also observed similar trend for other concentrations.

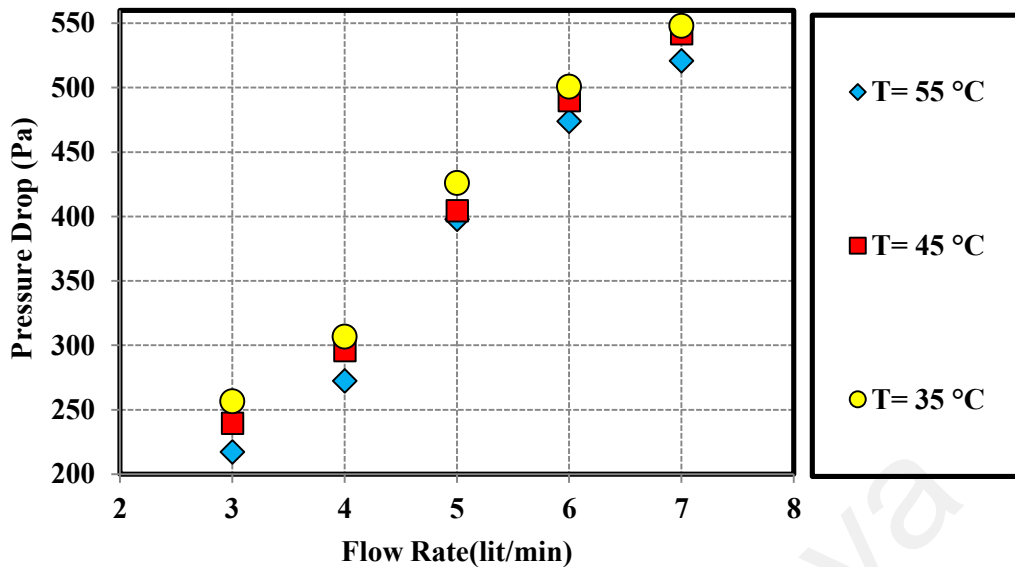


Figure 4.60: Effect of Inlet temperature of working fluid on the pressure drop at concentration of 0.1 wt%.

The friction factor for the radiator at different volume flow rates as well as weight concentrations of EG-treated GNP is shown in Figure 4.61 at constant inlet flow temperature of 55 °C. It is seen that the experimental friction factor decreases with the increasing of the volume flow rate at different concentrations. In addition, the friction factor increases as the concentration of EG-treated GNP increases, although there are some fluctuations in the measured friction factor for different volume flow rates. The minimum value of friction factor occurs for the base-fluid.

It is also seen as the volume flow rate increases, the dependence of friction factor on the concentration of EG-treated GNP decreases. At low extent of the Reynolds numbers, Brownian motion can be the main important parameter that influenced on the momentum transfer between the nanoparticles and base-fluid molecules. Thus, with the increase of the Brownian motion in the presence of GNP-WEG, the friction factor increases with higher slope as compared with base-fluid (Shanbedi et al., 2015; Shanbedi et al., 2012). However, this mechanism is not dominant when the high extent of Reynolds number is employed. In summary, the velocity of working fluids can be considered as the

most important parameter in increasing the friction factor at the high extent of Reynolds number. Overall, the low difference between the friction factors of the base fluid and the GNP-WEG suspensions at different volume flow rates is attributed to the insignificant gap between viscosities of basefluids and GNP-WEG.

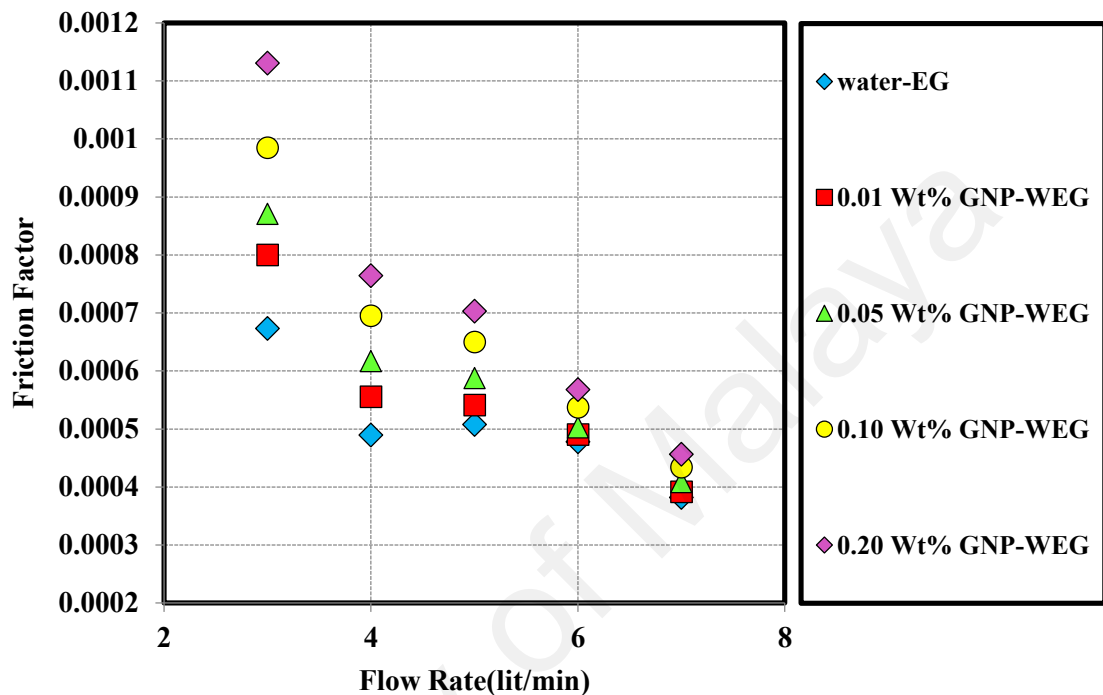


Figure 4.61: Effect of volume flow rate and concentration of EG-treated GNP on the friction factor at inlet temperature of 55 °C.

Also, Figure 4.62 shows the effect of inlet temperature of working fluid on the friction factor at the constant concentration of 0.1 wt%. It is observed that the friction factor increases with the decrease in temperature especially for volume flow rate less than 4 lit/min. Also, as the volume flow rate of working fluid (coolant) increases, the friction factor as well as the gap between the friction factors of working fluid at different temperatures decreases. As mentioned above, a drop in viscosity and/or pressure drop can be considered as the main reason for decreasing friction factor with the increasing of temperature.

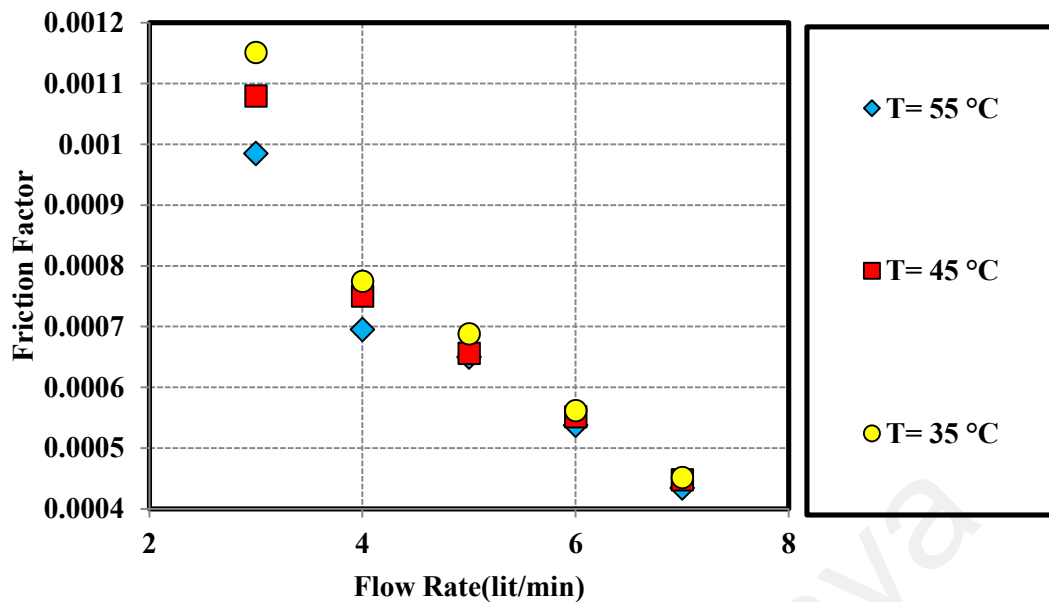


Figure 4.62: Effect of volume flow rate and inlet temperature of working fluid on the friction factor at concentration of 0.1 wt%.

The economic performance of working fluids for car radiator is typically evaluated using the performance index (ϵ), which expressed as the ratio of the heat transfer rate to the pressure drop. Earlier studies (e.g., (Samira et al., 2014)) showed that while the addition of nanoparticles increases the heat transfer rate, it also increases the pressure drop, which is undesirable. Performance index is then introduced to investigate the combined effect of both parameters. The variations of the performance indexes of the coolants are shown for different volume flow rates and various concentrations for a constant T_{in} of 55 °C in Figure 4.63. It is seen that the performance indexes of all the samples are greater than 1, which indicates the effectiveness of the prepared coolant samples for car radiators. This figure shows that the performance index curves for different concentrations reach their peaks for a volume flow rate of 6 lit/min, and that is followed by a gradual decrease of the performance index for further increase in the flow rate which refers the optimum value of flow rates. Also, an increase in the performance index is obtained with an increase in the weight fraction of GNP.

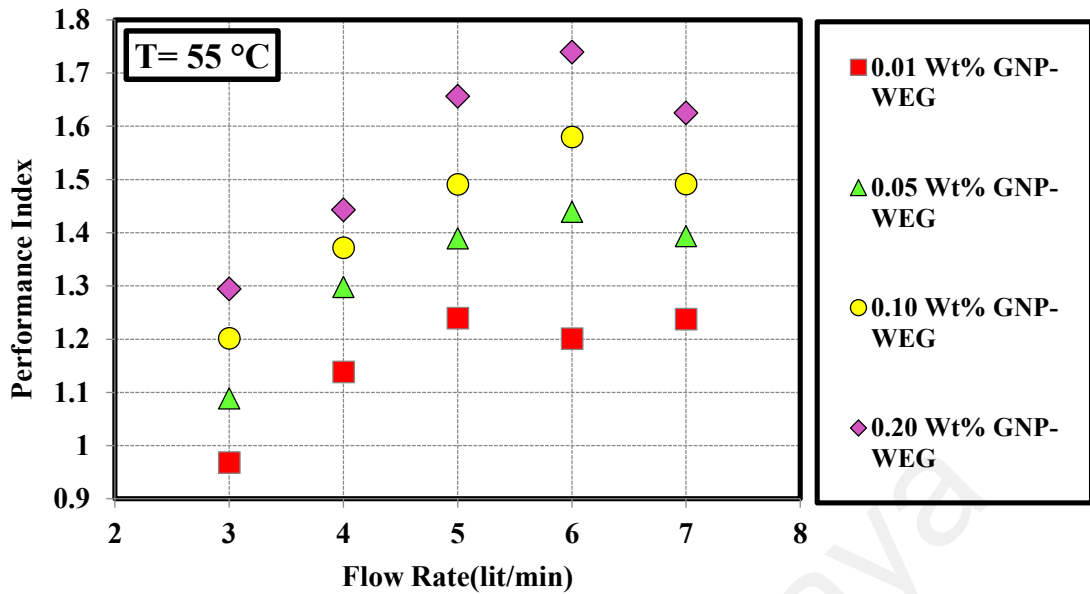


Figure 4.63: The performance index of the synthesized coolant versus flow rate at different concentrations of EG-treated GNP.

Figure 4.64 presents the performance indexes of GNP-WEG for the concentration of 0.1 wt% for different inlet temperatures and flow rates. This figure exhibits a rising trend of performance index with the volume flow rate. That is, as the volume flow rate increases, performance index increases. It is also seen that the performance indices of all the samples (except for volume flow rate of 3 lit/min and an inlet temperature of 35 °C) are greater than 1, indicating that GNP-WEG is an appropriate coolant for the car radiator at different volume flow rates.

These results also validate that the positive effects of heat transfer exceed the negative effects of pressure drop for GNP-WEG coolants for a wide range of inlet temperatures, concentrations, and volume flow rates; thus indicating excellent capability of the synthesized coolant for use in car radiators. In this study, it is also distinct that the performance index drops down after the flow rate of 6 lit/min which refers to the importance of optimization of the flow parameters for the best performance.

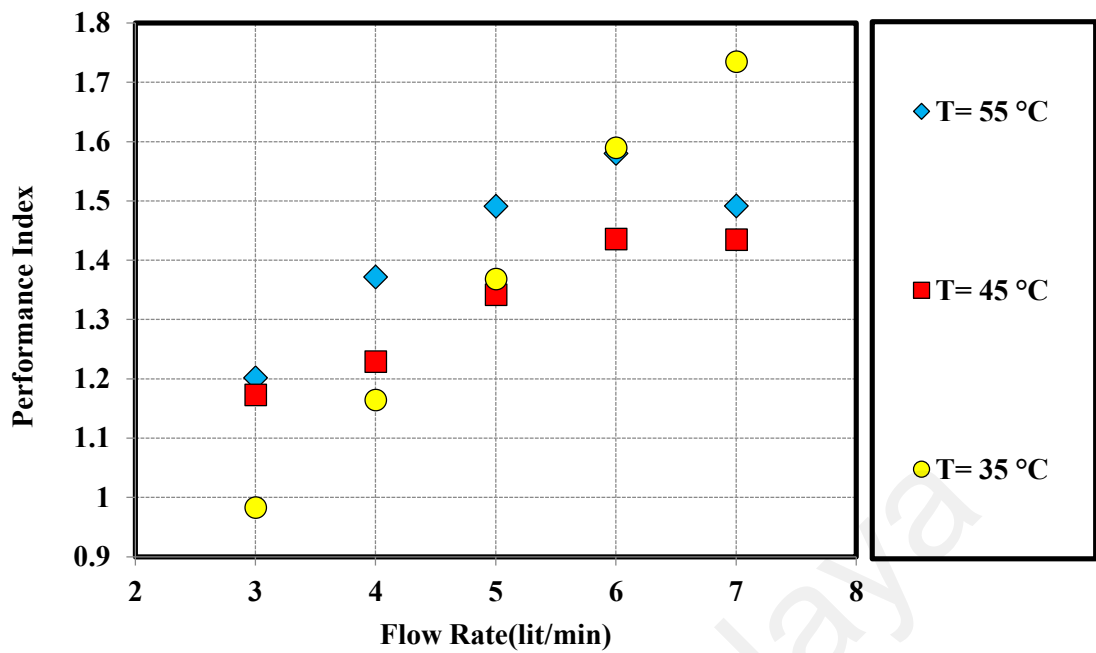


Figure 4.64: The performance index of the synthesized coolant versus flow rate at different temperatures and concentration of 0.1 wt%.

Power consumption and pumping characteristics in a loop is a critical parameter in terms of economy as well as energy-saving. Pumping power can be considered as an economic performance indicator in a loop system for evaluating the operability of fluid and performance of power plant. Figure 4.65 compares the pumping power of the car radiator coolant (GNP-WEG) at various concentrations of EG-treated GNP at different inlet temperatures with that of the base-fluid. This figure shows that there is a slight increase in the pumping power with the EG-treated GNP loading, and the effect of temperature variation is negligible (Wenhua Yu et al., 2012).

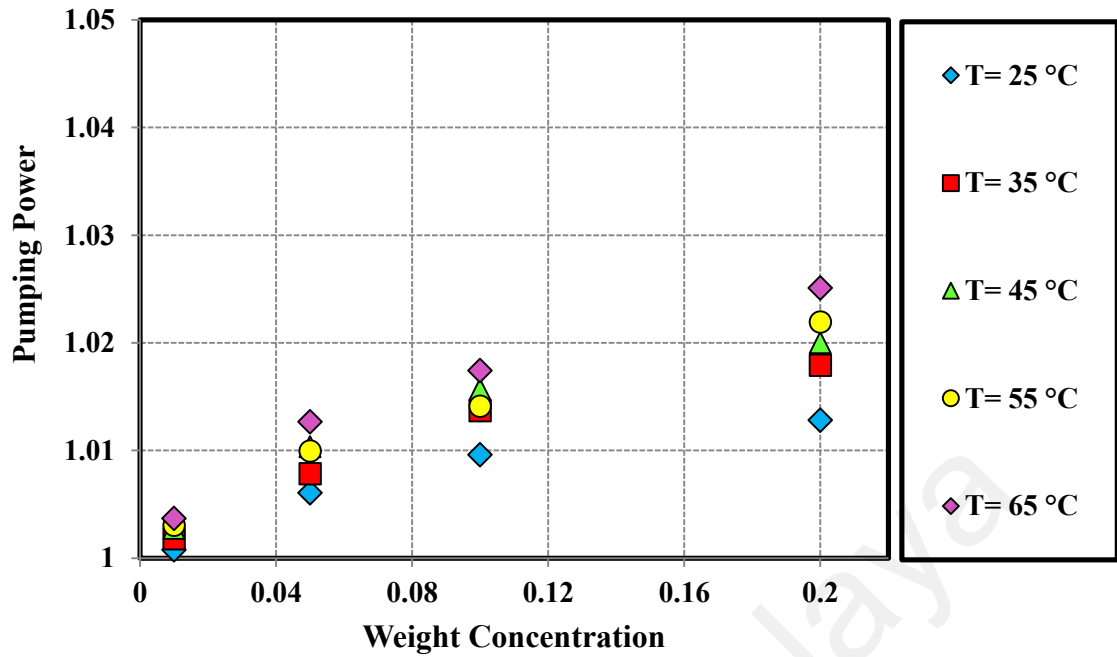
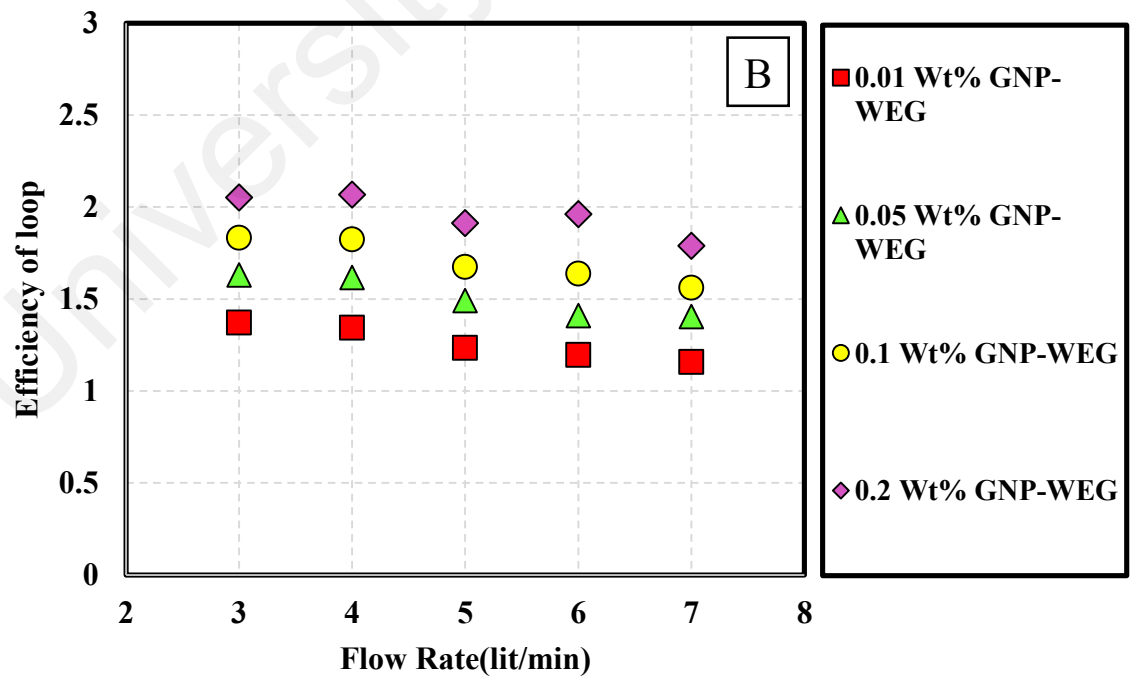
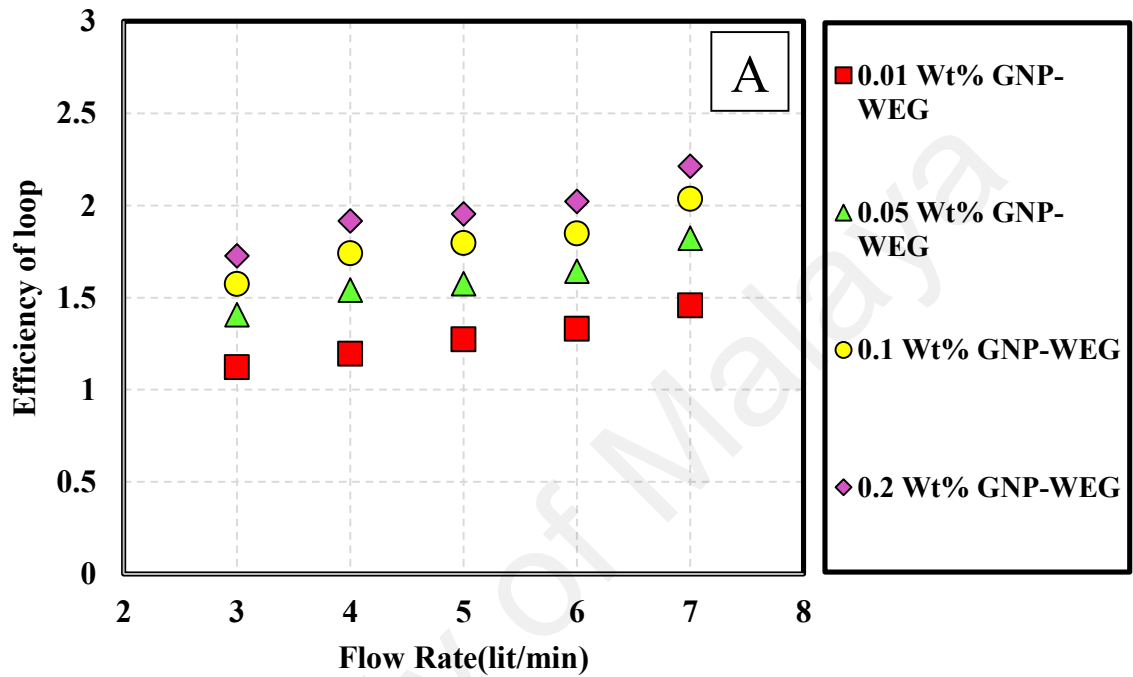


Figure 4.65: Pumping power of GNP-WEG for different concentrations and temperatures.

Performance index presented the radiator efficiency in terms of pressure drop and rate of heat transfer. The increase in needed pumping power is of course undesirable, while the heat transfer coefficient enhancement is highly desirable. To consider these conflicting parameters, Wenhua Yu et al. (2012) suggested another type of efficiency (efficiency of loop), which is a combination of the heat transfer coefficient (h) and the pumping power (W). The efficiency of radiator in automobile is then measured by the ratio of the heat transfer coefficient enhancement to the ratio of the pumping power increase (Wenhua Yu et al., 2009b; Wenhua Yu et al., 2012). That is represented by Equation 4.16.

$$\eta = \frac{h_{nf}/h_{bf}}{W_{nf}/W_{bf}} \quad (4-16)$$

As discussed above, the efficiency of loop should be higher than 1 for a cost-effective system. It can be seen in Figure 4.66 that the efficiency of loop is higher than 1 at different temperatures, concentrations and flow rates, indicating the promising potential of GNP-WEG for being an alternative coolant in the car radiators.



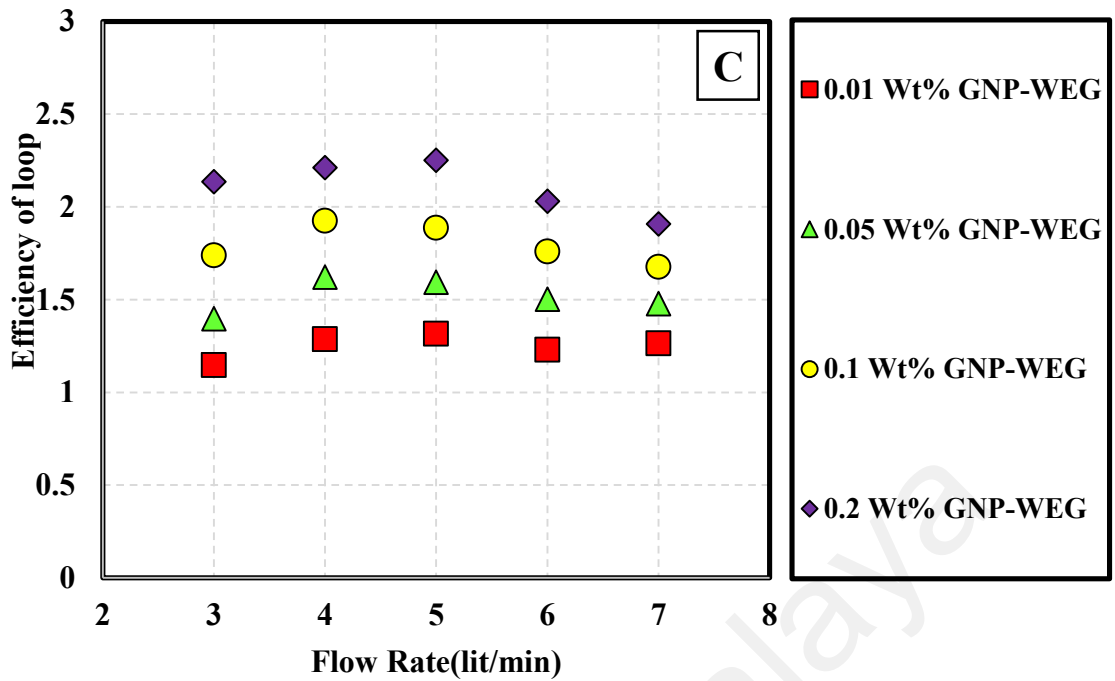


Figure 4.66: Radiator Efficiency of GNP-WEG at different concentrations and volume flow rates for different inlet temperatures of (a) 35 °C, (b) 45 °C and (c) 55 °C.

In conclusion, a series of tests on the physical properties of the new coolant were performed and the results were presented in graphical forms. The thermal conductivity, viscosity, specific heat capacity, and density of all the tested samples had shown reasonable performance for utilization in car radiators. The ratio of convective to conductive heat transfer for the new coolant has shown significantly higher than that of the conventional base-fluid, indicating that the new fluid can be an effective coolant for car radiator in terms of overall thermal properties and energy saving.

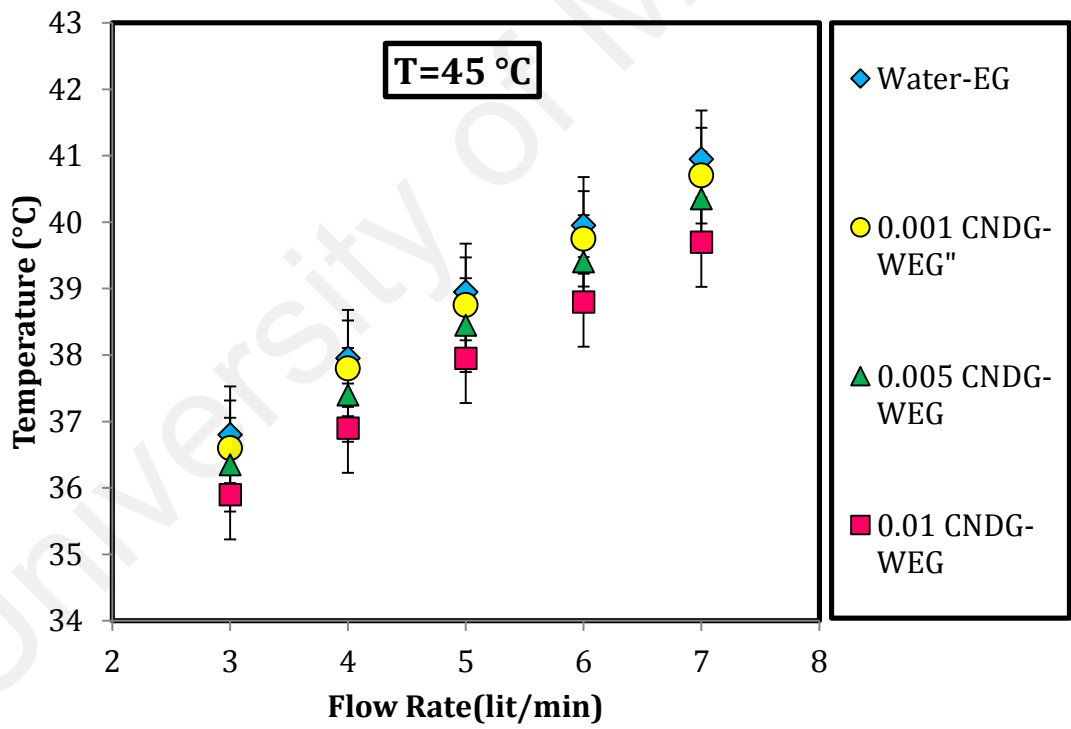
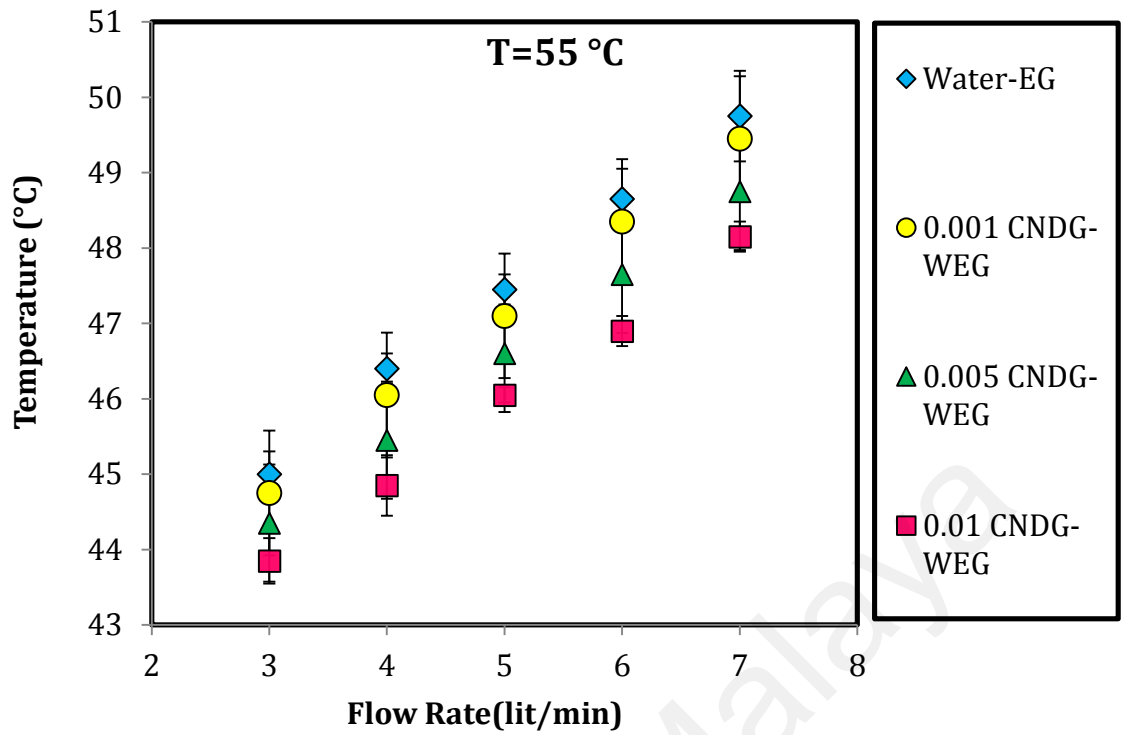
Also, other characteristics of the new coolant such as weak increase in the pressure drop for different concentrations and inlet temperatures, low friction factor, lack of corrosive agent, appropriate performance index ($\epsilon > 1$), and slight increase in the required pumping power are all highly favorable for introducing new fluid for wide industrial applications.

4.4.1.3.2 CNDG-WEG

To reach better results, CNDG-WEG with higher specific surface area than that of GNP-WEG were synthesized at different weight concentrations. The same experiments' phases were repeated for CNDG-WEG and the results are reported as follow.

The average outlet temperature (T_{out}) of the car radiator by using CNDG-WEG as a coolant fluid for inlet temperatures of 55, 45 and 35°C and different weight concentrations of CNDG are shown in Figure 4.67. The figures indicate an increasing trend of T_{out} with volume flow rate and a downward trend of T_{out} with concentration of CNDG. It means that, as the concentration of CNDG in base-fluid increases, T_{out} decreases. As mentioned earlier, higher weight concentration means higher thermal conductivity of the working fluid, resulting in higher heat transfer or lower difference between temperatures of bulk fluid and the radiator tube wall. Moreover, by increasing the volume flow rate in circulation system, the connection time for transfer heat in car radiator (time for transferring heat between air and tube surface) decreases, making the outlet temperature to be higher.

Additionally, it is observed that as the inlet temperature increases, the average outlet temperature increases too. Temperature drop of the car radiator associated with the increase of CNDG concentration is attributed to the increase of thermal conductivity of water-EG mixture in the presence of CNDG.



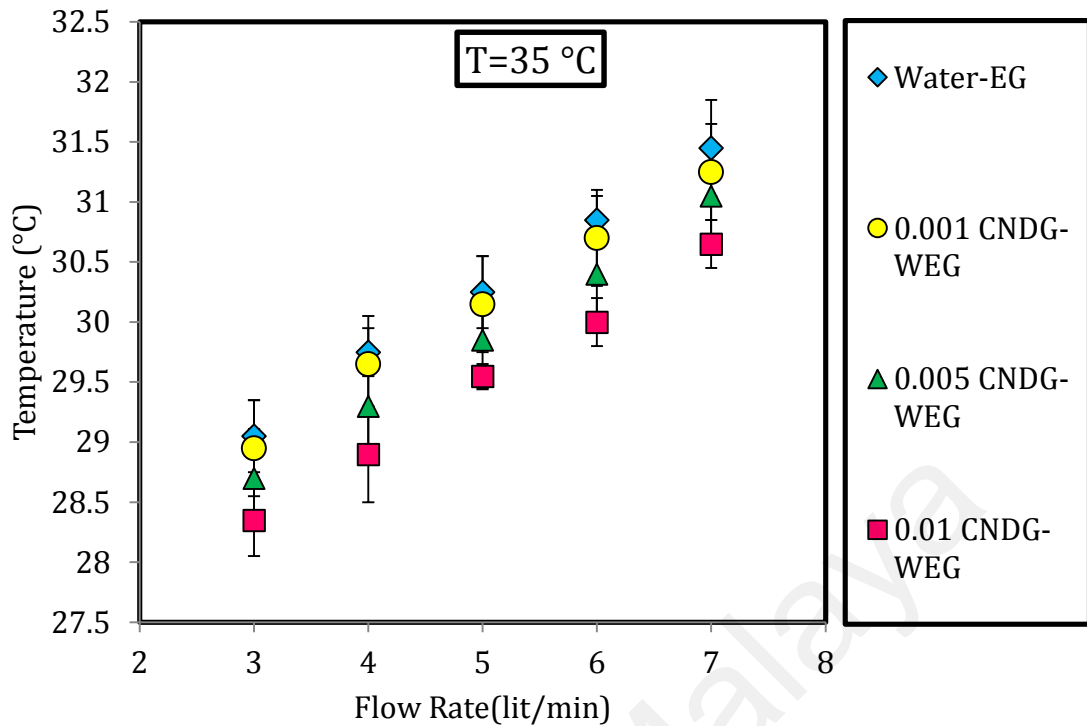
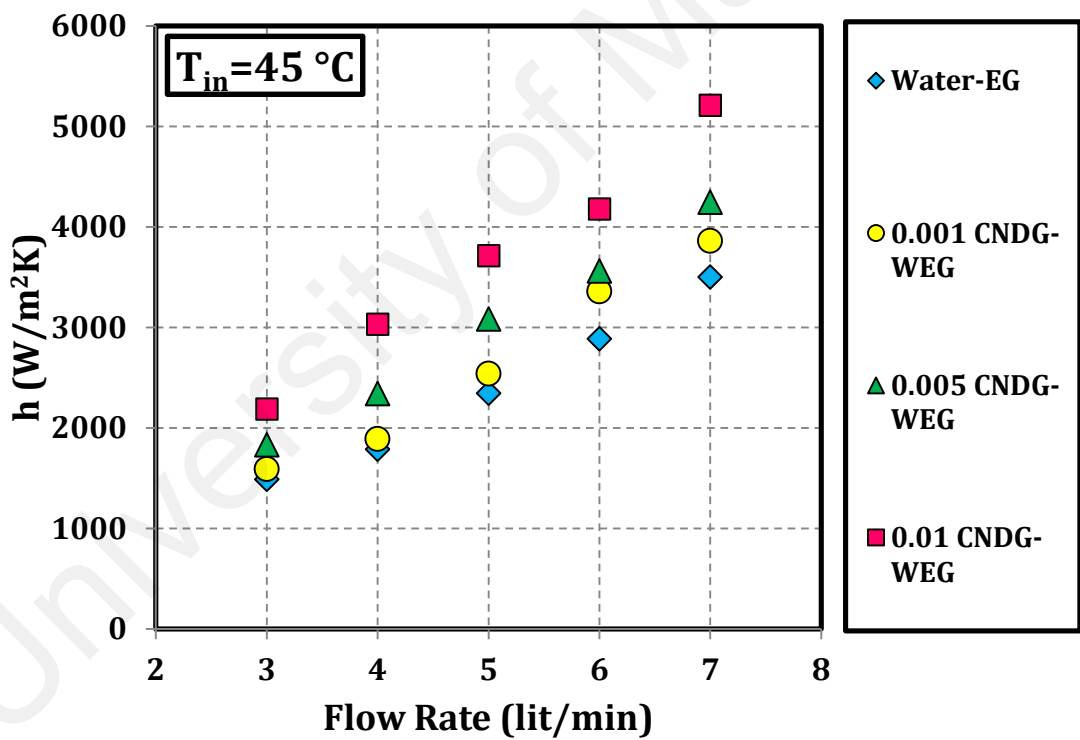
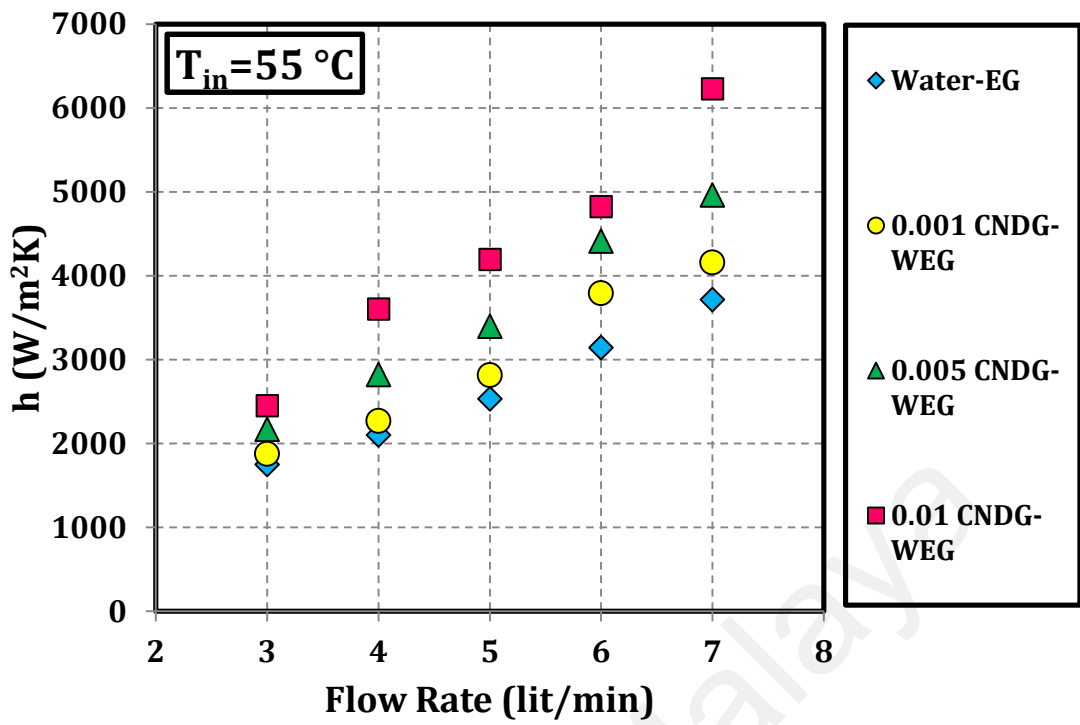


Figure 4.67: The average outlet temperature (T_{out}) of car radiator in the presence of CNDG-WEG as well as Water-EG mixture at different inlet temperatures.

Variations of the convective heat transfer coefficient of CNDG dispersed in a mixture of DI water-EG are studied and the results are systematically presented. Figures 4.68 compare convective heat transfer coefficients of CNDG-WEG for different weight concentrations at three different outlet temperatures. It is observed that the improvements of the convective heat transfer coefficient of CNDG-WEG are significantly higher than those of the thermal conductivity for different weight concentrations. This behavior can be qualitatively explained by a simple scale analysis. It is obvious that the heat-transfer coefficient is a macroscopic parameter and can be approximately given by k/δ_t with δ_t as the thickness of thermal boundary layer (Ding et al., 2006a). In a double tube heat exchanger, at the entrance of the test section ($x/D = 0$), where the theoretical boundary layer thickness is zero, the heat-transfer coefficient approaches infinity (S. J. Aravind & S. Ramaprabhu, 2013). With the increase in axial distance, the boundary layer increases

until fully developed, after which the boundary layer thickness and hence the convective heat-transfer coefficient are constant.

However, according to the results, the maximum heat transfer coefficient enhancements for CNDG-WEG is 83% for a volume fraction of 0.01 wt.%, whereas the maximum enhancements in thermal conductivity is respectively 19.4%. Therefore, it is obvious that the enhancement of the convective heat-transfer coefficient is much greater than that of the thermal conductivity, especially at high flow rates. So, the heat-transfer enhancement can be largely obtained by thinning of the thermal boundary layer thickness (S. J. Aravind et al., 2011). As mentioned by several studies, the possible reasons for this reduction in boundary layer thickness are particle migration in nanofluids due to shear action, viscosity gradient, and Brownian motion in the cross-section of the tube (S. Aravind & S. Ramaprabhu, 2013; Phillips et al., 1992). The increase of the thermal conduction under dynamic conditions could be another decisive factor for heat transfer improvement (Xuan & Li, 2003). It is also possible that as the surface area increases, Brownian motion increases, particle migration increases and a reduction in boundary layer thickness happens. More studies on a double tube heat exchanger should be conducted to get a clearer picture of the heat transfer enhancement mechanism. To reach a clearer picture of the heat transfer enhancement mechanism, more studies, typically flow visualization studies, need to be conducted.



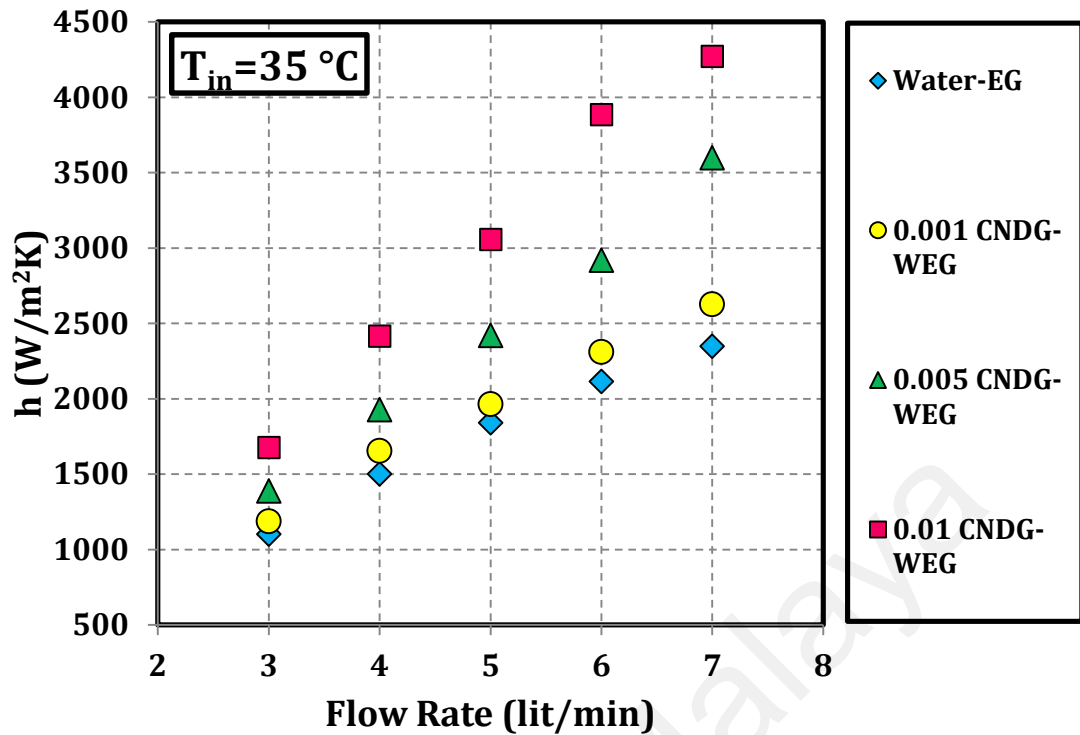
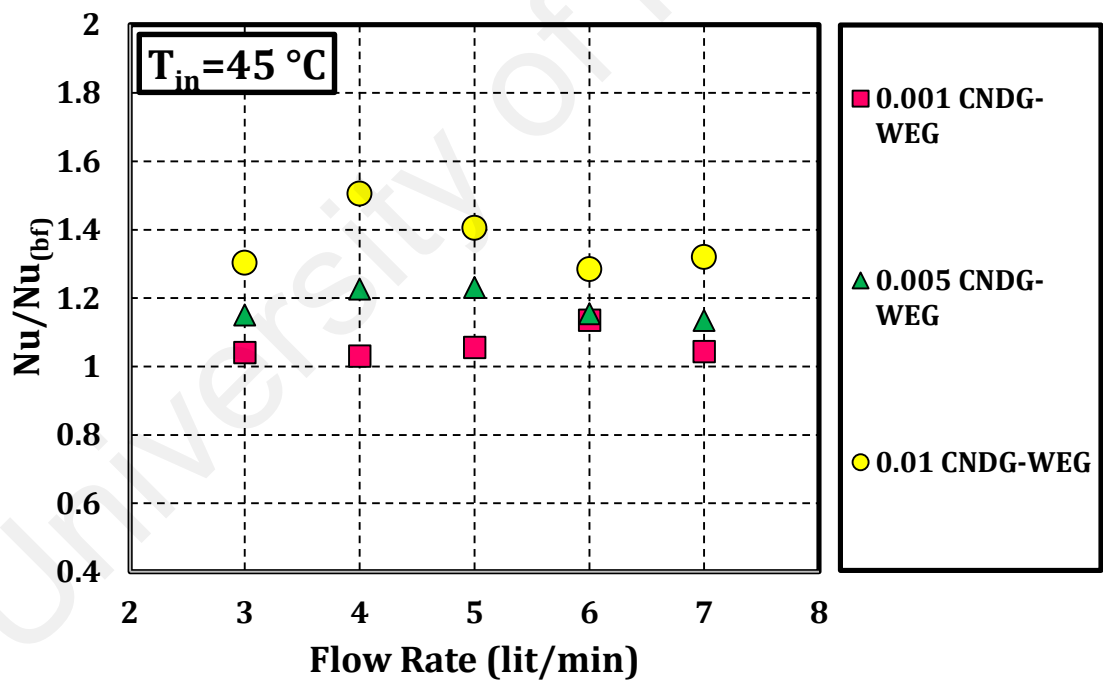
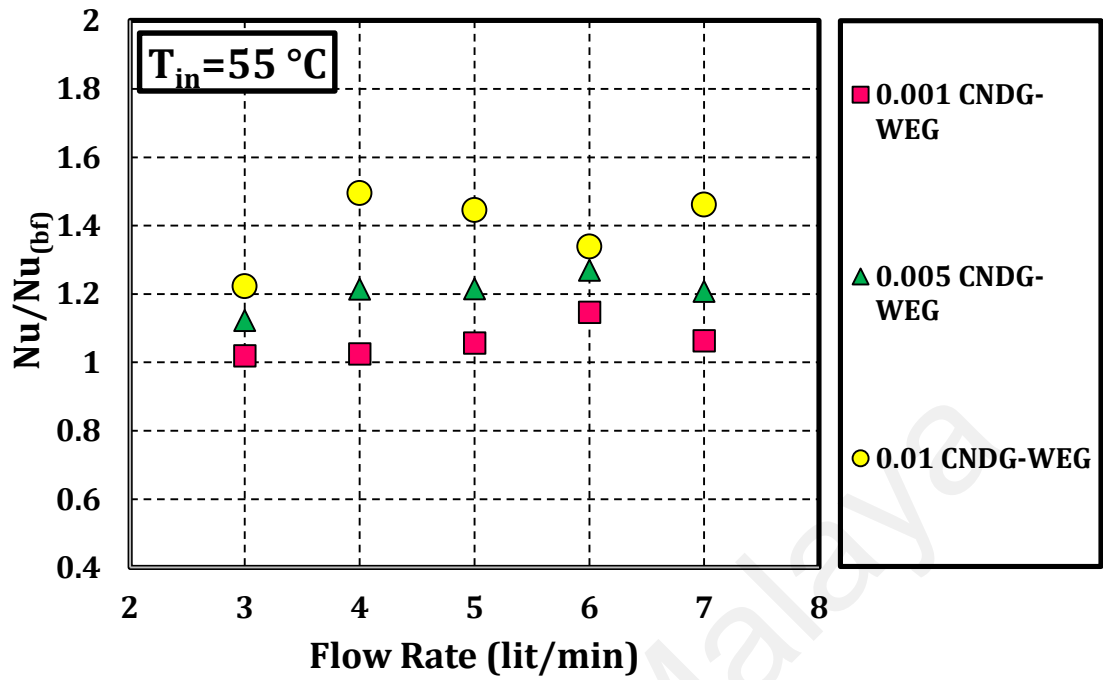


Figure 4.68: The effects of Reynolds numbers and weight concentrations of CNDG on the forced convective heat transfer coefficient at different inlet temperatures.

For evaluating the ratio of convective to conductive heat transfer of CNDG-WEG coolants as compared with the basefluid, some experiments were performed at different weight concentrations (0.001 wt.%, 0.005 wt.% and 0.01 wt.%), volume flow rates, inlet temperatures and the ratio of Nusselt number of coolants to the basefluid are assessed and indicated in Figure 4.69 for different input temperatures. This figure indicates that the ratio of Nusselt numbers of all the samples to the basefluid are greater than 1, and significantly increases with increasing weight concentration of CNDG in coolants. The higher ratio of Nusselt numbers to base fluid than 1 is attributed to the reduction of circulation temperature by increase in thermal conductivity of working fluid, leading to decrease in the temperature difference between the tube wall and the bulk fluid in the car radiator. The lower temperature difference between the tube wall and the working fluid can be explained by the increase in the heat transfer rate. This could result in a decrease in the size of radiator or heat exchanger.



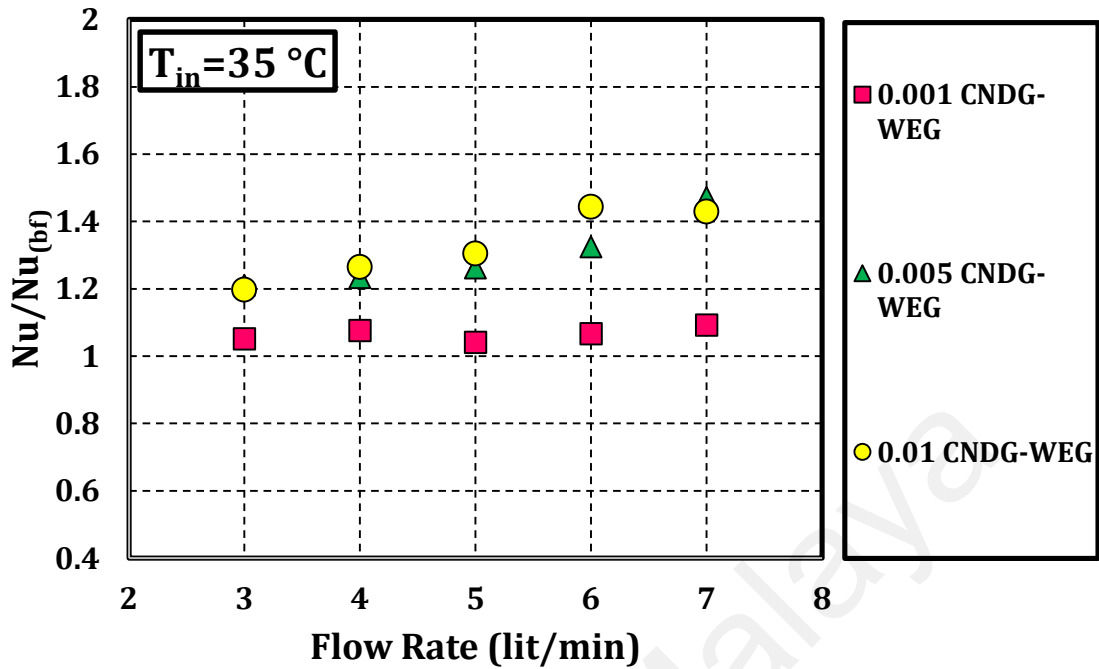
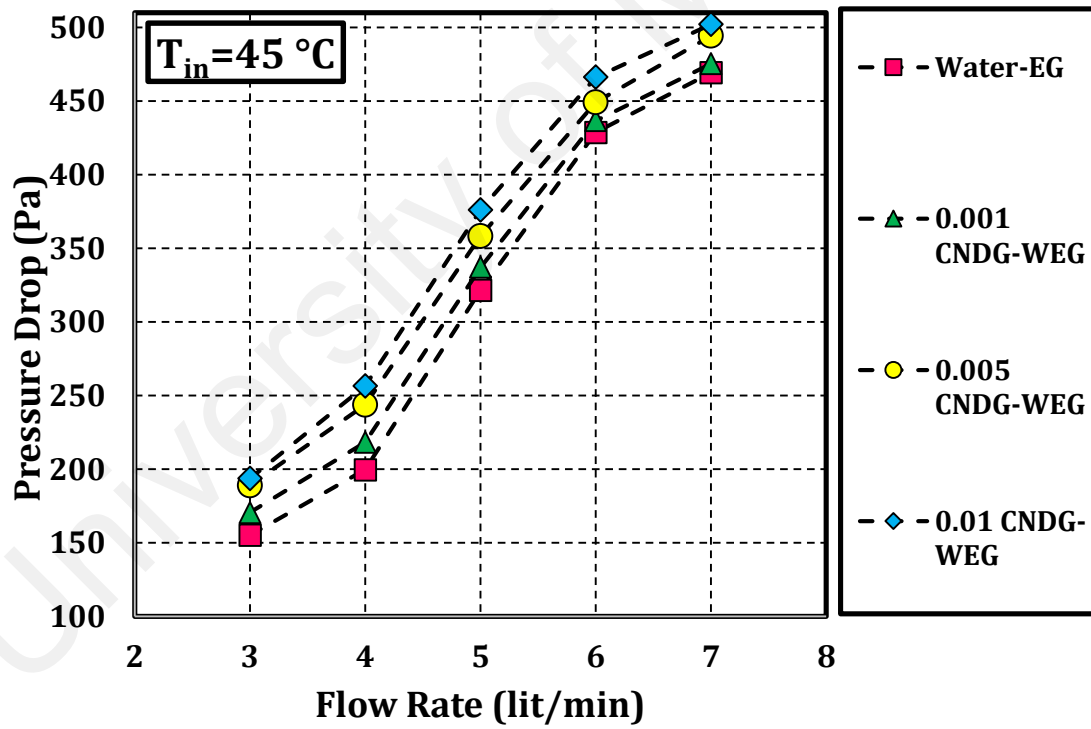
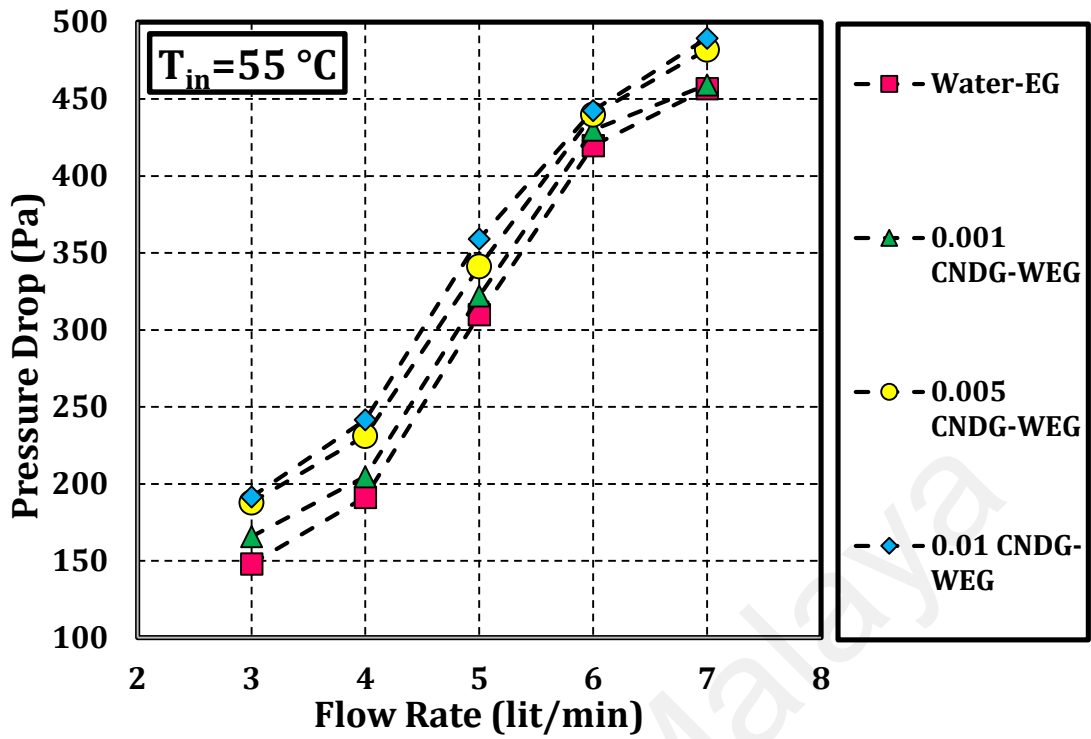


Figure 4.69: The Nusselt number enhancement of CNDG-WEG at different concentrations, inlet temperatures and volume flow rates.

Figure 4.70 indicates the pressure drop of the car radiator for different flow rates and weight concentrations of CNDG-WEG as well as DI water-EG mixture at $T_{in} = 55$ °C. It is observed that by increasing the volume flow rate and concentration of CNDG, the pressure drop increases too. The pressure drops for the coolant suspensions at different concentrations are very close to that for the mixture of DI water-EG. Figure 4.70 indicates that the highest pressure drop for the current range of measurement is for the pressure drop of the CNDG-WEG at the concentration of 0.01 wt.% and flow rate of 7 lit/min. It is of note that the similar trends are seen for pressure drop and viscosity curves, attributing to the direct relationship between pressure drop and viscosity. Also, Figure 4.70 shows the influence of inlet flow temperature and flow rate on pressure drop at the concentration of 0.01 wt.% of CNDG. It can be seen that as the weight concentration of CNDG in CNDG-WEG and/or inlet temperature of flow was increased, the higher pressure drop observed.



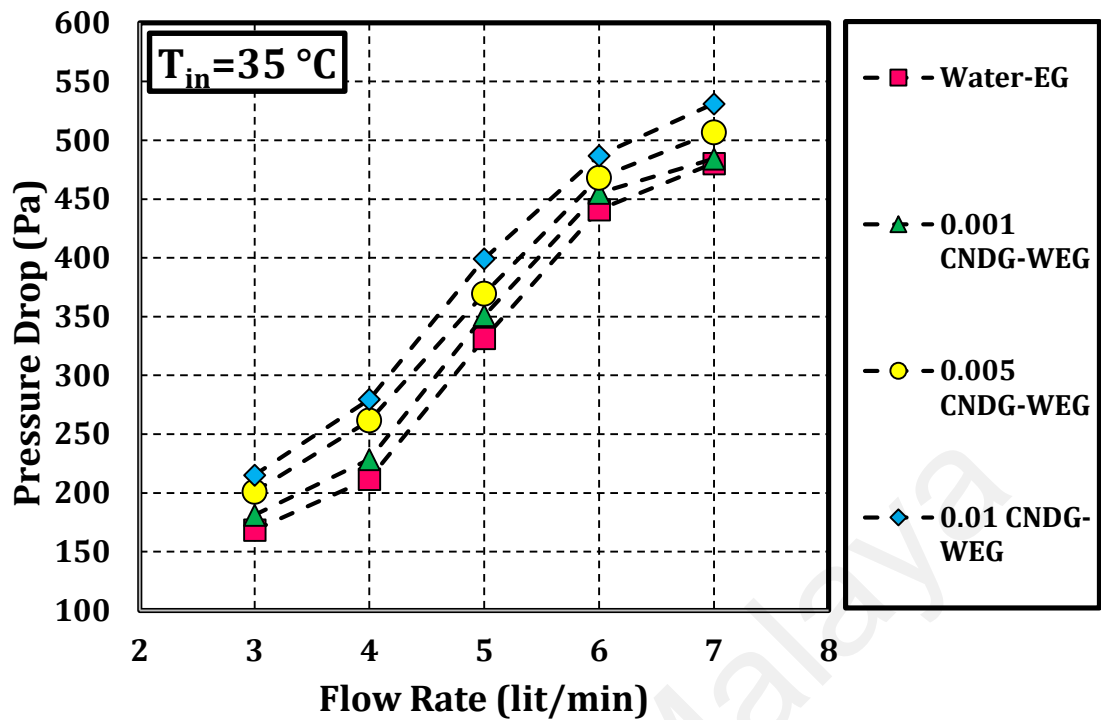


Figure 4.70: Pressure drop of the car radiator at different flow rates and weight concentrations of GNP-WEG and inlet temperatures.

Figure 4.71 represents the pressure drop of the car radiator for different T_f (the average temperature between inlet and outlet) and weight concentrations of CNDG-WEG at volume flow rate of 7 lit/min. There is a decrease in pressure drop at temperature range of 30-55 $^{\circ}\text{C}$ for the base fluids and coolant suspensions at different concentrations. Figure 4.71 indicates that the highest pressure drop for the current range of measurements for the pressure drop of the CNDG-WEG (0.01 wt.%) at T_f of 32.8 $^{\circ}\text{C}$ and flow rate of 7 lit/min.

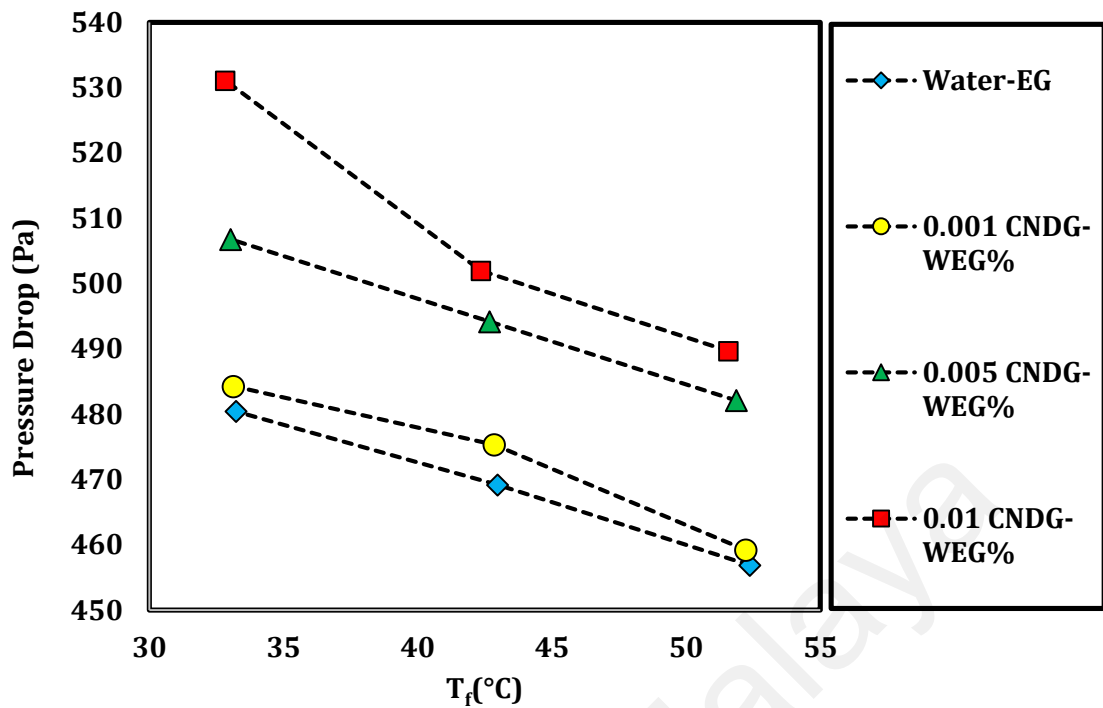
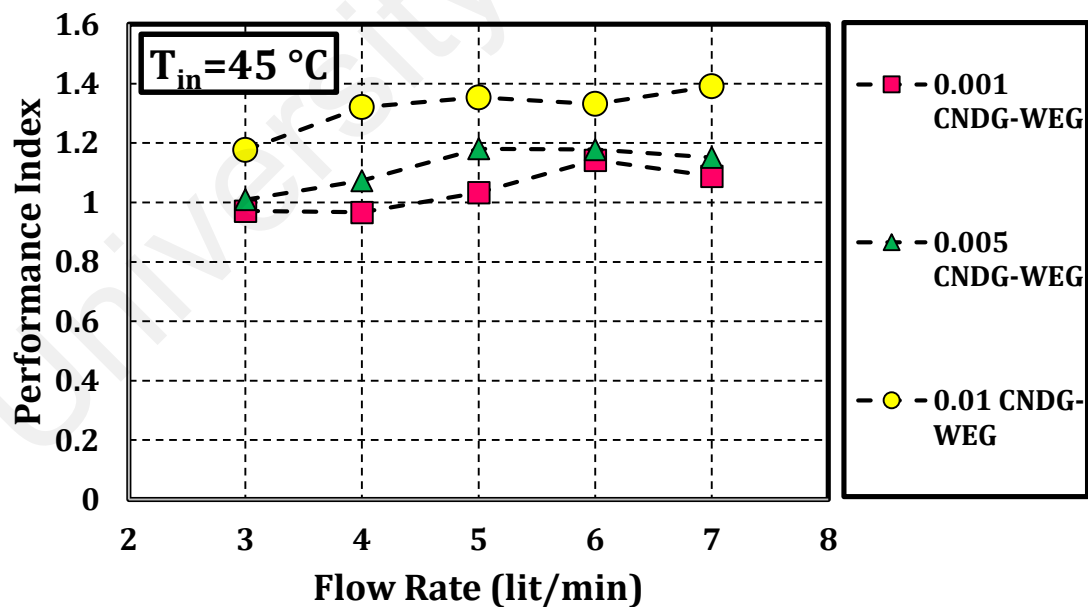
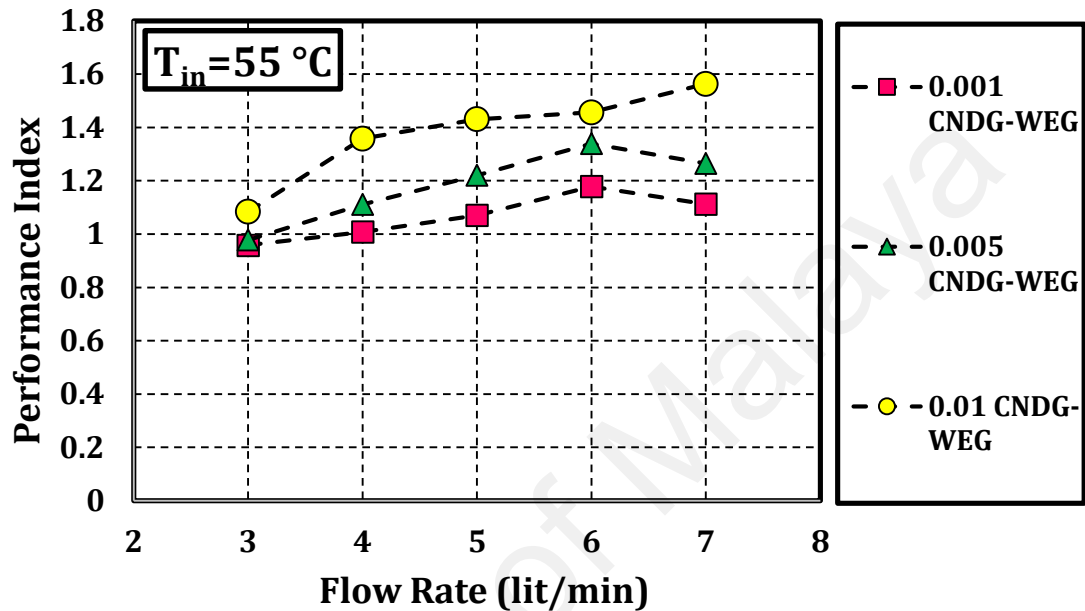


Figure 4.71: The pressure drop of the car radiator for different T_f (the average temperature between inlet and outlet) and weight concentrations of CNDG-WEG at volume flow rate of 7 lit/min.

The performance of working fluids in car radiator is commonly measured by performance index (ϵ), defined as the ratio of the heat transfer rate to the pressure drop. Previous researches (e.g., (Samira et al., 2014)) showed that adding nanoparticles increase the heat transfer rate as well as the pressure drop, which is undesirable. Thus, performance index is introduced to examine the combined effect of both parameters. Figure 4.72 shows the variations of performance index of the CNDG for different volume flow rates and various concentrations. It is observed that performance index is greater than 1 for all samples in a majority of experimental condition, indicating the effectiveness of the prepared coolant samples for car radiators. This figures also indicate that performance index curves showed some reasonable enhancements at different temperatures and concentrations, indicating a high potential alternative for car radiator in different conditions. Furthermore, as the weight concentration of CNDG increases, the amount of performance index increases, however the concentrations of CNDG in all samples are

fairly low. These results support that for a wide range of inlet temperatures, the concentrations and volume flow rates have the positive effects of heat transfer which are more than the negative effects of pressure drop for CNDG-WEG coolants; so the synthesized coolants have excellent capability for using in car radiators.



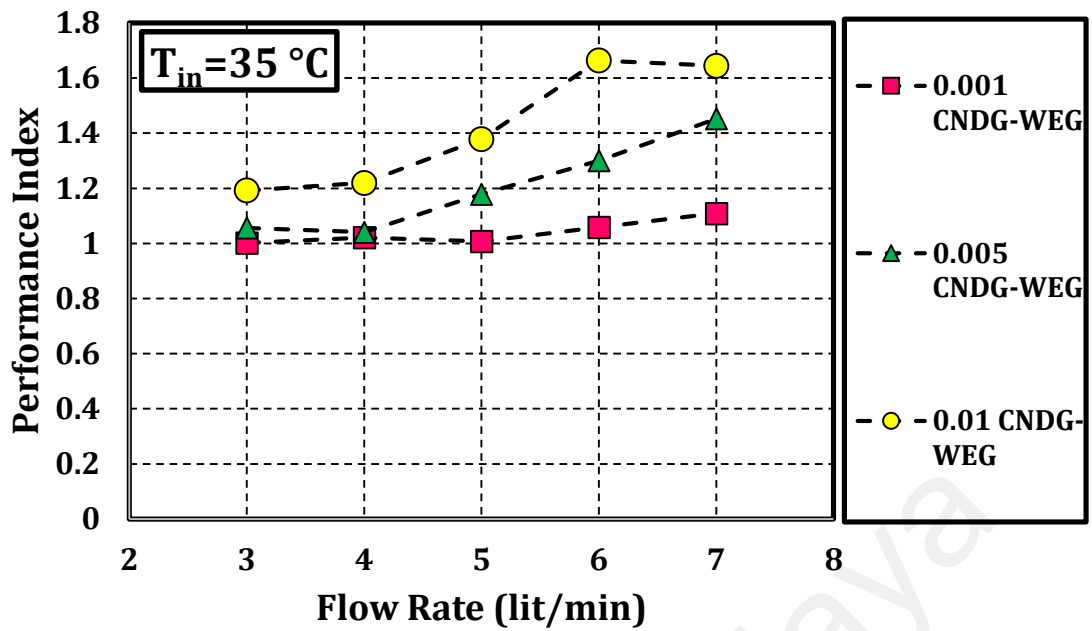
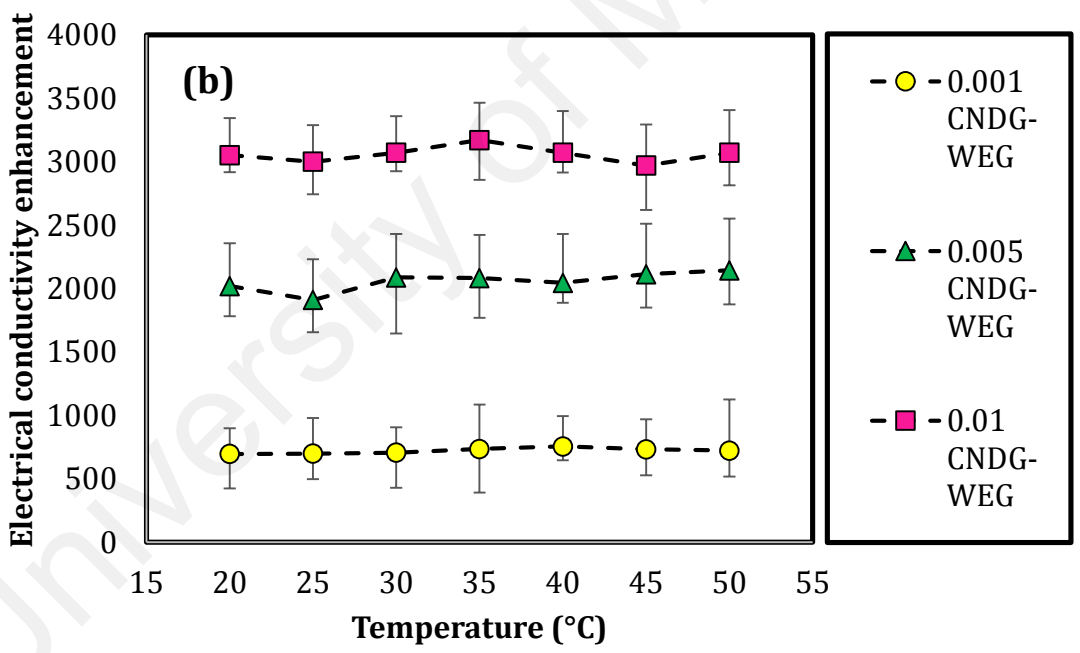
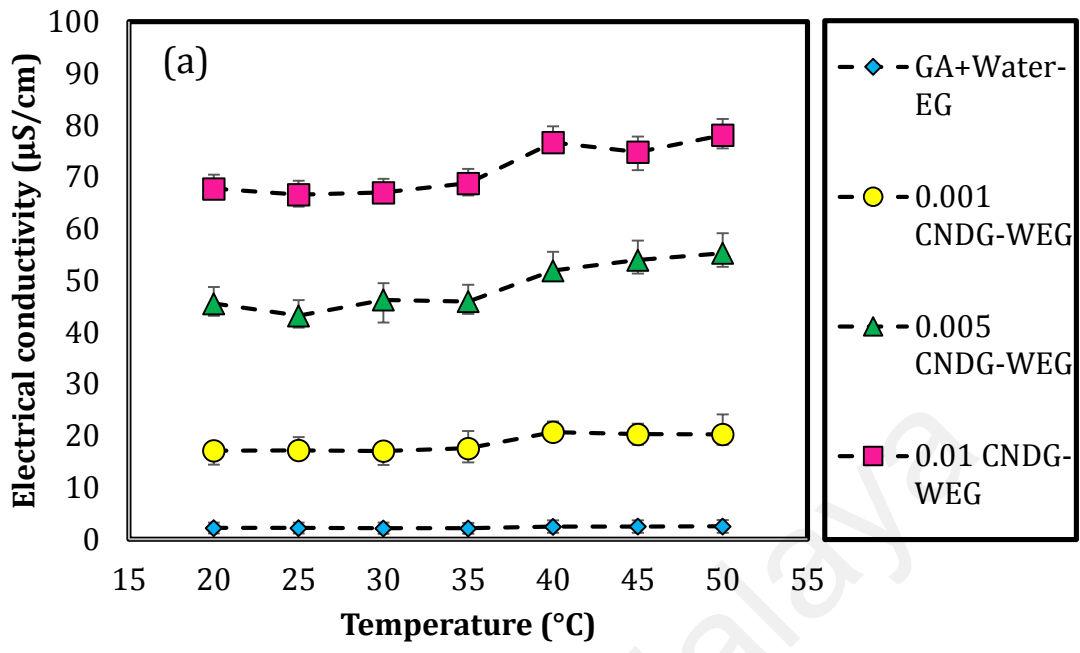


Figure 4.72: The performance index of the CNDG-WEG coolants at different flow rates, inlet temperatures and weight concentrations.

Low concentration of CNDG in prepared samples and high convective and conductive heat transfer coefficient of alternative coolant noted here can be presented as much more suitable and economical for being used in car radiator and can provide lower erosion, which should be further investigated. Also, NDG with special properties such as high number of electrons for carrying of charged ions “called activation region” which has attractive and unique electrical properties (Seyed Shirazi et al., 2015; Zakaria et al., 2015). Electrical conductivity behavior of fluids is a technological importance and has not been widely studied. The electrical conductivity and enhancement of CNDG-WEG for different weight concentrations were measured at the temperature range of 20–50 °C, which are illustrated in Figures 4.73a and b, respectively. It can be seen that the prepared samples are presented larger electrical conductivity enhancement at higher weight concentrations of CNDG, due to the presence of higher activation region in the base fluid. Thus, the intrinsic electron transfer capacity of the CNDG should be the main reason for electrical conductivity enhancement.



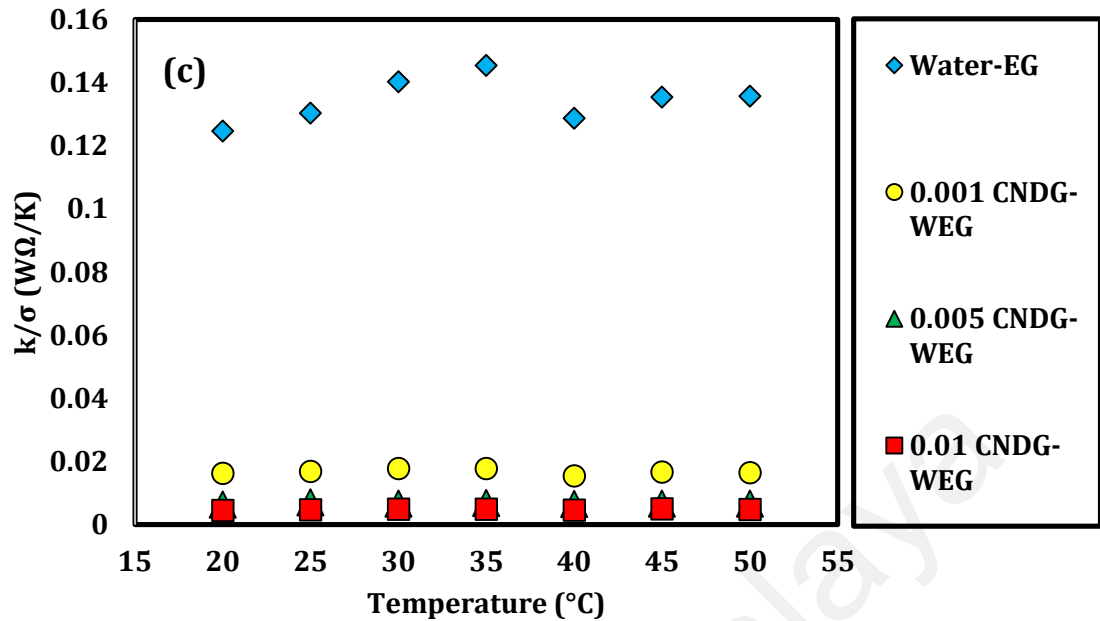


Figure 4.73: (a) Electrical conductivity and (b) enhancement in electrical conductivity of CNDG-WEG at different weight concentrations and temperatures (c) the ratio of the thermal conductivity (κ) to the electrical conductivity (σ) of CNDG-WEG for different weight percentages

Also, resistance of CNDG in solid phase was measured by using 4-point probe electrical measurements probe. The electrical conductivities of the CNDG were measured using a Jandel Multi Height Four-Point Probe. The electrical conductivity of the CNDG material was 2381 S/m, presumably due to the restoration of the graphene network by the formation of C–N bonded groups and N-doping (Li et al., 2009; X. Li, X. Wang, et al., 2008).

Also, the ratios of the thermal conductivity (κ) to the electrical conductivity (σ) of CNDG-WEG nanofluid at different weight concentrations are shown in Figure 4.73c. From this panel, the k/σ of the water-EG mixture versus temperature show some fluctuations, while the k/σ of the CNDG-WEG remains almost the same with the increase of temperature. A sharp increase in electrical conductivity and gradual increase in thermal conductivity resulted in decreasing k/σ with the increasing of temperature. It reached to about 0.007 WΩ/K for a weight fraction of 0.005 wt.% at the temperature range of 20-50 °C. No leveling off in k/σ of the present nanofluids by increasing weight concentration

was observed. The leveling off is due to the counter-ion condensation effect, indeed, it happens at high weight concentration (Steven et al., 2011), which is not observed here.

In the main results of this phase of study, the structural aspects, dispersion phenomena, electrical and thermal conductivity enhancement, and forced convective heat transfer coefficients affirm the superior electrical, thermal and rheological properties of CNDG-WEG. Further, the thermal conductivity and heat transfer enhancements in the presence of CNDG has been confirmed that the high specific surface area of CNDG and the thinning of the thermal boundary layer could be the main reasons for enhancing the heat transfer rate. The suitable stability without irreversible particle aggregation and improved thermal conductivity and heat transfer rate would enable the CNDG-WEG to be used as advanced alternative coolants in car radiators.

4.4.2 Ducts and channels with abrupt expansion

4.4.2.1 Introduction

Availability of highly-stable superconductive nanofluids (such as water-based HCFLG nanofluids, water-based SGr nanofluids) opens a new gateway for economical increase in the performance of thermal loops in industrial applications (Azmi et al., 2016; Cingarapu et al., 2014; Manimaran et al., 2014). Ducts and channels with abrupt expansion are broadly applied in different industrial applications and heat transfer equipment. These include passages of turbine blades, combustors, diffusers, and heat exchangers. Due to mixing of high and low energy fluids in the flow reattachment zone, the rate of heat transfer along with other thermal parameters are affected in the back-step flows. In particular, in the reattaching flow region, momentum, mass and heat transfer vary significantly due to the presence of reverse flows (Mohammed et al., 2015). There have been many mostly numerically performed studies in the literature to determine the effects of different parameters on the heat transfer performance as well as identifying the actual mechanism of flow separation and reattachment (Kherbeet, Mohammed, Salman,

et al., 2014; Kherbeet et al., 2015; Lancial et al., 2013; Mohammed et al., 2015; Sheikholeslami et al., 2015).

It is now known that one efficient way to increase the heat transfer rate in the separated flow regions is to use highly-conductive working fluids (E. Abu-Nada et al., 2008; Arzani et al., 2016; Solangi et al., 2016; Yarmand et al., 2016; Zeinali Heris et al., 2006). To take advantage of this potential, numerous researchers have been employing different suspension of metal and metal oxide nanoparticles (Mohammed, Al-Aswadi, et al., 2011; Zeinali Heris et al., 2006).

Eiyad Abu-Nada (2008) was one of the pioneers in studying the heat transfer of nanofluids in a backward-facing step flow. He synthesized CuO-, Al₂O₃-, Ag-, Cu- and TiO₂-based water nanofluids and investigated the rate of convective heat transfer enhancement for various nanofluids of different thermal conductivities. He concluded that the thermo-physical properties of the nanofluids, in particular the thermal conductivity, play the key roles in increasing Nusselt number particularly inside the recirculation zone.

In a similar work, Mohammed and coworkers (Mohammed et al., 2012; Mohammed, Al-aswadi, et al., 2011) studied the effects of different nanofluids on the mixed convective heat transfer coefficient in vertical and horizontal backward-facing steps. According to their results, the nanofluids with secondary recirculation regions have lower Nusselt number and the diamond-based water nanofluids showed a significant enhancement of Nusselt number. More recently, Kherbeet et al. (Kherbeet et al., 2012) studied the heat transfer rate of Al₂O₃-, CuO-, SiO₂- and ZnO-based water nanofluids in the laminar flow regime over a microscale backward-facing step. They reported that there was no recirculation region behind the step for all four nanofluids at various concentrations. They concluded that SiO₂-based water nanofluid showed the best performance among their prepared nanofluids.

The literature reviews of applications reveal that the majority of previous studies on the heat transfer over a backward-facing step used water-based suspension of metal or metal oxide nanofluids and the lack of highly-conductive nanofluids including the few-layered graphene with high stability and specific surface area is obvious. They were also mostly focused on heat transfer in the laminar regime and there is no reported study on transition and turbulent flow regimes over a backward-facing step. Thus, discovering the heat transfer behavior of water and highly-conductive nanofluids in the transition and turbulent flow regimes is the second target of this study.

To this end, three phases of study have been performed to investigate the heat transfer behavior of water-based highly crumpled few layered graphene nanofluids as well as water over a backward facing step. First of all, a quick and efficient functionalization procedure was developed to fabricate highly-crumpled, few layer graphene (HCFLG) and single layer graphene (SGr) flakes with large specific surface area (sections 4.2.1 and 4.2.2). Also, the methods of synthesizing HCFLG and SGR seem to be new, simple, cost-effective, and with the capability of mass-production. The HCFLG and SGR materials with nanoscopic porous morphology are of high specific surface areas based on BET analyses of nitrogen cryo-adsorption method. Morphology and structure of HCFLG and SGR were analyzed thoroughly (sections 4.2.1 and 4.2.2). Secondly, water-based HCFLG and water-based SGr nanofluids for different low weight concentrations were prepared, and thermo-physical properties and colloidal stability in the presence of covalent and non-covalent functional groups were investigated (sections 4.3.1 and 4.3.2). Lastly, heat transfers parameters such as Nusselt number (Nu) and the convective heat transfer coefficient (h) over a backward-facing step in both of the transitional and turbulent flow regimes were investigated for both the aforementioned nanofluids and compare with water as the basefluid. The results suggest that water-based

HCFLG and water-based SGr nanofluids are the highly conductive nanofluids at very low weight concentration.

4.4.2.2 Data Processing

Experimental measurements of the thermo-physical properties of water-based HCFLG and water-based SGr nanofluids including thermal conductivity, specific heat capacities, density and viscosities at different concentrations were performed. Heat transfer behavior and energy management of the synthesized coolant in the test-rig were studied and the convective heat transfer coefficient (h), Nusselt number (Nu), and pressure drop (ΔP) were evaluated. By measuring the temperatures at the inlet and outlet, and on the wall for different flow rates, the local convective heat transfer coefficients were obtained. The flow Reynolds number was calculated using,

$$Re = \frac{\rho U_{ave} D}{\mu} \quad (4.17)$$

where D , U_{ave} , μ and ρ are, respectively, the inner diameter of the test section, the average flow velocity, the viscosity, and the density of the working fluid. Also, U_{ave} is given as,

$$U_{ave} = \frac{\dot{m}}{\rho A_c} \quad (4.18)$$

where \dot{m} and A_c are the mass flow rate and surface area of the cross section. The local heat transfer coefficient " h_x " and local Nusselt number " Nu_x " can be obtained by the following equations:

$$Q = \dot{m} C_p (T_{out} - T_{in}) \quad (4.19)$$

$$q = \frac{Q}{A_w} \quad (4.20)$$

$$h_x = \frac{q}{T_{wx} - T_{bx}} \quad (4.21)$$

Also, the bulk temperature of fluid (T_{bx}) at the axial distance x is given as (Aravind et al., 2011):

$$T_{bx} = T_{in} + \frac{q/\pi Dx}{m^o C_p} \quad (4.22)$$

$$Nu_x = \frac{h_x D}{k} \quad (4.23)$$

In order to calculate the friction factor, “ f ”, the pressure drop across the test section was measured by a Foxboro™ differential pressure transmitter and Eq. (4.24) was used. That is,

$$f = \Delta P \frac{2D}{\rho U_{ave}^2 L} \quad (4.24)$$

Employing new working fluids as a coolant requires investigation of their thermal performance, as well as, their suitability as an appropriate alternative candidate for a range of Reynolds numbers and temperatures. According to researchers (Samira et al., 2014), use of nanofluids as the working fluids in heat exchangers provides increase in both heat transfer coefficient (positive effects) and pressure drop (negative effects). To assess the effectiveness of water-based HCFLG and water based SGr nanofluids, a performance index is evaluated which is represented by equation 4.25.

$$PI = \frac{h_{nf}/h_{bf}}{\Delta P_{nf}/\Delta P_{bf}} = \frac{R_h}{R_{\Delta P}} \quad (4.25)$$

Here R_h is the ratio of the heat transfer enhancement of the new coolant to the base-fluid, $R_{\Delta P}$ is the ratio of pressure drop of synthesized coolant to the base-fluid, and subscripts nf and bf , respectively, refer to the nanofluid and base fluid. As mentioned above, the use of nanofluids along with the sudden expansion in the duct not only increases the Nusselt number, but also increases the friction factor. In order to assess the overall performance of the system, including the thermal performance, as well as, the hydraulic performance of the system, the performance evaluation criterion (PEC) is evaluated. The PEC shows

the ratio of thermal performance of nanofluids in comparison to the Di-water to the hydraulic performance of nanofluids in comparison to Di-water. Mathematically, the PEC is given by (Manca et al., 2012),

$$PEC = \frac{Nu_{nf}/Nu_{bf}}{(f_{nf}/f_{bf})^{1/3}} \quad (4.26)$$

Equation (6.24) provides an appropriate parameter for clarifying the range of temperatures and velocities that the synthesized coolant can be used (Samira et al., 2014). To study the energy saving in the turbulent flow region, the pumping power can be measured (Mansour et al., 2007). Thus the pumping power ratio is represented by equation 4.27.

$$\frac{W_{nf}}{W_{bf}} = \left(\frac{\mu_{nf}}{\mu_{bf}}\right)^{0.25} \left(\frac{\rho_{bf}}{\rho_{nf}}\right)^2 \quad (4.27)$$

where W_{nf} and W_{bf} are, respectively, the pumping powers for the nanofluid and the basefluid.

The uncertainty analysis of the experimental data for the heat transfer and flow characteristics in the test-rig are of critical importance to ensure the range of validity and the applicability of the test results. Here uncertainty analysis according to the method described by Kline and McClintock (S. J. Kline, and F. A. McClintock, January 1953) was performed and the resulting uncertainties in the Nusselt number, heat transfer coefficient and friction factor measurements are listed in Table 4.13 and Appendix A. The measurement uncertainties in the friction factor, heat transfer coefficient, and performance index (ε) were calculated as follows:

$$\frac{\Delta\varphi}{\varphi} = \frac{1}{\varphi} \sqrt{\sum_{i=1}^n \left(\frac{\partial\varphi}{\partial x_i} \times \Delta x_i\right)^2} \quad (4.28)$$

where ϕ is the derived parameter, x represents the measured variables, and Δx represents the error of the measured variables.

Table 4.13: Measurement uncertainties.

Parameters	Maximum uncertainty (%)
Friction factor	5.3%
Nusselt number	4.1%
Performance index (ϵ)	5.7%

4.4.2.3 Heat transfer Over a Backward Facing Step Flow

4.4.2.3.1 Water-Based HCFLG Nanofluids

In this section, experimental investigations of heat transfer over a backward facing step flow of the HCFLG nanofluids in transitional and turbulent flow regimes are presented. The water-based highly crumpled few layer graphene nanofluids with different weight concentrations were synthesized and used in these experimentations. The experimental data for the rate of heat transfer for different Reynolds numbers in the range of $2000 \leq Re \leq 16000$ and HCFLG concentrations of 0.001, 0.005 and 0.01 wt.% of HCFLG were obtained. A constant heat flux of 600 W was provided after the expansion via two DC power supply units. The inlet fluid rate was in the range of 1 to 16 Lit/min. Also, the inlet flow temperature was always maintained at a constant temperature of 30 ± 1 °C.

Figure 4.74 shows the temperature of the heated wall (T_s), the temperature difference between the wall and the fluid bulk ($T_s - T_b$), local convective heat transfer coefficient (h) and Nusselt number (Nu) versus X/D for distilled water at different Reynolds numbers (Re). In both plots of T_s versus X/D and $T_s - T_b$ versus X/D , a U-shape variation of the T_s or $T_s - T_b$ with X/D is seen. Heat transfer in back ward facing step was studied by a number of researches (Eiyad Abu-Nada, 2008; Lancial et al., 2013; Mohammed et al., 2015) in the recent years. Here, the boundary layer flow separates at the sharp step edge and form a recirculation region, as shown schematically in Figure 3.6.

The shear layer, downstream, impinges on the surface and reattaches to the lower wall at the so-called the reattachment point (Eaton & Johnston, 1981). Downstream of the reattachment point, the boundary layer begins to redevelop and far downstream the flow approached fully developed flow in the larger diameter pipe. The separation and reattachment in this area cause major changes in the flow in this region. Close to the step, the velocity is insignificant, leading to the maximum wall temperature and consequently minimum Nusselt number. On the other hand, the velocity can reach the maximum amount in the recirculation zone, where the wall temperature is minimum and the Nusselt number is maximum. So, a U-shape variation of the T_s or T_s-T_b with X/D is reasonable and were reported by a majority of recent studies in this field (Eiyad Abu-Nada, 2008; Lancial et al., 2013; Mohammed et al., 2015).

Thus, there is a sharp downward trend of temperature with X/D up to ~ 2.66 , after which both of the temperature of the heated wall (T_s) and the temperature difference between the wall and the fluid bulk for the deionized water increase moderately with further increase of X/D . The heat transfer coefficient was computed from the temperature given by the thermocouples in different positions. Eqs. (6.18) and (6.20) indicate that the local convective heat transfer coefficient (h_x) and local Nusselt number (Nu_x) have an inverse relation with the temperature difference between the wall and the bulk fluid. Therefore, for X/D less than 2.66 for distilled water, the amount of local convective heat transfer coefficient (h) and local Nusselt number (Nu) increase. By contrast, the h and Nu show a downward trend for X/D higher than 2.66. Figures 4.75, 4.76 and 4.77 present the measured temperature of the heated wall (T_s), the measured temperature difference between the wall and the fluid bulk (T_s-T_b), local convective heat transfer coefficient (h) and Nusselt number (Nu) for different Re numbers and X/D location for water-based HCFLG nanofluids with concentrations of 0.001, 0.005 and 0.01 wt%, respectively.

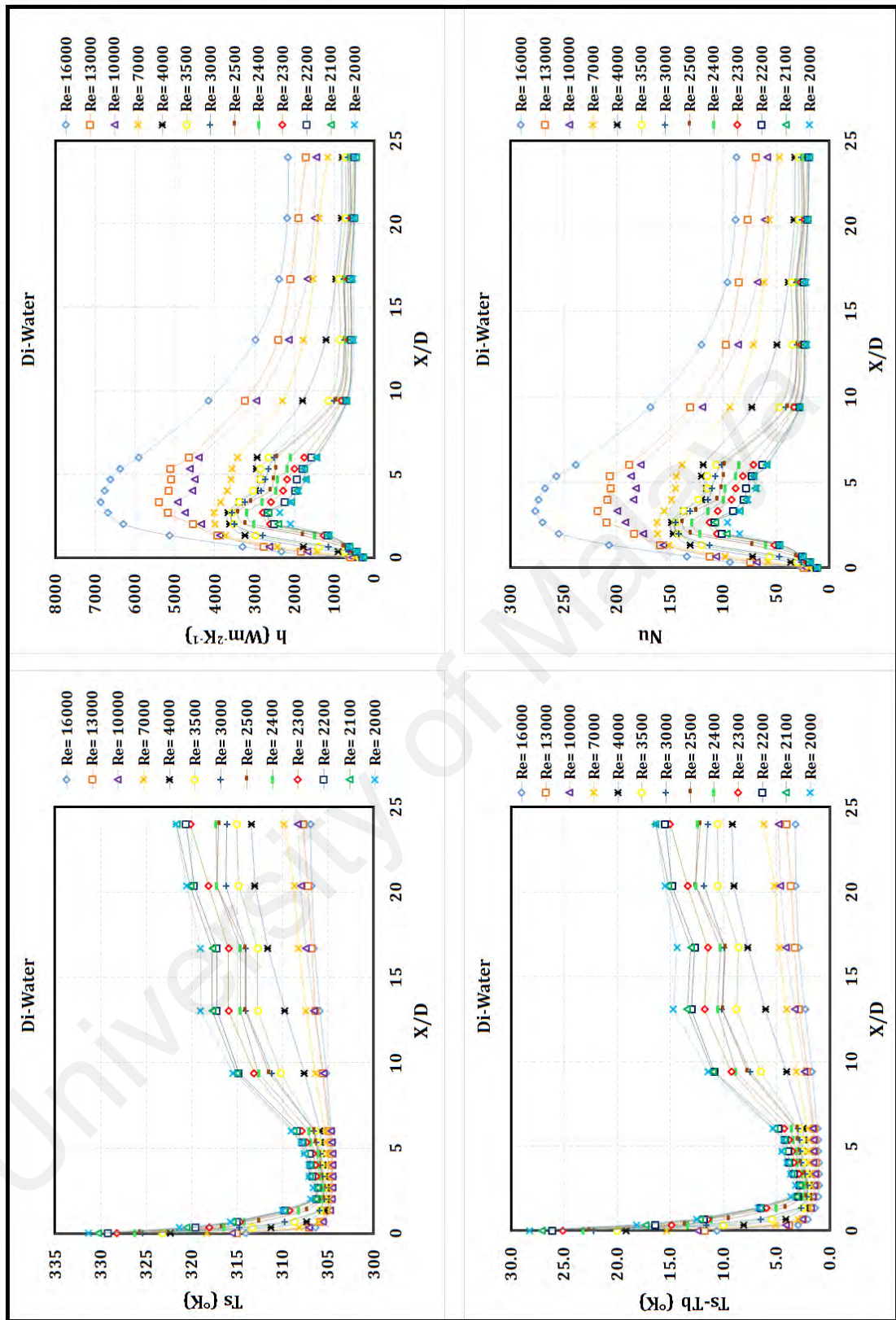


Figure 4.74: Measured temperature of the heated wall (T_s), the temperature difference between the wall and the fluid bulk ($T_s - T_b$), local convective heat transfer coefficient (h) and Nusselt number (Nu) versus X/D for distilled water at different Reynolds numbers (Re).

Like distilled water, these figures show a similar U-shape variation of the T_s or $T_s - T_b$ with X/D , representing a sudden decrease and a gradual increase. Also, the local convective heat transfer coefficient (h_x) and local Nusselt number (Nu_x) show the same trends as the variations of distilled water. From a comparison between Figures 4.74-4.77, it is observed that the measured temperature of the heated wall (T_s) and the measured temperature difference between the wall and the fluid bulk temperature ($T_s - T_b$) become closer for higher weight concentration of HCFLG, representing the key role of HCFLG in transferring heat in the recirculation zone. All of the Nusselt profiles present the same characteristic behavior: their values are low in the recirculation zone, increase through a maximum at the reattachment point and decrease in the recovery region to a stable value, as observed by Nie and Armaly (Nie & Armaly, 2002) for a confined configuration.

Also, as the concentration of HCFLG in nanofluids increases, the U-shape variation of the T_s or $T_s - T_b$ with X/D becomes wider. As mentioned above, the local convective heat transfer coefficient and local Nusselt number have the inverse relationship with the measured temperature difference between the wall temperature and the fluid bulk temperature.

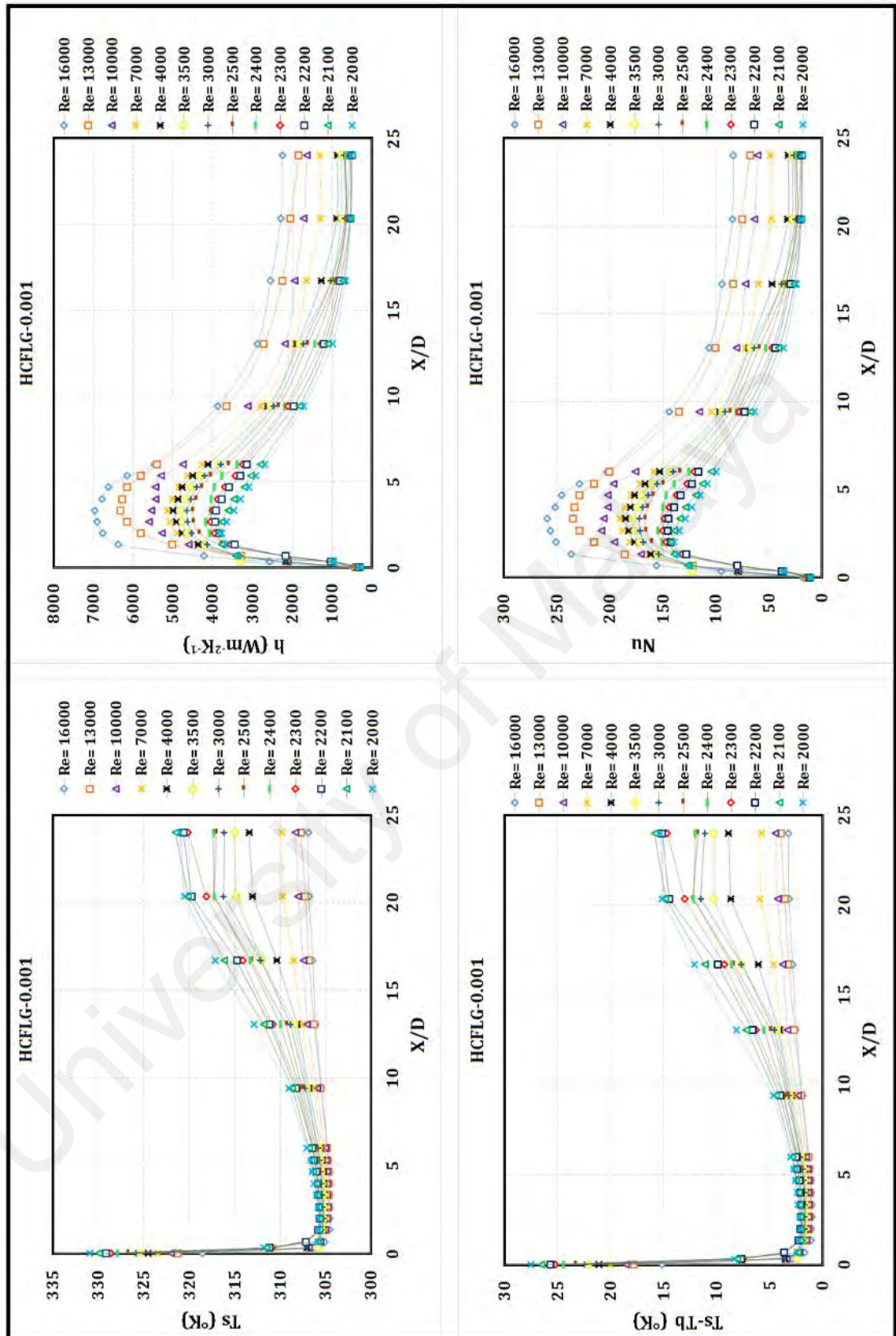


Figure 4.75: Measured temperature of the heated wall (T_s), the temperature difference between the wall and the fluid bulk ($T_s - T_b$), local convective heat transfer coefficient (h) and Nusselt number (Nu) versus X/D for water-based HCFLG nanofluid at 0.001 wt%.

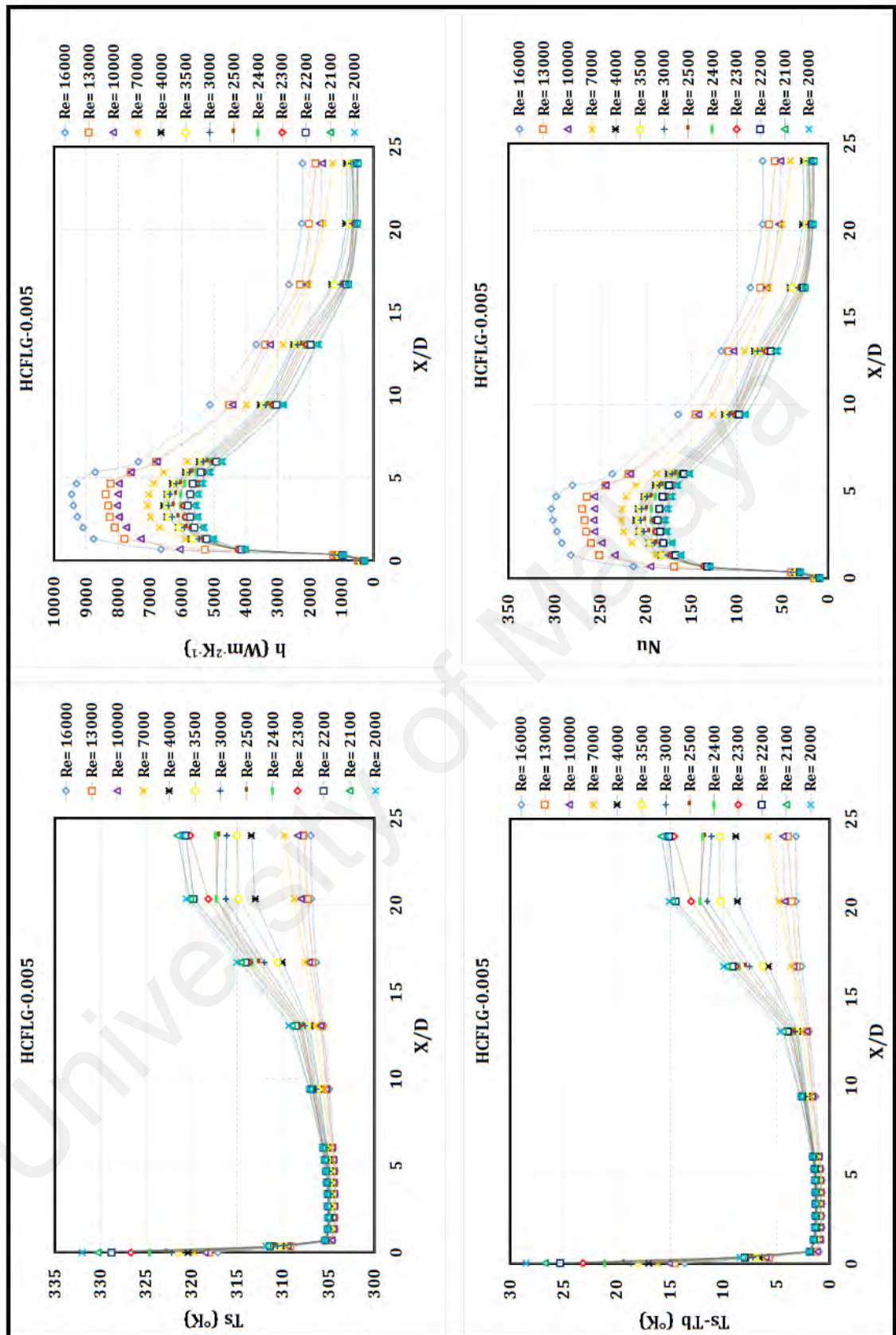


Figure 4.76: Measured temperature of the heated wall (T_s), the temperature difference between the wall and the fluid bulk ($T_s - T_b$), local convective heat transfer coefficient (h) and Nusselt number (Nu) versus X/D for water-based HCFLG nanofluid at 0.005 wt%.

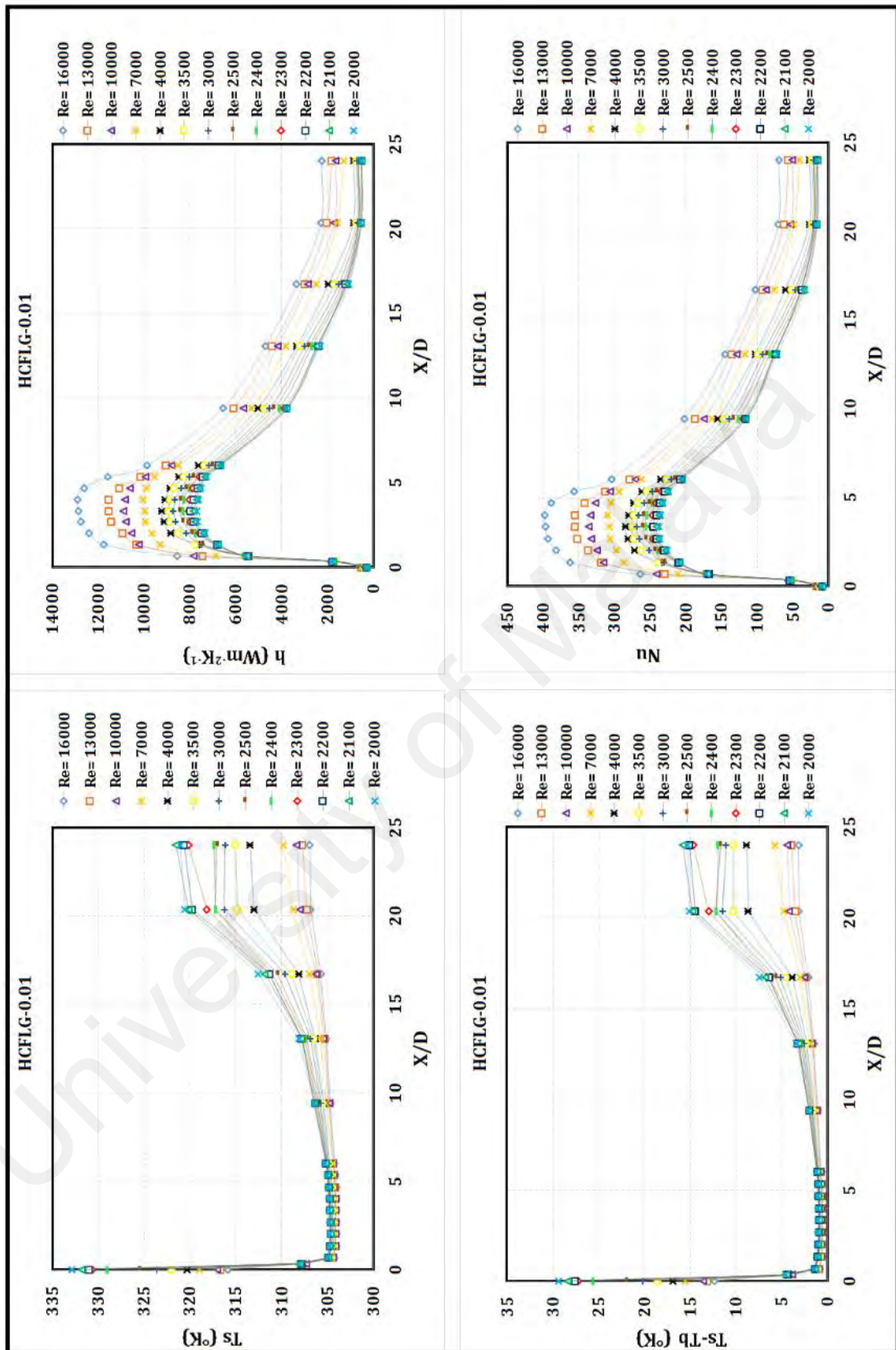


Figure 4.77: Measured temperature of the heated wall (T_s), the temperature difference between the wall and the fluid bulk ($T_s - T_b$), local convective heat transfer coefficient (h) and Nusselt number (Nu) versus X/D for water-based HCFLG nanofluids at 0.01wt%.

In order to perform an appropriate comparison, the variation of average heat transfer coefficient with the Reynolds number for water-based HCFLG nanofluids at different weight concentrations as well as water were evaluated, as shown in Figure 4.78. For all the samples, the average heat transfer coefficient increases with the Reynolds number and weight concentrations. The highest average heat transfer coefficient was achieved for water-based HCFLG nanofluid with weight concentration of 0.01% and Re number of 16,000, representing the average heat transfer coefficient of 5520.26 W/m²K. For instance, the maximum ratio of enhancement in the average heat transfer coefficient was almost 60% for water-based HCFLG nanofluid at 0.01 wt.% and Re number of 16,000 as compared with pure water, where the improvement is brilliant.

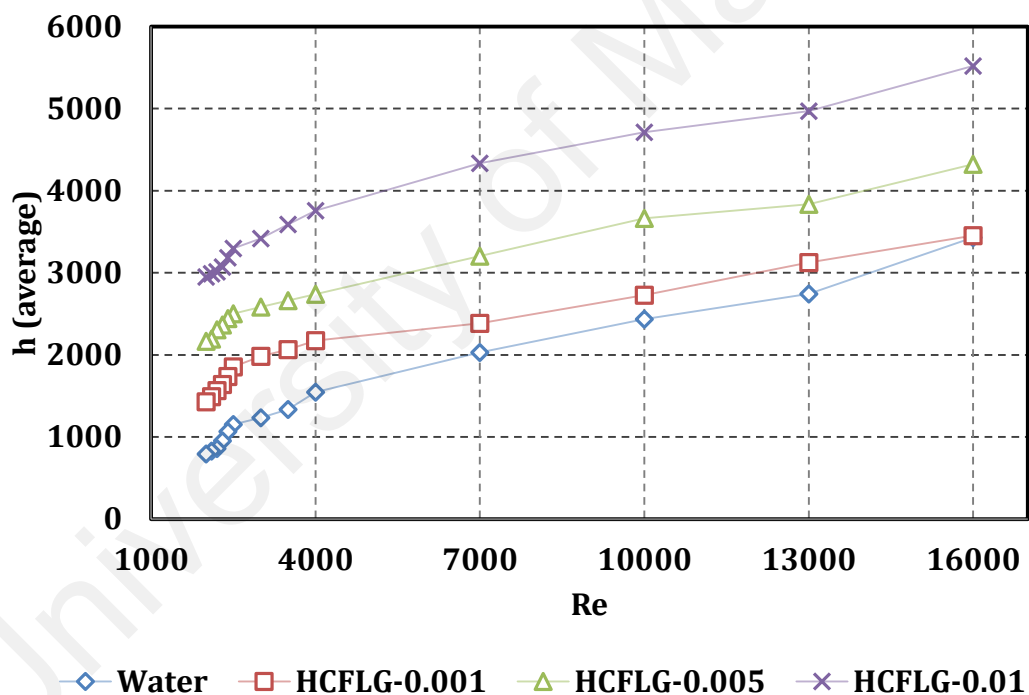


Figure 4.78: Average heat transfer coefficient of distilled water and water-based HCFLG nanofluids over a backward-facing step.

In order to clarify the key role of weight concentration of HCFLG, the measured results for Nusselt number are shown for the Reynolds numbers of 2000, 3500, 7000, 13000 in Figure 4.79. These four Reynolds numbers were selected as the candidates for

all the conditions. It is seen, as the concentration of HCFLG in nanofluids increases, the Nu number increases at a constant Re number. However, Figure 4.79 shows that the effects of HCFLG concentration on the Nusselt number term are more pronounced than other parameters. The reason for larger enhancement of the Nusselt number for the nanofluids compared to that of the distilled water was recommended by S. J. Aravind et al. (2011) using a simple analogy. Accordingly, the convective heat transfer is proportional to k/δ_t , where δ_t is the thickness of the thermal boundary layer. Thus, to increase the convective heat transfer coefficient, k should be increased and/or δ_t should be decreased. According to (S. J. Aravind et al., 2011; S. J. Aravind & S. Ramaprabhu, 2013), carbon nanomaterials such as carbon nanotubes and graphene have a tendency to decrease the thermal boundary layer thickness. On the other hand, as the concentration of HCFLG increases, the measured thermal conductivity of the nanofluids increases, implying higher convective heat transfer coefficient. Therefore, both the thermal boundary layer thickness term and thermal conductivity term have positive effects on increasing heat transfer rate. Therefore, nanofluids with higher weight concentration (higher thermal conductivity) have more enhancements on the value of the Nusselt number. This conclusion is consistent with the recent studies (Eiyad Abu-Nada, 2008). Obviously, the maximum value of Nusselt number coincides with the point of reattachment. Like other studies (Eiyad Abu-Nada, 2008; Heshmati et al., 2014), after the point of reattachment, an increase in Nusselt number is observed by increasing the weight concentration of the HCFLG. Therefore, the high Nusselt number inside the recirculation depends mainly on the thermo-physical properties of the nanoparticles. Also, both the Reynolds number and the thermo-physical properties of the nanofluids affect the values of Nusselt numbers outside the recirculation zone.

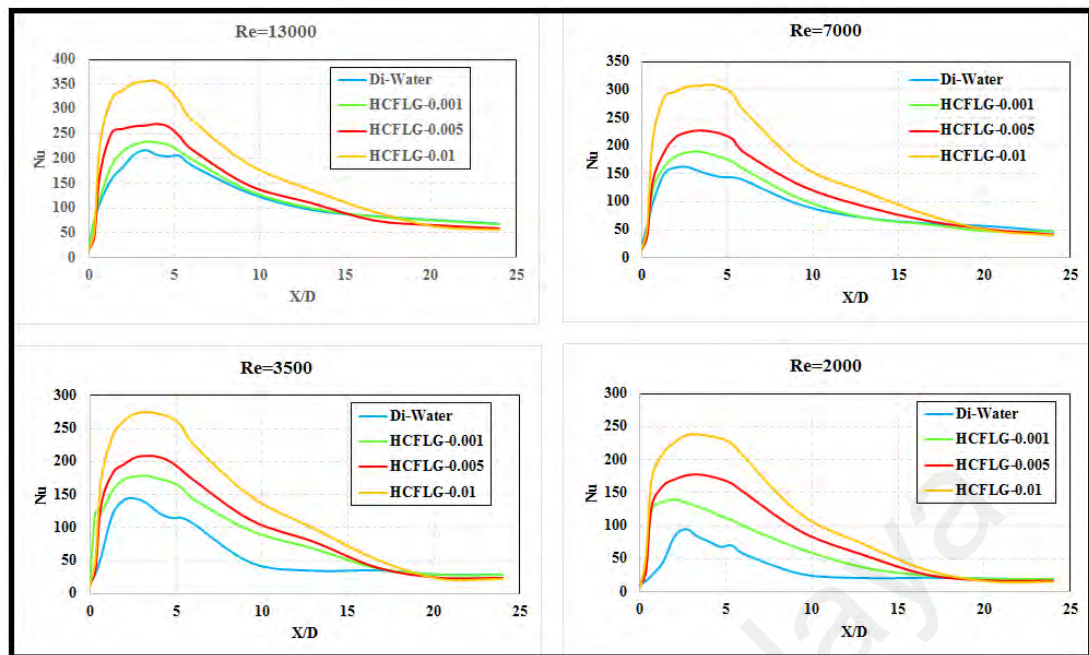


Figure 4.79: The effects of Reynolds numbers and weight concentrations of HCFLG on the Nusselt numbers at different axial ratios.

Figures 4.76, 4.77, 4.78 and 4.79 show that the position of maximum Nusselt number (X_{\max}/D) changes as the Re number changes. Figure 4.80 shows the variations of X_{\max}/D for water-based HCFLG nanofluids and distilled water for different Re numbers and weight% concentrations. It is seen that the position of maximum value of Nusselt number increases (shifts up) with the Re number and weight concentration of HCFLG. It is observed that as the concentration increased, the temperature difference between the tube wall and the working fluid decreased due to higher thermal conductivity, implying higher heat transfer rate. For the same expansion ratio of 2, it is observed that the higher Re number leads to the higher Nu_x . For the same expansion ratio of 2 and Re number of 16000, the experimentally measured values of X_{\max}/D are 4.66, 3.99, 3.33 and 3.33 for water-based HCFLG nanofluids at 0.01, 0.005, 0.001 and 0.0 wt% respectively. The position as well as the value of X_{\max}/D increased as the Re number increased, representing that X_{\max} is dependent of Re and concentration of additives (thermal conductivity).

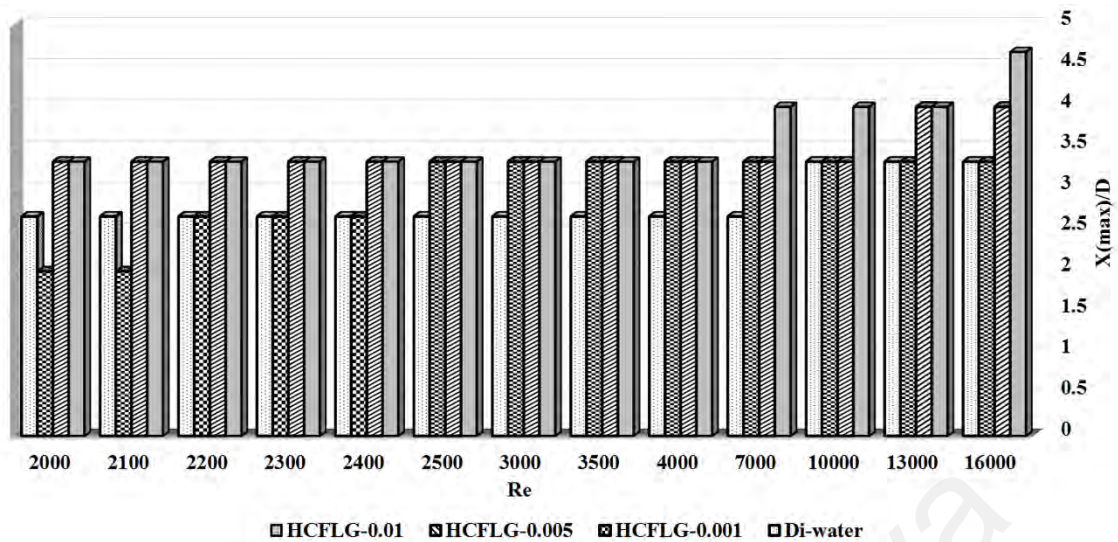
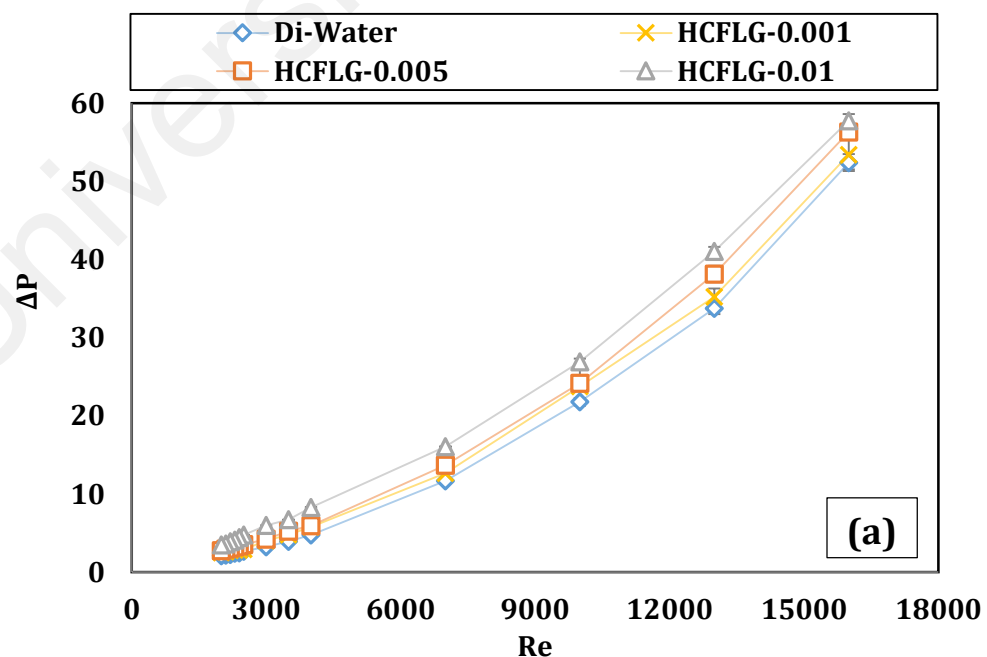


Figure 4.80: The effects of Reynolds numbers and weight concentrations of HCFLG on the position of maximum Nusselt numbers.

Figure 4.81a represents the plots of the pressure drop of flow over the backward-facing step for different Re numbers and weight concentrations of HCFLG including distilled water. It is seen that as the Re number and concentration of HCFLG in the basefluid increase, the pressure drop increases. It is noteworthy that the pressure drops for the prepared samples are quite close to that for the distilled water, which is attributed to the low concentrations of 0.001 wt%, 0.005 wt% and 0.01 wt%. Figure 4.81a also shows that the pressure drop for the water-based HCFLG nanofluids at the concentration of 0.01 wt.% and Re number of 16000 has the highest pressure drop for the current range of measurements. Note that the pressure drop is proportional to the viscosity of the working fluids, which exhibit the highest and the lowest amounts corresponding to the highest and the lowest viscosities in the similar conditions.

The friction factor for the flow over the backward-facing step at different Re numbers as well as weight concentrations of HCFLG is shown in Figure 4.81b. It is seen that the measured friction factor decreases with the increase of the Re number for different weight concentrations of HCFLG. In addition, the friction factor increases as the concentration of HCFLG increases, although percentage of enhancement is more obvious

in low values of the Re numbers. As expected, the minimum value of friction factor occurs for the base fluid. It is also seen as the Re number increases, the dependence of friction factor on the weight concentration of HCFLG decreases. At low Reynolds numbers, the Brownian motion is the main mechanism that influences the momentum transfer between the HCFLG and the base-fluid molecules. Thus, as the Brownian motion increases, the concentration of HCFLG in the nanofluids increases, which causes the increase of the friction factor with higher slope as compared with base fluid (Mohammed, Al-Aswadi, et al., 2011). In contrast, this mechanism loses its dominance for high Reynolds number flows, where turbulent agitations in flow play the key role. In summary, the turbulence of the working fluid can be considered as the most important parameters in increasing the friction factor at the high Reynolds numbers. Also, the small difference between the friction factors of the distilled water and the water-based HCFLG suspensions at different weight concentrations is attributed to the small difference between viscosities of base fluid and the prepared nanofluid samples.



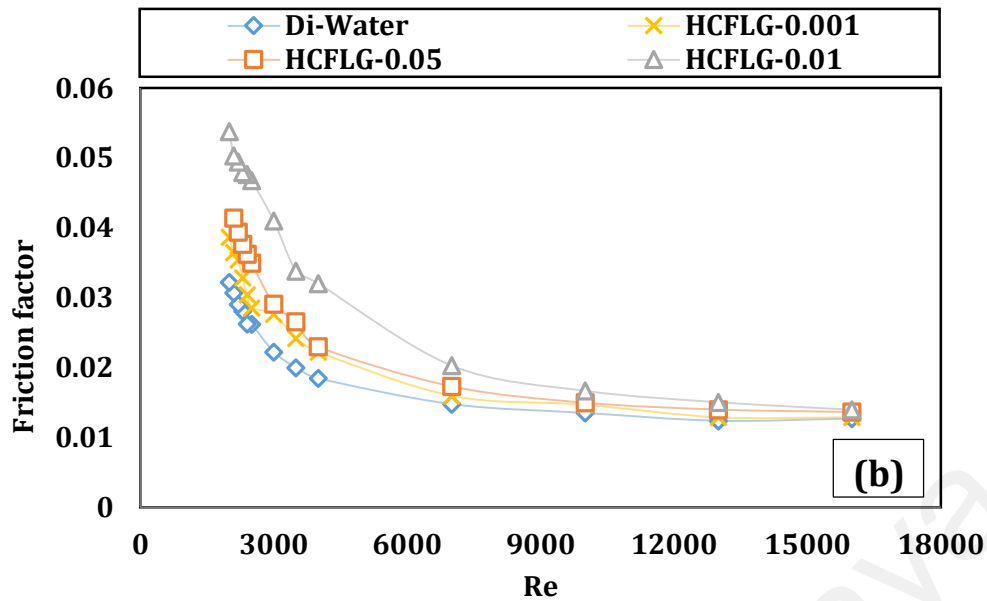
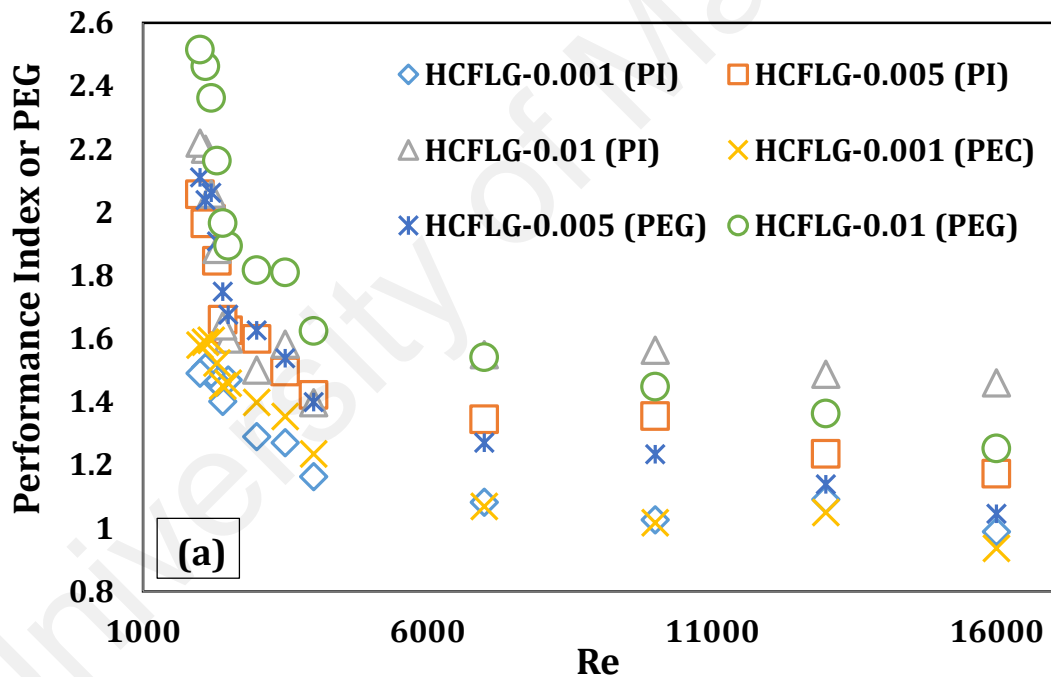


Figure 4.81: (a) The measured values of pressure drop in the set-up at different Re numbers for distilled water and water-based HCFLG nanofluids with different weight concentrations. (b) Experimental friction factor for distilled water and water-based HCFLG nanofluids with different weight concentrations at different Re numbers.

The economic performance of working fluids for different heat transfer equipment is measured via performance index (ϵ), which identified as the ratio of the heat transfer rate to the pressure drop ratios. Recent studies (e.g., (Samira et al., 2015)) suggested that while the addition of solid nanoparticles improves the heat transfer rate, the pressure drop in the flow loops also increases, which is undesirable. Therefore, performance index is presented to consider both parameters. The variations of the average performance index and PEC for water-based HCFLG nanofluids are illustrated for different Re numbers and weight concentrations in Figure 4.82a. It is seen that the average performance index as well as PEC of all the samples including HCFLG is higher than 1, representing the effectiveness of the prepared coolant samples for use over the backward-facing step flows. It is also seen, as the weight concentration of HCFLG in nanofluids increases, the average performance index as well as PEC increase, which shows that the enhancement in heat transfer is more effective compared to the increase in pressure drop. This figure

also shows that the average performance index curves for different Re numbers. Also, the performance index results showed a gradual decrease with Re numbers.

Pumping power ratio can be considered as an economic performance indicator in a loop system for evaluating the operability of fluid and performance of the power plant. Figure 4.82b compares the pumping power of the water-based HCFLG nanofluids for different weight concentrations with that of the base-fluid. This figure shows that there is a slight increase in the pumping power with the HCFLG loading but the percentage of pumping power increase is negligible. The small growth in the pumping power can be due to the low weight fraction of HCFLG in base fluid.



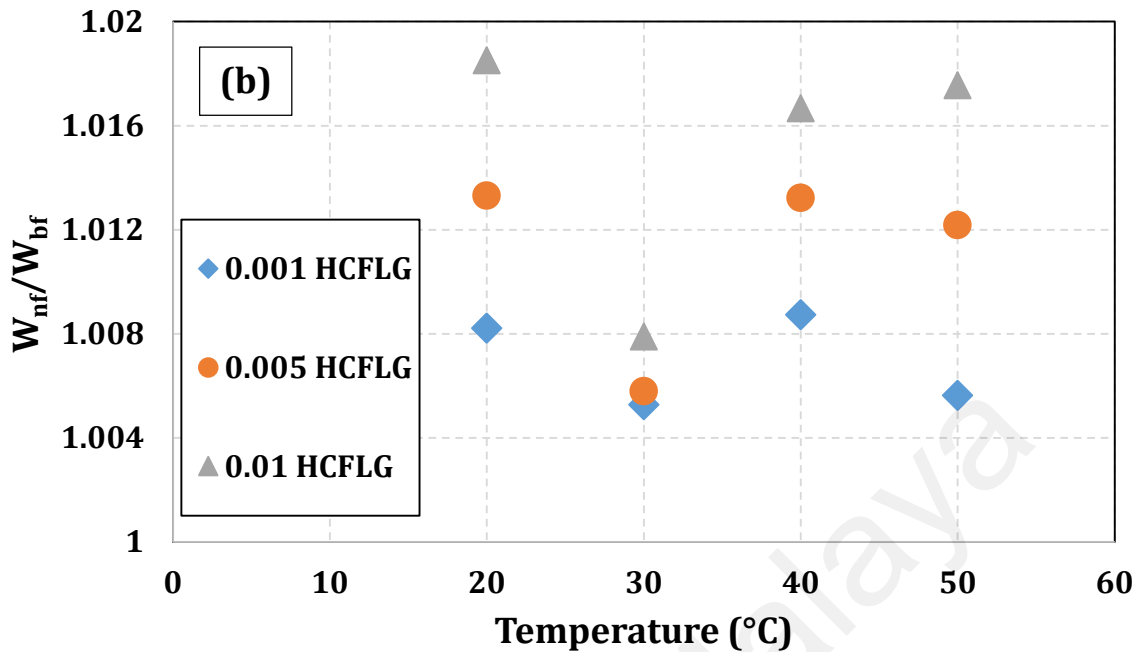


Figure 4.82: (a) Performance evaluation criterion (PEC) and performance index (PI) of water-based HCFLG nanofluid; (b) pumping power ratio for the backward-facing step in the presence of distilled water and water-based SGr nanofluids with different weight concentrations.

As a summary of study, a simple and cost-effective approach was utilized for mass production of the HCFLG with large specific surface area. Highly-crumpled few layer graphene was then used as an additive for preparing highly stable and highly conductive nanofluids with superior thermo-physical properties. The results suggested that the thermo-physical properties of water-based HCFLG nanofluids were enhanced, that makes the nanofluid well-suited for heat transfer applications. The heat transfer results showed that the water-based HCFLG nanofluids at very low concentrations exhibited noticeably higher heat transfer rate compared to the distilled water. The overall heat transfer rate showed a 90% enhancement by loading just 0.01 wt% of HCFLG into the distilled water. Also, experimental data for the Nu number and local heat transfer coefficient of water-based HCFLG nanofluids for transitional and turbulent flow regimes were presented. The data showed that as the wt% of HCFLG in the nanofluids and/or Re number increase over backward-facing step, the position of maximum heat transfer point

X_{\max}/D shifts to the higher distances, leading to larger recirculation zone. The presented results showed that the water-based HCFLG nanofluid is a great candidate for a new generation of heat transfer fluids.

4.4.2.3.2 Water-Based SGr Nanofluids

For the first time, experimental investigation of heat transfer over a backward facing step using nanofluids is presented for the transitional and turbulent flow regimes. A promising water-based SGr nanofluid with unique thermo-physical properties were synthesized. The experimental study examines the rate of heat transfer over a backward-facing step for different Reynolds numbers and weight concentrations of SGr. To address this issue, water-based SGr samples with three weight concentrations of 0.001, 0.005 and 0.01 wt% were utilized and Nusselt number as a candidate for introducing heat transfer rate were measured in the range of $2000 \leq Re \leq 16000$. Figure 4.83 shows the temperature of the heated wall (T_s) and the temperature difference between the wall and the fluid bulk ($T_s - T_b$) of water-based SGr nanofluids with different weight concentrations and distilled water for different Re numbers and X/D locations. In both plots of T_s vs. X/D and $T_s - T_b$ vs. X/D, a U-shape variation of the T_s or $T_s - T_b$ with X/D is seen. That is, there is a sharp downward trend of temperature with X/D up to almost 2.66, after which both the temperature of the heated wall (T_s) and the temperature difference between the wall and the fluid bulk for the deionized water increase gradually with further increase of X/D. From Figure 4.83, it is observed that the measured temperature of the heated wall (T_s) and the measured temperature difference between the wall and the fluid bulk temperature ($T_s - T_b$) become closer for higher weight concentration of SGr. Also, as the concentration of SGr in nanofluids increases, the U-shape variation of the T_s or $T_s - T_b$ with X/D becomes wider.

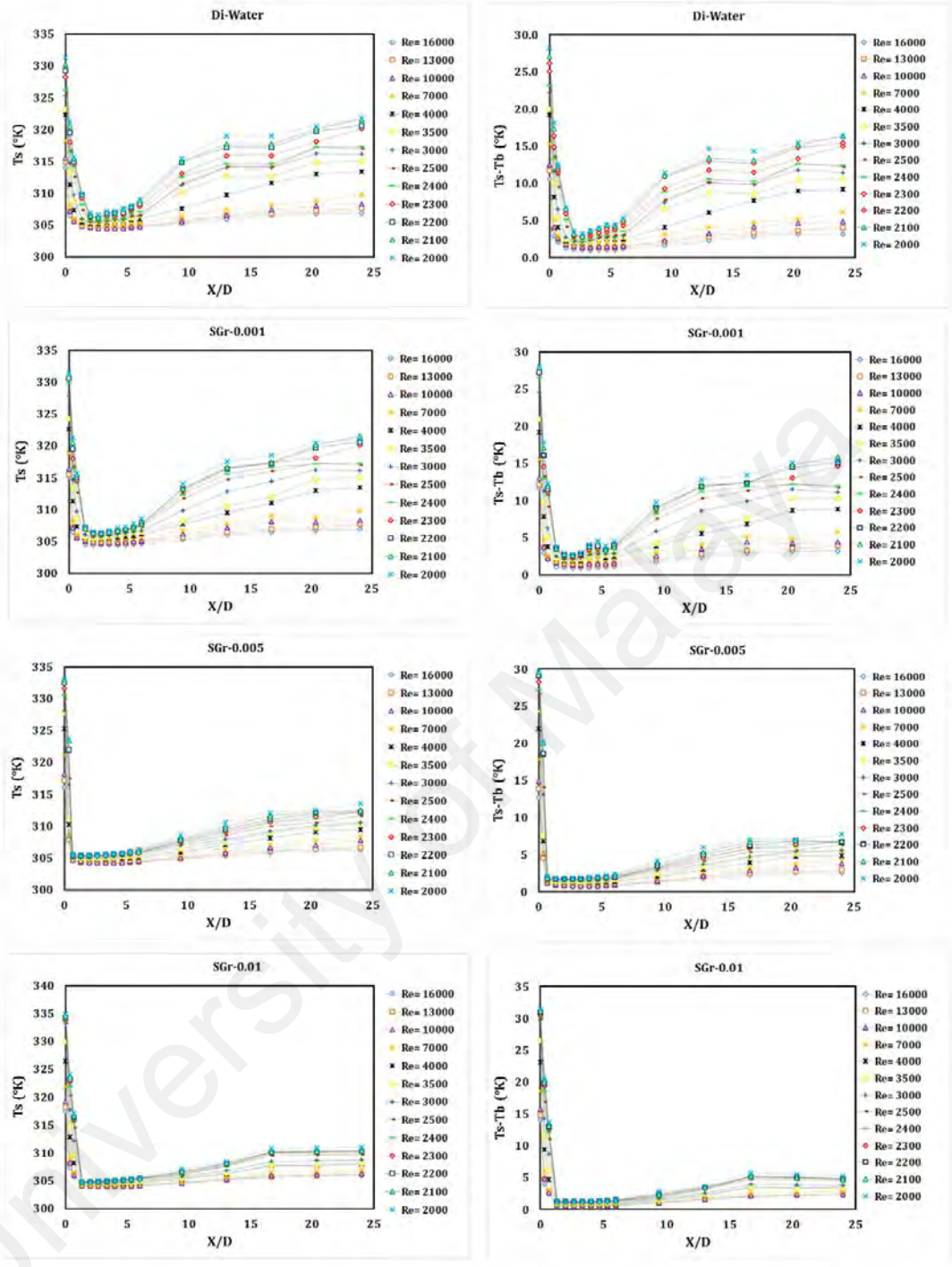


Figure 4.83: The temperature of the heated wall (T_s) and the temperature difference between the wall and the fluid bulk ($T_s - T_b$) for water and water-based SGr nanofluids.

Eqs. (6.18) and (6.20) indicate that the local convective heat transfer coefficient (h_x) and local Nusselt number (Nu_x) have a diverse connection with the temperature difference between the wall and the bulk fluid. Therefore, for X/D less than ~ 2.66 for distilled water, the amount of local convective heat transfer coefficient (h) and local

Nusselt number (Nu) should be increased. By contrary, the h and Nu show a downward trend for X/D higher than ~ 2.66 , which is obvious in Figure 4.84.

Figures 4.84 present the measured Nusselt number of water and samples with different weight concentrations of 0.001, 0.005 and 0.01 wt% for different Re numbers and X/D axial ratios. It can be seen that the local Nusselt number (Nu_x) peaked at the X/D range of 3 to 4 before starting to decrease gradually. From a comparison between panels in Figure 4.84, the local Nusselt number has the diverse relationship with the measured temperature difference between the wall temperature and the fluid bulk temperature. Note that as the weight concentration increases, the local Nusselt number for all axial ratios increases, representing higher heat transfer rate than that of base fluid.

In order to perform an appropriate comparison, the variation of average heat transfer coefficient with the Reynolds number for water-based SGr nanofluids at different weight concentrations as well as water were evaluated, as shown in Figure 4.85a. For all the samples, the average heat transfer coefficient increases with the Reynolds number and weight concentrations. The highest average heat transfer coefficient was achieved in water-based SGr nanofluid at the weight concentration of 0.01% and Re number of 16,000, such as the average heat transfer coefficient of 6306.18 W/m²K. For instance, the ratio of enhancement in the average heat transfer coefficient was 83.8% for water-based SGr nanofluid at 0.01 wt% and Re number of 16,000 as compared with pure water, which is a brilliant improvement.

From Figure 4.85b, despite some initial fluctuations, the average heat transfer coefficient ratio $(h_{nf} / h_{bf})_{ave}$ showed a downward trend with increasing of Reynolds number for all the concentrations. For example, as the Re number increased from 2000 to 16000, the $(h_{nf} / h_{bf})_{ave}$ ratio decreased from 233.5 % to only 83.8% at 0.01 wt%; from 132.9 % to 42.4% at 0.005 wt%; and from 5.6 % to only 18.4% at 0.001 wt%. From

which, it can be found that the increase in the weight concentration of SGr enhances the $(h_{nf} / h_{bf})_{ave}$ ratio.

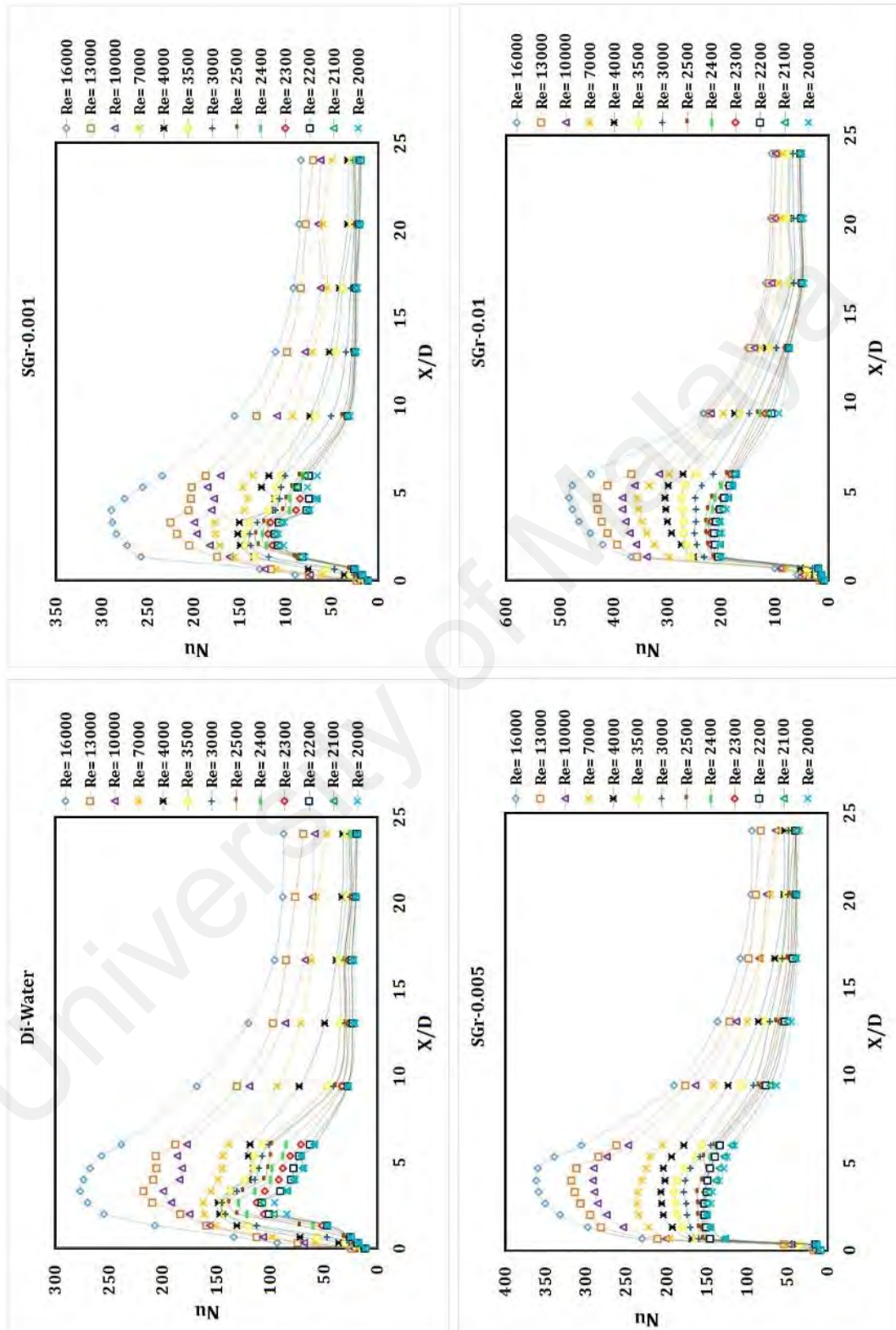


Figure 4.84: Experimental Nusselt number of distilled water and water-based SGr nanofluids at weight concentrations of 0.001, 0.005 and 0.01% for different Re numbers.

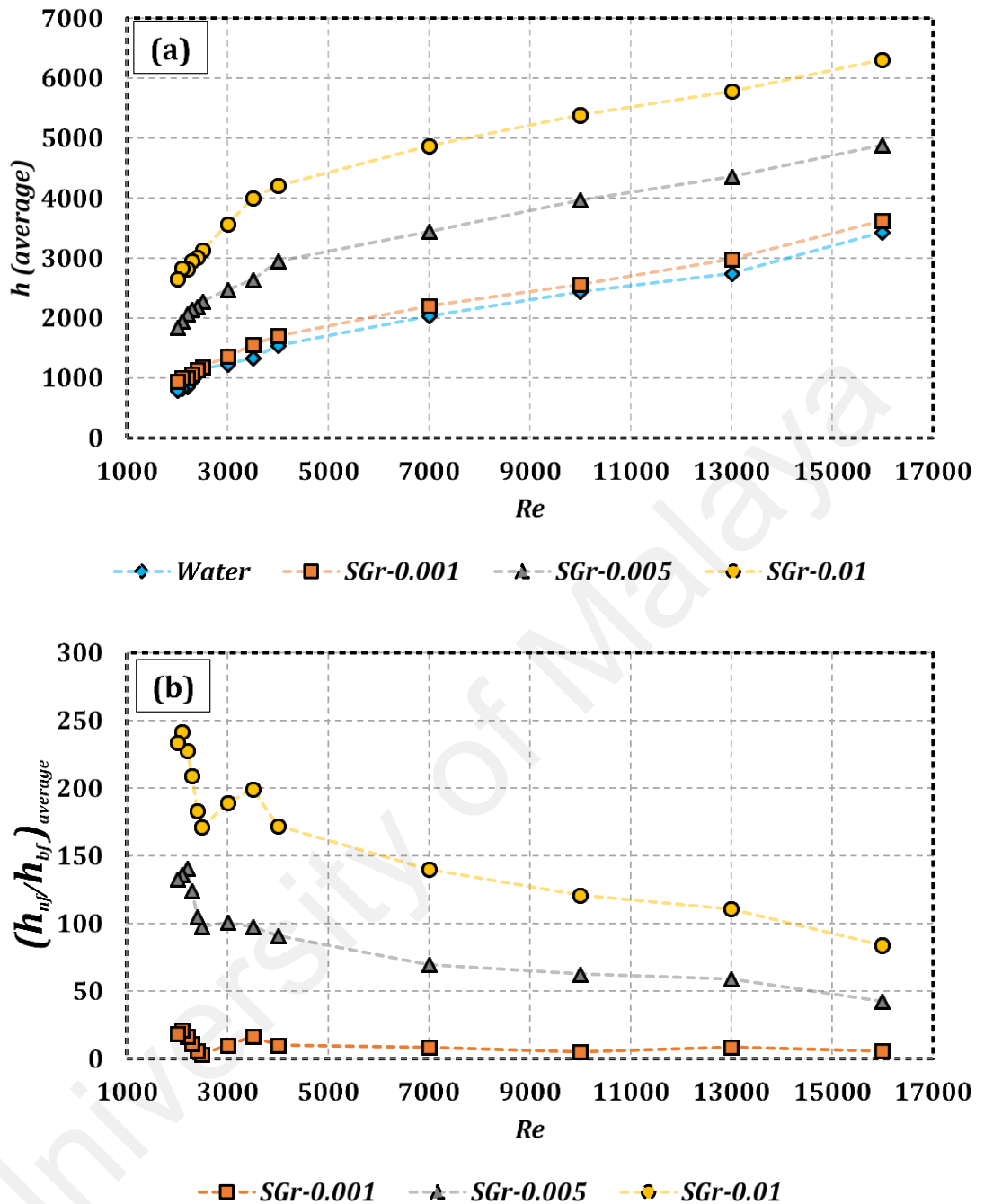


Figure 4.85: Average heat transfer coefficient of distilled water and water-based SGr nanofluids over a backward-facing step.

In order to clarify the key role of weight concentration of SGr in samples, the measured Nusselt number for Reynolds number of 2000, 3500, 7000, 16000 are shown in Figure 4.86. From Figure 4.86, as the weight concentration of SGr in nanofluids increases, the Nu number increases. The effect of weight concentration of SGr in water-

based nanofluids on the temperature gradient term ($T_s - T_b$) is not negligible. However, Figure 4.86 shows that the effects of weight concentration of SGr on the temperature gradient term and on the thermal conductivity term are more pronounced. The reason for larger enhancement of the Nusselt number of nanofluids compared to that of distilled water was introduced by S. J. Aravind et al. (2011) using a simple analogy that the convective heat transfer is proportional to k/δ_t where δ_t is the thickness of thermal boundary layer. Thus, to increase the convective heat transfer coefficient, k can be increased and/or δ_t can be decreased. According to (S. J. Aravind et al., 2011; S. J. Aravind & S. Ramaprabhu, 2013), carbon nanomaterials such as carbon nanotubes and graphene have a tendency to decrease the thermal boundary layer thickness. On the other hand, as the concentration of SGr increases, the measured thermal conductivity of nanofluids increases, implying higher convective heat transfer coefficient. Therefore, both the thermal boundary layer thickness term and thermal conductivity term have positive effects on increasing heat transfer rate in the presence of nanofluids including carbon nanostructures. It is interesting to note that nanofluids with higher weight concentration (higher thermal conductivity) show higher convective heat transfer coefficient, indicating the key role of carbon nanostructure on increasing thermal conductivity and decreasing the thermal boundary layer thickness. This conclusion is the same with the recent studies (Eiyad Abu-Nada, 2008). According to (Eiyad Abu-Nada, 2008), the maximum value of Nusselt number coincides with the point of reattachment. Like other studies (Eiyad Abu-Nada, 2008; Heshmati et al., 2014), after the point of reattachment, an increase in the convective heat transfer coefficient is observed by increasing the weight concentration of the nanoparticles. Therefore, the high convective heat transfer coefficient inside the recirculation depends mainly on the thermo-physical properties of the nanoparticles. Also, both of the Reynolds number and the thermo-

physical properties of the nanofluids affect the value of the heat transfer coefficient outside the recirculation zone.

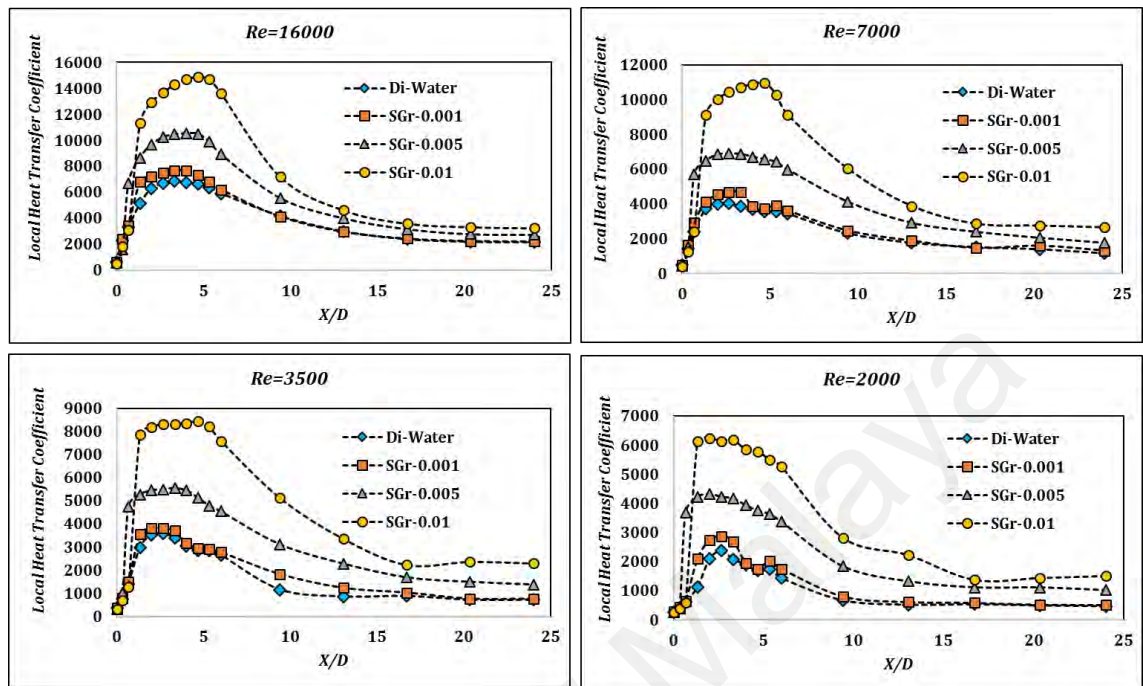


Figure 4.86: The effects of Reynolds number and weight concentration of SGr on the local heat transfer coefficient at different axial ratios.

From Figures 4.84 and 4.86, it can be seen that the position of maximum value of the heat transfer coefficient and/or Nusselt number (X_{max}/D) changes with the Re number. Figure 4.87 illustrates the X_{max}/D of water-based SGr nanofluids and distilled water for different Re numbers and weight concentrations. It can be seen that the position of maximum value of the heat transfer coefficient and/or Nusselt number increases (shifts up) with the Re number and weight concentration of SGr. Regarding weight concentration of SGr, the lower temperature difference between the tube wall and the working fluid explains the increase in the heat transfer rate.

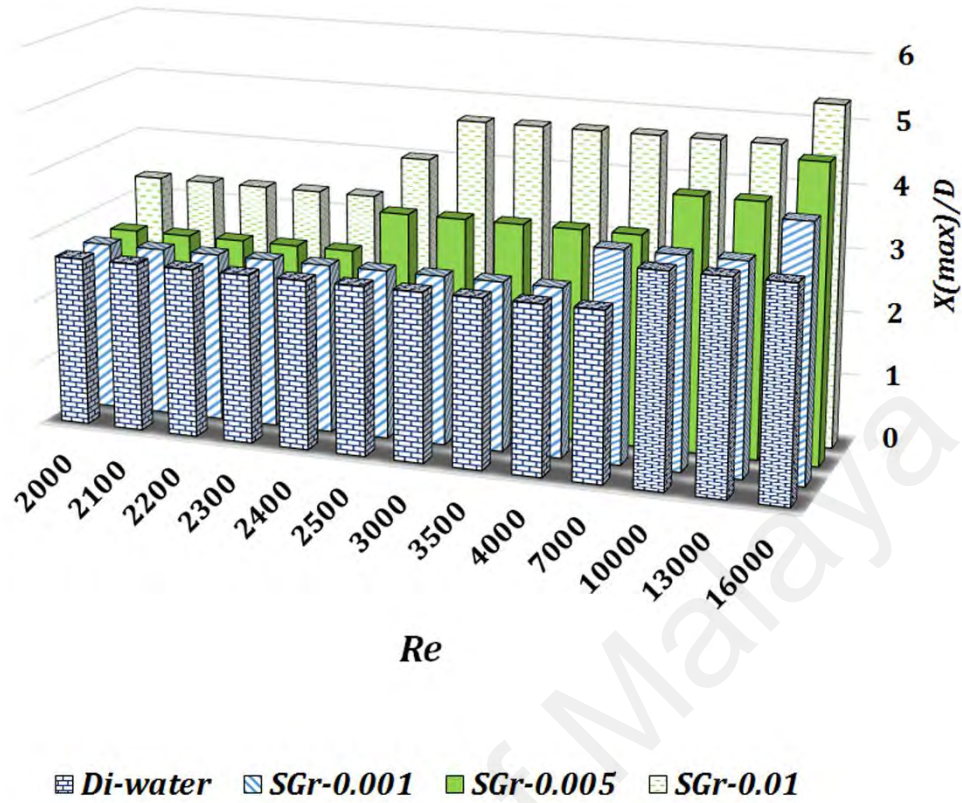


Figure 4.87: The effects of Reynolds number and weight concentration of SGr on the position of maximum local heat transfer coefficient.

Figure 4.88a plots the pressure drop of flow over the backward-facing step for different Re numbers and weight concentrations of SGr as well as distilled water. It is seen that as the Re number and concentration of SGr in basefluid increase, the pressure drop increases. It is noteworthy that the pressure drops for the prepared samples are quite close to that for the distilled water, which is attributed to the low concentrations of additive. Figure 4.88a also shows that the pressure drop for the water-based SGr nanofluids at the concentration of 0.01 wt.% and Re number of 16000 has the highest pressure drop for the current range of measurement. Note that the pressure drop and viscosity curves exhibit similar trends, which can be attributed to the direct relationship between pressure drop and viscosity.

The friction factor, f , over the backward-facing step is considered for different Re numbers and weight concentrations of SGr, which is shown in Figure 4.88b. It is seen that the measured friction factor decreases with increasing the Re Number at different weight concentrations of SGr. In addition, the friction factor increases as the concentration of SGr increases, although percentage of enhancement is more sensible in low amount of Re numbers. The minimum value of friction factor occurs for the base-fluid. It is also seen as the Re number increases, the dependence of friction factor on the weight concentration of SGr decreases. At low amount of the Reynolds number, Brownian motion is the main important parameter that influenced on the momentum transfer between the SGr and base-fluid molecules. Thus, as the Brownian motion increases, in the presence of water-based SGr nanofluids, the friction factor increases with higher slope as compared with base fluid (Mohammed, Al-Aswadi, et al., 2011). By contrary, this mechanism cannot be dominant for high amount of Reynolds number and agitation in flow plays the key role. In summary, the velocity of working fluid can be considered as the most important parameter in increasing the friction factor at the high amount of Reynolds number. Also, the small difference between friction factors of the distilled water and water-based SGr suspensions at different weight concentrations may be related to the insignificant gap between viscosities of base fluid and prepared samples.

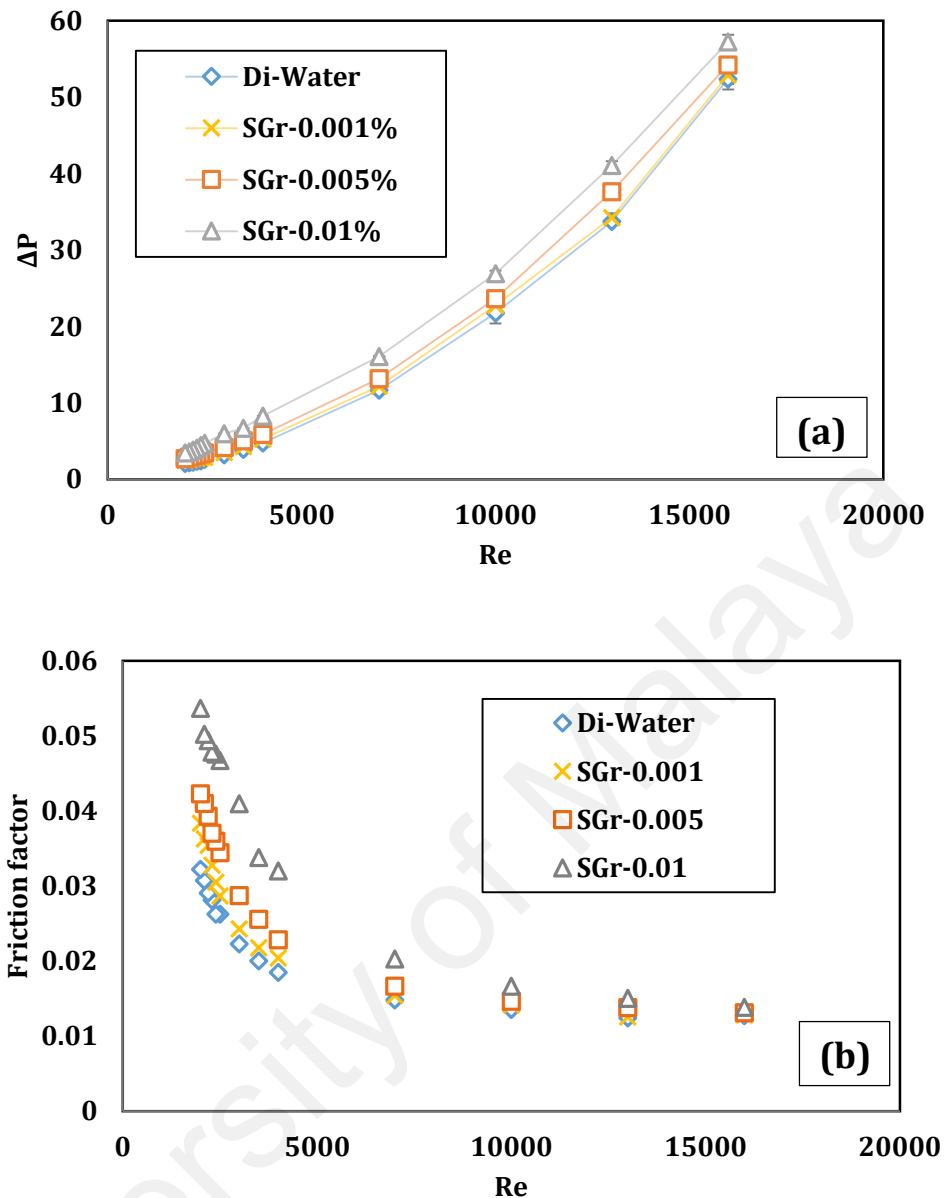


Figure 4.88: (a) The measured value of pressure drop of the set-up at different Re numbers for distilled water and water-based SGr nanofluids with different weight concentrations. (b) Experimental friction factor for distilled water and water-based SGr nanofluids with different weight concentrations at different Re numbers.

The economic performance of working fluids for different heat transfer equipment is measured via performance index (PI), which identified as the ratio of the heat transfer rate to the pressure drop. Recent studies in the field of heat transfer (e.g., (Samira et al., 2015)) presented that although the addition of solid nanoparticles improves the heat transfer rate, the pressure drop in the heat transfer loops also increases, which is significantly undesirable. Therefore, performance index is presented to consider both

parameters. The variations of the average performance index for water-based SGr nanofluids are illustrated for different Re numbers and weight concentrations in Figure 4.89a. It is seen that the average performance index of all samples including SGr (excluding water-based SGr nanofluids at weight concentration of 0.001% and $Re < 4000$) is higher than 1, representing the effectiveness of the prepared coolant samples for being used over the backward-facing step. It is also seen, as the weight concentration of SGr in nanofluids increases, the average performance index increases, which is an expecting phenomenon by looking at higher heat transfer coefficient in the presence of higher weight concentration. This figure also depicts that the average performance index curves for different Re numbers attain the best results for the weight concentration of 0.01 wt.%, which is followed by a gradual decrease of the average performance index for further increase in the Re numbers. As the second controller and in order to found a relation between the thermal performance and hydraulic performance of the test-rig in the presence of nanofluids, the performance evaluation criterion (PEC) is calculated (Manca et al., 2012). Like the PI, PEC is assessed as a criteria of optimization of employing both nanofluids and the backward-facing step as shown in Figure 4.89 panel (a). The PEC higher than 1 indicates that the enhancement in heat transfer rate is higher than that of an increase in the pressure drop penalty. Like PI trend, the same trend for PEC was repeated. From Figure 4.89 panel (a), the performance of nanofluids combined with set-up is higher than unit for water-based SGr nanofluids at different weight concentrations. Note that the enhancement in heat transfer become more significant than the pressure drop penalty at weight concentration > 0.005 wt%.

Also, power consumption and pumping characteristics in a loop is another critical parameter in terms of economy as well as energy-saving. Pumping power can be considered as an economic performance indicator in a loop system for evaluating the operability of fluid and performance of power plant.

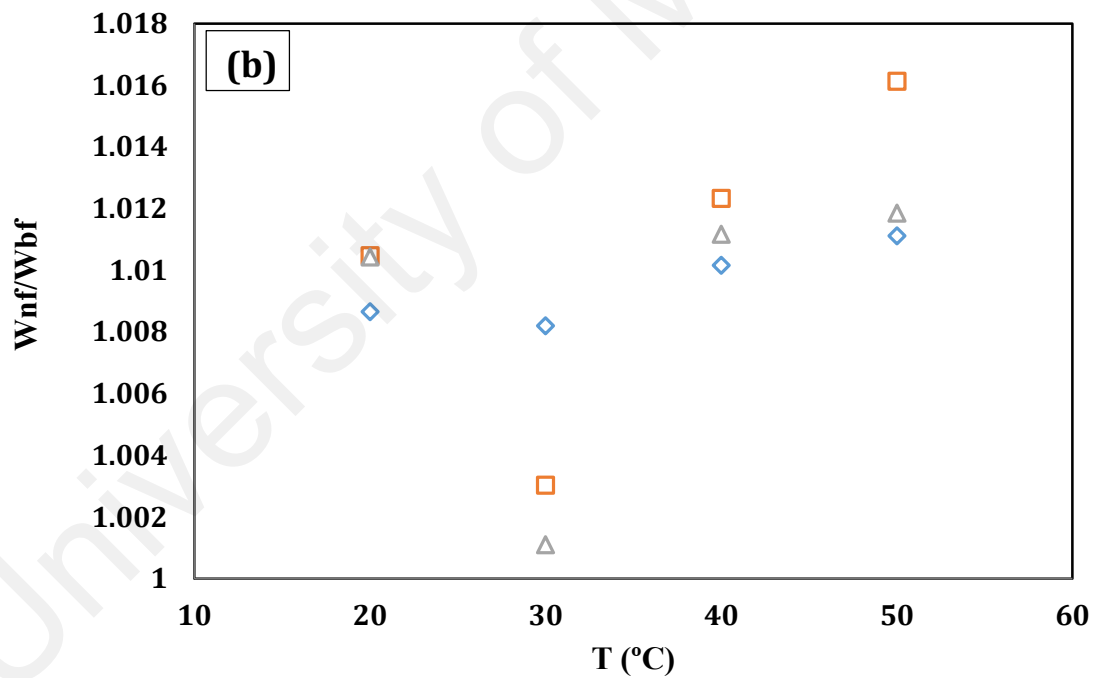
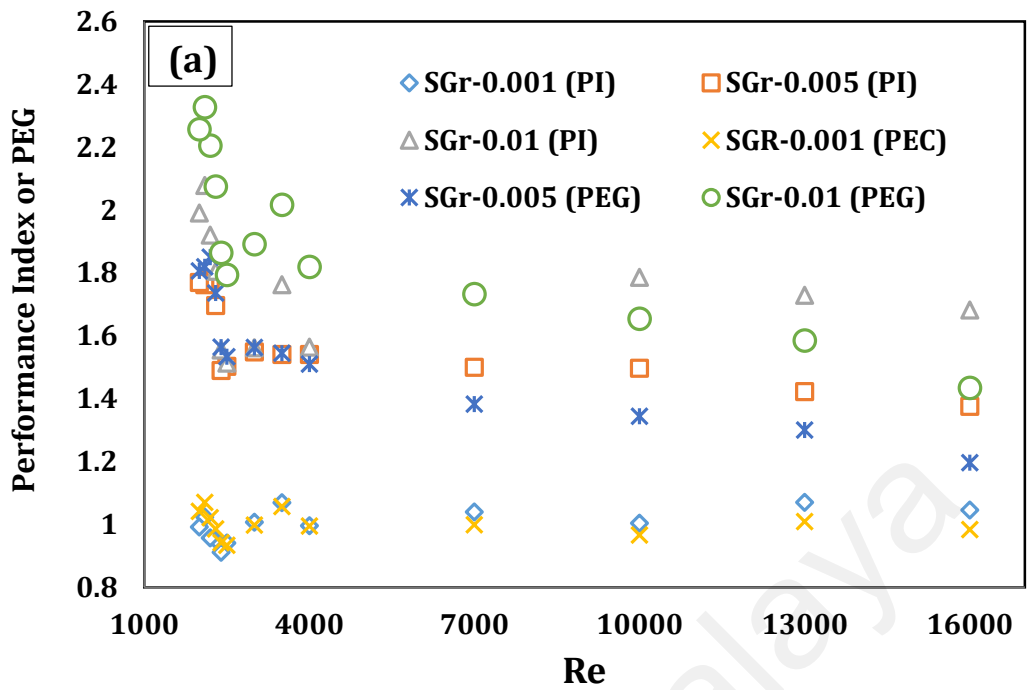


Figure 4.89: (a) Performance evaluation criterion (PEC) and performance index (PI) and (b) pumping power for the backward-facing step in the presence of distilled water and water-based SGr nanofluids with different weight concentrations.

Figure 4.89b compares the pumping power of the water-based SGr nanofluids for different weight concentrations and temperatures with that of the base fluid. This figure

shows that there is a small increase in the pumping power with the SGr loading and the percentage of pumping power growth is negligible. The small growth in the pumping power can be due to the low weight fraction of SGr in base fluid.

As a result, a simple and cost-effective approach was utilized for mass production of the SGr with large specific surface area. Mono layer graphene with high surface area was then used as additive for preparing highly stable and highly conductive nanofluids with superior thermo-physical properties. The results suggested that the thermo-physical properties of water-based SGr were increased significantly, and they are well-suited for heat transfer applications. A comprehensive study on the prepared nanofluids over a backward-facing step for transitional and turbulent flow regimes illustrated that water-based SGr nanofluids at very low concentrations exhibited higher rate of heat transfer as compared to the distilled water. Overall heat transfer rate showed a dramatic rise by loading only 0.01 wt% of SGr into the distilled water, representing more than 83% enhancement. Also, the Nu number and local heat transfer coefficient of distilled water and water-based nanofluids for transitional and turbulent flow regimes were measured for the first time. Regarding heat transfer in set-up, as the surface area of additive in nanofluids increases, the thermal conductivity increases. So, SGr with high thermal conductivity and high specific surface area can be a great candidate for a new generation of heat transfer equipment. In addition, as the thermal conductivity of nanofluids and/or Re number increase over backward-facing step, the position of X_{\max}/D shifts to the higher axial ratio.

4.4.3 Two-phase closed thermosyphon

4.4.3.1 Introduction

Different kinds of heat pipes are essential equipment in the electronics, thermal and electrical appliances. Also, heat pipes are commonly energy-efficient vehicles with

minimal maintenance requirements for a long period of time (Chehade et al., 2014; Z.-H. Liu et al., 2013). Heat pipes are commonly designed based on the characteristics of the apparatus including working fluid, temperature of the basefluid, the dimension and heat flux (Z.-H. Liu et al., 2013). In terms of design, heat pipes can be categorized into four groups: heat pipe with wick, loop heat pipe, thermosyphon heat pipe and thermosyphon loop. Each type of the heat pipes is appropriate for an special application based on the thermal performance, rate of heat transfer, the objective device to be cooled and the installation reason (Bojić & Lukić, 2002; Jaisankar et al., 2011).

Previous researches showed that various factors such as right filling ratio to the evaporator volume, basefluids, design, bent position and bend angle play key roles in the thermal performance of the thermosyphon heat pipe (Chien et al., 2011; Jouhara & Merchant, 2012). Finding optimal filling ratio, working fluids, the geometry, diameters and bend angles, application of vibration and rotation system have been considered as the main essential subjects to increase the performance of thermosyphons. Although all the mentioned novelties have appropriate influence on the thermal performance of thermosyphon heat pipe, employing of the new basefluids seems to be the most cost-effective, especially for systems which are already manufactured.

As mentioned above, the effects of working fluids on the performance of thermosyphon heat pipes were investigated extensively by some researchers (Z.-H. Liu et al., 2013; Shanbedi, Heris, Amiri, & Baniadam, 2014; Shanbedi et al., 2012; M Shanbedi et al., 2013). In addition, previous studies (Chol, 1995; S Zeinali Heris et al., 2006) confirmed that nanofluids made of the mixture of basefluids and nanoparticles with good thermal conductivity could enhance the thermal performance of the heat pipes. This observation showed that the thermal conductivity of nanoparticles plays an essential role in the heat transfer characteristics of nanofluids. A maximal reduction of the thermal resistance of about 24% was reported in the presence of water based titanium dioxide and

gold nanofluids by Buschmann and Franzke (2014). As another example, M Shanbedi et al. (2013) studied the influence of multiwalled carbon nanotubes (MWCNT) on the efficiency of two-phase closed thermosyphon (TPCT). They observed about 11% enhancement in the thermal efficiency of the TPCT at 90 kW in the presence of functionalized MWCNT. The recent results also showed that the thermo-physical properties like thermal conductivity of nanoparticles play a key role in their applications especially in heat transfer equipment (Afshar et al., 2009; Garg et al., 2009). The thermal conductivity of graphene nanoparticles (GNP) is much higher than the value presented by other carbon allotropes like MWNT, SWNT and diamond (Azizi et al., 2013). Due to the promising properties, GNP may have numerous applications in different scientific fields for making some equipment such as sensors, and batteries (Zhu, Murali, Cai, et al., 2010). A majority of these applications, however, cannot fully be realized because of insignificant interaction between GNP and other materials. Thus, in order to increase the interactivity of carbon nanostructures, covalent and non-covalent functionalizations were proposed as the common solutions elsewhere. Covalent and non-covalent functionalizations are two possible methods to increase the GNP dispersibility in aqueous/organic solvents. Non-covalent functionalization of carbon nanostructures is performed by employing various surfactants. In order to increase the dispersibility of carbon nanostructures in aqueous media, four common surfactants of gum Arabic (GA), sodium dodecyl sulphate (SDS), sodium dodecyl benzene sulphate (SDBS) and triton X-100 are commonly utilized. SDBS and triton X-100 have a benzene function, which produce powerful π - π interaction with the surface of carbon nanostructures. It is noteworthy that SDBS has higher dispersibility than that of Triton X-100. This is attributed to the steric hindrance of tip chains in triton X-100, which resulted in low concentration of triton on the carbon nanostructures surface (Islam et al., 2003). On the other hand, although GA can provide better condition for dispersion of carbon

nanostructures in comparison with SDBS and triton X-100, it significantly increases the viscosity of mixture, which may cause numerous problems including increase in pressure drop in thermal equipment (M Shanbedi et al., 2013). Thus, SDBS was selected as a suitable candidate for synthesizing non-covalent nanofluid. Also, covalent functionalization comprises the addition of hydrophobic or hydrophilic groups on the high energy features such as edges of GNP. To compare the effect of functionalization, in the present study, the GNPs with two methods based on covalent and non-covalent reactions were functionalized (section 4.2.6). These include rapid non-covalent functionalization of GNP with SDBS and the covalent functionalization with carboxyl groups. The samples were then characterized and the thermal performance in a thermosyphon was evaluated. The covalent and non-covalent functionalization effects on the thermal conductivity, viscosity, and thermosyphon performance were studied for various operating temperatures and concentrations. As discussed in section 4.2.6, in the presence of non-covalent groups, a significant increase in viscosity of suspension vitiates the enhancement in the heat transfer characteristics of GNP nanofluids. The presented results showed that the thermo-physical properties of covalent nanofluids (GNP-COOH/water) were more enhanced compared to those of non-covalent nanofluids (GNP-SDBS/water) and water. In this phase of study, overall heat transfer, entropy, thermal efficiency, thermal resistance and pressure drop are investigated in the presence of covalent nanofluids even at low concentrations.

4.4.3.2 Data Processing

A study on the heat transfer behavior of the thermosyphon was performed by evaluating the thermal efficiency, thermal resistance and overall heat transfer coefficient as well as thermo-physical properties such as viscosity and thermal conductivity of nanofluids. The overall heat transfer coefficient was obtained by measuring the values of

the inlet, outlet, and inner bulk fluid temperatures. The input power at the evaporator section was measured by using,

$$Q_{in} = VI \quad (4.29)$$

where V and I are the voltage and current, respectively. The output power at the condenser sections (Q_{out}) can be calculated as,

$$Q_{out} = \dot{m} C_p (T_{out} - T_{in}) \quad (4.30)$$

where \dot{m} is the mass flow rate, T_{in} and T_{out} are, respectively, the temperatures of the inlet and the outlet water to the condenser.

The ratio of output power to input power is commonly introduced as the thermal efficiency and is given as (Faghri, 1995; Shanbedi et al., 2012),

$$\eta_1 = \frac{Q_{out}}{Q_{in}} \quad (4.31)$$

The overall thermal resistance of the thermosyphon (R_{th}) is measured from the average temperature difference between the evaporator and the condenser sections and the input power. That is (Faghri, 1995; Shanbedi et al., 2012),

$$R_{th} = \frac{\bar{T}_e - \bar{T}_c}{Q_{in}} \quad (4.32)$$

where \bar{T}_e and \bar{T}_c are introduced as the average temperature of the evaporator and condenser sections, respectively. The overall heat transfer coefficient (U) can be calculated as (Faghri, 1995; Shanbedi et al., 2012),

$$U = \frac{Q_{in}}{\pi DL(\bar{T}_e - \bar{T}_c)} \quad (4.33)$$

where, D and L are the diameter and the length of the evaporator section, respectively. Based on the second law of thermodynamics, the thermal efficiency of thermosyphon can be evaluated as the ratio of exergy at the condenser to evaporator sections. That is (Khalkhali et al., 1999),

$$\eta_2 = \frac{e_{out}}{e_{in}} = \eta_1 \left(1 - \frac{1}{\left(\frac{\bar{T}_e}{\Delta T - 1} \right) \left(\frac{\bar{T}_e}{T_{out} - 1} \right)} \right) \quad (4.34)$$

Here, ΔT is the average temperature difference between the condenser and evaporator sections, which is given by $\Delta T = T_{out} - T_{in}$.

The entropy, S , can be calculated as by equation 4.35 (Khalkhali et al., 1999; Maheshkumar & Muraleedharan, 2011).

$$S = \frac{Q_{out}}{\bar{T}_c} - \frac{Q_{in}}{\bar{T}_e} \quad (4.35)$$

4.4.3.3 Heat Transfer Rate

In order to evaluate the thermal efficiency enhancement of the thermosyphon filled with water-based nanofluids and deionized water, different input powers (30.1, 59.7, 90.5, 119.9 and 149.8 W) were applied and the measured efficiency data are presented in Figure 4.90. It is seen that when GNP/water nanofluids is used, the thermal efficiency of thermosyphon improves considerably, which implies enhancement of the heat transfer effectiveness. The higher thermal efficiency of GNP/water nanofluids is attributed to the decrease in bubbles size produced at the evaporator interface. The lower thermal resistance between solid and liquid surfaces in the presence of smaller bubbles and/or air layer explains the increase in the heat transfer rate. It is also seen that the enhancement increases as volume concentration of GNP in both covalent and non-covalent nanofluids increases.

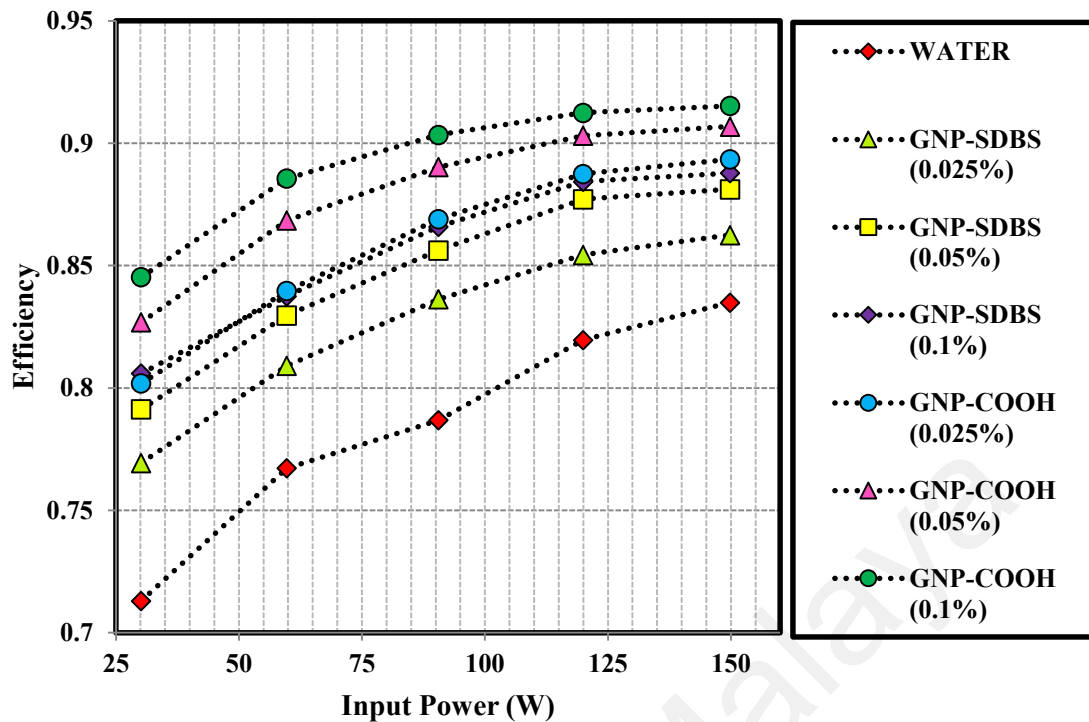


Figure 4.90: Efficiency of thermosyphon in the presence of GNP-based water nanofluids at various concentrations.

The thermal efficiency of thermosyphon also increases as the input power increases, although the increasing trends vary with concentrations and the type of GNP/water nanofluids. In general, the gradient of thermal efficiency (with respect to power) is larger at lower input powers compared to that at the higher input power for all the nanofluids as well as deionized water.

Shanbedi et al. (Shanbedi et al., 2015; Shanbedi, Heris, Amiri, & Baniadam, 2014; Shanbedi et al., 2012) reported that the geyser-effect (impulsive boiling at low pressures) can decrease the thermal efficiency of thermosyphon at the higher input power of 90 W in the presence of carbon nanostructures-nanofluids. A decrease in the slope of thermal efficiency versus input power at the range of 120–150 W can be attributed to the geyser-effect phenomenon.

According to the data presented in Figure 4.90, GNP-COOH/water nanofluids with various weight concentrations are more efficient than the corresponding GNP-

SDBS/water nanofluids, which can be considered as the best non-covalent nanofluids among the cases studied.

The heat transfer coefficient and thermal efficiency enhancements of the functionalized nanofluids can result mainly from the improvement of the thermo-physical properties, in which the synthesized covalent nanofluids at the same conditions show higher thermo-physical properties e.g. thermal conductivity than that of non-covalent nanofluids. Thus, the more increase in the thermal conductivity of basefluid in the presence of GNP-COOH in comparison with GNP-SDBS can possibly explain the corresponding increase in heat transfer coefficient (Mehta & Khandekar, 2007; Parametthanuwat et al., 2011). In addition, it is obvious that the thermal efficiency is influenced by many complementary parameters such as bubble diameter, nucleation site density and the average rise velocity of the individual bubbles. In terms of nucleation site density and bubble diameter as another possible mechanism, produced vapor bubbles easily burst during their generation due to contact with nanoparticles surfaces. This phenomenon prevents the formation of bubble layers in the solid and liquid interface, which are the main reason for the reduction of heat transfer. As a result, in the absence of bubbles, the amount of heat loaded on the evaporator decreased by removing the bubble layer on the evaporator surface. Thus, when the non-covalent groups warped around the GNP, it may decrease the effective surface of GNP, implying lower heat transfer rate in comparison with covalent samples (Kim et al., 2010). The presented results suggest that a maximum thermal efficiency of 91.5% was archived at the concentration of 0.1 wt% and the power of 150 W.

Figure 4.91 presents the measured average temperature difference (ΔT) between evaporator temperature and condenser temperature for different input powers and concentrations. This figure shows a rising trend of ΔT with the input power and a

decreasing trend of ΔT with the concentration of GNP. That is, as the concentration of GNP increases, ΔT decreases.

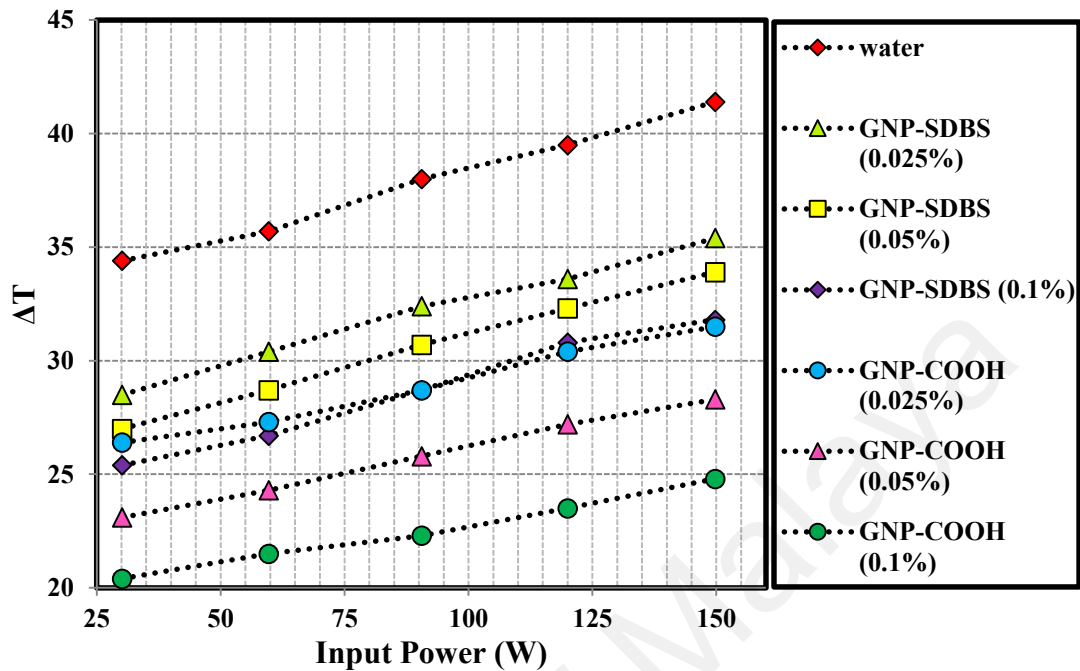


Figure 4.91: Effect of input power and concentration of GNP-based water nanofluids on the average temperature difference (ΔT) between the evaporator and the condenser.

As mentioned above, the higher bubble size means higher thermal resistance between solid and liquid surfaces in the evaporator, leading to a lower heat transfer rate (Duan et al., 2011; Kim et al., 2010). As a result, in the absence of bubbles, there is a lower heat load on the evaporator, while the formation of bubble layer on the evaporator surface lead to a higher heat load on the evaporator, which leads to an increase in the surface temperature of evaporator and subsequently larger ΔT .

Figure 4.92 shows the variation of evaporator temperature with concentration and power input. It is seen that the evaporator temperature rises with the input power and decreases with the increase of GNP concentration. The drop in the evaporator temperature associated with the increase of GNP concentration may be attributed to the enhancement of the bubble burst process in the presence of more nanoparticles that prevents the formation of air layer at the solid–liquid interfaces in the evaporator. This trend is in

agreement with the results presented for the efficiency in Figure 4.90. That is, the formation of smaller bubbles results in higher heat transfer rate and subsequently higher thermal efficiency compared to the basefluids.

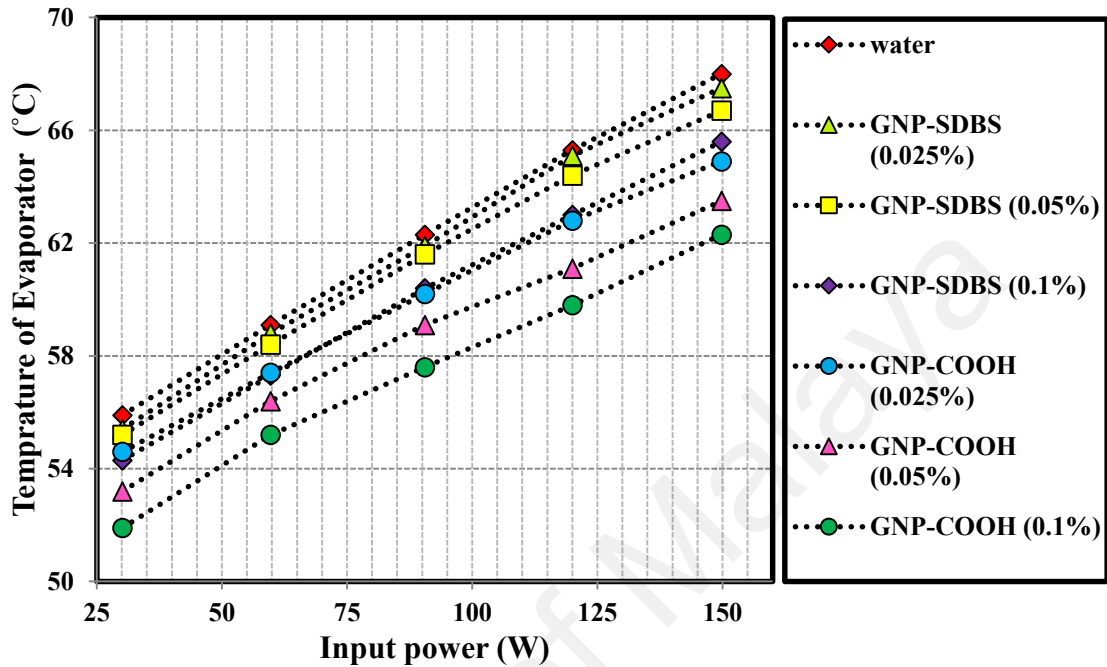


Figure 4.92: Effect of input power and concentration of GNP-based water nanofluids on the average temperature of the evaporator section.

Noteworthy, the higher enhancement in the thermal conductivity of basefluid in the presence of GNP-COOH in comparison with GNP-SDBS can possibly clarify the corresponding decrease in ΔT , implying lower heat load on the evaporator and followed by lower the evaporator temperature, as is apparent in the results.

Figure 4.93 compares the measured overall thermal resistance of nanofluids with various concentrations of GNP for different heat fluxes with that of deionized water. It is observed that the overall thermal resistance decreases rapidly with the increase in heat flux especially for power input less than 90 W. Also, as the concentration of GNP in nanofluids increases, the overall thermal resistance decreases. As mentioned above, the thermal conductivity of the basefluids is preferably high for minimizing the temperature gradient, which also repeated in GNP-COOH-based water nanofluids in comparison with

the non-covalent nanofluids. The reason of increasing the efficiency with the increasing of concentration of volume of nanofluid can also be related to the increasing of fluid thermal conductivity (Hussein et al., 2013; Mousa, 2011).

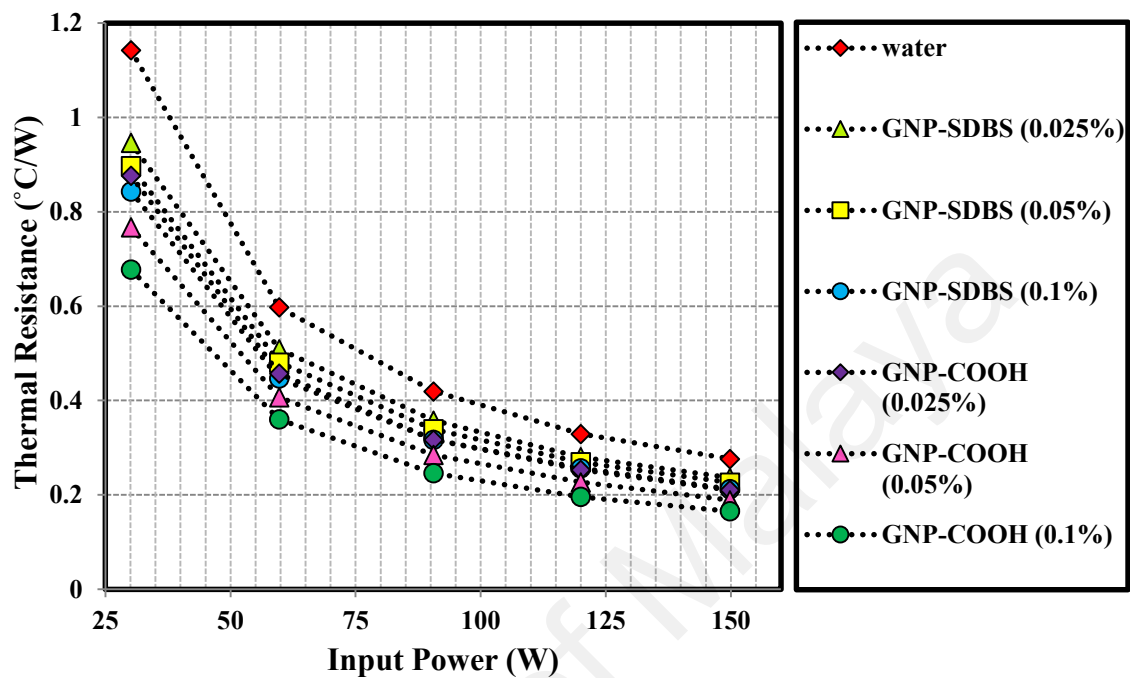


Figure 4.93: Effect of input power and concentration of GNP-based water nanofluids on the thermal resistance of thermosyphon.

On the effects of functional groups, it is seen that the increase of concentration of GNP-SDBS has lower influence on the overall thermal resistance as compared with covalent samples, which can be resulted from lower thermal conductivity of non-covalent nanofluids, implying the higher temperature gradient (Mousa, 2011). In agreement with the evaporator temperature variations, Figure 4.93 shows that the thermal resistance of the thermosyphon is the lowest for GNP-COOH nanofluids with concentration of 0.1 wt% which is the highest of the concentration being studied.

Figure 4.94 shows the overall heat transfer coefficient of thermosyphon for different input powers and GNP concentrations. It is seen that the overall heat transfer coefficient increases with the increasing of the input power and GNP concentration. Among the data shown in this figure, the heat transfer coefficient for the covalent samples of GNP-COOH show larger increases. In fact, the maximum overall heat transfer

coefficient of $601 \text{ Wm}^{-2} \text{ }^{\circ}\text{C}^{-1}$ was found for the GNP-COOH concentration of 0.1% and input power of 149.8 W. The maximum overall heat transfer coefficient enhancements for GNP-COOH and GNP-SDBS-based Water Nanofluids are respectively 35% and 68% for a weight fraction of 0.1%.

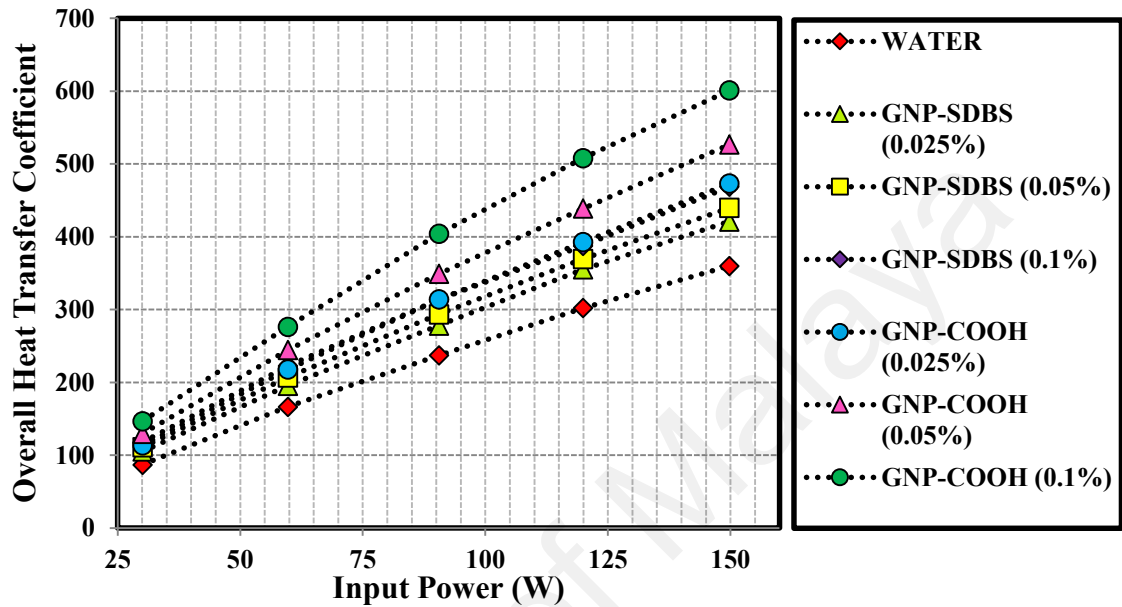


Figure 4.94: Effect of input power and concentration of GNP-based water nanofluids on the overall heat transfer coefficient of thermosyphon.

In agreement with the temperature gradient and thermal resistance results, the concentration and type of functionalization method play key roles in increasing the overall heat transfer coefficient. In thermosyphon studies, due to the higher thermal conductivity of the basefluids in the presence of GNP-COOH as well as GNP-SDBS, the lower temperature gradient obtained in the presence of nanofluids means the higher extent of overall heat transfer coefficient. Also, this reason can identify the gap between the covalent and non-covalent samples.

Entropy, S , is an important parameter that affects the thermosyphon performance. Variations of entropy of thermosyphon for water-based nanofluids versus input power for different concentrations of GNP-COOH and GNP-SDBS are presented in Figure 4.95.

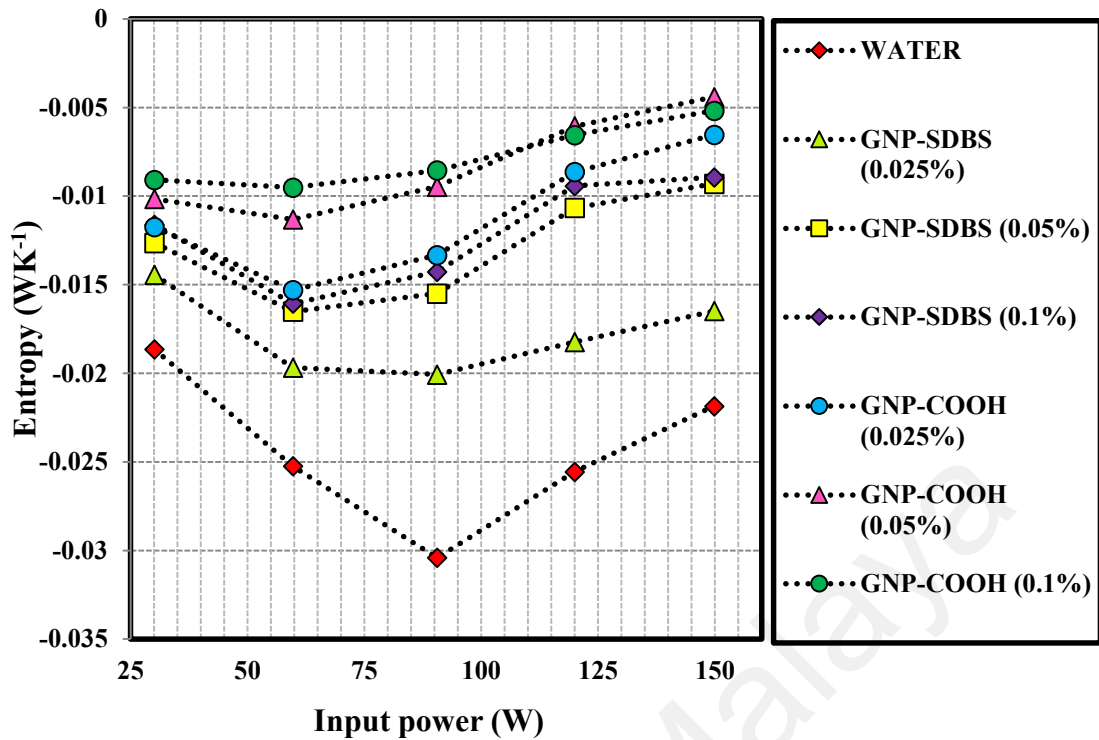


Figure 4.95: Effect of input power and concentration of GNP-based water nanofluids on the entropy of the thermosyphon.

For the deionized water, a U-shape variation of the entropy with input power is seen. That is, there is a downward trend of entropy with input power up to 90 W, after which the entropy for the deionized water increase with further increase of input power. Eq. (6.32) indicates that the entropy of the thermosyphon is given as the difference of Q_{out}/T_c and Q_{in}/T_e . For input powers less than 90 for water, the Q_{in}/T_e is larger than Q_{out}/T_c , due to a part of energy produced by heater consume for increasing temperature of bulk fluid in evaporator section (or refluxed fluid from condenser section). Therefore, the entropy shows a downward trend up to 90 W.

As the concentration of GNP in nanofluids increases, the entropy increases, and the amplitude of the variation of entropy with input power decreases. It can be attributed to the lower temperature gradient (although some fluctuations observed), since the range of input power and output power at various concentrations are insignificant. The same issue has also been occurred in the covalent and non-covalent nanofluids. The measured

data suggests the point of minimum entropy shifts to the lower input power to about 60 W for the range of concentrations studied. For high input power, a thin layer of vapor forms around the evaporator surfaces, which acts like an insulation layer and leads to low thermal conductivity. When the concentration of GNP increases, it is conjectured that the nanoparticle bursts the vapor bubbles and decrease the air layer (Kim et al., 2010), thus, providing a higher heat transfer rate from the heater to the bulk fluid in evaporator and shifting up the entropy.

Figure 4.96 plots the measured vacuum pressure drop of the thermosyphon for different input powers and concentrations of nanofluids as well as deionized water. It is seen, as the input power and concentration of nanofluids increases, the pressure drop increases. The pressure drops for GNP-COOH/water nanofluids at various concentrations are quite similar and close to that for deionized water pressure drop. This observation confirms that influence of GNP nanostructures on the effective viscosity of nanofluids and consequently on the pressure drop is small. On the other hand, as the concentration of GNP-SDBS increases, the variation of pressure drop with the input power shows sharper slope. That is, the GNP-SDBS/water nanofluids at the concentration of 0.1 wt% and input power of 149.8 W shows the maximum pressure drop. Expectedly, the pressure drop curve and viscosity curves show similar trends in the presence of covalent and non-covalent samples, which can be resulted from the direct connection between pressure drop and viscosity.

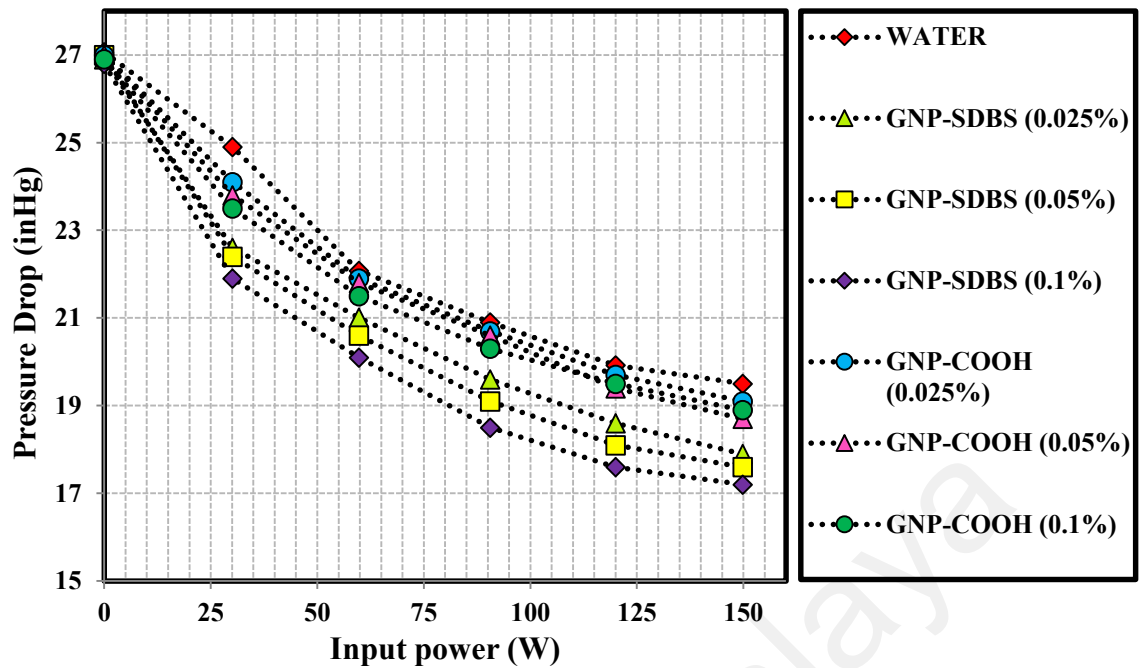


Figure 4.96: Effect of input power and concentration of GNP-based water nanofluids on the vacuum pressure drop of thermosyphon.

It should be pointed out that the uncertainties of the measured parameters are evaluated by the method described by S. J. Kline and McClintock (1953). Accordingly, the maximum error in evaluating all quantities was less than 4.5%.

As a summary of this phase of study, GNP-based water nanofluids were synthesized using two methods, one SDBS as one of the most effective surfactants (non-covalent functional group) and subsequently by acid treated GNP under microwave. The thermal performances of the nanofluids functionalized by two different methods are evaluated and compared for a range of concentrations and input powers. Acid treatment was introduced numerous carboxyl groups on the surface of GNP and due to attachment of COOH groups with main flake of GNPs, good dispersability was achieved. The prepared GNP-based water nanofluids exhibited higher thermo-physical properties compared to the distilled water. The experimental data suggests that the thermo-physical properties of covalent nanofluids (GNP-COOH/water) was more significantly enhanced compared with those of non-covalent nanofluids (GNP-SDBS/water). The

measured overall heat transfer, entropy, thermal efficiency, thermal resistance and pressure drop of covalent nanofluids showed promising results even at low nanofluid concentrations. The presented results suggest that the thermal performance of covalent nanofluids is better than that of non-covalent samples in the same experimental conditions. The results also suggest that the addition of GNP-SDBS to the deionized water increased the pressure drop and viscosity in thermosyphon more than GNP-COOH/water. In summary, the covalent functionalization under microwave radiation is quick and cost-effective with promising enhancement of thermal performance; therefore, it has the potential to replace the use of surfactant for synthesizing nanofluids.

4.5 Numerical Study on the Convective Heat Transfer Over a Backward-Facing Step

4.5.1 Introduction

The thermo-physical phenomena of separation and reattachment e.g. backward-facing step, involving heat transfer, are frequently encountered in many engineering problems like electrical rotating machines. Thus, investigation of the convection heat transfer over a backward facing step is one of the interesting topics in many research studies. Heat transfer applications of backward facing step appear in different industrial equipment such as combustors, aircraft, gas turbine engines, and buildings. It is obvious that the separation and reattachment of the flow can change the flow structure and has a direct influence on the heat transfer mechanism as well as thermal performance of the equipment (Eiyad Abu-Nada, 2008). Thus, numerous numerical studies have been investigated to determine the real mechanism of flow separation and reattachment, the best geometry for heat transfer applications, and the best type of working fluids in the past decades (Abu-Mulaweh et al., 1993; J.-T. Lin et al., 1991). Although, the flow over a backward-facing step with heat transfer was investigated by some scientists (Vradis &

Vannostrand, 1992; Vradis et al., 1993), a majority of studies considered the isothermal flow, commonly in two dimensional geometry.

A study on the two non-Newtonian liquids was performed in a sudden expansion in the presence of viscoelastic polyacrylamide (PAA) solutions and a purely viscous shear-thinning liquid (Vradis & Vannostrand, 1992). According to their results, the reattachment length of non-Newtonian fluid was shorter than that of Newtonian counterparts and surely water. Abu-Nada (Eiyad Abu-Nada, 2006) performed a numerical study on the entropy over a backward facing step for different expansion ratios. Different expansion ratios of $1/4$, $1/3$, $1/2$, $2/3$, and $3/4$ were selected and the results presented an increase in the Reynolds number with the value of total entropy generation number, which was for the high range of Reynolds number. A numerical study on the laminar regime in a rectangular duct including backward-facing step was performed by Nie and Armaly (2002). They suggested the appearance of the maximum reattachment length at the sidewall. Also, they concluded that as the step height enhances, the amount of Nusselt number increases. Biswas et al. (2004) investigated the laminar fluid flow behavior over a three dimensional backward-facing step with various expansion ratios. They concluded that the formation of wall jets at the side wall within the separating shear layer, formed by the spanwise of the velocity moves towards the symmetry channel plane. An experimental study have been done by Armaly et al. (2003) for measuring the velocity over a backward-facing step by using two-component laser Doppler velocimeter in laminar regime. In another similar study, Hsieh et al. (2010) studied the flow over a backward-facing step by the Direct Simulation Monte Carlo method (DSMC). According to their results, the side walls can significantly affect the flow structure and thermal characteristics in the 3-D structure. Bao and Lin (2011) also utilized the DSMC approach for investigation of the thermal performance over the microscale backward-facing step in the transition regime. They reported that the streamwise velocity is positive at the

Knudsen number of 0.136, indicating the lack of the reversed flow after the step. Also, they concluded that there is a non-linear connection between the mass flow rate and pressure drop ratio in traditional flow.

As mentioned above, a majority of studies focused on having novelty in changing design such as expansion ratio, in particular in the laminar regime, and neglected thermo-physical properties of working fluid. Thus, as another novelty for improving heat transfer rate over a backward-facing step is the utilization of nanofluids. A combination of nanofluids with thermal conductivity and backward-facing step can result in an effective approach for enhancing the heat transfer rate. In addition, previous studies (Solangi et al., 2015) showed that nanofluids made of the mixture of basefluids and nanoparticles with good thermal conductivity could enhance the thermal performance of the different heat transfer equipment.

Kherbeet et al. (2012) investigated the heat transfer behaviors of four types of nanofluids (Al_2O_3 -, CuO -, SiO_2 - and ZnO -based water nanofluid) in the laminar regime over a microscale backward-facing step. The results showed the lack of recirculation region behind the step for all the prepared samples at different concentrations. In addition, the results suggested that SiO_2 -based water nanofluid has the highest Nusselt number as compared with other nanofluids. In addition, the results showed that the amount of Nusselt number enhances with the increment of the volume fraction of the nanoparticles in the base fluid. Kherbeet, Mohammed, Munisamy, et al. (2014) performed a numerical study on the laminar mixed convection flow of nanofluids over a horizontal microscale forward-facing step (MFFS) using a finite volume method. Different nanofluids including SiO_2 -, Al_2O_3 -, CuO -, and ZnO -based ethylene glycol nanofluids at various volume fractions investigated in terms of heat transfer parameters and the results demonstrated that the SiO_2 -based ethylene glycol nanofluid had the maximum Nusselt number. They

also reported that the Nusselt number increases with decreasing nanoparticle density and diameter as well as increasing volume fraction of nanoparticles.

It is obvious from the above literature review that the terms of thermal conductivity of nanoparticles was neglected. In addition, most of the previous studies on the backward-facing step involved metal- or metal oxide-based water or ethylene glycol as the basefluid and there is no study concentrated on nanofluids including carbon nanostructures. It is known that the thermal conductivity of most carbon particles such as carbon nanotubes (CNTs) and graphene nanoplatelets (GNPs) are much higher than that of metal or metal oxide nanoparticles. This implies that the carbon-base nanoparticles have higher potential for enhancing the thermal conductivity of base fluids. Despite some promising thermal properties of graphene nanoplatelets in the field of nanofluids, the strong van der Waals interactions have limited their thermal applications. Non-covalent and covalent functionalization are the effective approaches to improve the dispersibility of GNPs. Also, there is no study in water–ethylene glycol media over the backward-facing step.

Herein, three phases of study have been performed for numerical investigation of heat transfer behavior in the presence of EG-treated GNP based water–EG coolants over a backward facing step. First, a promising and potentially industrially scalable functionalization approach is employed to prepare ethylene glycol-functionalized graphene nanoplatelets (EGNP) and EGNP based water–EG coolant (EGNP-WEG). First phase followed by analyzing EG-treated GNP samples in terms of functionality and morphology (section 4.2.4). Second phase of study comprises of the experimental-evaluation of the thermo-physical, rheological and colloidal properties of EGNP-WEG (section 4.3.4). As the three phase of study, a numerical analysis on the heat transfer over a backward-facing step is performed in the presence of EGNP-WEG at different weight concentrations. The main objective was to investigate the heat transfer enhancement and

pressure drop in the presence of EGNP in basefluid. The latter is obtained by the calculation of the performance index.

4.5.2 Numerical implementation

The numerical method available in the commercial CFD package of ANSYS-Fluent, V15, has been used here. Fluent uses a finite volume approach to convert the governing partial differential equations into a system of discrete algebraic equations. As the discretization methods, a second-order upwind scheme was selected for the momentum, turbulent kinetic energy and turbulent dissipation rate equations whereas the first order upwind for energy equation was selected. For two-phase calculations, the phase momentum equations with the shared pressure are solved in a coupled and segregated fashion. The phase coupled SIMPLE (PC-SIMPLE) algorithm was employed for the pressure–velocity coupling. PC-SIMPLE is an extension of the SIMPLE algorithm to multiphase flows. The scaled residuals for the velocity components and energy are set equal to 10^{-8} and 10^{-9} , respectively.

4.5.3 Governing equations

Considering the turbulent forced convection in a steady flow of an incompressible and Newtonian fluid, the governing equations can be written as follows (T. M. Shih, 1984):

- (a) Continuity equation

$$\nabla \cdot (\rho_{eff} \bar{V}) = 0 \quad (4.36)$$

- (b) Momentum equations

$$\nabla \cdot (\rho_{eff} \bar{V} \bar{V}) = -\nabla \bar{P} + \mu_{eff} \nabla^2 \bar{V} - \rho_{eff} \nabla \cdot (\bar{v} \bar{v}') \quad (4.37)$$

- (c) Conservation of energy

$$\nabla \cdot (\rho_{eff} C_{p,eff} \bar{V} \bar{T}) = \nabla \cdot ((k_{eff} + k_t) \nabla \bar{T}) \quad (4.38)$$

In the above equations, the symbols \bar{v} , \bar{P} and \bar{T} are the time averaged flow variables, while the symbol v' represents the fluctuations in velocity. The term in the momentum equations $\rho_{eff} \nabla \cdot (\overline{v'v'})$ represents the turbulent shear stress. The terms of k_{eff} and k_t represent the effective molecular conductivity and the turbulent thermal conductivity, respectively.

To model flow in the turbulent regime, the standard k - ϵ model can be employed based on the Launder and Spalding study (Launder & Spalding, 1974), which is as follows (equations 4.39 to 4.42):

$$\nabla \cdot (\rho_{eff} kV) = \nabla \cdot \left[\left(\frac{\mu_t}{\sigma_k} \right) \nabla (k) \right] + G_k - \rho_{eff} \epsilon \quad (4.39)$$

$$\nabla \cdot (\rho_{eff} \epsilon V) = \nabla \cdot \left[\left(\frac{\mu_t}{\sigma_\epsilon} \right) \nabla \epsilon \right] + \frac{\epsilon}{k} (C_{1\epsilon} G_k - C_{2\epsilon} \rho_{eff} \epsilon) \quad (4.40)$$

$$G_k = \mu_t (\nabla V + (\nabla V)^T), \quad \mu_t = \rho_{eff} C_\mu \frac{k^2}{\epsilon} \quad (4.41)$$

$$C_\mu = 0.09, \sigma_k = 1.00, \sigma_\epsilon = 1.30, C_{1\epsilon} = 1.44, C_{2\epsilon} = 1.92 \quad (4.42)$$

4.5.4 Physical model and assumptions

The geometry and flow domain are schematically illustrated in Figure 4.97. The geometrical dimensions were 12.7 (mm) inlet diameter, 200 (mm) upstream length, 25.4 (mm) outlet diameter and 1000 (mm) downstream length with an expansion ratio of 2. At the inlet, temperature was set up at 303 K and the downstream wall was exposed to the constant heat flux of 10,000 (W/m²) while all other walls were insulated.

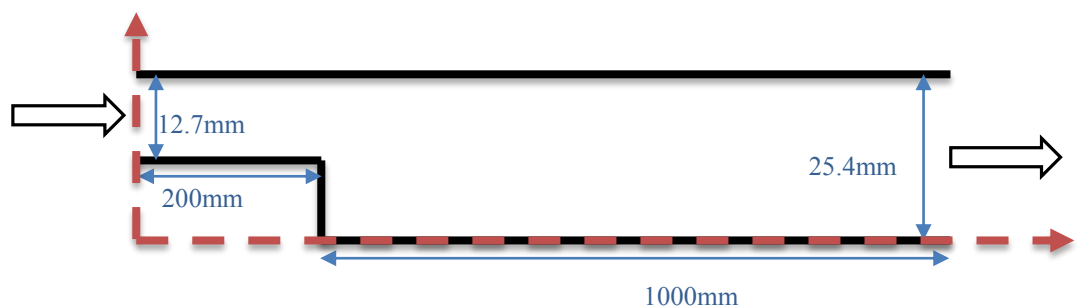


Figure 4.97: 2D geometrical configuration of backward-facing step.

The base fluid (ethylene glycol-water mixture) and the nanoparticles are assumed to have a thermal equilibrium and no slip condition occurs. The fluid flow is considered to be Newtonian and incompressible. The thermo-physical properties of the mixture of EG-water and EGNP-WEG coolants at different weight concentrations were obtained from experimental tests.

4.5.5 Grid study

The meshing tool available in ANSYS was used to construct the computational mesh. A structured mesh based on a rectangular grid was used throughout the domain. Several grid distributions had been tested and the results were compared to ensure that the calculated results were grid independent. Figure 4.98 shows the comparison of surface Nusselt numbers for Reynolds number of 5000 and pure water as a working fluid at three different grid distributions. It has shown that obtained results are independent of the number of grid points.

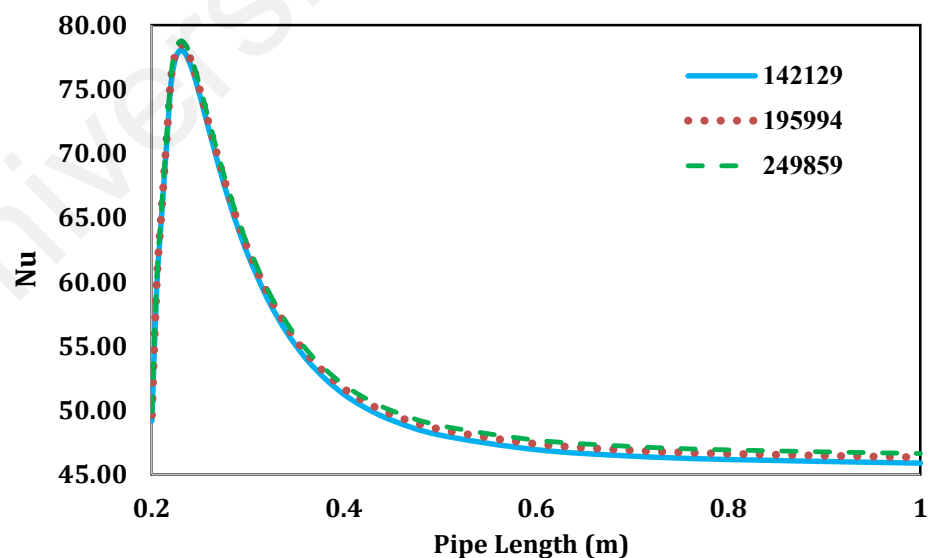


Figure 4.98: Local Nusselt numbers for $Re = 5000$ and pure water at three different grid distributions.

To reduce computational time and effort, the total grid points and the elements have employed throughout the tube are 142,129 and 140,800, respectively. A non-uniform grid was utilized in the meshing phase. Noteworthy, the grids are smaller where close to the separated region (backward phase of flow happen) for obtaining better results (see Figure 4.99).

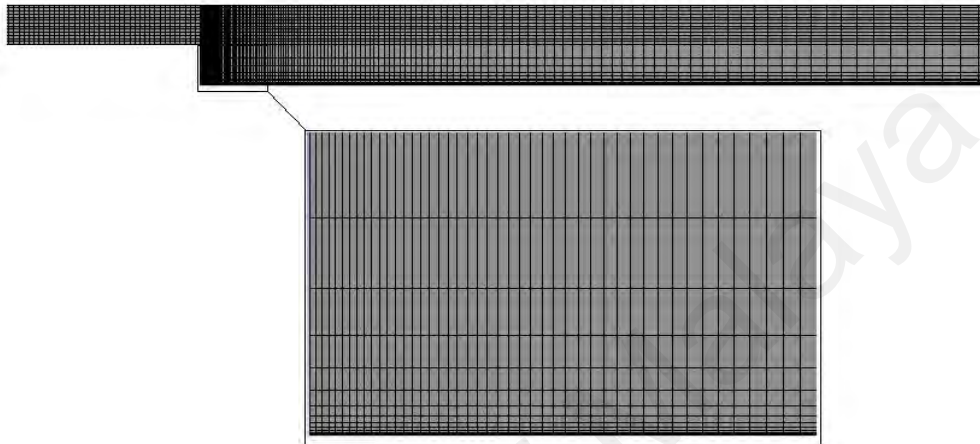


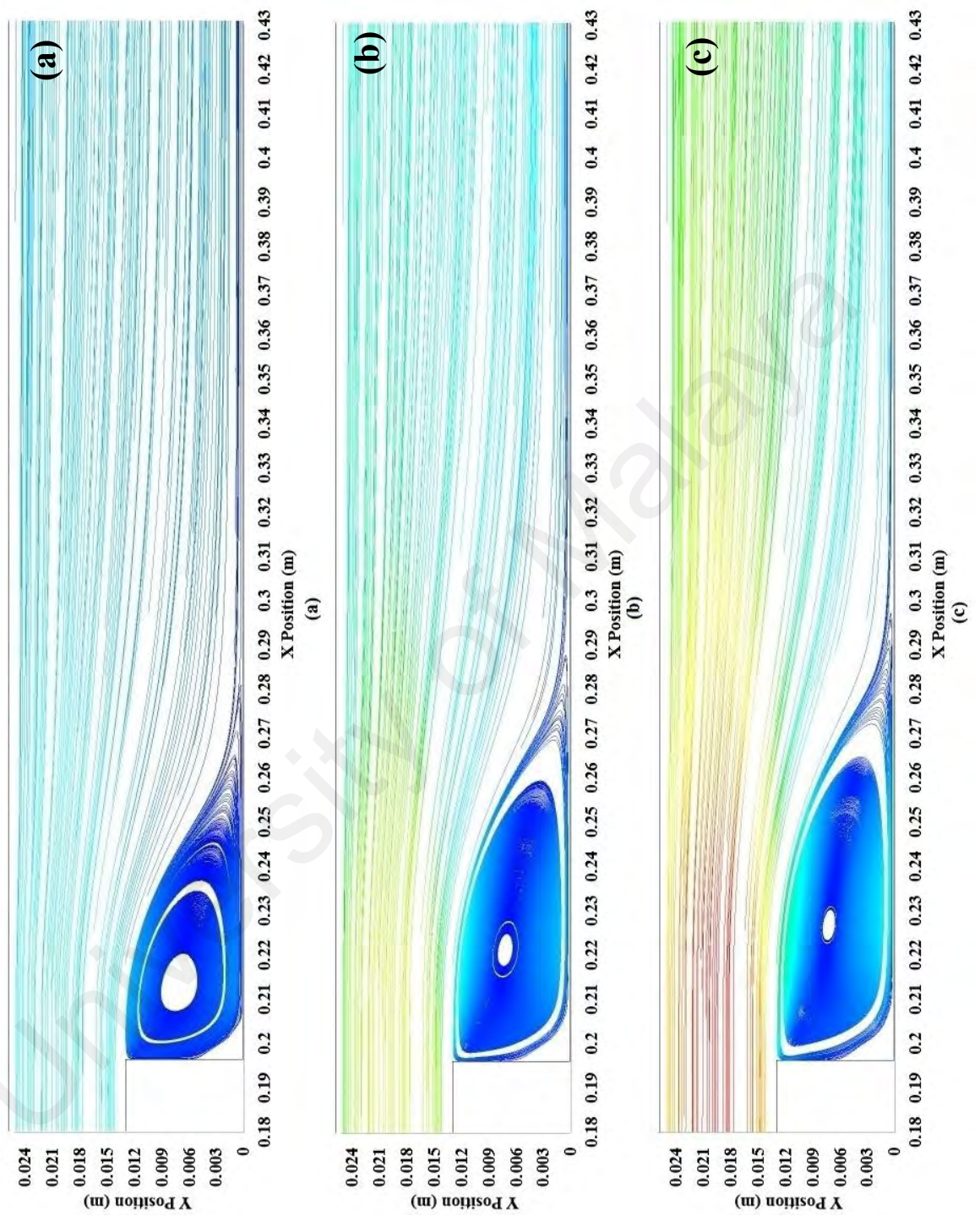
Figure 4.99: Mesh configuration of backward facing step.

4.5.6 Result and discussion

Dynamic viscosities, density, thermal conductivity and specific heat capacity of water-EG and EGNP-WEG mixtures were experimentally obtained and presented in section 4.3.4.

As a next phase of study, the numerical study on the forced convection heat transfer for the turbulent regime over a backward-facing step has been performed in the presence of EGNP-WEG coolants for various Reynolds numbers and weight concentrations. There are 15 cases of simulation, where weight concentrations of 0%, 0.01%, 0.05%, 0.1%, and 0.2% and the Reynolds numbers of 5000, 10,000 and 15,000 have been selected. The streamlines in the turbulent regime for the weight concentration of 0.2% and Reynolds number of 5000, 10,000 and 15,000 are presented in Figure 4.100

panels a, b and c, respectively. Streamline plots present the flow patterns for backward-facing step for the expansion ratio of 1:2.



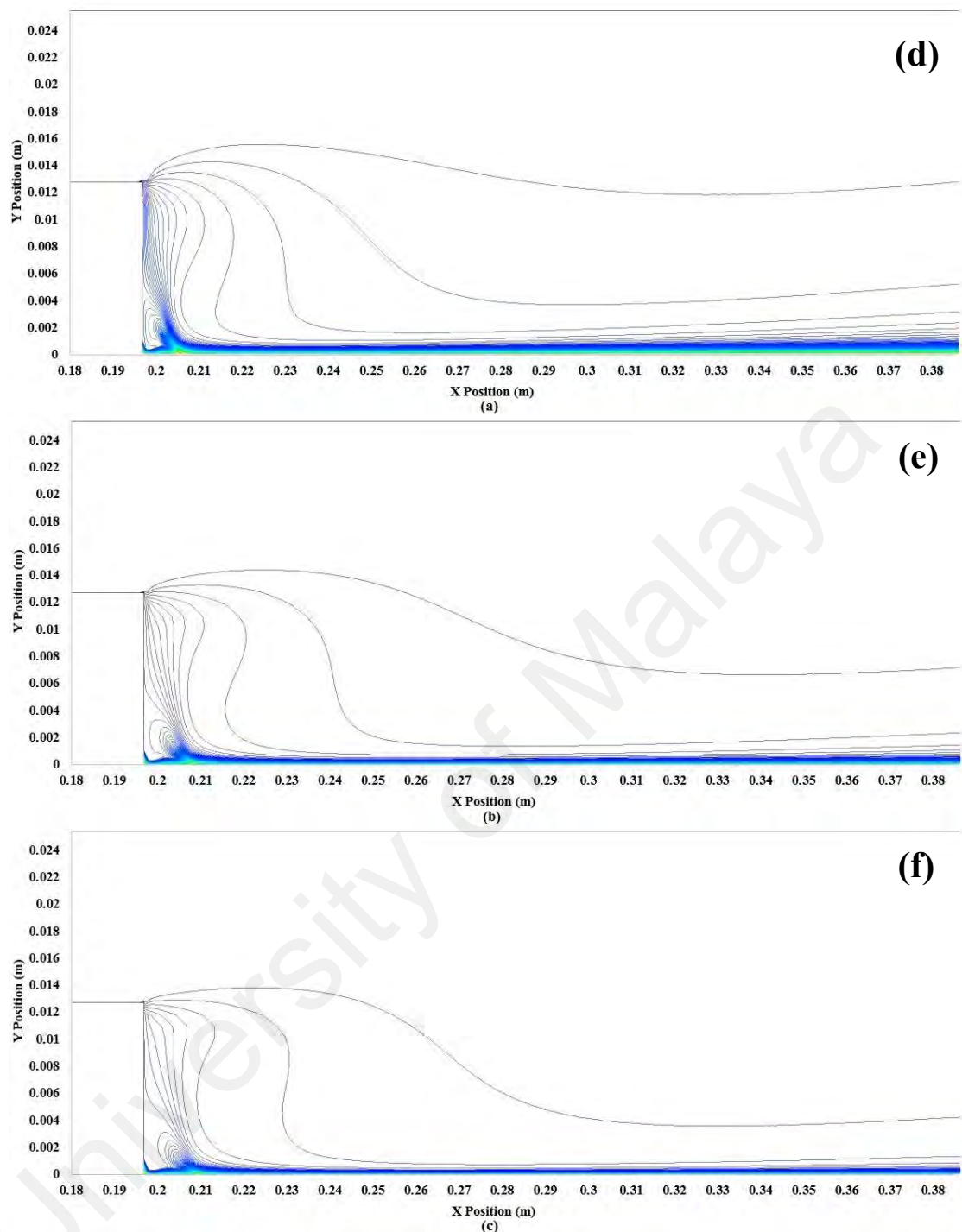


Figure 4.100: Streamline of velocity with weight fraction of 0.2% (a) $Re = 5000$, (b) $Re = 10,000$, (c) $Re = 15,000$, isothermal streamline with weight fraction of 0.2% (d) $Re = 5000$, (e) $Re = 10,000$, (f) $Re = 15,000$.

In addition, as the Reynolds number increases, the flow at the edge of the step separates and a recirculation zone is observed behind the step (Lancial et al., 2013). As another important phenomenon, the size of recirculation zone increases with an increase

in the Reynolds number. From the streamline plots, it is seen that the recirculation region expands in terms of length with the increase of Reynolds number. Thus, the largest recirculation region in our results is obtained for Re of 15,000, which can be resulted in higher heat transfer rate improvement due to the recirculation formation (Lancial et al., 2013). For more clarification, isothermal streamlines are presented in Figure 4.100d, e and f for three Reynolds numbers of 5000, 10,000 and 15,000, respectively.

Figure 4.101 (a–c) and (d–f) are presented the forced convective heat transfer coefficient (h_x) and the local Nusselt numbers (Nu_x) of EGNP-WEG as well as basefluid as a function of the Reynolds number and weight concentration, respectively. First, all of the forced convective heat transfer coefficient plots show the same characteristic behavior. Based on the results, both Nu_x and h_x values are small in the recirculation zone, significantly increase through the recirculation zone to reach a maximum in the reattachment region and followed by decreasing into the recovery region to a stable value, which is in agreement with Nie and Armaly (2002), Lancial et al. (2013), Cheng and Tsay (2006) and Heshmati et al. (2014). It can be observed that the Nusselt number and convective heat transfer coefficient are higher for the cases with higher Re number, with maximum Nu of 342.61 for Re of 15,000 and weight concentration of 0.2%. Consequently, the higher Re number, the higher Nu is and the higher the position of the happened maximum Nusselt number is. It can be seen that the maximum Nusselt number and heat transfer points move depending on the Reynolds number. Also, all of the plots regarding the Nusselt number profile and heat transfer coefficient at constant Re number present the same maximum points, indicating X_{max} is independent of weight concentration of nanofluids, which is confirmed by Heshmati et al. (2014). The value of X_{max} is 0.24.5, 0.25.5, and 0.26 m for Re numbers of 5000, 10,000, and 15,000, respectively.

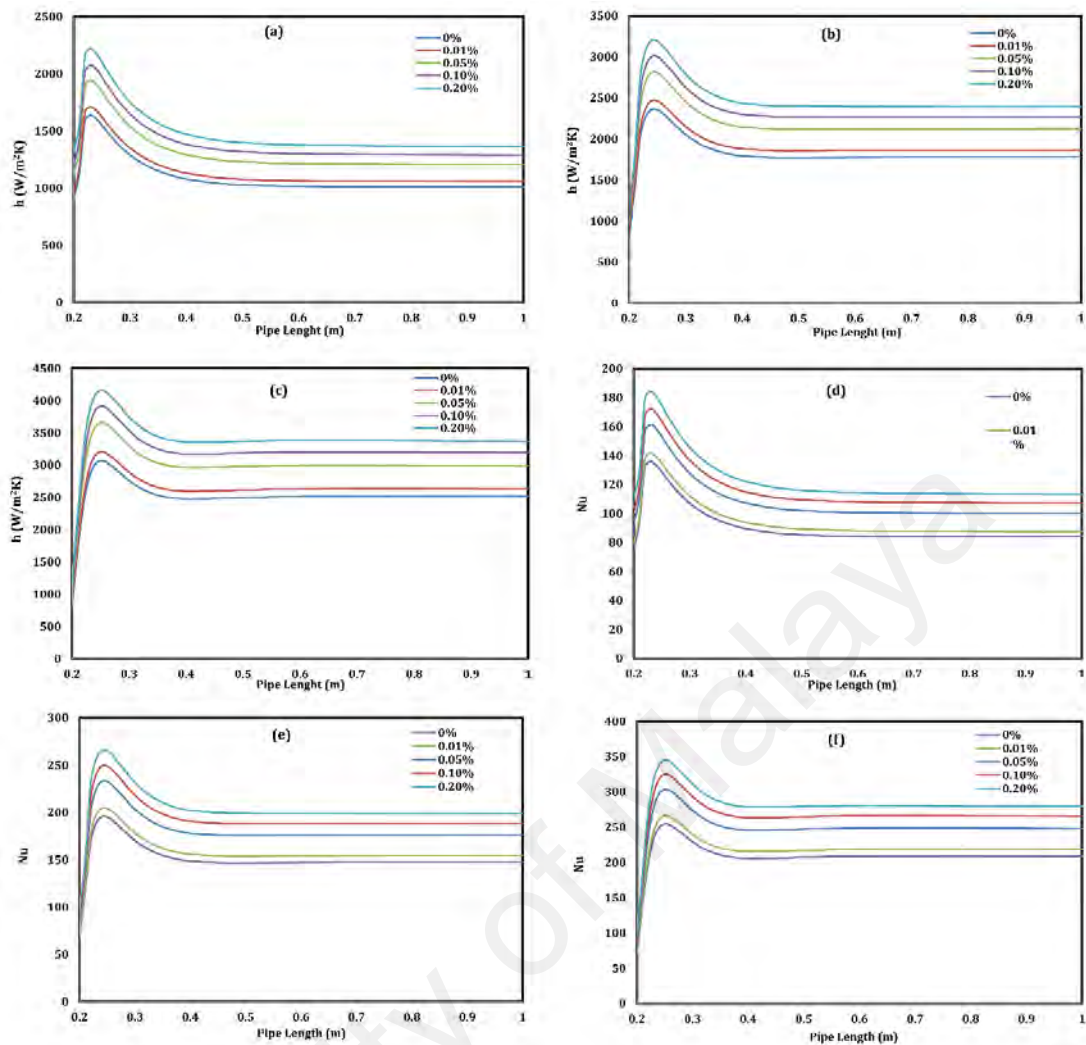


Figure 4.101: Convective heat transfer coefficient as a function of different weight concentrations at different Reynolds numbers of (a) 5000, (b) 10,000, and (c) 15,000 and the local Nusselt number as a function of different concentrations at (d) $Re = 5000$, (e) $Re = 10,000$, and (f) $Re = 15,000$.

Further downstream, where the variation of Nu tends to be constant, the flow become fully-developed. All samples showed similar results in terms of weight concentration, meaning the higher weight concentration, the higher heat transfer coefficient and Nusselt number as well.

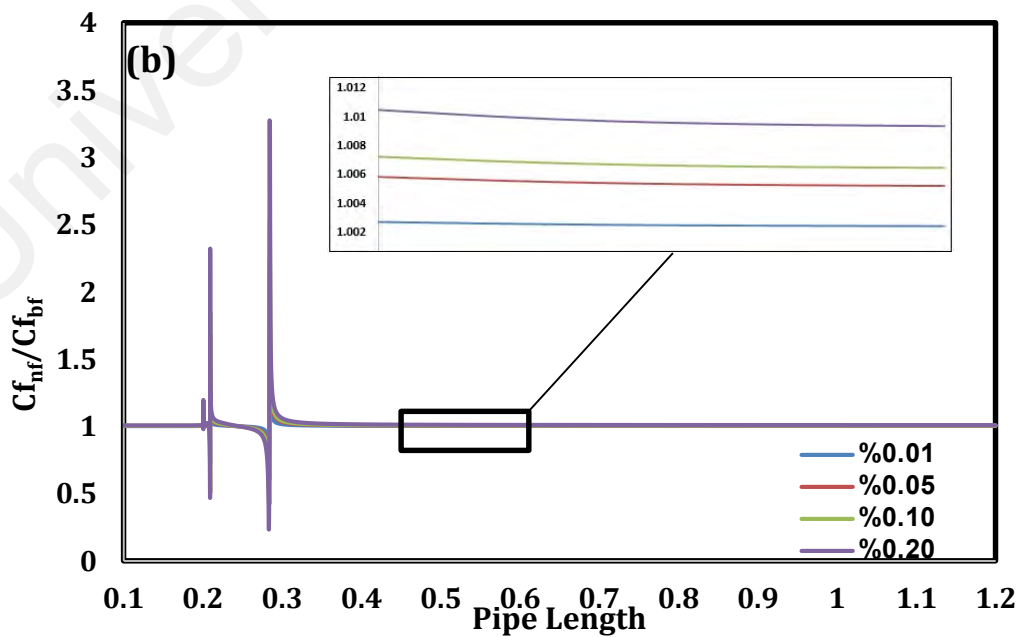
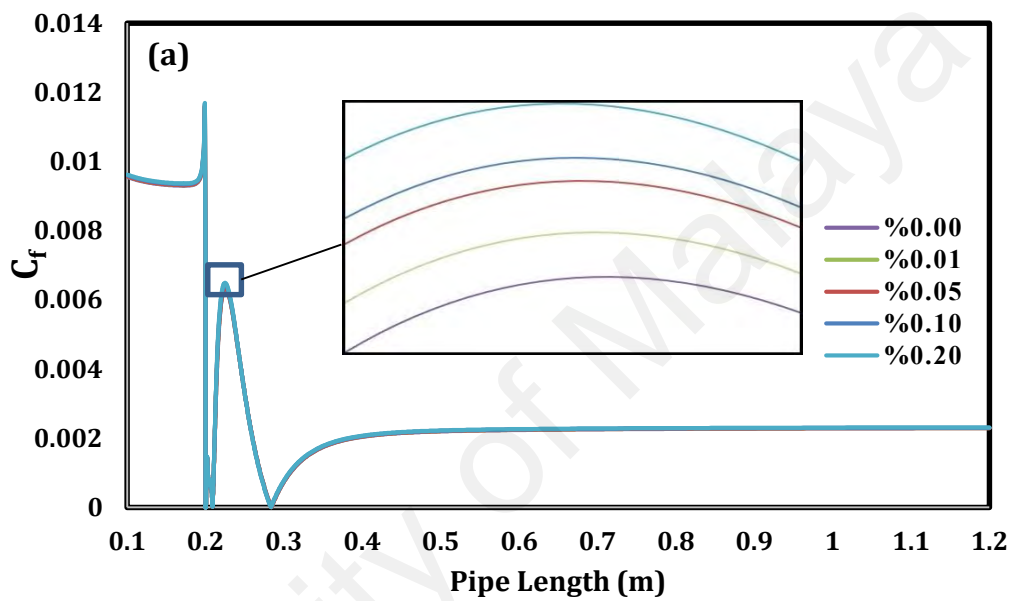
As it is seen in Figure 4.101, the maximum enhancement in the forced convective heat transfer coefficient for EGNP-WEG is 50% at X_{max} . The reason for larger enhancement of the convective heat transfer with increasing concentration was discussed above by S. J. Aravind et al. (2011) using a simple analogy that the connective heat

transfer can be introduced with k/σ , where σ and k are the thickness of the thermal boundary layer and thermal conductivity of sample, respectively. According to S. J. Aravind et al. (2011), carbon nanostructures such as carbon nanotubes and graphene decrease the thermal boundary layer thickness. On the other hand, they increase the thermal conductivity of working fluids such as water and EG, as it is obvious in the present experimental results, indicating a significant increase in the convective heat transfer coefficient.

Also, the higher Nusselt number for the EGNP-WEG coolants in comparison with basefluid is attributed to the improved thermal conductivity, which leads to the lower temperature difference between the tube wall and the bulk fluid.

The friction factor for the upper and lower walls at different weight concentrations of EGNP is shown in Figure 4.102a at constant inlet flow temperature of 35 °C. It is also clear from Figure 4.102a, as there are two peaks for skin friction coefficient for all cases. It is seen that the numerical friction shows some fluctuations, which is attributed to the circulation zone and followed by showing similar friction factor in the fully-developed regime. In addition, although the difference is not significant, the friction factor increases as the concentration of EGNP increases, which is in agreement with many experimental results in different regimes of flow, meaning basefluid has the lowest friction factor. The second peak can be attributed to the secondary recirculation region. Figure 4.102b is shown the ratio of skin friction factor of nanofluid to basefluid at different weight concentrations. It can be seen as the weight concentration increases, the ratio of the ratio of skin friction factor of nanofluid to basefluid increases. Figure 4.102c presents the performance index of EGNP-WEG for different weight concentration and Reynolds numbers. The performance index (ϵ) is the ratio of the heat transfer rate to the pressure drop. Some studies (e.g., Solangi et al. (2016)) illustrate that the addition of nanoparticles increases the heat transfer rate enhancement and the pressure drop together, which is

desirable and undesirable, respectively. Noticeably, the performance index results of all samples in X_{\max} for all Reynolds number is greater than 1, indicating the effectiveness of the prepared coolant over a backward facing step. This figure also shows that the performance index curves for different Reynolds number reach their peaks for a weight concentration of 0.05%, and that is followed by a decrease of the performance index for further increase in the weight concentration of EGNP.



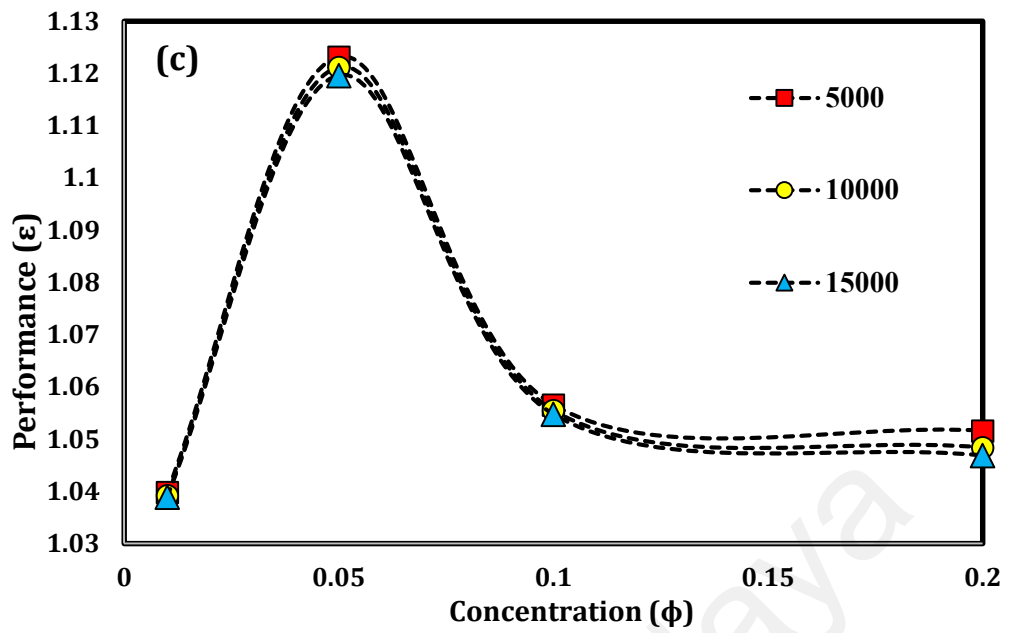


Figure 4.102: (a) Prediction of skin friction factor, (b) the ratio of skin friction factors of EGNP to basefluid, and (c) the performance index of the synthesized coolant versus weight concentrations of EGNP for various Reynolds numbers.

As a summary, this numerical study analyses the recirculation phenomena in a turbulent flow downstream over a backward facing step in the presence of a new type of coolant. Numerical simulation showed that the value and the position of maximum Nu depends on Re in the turbulent regime.

CHAPTER 5: CONCLUSIONS AND RECOMMENDATIONS

5.1 Conclusions

Present research work focused on investigation of a facile and economical method for the scalable synthesis of few-layered graphene sheets by the microwave-assisted functionalization. Here, single-layered graphene, few-layered graphene, highly-crumpled, few-layered graphene and highly-crumpled nitrogen-doped graphene with high surface area were produced by dispersion and liquid-phase exfoliation of functionalized graphite.

As the first phase of study, for mass-production of single and few-layered graphene, the treated graphite with PEG was firstly synthesized by covalent functionalization under microwave irradiation to enhance its dispersibility in polar aprotic organic solvents. Functionalization was confirmed by necessary characterization of the samples and statistically obtained about 90% of few-layered graphene containing one and two layers, about 84% of which were single-layered. The highly-porous, single-layered structure of graphene provides a special condition for using as additive in basefluids due to the specific surface area of the sheets. The nanoscopic porous morphology of single-layered graphene-based nanofluids have an important role in increasing BET surface. Furthermore, thermal treatment is a successful approach to prepare pure graphene without functional groups. The obtained results show that this procedure can be applied to prepare both functionalized sample and the pure graphene and product has been labeled as thermally-treated graphene (T-GR). Also, BET analysis indicated that the specific surface area of CE-GR and T-GR were up to 761 and 1559 m²/g, respectively. Another industrially-scalable, cost-effective, and simple approach was introduced for the first time to synthesize highly-crumpled, few-layered graphene and highly-crumpled nitrogen-doped graphene with large specific surface area. Highly-crumpled graphene and highly-crumpled nitrogen-doped graphene with appropriate specific surface area of 1689 and

1568 m²/g were synthesized and used as the additives for preparing highly-conductive coolants, respectively.

Owing to unique surface chemistry, superior specific surface area and high functionalization degree, the single-layered graphene, highly-crumpled, few-layered graphene and highly-crumpled nitrogen-doped graphene demonstrate excellent potential for using as additive in heat transfer liquids. So, all of the prepared materials with high degree of hydrophilic-functionalization and extremely high specific surface area have been introduced as promising candidates for heat transfer applications.

As the second phase of study, after manufacture of graphene sheets as additives, the colloidal stability of the samples in the presence of different functional groups has been investigated. The covalently functionalization of carbon-based nanostructures with highly-branched molecules are more effective than small molecules in terms of colloidal stability. It means, a functional group with higher hydrophilic branches is, a higher stability is, implying lower sediment in a specific period of time. The results suggest that the loss of weight concentration for the distilled water-based SGr nanofluids after 30 days was less than 13%. Thus the suitable colloidal stability of distilled water-based SGr nanofluids is attributed to the hydrophilic functional PEG which makes the small particle size of SGr associated with very high SSA as stable suspension in distilled water. Mostly, the easily-miscible PEG functionalities may explain the higher dispersion of the SGr in aqueous media. As the second sample, the prepared water-based HCFLG nanofluids were shown to be stable with less than 2% sedimentation after 30 days, which is the most stable sample in this study. As other samples, the maximum sediment of 26%, 15% and 25% were obtained for water/ethylene glycol-based CNDG nanofluid, water-based PEG-treated GNP nanofluid, and water-based Azo-treated GNP, respectively.

As the third phase of study, the thermo-physical properties of water-based HCFLG nanofluids and water-based SGr nanofluids were enhanced significantly, which make the nanofluids well-suited for heat transfer applications. The maximum enhancement in the thermal conductivity of water-based HCFLG nanofluids, water-based SGr nanofluids, water/ethylene glycol-based CNDG nanofluids, water/ethylene glycol-based EG-GNP nanofluids and water-based GNP-COOH nanofluids was 42.5%, 26%, 20%, 55% and 27%, respectively. These rates of enhancement are quite impressive even for some case in low weight concentration of 0.01 wt%. The thermal conductivity enhancements in the presence of different graphene-based additives have been confirmed that the high specific surface area of graphene family and the thinning of the thermal boundary layer can be the main reasons for enhancement of heat transfer rate.

Average drops in the range of 0.1–1% in specific heat capacity were observed after addition of SGr and HCFLG into the water with the weight concentration of 0.001–0.01 wt%. Also, the results show that the effective viscosity of water-based HCFLG nanofluids, water-based SGr nanofluids, water/ethylene glycol-based CNDG nanofluids, water/ethylene glycol-based EG-GNP nanofluids and water-based GNP-COOH nanofluids is higher than that of base fluid and increases as the weight concentration increases. Furthermore, the effective viscosity decreases with an increase in the temperature. Interestingly, the amounts of enhancement in viscosity are insignificant and negligible, resulting in maintaining the Newtonian behavior of base fluids. The maximum enhancement in viscosity was almost 10% in the presence of different graphene-based nanofluids. Also, the density of the water-based HCFLG nanofluids, water-based SGr nanofluids, and water/ethylene glycol-based EG-GNP nanofluids at weight concentration of 0.01% decreases by 1.01 and 0.99%, 0.87 and 0.88%, and 0.01 and 0.1%, when the temperature increases from 20 to 50 °C, respectively, which are really insignificant.

As the forth phase of study, the suitable stability without irreversible particle aggregation, improved thermal conductivity, low drop in specific heat capacity and density, and maintaining Newtonian behavior would enable the graphene-based nanofluids to be used as advanced alternative coolants in different heat transfer equipment e.g., car radiators, thermosyphon, and heat exchangers. The experimental results showed that both of the water-based HCFLG and water-based SGr nanofluids at very low concentrations exhibited noticeably higher heat transfer rate compared to the distilled water over a duct with a backward-facing step. As compared to the base fluid, the maximum enhancement in average heat transfer coefficient for transitional and turbulent flow regimes was 271% and 177% in the presence of water-based SGr nanofluid at 0.01 wt%, respectively. The amount of enhancement was 233.5% and 199% for water-based HCFLG nanofluids, respectively. Moreover, as the Re number increased from 2000 to 16000, the average ratio of enhancement decreased from 233.5% to only 83.8% at 0.01 wt%; from 132.9% to 42.4% at 0.005 wt%; and from 18.4% to only 5.6% at 0.001 wt% in the presence of water-based SGr nanofluids.

Also, Nu number and local heat transfer coefficient of water-based nanofluids for transitional and turbulent flow regimes showed that as the wt% of HCFLG as well as SGr in the nanofluids and/or Re number increase over backward-facing step, the position of maximum heat transfer point X_{\max}/D shifts to the higher distances, leading to larger recirculation zone. For example, for the same expansion ratio of 2 and Re number of 16000, the experimentally measured values of X_{\max}/D are, 4.66, 3.99, 3.33 and 3.33 for water-based HCFLG nanofluids at 0.01, 0.005, 0.001 and 0.00 wt%, respectively. The position as well as the amount of X_{\max}/D increased as the Re number increased, showing that X_{\max} is dependent on Re and the concentration of additives (thermal conductivity). It should be mentioned that the average overall performance index of duct including

expansion was 1.8 and 1.6 in the presence of water-based SGr nanofluids and water-based HCFLG nanofluids, respectively.

Also, crumpled nitrogen-doped graphene nanosheet and ethylene glycol-treated GNP were tested as the new additives for preparing a new engine coolant. The prepared two-dimensional crumpled nitrogen-doped graphene nanosheet feature high electrical conductivity, excellent thermal conductivity and heat transfer properties, permitting the water-ethylene glycol-based CNDG coolants to exhibit excellent Moudramtseff number, electrical properties and heat transfer performance for all temperatures and weight concentrations in a car radiator. Also, using ethylene glycol-treated GNP in GNP-WEG, without acid treatment phase, a new type of coolant with promising thermo-physical properties was developed for use in the car radiator. The average thermal performance of car radiator in the presence of water/EG-based ethylene glycol-treated GNP nanofluids increased by 99.9%, 102.2% and 115.3% for inlet temperature of 35, 45 and 55 °C, respectively. Other characteristics of the new coolant such as weak increase in the pressure drop for different concentrations (and inlet temperature, low friction factor, lack of corrosive agent, appropriate performance index ($PI > 1$), and slight increase in the required pumping power (less than 2%) are all highly favorable for introducing new fluid for wide industrial applications.

In thermosyphon, the experimental data suggests that the thermo-physical property of covalent nanofluids (GNP-COOH/water) was more significantly enhanced compared with those of non-covalent nanofluids (GNP-SDBS/water). The measured overall heat transfer, entropy, thermal efficiency, thermal resistance and pressure drop of covalent nanofluids showed promising results even at low nanofluid concentrations. The presented results suggest that the thermal performance of covalent nanofluids is significantly better than that of non-covalent samples in same experimental conditions. In summary, the covalent functionalization under microwave radiation is quick and cost-

effective with promising enhancement of thermal performance; therefore, it has the potential to replace the use of surfactant for synthesizing nanofluids and simple basefluids.

5.2 Recommendations for Future Work

- 1- Investigation heat transfer performance of heat pipes in the presence of water-based graphene nanofluids
- 2- Investigation of miniature thermosyphons in terms of convective heat transfer rate in the presence of water-based graphene nanofluids
- 3- Mass production of highly-porous graphene sheets for heat transfer application
- 4- Investigation of heat transfer performance of thermosyphons in the presence of graphene quantum dots as additive
- 5- Investigation heat transfer performance of heat pipes in the presence of water-based graphene quantum dots nanofluids
- 6- Investigation of miniature thermosyphons in terms of convective heat transfer rate in the presence of water-based graphene quantum dots nanofluids
- 7- Investigation of colloidal stability of graphene quantum dots in different solvents such as water, ethylene glycol, DMF, etc.
- 8- Investigation of thermo-physical properties of different graphene quantum dots nanofluids.

REFERENCES

- Abdelkader, A., Cooper, A., Dryfe, R., & Kinloch, I. (2015). How to get between the sheets: a review of recent works on the electrochemical exfoliation of graphene materials from bulk graphite. *Nanoscale*, 7(16), 6944-6956.
- Abu-Mulaweh, H., Armaly, B. F., & Chen, T. (1993). Measurements in buoyancy-assisting laminar boundary layer flow over a vertical backward-facing step—uniform wall heat flux case. *Experimental thermal and fluid science*, 7(1), 39-48.
- Abu-Nada, E. (2006). Entropy generation due to heat and fluid flow in backward facing step flow with various expansion ratios. *International Journal of Exergy*, 3(4), 419-435.
- Abu-Nada, E. (2008). Application of nanofluids for heat transfer enhancement of separated flows encountered in a backward facing step. *International Journal of Heat and Fluid Flow*, 29(1), 242-249.
- Abu-Nada, E., Masoud, Z., & Hijazi, A. (2008). Natural convection heat transfer enhancement in horizontal concentric annuli using nanofluids. *International Communications in Heat and Mass Transfer*, 35(5), 657-665.
doi:<http://dx.doi.org/10.1016/j.icheatmasstransfer.2007.11.004>
- Afshar, H., Shams, M., Nainian, S., & Ahmadi, G. (2009). Microchannel heat transfer and dispersion of nanoparticles in slip flow regime with constant heat flux. *International communications in heat and mass transfer*, 36(10), 1060-1066.
- Akhavan-Zanjani, H., Saffar-Avval, M., Mansourkiaei, M., Ahadi, M., & Sharif, F. (2014). Turbulent convective heat transfer and pressure drop of graphene–water nanofluid flowing inside a horizontal circular tube. *Journal of Dispersion Science and Technology*, 35(9), 1230-1240.
- Al-Hazmi, F. S., Al-Harbi, G. H., Beall, G. W., Al-Ghamdi, A. A., Obaid, A. Y., & Mahmoud, W. E. (2015). One pot synthesis of graphene based on microwave assisted solvothermal technique. *Synthetic Metals*, 200, 54-57.
doi:<http://dx.doi.org/10.1016/j.synthmet.2014.12.028>
- Alzari, V., Nuvoli, D., Sanna, R., Scognamillo, S., Piccinini, M., Kenny, J. M., Mariani, A. (2011). In situ production of high filler content graphene-based polymer nanocomposites by reactive processing. *Journal of Materials Chemistry*, 21(41), 16544-16549.
- A. Amiri, M. M., M. Baniadam, S. Zeinali Heris. (2011). One-pot, efficient functionalization of multi-walled carbon nanotubes with diamines by microwave method. *Applied Surface Science*, 257, 10261 - 11026.
- An, W., Zhang, J., Zhu, T., & Gao, N. (2016). Investigation on a spectral splitting photovoltaic/thermal hybrid system based on polypyrrole nanofluid: Preliminary test. *Renewable Energy*, 86, 633-642.
doi:<http://dx.doi.org/10.1016/j.renene.2015.08.080>

An, X., Butler, T. W., Washington, M., Nayak, S. K., & Kar, S. (2011). Optical and sensing properties of 1-pyrenecarboxylic acid-functionalized graphene films laminated on polydimethylsiloxane membranes. *ACS nano*, 5(2), 1003-1011.

An, X., Simmons, T., Shah, R., Wolfe, C., Lewis, K. M., Washington, M., Kar, S. (2010). Stable aqueous dispersions of noncovalently functionalized graphene from graphite and their multifunctional high-performance applications. *Nano letters*, 10(11), 4295-4301.

Aravind, S. J., Baskar, P., Baby, T. T., Sabareesh, R. K., Das, S., & Ramaprabhu, S. (2011). Investigation of structural stability, dispersion, viscosity, and conductive heat transfer properties of functionalized carbon nanotube based nanofluids. *The Journal of Physical Chemistry C*, 115(34), 16737-16744.

Aravind, S. J., & Ramaprabhu, S. (2011). Surfactant free graphene nanosheets based nanofluids by in-situ reduction of alkaline graphite oxide suspensions. *Journal of Applied Physics*, 110(12), 124326.

Aravind, S. S. J., & Ramaprabhu, S. (2013). Graphene-multiwalled carbon nanotube-based nanofluids for improved heat dissipation. *RSC Advances*, 3(13), 4199-4206. doi:10.1039/C3RA22653K

Armaly, B. F., Li, A., & Nie, J. (2003). Measurements in three-dimensional laminar separated flow. *International Journal of Heat and Mass Transfer*, 46(19), 3573-3582.

Arnold, E. (1970). UK steam tables in SI units. *United Kingdom Committee on the Properties of Steam, London, UK*.

Arzani, H. K., Amiri, A., Kazi, S., Chew, B., & Badarudin, A. (2016). Experimental investigation of thermophysical properties and heat transfer rate of covalently functionalized MWCNT in an annular heat exchanger. *International communications in heat and mass transfer*, 75, 67-77.

Ayan-Varela, M., Paredes, J., Villar-Rodil, S., Rozada, R., Martinez-Alonso, A., & Tascón, J. (2014). A quantitative analysis of the dispersion behavior of reduced graphene oxide in solvents. *Carbon*, 75, 390-400.

Azizi, M., Hosseini, M., Zafarnak, S., Shanbedi, M., & Amiri, A. (2013). Experimental analysis of thermal performance in a two-phase closed thermosiphon using graphene/water nanofluid. *Industrial & Engineering Chemistry Research*, 52(29), 10015-10021.

Azmi, W., Hamid, K. A., Mamat, R., Sharma, K., & Mohamad, M. (2016). Effects of working temperature on thermo-physical properties and forced convection heat transfer of TiO₂ nanofluids in water–Ethylene glycol mixture. *Applied Thermal Engineering*, 106, 1190-1199.

Baby, T. T., & Ramaprabhu, S. (2010). Investigation of thermal and electrical conductivity of graphene based nanofluids. *Journal of Applied Physics*, 108(12), 124308.

Baby, T. T., & Ramaprabhu, S. (2011a). Enhanced convective heat transfer using graphene dispersed nanofluids. *Nanoscale research letters*, 6(1), 1.

Baby, T. T., & Ramaprabhu, S. (2011b). Synthesis and nanofluid application of silver nanoparticles decorated graphene. *Journal of Materials Chemistry*, 21(26), 9702-9709.

Baby, T. T., & Sundara, R. (2011). Synthesis and transport properties of metal oxide decorated graphene dispersed nanofluids. *The Journal of Physical Chemistry C*, 115(17), 8527-8533.

Baby, T. T., & Sundara, R. (2013). Synthesis of silver nanoparticle decorated multiwalled carbon nanotubes-graphene mixture and its heat transfer studies in nanofluid. *AIP Advances*, 3(1), 012111.

Bai, H., Xu, Y., Zhao, L., Li, C., & Shi, G. (2009). Non-covalent functionalization of graphene sheets by sulfonated polyaniline. *Chemical Communications*(13), 1667-1669.

Balandin, A. A., Ghosh, S., Bao, W., Calizo, I., Teweldebrhan, D., Miao, F., & Lau, C. N. (2008). Superior thermal conductivity of single-layer graphene. *Nano letters*, 8(3), 902-907.

Bao, F.-b., & Lin, J.-z. (2011). Continuum simulation of the microscale backward-facing step flow in a transition regime. *Numerical Heat Transfer, Part A: Applications*, 59(8), 616-632.

Becerril, H. A., Mao, J., Liu, Z., Stoltenberg, R. M., Bao, Z., & Chen, Y. (2008). Evaluation of solution-processed reduced graphene oxide films as transparent conductors. *ACS nano*, 2(3), 463-470.

Bellos, E., Tzivanidis, C., Antonopoulos, K. A., & Gkinis, G. (2016). Thermal enhancement of solar parabolic trough collectors by using nanofluids and converging-diverging absorber tube. *Renewable Energy*, 94, 213-222.
doi:<http://dx.doi.org/10.1016/j.renene.2016.03.062>

Berger, C., Song, Z., Li, X., Wu, X., Brown, N., Naud, C., Marchenkov, A. N. (2006). Electronic confinement and coherence in patterned epitaxial graphene. *science*, 312(5777), 1191-1196.

Bergin, S. D., Nicolosi, V., Streich, P. V., Giordani, S., Sun, Z., Windle, A. H., Carpenter, L. (2008). Towards solutions of single-walled carbon nanotubes in common solvents. *ADVANCED MATERIALS-DEERFIELD BEACH THEN WEINHEIM-*, 20(10), 1876.

Biswas, G., Breuer, M., & Durst, F. (2004). Backward-facing step flows for various expansion ratios at low and moderate Reynolds numbers. *Journal of fluids engineering*, 126(3), 362-374.

Blake, P., Brimicombe, P. D., Nair, R. R., Booth, T. J., Jiang, D., Schedin, F., Hill, E. W. (2008). Graphene-based liquid crystal device. *Nano letters*, 8(6), 1704-1708.

Bojić, M., & Lukić, N. (2002). Controlling evaporative three finger thermosyphon. *Energy Conversion and Management*, 43(5), 709-720.

Botelho, E. C., Edwards, E. R., Bittmann, B., & Burkhart, T. (2011). Dispersing carbon nanotubes in phenolic resin using an aqueous solution. *Journal of the Brazilian Chemical Society*, 22(11), 2040-2047.

Bourlinos, A. B., Georgakilas, V., Zboril, R., Steriotis, T. A., & Stubos, A. K. (2009). Liquid-Phase Exfoliation of Graphite Towards Solubilized Graphenes. *Small*, 5(16), 1841-1845.

Bourlinos, A. B., Georgakilas, V., Zboril, R., Steriotis, T. A., Stubos, A. K., & Trapalis, C. (2009). Aqueous-phase exfoliation of graphite in the presence of polyvinylpyrrolidone for the production of water-soluble graphenes. *Solid State Communications*, 149(47), 2172-2176.

Bracamonte, M. V., Lacconi, G. I., Urreta, S. E., & Foa Torres, L. (2014). On the nature of defects in liquid-phase exfoliated graphene. *The Journal of Physical Chemistry C*, 118(28), 15455-15459.

Buschmann, M. H., & Franzke, U. (2014). Improvement of thermosyphon performance by employing nanofluid. *International Journal of Refrigeration*, 40, 416-428.

Cai, M., Thorpe, D., Adamson, D. H., & Schniepp, H. C. (2012). Methods of graphite exfoliation. *Journal of Materials Chemistry*, 22(48), 24992-25002.

Cai, W., Piner, R. D., Stadermann, F. J., Park, S., Shaibat, M. A., Ishii, Y., Stoller, M. (2008). Synthesis and solid-state NMR structural characterization of ¹³C-labeled graphite oxide. *science*, 321(5897), 1815-1817.

Can, W., Liang, Z., Qiao, W.-m., & Ling, L.-c. (2011). Preparation of graphene nanosheets through detonation. *New Carbon Materials*, 26(1), 21-25.

Cappella, B., & Dietler, G. (1999). Force-distance curves by atomic force microscopy. *Surface Science Reports*, 34(1-3), 1-104.
doi:[http://dx.doi.org/10.1016/S0167-5729\(99\)00003-5](http://dx.doi.org/10.1016/S0167-5729(99)00003-5)

Chandrasekaran, P., Cheralathan, M., Kumaresan, V., & Velraj, R. (2014). Enhanced heat transfer characteristics of water based copper oxide nanofluid PCM (phase change material) in a spherical capsule during solidification for energy efficient cool thermal storage system. *Energy*, 72(0), 636-642.
doi:<http://dx.doi.org/10.1016/j.energy.2014.05.089>

Chang, Y.-I., Chang, C.-C., & Cheng, W.-Y. (2011). Can nanoparticles stabilize microparticle suspension? *Separation and Purification Technology*, 79(3), 393-398.

Chehade, A., Louahlia-Gualous, H., Le Masson, S., Victor, I., & Abouzahab-Damaj, N. (2014). Experimental investigation of thermosyphon loop thermal performance. *Energy Conversion and Management*, 84, 671-680.

Chen, C., Zhai, W., Lu, D., Zhang, H., & Zheng, W. (2011). A facile method to prepare stable noncovalent functionalized graphene solution by using thionine. *Materials Research Bulletin*, 46(4), 583-587.

Cheng, J.-C., & Tsay, Y.-L. (2006). Effects of solid and slotted baffles on the convection characteristics of backward-facing step flow in a channel. *Heat and Mass Transfer*, 42(9), 843-852.

Chien, C., Kung, C., Chang, C., Lee, W., Jwo, C., & Chen, S. (2011). Theoretical and experimental investigations of a two-phase thermosyphon solar water heater. *Energy*, 36(1), 415-423.

Choi, E.-Y., Han, T. H., Hong, J., Kim, J. E., Lee, S. H., Kim, H. W., & Kim, S. O. (2010). Noncovalent functionalization of graphene with end-functional polymers. *Journal of Materials Chemistry*, 20(10), 1907-1912.

Choi, E.-Y., San Choi, W., Lee, Y. B., & Noh, Y.-Y. (2011). Production of graphene by exfoliation of graphite in a volatile organic solvent. *Nanotechnology*, 22(36), 365601.

Choi, J., Kim, K.-j., Kim, B., Lee, H., & Kim, S. (2009). Covalent functionalization of epitaxial graphene by azidotrimethylsilane. *The Journal of Physical Chemistry C*, 113(22), 9433-9435.

Choi, S., Zhang, Z., Yu, W., Lockwood, F., & Grulke, E. (2001). Anomalous thermal conductivity enhancement in nanotube suspensions. *Applied Physics Letters*, 79(14), 2252-2254.

Choi, S. Y., Mamak, M., Cordola, E., & Stadler, U. (2011). Large scale production of high aspect ratio graphite nanoplatelets with tunable oxygen functionality. *Journal of Materials Chemistry*, 21(13), 5142-5147.

Chol, S. (1995). Enhancing thermal conductivity of fluids with nanoparticles. *ASME-Publications-Fed*, 231, 99-106.

Chon, C., & Kihm, K. (2005). Thermal conductivity enhancement of nanofluids by Brownian motion. *Journal of Heat Transfer*, 127(8), 810-810.

Cingarapu, S., Singh, D., Timofeeva, E. V., & Moravek, M. R. (2014). Nanofluids with encapsulated tin nanoparticles for advanced heat transfer and thermal energy storage. *International Journal of Energy Research*, 38(1), 51-59. doi:10.1002/er.3041

Dabiri, M., Kasmaei, M., Salari, P., & Movahed, S. K. (2016). Copper nanoparticle decorated three dimensional graphene with high catalytic activity for Huisgen 1, 3-dipolar cycloaddition. *Rsc Advances*, 6, 57019-57023. doi: 10.1039/C5RA25317A

Dalir, N., Dehsara, M., & Nourazar, S. S. (2015). Entropy analysis for magnetohydrodynamic flow and heat transfer of a Jeffrey nanofluid over a stretching sheet. *Energy*, 79(0), 351-362. doi:<http://dx.doi.org/10.1016/j.energy.2014.11.021>

Das, B., Voggu, R., Rout, C. S., & Rao, C. N. R. (2008). Changes in the electronic structure and properties of graphene induced by molecular charge-transfer. *Chemical Communications*(41), 5155-5157. doi:10.1039/B808955H

Das, A., Pisana, S., Chakraborty, B., Piscanec, S., Saha, S. K., Waghmare, U. V., Sood, A. K. (2008). Monitoring dopants by Raman scattering in an

electrochemically top-gated graphene transistor. *Nat Nano*, 3(4), 210-215.
doi:http://www.nature.com/nnano/journal/v3/n4/supinfo/nnano.2008.67_S1.html

De Carli, M., Fiorenzato, S., & Zarrella, A. (2015). Performance of heat pumps with direct expansion in vertical ground heat exchangers in heating mode. *Energy Conversion and Management*, 95(0), 120-130.
doi:<http://dx.doi.org/10.1016/j.enconman.2015.01.080>

De, S., King, P. J., Lotya, M., O'Neill, A., Doherty, E. M., Hernandez, Y., Coleman, J. N. (2010). Flexible, Transparent, Conducting Films of Randomly Stacked Graphene from Surfactant-Stabilized, Oxide-Free Graphene Dispersions. *Small*, 6(3), 458-464.

Delfani, S., Karami, M., & Behabadi, M. A. A. (2016). Performance characteristics of a residential-type direct absorption solar collector using MWCNT nanofluid. *Renewable Energy*, 87, Part 1, 754-764.
doi:<http://dx.doi.org/10.1016/j.renene.2015.11.004>

Dhakate, S., Chauhan, N., Sharma, S., Tawale, J., Singh, S., Sahare, P., & Mathur, R. (2011). An approach to produce single and double layer graphene from re-exfoliation of expanded graphite. *Carbon*, 49(6), 1946-1954.

Dhar, P., Gupta, S. S., Chakraborty, S., Pattamatta, A., & Das, S. K. (2013). The role of percolation and sheet dynamics during heat conduction in poly-dispersed graphene nanofluids. *Applied Physics Letters*, 102(16), 163114.

Dikin, D. A., Stankovich, S., Zimney, E. J., Piner, R. D., Dommett, G. H., Evmenenko, G., Ruoff, R. S. (2007). Preparation and characterization of graphene oxide paper. *Nature*, 448(7152), 457-460.

Dimiev, A., Kosynkin, D. V., Sinitskii, A., Slesarev, A., Sun, Z., & Tour, J. M. (2011). Layer-by-layer removal of graphene for device patterning. *Science*, 331(6021), 1168-1172.

Ding, Y., Alias, H., Wen, D., & Williams, R. A. (2006a). Heat transfer of aqueous suspensions of carbon nanotubes (CNT nanofluids). *International Journal of Heat and Mass Transfer*, 49(1), 240-250.

Ding, Y., Alias, H., Wen, D., & Williams, R. A. (2006b). Heat transfer of aqueous suspensions of carbon nanotubes (CNT nanofluids). *International Journal of Heat and Mass Transfer*, 49(1-2), 240-250.
doi:<http://dx.doi.org/10.1016/j.ijheatmasstransfer.2005.07.009>

Ding, Y., & Wen, D. (2005). Particle migration in a flow of nanoparticle suspensions. *Powder Technology*, 149(2), 84-92.

Dittus, F. W., & Boelter, L. M. K. (1985). Heat transfer in automobile radiators of the tubular type. *International Communications in Heat and Mass Transfer*, 12(1), 3-22. doi:[http://dx.doi.org/10.1016/0735-1933\(85\)90003-X](http://dx.doi.org/10.1016/0735-1933(85)90003-X)

Dong, J., Zeng, B., Lan, Y., Tian, S., Shan, Y., Liu, X., Ren, Z. (2010). Field emission from few-layer graphene nanosheets produced by liquid phase exfoliation of graphite. *Journal of nanoscience and nanotechnology*, 10(8), 5051-5055.

- Dong, X., Shi, Y., Zhao, Y., Chen, D., Ye, J., Yao, Y., Shen, Z. (2009). Symmetry breaking of graphene monolayers by molecular decoration. *Physical review letters*, 102(13), 135501.
- Dreyer, D. R., Park, S., Bielawski, C. W., & Ruoff, R. S. (2010). The chemistry of graphene oxide. *Chemical Society Reviews*, 39(1), 228-240.
- Du, Q., Zheng, M., Zhang, L., Wang, Y., Chen, J., Xue, L., Cao, J. (2010). Preparation of functionalized graphene sheets by a low-temperature thermal exfoliation approach and their electrochemical supercapacitive behaviors. *Electrochimica Acta*, 55(12), 3897-3903.
- Du, W., Jiang, X., & Zhu, L. (2013). From graphite to graphene: direct liquid-phase exfoliation of graphite to produce single- and few-layered pristine graphene. *Journal of Materials Chemistry A*, 1(36), 10592-10606.
- Duan, W. H., Wang, Q., & Collins, F. (2011). Dispersion of carbon nanotubes with SDS surfactants: a study from a binding energy perspective. *Chemical Science*, 2(7), 1407-1413.
- Eapen, J., Li, J., & Yip, S. (2007). Beyond the Maxwell limit: thermal conduction in nanofluids with percolating fluid structures. *Physical Review E*, 76(6), 062501.
- Eastman, J. A., Phillpot, S., Choi, S., & Keblinski, P. (2004). Thermal transport in nanofluids 1. *Annu. Rev. Mater. Res.*, 34, 219-246.
- Eaton, J., & Johnston, J. (1981). A review of research on subsonic turbulent flow reattachment. *AIAA journal*, 19(9), 1093-1100.
- Edwards, R. S., & Coleman, K. S. (2013). Graphene synthesis: relationship to applications. *Nanoscale*, 5(1), 38-51.
- Englert, J. M., Röhr, J., Schmidt, C. D., Graupner, R., Hundhausen, M., Hauke, F., & Hirsch, A. (2009). Soluble Graphene: Generation of Aqueous Graphene Solutions Aided by a Perylenebisimide-Based Bolaamphiphile. *Advanced Materials*, 21(42), 4265-4269.
- Evans, W., Fish, J., & Keblinski, P. (2006). Role of Brownian motion hydrodynamics on nanofluid thermal conductivity. *Applied Physics Letters*, 88(9), 093116.
- Faghri, A. (1995). *Heat pipe science and technology*: Global Digital Press.
- Fang, M., Long, J., Zhao, W., Wang, L., & Chen, G. (2010). pH-responsive chitosan-mediated graphene dispersions. *Langmuir*, 26(22), 16771-16774.
- Fang, M., Wang, K., Lu, H., Yang, Y., & Nutt, S. (2009). Covalent polymer functionalization of graphene nanosheets and mechanical properties of composites. *Journal of Materials Chemistry*, 19(38), 7098-7105.
- Feng, L., Yang, L., Huang, Z., Luo, J., Li, M., Wang, D., & Chen, Y. (2013). Enhancing electrocatalytic oxygen reduction on nitrogen-doped graphene by active sites implantation. *Scientific reports*, 3, 3306.

Feng, Y., Liu, H., Luo, W., Liu, E., Zhao, N., Yoshino, K., & Feng, W. (2013). Covalent functionalization of graphene by azobenzene with molecular hydrogen bonds for long-term solar thermal storage. *Scientific reports*, 3, 3260.

Ferrari, A., Meyer, J., Scardaci, V., Casiraghi, C., Lazzeri, M., Mauri, F., Roth, S. (2006). Raman spectrum of graphene and graphene layers. *Physical review letters*, 97(18), 187401.

Filonenko, G. K. (1954). Hydraulic Resistance in Pipes (in Russian). *Teploenergetika*, 1(4), 40-44.

Fischer, A., Antonietti, M., & Thomas, A. (2007). Growth confined by the nitrogen source: synthesis of pure metal nitride nanoparticles in mesoporous graphitic carbon nitride. *Advanced Materials*, 19(2), 264-267.

Fischer, A., Müller, J. O., Antonietti, M., & Thomas, A. (2008). Synthesis of ternary metal nitride nanoparticles using mesoporous carbon nitride as reactive template. *ACS nano*, 2(12), 2489-2496.

Fu, Y., Zhang, J., Liu, H., Hiscox, W. C., & Gu, Y. (2013). Ionic liquid-assisted exfoliation of graphite oxide for simultaneous reduction and functionalization to graphenes with improved properties. *Journal of Materials Chemistry A*, 1(7), 2663-2674.

Garg, P., Alvarado, J. L., Marsh, C., Carlson, T. A., Kessler, D. A., & Annamalai, K. (2009). An experimental study on the effect of ultrasonication on viscosity and heat transfer performance of multi-wall carbon nanotube-based aqueous nanofluids. *International Journal of Heat and Mass Transfer*, 52(21), 5090-5101.

Geim, A. K., & Novoselov, K. S. (2007). The rise of graphene. *Nature materials*, 6(3), 183-191.

Geng, J., & Jung, H.-T. (2010). Porphyrin functionalized graphene sheets in aqueous suspensions: from the preparation of graphene sheets to highly conductive graphene films. *The Journal of Physical Chemistry C*, 114(18), 8227-8234.

Geng, J., Kong, B.-S., Yang, S. B., & Jung, H.-T. (2010). Preparation of graphene relying on porphyrin exfoliation of graphite. *Chemical Communications*, 46(28), 5091-5093.

Georgakilas, V., Bourlinos, A., Gournis, D., Tsoufis, T., Trapalis, C., Mateo-Alonso, A., & Prato, M. (2008). Multipurpose organically modified carbon nanotubes: from functionalization to nanotube composites. *Journal of the American Chemical Society*, 130(27), 8733-8740.

Georgakilas, V., Bourlinos, A. B., Zboril, R., Steriotis, T. A., Dallas, P., Stubos, A. K., & Trapalis, C. (2010). Organic functionalisation of graphenes. *Chemical Communications*, 46(10), 1766-1768.

Georgakilas, V., Otyepka, M., Bourlinos, A. B., Chandra, V., Kim, N., Kemp, K. C., Kim, K. S. (2012). Functionalization of graphene: covalent and non-covalent approaches, derivatives and applications. *Chemical Reviews*, 112(11), 6156-6214.

Gerardi, C., Cory, D., Buongiorno, J., Hu, L. W., & McKrell, T. (2009). Nuclear magnetic resonance-based study of ordered layering on the surface of alumina nanoparticles in water. *Applied Physics Letters*, 95(25), 253104.

Gharehkhani, S., Seyed Shirazi, S. F., Pilban Jahromi, S., Sookhajian, M., Baradaran, S., Yarmand, H., Basirun, W. J. (2015). Spongy nitrogen-doped activated carbonaceous hybrid derived from biomass material/graphene oxide for supercapacitor electrodes. *RSC Advances*, 5(51), 40505-40513. doi:10.1039/C5RA01525A

Ghiadi, B., Baniadam, M., Maghrebi, M., & Amiri, A. (2013). Rapid, one-pot synthesis of highly-soluble carbon nanotubes functionalized by L-arginine. *Russian Journal of Physical Chemistry A*, 87(4), 649-653.

Ghosh, A., Rao, K. V., George, S. J., & Rao, C. (2010). Noncovalent functionalization, exfoliation, and solubilization of graphene in water by employing a fluorescent coronene carboxylate. *Chemistry—A European Journal*, 16(9), 2700-2704.

Ghozatloo, A., Rashidi, A., & Shariaty-Niassar, M. (2014). Convective heat transfer enhancement of graphene nanofluids in shell and tube heat exchanger. *Experimental Thermal and Fluid Science*, 53, 136-141.

Ghozatloo, A., Shariaty-Niasar, M., & Rashidi, A. (2014). Investigation of Heat Transfer Coefficient of Ethylene Glycol/Graphenenanofluid in Turbulent Flow Regime. *International Journal of Nanoscience and Nanotechnology*, 10(4), 237-244.

Ghozatloo, A., Shariaty-Niasar, M., & Rashidi, A. M. (2013). Preparation of nanofluids from functionalized graphene by new alkaline method and study on the thermal conductivity and stability. *International Communications in Heat and Mass Transfer*, 42, 89-94.

Godson, L., Raja, B., Lal, D. M., & Wongwises, S. (2010). Experimental investigation on the thermal conductivity and viscosity of silver-deionized water nanofluid. *Experimental Heat Transfer*, 23(4), 317-332.

Green, A. A., & Hersam, M. C. (2009). Solution phase production of graphene with controlled thickness via density differentiation. *Nano letters*, 9(12), 4031-4036.

Gu, W., Zhang, W., Li, X., Zhu, H., Wei, J., Li, Z., Shen, W. (2009). Graphene sheets from worm-like exfoliated graphite. *Journal of Materials Chemistry*, 19(21), 3367-3369.

Guardia, L., Fernández-Merino, M., Paredes, J., Solis-Fernandez, P., Villar-Rodil, S., Martinez-Alonso, A., & Tascón, J. (2011). High-throughput production of pristine graphene in an aqueous dispersion assisted by non-ionic surfactants. *Carbon*, 49(5), 1653-1662.

Gunasekaran, S., & Dharmendirakumar, M. (2014). Carboxyl-tailed ionic liquid promoted aqueous dispersion of multi-walled carbon nanotubes. *High Performance Polymers*, 26(3), 274-282.

Guo, Y., Deng, L., Li, J., Guo, S., Wang, E., & Dong, S. (2011). Hemin-graphene hybrid nanosheets with intrinsic peroxidase-like activity for label-free colorimetric detection of single-nucleotide polymorphism. *ACS nano*, 5(2), 1282-1290.

Gupta, S. S., Siva, V. M., Krishnan, S., Sreepasad, T., Singh, P. K., Pradeep, T., & Das, S. K. (2011). Thermal conductivity enhancement of nanofluids containing graphene nanosheets. *Journal of Applied Physics*, 110(8), 084302.

Hadadian, M., Goharshadi, E. K., & Youssefi, A. (2014). Electrical conductivity, thermal conductivity, and rheological properties of graphene oxide-based nanofluids. *Journal of Nanoparticle Research*, 16(12), 1-17. doi:10.1007/s11051-014-2788-1

Hajjar, Z., morad Rashidi, A., & Ghozatloo, A. (2014). Enhanced thermal conductivities of graphene oxide nanofluids. *International Communications in Heat and Mass Transfer*, 57, 128-131.

Halelfadl, S., Maré, T., & Estellé, P. (2014). Efficiency of carbon nanotubes water based nanofluids as coolants. *Experimental Thermal and Fluid Science*, 53, 104-110.

Hamilton, C. E., Lomeda, J. R., Sun, Z., Tour, J. M., & Barron, A. R. (2009). High-yield organic dispersions of unfunctionalized graphene. *Nano letters*, 9(10), 3460-3462.

Hao, R., Qian, W., Zhang, L., & Hou, Y. (2008). Aqueous dispersions of TCNQ-anion-stabilized graphene sheets. *Chemical Communications*(48), 6576-6578. doi:10.1039/B816971C

Haque, A. M., Kwon, S., Kim, J., Noh, J., Huh, S., Chung, H., & Jeong, H. (2015). An experimental study on thermal characteristics of nanofluid with graphene and multi-wall carbon nanotubes. *Journal of Central South University*, 22(8), 3202-3210.

Hasan, S. A., Tsekoura, E. K., Sternhagen, V., & Strømme, M. (2012). Evolution of the composition and suspension performance of nitrogen-doped graphene. *The Journal of Physical Chemistry C*, 116(11), 6530-6536.

Hasan, T., Scardaci, V., Tan, P., Rozhin, A. G., Milne, W. I., & Ferrari, A. C. (2007). Stabilization and “debundling” of single-wall carbon nanotube dispersions in N-methyl-2-pyrrolidone (NMP) by polyvinylpyrrolidone (PVP). *The Journal of Physical Chemistry C*, 111(34), 12594-12602.

Hasan, T., Torrisi, F., Sun, Z., Popa, D., Nicolosi, V., Privitera, G., Ferrari, A. (2010). Solution-phase exfoliation of graphite for ultrafast photonics. *physica status solidi (b)*, 247(11-12), 2953-2957.

Hatami, M., Ganji, D. D., & Gorji-Bandpy, M. (2015). Experimental and numerical analysis of the optimized finned-tube heat exchanger for OM314 diesel exhaust exergy recovery. *Energy Conversion and Management*, 97(0), 26-41. doi:<http://dx.doi.org/10.1016/j.enconman.2015.03.032>

He, H., & Gao, C. (2010). General approach to individually dispersed, highly soluble, and conductive graphene nanosheets functionalized by nitrene chemistry. *Chemistry of Materials*, 22(17), 5054-5064.

He, H., Klinowski, J., Forster, M., & Lerf, A. (1998). A new structural model for graphite oxide. *Chemical Physics Letters*, 287(1), 53-56.

Heris, S. Z., Etemad, S. G., & Esfahany, M. N. (2006). Experimental investigation of oxide nanofluids laminar flow convective heat transfer. *International communications in heat and mass transfer*, 33(4), 529-535.

Heris, S. Z., Shokrgozar, M., Poorpharhang, S., Shanbedi, M., & Noie, S. H. (2013). Experimental Study of Heat Transfer of a Car Radiator with CuO/Ethylene Glycol-Water as a Coolant. *Journal of Dispersion Science and Technology*, 35(5), 677-684. doi:10.1080/01932691.2013.805301

Hernandez, Y., Nicolosi, V., Lotya, M., Blighe, F. M., Sun, Z., De, S., Gun'Ko, Y. K. (2008). High-yield production of graphene by liquid-phase exfoliation of graphite. *Nature nanotechnology*, 3(9), 563-568.

Heshmati, A., Mohammed, H., & Darus, A. (2014). Mixed convection heat transfer of nanofluids over backward facing step having a slotted baffle. *Applied Mathematics and Computation*, 240, 368-386.

Hossain, M. Z., Walsh, M. A., & Hersam, M. C. (2010). Scanning tunneling microscopy, spectroscopy, and nanolithography of epitaxial graphene chemically modified with aryl moieties. *Journal of the American Chemical Society*, 132(43), 15399-15403.

Hsieh, T.-Y., Hong, Z.-C., & Pan, Y.-C. (2010). Flow characteristics of three-dimensional microscale backward-facing step flows. *Numerical Heat Transfer, Part A: Applications*, 57(5), 331-345.

Hu, C., Yu, C., Li, M., Wang, X., Dong, Q., Wang, G., & Qiu, J. (2015). Nitrogen-doped carbon dots decorated on graphene: a novel all-carbon hybrid electrocatalyst for enhanced oxygen reduction reaction. *Chemical Communications*, 51(16), 3419-3422. doi:10.1039/C4CC08735F

Hu, H., Zhao, Z., Zhou, Q., Gogotsi, Y., & Qiu, J. (2012). The role of microwave absorption on formation of graphene from graphite oxide. *Carbon*, 50(9), 3267-3273.

Huang, X., Yin, Z., Wu, S., Qi, X., He, Q., Zhang, Q., Zhang, H. (2011). Graphene-based materials: synthesis, characterization, properties, and applications. *Small*, 7(14), 1876-1902.

Hussein, A. M., Sharma, K., Bakar, R., & Kadirgama, K. (2013). The effect of nanofluid volume concentration on heat transfer and friction factor inside a horizontal tube. *Journal of Nanomaterials*, 2013, 1.

Huxtable, S. T., Cahill, D. G., Shenogin, S., Xue, L., Ozisik, R., Barone, P., Shim, M. (2003). Interfacial heat flow in carbon nanotube suspensions. *Nature Materials*, 2(11), 731-734.

Imke, U. (2004). Porous media simplified simulation of single- and two-phase flow heat transfer in micro-channel heat exchangers. *Chemical Engineering Journal*, 101(1-3), 295-302. doi:<http://dx.doi.org/10.1016/j.cej.2003.10.012>

Islam, M., Rojas, E., Bergey, D., Johnson, A., & Yodh, A. (2003). High weight fraction surfactant solubilization of single-wall carbon nanotubes in water. *Nano letters*, 3(2), 269-273.

Israelachvili, J. N. (2011). *Intermolecular and surface forces: revised third edition*: Academic press.

Jaegfeldt, H., Kuwana, T., & Johansson, G. (1983). Electrochemical stability of catechols with a pyrene side chain strongly adsorbed on graphite electrodes for catalytic oxidation of dihydronicotinamide adenine dinucleotide. *Journal of the American Chemical Society*, *105*(7), 1805-1814.

Jaisankar, S., Radhakrishnan, T., & Sheeba, K. (2011). Experimental studies on heat transfer and thermal performance characteristics of thermosyphon solar water heating system with helical and left–right twisted tapes. *Energy Conversion and Management*, *52*(5), 2048-2055.

Jang, J.-H., Rangappa, D., Kwon, Y.-U., & Honma, I. (2011). Direct preparation of 1-PSA modified graphene nanosheets by supercritical fluidic exfoliation and its electrochemical properties. *Journal of Materials Chemistry*, *21*(10), 3462-3466.

Janowska, I., Chizari, K., Ersen, O., Zafeiratos, S., Soubane, D., Da Costa, V., Bégin, D. (2010). Microwave synthesis of large few-layer graphene sheets in aqueous solution of ammonia. *Nano Research*, *3*(2), 126-137.

Jeong, H. M., Lee, J. W., Shin, W. H., Choi, Y. J., Shin, H. J., Kang, J. K., & Choi, J. W. (2011). Nitrogen-doped graphene for high-performance ultracapacitors and the importance of nitrogen-doped sites at basal planes. *Nano letters*, *11*(6), 2472-2477.

Jha, N., & Ramaprabhu, S. (2008). Synthesis and Thermal Conductivity of Copper Nanoparticle Decorated Multiwalled Carbon Nanotubes Based Nanofluids. *The Journal of Physical Chemistry C*, *112*(25), 9315-9319. doi:10.1021/jp8017309

Jin, M., Jeong, H.-K., Kim, T. H., So, K. P., Cui, Y., Yu, W. J., Lee, Y. H. (2010). Synthesis and systematic characterization of functionalized graphene sheets generated by thermal exfoliation at low temperature. *Journal of Physics D: Applied Physics*, *43*(27), 275402.

Jin, Z., Lomeda, J. R., Price, B. K., Lu, W., Zhu, Y., & Tour, J. M. (2009). Mechanically assisted exfoliation and functionalization of thermally converted graphene sheets. *Chemistry of Materials*, *21*(14), 3045-3047.

Jo, K., Lee, T., Choi, H. J., Park, J. H., Lee, D. J., Lee, D. W., & Kim, B.-S. (2011). Stable aqueous dispersion of reduced graphene nanosheets via non-covalent functionalization with conducting polymers and application in transparent electrodes. *Langmuir*, *27*(5), 2014-2018.

Johnson, D. W., Dobson, B. P., & Coleman, K. S. (2015). A manufacturing perspective on graphene dispersions. *Current Opinion in Colloid & Interface Science*, *20*(5–6), 367-382. doi:<http://dx.doi.org/10.1016/j.cocis.2015.11.004>

Jouhara, H., & Merchant, H. (2012). Experimental investigation of a thermosyphon based heat exchanger used in energy efficient air handling units. *Energy*, *39*(1), 82-89.

Kalinina, I., Worsley, K., Lugo, C., Mandal, S., Bekyarova, E., & Haddon, R. C. (2011a). Synthesis, dispersion, and viscosity of poly (ethylene glycol)-functionalized

water-soluble single-walled carbon nanotubes. *Chemistry of Materials*, 23(5), 1246-1253.

Kalinina, I., Worsley, K., Lugo, C., Mandal, S., Bekyarova, E., & Haddon, R. C. (2011b). Synthesis, Dispersion, and Viscosity of Poly(ethylene glycol)-Functionalized Water-Soluble Single-Walled Carbon Nanotubes. *Chemistry of Materials*, 23(5), 1246-1253. doi:10.1021/cm103030s

Kaloudis, E., Papanicolaou, E., & Belessiotis, V. (2016). Numerical simulations of a parabolic trough solar collector with nanofluid using a two-phase model. *Renewable Energy*, 97, 218-229. doi:<http://dx.doi.org/10.1016/j.renene.2016.05.046>

Kamiya, H., Gotoh, K., Shimada, M., Uchikoshi, T., Otani, Y., Fuji, M., Higashitani, K. (2012). Characteristics and behavior of nanoparticles and its dispersion systems. *Nanoparticle Technology Handbook*, 5, 115-119.

Kang, H. U., Kim, S. H., & Oh, J. M. (2006). Estimation of thermal conductivity of nanofluid using experimental effective particle volume. *Experimental Heat Transfer*, 19(3), 181-191.

Kaniyoor, A., Baby, T. T., & Ramaprabhu, S. (2010). Graphene synthesis via hydrogen induced low temperature exfoliation of graphite oxide. *Journal of Materials Chemistry*, 20(39), 8467-8469.

Keblinski, P., Phillpot, S., Choi, S., & Eastman, J. (2002). Mechanisms of heat flow in suspensions of nano-sized particles (nanofluids). *International Journal of Heat and Mass Transfer*, 45(4), 855-863.

Khaled, A.-R., & Vafai, K. (2005). Heat transfer enhancement through control of thermal dispersion effects. *International Journal of Heat and Mass Transfer*, 48(11), 2172-2185.

Khalkhali, H., Faghri, A., & Zuo, Z. (1999). Entropy generation in a heat pipe system. *Applied Thermal Engineering*, 19(10), 1027-1043.

Khan, U., May, P., O'Neill, A., & Coleman, J. N. (2010). Development of stiff, strong, yet tough composites by the addition of solvent exfoliated graphene to polyurethane. *Carbon*, 48(14), 4035-4041.

Khan, U., O'Neill, A., Lotya, M., De, S., & Coleman, J. N. (2010). High-Concentration Solvent Exfoliation of Graphene. *Small*, 6(7), 864-871.

Khan, U., Porwal, H., O'Neill, A., Nawaz, K., May, P., & Coleman, J. N. (2011). Solvent-exfoliated graphene at extremely high concentration. *Langmuir*, 27(15), 9077-9082.

Khanra, P., Kuila, T., Bae, S. H., Kim, N. H., & Lee, J. H. (2012). Electrochemically exfoliated graphene using 9-anthracene carboxylic acid for supercapacitor application. *Journal of Materials Chemistry*, 22(46), 24403-24410.

Khare, B., Wilhite, P., Tran, B., Teixeira, E., Fresquez, K., Mvondo, D. N., Meyyappan, M. (2005). Functionalization of carbon nanotubes via nitrogen glow discharge. *The Journal of Physical Chemistry B*, 109(49), 23466-23472.

Kherbeet, A. S., Mohammed, H., Munisamy, K. M., & Salman, B. (2014). Combined convection nanofluid flow and heat transfer over microscale forward-facing step. *International Journal of Nanoparticles*, 7(1), 1-25.

Kherbeet, A. S., Mohammed, H., Salman, B., Ahmed, H. E., & Alawi, O. A. (2014). Experimental and numerical study of nanofluid flow and heat transfer over microscale backward-facing step. *International Journal of Heat and Mass Transfer*, 79, 858-867.

Kherbeet, A. S., Mohammed, H., Salman, B., Ahmed, H. E., Alawi, O. A., & Rashidi, M. (2015). Experimental study of nanofluid flow and heat transfer over microscale backward-and forward-facing steps. *Experimental Thermal and Fluid Science*, 65, 13-21.

Kherbeet, A. S., Mohammed, H. A., & Salman, B. (2012). The effect of nanofluids flow on mixed convection heat transfer over microscale backward-facing step. *International Journal of Heat and Mass Transfer*, 55(21), 5870-5881.

Kim, S., Kim, H. D., Kim, H., Ahn, H. S., Jo, H., Kim, J., & Kim, M. H. (2010). Effects of nano-fluid and surfaces with nano structure on the increase of CHF. *Experimental thermal and fluid science*, 34(4), 487-495.

Kline, S. J., and F. A. McClintock. (January 1953). Describing Uncertainties in Single-Sample Experiments. *Mechanical Engineering* 75(1), 3-8.

Kline, S. J., & McClintock, F. (1953). Describing uncertainties in single-sample experiments. *Mechanical engineering*, 75(1), 3-8.

Ko, G. H., Heo, K., Lee, K., Kim, D. S., Kim, C., Sohn, Y., & Choi, M. (2007). An experimental study on the pressure drop of nanofluids containing carbon nanotubes in a horizontal tube. *International Journal of Heat and Mass Transfer*, 50(23), 4749-4753.

Kodali, V. K., Scrimgeour, J., Kim, S., Hankinson, J. H., Carroll, K. M., De Heer, W. A., Curtis, J. E. (2010). Nonperturbative chemical modification of graphene for protein micropatterning. *Langmuir*, 27(3), 863-865.

Kole, M., & Dey, T. (2013). Investigation of thermal conductivity, viscosity, and electrical conductivity of graphene based nanofluids. *Journal of Applied Physics*, 113(8), 084307.

Koo, J., & Kleinstreuer, C. (2005). Impact analysis of nanoparticle motion mechanisms on the thermal conductivity of nanofluids. *International Communications in Heat and Mass Transfer*, 32(9), 1111-1118.

Kostarelos, K., Lacerda, L., Pastorin, G., Wu, W., Wieckowski, S., Luangsivilay, J., Muller, S. (2007). Cellular uptake of functionalized carbon nanotubes is independent of functional group and cell type. *Nature Nanotechnology*, 2(2), 108-113.

Kosynkin, D. V., Higginbotham, A. L., Sinitskii, A., Lomeda, J. R., Dimiev, A., Price, B. K., & Tour, J. M. (2009). Longitudinal unzipping of carbon nanotubes to form graphene nanoribbons. *Nature*, 458(7240), 872-876.

Kovtyukhova, N. I., Wang, Y., Berkdemir, A., Cruz-Silva, R., Terrones, M., Crespi, V. H., & Mallouk, T. E. (2014). Non-oxidative intercalation and exfoliation of graphite by Brønsted acids. *Nature chemistry*, 6, 957–963.

Kudin, K. N., Ozbas, B., Schniepp, H. C., Prud'Homme, R. K., Aksay, I. A., & Car, R. (2008). Raman spectra of graphite oxide and functionalized graphene sheets. *Nano letters*, 8(1), 36-41.

Kuila, T., Khanra, P., Kim, N. H., Choi, S. K., Yun, H. J., & Lee, J. H. (2013). One-step electrochemical synthesis of 6-amino-4-hydroxy-2-naphthalene-sulfonic acid functionalized graphene for green energy storage electrode materials. *Nanotechnology*, 24(36), 365706.

Kulkarni, D. P., Vajjha, R. S., Das, D. K., & Oliva, D. (2008). Application of aluminum oxide nanofluids in diesel electric generator as jacket water coolant. *Applied Thermal Engineering*, 28(14–15), 1774-1781.
doi:<http://dx.doi.org/10.1016/j.applthermaleng.2007.11.017>

Lancial, N., Beaubert, F., Harmand, S., & Rolland, G. (2013). Effects of a turbulent wall jet on heat transfer over a non-confined backward-facing step. *International Journal of Heat and fluid flow*, 44, 336-347.

Lauder, B. E., & Spalding, D. (1974). The numerical computation of turbulent flows. *Computer methods in applied mechanics and engineering*, 3(2), 269-289.

Lee, D.-W., Kim, T., & Lee, M. (2011). An amphiphilic pyrene sheet for selective functionalization of graphene. *Chemical Communications*, 47(29), 8259-8261.

Lee, D., Kim, J.-W., & Kim, B. G. (2006). A new parameter to control heat transport in nanofluids: surface charge state of the particle in suspension. *The Journal of Physical Chemistry B*, 110(9), 4323-4328.

Lee, G.-J., & Rhee, C. K. (2014). Enhanced thermal conductivity of nanofluids containing graphene nanoplatelets prepared by ultrasound irradiation. *Journal of Materials Science*, 49(4), 1506-1511.

Lee, S., Choi, S.-S., Li, S., and, & Eastman, J. (1999). Measuring thermal conductivity of fluids containing oxide nanoparticles. *Journal of Heat Transfer*, 121(2), 280-289.

Li, D., Mueller, M. B., Gilje, S., Kaner, R. B., & Wallace, G. G. (2008). Processable aqueous dispersions of graphene nanosheets. *Nature Nanotechnology*, 3(2), 101-105.

Li, F., Bao, Y., Chai, J., Zhang, Q., Han, D., & Niu, L. (2010). Synthesis and application of widely soluble graphene sheets. *Langmuir*, 26(14), 12314-12320.

Li, G. L., Liu, G., Li, M., Wan, D., Neoh, K., & Kang, E. (2010). Organo-and water-dispersible graphene oxide– polymer nanosheets for organic electronic memory and gold nanocomposites. *The Journal of Physical Chemistry C*, 114(29), 12742-12748.

Li, J., Niu, L., Zheng, Z., & Yan, F. (2014). Photosensitive graphene transistors. *Advanced Materials*, 26(31), 5239-5273.

Li, X., Chen, Y., Mo, S., Jia, L., & Shao, X. (2014). Effect of surface modification on the stability and thermal conductivity of water-based SiO₂-coated graphene nanofluid. *Thermochimica Acta*, 595, 6-10.

Li, X., Wang, H., Robinson, J. T., Sanchez, H., Diankov, G., & Dai, H. (2009). Simultaneous nitrogen doping and reduction of graphene oxide. *Journal of the American Chemical Society*, 131(43), 15939-15944.

Li, X., Wang, X., Zhang, L., Lee, S., & Dai, H. (2008). Chemically derived, ultrasmooth graphene nanoribbon semiconductors. *Science*, 319(5867), 1229-1232.

Li, X., Zhang, G., Bai, X., Sun, X., Wang, X., Wang, E., & Dai, H. (2008). Highly conducting graphene sheets and Langmuir–Blodgett films. *Nature Nanotechnology*, 3(9), 538-542.

Liang, Y., Wu, D., Feng, X., & Müllen, K. (2009). Dispersion of graphene sheets in organic solvent supported by ionic interactions. *Advanced Materials*, 21(17), 1679-1683.

Liang, Y. T., & Hersam, M. C. (2010). Highly concentrated graphene solutions via polymer enhanced solvent exfoliation and iterative solvent exchange. *Journal of the American Chemical Society*, 132(50), 17661-17663.

Lin, J.-T., Armaly, B., & Chen, T. (1991). Mixed convection heat transfer in inclined backward-facing step flows. *International Journal of Heat and Mass Transfer*, 34(6), 1568-1571.

Lin, W., Moon, K.-S., Zhang, S., Ding, Y., Shang, J., Chen, M., & Wong, C.-p. (2010). Microwave makes carbon nanotubes less defective. *ACS nano*, 4(3), 1716-1722.

Liu, F., Choi, J. Y., & Seo, T. S. (2010). DNA mediated water-dispersible graphene fabrication and gold nanoparticle-graphene hybrid. *Chemical Communications*, 46(16), 2844-2846.

Liu, H., Gao, J., Xue, M., Zhu, N., Zhang, M., & Cao, T. (2009). Processing of graphene for electrochemical application: noncovalently functionalize graphene sheets with water-soluble electroactive methylene green. *Langmuir*, 25(20), 12006-12010.

Liu, H., Ryu, S., Chen, Z., Steigerwald, M. L., Nuckolls, C., & Brus, L. E. (2009). Photochemical reactivity of graphene. *Journal of the American Chemical Society*, 131(47), 17099-17101.

Liu, J., Li, Y., Li, Y., Li, J., & Deng, Z. (2010). Noncovalent DNA decorations of graphene oxide and reduced graphene oxide toward water-soluble metal–carbon hybrid nanostructures via self-assembly. *Journal of Materials Chemistry*, 20(5), 900-906.

Liu, J., Wang, F., Zhang, L., Fang, X., & Zhang, Z. (2014). Thermodynamic properties and thermal stability of ionic liquid-based nanofluids containing graphene as advanced heat transfer fluids for medium-to-high-temperature applications. *Renewable Energy*, 63, 519-523.

Liu, J., Yang, W., Tao, L., Li, D., Boyer, C., & Davis, T. P. (2010). Thermosensitive graphene nanocomposites formed using pyrene-terminal polymers

made by RAFT polymerization. *Journal of Polymer Science Part A: Polymer Chemistry*, 48(2), 425-433.

Liu, L.-H., Lerner, M. M., & Yan, M. (2010). Derivatization of pristine graphene with well-defined chemical functionalities. *Nano letters*, 10(9), 3754-3756.

Liu, N., Luo, F., Wu, H., Liu, Y., Zhang, C., & Chen, J. (2008). One-step ionic-liquid-assisted electrochemical synthesis of ionic-liquid-functionalized graphene sheets directly from graphite. *Advanced Functional Materials*, 18(10), 1518-1525.

Liu, S., Tian, J., Wang, L., Li, H., Zhang, Y., & Sun, X. (2010). Stable aqueous dispersion of graphene nanosheets: noncovalent functionalization by a polymeric reducing agent and their subsequent decoration with Ag nanoparticles for enzymeless hydrogen peroxide detection. *Macromolecules*, 43(23), 10078-10083.

Liu, Z.-H., Hu, R.-L., Lu, L., Zhao, F., & Xiao, H.-s. (2013). Thermal performance of an open thermosyphon using nanofluid for evacuated tubular high temperature air solar collector. *Energy Conversion and Management*, 73, 135-143.

Loh, K. P., Bao, Q., Eda, G., & Chhowalla, M. (2010). Graphene oxide as a chemically tunable platform for optical applications. *Nature chemistry*, 2(12), 1015-1024.

Lomeda, J. R., Doyle, C. D., Kosynkin, D. V., Hwang, W.-F., & Tour, J. M. (2008). Diazonium functionalization of surfactant-wrapped chemically converted graphene sheets. *Journal of the American Chemical Society*, 130(48), 16201-16206.

Lopes, M., Candini, A., Urdampilleta, M., Reserbat-Plantey, A., Bellini, V., Klyatskaya, S., Wernsdorfer, W. (2010). Surface-enhanced Raman signal for terbium single-molecule magnets grafted on graphene. *ACS nano*, 4(12), 7531-7537.

Lotya, M., Hernandez, Y., King, P. J., Smith, R. J., Nicolosi, V., Karlsson, L. S., McGovern, I. (2009). Liquid phase production of graphene by exfoliation of graphite in surfactant/water solutions. *Journal of the American Chemical Society*, 131(10), 3611-3620.

Lotya, M., King, P. J., Khan, U., De, S., & Coleman, J. N. (2010). High-concentration, surfactant-stabilized graphene dispersions. *ACS nano*, 4(6), 3155-3162.

Lu, J., Yang, J.-x., Wang, J., Lim, A., Wang, S., & Loh, K. P. (2009). One-Pot Synthesis of Fluorescent Carbon Nanoribbons, Nanoparticles, and Graphene by the Exfoliation of Graphite in Ionic Liquids. *ACS nano*, 3(8), 2367-2375. doi:10.1021/nn900546b

Lv, W., Tang, D.-M., He, Y.-B., You, C.-H., Shi, Z.-Q., Chen, X.-C., Yang, Q.-H. (2009). Low-temperature exfoliated graphenes: vacuum-promoted exfoliation and electrochemical energy storage. *ACS nano*, 3(11), 3730-3736.

Ma, W., Yang, F., Shi, J., Wang, F., Zhang, Z., & Wang, S. (2013). Silicone based nanofluids containing functionalized graphene nanosheets. *Colloids and Surfaces A: Physicochemical and Engineering Aspects*, 431, 120-126.

Maheshkumar, P., & Muraleedharan, C. (2011). Minimization of entropy generation in flat heat pipe. *International Journal of Heat and Mass Transfer*, 54(1), 645-648.

Manca, O., Nardini, S., & Ricci, D. (2012). A numerical study of nanofluid forced convection in ribbed channels. *Applied Thermal Engineering*, 37, 280-292.

Manimaran, R., Palaniradja, K., Alagumurthi, N., & Hussain, J. (2014). Experimental comparative study of heat pipe performance using CuO and TiO₂ nanofluids. *International Journal of Energy Research*, 38(5), 573-580.
doi:10.1002/er.3058

Mansour, R. B., Galanis, N., & Nguyen, C. T. (2007). Effect of uncertainties in physical properties on forced convection heat transfer with nanofluids. *Applied Thermal Engineering*, 27(1), 240-249.
doi:<http://dx.doi.org/10.1016/j.applthermaleng.2006.04.011>

Marcano, D. C., Kosynkin, D. V., Berlin, J. M., Sinitskii, A., Sun, Z., Slesarev, A., Tour, J. M. (2010). Improved synthesis of graphene oxide. *ACS nano*, 4(8), 4806-4814.

Marchini, S., Günther, S., & Wintterlin, J. (2007). Scanning tunneling microscopy of graphene on Ru (0001). *Physical Review B*, 76(7), 075429.

Martin-Gallego, M., Verdejo, R., Khayet, M., de Zarate, J. M. O., Essalhi, M., & Lopez-Manchado, M. A. (2011). Thermal conductivity of carbon nanotubes and graphene in epoxy nanofluids and nanocomposites. *Nanoscale research letters*, 6(1), 1-7.

Mason, T. J., & Lorimer, J. P. (2002). Introduction to applied ultrasonics. *Applied Sonochemistry: Uses of Power Ultrasound in Chemistry and Processing*, 5, 1-24.

Matsumoto, M., Saito, Y., Park, C., Fukushima, T., & Aida, T. (2015a). Ultrahigh-throughput exfoliation of graphite into pristine 'single-layer' graphene using microwaves and molecularly engineered ionic liquids. *Nat Chem*, 7(9), 730-736.
doi:10.1038/nchem.2315,
<http://www.nature.com/nchem/journal/v7/n9/abs/nchem.2315.html#supplementary-information>

Matsumoto, M., Saito, Y., Park, C., Fukushima, T., & Aida, T. (2015b). Ultrahigh-throughput exfoliation of graphite into pristine 'single-layer' graphene using microwaves and molecularly engineered ionic liquids. *Nature chemistry*, 7(9), 730-736.

Maxwell, J. C. (1881). A treatise on electricity and magnetism (Vol. 1): *Clarendon press*, 1.

May, P., Khan, U., Hughes, J. M., & Coleman, J. N. (2012). Correction to "Role of Solubility Parameters in Understanding the Steric Stabilization of Exfoliated Two-Dimensional Nanosheets by Adsorbed Polymers". *The Journal of Physical Chemistry C*, 116(45), 24390-24391.

McAllister, M. J., Li, J.-L., Adamson, D. H., Schniepp, H. C., Abdala, A. A., Liu, J., Prud'homme, R. K. (2007). Single sheet functionalized graphene by oxidation and thermal expansion of graphite. *Chemistry of Materials*, 19(18), 4396-4404.

Mehrali, M., Sadeghinezhad, E., Latibari, S. T., Kazi, S. N., Mehrali, M., Zubir, M. N. B. M., & Metselaar, H. S. C. (2014). Investigation of thermal conductivity and rheological properties of nanofluids containing graphene nanoplatelets. *Nanoscale research letters*, 9(1), 1-12.

Mehrali, M., Sadeghinezhad, E., Latibari, S. T., Mehrali, M., Togun, H., Zubir, M., Metselaar, H. S. C. (2014). Preparation, characterization, viscosity, and thermal conductivity of nitrogen-doped graphene aqueous nanofluids. *Journal of Materials Science*, 49(20), 7156-7171.

Mehrali, M., Sadeghinezhad, E., Rosen, M. A., Akhiani, A. R., Latibari, S. T., Mehrali, M., & Metselaar, H. S. C. (2015). Heat transfer and entropy generation for laminar forced convection flow of graphene nanoplatelets nanofluids in a horizontal tube. *International Communications in Heat and Mass Transfer*, 66, 23-31.

Mehrali, M., Sadeghinezhad, E., Rosen, M. A., Latibari, S. T., Mehrali, M., Metselaar, H. S. C., & Kazi, S. N. (2015). Effect of specific surface area on convective heat transfer of graphene nanoplatelet aqueous nanofluids. *Experimental Thermal and Fluid Science*, 68, 100-108.

Mehrali, M., Sadeghinezhad, E., Tahan Latibari, S., Kazi, S. N., Mehrali, M., Zubir, M. N. B. M., & Metselaar, H. S. C. (2014). Investigation of thermal conductivity and rheological properties of nanofluids containing graphene nanoplatelets. *Nanoscale Research Letters*, 9(1), 1-12.

Mehta, B., & Khandekar, S. (2007). Two-phase closed thermosyphon with nanofluids. *14th International Heat Pipe Conference*, 1, 25-48.

Mensing, J. P., Kerdcharoen, T., Sriprachuabwong, C., Wisitsoraat, A., Phokharatkul, D., Lomas, T., & Tuantranont, A. (2012). Facile preparation of graphene-metal phthalocyanine hybrid material by electrolytic exfoliation. *Journal of Materials Chemistry*, 22(33), 17094-17099.

Meyer, J., Geim, A., Katsnelson, M., Novoselov, K., Obergfell, D., Roth, S., Zettl, A. (2007). On the roughness of single- and bi-layer graphene membranes. *Solid State Communications*, 143(1), 101-109.

Meyer, J. C., Geim, A. K., Katsnelson, M. I., Novoselov, K. S., Booth, T. J., & Roth, S. (2007). The structure of suspended graphene sheets. *Nature*, 446(7131), 60-63.

Minea, A., Manca, O., Moldoveanu, M. (2015) Fom comparison on al₂o₃, cuo and tio₂ water based nanofluids in laminar and turbulent flow, *Conference on Thermal Energy Systems*, 8, 21-45.

Moaseri, E., Maghrebi, M., & Baniadam, M. (2014). Improvements in mechanical properties of carbon fiber-reinforced epoxy composites: a microwave-assisted approach in functionalization of carbon fiber via diamines. *Materials & Design*, 55, 644-652.

Moffat, R. J. (1988). Describing the uncertainties in experimental results. *Experimental Thermal and Fluid Science*, 1(1), 3-17.
doi:[http://dx.doi.org/10.1016/0894-1777\(88\)90043-X](http://dx.doi.org/10.1016/0894-1777(88)90043-X)

Mohammad Zadeh, P., Sokhansefat, T., Kasaeian, A. B., Kowsary, F., & Akbarzadeh, A. (2015). Hybrid optimization algorithm for thermal analysis in a solar parabolic trough collector based on nanofluid. *Energy*, 82(0), 857-864.
doi:<http://dx.doi.org/10.1016/j.energy.2015.01.096>

Mohammed, H., Al-Aswadi, A., Shuaib, N., & Saidur, R. (2011). Convective heat transfer and fluid flow study over a step using nanofluids: a review. *Renewable and Sustainable Energy Reviews*, 15(6), 2921-2939.

Mohammed, H., Al-Aswadi, A., Yusoff, M., & Saidur, R. (2012). Mixed convective flows over backward facing step in a vertical duct using various nanofluids-buoyancy-assisting case. *Thermophys. Aeromech*, 42(1), 1-30.

Mohammed, H., Al-aswadi, A., Abu-Mulaweh, H., & Shuaib, N. (2011). Influence of nanofluids on mixed convective heat transfer over a horizontal backward-facing step. *Heat Transfer—Asian Research*, 40(4), 287-307.

Mohammed, H., Alawi, O. A., & Wahid, M. (2015). Mixed convective nanofluid flow in a channel having backward-facing step with a baffle. *Powder Technology*, 275, 329-343.

Mousa, M. (2011). Effect of nanofluid concentration on the performance of circular heat pipe. *Ain shams engineering journal*, 2(1), 63-69.

Murphy, D., & Hull Jr, G. (1975). Monodispersed tantalum disulfide and adsorption complexes with cations. *The Journal of Chemical Physics*, 62(3), 973-978.

Murshed, S., Leong, K., & Yang, C. (2006). A model for predicting the effective thermal conductivity of nanoparticle-fluid suspensions. *International Journal of Nanoscience*, 5(01), 23-33.

Murshed, S., Leong, K., & Yang, C. (2008). Investigations of thermal conductivity and viscosity of nanofluids. *International Journal of Thermal Sciences*, 47(5), 560-568.

Nan, C.-W., Birringer, R., Clarke, D. R., & Gleiter, H. (1997). Effective thermal conductivity of particulate composites with interfacial thermal resistance. *Journal of Applied Physics*, 81(10), 6692-6699.

Nanda, J., Maranville, C., Bollin, S. C., Sawall, D., Ohtani, H., Remillard, J. T., & Ginder, J. (2008). Thermal conductivity of single-wall carbon nanotube dispersions: role of interfacial effects. *The Journal of Physical Chemistry C*, 112(3), 654-658.

Nemes-Incze, P., Osváth, Z., Kamarás, K., & Biró, L. (2008). Anomalies in thickness measurements of graphene and few layer graphite crystals by tapping mode atomic force microscopy. *Carbon*, 46(11), 1435-1442.

Nie, J., & Armaly, B. F. (2002). Three-dimensional convective flow adjacent to backward-facing step-effects of step height. *International Journal of Heat and Mass Transfer*, 45(12), 2431-2438.

Niu, L., Coleman, J. N., Zhang, H., Shin, H., Chhowalla, M., & Zheng, Z. (2016). Production of Two-Dimensional Nanomaterials via Liquid-Based Direct Exfoliation. *Small*, 12(3), 272-293.

Niyogi, S., Bekyarova, E., Itkis, M. E., Zhang, H., Shepperd, K., Hicks, J., Deheer, W. A. (2010). Spectroscopy of covalently functionalized graphene. *Nano letters*, 10(10), 4061-4066.

Notley, S. M. (2012). Highly concentrated aqueous suspensions of graphene through ultrasonic exfoliation with continuous surfactant addition. *Langmuir*, 28(40), 14110-14113.

Novoselov, K., Geim, A. K., Morozov, S., Jiang, D., Katsnelson, M., Grigorieva, I., Firsov, A. (2005). Two-dimensional gas of massless Dirac fermions in graphene. *Nature*, 438(7065), 197-200.

Novoselov, K., Jiang, D., Schedin, F., Booth, T., Khotkevich, V., Morozov, S., & Geim, A. (2005). Two-dimensional atomic crystals. *Proceedings of the National Academy of Sciences of the United States of America*, 102(30), 10451-10453.

Novoselov, K. S., Fal, V., Colombo, L., Gellert, P., Schwab, M., & Kim, K. (2012). A roadmap for graphene. *Nature*, 490(7419), 192-200.

Novoselov, K. S., Geim, A. K., Morozov, S., Jiang, D., Zhang, Y., Dubonos, S. a., Firsov, A. (2004). Electric field effect in atomically thin carbon films. *science*, 306(5696), 666-669.

O'Neill, A., Khan, U., Nirmalraj, P. N., Boland, J., & Coleman, J. N. (2011). Graphene dispersion and exfoliation in low boiling point solvents. *The Journal of Physical Chemistry C*, 115(13), 5422-5428.

Obraztsov, A. N. (2009). Chemical vapour deposition: making graphene on a large scale. *Nature nanotechnology*, 4(4), 212-213.

Ohta, T., El Gabaly, F., Bostwick, A., McChesney, J. L., Emtsev, K. V., Schmid, A. K., Rotenberg, E. (2008). Morphology of graphene thin film growth on SiC (0001). *New Journal of Physics*, 10(2), 023034.

Olah, G. A., Germain, A., Lin, H. C., & Forsyth, D. A. (1975). Electrophilic reactions at single bonds. XVIII. Indication of protosolvated de facto substituting agents in the reactions of alkanes with acylium and nitronium ions in superacidic media. *Journal of the American Chemical Society*, 97(10), 2928-2929.

Ou, B., Zhou, Z., Liu, Q., Liao, B., Yi, S., Ou, Y., Li, D. (2012). Covalent functionalization of graphene with poly (methyl methacrylate) by atom transfer radical polymerization at room temperature. *Polymer Chemistry*, 3(10), 2768-2775.

Pak, B. C., & Cho, Y. I. (1998). Hydrodynamic and heat transfer study of dispersed fluids with submicron metallic oxide particles. *Experimental Heat Transfer*, 11(2), 151-170. doi:10.1080/08916159808946559

Pak, B. C., & Cho, Y. I. (1998). Hydrodynamic and heat transfer study of dispersed fluids with submicron metallic oxide particles. *Experimental Heat Transfer an International Journal*, 11(2), 151-170.

Pan, S., Zhu, J., & Liu, X. (2013). Preparation, electrochemical properties, and adsorption kinetics of Ni₃S₂/graphene nanocomposites using alkyldithiocarbamate complexes of nickel (ii) as single-source precursors. *New Journal of Chemistry*, 37(3), 654-662.

Paramethanuwat, T., Rittidech, S., Pattiya, A., Ding, Y., & Witharana, S. (2011). Application of silver nanofluid containing oleic acid surfactant in a thermosyphon economizer. *Nanoscale research letters*, 6(1), 1-10.

Paredes, J. I., Villar-Rodil, S., Martínez-Alonso, A., & Tascón, J. M. D. (2008). Graphene Oxide Dispersions in Organic Solvents. *Langmuir*, 24(19), 10560-10564. doi:10.1021/la801744a

Park, S.-H., Bak, S.-M., Kim, K.-H., Jegal, J.-P., Lee, S.-I., Lee, J., & Kim, K.-B. (2011). Solid-state microwave irradiation synthesis of high quality graphene nanosheets under hydrogen containing atmosphere. *Journal of Materials Chemistry*, 21(3), 680-686.

Park, S., An, J., Jung, I., Piner, R. D., An, S. J., Li, X., Ruoff, R. S. (2009). Colloidal suspensions of highly reduced graphene oxide in a wide variety of organic solvents. *Nano letters*, 9(4), 1593-1597.

Park, S., Lee, K.-S., Bozoklu, G., Cai, W., Nguyen, S. T., & Ruoff, R. S. (2008). Graphene oxide papers modified by divalent ions—enhancing mechanical properties via chemical cross-linking. *ACS nano*, 2(3), 572-578.

Park, S., Mohanty, N., Suk, J. W., Nagaraja, A., An, J., Piner, R. D., Ruoff, R. S. (2010). Biocompatible, robust free-standing paper composed of a tween/graphene composite. *Advanced Materials*, 22(15), 1736-1740.

Park, S., & Ruoff, R. S. (2009). Chemical methods for the production of graphenes. *Nature Nanotechnology*, 4(4), 217-224.

Park, S., & Ruoff, R. S. (2015). Synthesis and characterization of chemically modified graphenes. *Current Opinion in Colloid & Interface Science*, 20(5), 322-328.

Park, S. D., Lee, S. W., Kang, S., Bang, I. C., Kim, J. H., Shin, H. S., Lee, D. W. (2010). Effects of nanofluids containing graphene/graphene-oxide nanosheets on critical heat flux. *Applied Physics Letters*, 97(2), 023103.

Park, S. S., & Kim, N. J. (2014). Influence of the oxidation treatment and the average particle diameter of graphene for thermal conductivity enhancement. *Journal of Industrial and Engineering Chemistry*, 20(4), 1911-1915.

Parvez, K., Li, R., Puniredd, S. R., Hernandez, Y., Hinkel, F., Wang, S., Müllen, K. (2013). Electrochemically exfoliated graphene as solution-processable, highly conductive electrodes for organic electronics. *ACS nano*, 7(4), 3598-3606.

Parvez, K., Wu, Z.-S., Li, R., Liu, X., Graf, R., Feng, X., & Müllen, K. (2014). Exfoliation of graphite into graphene in aqueous solutions of inorganic salts. *Journal of the American Chemical Society*, 136(16), 6083-6091.

- Parviz, D., Das, S., Ahmed, H. T., Irin, F., Bhattacharia, S., & Green, M. J. (2012). Dispersions of non-covalently functionalized graphene with minimal stabilizer. *ACS nano*, 6(10), 8857-8867.
- Paton, K. R., Varrla, E., Backes, C., Smith, R. J., Khan, U., O'Neill, A., King, P. (2014). Scalable production of large quantities of defect-free few-layer graphene by shear exfoliation in liquids. *Nature materials*, 13(6), 624-630.
- Phillips, R. J., Armstrong, R. C., Brown, R. A., Graham, A. L., & Abbott, J. R. (1992). A constitutive equation for concentrated suspensions that accounts for shear-induced particle migration. *Physics of Fluids A: Fluid Dynamics (1989-1993)*, 4(1), 30-40.
- Pisana, S., Lazzeri, M., Casiraghi, C., Novoselov, K. S., Geim, A. K., Ferrari, A. C., & Mauri, F. (2007). Breakdown of the adiabatic Born–Oppenheimer approximation in graphene. *Nature materials*, 6(3), 198-201.
- Popiel, C. O., & Wojtkowiak, J. (1998). Simple Formulas for Thermophysical Properties of Liquid Water for Heat Transfer Calculations (from 0°C to 150°C). *Heat transfer engineering*, 19(3), 87-101. doi:10.1080/01457639808939929
- Qi, X., Pu, K. Y., Li, H., Zhou, X., Wu, S., Fan, Q. L., Zhang, H. (2010). Amphiphilic graphene composites. *Angewandte Chemie International Edition*, 49(49), 9426-9429.
- Qian, W., Hao, R., Hou, Y., Tian, Y., Shen, C., Gao, H., & Liang, X. (2009). Solvothermal-assisted exfoliation process to produce graphene with high yield and high quality. *Nano Research*, 2(9), 706-712.
- Quintana, M., Spyrou, K., Grzelczak, M., Browne, W. R., Rudolf, P., & Prato, M. (2010). Functionalization of graphene via 1, 3-dipolar cycloaddition. *ACS nano*, 4(6), 3527-3533.
- Radic, S., Geitner, N. K., Podila, R., Käkinen, A., Chen, P., Ke, P. C., & Ding, F. (2013). Competitive binding of natural amphiphiles with graphene derivatives. *Scientific reports*, 3, 2273.
- Rao, K. S., Sentilnathan, J., Cho, H. W., Wu, J. J., & Yoshimura, M. (2015). Soft Processing of Graphene Nanosheets by Glycine-Bisulfate Ionic-Complex-Assisted Electrochemical Exfoliation of Graphite for Reduction Catalysis. *Advanced Functional Materials*, 25(2), 298-305.
- Rashidi, M., & Abbasbandy, S. (2011). Analytic approximate solutions for heat transfer of a micropolar fluid through a porous medium with radiation. *Communications in Nonlinear Science and Numerical Simulation*, 16(4), 1874-1889.
- Rocquefelte, X., Boucher, F., Gressier, P., Ouvrard, G., Blaha, P., & Schwarz, K. (2000). Mo cluster formation in the intercalation compound LiMoS₂. *Physical Review B*, 62(4), 2397.
- Ruoff, R. (2008). Graphene: Calling all chemists. *Nature nanotechnology*, 3(1), 10-11.

Sadeghinezhad, E., Mehrali, M., Tahan Latibari, S., Mehrali, M., Kazi, S., Oon, C. S., & Metselaar, H. S. C. (2014). Experimental Investigation of Convective Heat Transfer Using Graphene Nanoplatelet Based Nanofluids under Turbulent Flow Conditions. *Industrial & Engineering Chemistry Research*, 53(31), 12455-12465.

Sadeghinezhad, E., Togun, H., Mehrali, M., Nejad, P. S., Latibari, S. T., Abdulrazzaq, T., Metselaar, H. S. C. (2015). An experimental and numerical investigation of heat transfer enhancement for graphene nanoplatelets nanofluids in turbulent flow conditions. *International Journal of Heat and Mass Transfer*, 81, 41-51.

Saidi, M., & Karimi, G. (2014). Free convection cooling in modified L-shape enclosures using copper–water nanofluid. *Energy*, 70(0), 251-271.
doi:<http://dx.doi.org/10.1016/j.energy.2014.03.121>

Samira, P., Saeed, Z., Motahare, S., & Mostafa, K. (2014). Pressure drop and thermal performance of CuO/ethylene glycol (60%)-water (40%) nanofluid in car radiator. *Korean Journal of Chemical Engineering*, 5, 1-8. doi:10.1007/s11814-014-0244-7

Samira, P., Saeed, Z. H., Motahare, S., & Mostafa, K. (2015). Pressure drop and thermal performance of CuO/ethylene glycol (60%)-water (40%) nanofluid in car radiator. *Korean Journal of Chemical Engineering*, 32(4), 609-616.

Sarsam, W., Amiri, A., Kazi, S., & Badarudin, A. (2016). Stability and thermophysical properties of non-covalently functionalized graphene nanoplatelets nanofluids. *Energy Conversion and Management*, 116, 101-111.

Sarsam, W., Amiri, A., Zubir, M. N. M., Yarmand, H., Kazi, S. N., & Badarudin, A. (2016b). Stability and thermophysical properties of water-based nanofluids containing triethanolamine-treated graphene nanoplatelets with different specific surface areas. *Colloids and Surfaces A: Physicochemical and Engineering Aspects*, 500, 17-31. doi:<http://dx.doi.org/10.1016/j.colsurfa.2016.04.016>

Schlierf, A., Yang, H., Gebremedhn, E., Treossi, E., Ortolani, L., Chen, L., Casiraghi, C. (2013). Nanoscale insight into the exfoliation mechanism of graphene with organic dyes: effect of charge, dipole and molecular structure. *Nanoscale*, 5(10), 4205-4216.

Schniepp, H. C., Li, J.-L., McAllister, M. J., Sai, H., Herrera-Alonso, M., Adamson, D. H., Aksay, I. A. (2006). Functionalized single graphene sheets derived from splitting graphite oxide. *The Journal of Physical Chemistry B*, 110(17), 8535-8539.

Sensale-Rodriguez, B., Fang, T., Yan, R., Kelly, M. M., Jena, D., Liu, L., & Xing, H. G. (2011). Unique prospects for graphene-based terahertz modulators. *Applied Physics Letters*, 99(11), 113104.

Seyed Shirazi, S. F., Gharekhani, S., Yarmand, H., Badarudin, A., Cornelis Metselaar, H. S., & Kazi, S. N. (2015). Nitrogen doped activated carbon/graphene with high nitrogen level: Green synthesis and thermo-electrical properties of its nanofluid. *Materials Letters*, 152, 192-195. doi:<http://dx.doi.org/10.1016/j.matlet.2015.03.110>

Shanbedi, M., Amiri, A., Rashidi, S., Heris, S. Z., & Baniadam, M. (2015). Thermal Performance Prediction of Two-Phase Closed Thermosyphon Using Adaptive Neuro-Fuzzy Inference System. *Heat Transfer Engineering*, 36(3), 315-324.

Shanbedi, M., Heris, S. Z., Amiri, A., Adyani, S., Alizadeh, M., & Baniadam, M. (2014). Optimization of the thermal efficiency of a two-phase closed thermosyphon using active learning on the human algorithm interaction. *Numerical Heat Transfer, Part A: Applications*, 66(8), 947-962.

Shanbedi, M., Heris, S. Z., Amiri, A., & Baniadam, M. (2014). Improvement in heat transfer of a two-phased closed thermosyphon using silver-decorated MWCNT/water. *Journal of Dispersion Science and Technology*, 35(8), 1086-1096.

Shanbedi, M., Heris, S. Z., Baniadam, M., Amiri, A., & Maghrebi, M. (2012). Investigation of heat-transfer characterization of EDA-MWCNT/DI-water nanofluid in a two-phase closed thermosyphon. *Industrial & Engineering Chemistry Research*, 51(3), 1423-1428.

Shanbedi, M., Jafari, D., Amiri, A., Heris, S. Z., & Baniadam, M. (2013). Prediction of temperature performance of a two-phase closed thermosyphon using Artificial Neural Network. *Heat and Mass Transfer*, 49(1), 65-73.

Shanbedi, M., Zeinali Heris, S., Baniadam, M., & Amiri, A. (2013). The effect of multi-walled carbon nanotube/water nanofluid on thermal performance of a two-phase closed thermosyphon. *Experimental Heat Transfer*, 26(1), 26-40.

Sharma, R., Baik, J. H., Perera, C. J., & Strano, M. S. (2010). Anomalously large reactivity of single graphene layers and edges toward electron transfer chemistries. *Nano letters*, 10(2), 398-405.

Sheikholeslami, M., Ganji, D. D., Javed, M. Y., & Ellahi, R. (2015). Effect of thermal radiation on magnetohydrodynamics nanofluid flow and heat transfer by means of two phase model. *Journal of Magnetism and Magnetic Materials*, 374, 36-43.

Shen, Y., & Lua, A. C. (2013). A facile method for the large-scale continuous synthesis of graphene sheets using a novel catalyst. *Scientific reports*, 3.

Shende, R., & Sundara, R. (2015). Nitrogen doped hybrid carbon based composite dispersed nanofluids as working fluid for low-temperature direct absorption solar collectors. *Solar Energy Materials and Solar Cells*, 140, 9-16.

Shih, C.-J., Lin, S., Sharma, R., Strano, M. S., & Blankshtein, D. (2011). Understanding the pH-dependent behavior of graphene oxide aqueous solutions: a comparative experimental and molecular dynamics simulation study. *Langmuir*, 28(1), 235-241.

Shih, T. M. (1984). Numerical heat transfer: *CRC Press*, 11, 250-290.

Shinde, D. B., Brenker, J., Easton, C. D., Tabor, R. F., Neild, A., & Majumder, M. (2016). Shear Assisted Electrochemical Exfoliation of Graphite to Graphene. *Langmuir*, 32(14), 3552-3559. doi:10.1021/acs.langmuir.5b04209

Shirazi, S. F. S., Gharekhani, S., Yarmand, H., Badarudin, A., Metselaar, H. S. C., & Kazi, S. N. (2015). Nitrogen doped activated carbon/graphene with high nitrogen

level: green synthesis and thermo-electrical properties of its nanofluid. *Materials Letters*, 152, 192-195.

Singh, M. S. (2004). *Advanced organic chemistry: reactions and mechanisms: Pearson Education India*, 9, 243.

Sinitskii, A., Dimiev, A., Corley, D. A., Fursina, A. A., Kosynkin, D. V., & Tour, J. M. (2010). Kinetics of diazonium functionalization of chemically converted graphene nanoribbons. *ACS nano*, 4(4), 1949-1954.

Skaltsas, T., Karousis, N., Yan, H.-J., Wang, C.-R., Pispas, S., & Tagmatarchis, N. (2012). Graphene exfoliation in organic solvents and switching solubility in aqueous media with the aid of amphiphilic block copolymers. *Journal of Materials Chemistry*, 22(40), 21507-21512.

Smith, R. J., Lotya, M., & Coleman, J. N. (2010). The importance of repulsive potential barriers for the dispersion of graphene using surfactants. *New Journal of Physics*, 12(12), 125008.

Solangi, K., Amiri, A., Luhur, M., Ghavimi, S. A. A., Zubir, M. N. M., Kazi, S., & Badarudin, A. (2016). Experimental investigation of the propylene glycol-treated graphene nanoplatelets for the enhancement of closed conduit turbulent convective heat transfer. *International communications in heat and mass transfer*, 73, 43-53.

Solangi, K., Kazi, S., Luhur, M., Badarudin, A., Amiri, A., Sadri, R., Teng, K. (2015). A comprehensive review of thermo-physical properties and convective heat transfer to nanofluids. *Energy*, 89, 1065-1086.

Stankovich, S., Dikin, D. A., Dommett, G. H., Kohlhaas, K. M., Zimney, E. J., Stach, E. A., Ruoff, R. S. (2006). Graphene-based composite materials. *Nature*, 442(7100), 282-286.

Stankovich, S., Dikin, D. A., Piner, R. D., Kohlhaas, K. A., Kleinhammes, A., Jia, Y., Ruoff, R. S. (2007). Synthesis of graphene-based nanosheets via chemical reduction of exfoliated graphite oxide. *Carbon*, 45(7), 1558-1565.

Stankovich, S., Piner, R. D., Chen, X., Wu, N., Nguyen, S. T., & Ruoff, R. S. (2006). Stable aqueous dispersions of graphitic nanoplatelets via the reduction of exfoliated graphite oxide in the presence of poly (sodium 4-styrenesulfonate). *Journal of Materials Chemistry*, 16(2), 155-158.

Stankovich, S., Piner, R. D., Nguyen, S. T., & Ruoff, R. S. (2006). Synthesis and exfoliation of isocyanate-treated graphene oxide nanoplatelets. *Carbon*, 44(15), 3342-3347.

Steven, B., Albert, J., & Kevin, P. (2011). Investigation of the electrical conductivity of propylene glycol-based ZnO nanofluids. *Nanosca. Res. Lett*, 6, 346-351.

Strom, T. A., Dillon, E. P., Hamilton, C. E., & Barron, A. R. (2010). Nitrene addition to exfoliated graphene: a one-step route to highly functionalized graphene. *Chemical Communications*, 46(23), 4097-4099.

Su, Q., Pang, S., Alijani, V., Li, C., Feng, X., & Müllen, K. (2009). Composites of graphene with large aromatic molecules. *Advanced Materials*, 21(31), 3191-3195.

- Sun, G., Li, X., Yan, H., Qiu, J., & Zhang, Y. (2008). Production of nanosized graphite powders from natural graphite by detonation. *Carbon*, 46(3), 476-481.
- Sun, Z., James, D. K., & Tour, J. M. (2011). Graphene chemistry: synthesis and manipulation. *The Journal of Physical Chemistry Letters*, 2(19), 2425-2432.
- Sun, Z., Kohama, S.-i., Zhang, Z., Lomeda, J. R., & Tour, J. M. (2010). Soluble graphene through edge-selective functionalization. *Nano Research*, 3(2), 117-125.
- Sun, Z., Nicolosi, V., Rickard, D., Bergin, S. D., Aherne, D., & Coleman, J. N. (2008). Quantitative evaluation of surfactant-stabilized single-walled carbon nanotubes: dispersion quality and its correlation with zeta potential. *The Journal of Physical Chemistry C*, 112(29), 10692-10699.
- Sun, Z., Pöller, S., Huang, X., Guschin, D., Taetz, C., Ebbinghaus, P., Schuhmann, W. (2013). High-yield exfoliation of graphite in acrylate polymers: A stable few-layer graphene nanofluid with enhanced thermal conductivity. *Carbon*, 64, 288-294.
- Sundar, L. S., Singh, M. K., & Sousa, A. C. (2014). Enhanced heat transfer and friction factor of MWCNT-Fe₃O₄/water hybrid nanofluids. *International Communications in Heat and Mass Transfer*, 52, 73-83.
- Sutter, P. W., Flege, J.-I., & Sutter, E. A. (2008). Epitaxial graphene on ruthenium. *Nature materials*, 7(5), 406-411.
- Tian, R., Wang, X., Li, M., Hu, H., Chen, R., Liu, F., Wan, L. (2008). An efficient route to functionalize single-walled carbon nanotubes using alcohols. *Applied Surface Science*, 255(5), 3294-3299.
- Tong, Y., Kim, J., & Cho, H. (2015). Effects of thermal performance of enclosed-type evacuated U-tube solar collector with multi-walled carbon nanotube/water nanofluid. *Renewable Energy*, 83, 463-473.
doi:<http://dx.doi.org/10.1016/j.renene.2015.04.042>
- Tran, T. S., Park, S. J., Yoo, S. S., Lee, T.-R., & Kim, T. (2016). High shear-induced exfoliation of graphite into high quality graphene by Taylor-Couette flow. *Rsc Advances*, 6(15), 12003-12008. doi:10.1039/C5RA22273G
- Tu, W., Lei, J., Zhang, S., & Ju, H. (2010). Characterization, Direct Electrochemistry, and Amperometric Biosensing of Graphene by Noncovalent Functionalization with Picket-Fence Porphyrin. *Chemistry—A European Journal*, 16(35), 10771-10777.
- Vadasz, P. (2006). Heat conduction in nanofluid suspensions. *Journal of Heat Transfer*, 128(5), 465-477.
- Vadukumpully, S., Gupta, J., Zhang, Y., Xu, G. Q., & Valiyaveetil, S. (2011). Functionalization of surfactant wrapped graphene nanosheets with alkylazides for enhanced dispersibility. *Nanoscale*, 3(1), 303-308.
- Vadukumpully, S., Paul, J., & Valiyaveetil, S. (2009). Cationic surfactant mediated exfoliation of graphite into graphene flakes. *Carbon*, 47(14), 3288-3294.

Vandsberger, L. (2009). Synthesis and Covalent Surface Modification of Carbon Nanotubes for Preparation of Stabilized Nanofluid Suspensions. *McGill University*, 6, 2002.

Vázquez, E., & Prato, M. (2009). Carbon nanotubes and microwaves: interactions, responses, and applications. *ACS nano*, 3(12), 3819-3824.

Vradis, G. C., & Vannostrand, L. (1992). Laminar coupled flow downstream of an asymmetric sudden expansion. *Journal of thermophysics and heat transfer*, 6(2), 288-295.

Vradis, G. C., Volkan Otugen, M., & Sanchez, J. G. (1993). Heat Transfer Over a Backward-Facing Step: Solutions to a Benchmark Problem. *ASME-Publications-HTD*, 222, 27-27.

Wang, G., Wang, B., Park, J., Wang, Y., Sun, B., & Yao, J. (2009). Highly efficient and large-scale synthesis of graphene by electrolytic exfoliation. *Carbon*, 47(14), 3242-3246.

Wang, G., Yang, J., Park, J., Gou, X., Wang, B., Liu, H., & Yao, J. (2008). Facile synthesis and characterization of graphene nanosheets. *The Journal of Physical Chemistry C*, 112(22), 8192-8195.

Wang, H., Robinson, J. T., Li, X., & Dai, H. (2009). Solvothermal reduction of chemically exfoliated graphene sheets. *Journal of the American Chemical Society*, 131(29), 9910-9911.

Wang, J., Manga, K. K., Bao, Q., & Loh, K. P. (2011). High-yield synthesis of few-layer graphene flakes through electrochemical expansion of graphite in propylene carbonate electrolyte. *Journal of the American Chemical Society*, 133(23), 8888-8891.

Wang, X., Fulvio, P. F., Baker, G. A., Veith, G. M., Unocic, R. R., Mahurin, S. M., Dai, S. (2010). Direct exfoliation of natural graphite into micrometre size few layers graphene sheets using ionic liquids. *Chemical Communications*, 46(25), 4487-4489.

Wang, X., Xu, X., & S. Choi, S. U. (1999). Thermal conductivity of nanoparticle-fluid mixture. *Journal of thermophysics and heat transfer*, 13(4), 474-480.

Wang, X. J., Li, X. F., Xu, Y. H., & Zhu, D. S. (2014). Thermal energy storage characteristics of Cu-H₂O nanofluids. *Energy*, 78(0), 212-217.
doi:<http://dx.doi.org/10.1016/j.energy.2014.10.005>

Wang, Y., Chen, X., Zhong, Y., Zhu, F., & Loh, K. P. (2009). Large area, continuous, few-layered graphene as anodes in organic photovoltaic devices. *Applied Physics Letters*, 95(6), 063302.

Wang, Y., Iqbal, Z., & Mitra, S. (2006). Rapidly functionalized, water-dispersed carbon nanotubes at high concentration. *Journal of the American Chemical Society*, 128(1), 95-99.

Wang, Y., Shi, Z., & Yin, J. (2011). Facile synthesis of soluble graphene via a green reduction of graphene oxide in tea solution and its biocomposites. *ACS applied materials & interfaces*, 3(4), 1127-1133.

Wang, Y., Zheng, Y., Xu, X., Dubuisson, E., Bao, Q., Lu, J., & Loh, K. P. (2011). Electrochemical delamination of CVD-grown graphene film: toward the recyclable use of copper catalyst. *ACS nano*, 5(12), 9927-9933.

Wang, Z., Dong, Y., Li, H., Zhao, Z., Wu, H. B., Hao, C., Lou, X. W. D. (2014). Enhancing lithium-sulphur battery performance by strongly binding the discharge products on amino-functionalized reduced graphene oxide. *Nature communications*, 5, 5002.

Watcharotone, S., Dikin, D. A., Stankovich, S., Piner, R., Jung, I., Dommett, G. H., Liu, C.-P. (2007). Graphene-silica composite thin films as transparent conductors. *Nano letters*, 7(7), 1888-1892.

Wei, D., Li, H., Han, D., Zhang, Q., Niu, L., Yang, H., Ryhänen, T. (2011). Properties of graphene inks stabilized by different functional groups. *Nanotechnology*, 22(24), 245702.

Wen, D., & Ding, Y. (2005). Effect of particle migration on heat transfer in suspensions of nanoparticles flowing through minichannels. *Microfluidics and Nanofluidics*, 1(2), 183-189.

Wen, Z., Wang, X., Mao, S., Bo, Z., Kim, H., Cui, S., Chen, J. (2012). Crumpled Nitrogen-Doped Graphene Nanosheets with Ultrahigh Pore Volume for High-Performance Supercapacitor. *Advanced Materials*, 24(41), 5610-5616.

White, B., Banerjee, S., O'Brien, S., Turro, N. J., & Herman, I. P. (2007). Zeta-potential measurements of surfactant-wrapped individual single-walled carbon nanotubes. *The Journal of Physical Chemistry C*, 111(37), 13684-13690.

Wu, Z.-S., Ren, W., Gao, L., Liu, B., Jiang, C., & Cheng, H.-M. (2009). Synthesis of high-quality graphene with a pre-determined number of layers. *Carbon*, 47(2), 493-499.

Wu, Z.-S., Ren, W., Gao, L., Zhao, J., Chen, Z., Liu, B., Cheng, H.-M. (2009). Synthesis of graphene sheets with high electrical conductivity and good thermal stability by hydrogen arc discharge exfoliation. *ACS nano*, 3(2), 411-417.

Wu, Z. S., Liu, Z., Parvez, K., Feng, X., & Müllen, K. (2015). Ultrathin Printable Graphene Supercapacitors with AC Line-Filtering Performance. *Advanced Materials*, 27(24), 3669-3675.

Xie, Y., Huang, Q., Liu, M., Wang, K., Wan, Q., Deng, F., Wei, Y. (2015). Mussel inspired functionalization of carbon nanotubes for heavy metal ion removal. *RSC Advances*, 5(84), 68430-68438. doi:10.1039/C5RA08908E

Xu, L., McGraw, J.-W., Gao, F., Grundy, M., Ye, Z., Gu, Z., & Shepherd, J. L. (2013). Production of high-concentration graphene dispersions in low-boiling-point organic solvents by liquid-phase noncovalent exfoliation of graphite with a hyperbranched polyethylene and formation of graphene/ethylene copolymer composites. *The Journal of Physical Chemistry C*, 117(20), 10730-10742.

Xu, Y., Bai, H., Lu, G., Li, C., & Shi, G. (2008). Flexible graphene films via the filtration of water-soluble noncovalent functionalized graphene sheets. *Journal of the American Chemical Society*, 130(18), 5856-5857.

- Xuan, Y., & Li, Q. (2000). Heat transfer enhancement of nanofluids. *International Journal of heat and fluid flow*, 21(1), 58-64.
- Xuan, Y., & Li, Q. (2003). Investigation on convective heat transfer and flow features of nanofluids. *Journal of Heat transfer*, 125(1), 151-155.
- Xue, L., Keblinski, P., Phillpot, S., Choi, S., & Eastman, J. (2004). Effect of liquid layering at the liquid–solid interface on thermal transport. *International Journal of Heat and Mass Transfer*, 47(19), 4277-4284.
- Yang, H., Hernandez, Y., Schlierf, A., Felten, A., Eckmann, A., Johal, S., Mullen, K. (2013). A simple method for graphene production based on exfoliation of graphite in water using 1-pyrenesulfonic acid sodium salt. *Carbon*, 53, 357-365.
- Yang, H., Zhang, Q., Shan, C., Li, F., Han, D., & Niu, L. (2010). Stable, conductive supramolecular composite of graphene sheets with conjugated polyelectrolyte. *Langmuir*, 26(9), 6708-6712.
- Yang, Q., Pan, X., Huang, F., & Li, K. (2010). Fabrication of high-concentration and stable aqueous suspensions of graphene nanosheets by noncovalent functionalization with lignin and cellulose derivatives. *The Journal of Physical Chemistry C*, 114(9), 3811-3816.
- Yang, Y., Lu, F., Zhou, Z., Song, W., Chen, Q., & Ji, X. (2013). Electrochemically cathodic exfoliation of graphene sheets in room temperature ionic liquids N-butyl, methylpyrrolidinium bis (trifluoromethylsulfonyl) imide and their electrochemical properties. *Electrochimica Acta*, 113, 9-16.
- Yang, Y., Oztekin, A., Neti, S., & Mohapatra, S. (2011). Characterization and convective heat transfer with nanofluids. *Thermal Engineering Joint Conference*, 2, 202-207.
- Yarmand, H., Gharehkhani, S., Ahmadi, G., Shirazi, S. F. S., Baradaran, S., Montazer, E., Dahari, M. (2015). Graphene nanoplatelets–silver hybrid nanofluids for enhanced heat transfer. *Energy Conversion and Management*, 100, 419-428. doi:<http://dx.doi.org/10.1016/j.enconman.2015.05.023>
- Yarmand, H., Gharehkhani, S., Shirazi, S. F. S., Amiri, A., Montazer, E., Arzani, H. K., Kazi, S. (2016). Nanofluid based on activated hybrid of biomass carbon/graphene oxide: Synthesis, thermo-physical and electrical properties. *International communications in heat and mass transfer*, 72, 10-15.
- Yeh, C.-N., Raidongia, K., Shao, J., Yang, Q.-H., & Huang, J. (2015). On the origin of the stability of graphene oxide membranes in water. *Nature chemistry*, 7(2), 166-170.
- You, S., Kim, J., & Kim, K. (2003). Effect of nanoparticles on critical heat flux of water in pool boiling heat transfer. *Applied Physics Letters*, 83(16), 3374-3376.
- Yu, W., & Choi, S. (2003). The role of interfacial layers in the enhanced thermal conductivity of nanofluids: a renovated Maxwell model. *Journal of Nanoparticle Research*, 5(1-2), 167-171.

Yu, W., & Choi, S. (2004). The role of interfacial layers in the enhanced thermal conductivity of nanofluids: a renovated Hamilton–Crosser model. *Journal of Nanoparticle Research*, 6(4), 355-361.

Yu, W., France, D., Timofeeva, E., Singh, D., & Routbort, J. (2010). Thermophysical property-related comparison criteria for nanofluid heat transfer enhancement in turbulent flow. *Applied physics letters*, 96(21), 213109.

Yu, W., France, D. M., Smith, D. S., Singh, D., Timofeeva, E. V., & Routbort, J. L. (2009a). Heat transfer to a silicon carbide/water nanofluid. *International Journal of Heat and Mass Transfer*, 52(15), 3606-3612.

Yu, W., France, D. M., Smith, D. S., Singh, D., Timofeeva, E. V., & Routbort, J. L. (2009b). Heat transfer to a silicon carbide/water nanofluid. *International Journal of Heat and Mass Transfer*, 52(15–16), 3606-3612.
doi:<http://dx.doi.org/10.1016/j.ijheatmasstransfer.2009.02.036>

Yu, W., France, D. M., Timofeeva, E. V., Singh, D., & Routbort, J. L. (2012). Comparative review of turbulent heat transfer of nanofluids. *International Journal of Heat and Mass Transfer*, 55(21–22), 5380-5396.
doi:<http://dx.doi.org/10.1016/j.ijheatmasstransfer.2012.06.034>

Yu, W., Timofeeva, E. V., Singh, D., France, D. M., & Smith, R. K. (2013). Investigations of heat transfer of copper-in-Therminol 59 nanofluids. *International Journal of Heat and Mass Transfer*, 64, 1196-1204.

Yu, W., Xie, H., Chen, L., Li, Y., & Li, D. (2010). The Preparation and Thermal Conductivities Enhancement of Nanofluids Containing Graphene Oxide Nanosheets. *Paper presented at the 2010 14th International Heat Transfer Conference*, 7, 2423.

Yu, W., Xie, H., Wang, X., & Wang, X. (2011). Significant thermal conductivity enhancement for nanofluids containing graphene nanosheets. *Physics Letters A*, 375(10), 1323-1328.

Zakaria, I., Azmi, W., Mohamed, W., Mamat, R., & Najafi, G. (2015). Experimental Investigation of Thermal Conductivity and Electrical Conductivity of Al₂O₃ Nanofluid in Water-Ethylene Glycol Mixture for Proton Exchange Membrane Fuel Cell Application. *International communications in heat and mass transfer*, 61, 61-68.

Zardini, H. Z., Amiri, A., Shanbedi, M., Maghrebi, M., & Baniadam, M. (2012). Enhanced antibacterial activity of amino acids-functionalized multi walled carbon nanotubes by a simple method. *Colloids and Surfaces B: Biointerfaces*, 92, 196-202.

Zardini, H. Z., Davarpanah, M., Shanbedi, M., Amiri, A., Maghrebi, M., & Ebrahimi, L. (2014). Microbial toxicity of ethanolamines—Multiwalled carbon nanotubes. *Journal of Biomedical Materials Research Part A*, 102(6), 1774-1781.

Zare-Zardini, H., Amiri, A., Shanbedi, M., Taheri-Kafrani, A., Kazi, S., Chew, B., & Razmjou, A. (2015a). In vitro and in vivo study of hazardous effects of Ag nanoparticles and Arginine-treated multi walled carbon nanotubes on blood cells: Application in hemodialysis membranes. *Journal of Biomedical Materials Research Part A*, 103(9), 2959-2965.

Zare-Zardini, H., Amiri, A., Shanbedi, M., Taheri-Kafrani, A., Kazi, S., Chew, B. T., & Razmjou, A. (2015b). In vitro and in vivo study of hazardous effects of Ag nanoparticles and Arginine-treated multi walled carbon nanotubes on blood cells: Application in hemodialysis membranes. *Journal of Biomedical Materials Research Part A*, *103*, 2959–2965.

Zeinali Heris, S., Etemad, S. G., & Nasr Esfahany, M. (2006). Experimental investigation of oxide nanofluids laminar flow convective heat transfer. *International Communications in Heat and Mass Transfer*, *33*(4), 529-535.
doi:<http://dx.doi.org/10.1016/j.icheatmasstransfer.2006.01.005>

Zeng, F., Sun, Z., Sang, X., Diamond, D., Lau, K. T., Liu, X., & Su, D. S. (2011). In situ one-step electrochemical preparation of graphene oxide nanosheet-modified electrodes for biosensors. *ChemSusChem*, *4*(11), 1587-1591.

Zeng, Z., Yin, Z., Huang, X., Li, H., He, Q., Lu, G., Zhang, H. (2011). Single-Layer Semiconducting Nanosheets: High-yield preparation and device fabrication. *Angewandte Chemie International Edition*, *50*(47), 11093-11097.

Zhang, H.B., Wang, J.-W., Yan, Q., Zheng, W.-G., Chen, C., & Yu, Z.-Z. (2011). Vacuum-assisted synthesis of graphene from thermal exfoliation and reduction of graphite oxide. *Journal of Materials Chemistry*, *21*(14), 5392-5397.

Zhang, M., Parajuli, R. R., Mastrogiovanni, D., Dai, B., Lo, P., Cheung, W., Liu, Z. (2010). Production of graphene sheets by direct dispersion with aromatic healing agents. *Small*, *6*(10), 1100-1107.

Zhang, Q., Li, W., Kong, T., Su, R., Li, N., Song, Q., Cheng, G. (2013). Tailoring the interlayer interaction between doxorubicin-loaded graphene oxide nanosheets by controlling the drug content. *Carbon*, *51*, 164-172.

Zhang, S., Tang, S., Lei, J., Dong, H., & Ju, H. (2011). Functionalization of graphene nanoribbons with porphyrin for electrocatalysis and amperometric biosensing. *Journal of Electroanalytical Chemistry*, *656*(1), 285-288.

Zhang, X., Coleman, A. C., Katsonis, N., Browne, W. R., Van Wees, B. J., & Feringa, B. L. (2010). Dispersion of graphene in ethanol using a simple solvent exchange method. *Chemical Communications*, *46*(40), 7539-7541.

Zhang, X., Hou, L., Cnossen, A., Coleman, A. C., Ivashenko, O., Rudolf, P., Feringa, B. L. (2011). One-Pot Functionalization of Graphene with Porphyrin through Cycloaddition Reactions. *Chemistry—A European Journal*, *17*(32), 8957-8964.

Zhang, Y., Tan, Y.-W., Stormer, H. L., & Kim, P. (2005). Experimental observation of the quantum Hall effect and Berry's phase in graphene. *Nature*, *438*(7065), 201-204.

Zheng, R., Gao, J., Wang, J., Feng, S.-P., Ohtani, H., Wang, J., & Chen, G. (2011). Thermal percolation in stable graphite suspensions. *Nano letters*, *12*(1), 188-192.

Zhong, X., Jin, J., Li, S., Niu, Z., Hu, W., Li, R., & Ma, J. (2010). Aryne cycloaddition: highly efficient chemical modification of graphene. *Chemical Communications*, *46*(39), 7340-7342.

Zhou, M., Tang, J., Cheng, Q., Xu, G., Cui, P., & Qin, L.-C. (2013). Few-layer graphene obtained by electrochemical exfoliation of graphite cathode. *Chemical Physics Letters*, 572, 61-65.

Zhou, S., Siegel, D., Fedorov, A., El Gabaly, F., Schmid, A., Neto, A. C., Lanzara, A. (2008). Origin of the energy bandgap in epitaxial graphene. *Nature materials*, 7(4), 259-260.

Zhou, X., Wu, T., Ding, K., Hu, B., Hou, M., & Han, B. (2010). Dispersion of graphene sheets in ionic liquid [bmim][PF6] stabilized by an ionic liquid polymer. *Chemical Communications*, 46(3), 386-388.

Zhu, Y., Murali, S., Cai, W., Li, X., Suk, J. W., Potts, J. R., & Ruoff, R. S. (2010). Graphene and graphene oxide: synthesis, properties, and applications. *Advanced Materials*, 22(35), 3906-3924.

Zhu, Y., Murali, S., Stoller, M. D., Ganesh, K., Cai, W., Ferreira, P. J., Thommes, M. (2011). Carbon-based supercapacitors produced by activation of graphene. *science*, 332(6037), 1537-1541.

Zhu, Y., Murali, S., Stoller, M. D., Velamakanni, A., Piner, R. D., & Ruoff, R. S. (2010). Microwave assisted exfoliation and reduction of graphite oxide for ultracapacitors. *Carbon*, 48(7), 2118-2122.

Zhu, Y., Stoller, M. D., Cai, W., Velamakanni, A., Piner, R. D., Chen, D., & Ruoff, R. S. (2010). Exfoliation of graphite oxide in propylene carbonate and thermal reduction of the resulting graphene oxide platelets. *ACS nano*, 4(2), 1227-1233.

Zu, S. Z., & Han, B.-H. (2009). Aqueous dispersion of graphene sheets stabilized by pluronic copolymers: formation of supramolecular hydrogel. *The Journal of Physical Chemistry C*, 113(31), 13651-13657.

Zubir, M. N. M., Badarudin, A., Kazi, S., Huang, N. M., Misran, M., Sadeghinezhad, E., Gharekhani, S. (2015). Experimental investigation on the use of reduced graphene oxide and its hybrid complexes in improving closed conduit turbulent forced convective heat transfer. *Experimental Thermal and Fluid Science*, 66, 290-303.

Zubir, M. N. M., Badarudin, A., Kazi, S., Huang, N. M., Misran, M., Sadeghinezhad, E., Yusoff, N. (2015). Highly dispersed reduced graphene oxide and its hybrid complexes as effective additives for improving thermophysical property of heat transfer fluid. *International Journal of Heat and Mass Transfer*, 87, 284-294.

Zubir, M. N. M., Badarudin, A., Kazi, S., Misran, M., Amiri, A., Sadri, R., & Khalid, S. (2015). Experimental investigation on the use of highly charged nanoparticles to improve the stability of weakly charged colloidal system. *Journal of colloid and interface science*, 454, 245-255.

LIST OF PUBLICATIONS AND AWARDS

- [1] A. Amiri, M. Shanbedi, B. Chew, S. Kazi, K. Solangi, Toward improved engine performance with crumpled nitrogen-doped graphene based water–ethylene glycol coolant, *Chemical Engineering Journal*, 289 (2016) 583-595.
- [2] A. Amiri, M. Shanbedi, H. Yarmand, H.K. Arzani, S. Gharehkhani, E. Montazer, R. Sadri, W. Sarsam, B. Chew, S. Kazi, Laminar convective heat transfer of hexylamine-treated MWCNTs-based turbine oil nanofluid, *Energy Conversion and Management*, 105 (2015) 355-367.
- [3] A. Amiri, M. Shanbedi, A.R. Rafieerad, M. M. Rashidi, Tuan Zaharinie, M. N. Mohd Zubir, S.N. Kazi, B.T. Chew, Functionalization and exfoliation of graphite into mono layer graphene for improved heat dissipation, *Journal of the Taiwan Institute of Chemical Engineers*, (2017), Doi: <http://dx.doi.org/10.1016/j.jtice.2016.12.009>
- [4] A. Amiri, G. Ahmadi, M. Shanbedi, M. Etemadi, M.N.M. Zubir, B. Chew, S. Kazi, Heat transfer enhancement of water-based highly crumpled few-layer graphene nanofluids, *RSC Advances*, 6 (2016) 105508-105527.
- [5] A. Amiri, M. Shanbedi, H. Amiri, S.Z. Heris, S. Kazi, B. Chew, H. Eshghi, Pool boiling heat transfer of CNT/water nanofluids, *Applied Thermal Engineering*, 71 (2014) 450-459.
- [6] A. Amiri, H.K. Arzani, S. Kazi, B. Chew, A. Badarudin, Backward-facing step heat transfer of the turbulent regime for functionalized graphene nanoplatelets based water–ethylene glycol nanofluids, *International Journal of Heat and Mass Transfer*, 97 (2016) 538-546.
- [7] A. Amiri, M. Shanbedi, G. Ahmadi, H. Eshghi, S. Kazi, B. Chew, M. Savari, M.N.M. Zubir, Mass production of highly-porous graphene for high-performance supercapacitors, *Scientific Reports-Nature*, 6 (2016), 32686.
- [8] A. Amiri, G. Ahmadi, M. Shanbedi, M. Savari, S. Kazi, B. Chew, Microwave-assisted synthesis of highly-crumpled, few-layered graphene and nitrogen-doped graphene for use as high-performance electrodes in capacitive deionization, *Scientific Reports-Nature*, 5 (2015), 17503.
- [9] A. Amiri, R. Sadri, M. Shanbedi, G. Ahmadi, B. Chew, S. Kazi, M. Dahari, Performance dependence of thermosyphon on the functionalization approaches: an experimental study on thermo-physical properties of graphene nanoplatelet-based water nanofluids, *Energy Conversion and Management*, 92 (2015) 322-330.
- [10] A. Amiri, R. Sadri, M. Shanbedi, G. Ahmadi, S. Kazi, B. Chew, M.N.M. Zubir, Synthesis of ethylene glycol-treated graphene nanoplatelets with one-pot, microwave-assisted functionalization for use as a high performance engine coolant, *Energy Conversion and Management*, 101 (2015) 767-777.
- [11] A. Amiri, S. Kazi, M. Shanbedi, M.N.M. Zubir, H. Yarmand, B. Chew, Transformer oil based multi-walled carbon nanotube–hexylamine coolant with optimized electrical, thermal and rheological enhancements, *RSC Advances*, 5 (2015) 107222-107236.

[12] A. Amiri, R. Sadri, G. Ahmadi, B. Chew, S. Kazi, M. Shanbedi, M.S. Alehashem, Synthesis of polyethylene glycol-functionalized multi-walled carbon nanotubes with a microwave-assisted approach for improved heat dissipation, *RSC Advances*, 5 (2015) 35425-35434.

[13] A. Amiri, M. Shanbedi, G. Ahmadi, H. Eshghi, B. Chew, S. Kazi, Microwave-assisted direct coupling of graphene nanoplatelets with poly ethylene glycol and 4-phenylazophenol molecules for preparing stable-colloidal system, *Colloids and Surfaces A: Physicochemical and Engineering Aspects*, 487 (2015) 131-141.

[14] A. Amiri, M. Shanbedi, M. Savari, B. Chew, S. Kazi, Cadmium ion sorption from aqueous solutions by high surface area ethylenediaminetetraacetic acid-and diethylene triamine pentaacetic acid-treated carbon nanotubes, *RSC Advances*, 5 (2015) 71144-71152.

Collaborative article

[1] H.K. Arzani, A. Amiri, H.K. Arzani, S.B. Rozali, S. Kazi, A. Badarudin, Toward improved heat transfer performance of annular heat exchangers with water/ethylene glycol-based nanofluids containing graphene nanoplatelets, *Journal of Thermal Analysis and Calorimetry*, 126 (2016) 1427-1436.

[2] H.K. Arzani, A. Amiri, S. Kazi, A. Badarudin, B. Chew, Heat transfer performance of water-based tetrahydrofurfuryl polyethylene glycol-treated graphene nanoplatelet nanofluids, *RSC Advances*, 6 (2016) 65654-65669.

[3] H.K. Arzani, A. Amiri, S. Kazi, B. Chew, A. Badarudin, Experimental and numerical investigation of thermophysical properties, heat transfer and pressure drop of covalent and noncovalent functionalized graphene nanoplatelet-based water nanofluids in an annular heat exchanger, *International communications in heat and mass transfer*, 68 (2015) 267-275.

[4] H.K. Arzani, A. Amiri, S. Kazi, B. Chew, A. Badarudin, Experimental investigation of thermophysical properties and heat transfer rate of covalently functionalized MWCNT in an annular heat exchanger, *International communications in heat and mass transfer*, 75 (2016) 67-77.

[5] W.S. Sarsam, A. Amiri, S. Kazi, A. Badarudin, Stability and thermophysical properties of non-covalently functionalized graphene nanoplatelets nanofluids, *Energy Conversion and Management*, 116 (2016) 101-111.

[6] W.S. Sarsam, A. Amiri, M.N.M. Zubir, H. Yarmand, S. Kazi, A. Badarudin, Stability and thermophysical properties of water-based nanofluids containing triethanolamine-treated graphene nanoplatelets with different specific surface areas, *Colloids and Surfaces A: Physicochemical and Engineering Aspects*, 500 (2016) 17-31.

[7] M. Savari, S. Rashidi, A. Amiri, M. Shanbedi, S. Zeinali Heris, S. Kazi, Hydrodynamic and thermal performance prediction of functionalized MWNT-based water nanofluids under the laminar flow regime using the adaptive neuro-fuzzy inference system, *Numerical Heat Transfer, Part A: Applications*, (2016) 1-14.

[8] M. Shanbedi, S.Z. Heris, A. Amiri, E. Hosseinipour, H. Eshghi, S. Kazi, Synthesis of aspartic acid-treated multi-walled carbon nanotubes based water coolant and experimental investigation of thermal and hydrodynamic properties in circular tube, *Energy Conversion and Management*, 105 (2015) 1366-1376.

[9] K. Solangi, A. Amiri, M. Luhur, S.A.A. Ghavimi, S. Kazi, A. Badarudin, M.N.M. Zubir, Experimental investigation of heat transfer performance and frictional loss of functionalized GNP-based water coolant in a closed conduit flow, *RSC Advances*, 6 (2016) 4552-4563.

[10] K. Solangi, A. Amiri, M. Luhur, S.A.A. Ghavimi, M.N.M. Zubir, S. Kazi, A. Badarudin, Experimental investigation of the propylene glycol-treated graphene nanoplatelets for the enhancement of closed conduit turbulent convective heat transfer, *International communications in heat and mass transfer*, 73 (2016) 43-53.

[11] K. Solangi, S. Kazi, M. Luhur, A. Badarudin, A. Amiri, R. Sadri, M. Zubir, S. Gharehkhani, K. Teng, A comprehensive review of thermo-physical properties and convective heat transfer to nanofluids, *Energy*, 89 (2015) 1065-1086.

[12] K. Teng, A. Amiri, S. Kazi, M. Bakar, B. Chew, Fouling mitigation on heat exchanger surfaces by EDTA-treated MWCNT-based water nanofluids, *Journal of the Taiwan Institute of Chemical Engineers*, 60 (2016) 445-452.

[13] K. Teng, A. Amiri, S. Kazi, M. Bakar, B. Chew, A. Al-Shamma'a, A. Shaw, Retardation of heat exchanger surfaces mineral fouling by water-based diethylenetriamine pentaacetate-treated CNT nanofluids, *Applied Thermal Engineering*, 110 (2017) 495-503.

[14] H. Zare-Zardini, A. Amiri, M. Shanbedi, A. Taheri-Kafrani, S. Kazi, B. Chew, A. Razmjou, In vitro and in vivo study of hazardous effects of Ag nanoparticles and Arginine-treated multi walled carbon nanotubes on blood cells: Application in hemodialysis membranes, *Journal of Biomedical Materials Research Part A*, 103 (2015) 2959-2965.

[15] M.N.M. Zubir, A. Badarudin, S.N. Kazi, M. Misran, R. Ibrahim, A. Amiri, R. Sadri, Exploration of the environmentally benign and highly effective approach for improving carbon nanotube homogeneity in aqueous system, *Journal of Thermal Analysis and Calorimetry*, 124 (2016) 815-825.

[16] A. Amiri, H.K. Arzani, S. Kazi, B. Chew, Numerical Heat Transfer Performance of Water-Based Graphene Nanoplatelets, *Numerical Heat Transfer*, 3 (2016) 54948.

Book Chapters

[1] Ahmad Amiri, Hadi Zare-Zardini, Mehdi Shanbedi, Salim Newaz Kazi, Asghar Taheri-Kafrani, Bee Teng Chew and Ali Zarrabi, Microbial toxicity of different functional groups-treated carbon nanotubes, chapter 2, *Surface Chemistry of Nanobiomaterials Applications of Nanobiomaterials*, vol. 3, Elsevier, ISBN: 978-0-323-42861-3, 2016.

[2] Mehdi Shanbedi, Ahmad Amiri, Saeed Zeinali Heris, Salim Newaz Kazi, and Chew Bee Teng, Nanofluids: Basic Principles and Modern Aspects, chapter 57, Encyclopedia of Nanotechnology, CRC Press, Taylor & Francis, 2016.

Conference

[1] Ahmad Amiri, Hamed K Arzani, SN Kazi, BT Chew, Numerical Heat Transfer Performance of Water-Based Graphene Nanoplatelets, World Academy of Science, Engineering and Technology International Journal of Chemical, Molecular, Nuclear, Materials and Metallurgical Engineering 2016, 10, 10-16.

[2] Ahmad Amiri, Chew Bee Teng, S. N. Kazi, Mass production of few-layer graphene, Putrajaya International Built Environment, Technology and Engineering Conference, PIBEC 2016, 1, 58-62.

[3] BT Chew, SN Kazi, A Amiri, Adaptive Thermal Comfort Model for Air-Conditioned Lecture Halls in Malaysia, World Academy of Science, Engineering and Technology, International Journal of Civil, Environmental, Structural, Construction and Architectural Engineering, 2015, 9, 150-157.

University of Malaya